THE UNIVERSITY OF SHEFFIELD

Department of Mechanical Engineering

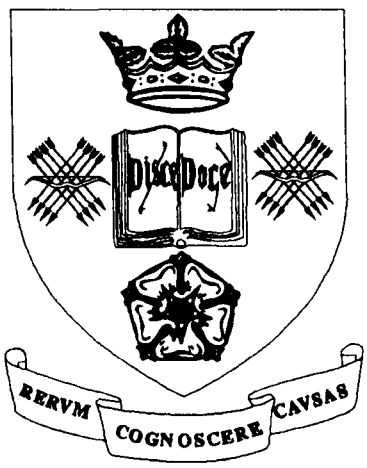

THE DYNAMICS OF TENNIS BALL IMPACTS ON TENNIS RACKETS

Simon Richard Goodwill

Submitted for the Degree

of

Doctor of Philosophy

July 2002

DAMAGED TEXT IN ORIGINAL

THE UNIVERSITY OF SHEFFIELD

Department of Mechanical Engineering

The dynamics of tennis ball impacts on tennis rackets

Simon Richard Goodwill

Submitted for the Degree of Doctor of Philosophy

July 2002

A model of a tennis ball impact on a tennis racket has been developed in this study. An experimental investigation was conducted to determine the dynamic properties of several different tennis balls. The balls were propelled at a piezoelectric force platform and the force acting on the ball was sampled, along with the ball rebound velocity. A visco-elastic model of this impact was developed and a set of model parameters were determined empirically for each ball type. The values of these parameters were independent of the ball impact velocity.

The next stage of the study involved an experimental investigation of a ball impact on a head clamped tennis racket. In this experiment, tennis balls were propelled at the geometric string centre of a tennis racket. High speed cinematography was used to determine the ball and stringbed deformation during impact, and speed gates were used to measure the ball rebound velocity. A visco-elastic model of this impact was developed. The ball component of this model was identical to that for a model of a ball impact on a rigid force platform. The model parameter for the stringbed component was obtained from a simple quasi-static compression of the stringbed in which the applied force and resulting deformation were measured.

The final stage of this study involved an investigation of the impact between a tennis ball and a freely supported tennis racket (this support method has been shown to be equivalent to a player gripping the tennis racket). In these experiments, the ball, stringbed and racket deformation were measured *during* impact, along with the velocity of the ball and racket *after* impact. A model was developed to simulate this impact in which it was assumed that the racket acted as a one-dimensional flexible beam.

The models which have been developed in this study are advancements of those which have been used in previously published literature. Experimental data was used to assess the accuracy of the results which were calculated by the models. An excellent correlation was found between the data calculated by the model and that measured experimentally.

A model of the impact between a ball and a tennis racket has been developed, as mentioned above. This model was incorporated into a PC software package (*Racket Impact v1.1*) that has been written in this study. This software allows the user to predict the rebound velocity of the ball for an impact between a tennis ball and racket. The user has the ability to control many parameters related to the impact including, (1) impact location on the racket, (2) ball/racket type and (3) type of shot. This software will be a useful tool for both the manufacturers of tennis equipment and the governing body of tennis.

Keywords: tennis ball, tennis racket, high speed cinematography, visco-elastic modelling.

Acknowledgements

I would like to thank Dr Steve Haake, who has been a continual source of advice, support and guidance throughout this entire study.

I would also like to thank Nicola Bellenger, Janet Page, Paul Rose and all the other members of the Technical Centre at the International Tennis Federation for providing support and funding for this work.

I am very grateful to Terry Senior and the rest of the technician staff at the University of Sheffield for their assistance in the design and building of the experimental apparatus used in this study.

I would like to make a special mention to Dr Matt Carré, David James, Nick Hamilton, Owain Pedgley and all the past and present members of the Sports Engineering Research Group at the University of Sheffield who have made significant contributions to this study through many valuable informal discussions.

Finally, I would like to thank Helen Cope for her constant support, patience and encouragement which has enabled me to complete this study.

Contents

Nomenclature

A_C	Dashpot damper constant (ball).
$ACOR$	Apparent coefficient of restitution.
A_K	Spring stiffness constant (ball).
B_R	Balance point of racket.
c_B	Dashpot coefficient used to model the hysteresis losses in the ball.
c_M	Dashpot coefficient used to model the momentum flux force which acts on the ball.
c_S	Dashpot coefficient used to model the hysteresis losses in the stringbed.
COR	Coefficient of restitution.
COP	Centre of percussion.
d	Distance between the impact point on racket and its centre-of-mass.
d_{CONT}	Diameter of the ball/stringbed contact surface.
E	Young's Modulus.
F_0	Distributed loading (force per unit length of the beam).
GSC	Geometric string centre.
I	Area moment of inertia.
I_B	Mass moment of inertia of ball (around its centre-of-mass).
I_{BUTT}	Mass moment of inertia of racket (around its butt end).
I_R	Mass moment of inertia of racket (around its centre-of-mass).
k	Compression factor.
k_B	Spring stiffness (ball).
$k_{B(0)}$	Spring stiffness (ball) at zero displacement.
k_S	Spring stiffness (stringbed).
$\tilde{k}_S$	Normalised spring stiffness (stringbed).
λ	Eigenvalue.
L_F	Length of frame.
L_H	Length of handle.
m_B	Mass of ball.
M_F	Mass of frame.
M_H	Mass of handle.
m_K	Spring stiffness gradient (for the ball).
m_R	Mass of racket.
$NStep$	Number of steps used to solve the model.
N	Number of beam segments.
r_B	Radius of ball.
s	Segment length.
T_C	Contact time.

t	Time.
V	Voltage.
V'_B	Rebound velocity of the ball.
V_B	Inbound velocity of the ball.
V'_{IP}	Rebound velocity of the racket (at the impact position).
V_{IP}	Inbound velocity of the racket (at the impact position).
x_B	Displacement of ball centre of mass (*COM*).
$\dot{x}_B$	Velocity of ball *COM*.
$\ddot{x}_B$	Acceleration of ball *COM*.
x_{IP}	Displacement of the racket (at the impact position).
$\dot{x}_{IP}$	Velocity of the racket (at the impact position).
x_S	Displacement of stringbed (at the impact position).
$\dot{x}_S$	Velocity of stringbed (at the impact position).
x_T	Displacement of a stringbed motion tracker.
Δt	Time step.
δ_{BALL}	Ball deformation.
δ_S	Stringbed deformation.
θ_R	Angular orientation of the racket.
ρ_{AREA}	Mass per unit surface area of the ball.
ω_B	Ball inbound spin.
ω'_B	Ball rebound spin.
ω_T	Rotational velocity of racket around its transverse axis *before* impact.
ω'_T	Rotational velocity of racket around its transverse axis *after* impact.

This thesis is dedicated to my parents.

1. Introduction

The following chapters describe a three year study examining the dynamic interaction between a tennis ball and tennis racket.

(a) Motivation for the study

The game of tennis has changed drastically over the last 30 years. Arguably, the most significant transformation in the game is in the speed of the serves and ground strokes, in both the men's and women's game. It is generally agreed that some part of this change can be assigned to the improved training, athleticism and physique of modern players, and also the higher rewards which are bestowed upon the successful athletes. However, the International Tennis Federation (*ITF*)[1] have still been criticised for not imposing some control on the equipment used by players. Many commentators cite the allowance of new technologies/materials in the manufacturing of tennis rackets as a major factor in the increased speed of the game. This criticism is not wholly justified as the *ITF* constantly review the rules of tennis to ensure that the game is not detrimentally affected by the introduction of certain new technologies. For example, a rule change was implemented in response to the widespread use of graphite composites in the manufacturing of tennis rackets. It was noted that the use of this material allowed manufacturers to produce rackets which were longer and wider than was previously possible with other materials. The *ITF* acted by introducing a maximum length and width dimension for all rackets which are approved for tournament play.

This decision itself was met with some criticism from certain parts of the industry. In commenting on this decision in 1996, Jim Baugh, President of Wilson Sporting Goods, said "*The actions the ITF is taking for the professional game is too late. The pro's that are playing today are playing with rackets from ten years ago. The goals of the Wilson's, Prince's and Dunlop's are to bring up new kids and have them start out with the latest technology frames. That would mean in five to ten years we are going to have young pro players with very large, stiff, head heavy rackets. Then that power level would reach the pro game in the years to come..... So my fear is that in five to ten years the professional game may be too quick.*" (Coe 2000).

The issue regarding the speed of the game of tennis is a complicated argument that requires careful, rational analysis in order for it to be fully understood. It should be noted that most comments which support the view that the game is 'too fast' refer to tournaments that are played on 'fast' surfaces, such as the grass court championships at Wimbledon. Furthermore, when stating that the game is 'too fast', commentators and spectators are generally referring to the fact that the game is dominated by the serve as the ball is travelling at such a speed that it cannot be returned by the receiver. Commenting on the 1994 Wimbledon Final between Sampras and Ivanisevic, in which only three points played lasted more than four shots, Fred Perry called it "*...one of the most boring finals in history....*". Intuitively, it would be expected that comments like these would be

[1] The International Tennis Federation are the governing body of tennis and are based at Roehampton, London, UK.

supported by evidence of a decreasing number of people visiting tournaments which are played on 'fast' surfaces, such as Wimbledon. However, this years championships at Wimbledon have, yet again, attracted a record number of visitors. On this evidence, the current speed of the game of tennis, even on 'fast' surfaces, does not appear to be affecting the popularity of the game. However, if developments in technology and the physique of players continues at a similar rate that has been evident in the last 20 years, then the nature of the game may be changed detrimentally in the future. The International Tennis Federation's role is to preserve the nature of the game, and therefore this observation has motivated the governing body to embark on research projects which are aimed at advancing their existing knowledge of the mechanics of the game. These extensive projects involve studies of the court surfaces, ball types, racket construction and the physique of the players.

The current study, described in this thesis, involves an investigation of the mechanism involved in the impact between a tennis ball and tennis racket, and forms an integral part of the *ITF's* overall investigation.

(b) Aim and Objectives

The aim of this study is to develop an understanding of the dynamic interaction which occurs during an impact between a tennis ball and a tennis racket. This will be achieved using both experimental investigations and theoretical modelling techniques.

The objectives of the study are as follows,

1. To obtain the static physical properties of a tennis ball and stringbed.
2. To measure the dynamic response of a tennis ball for an impact with a rigid surface.
3. To develop a model of a tennis ball impact on a rigid surface and to use this model to define the dynamic properties of the ball.
4. To measure the dynamic response of a tennis ball and racket stringbed for an impact between a tennis ball and a head clamped racket.
5. To develop a model of a tennis ball impact on a head clamped tennis racket.
6. To measure the dynamic response of a tennis ball, stringbed and racket for an impact between a tennis ball and a tennis racket; the racket being supported in a manner that is equivalent to a player's grip.
7. To develop a model that can be used to predict the dynamic response of a tennis ball impact on a tennis racket, and use this model to gain a further understanding of the mechanics of the impact.

(c) Structure of the study

The main objective of this work is to develop a model of a tennis ball impacting on a tennis racket. In this model, the racket is supported using a method which is equivalent to a player's grip. This model must have the ability to predict the dynamic response of the tennis ball and racket, for the impact. The impact between a tennis ball and racket is a complex non-linear system which involves a large number of variables. To successfully achieve the main objective, the model is to be constructed in a finite number of stages, as outlined in the list of objectives. These objectives define a logical procedure in which a simple model of a tennis ball impact on a rigid surface is developed into a model of a ball impact on a tennis racket.

This thesis is composed of a number of chapters which document the development of the model. At each stage of the development, data from relevant experimental investigations will be used to verify the accuracy of the model.

2. Literature Review

2.1 Introduction

There is a vast amount of literature which documents studies into different aspects of the game of tennis. Indeed, one of the very first papers in the field of sports engineering was on the irregular flight of a tennis ball by the physician Lord Rayleigh back in 1877. Since then, material has been published by researchers from a range of disciplines such as physics, engineering, sports science and commercial design. The magnitude and diversity of this material has lead to much duplication of work resulting in the reinforcement of certain, well-established conclusions. It has also lead to some contradiction between authors where different findings have been determined for the same investigation. This review attempts to explain and resolve these differences, as well as highlighting the undisputed existing knowledge in the field.

It has been noted that the published material has originated from a variety of disciplines and for a wide range of sports. This review aims to discuss the relevance of each study on the game of tennis for which this project is concerned.

This project is aimed at developing an understanding and model for the impact between a tennis ball and racket. The procedure adopted in this study was to first gain an understanding of how the ball impacts on a rigid surface. This is to be followed by an understanding of the interaction of the ball and stringbed. The research then culminates in an understanding of the entire ball, string and racket frame system. The literature discussed in this section follows a similar order where possible.

The sponsors for this work are the International Tennis Federation who are the governing body of tennis. The conclusions drawn from this work will be used by them as an aid when deciding upon new rules and regulations. For example, in the definition of a test for the power of a tennis racket the governing body must have a full understanding of the parameters which contribute to this property. The sport of golf has strict rules already in place on the equipment used to ensure that the nature of the game is not changed by courses becoming obsolete (Royal and Ancient & USGA (2000)). For example, these rules define tests to regulate the speed of the ball as it leaves the club and the maximum distance that a ball may travel for a specified standard shot.

2.2 The Ball

2.2.1 ITF Rules and Regulations for a Tennis Ball

For a ball or racket to be labelled *'ITF Approved'* it must conform to a stringent set of approval tests described in the Rules of Tennis (ITF, 2000a) as defined by the International Tennis Federation. In regard to the ball, these standard tests cover such properties as mass, diameter, stiffness and bound height for an impact with a flat, rigid surface. The Rules of Tennis are revised annually and cover all aspects of the game in great detail.

Relevant extracts from Rules of Tennis regarding the ball are given below. The first passage refers to a Type 2 (medium) ball, which is the category that the majority of tennis balls are manufactured and qualify for.

> *The ball shall be more than 1.975 ounces (56.0 grams) and less than 2.095 ounces (59.4 grams) in weight.*
>
> *The ball shall have a bound of more than 53 inches (134.62 cm) and less than 58 inches (147.32 cm) when dropped 100 inches (254.00 cm) upon a flat, rigid surface e.g. concrete. The ball shall have a forward deformation of more than 0.220 of an inch (0.559 cm) and less than 0.290 of an inch (0.737 cm) and return deformation of more than 0.315 of an inch (0.800 cm) and less than 0.425 of an inch (1.080 cm) at 18 lb. (8.165 kg) load. The two deformation figures shall be the averages of three individual readings along three axes of the ball and no two individual readings shall differ by more than 0.030 of an inch (0.076 cm) in each case.*
>
> *The ball shall be more than 2.575 inches (6.541 cm) and 2.700 inches (6.858 cm) in diameter.*

An additional section was added to the Rules of Tennis in 2000 describing two new types of balls; the Type 1 ball being a 'stiffer' ball than Type 2, and the Type 3 ball being larger than the Type 2 ball.

> *From 1st January 2000 until 31st December 2001 two further types of tennis ball may be used on an experimental basis.*
>
> *The first type is identical to those described in paragraphs a. to c.* (in the Rules of Tennis which are summarised above) *except that the ball shall have a forward deformation of more than 0.195 inches (0.495 cm) and less than 0.235 inches (0.597 cm) and return deformation of more than 0.295 inches (0.749 cm) and less than 0.380 inches (0.965 cm). This type of ball shall be described as Type 1 and may be used in either a pressurised or non-pressurised form.*
>
> *Another type is identical to those described in paragraphs a. to c. above except that the size shall be more than 2.750 inches (6.985 cm) and less than 2.875 inches (7.302 cm) in diameter as determined by ring gauges and detailed in Appendix I section (iv). This type of*

ball shall be described as Type 3 and may be used in either a pressurised or non-pressurised form.

All other type of ball defined by Rule 3 shall be described as ball Type 2.

For the purpose of tournaments played under this experiment:

1. *Ball Type 1 (fast) should only be used for play on court surface types which have been classified as Category 1 (slow pace).*
2. *Ball Type 2 (medium) should only be used for play on court surface types which have been classified as Category 2 (medium/medium-fast pace).*
3. *Ball Type 3 (slow) should only be used for play on court surface types which have been classified as Category 3 (fast pace).*

For non-professional play any ball type may be used on any surface type.

The method used to determine the diameter of a tennis ball is summarised below.

In all tests for diameter a ring gauge shall be used consisting of a metal plate, preferably non-corrosive, of a uniform thickness of one-eighth of an inch (0.318cm). In the case of Type 1 (fast) and Type 2 (medium) balls there shall be two circular openings in the plate measuring 2.575 inches (6.541cm) and 2.700 inches (6.858cm) in diameter respectively. In the case of Type 3 (slow) balls there shall be two circular openings in the plate measuring 2.750 inches (6.985cm) and 2.875inches (7.302cm) in diameter respectively. The inner surface of the gauge shall have a convex profile with a radius of one-sixteenth of an inch (0.159cm) The ball shall not drop through the smaller opening by its own weight and shall drop through the larger opening by its own weight.

Tennis balls are known to exhibit a phenomenon often referred to as 'set'. This refers to the stiffness property of the rubber which appears to be highest for the initial couple of compressions than for all subsequent compressions, if the ball has been left to stand for a significant amount of time. The following extract describes the procedure used to minimise the effect of this 'set'.

Before carrying out any of the tests, a ball should be pre-compressed by approximately one inch (2.54 cm) on each of three mutually perpendicular axes. This should be carried out three times on each axis, and the tests completed within two hours of pre-compression.

2.2.2 Construction of a Tennis Ball

The Approved Tennis Balls (ITF, 2000b) states that *'a tennis ball consists of a hollow rubber core...covered by Melton consisting of textile material composed of wool, nylon and cotton'*. This textile material must be white or yellow in colour. Penn (2002) describes the complete process of making a tennis ball. In brief, two rubber hemispheres are bonded together and then covered with adhesive. If the balls are to be internally pressurised then this process occurs in a pressure chamber. Two dumbbell shaped pieces of felt cover the rubber sphere and then the further

adhesive is used to create the familiar white seam that is characteristic of all tennis balls. There are two main constructions of tennis balls which are generally defined in ITF (2000a) as,

1. *Pressurised* – a ball with a typical wall thickness of 3mm and internally pressurised with air at approximately 1bar.
2. *Pressureless* – a ball with a typical wall thickness of 4mm and has an internal air pressure equal to that of atmosphere.

A further ball construction method involves filling the rubber core with a micro-cellular material that is designed to simulate the internal pressurisation of a *Pressurised* ball. This is often referred to as a *Foam-Filled* ball.

The manufacturers of *Pressureless* and *Foam-Filled* balls claim that their products have a more durable performance property because *Pressurised* balls suffer from pressure loss over time. This loss in internal air pressure is a well established phenomenon and has been studied by various researchers and manufacturers who have investigated methods of minimising it. A patent by Koziol & Reed (1978) claimed that the a ball which was internally pressurised using a mixture of sulphur hexafluoride and air only suffered a 6% loss in stiffness over a period of 236 days. This compared to a loss of 23% in the ball pressurised with air over a similar time period. Reed & Thomas (1988) investigated the effectiveness of using low permeability gases in different concentrations to pressurise a tennis ball. A compression test was performed on the balls to monitor the change in stiffness over a period of 60 days. It was found that the stiffness of the ball pressurised with air reduced by approximately 7% in this time. In the same time the stiffness of the ball pressurised with the low permeability gas actually increased, due to the surrounding air permeating into the ball as a consequence of the gradient in the partial pressure of the air on either side of the rubber core. It was accepted that the use of low permeability gases to pressurise tennis balls may not be economically viable which is why this method is not used commercially.

Wilson Sporting Goods (2001) have recently introduced utilised a coated inner core in their pressurised balls which they claim reduces air permeation by 200%, thus preserving the life of the ball.

The Rules of Tennis aim to ensure that a ball is a homogenous structure by ensuring that the deformation in the three axis's does not differ by a pre-defined amount. Thomson (2000) tested the homogeneity of a range of tennis balls for compressions of approximately 30mm, which is higher than those used in the standard ITF test. Thomson confirmed that all the balls tested could be considered homogenous. At these high compressions it was found that a *Pressurised* ball was significantly stiffer than a *Pressureless* ball.

Due to the nature of the ball construction it is likely that the properties will change with the atmospheric temperature. Rose *at al* (2000) measured the variation in static and dynamic tennis ball properties with temperature. The properties measured were the ball rebound from 100inches, ball deformation for a load of 18lbs, and coefficient of restitution for normal impacts on a rigid surface at velocities up to 45m/s. It was found that the *Pressurised* balls exhibited the largest

variation with temperature for the 100inch drop, compared with the *Pressureless* balls. The deformation test showed little variation of the forward or return deformation with temperature. The coefficient of restitution increased with temperature for all impact velocities and ball types.

In summary, the literature highlights the considerations which should be noted when testing tennis balls. The temperature at which the tests are conducted must be regulated and the errors caused by pressure loss inside *Pressurised* tennis balls should be minimised by whatever suitable method.

2.2.3 Properties of a Tennis Ball

This section discusses the existing knowledge of the static and dynamic properties of a tennis ball, such as the structural stiffness or coefficient of restitution, for an impact with a rigid surface. It is also a suitable point to describe the experimental methods used to obtain this data.

(a) Quasi-static ball compression testing

Although a relevantly simple property, the quasi-static stiffness of the ball has been of interest to many researchers as it is an obvious starting point of any modelling procedure. The simplest test is that carried out in the Rules of Tennis which states that the deformation of the ball should be between 0.559cm and 0.737cm for a load of 80N, when compressed between two plates. During this test the ball sits in an indentation in the plate. However, the dimension of this concave shape is not specified. This test implies that a ball should have a linear stiffness of between 14.3kN/m and 10.9kN/m for the applied load of 80N.

A simple calculation can be used to show that the forces acting on the ball during an impact with a racket are considerably higher than 80N. This motivated researchers to investigate the stiffness of the ball for typical loads found, for example, during a typical serve. This has been approached in different ways using different apparatus. The simplest method involves deforming the ball between two flat plates (Leigh & Lu 1992, Cross 1999b, Thomson 2000). Leigh & Lu determined a linear stiffness of 9.2kN/m and 11.9kN/m for ball deformations of 5mm and 30mm respectively. Thomson determined a linear stiffness of between 10.0kN/m and 17.2kN/m for a similar deformation range. The linear stiffness referred to here are the ratio of the load and deformation. The most likely reason for the differences is that Leigh and Thomson used old and new balls respectively. In both these studies the stiffness values obtained for a compression test between two flat plates was compared to the stiffness of the ball during a dynamic impact with a rigid surface. Both authors claimed that the obtained deformation values should be halved because in a dynamic impact only one side of the ball deforms. A similar claim was made by Kawazoe (1993) who made the observation from still images of a ball hitting a racket. One consequence of this is that the stiffness values which are quoted above should be doubled. However, none of these publications give quantitative evidence that this is a valid assumption.

Brody (1979) performed a compression test where the ball was placed in a rigid hemispherical cup so that only one side was deformed. A value of 12.5kN/m was quoted for the ball stiffness, for

deformations of up to 12mm. Although this method gives a realistic deformation shape, the cup provides a restoring force to the ball which is not present in an impact between a ball and surface.

A further alternative is to compress the ball into a stringbed, and measure both the deformation of the ball and stringbed. This was performed by Casolo & Ruggieri (1991) who applied a load of up to 1500N giving a ball stiffness of between 50 and 80kN/m. These are much higher values than those quoted by any other author.

Leigh & Lu acknowledged that no quasi-static compression test method can possibly recreate what happens to the ball in an impact with a rigid surface or stringbed.

(b) Dynamic impacts

In this section, methods are discussed for analysing the impact between a ball and surface (whether it be rigid or deformable).

Ball Projection devices

A method of propelling a ball with controllable velocity, and often spin, is a general requirement of many studies of ball sports. This has been attempted using three main methods as follows,

1. Dropping the ball from a range of heights
2. Propel the ball between two rotating wheels.
3. Launch the ball from an air cannon gun.

The first method simply uses gravity to accelerate the ball and it gives an accurate, repeatable impact velocity. Many authors (Brody (1979), Grabiner *et al.* (1983), Leigh and Lu (1992), Goodwill (1997), Cross (2002a)) have successfully used this method. The principle drawback of this method is that the maximum impact speeds which can be obtained are in the order of 8m/s – corresponding to a drop height of 3.5m. This may be suitable for many ball-surface impacts, but the relative impact velocity is far lower than that occurring in a ball-racket impact. This general comment was noted by Kotze (2000) in his overview of published tennis racket research. Also, another weakness is that, in its standard form, the ball must impact perpendicular to the surface and have no initial spin. However, Cross (2002a) illustrated how oblique impacts could be performed by rotating the surface and clamping it at the desired angle. Also, Chadwick (2002) developed a dropping mechanism that could apply a user defined magnitude of spin to the ball prior to it being released.

Many authors (Haake (1989), Cross (1999b), Carré (2000)) have used a projection device based on two counter-rotating inflated wheels which were in the same vertical plane. Haake (1989) used a modified baseball pitching machine which was capable of propelling golf balls at up to 35m/s with up to 700rad/s of top or back spin. These speeds are considerably higher than those which could be obtained from drop tests, and much more representative of the speed that a ball hits the turf. Carré (2000) used a modified bowling machine to apply spin to a cricket ball, in any chosen axis. Carré

comments that one weakness of this propulsion method is the repeatability of the impact position is low, possibly due to the compressibility of the wheels.

An alternative method of propelling the ball is to use an air cannon. This technique is used in the *ITF surface pace rating* test (ITF 2001) and by many other authors (Gobush (1990), Ujihashi (1994), Neville (2000)). The device works by storing air in a cylinder and then rapidly discharging it behind the ball. The cannon tube is generally of a similar diameter to that of the ball. The main advantage of an air cannon is the high repeatability in the impact position, compared with that of the rotating wheel system. The disadvantage of using an air cannon is that initial spin can not be easily applied to the ball. Mish & Hubbard (2001) successfully built and tested a pneumatic system which was capable of applying spin in any axis to a baseball. The ball was then fired down a cannon and the flight of the ball was recorded using a high speed video system which confirmed that the device applied consistent spin magnitude and orientation.

Measuring Dynamic Parameters

In the study of a ball-surface impact, there are many parameters that could be measured before, during and after the contact period. These measurements are measured in an effort to understand the impact mechanism and the contribution of each parameter (e.g. ball stiffness) on the system. These are listed below,

1. Linear and angular velocity of the ball (and surface, if applicable) before, during and after impact.
2. Ball (and surface) deformation during impact
3. Force and Torque acting on the ball (and surface) during impact
4. Amplitude and frequency of the induced sound wave.

There are four main categories of apparatus which can be used to individually determine one or more of the above parameters; stroboscopic photography, cinematic photography, load transducers and photo sensors.

Carré (2000) used stroboscopic photography to obtain a single image showing a spinning cricket ball impacting obliquely on natural turf. The image was later analysed using PC software to give the velocity, angle and spin of the ball, before and after the impact. Haake (1989) and Lieberman (1990) used a similar method for the study of golf balls impacting on natural turf and rigid surfaces respectively. Carré commented that an advantage of this method was that impacts could be recorded and stored very quickly once the experimental arrangement had been set up. A disadvantage of this system is that all background light must be blocked out in order to produce clear images. Also, an automatic trigger mechanism is generally required due to the short amount of time that the film is exposed for. The system is not suitable for any impact in which two or more images cover each other, i.e. in a normal impact or in an experiment aimed at determining the ball compression during impact.

A more commonly used photographic technique in recent studies has been the use of video cameras to record the impact. The required speed of the camera is dependant on the actual parameter being measured. Cross (2002a) used a camera with a recording rate of only 100fps as this was sufficient to determine the velocity, angle and spin of the ball before and after an oblique impact on a range of surfaces. Similarly, Plagenhoef (1970) used a camera with a frame rate of 64fps to determine the motion of a tennis racket during a serve. This was sufficient to provide data for coaching but was not fast enough to determine the speed of the racket at the point of impact.

Dignall, Haake & Chadwick (2000a) used a Kodak EktaPro 4540 camera operating at 9000 fps to record an oblique impact between a ball and acrylic surface. This was used to determine the velocity, angle and spin of the ball before and after impact, and also the deformation of the ball during impact. Groppel *et al.* (1987a) recorded the impact between a ball and handle-clamped tennis racket using a camera operating at 3500fps. The optical axis of the camera had an angle of 8.7° from the string plane which allowed the entire stringbed to be seen during impact. The images were analysed using an out-of-plane adjustment algorithm to determine the stringbed and racket displacement during impact.

UC Davis (2001) used a video camera operating at 250fps to determine the ball and racket velocity in matches filmed at the US Open. This study highlights the main benefits of using cinematic techniques. The method is non-intrusive which not only means that the technique can be used in real field situations, but also the properties of, for example the racket, are not changed by the introduction of markers. Also, the equipment is highly suited for lab work where the experimental arrangement is often constantly being changed for different investigations. Another fundamental advantage is that cinematic cameras are more versatile than stroboscopic cameras because individual frames are obtained, as opposed to one combined image of the impact.

Mitchell *et al.* (2000) used both a high speed video and a three-dimensional active marker system (CODA) in a study of tennis racket velocities in a serve. The main finding was that the CODA could determine the motion of the racket much more accurately than the two dimensional high speed video images, due to the considerable out-of-plane motion of the tennis racket. However, the video system has the ability to measure the ball rebound velocity which the CODA was unable to do. Elliott *et al.* (1986) performed a similar study to Mitchell *et al.* using two phase-locked high speed video cameras and the direct linear transformation (DLT) technique to build up a three dimensional reconstruction of the motion of a tennis racket. This gave results which were similar to those determined using a marker system but suffered from a lower resolution and longer processing times.

Neville (2001) described the use of one-dimensional speed gates to determine the impact and rebound velocity of a tennis ball impacting normal to a rigid surface. These speed gates used two sets of fluorescent lights and photo detectors coupled to a simple sampling system which directly displayed the ball impact and rebound velocity. If these are the only two parameters which are required then this is easily the most suitable method.

ITF (2001) describes the standard test for measuring the pace of a tennis surface which involves propelling a non-spinning tennis ball onto the surface at an angle of 16°. The apparatus used is called a *Sesteé* which contains four sets of infra-red photocell arrays that determine the trajectory of the ball. A PC is used to sample the data and calculate the ball velocity and angle, before and after impact, and also the contact distance of the ball on the surface. This equipment is not capable of determining the spin on the ball.

Many authors have used either a single component (Cross (1999a, 1999b, 2000a), Thomson (2000), Neville (2001)) or a multi-component (Gobush (1990)) piezoelectric force platform to measure the *Force-Time* plot for a range of sports ball impacts on a rigid surface. Piezoelectric transducers have a very high stiffness relative to the ball which results in rapid response times of the load sensor, in comparison to strain-gauge based load cells.

The majority of the work done on tennis ball impacts has been for normal impacts, at speeds of up to 20m/s. The single component force platform is used in conjunction with a method of measuring the ball velocity. Analysis of this data determines the following parameters,

1. *Coefficient of restitution* for the impact
2. *Force-Time* plot
3. *Contact time* for the impact
4. Velocity/Displacement of the ball COM during impact. (these are obtained by successive integration of the *Force-Time* plots.)

An important point to note is that the ball COM displacement is not equal to the ball deformation, and therefore it is difficult to compare these results with the quasi-static compression data discussed above. To the authors knowledge, no work has been done which gives the force and ball deformation during the impact between a tennis ball and force platform. However, this could easily have been achieved using a high speed video system as done by Ujihashi (1994) for golf ball impacts.

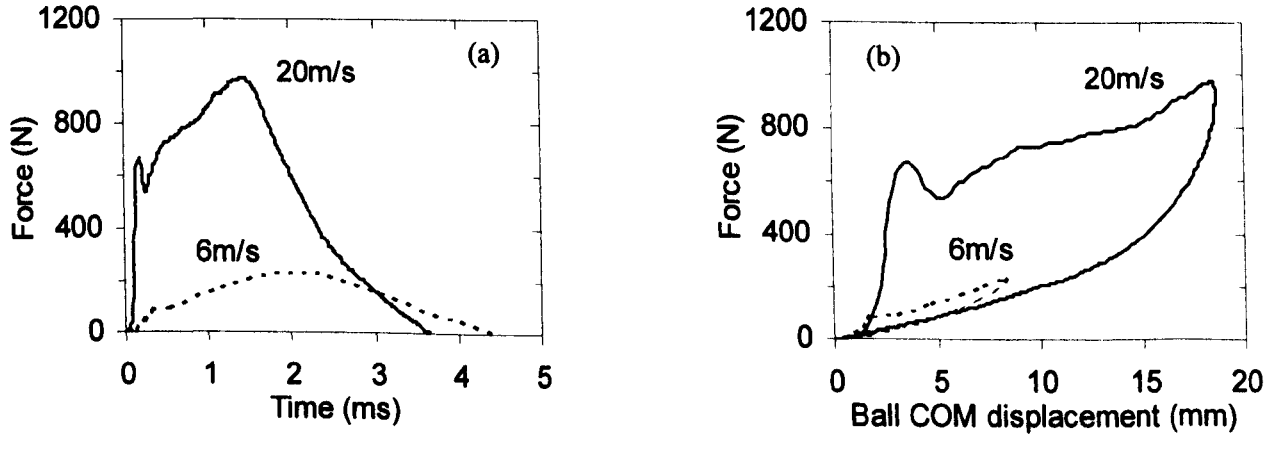

Figure 2.1 Typical plots for a normal impact on force platform for two different impact velocities. (a) *Force-Time* and (b) *Force-Displacement* (Reproduced from Neville 2001).

Figure 2.1(a) & (b) show typical results obtained from a piezoelectric force platform (Neville 2001), at 6m/s (the ITF standard 100in. drop height) and 20m/s. The precise shape of the curves differs slightly between ball types, but the general shape is similar to that in Figure 2.1 (a) & (b). In the initial phase of impact the ball is subject to a relatively low load, as shown in Figure 2.1 (b), which is assigned to the low stiffness of the cloth. The load then rises rapidly for approximately 0.2ms which is followed by a characteristic kink in the curve, particularly at higher speeds. Most researchers (Cross (1999a), Dignall & Haake (2000b), Thomson (2000), Neville (2001)) agree that this is due to the buckling of the ball wall.

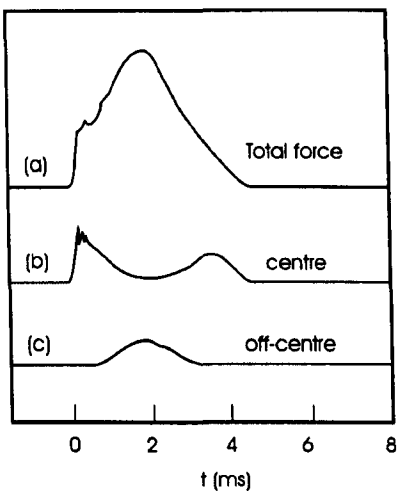

Figure 2.2 Oscilloscope traces for a normal impact on a two piece force platform. The central section has a diameter of 13mm (Reproduced from Cross (1999a)).

Figure 2.2 illustrates the buckling of the ball wall by the transition of the majority of the load from the centre of the impact area (t<0.2ms), to the outer regions during impact (Cross 1999a). The impact shown was for a ball impact velocity of 7m/s.

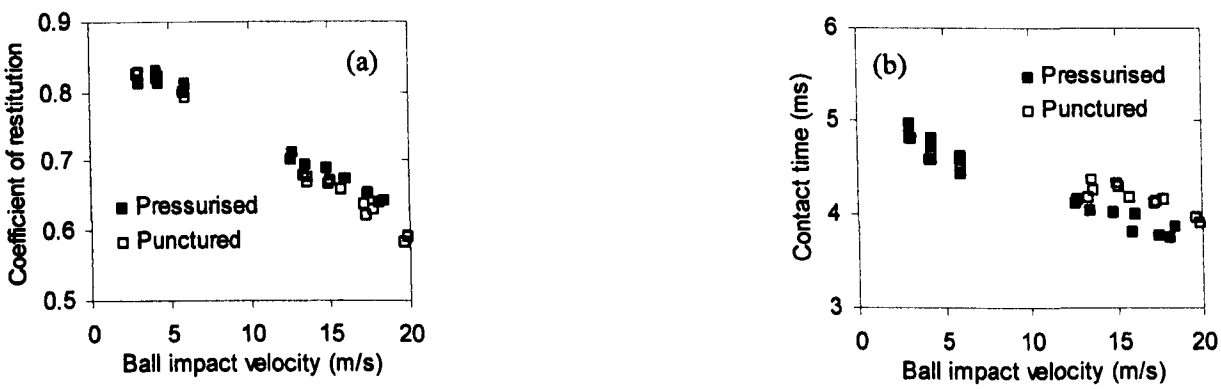

Figure 2.3 Relationship between ball impact velocity and (a) coefficient of restitution and (b) contact time, for an impact between a ball and a rigid surface.

Thomson (2000) and Neville (2001) used a force platform and speed gates to compare the *Force-Time* and *Force-Displacement* curves for a range of different ball types, including *Pressurised* and *Pressureless*, at impact velocities from 2 to 20m/s. It was found that all ball types exhibited similar responses for impact velocities of 6m/s and below, with similar *Force-Time* curves, coefficient of

restitution and contact time values being obtained. However, at higher speeds the *Pressureless* ball had a lower *COR* and longer contact time than the *Pressurised* ball as shown in Figure 2.3. It was deduced that the *Pressureless* ball was therefore less stiff than the *Pressurised* ball.

Figure 2.3 also shows that the coefficient of restitution reduces with ball impact velocity V_B which implies that the energy losses increase with V_B. The contact time also decreases with V_B. Neville, amongst many authors, has concluded that this is because the effective stiffness of the ball increases with ball impact velocity. This correlates with the quasi static compression data.

2.2.4 Summary

The Rules of Tennis define the size, mass, stiffness and coefficient of restitution of a tennis ball. There are two main constructions of tennis ball; *Pressurised* and *Pressureless*. *Pressurised* balls have an internal air pressure of 1bar gauge (15psi) and a rubber wall thickness of 3mm. *Pressureless* balls having a lower internal pressure (0 bar gauge) and a wall thickness of 4mm.

The Rules of Tennis specify the quasi-static stiffness of a tennis ball for a load of only 80N. The literature shows that the stiffness increases considerably with deformation and at high compressions a *Pressurised* ball is stiffer than a *Pressureless* ball. The correlates with impact test results that have shown that the former ball has a shorter contact time, implying a higher stiffness.

2.3 The Strings

2.3.1 Introduction

Tennis strings are generally manufactured from either natural gut, Kevlar, polyester or nylon. They are available in a range of diameters from 15 gauge (~1.4mm) to 18 gauge (~1.2 mm). Cross (2000b) highlighted that there is no International Tennis Federation ruling on the properties of tennis strings. Therefore the manufacturers are allowed to produce strings with any stiffness and friction properties that they chose. Also, they can use any materials and construction techniques in order to achieve the desired combination of these two properties.

It is well established that players prefer the 'feel' of natural gut and this is backed up by the fact that 14 out of the top 20 male professionals use this type of string (Racket Tech (2001)). The string tension generally ranges from 40lbs to 70lbs. It is claimed that many professional players use very high tensions, e.g. Pete Sampras is reported to use a tension of 75lbs.

The main disadvantages of natural gut are its poor durability and high cost, making it unsuitable for many 'leisure' standard players. Attempts have been made to replicate the playing properties of this material in the form of a synthetic gut. ICI (1986) filed a patent for a new synthetic material which was designed to replicate the performance of natural gut. ICI highlighted the features of

natural gut which appear to make it attractive to players. They stated that the dynamic stiffness of the material should not increase substantially as the mean tension is increased. Many synthetic strings exhibit a rapid increase in stiffness with mean tension which leads to a 'boardy' response when the racket is strung at a high tension. It is quoted that a high tension is favoured by many players for the higher level of control that it offers.

2.3.2 Properties of Tennis Strings

The static stiffness of a tennis string can easily be obtained using a tensile testing machine, for example an Instron test device (Cross, 2000c). However, the impact between a ball and racket is a dynamic event which involves high strain rates. Tipton (1955) described an apparatus which could be used to determine the dynamic Young's Modulus of a range of textile filaments and yarns including various nylons. This paper illustrates the concept of the relationship between the Dynamic Young's Modulus and the Loss Modulus which leads to a dwell, or loss, angle. The loss angle gives a good indication of the relative damping in the material. Results are presented for several nylon specifications, for a range of static and dynamic strain amplitudes. The data shows that the dynamic Young's Modulus increases with static strain, but remains approximately unchanged with dynamic strain amplitude. The loss angle increases with dynamic strain amplitude, but decreases with static strain. The applicability of this work is limited because production tennis strings were not tested and the static and dynamic strain amplitudes were not related to those in tennis.

Calder (1987) advanced the work of Tipton in his study of the dynamic properties of a tennis strings. This paper focused on a comparison between synthetic and natural gut strings. A strain gauge based transducer was placed in-line with a main string of a mid-sized tennis racket strung at 50lbs. When this head clamped tennis racket was subjected to a ball impact the string tension increased to a maximum of 70lbs, during the contact time of 3.5ms. The ball velocity for this test was not quoted. A single string was then tested in a purpose built rig which simulated both the static and dynamic loading that was determined from the in-line transducer. At high preloads the hysteresis losses in both natural and synthetic gut are very low. It shows that the stiffness of natural gut is not dependent on the pre-load, whereas it is strongly dependent on the pre-load for synthetic gut. The data also shows that the natural gut is significantly less stiff than synthetic gut, for a specific string tension. Calder found that the hysteresis loss reduced when the static strain was increased, which is in agreement with Tipton.

Cross (2000b) performed a dynamic impact on a single, pre-loaded string, using a 0.292kg hammer. The tension was measured using an in-line strain gauge load transducer and the transverse displacement of the string was measured using a 1mm optical grid and laser beam. A preload of 270N (60lbs) was used and it was shown that natural gut was significantly softer than nylon. This was concluded from the fact that the stiffness of the natural gut did not increase as much during impact in comparison to the nylon string. This supported the findings of Calder.

Calder (1987) and Cross (2000c) have both commented that the most noticeable source of tension loss is in the first five minutes after stringing. Cross (2000c) showed that the loss in tension for a natural gut string was approximately 30N(6lbs) in 1 hour, compared to 70N(15lbs) for a typical synthetic string. The rate of tension loss reduced with time.

The discussion above has focused on the characteristics of an individual string. To determine the actual 'playability' of the string the properties of the interwoven stringbed must be investigated. (Casolo & Ruggieri (1991), Leigh and Lu (1992), Kawazoe (1993) and Cross (2000b, 2000c, 2000d)). Leigh & Lu (1992) compressed a tennis ball onto a head clamped racket using a force of up to 200N, giving a stringbed stiffness of up to 30kN/m. Kawazoe (1993) performed a similar experiment and determined a stiffness of 30kN/m for very small loads, and over 100kN/m for a load of 1200N. There is little data available regarding the dynamic stiffness of a stringbed.

The hysteresis loss in tennis strings has also been determined for normal impacts on an interwoven stringbed. Leigh and Lu (1992) dropped a (rigid) Pool ball, with a mass of 164g, onto a head clamped racket at velocities of up to ~7m/s. This gives approximately the same amount of kinetic energy as a tennis ball being propelled at 12m/s (27mph). It was found that the pool ball rebounded up to a point that was 95% of the original height. Leigh and Lu determined the impact and rebound velocity by considering the drag force acting on the ball during its flight. They calculated that the coefficient of restitution for the impact was ~1, implying that the strings did not lose any energy during impact. Cross (2000b) performed a similar experiment with a 760g steel ball, dropped from similar heights and found that it rebounded with approximately 95% of the original velocity. Cross compared the kinetic energy of the balls to conclude that this was equivalent to a tennis ball impacting at 24m/s (54mph). Hatze (1993) concluded that the strings contributed to approximately only 3% of the total energy loss in an impact between a ball and racket.

Cross (2000d) highlighted anecdotal evidence that players say that old strings are less responsive than new ones. This is not consistent with laboratory tests for normal impacts on a racket which have shown that the ball rebounded at the same velocity whatever the ages of the strings (Cross (2000d)). However, most impacts between a racket and ball are oblique and therefore this laboratory test is not necessarily sufficient to analyse the impact.

Cross (2000c) discussed the influence of string friction on the impact between a ball and racket. An experiment was conducted to find the coefficient of friction (*COF*) between a tennis ball and stringbed for normal reaction loads of up to 100N. This is much lower than the peak loads quoted by Cross (2000b) of 1500N in an impact. It was shown that the *COF* varied between 0.27 and 0.42 for a range of string types. The relationship between *COF* and applied load is not presented. Cross suggested that a possible reason why older strings 'felt worse' compared to new ones was that strings will feel much less responsive if *COF* drops below about 0.3. It was shown that, in this case, the ball rebound velocity does not drop significantly but the rebound angle does change. This results in the ball dropping short of the intended target which the player perceives as a loss in power. It is not, however, shown that the friction of a string does drop significantly with age.

Isospeed Professional string has the highest *COF* tested, and is a very popular string which may be because this high friction leads to a more 'responsive' string.

Knudson (1991 & 1993) concluded that string type and tension effected the rebound angle and speed for an oblique impact test on a handle clamped racket. It was found that the rebound angle increased significantly with string tension for natural gut, but only fractionally for synthetic gut. It was found that the rebound velocity dropped significantly (8%) for a change in string tension of 20lbs for the natural gut, but only changed by approximately 3% for the same tension change in synthetic gut. The rebound spin was not measured in this test.

Knudson (1997) propelled tennis balls at a freely suspended racket which was strung at 50, 60 and 70lbs with nylon string. The ball was propelled at an angle of 5° to simulate a topspin shot, at a point approximately 20mm from the longitudinal axis. The data showed that an increase in string tension reduced the angle of rebound. This was explained by the fact that a higher tension gives a shorter contact time and therefore the racket rotation is minimized at the highest string tension.

2.3.3 Summary

The review of literature that covers the properties of tennis strings has revealed many issues which should be considered in the study of the impact between a ball and tennis racket.

1. A range of materials are used in the manufacture of strings which all have different playing properties. The diameter ranges from 1.2mm to 1.4mm.
2. The hysteresis losses in tennis strings are generally less than 5%.
3. Generally strings made from natural gut have a lower stiffness than those made from synthetic gut.
4. The tension in the strings reduces immediately once the racket is strung. The rate of loss decreases with time. This loss in tension should be accommodated for in any model which is generated to simulate the impact.

2.4 The Racket

2.4.1 Tennis racket development

Traditionally a tennis racket frame was constructed from wood (eg. Ash). One of the main limitations of this material was that the frame had to be solid. The consequence of this was that the head sizes were generally small and the frames were relatively flexible to maintain a sensible weight of racket. The introduction of metal rackets in the 1970's brought with it new manufacturing methods which allowed lighter, larger and stiffer rackets to be economically manufactured. This innovation was closely followed by the advent of composite rackets with even more versatile manufacturing methods.

A modern racket is typically made from a long, hollow tube of graphite, as described in Cross (2001b). A typical composite racket weighs 332g and consists of a frame (286g), a grip (10g), grommets (20g) and strings (16g). This breakdown gives an indication of the contribution of each section to the mass of the racket.

Marketing of sports products is often heavily surrounded by hype and unfortified claims and tennis racket advertising is no exception to this trend. However, some of the fundamental claims and ideas are based on well-established scientific findings. For example, the main developments have been to reduce the mass, increase the frame stiffness and head size, and shift the balance point towards the tip. Brody (1979), amongst others, highlighted that an increase in frame stiffness will increase the ball rebound velocity, as less energy will be lost due to racket deformation. Reducing the mass of the racket allows the player to generate higher head speeds and thus be able to hit the ball faster. The head size has been increased to provide a larger 'sweet spot' for the player, effectively increasing the probability that the player will hit a good shot. All these points shall be expanded upon in the following sections.

2.4.2 ITF Rules and Regulations

Prior to the 1970's there were few rules to regulate the characteristics of a tennis racket, allowing it to be of any shape, size or material. It was around this time when oversize rackets were introduced that the governing body became concerned about racket designs and the *ITF* implemented rules to limit the size of the racket head. Before then the racket was simply defined as an implement which could be used to hit the ball.

The current regulations which apply to the racket describe the overall dimensions and characteristics of the hitting surface. Relevant extracts from Rules of Tennis regarding the racket are given below.

> *The hitting surface of the racket shall be flat and consist of a pattern of crossed strings connected to a frame and alternatively interlaced or bonded where they cross; and the stringing pattern shall be generally uniform, and in particular not less dense in the centre*

than in any other area. The racket shall be designed and strung such that the playing characteristics are identical on both faces. The strings shall be free of attached objects and protrusions other than those utilised solely and specifically to limit or prevent wear and tear or vibration, and which are reasonable in size and placement for such purposes.

The frame of the racket shall not exceed 29 inches (73.66cm) in overall length, including the handle. The frame of the racket shall not exceed $12^1/_2$ inches (31.75cm) in overall width. The hitting surface shall not exceed $15^1/_2$ inches in overall length, and $11^1/_2$ inches (29.21cm) in overall width.

2.4.3 Simulating a player's grip on a racket during impact

In the experimental analysis of the interaction between a ball and racket during impact, the racket would ideally be swung by a player and the testing would be conducted on a tennis court to recreate actual playing conditions. However, the nature of the equipment used to analyse the impact makes it more convenient to conduct the testing in a laboratory and using a player to swing the racket in the test introduces an extra variable into the study. Also, the velocity of the racket, when swung by a player, is difficult to measure accurately due to the high accelerations occurring at impact. It has been achieved by some authors (Groppel (1975), Elliott *et al.* (1986), Mitchell *et al.* (2000), Schleihauf *et al.* (2000)). However, the necessity of conducting this complicated testing needs to be established.

Ideally the testing should be conducted with full control of all the input variables (ball/racket impact velocities, ball impact position, etc) and a realistic simulation used for the player's grip. Initially it would seem obvious to conduct the laboratory testing with a player holding the racket. However, this is not consistent with the above requisite of the experiment in that it needs to be simple and repeatable. If the hand gives no support during impact, then it would be much simpler to just use a freely supported racket. Alternatively, if the hand does provide some support then using a player to hold the racket does not lead to a repeatable experiment as it is difficult for a player to control the level of grip firmness.

There has been extensive debate regarding the method used to support a racket during laboratory tests to correctly simulate a player's grip. A review of the relevant publications has shown that the gripping methods used have ranged from rigidly clamping the handle to freely supporting the racket. Some earlier published results initially seem to contradict each other. However, much of this confusion can generally be resolved by re-interpreting the authors actual claims.

Early published research into the issue of grip firmness concluded that a high level of firmness increased the ball rebound velocity (Broer (1973), Tilmanis (1975)) by reducing the recoil velocity of the racket. Plagenhoef (1970) commented that the effective racket mass, and therefore the ball rebound velocity, was dependent on the level of grip firmness. These publications are aimed at coaches and players, and the comments made are based on experience on-court and were not controlled laboratory experiments. These comments were not aimed at any specific shot so

effectively it is being claimed that for any shot and impact position it is desirable to have a firm grip and a 'set wrist'. Also, it should be noted that these comments are aimed at recreational level players who are likely to hit many shots from all points of the racket. Therefore these comments are encompassing off-centre shots, near the throat and near the tip.

Hatze (1976) performed a theoretical analysis of the impact between a tennis ball and racket and simplified the frame and stringbed as a non-uniform one dimensional beam. Therefore an inherent assumption in this work was that the ball impacted along the longitudinal axis. The racket was modelled in great detail by determining the magnitude of the cross-sectional area and area moment of inertia as a function of the position along the racket. Strain gauges were placed on the frame of the racket (wooden Dunlop MaxPly) to measure the impulse, and it was stated that the model was in good agreement with this empirical data. The model was used to quantify the difference in impulse acting on the ball which occurred for different grip firmnesses. It was found that the impulse increased by 10-15% by gripping the racket tightly, as opposed to loosely, although the ball rebound velocity was not actually measured to confirm this. Hatze concluded that an increased grip firmness resulted in increased power in the stroke. However, it was also pointed out that it was a fallacious belief that a very firm grip could be used to prevent the racket recoiling in the hand, as the required force/torque would be 16 times the value that the human hand can exert (for a relative ball-racket impact velocity of 35m/s).

Watanabe *et al.* (1979) performed an interesting series of experiments in which the coefficient of restitution (*COR*) was measured for a range of gripping conditions (freely suspended, handle clamped and hand held). The ball was propelled at a wooden racket at velocities between 5 and 25m/s, and it was shown that the *COR* values were independent of grip condition. Although it is not explicitly said, it is assumed that the ball impacted at the geometric string centre (GSC). Superficially this work seems to confirm beyond doubt that the level of grip firmness does not effect the ball rebound velocity, and therefore conflicts with Tilmanis, Broer and Hatze. However, it should be noted that this is only applicable for the impact position tested, not for off centre impacts or impacts towards the throat. Also, the testing was conducted in 1979 using a wooden tennis racket with a fundamental frequency of ~100Hz. Modern tennis rackets are much stiffer and lighter and therefore have higher fundamental frequencies. Therefore the force wave travels much faster in these rackets which may effect the conclusions. Also, impacts should be conducted at various positions on the racket to deduce whether the obtained result was only applicable at the chosen impact position.

Elliott (1982) conducted a detailed experiment into the effect of grip firmness on the ball rebound velocity. A college player was asked to grip a racket fitted with four pressure transducers to benchmark three different levels of grip firmness; light, moderate and firm. This was then replicated in a grip mechanism of a pneumatic arm which was used to swing a racket at approximately 7m/s (16mph). Balls were projected at a range of points on the racket all referenced from the GSC; at the GSC, 50mm towards the butt end, 50mm towards the tip, and 50mm towards the edge of the frame. It was found that there was a 7% increase ball rebound velocity for the firm grip compared with the light grip, for central impacts. It was determined that this was not

significant and therefore it was concluded that grip firmness does not effect ball rebound velocity. For the off-centre impacts, significant increases were determined for the ball rebound velocity for the increased grip firmness, up to 20% in magnitude. Therefore it was concluded that the level of grip firmness affects the ball rebound velocity insignificantly for impacts at the GSC, but significantly for off centre impacts. This goes some way to support the anecdotal coaching evidence given by Broer and Tilmanis.

In Baker & Putnam (1979) tennis balls were propelled at the GSC of both freely supported and handle clamped rackets. The motion of the racket during impact and the ball rebound velocity were measured using high speed cinematographic analysis. A wide range of rackets and strings were tested and it was concluded that the ball rebound velocity was independent of the method of supporting the racket. A supplementary experiment determined that the motion of the racket was very similar for both supporting methods during impact. This implies that effectively the ball does not 'know' what the gripping condition is during impact because the racket acts very similarly. A final comment was made that preliminary testing for off-centre impacts showed that the ball rebound velocity was different for the two support methods due to the inherent twisting of the freely suspended racket during impact.

To compare Baker & Putnam (1979) and Elliott (1982) it is noted that Elliott performed the investigation for more impact points, but Baker tests the extremes of grip firmness more appropriately by using a free condition instead of a light grip. Elliott assumed that different grip levels could be simulated by adjusting the torque on the bolts which clamped the racket handle in the rubber. However, it is difficult to apply Elliott's results because no player's grip is strong enough to act like any handle gripped condition (Hatze 1976).

Missavage *et al.* (1984) conducted a theoretical analysis of the impact between a ball and racket to investigate the effect of grip firmness on ball rebound velocity, using a one-dimensional beam to represent the racket. The beam was clamped at the butt end and free at the other, and the model showed that the moment acting on the clamped end was zero during impact, for a regular racket. This inferred that the ball rebound velocity was independent of the grip condition, for the simulated impact at the GSC. The model also predicted that the moment was non-zero for a drastically stiffened or shortened racket because the impulse reaches the handle more quickly. The model predicted that the stiffness of the conventional frame must be doubled, for a constant mass, for the moment at the handle to be non-zero. Experiments using a conventional racket verified that the ball rebound velocity was identical for freely suspended and handle clamped conditions. Tests carried out using the stiffened racket revealed that the COR increased from 0.36 to 0.42 for the free and grip clamped conditions respectively. It is noted that the racket used in this testing was wooden and new carbon fibre composite rackets may be sufficiently stiff for the moment at the handle to be non-zero. Also, the stiffness of the 'stiffened' racket used in the experiment was not given.

Kawazoe (1997a) used a rigid body model to compare a freely suspended racket with a hand-held racket. It was assumed that a hand held support could be modelled as a pin jointed structure. This

contradicted Hatze (1976) who claimed that a human hand did not have the strength to act like a pin jointed structure. However, Hatze's claim was blurred in that it did not differentiate between the linear and angular impulse which the hand must react against. For example, it may be possible for the hand to react against the linear impulse but not against the angular impulse. Kawazoe's rigid body assumption regarding the racket frame puts this work into context. It was claimed that the method of supporting a racket does effect the ball rebound velocity. In fact, the real conclusion was that a rigid body which is pin jointed at one end and free at the other gives a different result to a free-free rigid body.

Cross (1999c) conducted a similar study of grip conditions but used a more realistic one dimensional flexible beam model for the racket. Theoretical solutions were obtained for the impact between a ball and a racket that was supported using a range of methods (grip clamped, grip pivoted and freely suspended). It was shown that, for impacts along the longitudinal axis, all three methods of supporting the racket give almost identical results, for the majority of the stringbed. For impacts within approximately 100mm of the throat piece, the grip clamped method gives a fractionally higher ball rebound velocity than the other two methods. It also showed that the free and grip pivoted cases gave very similar ball rebound results for practically all the hitting area along the longitudinal axis of the racket.

An alternative method of investigating the importance of grip pressure is to consider the vibrations of a tennis racket for all the different clamping conditions. A great deal of work has been done in this area, including much duplication, so only a brief summary of the available literature is presented here.

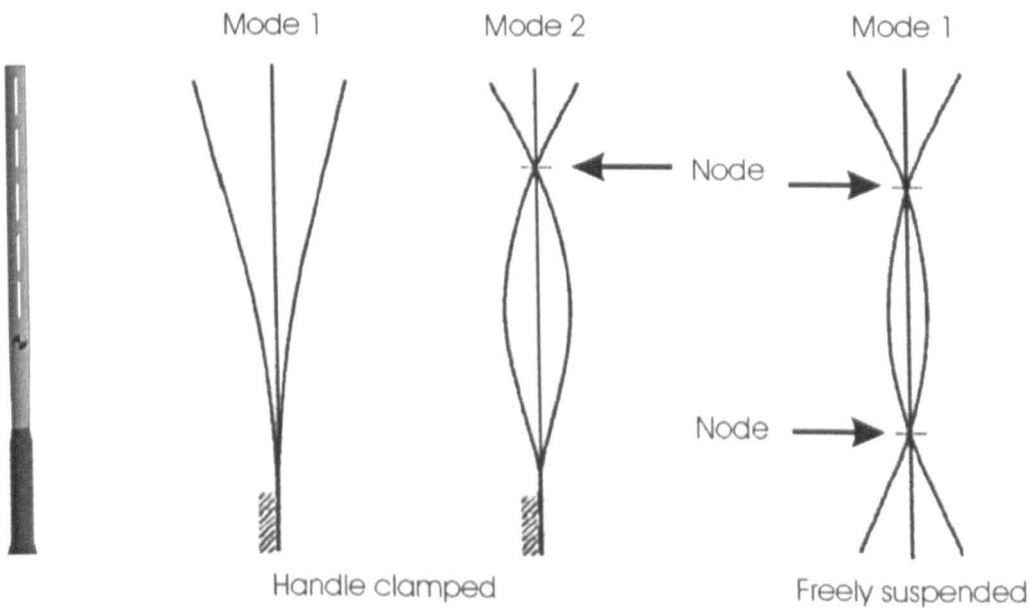

Figure 2.4 Vibration modes of a handle clamped and freely suspended racket. (Reproduced from Brody (1987)).

Brody (1981) combined his own data with that of Hedrick *et al.* (1979) to benchmark the modes of vibration for the two extremes of grip condition; handle clamped and freely suspended. This

comparison is shown in Figure 2.4. When a racket is handle clamped and a ball impacts on the stringbed it can oscillate in a number of modes. For a typical racket, the frequency of Mode 1 is 25-40Hz. The racket may also oscillate in Mode 2 (100-175Hz) providing the ball did not impact at the node of vibration, which is close to the centre of the stringbed. A freely suspended racket can not oscillate at a frequency comparable to Mode 1 of a handle clamped racket. Its lowest frequency is in the order of 100-175Hz.

Brody (1987) extended this analysis to compare the vibration of a hand held racket with the two extremes of grip condition. A modal analysis was conducted by attaching a thin piezoelectric film on the handle. The racket was struck with the ball at various points along the longitudinal axis to identify the node points and the induced vibration frequencies. It was determined that the head clamped Mode 1 frequency was not present in the hand held racket. The frequency of oscillation in the hand held racket was much closer to that of a freely suspended racket although no quantitative comparison was given.

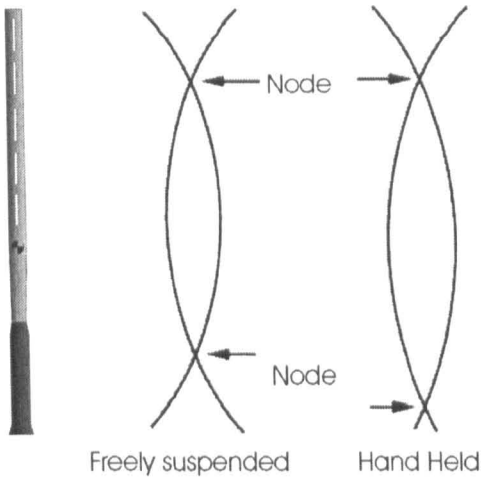

Figure 2.5 Comparison of fundamental mode of vibration for a freely suspended and hand held racket (reproduced from Cross (1998)).

A recent study which comprehensively covered the modal analysis of a tennis rackets was conducted by Cross (1998). A 1990 vintage Wilson graphite composite racket weighing 370g was used throughout the testing. Several piezoelectric transducers were placed along the handle and frame to identify the vibration frequency, mode shape and node location. Only the fundamental frequency of vibration was considered to be important as the higher frequency modes are small in amplitude and damp out very quickly (Brody (1979, 1981, 1995), (Cross (1997, 1999c)). The magnitude of the measured parameters for free and hand held conditions were 109Hz and 102Hz respectively for the vibration frequency, and 15cm and 5cm respectively for the node position (butt end). This shift in node point is illustrated in Figure 2.5. It was deduced that the hand held condition, which vibrated at 102Hz, was significantly closer to that of a free racket (109Hz) compared to a handle clamped racket (25-40Hz). An illustration was given which showed that adding a 40g mass to the handle of the freely suspended racket reduced the frequency from 109Hz to 103Hz and to 100Hz when an 80g mass was added. This showed that the observed frequency shift caused by the hand could be modelled by adding 40g to the handle, as noted by Brody (1995,

1997). However, it was noted that the shift in node position required an additional 80g to be added to the handle, which shows that further work would need to be done to define the precise mass required to simulate a player's grip.

Brody (1997) furthered this 'additional mass' theory by using a rigid body model to show that adding a mass at this point has negligible effect on the ball rebound velocity. This 'additional mass' theory is an interesting illustration and is only slightly flawed in that it does not truly account for the moment applied by the hand on the racket. However, Hatze (1976) has shown that the human hand can not apply a sufficiently high torque to affect the motion of the racket during impact anyway.

Cross (1998) showed that the axis of rotation, the point at which the racket is effectively stationary during impact, was the same for impacts between the GSC and the throat, for both methods of grip. It was also claimed that the axis of rotation was different for hand held and free racket conditions for other impact positions. This was based on velocity data for a range of points on the racket that was sampled for an 80ms period. It is accepted that the data suggests that the axis of rotation is shifted during this long time period. However, if only the data for the 5ms of impact is studied, the velocity of the racket appears identical for both grip conditions. Cross did not mention this. The analysis was continued and incorporated the momentum of the arm system to explain the shift in axis of rotation. It is commented that, after 10-20ms, the internal forces in the arm modify the initial response of the forearm. This implies that the response on the racket changes in the 80ms period which was initially used to conclude that the axis of rotation had shifted during impact. This confusion prevents any conclusions being drawn on the position of the axis of rotation for a hand held racket.

A similar analysis could be conducted, similar to that summarised by Hatze (1976), to determine whether the hand is strong enough to change the axis of rotation during impact. This would involve calculating the force that the hand would have to apply to the racket to make the axis of rotation be centred within the hand.

Hatze (1993) developed a theoretical model based on the energy losses in the ball, strings and frame. Experimental data was obtained for the ball rebound velocity for tests where the handle of the racket was either rigidly clamped or held in a manusimulator. The manusimulator was designed to realistically simulate the magnitude of force that a human hand can exert on the racket. It was found that generally the manusimulator gave higher ball rebound velocities than the handle clamped condition, by approximately 5-10%.. This lead Hatze to conclude that the level of grip firmness does effect the ball rebound velocity. The criticism here is that Hatze did not address the fact that the data suggests a firm grip (rigidly clamped) gives a lower ball rebound velocity than the hand grip (manusimulator). This contradicts findings by Hatze (1976) and Elliot (1982). The likely reason being that, yet again, an unrealistic rigidly clamped handle is used to represent a 'firm grip'; Brody (1987) having shown that the vibration mode excited in a handle clamped racket is not present in a hand held racket.

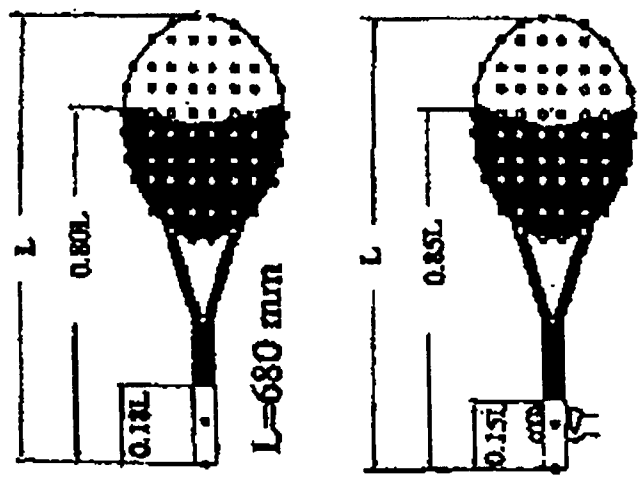

Figure 2.6 Node positions for the fundamental mode of vibration on (a) a freely suspended racket and (b) a hand held racket (Node lines represented by the boundary of the black and white regions) (Reproduced from Kawazoe (1997a)).

Kawazoe (1997a) performed an experimental modal analysis on a freely suspended and hand held racket. It was found that the fundamental frequencies for the freely suspended and hand held rackets were 122Hz and 117Hz respectively. The node positions for the two rackets are shown in Figure 2.6, which shows that the node near the handle is shifted by only 20mm (0.03L) when the racket was hand held. Cross (1998) obtained a similar difference in fundamental frequency but a larger shift in the node position (~100mm.) It was also claimed that the node near the centre of the stringbed shifts by approximately 35mm (0.05L), although the graphical results presented in the paper imply that it is shifted by a much smaller amount.

The work by Kawazoe (1997a) and Cross (1998) shows that the mode of vibration for hand held and freely suspended rackets are very similar, but the frequency and node positions are shifted slightly. Cross (2002b) extended the analysis to consider the modes of vibration of a pivoted racket. It was shown that a racket pivoted at the handle has a fundamental frequency of vibration of 85Hz, compared to 102Hz (hand-held) and 109Hz (freely suspended). The shift in the node for the hand-held racket, from its freely suspended racket position and the corresponding decrease in frequency, suggests that the vibration of a hand held racket lies somewhere between that of a freely suspended and pivoted racket. This implies that either a free or pivoted boundary condition was suitable to simulate a player's swing, although the comparison does suggest a slight bias towards the free condition.

An alternative approach to determine the ideal grip simulation is to discover why a handle clamped and freely suspended racket give similar ball rebound velocities. Brody (1997) commented that the transverse force wave that is induced from the ball impact must be reflected from the butt end and arrive back at the impact point during contact for the ball to have any knowledge of the gripping mechanism. The propagation time of the wave can be estimated from the frequency of the oscillation and the distance between the node points. Assuming a fundamental frequency of 150Hz

then the time taken is 8ms, which is longer than a typical contact time of 5ms. This implies that the ball has already left the stringbed before the impulse has returned. The ball rebound velocity is therefore independent of the gripping condition, which is why the handle clamped and freely suspended rackets give the same ball rebound velocity.

Cross (1998) analysed the wave propagation idea in more detail by performing both experimental and theoretical analyses. The propagation delay was measured by sampling piezoelectric disks which were placed at various points on the racket; one at the centre of the stringbed and one at each 50mm increment along the frame. It was found that the time taken for the pulse to travel from the centre of the strings to a point 120mm from the butt was 1.5ms. The racket handle therefore began to move well before the ball leaves the strings. This is much faster than that determined by Brody (1997) who only considered the fundamental mode of transverse vibration. In reality, the impact excites a broad spectrum of vibration frequencies which are superimposed to give the resultant motion. The higher frequency components, although small in amplitude, travel at a much faster speed and therefore result in the faster propagation time measured at 1.5ms.

The above discussion has shown that there is some conflict between the findings of the different authors in regard to the method of simulating a player's grip during impact. However, this can be clarified by considering the different impact positions separately.

(a) For impacts taking place between the GSC and the tip almost all authors agree that the ball rebound velocity is independent of grip firmness. The theoretical solutions predict that a free, handle clamped and pivoted handle all give the same ball rebound velocity. Experimental data shows that free, handle held and handle clamped conditions all give similar results. However, it was noted that are some anomalies identified between certain published data which requires clarification.

(b) For impacts taking place between the GSC and the throat, it is generally agreed that a grip clamped racket gives a higher ball rebound velocity compared with a freely suspended racket. However, it is shown that a grip clamped condition is not a realistic representation of a firm grip. Pivoted and free end conditions give similar results in this area.

(c) For impacts not on the longitudinal axis the published data implies that grip firmness does effect the ball rebound velocity.

Supplementary points to note are,

1. The mode of vibration of a hand held racket is closest to that of a freely suspended racket.
2. The theoretical time taken for the force wave to travel from the impact point, to the handle, and back is generally longer than the contact time, implying that the grip condition has no effect. However, this analysis only considers the fundamental transverse mode of vibration. The higher frequency modes will cause the gripping condition to effect the racket response. The magnitude of this effect being dependent on the amplitude of the mode.

The main conclusion from this section is that, for impacts along the longitudinal axis, a players grip can be replicated by a freely supported racket. Clearly this would initially imply that a racket must

be propelled freely at a ball in the laboratory. However, a simple transformation of the Newtonian reference frame, as discussed by Brody (1997), can be used to replicate the relative ball-racket impact velocities. For example, a typical serve can be simulated by propelling a tennis ball at 35m/s, towards a stationary racket (Mitchell *et al.* (2000)).

2.4.4 Coefficient of restitution for an impact between a ball and racket

The coefficient of restitution (*COR*) is a parameter which is used to indicate the proportion of recovered energy in a collision. In its reduced form it is defined as,

$$COR = \frac{(v'_B - v'_R)}{(v_B - v_R)} \qquad [2.1]$$

where v_B and v_R are the ball and racket velocities before impact, respectively, and v'_B and v'_R are the respective velocities after impact. The velocities v_R and v'_R are measured for the contact point of the racket. Initial investigation of published data identified that a wide range of *COR* values were being quoted by authors. This was primarily because the definition used by some authors differed from that in [2.1], and also the method used to restrain the racket differed.

1. *Coefficient of restitution for an impact on a head clamped racket*

The simplest, most unambiguous definition for *COR* is when the racket head is clamped, and therefore $v'_R = v_R = 0$. In this case, [2.1] reduces to,

$$COR_{HC} = \frac{v'_B}{v_B} \qquad [2.2]$$

Brody (1979) measured the values of COR_{HC} for a range of rackets and found them to be in the region of 0.85, for an impact velocity of 8.5m/s. Leigh & Lu (1992) used an impact velocity of 5.3m/s and obtained COR_{HC} of 0.90 and 0.85 for rackets strung at 178N and 356N respectively. This data showed that the COR_{HC} reduced with increasing string tension.

Kawazoe (1993) obtained a value of COR_{HC} equal to 0.83 for a ball impact velocity ranging between 15 and 25m/s. The racket was strung using natural gut (45lbs tension). By contrast the COR_{HC} for a synthetic gut (60lbs) reduced from 0.83 to 0.80 in this same velocity range. The natural gut was strung at a considerably lower tension than the synthetic gut and therefore it is difficult to draw comparisons between the two.

Williams (2000) performed an impact test which involved propelling a tennis ball at a range of points on a head clamped racket. The data was used to map the COR_{HC} distribution across the face, to give an indication of the magnitude of the area which could be considered to give a constant value of COR_{HC}. It was found that COR_{HC} was constant over an area approximately 60mm in diameter, centred at the GSC of the racket. The COR_{HC} then reduced towards the racket frame.

Goodwill & Haake (2000) determined COR_{HC} for standard and oversize tennis balls for a range of impact velocities between 20 and 50m/s, using a racket strung at 70lbs. It was shown that the value generally dropped from 0.83 to 0.75 over this large velocity range.

2. *Coefficient of restitution for an impact on a grip clamped racket*

If it is initially assumed that the recoil velocity of the racket can be ignored then the coefficient of restitution is defined as COR_{GC} and is calculated using,

$$COR_{GC} = \frac{v'_B}{v_B} \qquad [2.3]$$

If a tennis racket was rigid then clearly $COR_{GC} = COR_{HC}$. The published results confirm that this is not the case. Groppel *et al.* (1987b) propelled tennis balls at both midsize and oversize rackets which were clamped at the grip, and strung at a range of string tensions from between 40 and 80lbs using natural gut and nylon. The ball was propelled at 23m/s, at the geometric string centre of the racket. It was found that COR_{GC} typically ranged from 0.51 to 0.47 for a string tension range of 40 to 80lbs, for the oversize racket. For the same range of string tension the COR_{GC} reduced from 0.40 to 0.34 for the midsize racket.

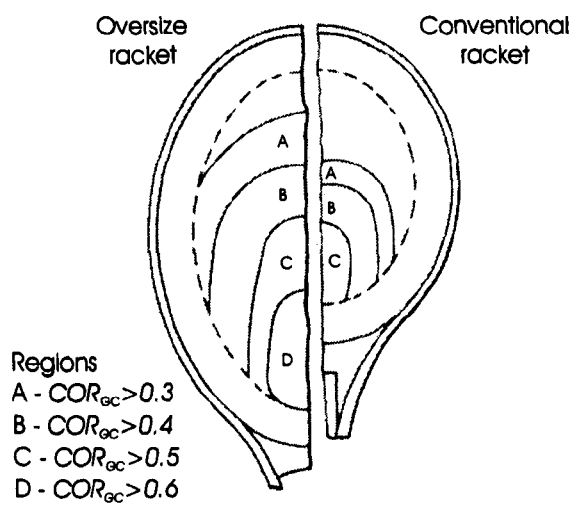

Figure 2.7 COR_{GC} distribution on a grip clamped racket for an oversize and conventional racket (reproduced from Head (1976)).

A comprehensive account of the coefficient of restitution for a grip clamped racket was given by Head (1976). The testing was conducted to illustrate the benefits of an oversize racket compared with a conventional racket. Figure 2.7 shows that the COR_{GC} increases towards the throat end of the racket and, due to its extended shape, is largest in the oversize racket. These values of coefficient of restitution are all much lower than those found for the head clamped racket. The increase in COR_{GC} at the throat is due to two main reasons, which have been thoroughly covered by many authors. Firstly, the racket is effectively stiffer at this point so less energy is 'lost' in the deformation of the racket (Brody (1997)). Secondly, the throat is closer to the racket COM and therefore the effective, or 'reduced', mass of the racket will be higher at this point (Kawazoe 1993). The ball velocity used by Head was between 30-60mph (13-36m/s) and the COR_{GC} data corresponds well with Groppel *et al.* (1987b) and other published material. The COR_{GC} is highest

along the longitudinal axis because off-centre impacts cause the racket to rotate around this axis due to the reduced 'effective' mass of the racket. The 'effective' mass was determined from the polar moment of inertia, which was highest for the oversize racket. This explains why the COR_{GC} was higher for this racket.

Groppel *et al.* (1987a) determined the coefficient of restitution for a range of grip clamped rackets, for impacts at the GSC. The obtained values of COR_{GC} were between 0.84 to 0.75 which are higher than those published by any other researcher. However, the anomaly was easily resolved in that Groppel included the recoil velocity of the racket in the calculation of COR_{GC}. Therefore [2.3] would need to be modified to incorporate this.

It should be noted that it was shown in section 2.4.3 that hand held and grip clamped rackets act very differently during impact, and therefore the results of COR_{GC} are mostly of academic interest.

3. *Coefficient of restitution for an impact on a freely suspended racket*

Many authors have conducted impact tests in which the ball is propelled at a freely supported racket (Watanabe *et al.* (1979), Hatze (1993), Brody (1997)). Generally the racket is stationary and either stands on its butt or is suspended from a small pin, and in this section it is assumed that the initial racket velocity is zero. The precise definition of *COR*, as given by [2.1], is the ratio of the separation and approach velocities of the ball and racket. As the racket will naturally recoil after impact, the correct definition of COR_{FS} is,

$$COR_{FS} = \frac{v'_B - v'_R}{v_B} \qquad [2.4]$$

An alternative definition of the *COR* is called the apparent coefficient of restitution, *ACOR* (Hatze 1993). Whilst this is not an exact term for the coefficient of restitution of the ball-racket interaction, if the only concern is the ball rebound velocity (as is true in many cases) then this *ACOR* term is adequate. It is defined as,

$$ACOR_{FS} = \frac{v'_B}{v_B} \qquad [2.5]$$

and therefore does not take into account the recoil velocity of the racket.

Brody (1997) measured the $ACOR_{FS}$ distribution along the longitudinal axis of a conventional tennis racket. The racket had a mass of 0.287kg, a balance point at 372mm from the butt and a swingweight of 0.0527kgm^2 (around the butt). The data for distinct points is shown in Figure 2.8. This shows that the $ACOR_{FS}$ increases from 0.17 at the tip to a maximum of 0.49 about 40mm from the throat section. At the throat section there is a slight decrease in $ACOR_{FS}$. Kawazoe (1993) using a different tennis racket but a similar ball impact velocity found different $ACOR_{FS}$ values along the longitudinal axis. Unfortunately Kawazoe did not give the details of the racket used in the testing, but clearly it is likely to be different to Brody's. Both $ACOR_{FS}$ distribution, and the likely reason for differences between Brody and Kawazoe, can easily be explained using a simple

rigid body model of the impact (Brody 1997). This model shows that $ACOR_{FS}$ is dependent on the mass and swingweight of the racket, and the impact position of the ball relative to the centre of mass. (The model is discussed in depth in section 2.5).

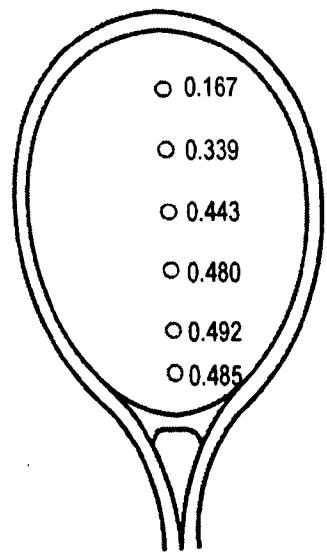

Figure 2.8 Apparent coefficient of restitution distribution for a stationary, freely suspended racket (reproduced from Brody (1997)).

Haake *et al.* (2000) determined the $ACOR_{FS}$ for impacts at the GSC of a racket with mass 343g, balance point of 320mm and swingweight 0.0505kgm^2 (referenced from the butt). The values reduced from 0.35 to 0.3 over the ball impact velocity range of 25m/s to 60m/s. This illustrates that $ACOR_{FS}$ reduces with impact velocity, as did the coefficient of restitution measured for an impact with a head clamped racket. The $ACOR_{HH}$ value at the GSC in Haake *et al.* is lower than that in Brody (1997). This can easily be accounted for using a rigid body model accompanying the fact that Brody's racket was considerably more 'head heavy' than that used by Haake *et al.*.

The above results show that $ACOR_{FS}$ varies greatly across a tennis racket, and is different for different rackets. This is clearly due to a combination of the mass/swingweight of the racket and the location of the impact. Therefore all $ACOR_{FS}$ data should be accompanied with this relevant extra data. This data can easily be used to predict how the racket will perform 'on-court' by changing the frame of reference so that the racket has an initially velocity (Brody (1997)).

4. *Coefficient of restitution for an impact on a hand held racket*

There is a limited amount of published material for the coefficient of restitution for an impact on a hand held racket. This data can easily be categorised into two main sets; the racket is held stationary and the racket is being swung by a player. The latter category is discussed in section 2.6, and the former is discussed below.

When a racket is held by a player it is very difficult to obtain the precise velocity of the racket immediately after impact. Three-dimensional marker systems have been used but the high accelerations involved around the time of impact make it difficult to measure an accurate velocity.

As for impacts on a freely suspended racket, a useful parameter is the coefficient of restitution which disregards the recoil velocity of the racket. This parameter is termed 'apparent' and the equation for $ACOR_{HH}$ is,

$$ACOR_{HH} = \frac{v'_B}{v_B} \qquad [2.6]$$

Elliot *et al.* (1980) performed $ACOR_{HH}$ measurements for a range of points along the longitudinal and transverse axes of the stringbed for conventional and oversize rackets. The racket was held stationary against a locating frame to ensure control of the impact positions and the ball was propelled at 21m/s (45mph). The vibration amplitude of the frame and the ball rebound velocity were measured using accelerometer and stroboscopic techniques respectively. Along the longitudinal axis the $ACOR_{HH}$ increased from almost zero at the tip to a maximum at 20mm from the throat, and then a slight reduction at the throat. Across the transverse axis the measurement was almost zero at the frame and a maximum at the longitudinal axis. The resulting $ACOR_{HH}$ map was similar to that found by Head (1976) for grip clamped rackets. The maximum values for the oversize and conventional rackets were 0.50 and 0.44 respectively. Also, for impacts off the longitudinal axis the difference is even greater. These maps confirmed Head's theory that the increase in polar moment of inertia for oversize rackets reduced the twisting of the racket during impact, and thus increased the ball rebound velocity. However, it should be noted that Elliott claimed that the determination of the polar moment of inertia of the rackets was beyond the scope of his paper.

2.4.5 The 'sweet spot' of a racket

In the last decade it has generally been impossible to see an advert for a new tennis racket which does not refer to the product as having a larger 'sweet spot'. The incentive for manufacturers to make these claims is that players are aware that a larger 'sweet spot' may improve their game due to the increased probability that they are able to hit the ball in this area. In these articles the implication is that the shot will 'feel sweeter' when the ball hits this position, although a precise definition of the claim is very rarely given. In the following review of the 'sweet spot', an attempt is made to highlight the definitions used by different authors to clarify what the manufacturers claims may be based upon. A very complete description of the sweet spot of a tennis racket can be found in Kotze (2000). This literature review is not intended to give a complete account of all available literature but it will clarify the terms used to quantify the positions which have become collectively known as the 'sweet spot'.

The earliest notable reference to the 'sweet spot' of a racket was in the US Patent for Prince's oversized racket (Head (1976)). It was claimed that its wider, longer head had a sweet spot or

power zone which was almost four times bigger than on a conventional racket. The size of this power zone was determined by propelling tennis balls at a grip clamped racket and measuring the COR_{GC} at various locations. The size of the sweet spot was defined as the area in which the COR_{GC} was greater than a certain level, as illustrated in Figure 2.7. The larger sweet spot has been achieved by effectively extending the stringbed closer to the racket COM. Also, the width of the racket head was increased which increased the polar moment of inertia, and thus reduced the magnitude of the twisting of the racket during impact. The combined effect of these two developments increased the size of the sweet spot on the racket.

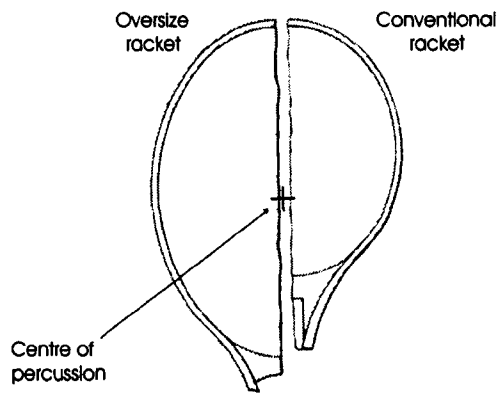

Figure 2.9 Comparison of the centre of percussion position for an oversize and conventional racket (reproduced from Head (1976)).

Head also described an alternative definition of the 'sweet spot' which was the point at which the hand experiences no linear impulse, or 'jar', when the ball is struck. This point was defined as the centre of percussion (COP) and is a function of the mass distribution along the longitudinal axis. The COP is described in more depth later in this section. On a conventional racket the COP is located near the throat but on the oversize racket it is located close to the GSC as illustrated in Figure 2.9. Head claimed that most players aim to hit the ball at the GSC, which was later supported by Hatze (1994), which highlighted the benefit of this oversize design.

Head's reported results for the COR_{GC} distribution clearly illustrate the benefits of the oversize racket design but their relevance to the playing characteristics of the racket is brought into question by the review of the literature regarding the simulation of player's grip. It has been shown that the grip clamped method is not representative of a player's grip. However, Head does illustrate why the maximum power region is close to the racket COM.

Head's patent was issued in 1976, around the time of the 'spaghetti' strung racket and the introduction of metal/composite rackets, and it was being acknowledged that the physics of a tennis racket was not very well established. Brody (1979) attempted to resolve this and identified information which could (a) explain the performance advantage of the Prince Oversize racket (Head (1976)) and (b) optimise the size, shape and weight of a tennis racket. A key area of this work was to further the understanding of the 'sweet spot'. The first point to be considered was the Centre of Percussion (COP) and a full derivation is given by Brody (1979). An illustration of the concept of the centre of percussion is given in Figure 2.10.

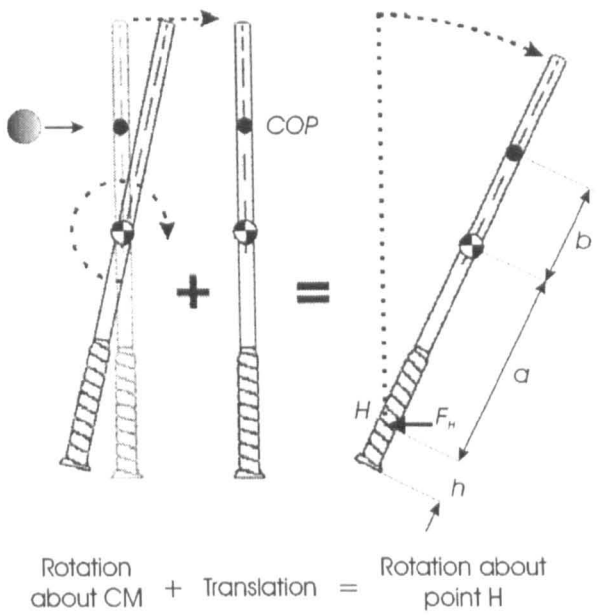

Figure 2.10 Illustration of the centre of percussion COP for a rigid body racket (Reproduced from Kotze (2000)).

The equation of the position of the COP in a rigid body is given in Brody (1979) as

$$b = \frac{I_R}{a.m_R} \qquad [2.7]$$

where I_R is the moment of inertia of the racket around its centre of mass, m_R is the mass of the racket and a is defined in Figure 2.10.

When a tennis ball hits the racket at a distance b from the racket COM there is no hand reaction force F_H, and therefore no overall 'shock' or 'jar' is felt during impact. This shows that the centre of percussion is not a unique position on the racket because it depends where the racket is gripped. Approximate values of h are 5cm and 7cm for a serve and ground stroke respectively. In a typical racket it can be shown that the COP lies between the throat and the GSC. Clearly a designer must attempt to make the position of the COP as close to the GSC as possible. Head (1976) achieved this by increasing the size of the head. An alternative method is to add weight to the tip of the racket to adjust the position of the COM (and increase I_R).

Another topic raised by Brody (1979) was how to maximise the ball rebound velocity. This questioned the argument that the COP was the best place to hit the ball. Head (1976) had determined that the coefficient of restitution would be maximised for impacts close to the racket COM, for an analysis on a grip clamped racket. If the analysis was extended to stationary, freely suspended rackets then a similar result would be obtained. However, it is noted that in a serve the actual point of maximum ball rebound velocity would be a function of the linear and angular velocity of the racket; the racket is rotating and therefore the tip is moving faster the COM. A simple rigid body analysis (Brody (1997)) can be used to predict the point on the racket which results in maximum ball rebound velocity. This quantifies the mechanics of the impact and illustrates how the ball rebound velocity is dependent on the effective mass of the racket at the

impact point. The racket mass is maximised when the player hits the ball on the longitudinal axis. However, this is not always achieved and therefore to increase the effective mass of the hitting point the polar moment of inertia must be maximised. This can either be achieved by increasing the width of the racket head, or by adding peripheral tungsten weights to the frame.

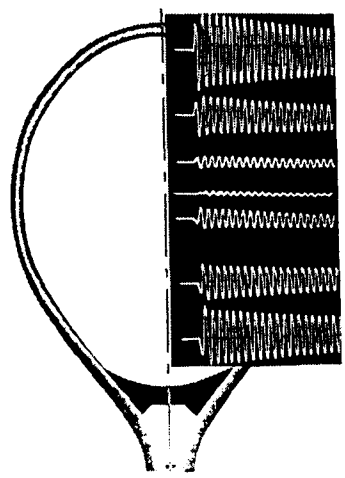

Figure 2.11 Measured vibration amplitudes along the longitudinal axis of a racket, illustrating a nodal point (Reproduced from Brody (1995)).

In section 2.4.3 the modes of vibration for a tennis racket were discussed. This analysis identified that a node point for the transverse mode was at a position approximately $^{1}/_{5}L$ along a racket of length L, from the tip (Kawazoe (1997a)). Hatze (1994) concluded that most players hit the ball at this nodal point of transverse vibrations. Impacts at this point clearly do not excite the fundamental frequency and therefore the player does not feel any unpleasant vibrations of the frame. This point is a further definition of the 'sweet spot'. Brody (1995) illustrated the vibration amplitudes for a range of points along the longitudinal axis of the racket and this is shown in Figure 2.11. This diagram illustrates that, for impacts at the node, there was very little vibration of the frame and therefore the energy loss was minimised.

A final definition of a 'sweet spot' was defined by Cross (1997) and called, rather ironically, the 'dead spot'. This is a point close to the tip, at which a ball impacts on a stationary freely suspended racket and rebounds with almost zero velocity, hence the term 'dead'. This is explained by considering the law of conservation of momentum and a knowledge that the effective mass of the impact point on the racket is similar to that of the ball. (Cross uses an analogy of a moving and a stationary snooker ball colliding head-on, where the momentum is transferred wholly from one to the other). It is assumed that in a serve the racket is rotating around a point close to the butt end (Mitchell *et al.* (2000)), and the ball impacts at the 'dead spot'. Given the correct linear and angular velocity of the racket, the racket will be brought to rest and the maximum momentum will be transferred to the ball. This impact point is close to the tip and, as Figure 2.11 suggests, this excites considerable vibrations in the frame, dissipating the maximum possible amount of available energy. Therefore this point may not 'feel' the best place to hit a ball as it leads to unpleasant vibrations and possibly fatigue.

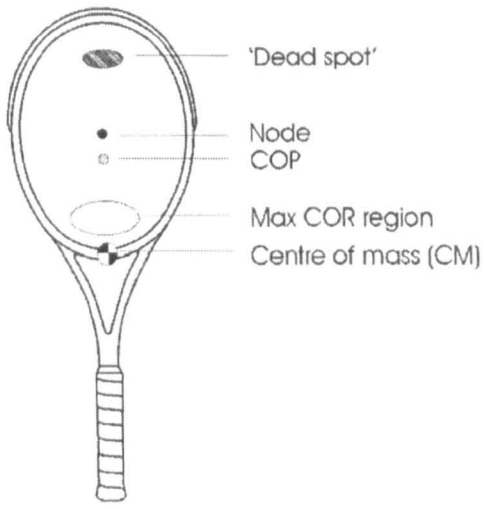

Figure 2.12 Illustration of the four definitions of a sweet spot (Reproduced from Kotze (2000)).

In this section four definitions have been discussed for the point commonly known as the 'sweet spot' and these are shown in Figure 2.12. They are,

1. Maximum coefficient of restitution – For a stationary racket this is located close to the racket COM, and results in the maximum ball rebound velocity. For a moving racket, the precise location of the maximum ball rebound velocity is dependent on the linear and angular racket velocity.
2. The Centre of Percussion – This is located near the GSC and represents the impact point which results in minimum 'jar' felt by the hand. This is dependent on the inertia of the racket and the grip position.
3. Node – This is the impact point which results in minimum vibration of the transverse mode of bending for a hand-held racket.
4. The 'Dead spot' – This point results in the maximum transfer of momentum from the racket to the ball, during a typical serve, for a given racket velocity.

2.5 Modelling of the Ball and Racket during Impact

Published research on the general modelling of sports ball impacts can be categorised into four main areas,

1. Rigid body analysis based on classical Newtonian mechanics
2. Flexible body analysis based on classical Solid mechanics.
3. Visco-elastic models in which the displacements of the two impacting bodies are modelled as a combination of springs and dampers.
4. Finite element analysis of the impact mechanism.

The published models vary in their applicability, accuracy and thoroughness, and these points are discussed in the following literature review. A complete model would be able to predict the compression and displacement of the colliding bodies during contact, and then predict the resulting velocity of the two objects after impact. The input parameters to this model would typically be the initial velocities and the physical properties of the bodies (eg. ball stiffness). Also, the boundary conditions must be suitably modelled (eg. player's grip).

2.5.1 Rigid Body Analysis

(a) Modelling an oblique impact between a ball and surface

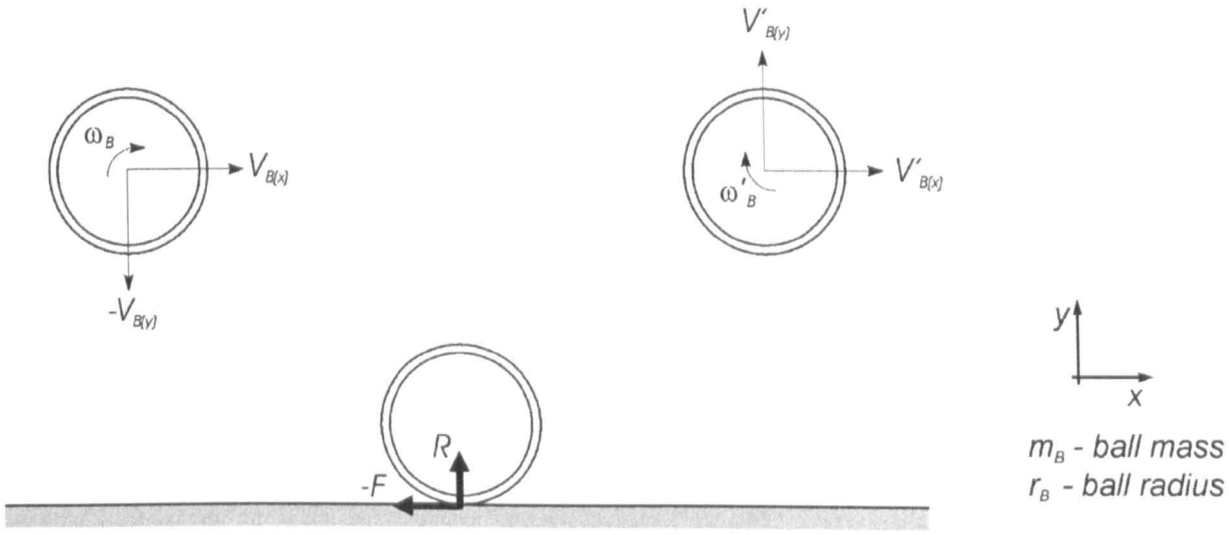

Figure 2.13 The impact between a rigid hollow sphere and a rigid surface.

The most comprehensive studies of rigid body ball-surface impacts have been conducted by Daish (1972) and Brody (1984). Both papers discuss the basic mechanism occurring during the impact between a rigid sphere and surface, as illustrated in Figure 2.13. This figure shows a rigid hollow ball travelling from left-to-right, impacting on a rigid surface – the positive x and y directions are shown by the co-ordinate system and the angular velocity is shown as positive. During impact a frictional and reactive force, F and R respectively, act on the sphere. The sphere has a mass of m_B

and radius r_B, and if it is assumed that the wall thickness is thin then its moment of inertia is $I_B = \frac{2}{3} m_B r_B^2$.

Daish and Brody state that there are two possible cases, depending on the magnitude of the friction.

1 – Ball slides throughout impact

In this case sliding friction applies throughout and therefore

$$F = -\mu_S R \qquad [2.8]$$

where μ_S is the sliding friction. Considering the impulses acting on the ball,

$$m_B\left(V'_{B(x)} - V_{B(x)}\right) = \int F.dt \qquad [2.9]$$

$$m_B\left(V'_{B(y)} - V_{B(y)}\right) = \int R.dt \qquad [2.10]$$

$$I_B\left(\omega'_B - \omega_B\right) = -r_B \int F.dt \qquad [2.11]$$

The coefficient of restitution is defined as

$$e = -\frac{V'_{B(y)}}{V_{B(y)}} \qquad [2.12]$$

[2.8] - [2.12] can be used to derive the following equations

$$V'_{B(x)} = V_{B(x)} - \mu_S V_{B(y)}(1+e) \qquad [2.13]$$

$$V'_{B(y)} = -eV_{B(y)} \qquad [2.14]$$

$$\omega'_B = \frac{3\mu_S V_{B(y)}}{2r_B}(1+e) + \omega_B \qquad [2.15]$$

[2.13]-[2.15] can be used to determine the rebound parameters $V'_{B(y)}$, $V'_{B(x)}$ and ω'_B if the parameters μ_S and e are known.

2 – Ball rolls off the surface

In this case [2.9]-[2.12] still apply, but it is no longer valid to assume that $F = \mu_S R$. Equating [2.2] and [2.4] gives,

$$\left(V'_{B(x)} - V_{B(x)}\right) m_B = -\frac{I_B}{r_B}\left(\omega'_B - \omega_B\right) \qquad [2.16]$$

$$\left(V_{B(x)} - V'_{B(x)}\right) = \frac{2r_B}{3}\left(\omega'_B - \omega_B\right) \quad [2.17]$$

And for the ball to be rolling at the end of impact,

$$\omega_B' = \frac{V'_{B(x)}}{r_B} \quad [2.18]$$

Substituting [2.18] into [2.17] gives

$$V'_{B(x)} = \frac{3V_{B(x)} + 2r_B\omega_B}{5} \quad [2.19]$$

$$V'_{B(y)} = -eV_{B(y)} \quad [2.20]$$

$$\omega'_B = \frac{3V_{B(x)} + 2r_B\omega_B}{5r_B} \quad [2.21]$$

This second case will apply if the friction is sufficiently great. The minimum value of μ_S for rolling to occur is defined by,

$$\mu_S \geq \frac{2\left(V_{B(x)} - r_B w_B\right)}{5V_B(1+e)} \quad [2.22]$$

The above formula can be used to obtain a basic understanding of the mechanisms occurring in an oblique impact between a ball and stringbed. However, the assumption that a ball (and stringbed) is rigid is the main weakness of the model as they both deform considerably. Brody (2000) develops these rigid body formulae to account for the fact that the ball COM deforms during impact.

Although it is not explicitly stated in this paper, Brody's analysis assumes that the ball slips throughout impact therefore the following equations still apply,

$$F = -\mu_S R \quad [2.23]$$

$$m_B\left(V'_{B(x)} - V_{B(x)}\right) = \int F.dt \quad [2.24]$$

$$m_B\left(V'_{B(y)} - V_{B(y)}\right) = \int R.dt \quad [2.25]$$

where μ_S is the sliding friction.

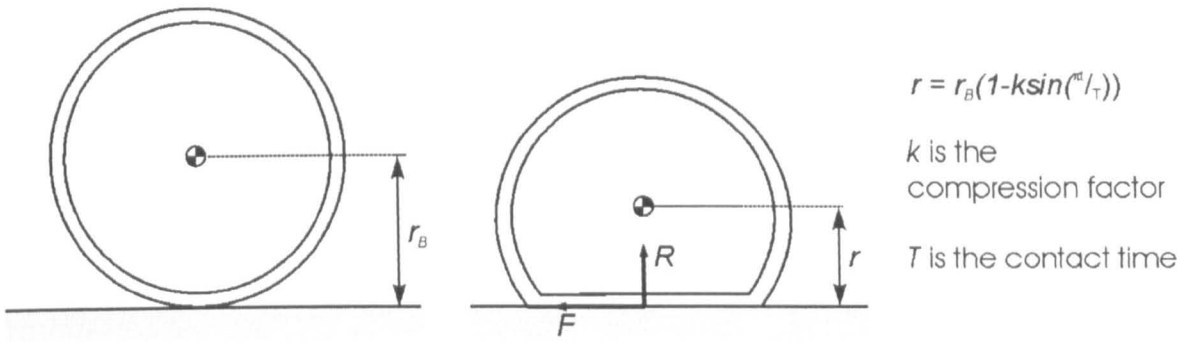

Figure 2.14 Definition of the parameter r which defines the deformation of the ball during an oblique impact (deduced from Brody (2000)).

Figure 2.14 shows the assumed motion of the ball COM during impact and the resulting distance between the COM and surface, r. Brody assumed this to be,

$$r = r_B\left(1 - k\,sin\left(\frac{\pi t}{T}\right)\right) \qquad [2.26]$$

where k is a constant, T is the contact time and t the instant during contact.

k can be considered a compression factor and defines the maximum displacement of the COM as a ratio of the original radius, r_B. From [2.26] it can be deduced the motion of the ball COM is undamped simple harmonic motion, although this was not actually stated in Brody (2000). In this paper it is assumed that the moment of inertia does not change throughout impact and is equal to that of a hollow sphere which is,

$$I_B = \frac{2}{3} m_B r_B^2 \qquad [2.27]$$

For simple harmonic motion the general equation for the force F is,

$$F = Q\,sin\left(\frac{\pi t}{T}\right) \qquad [2.28]$$

where Q is a constant.

Considering the angular impulse acting on the ball gives,

$$\int I_B . d\omega_B = \int (F.r) dt \qquad [2.29]$$

Substituting [2.28] into [2.24] and integrating between t=0 and t=T gives,

$$Q = -\frac{m_B \pi}{2T}\left(V'_{B(x)} - V_{B(x)}\right) \qquad [2.30]$$

From [2.29]

$$\frac{I_B}{r_B}\left(\omega'_{B(x)} - \omega_{B(x)}\right) = -\int_0^T \left[\frac{m_B \pi}{2T}\left(V'_{B(x)} - V_{B(x)}\right)\sin\left(\frac{\pi t}{T}\right)\right]\left[1 - k\sin\left(\frac{\pi t}{T}\right)\right] dt \qquad [2.31]$$

Which gives,

$$\omega'_{B(x)} = \omega_{B(x)} + \frac{3}{2r_B}\left(1 - \frac{k\pi}{4}\right)\left(V'_{B(x)} - V_{B(x)}\right) \qquad [2.32]$$

[2.32] shows that the rebound spin can be determined from the compression of the ball, k, and the change in the *x-component* of the ball velocity $\left(V'_{B(x)} - V_{B(x)}\right)$. The main weaknesses of this model are that it assumes that the ball slips throughout impact, and that the impact is perfectly elastic, i.e. the *COR* is unity. However, the analysis could easily be repeated with modified assumptions.

(b) Modelling a normal impact between a tennis racket and ball

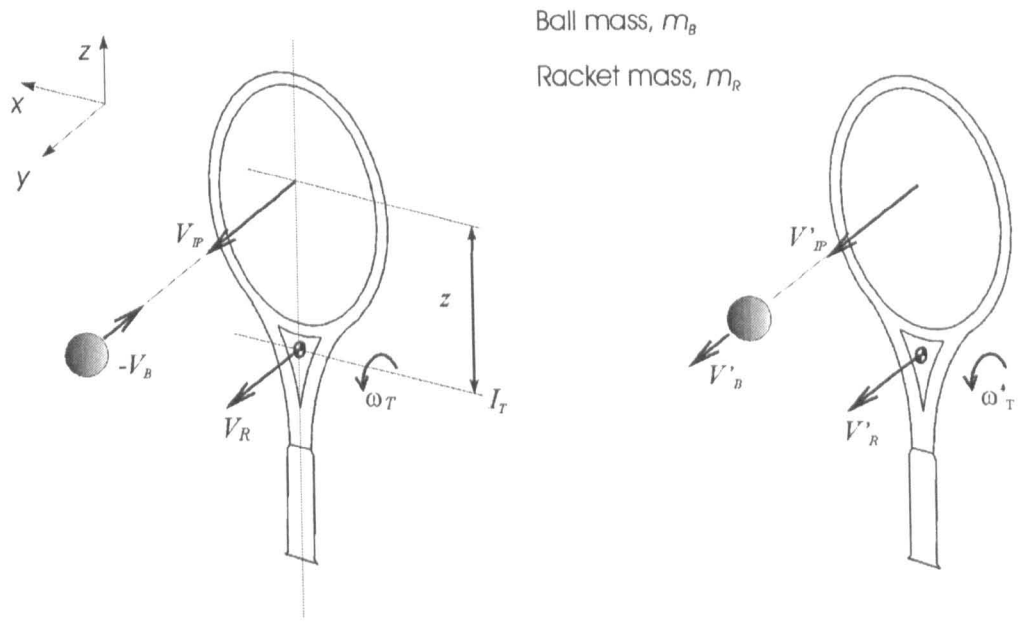

Figure 2.15 Rigid body model of an impact between a ball and freely suspended racket

A tennis racket is constructed using a material which clearly has a finite stiffness and is therefore not rigid. Whilst it is never claimed that a rigid body model of the racket can be used to fully analysis an impact, it can be used as a first approximation to understand the fundamental dynamics that occur during impact. Indeed, modelling a tennis racket as a rigid body is one of the most common methods for this piece of equipment (Liu (1983), Casolo & Ruggieri (1991), Kawazoe (1997a), Brody (1997), Cross (1999c , 2000e)).

Brody (1997) gives the most succinct account of the application of a one-dimensional rigid body model of a tennis racket. Figure 2.15 defines the parameters for an impact between a tennis ball and freely supported racket. Brody used the conservation of both linear and angular momentum to determine the velocity of the ball and racket after impact.

By conservation of linear momentum,

$$m_B V_B + m_R V_R = m_B V'_B + m_R V'_R \qquad [2.33]$$

By conservation of angular momentum,

$$m_B V_B z + I_R \omega_T = m_B V'_B z + I_R \omega'_T \qquad [2.34]$$

Using the definition of the coefficient of restitution,

$$COR = -\frac{V'_B - V'_{IP}}{V_B - V_{IP}} \qquad [2.35]$$

where V_{IP} and V'_{IP} are the velocity of the impact point before and after impact, respectively.

Solving [2.33]-[2.35] gives

$$V'_B = \frac{V_B\left(m_B z^2 + I_R\left(\frac{m_B}{m_R} - COR\right)\right) + V_{IP} I_R (1 + COR)}{m_B z^2 + I_R\left(1 + \frac{m_B}{m_R}\right)} \qquad [2.36]$$

[2.36] gives the rebound velocity for an impact between a ball and racket, for specific initial conditions. The value of V_B is a function of a group of known variables (m_B, m_R, z, I_R) and an unknown variable (COR). In Brody (1997) it was assumed that the value of COR was 0.85, which was the coefficient of restitution determined for an impact between a ball and head-clamped racket. In this paper the racket was initially at rest (i.e. V_{IP}=0). Both theoretical and experimental data was obtained for ball rebound velocity for impacts at various points along the longitudinal axis, at an impact velocity of 20m/s. Comparison of these two sets of data showed that the model was in good agreement with the experimental data for impacts close to the GSC, but less accurate for impacts close to the throat or tip. This is most likely to be due to the fact that the GSC corresponds very closely to the node of vibration. Therefore vibrational energy losses are minimised at this point and the rackets acts very similar to a rigid body. At other points the rigid body model overestimates the ball rebound velocity.

2.5.2 Flexible Body Analysis

(a) The Racket

In the previous section the racket was modelled as a freely suspended, rigid body. It was shown that this model was accurate for impacts at the GSC, but less reliable for impacts away from this point (Brody (1997), Goodwill & Haake (2001)). This has been accounted for by the fact the GSC corresponded to a node of vibration for the transverse fundamental frequency of a tennis racket and therefore the energy losses due to vibration were minimal at this point. Cross (1999c) comments that a rigid body model uses contradictory boundary conditions because (a) it is assumed that the propagation time of the force pulse to be reflected back from the handle is greater than the contact time, and (b) by assuming a rigid body, the propagation time for a pulse to travel this distance is infinitely short.

To predict the vibration energy losses in a tennis racket, the frame can be modelled as a simplified geometrical shape, which can be given finite material properties. Although a racket frame is a relatively complex shape many authors (Brody (1987), Kawazoe (1997a), Cross (1998)) have shown that the vibration modes and location of the nodes for a freely suspended racket are very

similar to the well established result for a simple one-dimensional beam (as shown previously in Figure 2.4). Van Zandt (1992) successfully studied the vibration of a baseball bat by assuming that the geometry could be simplified to a one dimensional beam with a non-uniform mass distribution.

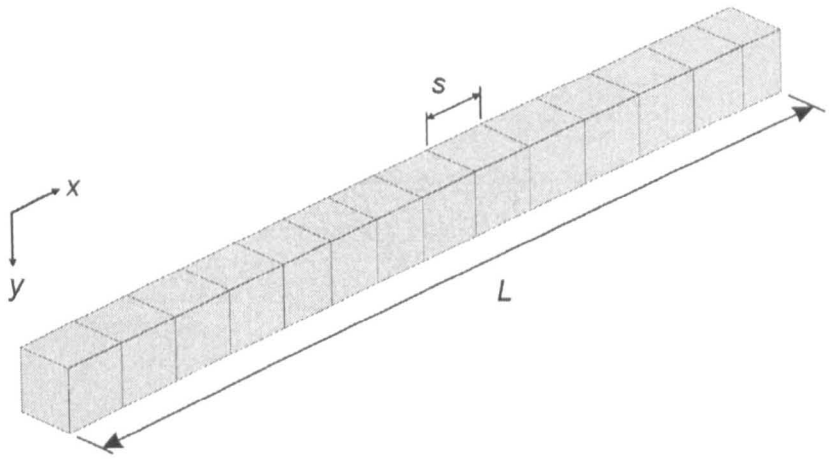

Figure 2.16 Segmented uniform beam.

Cross (1999c) performed a theoretical study to model the impact between a ball and a uniform aluminium bar. The model results were compared with experimental data for a range of boundary conditions and beam dimensions, and the findings were related to the impact between a ball and tennis racket. The equation of motion for a one dimensional beam subjected to a distributed force, F_0 per unit length, has the form (Goldsmith 1960),

$$\rho A \frac{\partial^2 y}{\partial t^2} = F_0 - \frac{\partial^2}{\partial x^2}\left(EI \frac{\partial^2 y}{\partial x^2} \right) \qquad [2.37]$$

where ρ is the density of the beam, A is its cross-sectional area, E is the Young's modulus, I is the area moment of inertia and y is the transverse displacement of the beam at coordinate x along the beam, as defined in Figure 2.16.

This equation neglects the shear force which is of negligible significance for the low frequencies of vibration which are of most interest in this work (Van Zandt 1992). In this case the beam is uniform and has a mass M and length L. A numerical solution of [2.37] can be obtained by splitting the beam into N equal sized segments, where the mass of each element is $m_N=M/N$ and the length of each segment is $s=L/N$.

The equation of motion for the nth segment is obtained by multiplying all terms in [2.37] by s, which gives,

$$m_N \frac{\partial^2 y_n}{\partial t^2} = F_0 s - \left(EIs \frac{\partial^4 y_n}{\partial x^2} \right) \qquad [2.38]$$

Although the force exerted by the ball may act over a number of segments it was assumed only one segment was subjected to a time-dependent force, F. The equation of motion for this segment is given by,

$$m_N \frac{\partial^2 y_n}{\partial t^2} = F - \left(EIs \frac{\partial^4 y_n}{\partial x^4} \right) \quad [2.39]$$

and for all other segments,

$$m_N \frac{\partial^2 y_n}{\partial t^2} = -\left(EIs \frac{\partial^4 y_n}{\partial x^4} \right) \quad [2.40]$$

In this case it was assumed that, as the beam was uniform, the values of E and I were constant along the beam. The possible types of boundary conditions are as follows,

1. At a freely suspended end – $\left(\frac{\partial^2 y}{\partial x^2} = 0 \right)$ and $\left(\frac{\partial^3 y}{\partial x^3} = 0 \right)$
2. At a rigidly clamped end – $(y = 0)$ and $\left(\frac{\partial y}{\partial x} = 0 \right)$
3. At a pin-jointed end – $(y = 0)$ and $\left(\frac{\partial^2 y}{\partial x^2} = 0 \right)$

The ball was modelled as a simple spring, with an assumed spring constant k_B, and this gives an equation of motion,

$$m_B \frac{\partial^2 y_B}{\partial t^2} = -F = -k_B (y_B - y_n) \quad [2.41]$$

The subsequent motion of the ball and beam was evaluated numerically using finite difference equations of [2.39]-[2.41]. The exact details of this technique are thoroughly explained in Cross (1999c).

The validity of the model was assessed by comparing the results with those for an experimental impact between a superball COR on a rigid surface (e = 0.85) and aluminium rod, for various rod dimensions and impact points. The vibration of the rod and the rebound ball velocity were compared with theoretical results and a high accuracy was obtained.

The paper carries on to describe the application of this method to the modelling of a tennis racket-ball impact. It is stated that the vibration modes and node locations of a racket can be accurately modelled by assuming that the racket behaves like a uniform beam. The zero frequency response of the racket will clearly only be modelled by the one dimensional beam for impacts along the longitudinal axis. It was still assumed that the ball only impacts on one of the N segments.

The paper gave a very good model for an impact between an aluminium bar and a ball, with experimental evidence to verify it. However, there was no experimental work done to validate the use of a uniform beam to model a tennis racket which would clearly be the next stage for this work.

Cross (2001b) advances the work of Cross (1999c) by assuming that the racket can be modelled as a one dimensional beam with a non-uniform mass distribution. This work discusses the effect of the mass distribution on the swingweight of the racket. It was assumed that the mass distribution of the racket can be simulated using a beam which is split into two equal lengths. The mass of each of these lengths was chosen to give the desired balance point for the racket. It was assumed that the values of E and I were constant along the bar, as much of the racket was made from a constant section beam. The accuracy of the model prediction for ball rebound velocity was tested for a ball impact velocity of only 1.6m/s. It is appreciated that this is not representative of the velocities used in tennis, but the aim of this paper was to investigate the effects of adding mass to certain sections of the racket. However, yet again the main criticism was that the model was not tested for high speed impacts.

Missavage *et al.* (1984) performed a theoretical analysis of the impact between a tennis ball and racket and simplified the frame and stringbed as a non-uniform one dimensional elastic beam, similar to Cross (1999c, 2001b). The model was more complex than Cross as it accounts for the shear force in the beam and assumed that the applied force acted uniformly over the entire head of the racket. An attempt was made to model the racket very precisely by determining the magnitude of the cross-sectional area and area moment of inertia as a function of the position along the racket. This was achieved by cutting the racket into 22 pieces. The beam was clamped at the butt end and free at the other, and the model was used to prove that the moment acting on the clamped end was zero during impact, for a regular racket. As with Cross (1999c, 2001b) no actual quantitative comparison was made between the model and experiment for realistic ball-racket impact velocities.

Brannigan & Adali (1981) constructed a mathematical model of a ball hitting a tennis racket. The individual components of the racket, for example the strings, were modelled discretely. The aim was to develop a model which could be used to investigate the contribution of each constituent of the racket on the ball rebound velocity and vibration of the racket. The standard equation [2.37] for a one dimensional, elastic beam subjected to bending was used, but parameters were also added to account for the material damping of the frame and the stiffness/damping of the hand. The ball was modelled as an undamped spring with constant stiffness. It was assumed that the force travelling through the stringbed arrived simultaneously at the racket rim. Incorporating damping into the material and accounting for the soft tissue in the hand, meant that the vibrations died out as they are found to do experimentally. However, it was not stated precisely how the level of damping effects the ball rebound velocity.

The main conclusion regarding the flexible beam modelling literature is that models already exist but they have not been experimentally verified for tennis ball-racket impacts, at high velocities.

(b) The Ball

Hubbard & Stronge (2001) used a table tennis ball to illustrate the mechanism of a hollow ball bouncing on a flat surface. In this study analytical equations were developed for the individual components which make up the stiffness of the ball, i.e. the shell stiffness and internal air pressure. These equations were used to model the impact of the ball on a flat surface. The model was

simplified so as not to include hysteresis losses in the materials, but did account for the contribution made by the momentum flux component of the force which acts on the ball. During the compression phase, an increasingly large proportion of the ball, that was initially moving towards the surface, will be brought to rest. The force due to the momentum flux is equal to the rate of change of momentum of the volume of material which is being brought to rest on the surface. The momentum flux is tensile during the restitution phase and therefore does not contribute to the force in this stage.

The analytical equations for the momentum flux force require an assumption to be made regarding the shape of the deformed ball. Hubbard & Stronge assumed that the ball shape was a truncated sphere throughout impact and that each point on this sphere was moving at an identical velocity. A similar study had been previously conducted for footballs by Johnson *et al.* (1972) and Percival (1976). Percival also assumed that the shell was inextensible and the undeformed section of the shell remained spherical. High speed video images of a tennis ball impacting on a rigid surface show that this assumption may be justified for low speed impacts but becomes less accurate at high speeds. Also, Hubbard & Stronge, Johnson *et al.* and Percival do not account for any material hysteresis losses which occur during the impact.

To apply a model such as Hubbard & Stronge to a tennis ball, analytical equations for the stiffness of the sphere need to be generated, and a method of introducing material damping would also be required.

2.5.3 Visco-Elastic models

Many authors (Haake (1989), Leigh & Lu (1992), Lieberman & Johnson (1994), Dignall & Haake (2000b), Pratt (2000), Carré (2000)) have attempted to use a visco-elastic model to simulate a sports ball-surface impact. These models use a combination of springs and dashpot dampers to represent the stiffness and damping respectively of the components in the impact.

(a) The Ball

Dignall & Haake (2000b) and Pratt (2000) used a simple 1 degree of freedom (1-DOF) model to simulate the normal impact between a tennis ball and rigid surface, as shown in Figure 2.17. The displacement x_B represents the motion of the centre of mass (COM) of the ball m_B. In this model the values of k_B and c_B represent the linear stiffness and damping of the ball. Both authors assumed that the values of these parameters were constant throughout impact, although they may vary with ball impact velocity. The governing equation for this system is,

$$m_B\ddot{x}_B + c_B\dot{x}_B + k_B x_B = 0 \qquad [2.42]$$

Given the first initial condition of $x_B = 0$ at time $t = 0$, the solution to [2.42] is,

$$x_B = ae^{-bt}\sin(\omega t) \qquad [2.43]$$

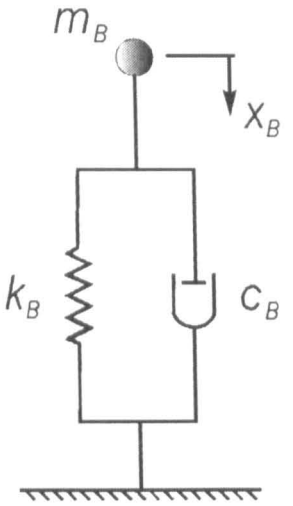

Figure 2.17 Kelvin-Voigt spring-dashpot model of a tennis ball impact on a rigid surface

Differentiating [2.43] gives

$$\dot{x}_B = ae^{-bt}\left[\omega\cos(\omega t) - b\sin(\omega t)\right] \qquad [2.44]$$

and

$$\ddot{x}_B = ae^{-bt}\left[\left(b^2 - \omega^2\right)\sin(\omega t) - 2b\omega\cos(\omega t)\right] \qquad [2.45]$$

It was assumed that the displacement of the ball COM would be zero at the end of impact, which is supported by the experimental data in Cross (1999a). Therefore a second initial condition is $x_B = 0$ at $t = T_C$ where T_C is the contact time. This gives,

$$\omega = \frac{\pi}{T_C} \qquad [2.46]$$

Two more initial conditions are obtained by substituting the incoming and outgoing ball velocities, V_B and V'_B, into [2.46] which gives,

$$\dot{x}_{t=0} = V_B = a\omega \qquad [2.47]$$

$$\dot{x}_{t=T_C} = V'_B = a\omega e^{-bT_C} \qquad [2.48]$$

Equating [2.46] and [2.47] gives

$$a = V_B \frac{T_C}{\pi} \qquad [2.49]$$

Equating [2.47] and [2.48] gives

$$b = -\frac{1}{T_C}\ln(e) \qquad [2.50]$$

where e is the coefficient of restitution.

Dignall & Haake assumed that the contact time was very similar to that of an undamped model and therefore the stiffness parameter k_B was determined using,

$$k_B = m_B \frac{\pi^2}{T_C^2} \qquad [2.51]$$

And for the damping parameter c_B

$$c_B = -\frac{2m_B}{T_C} \cdot \ln(e) \qquad [2.52]$$

Dignall & Haake illustrated how k_B and c_B could simply be obtained from the experimentally measured values of T_C and e, obtained using a force platform and light beam timers. It was shown that the stiffness k_B increased from 28kN/m to 41kN/m for a ball impact velocity ranging from 6m/s to 20m/s. The damping coefficient c_B increased from 6Ns/m to 15Ns/m in the same velocity range. The stiffness values that were published suggested a linear relationship between k_B and the ball impact velocity V_B. Also, a linear fit was found between the c_B and V_B. Unfortunately only a very small number of data points were used to support this claim. Also, this work involved the modelling of surfaces and therefore the maximum ball impact velocity was 20m/s. This may not be high enough to encompass the magnitude of ball deformations found in an impact between a ball and racket.

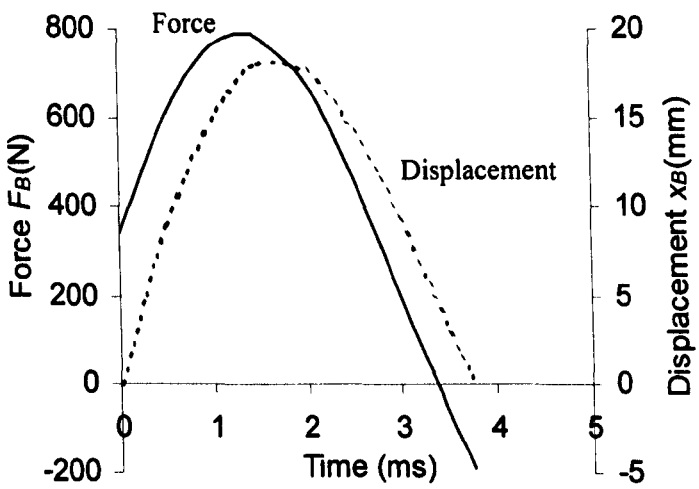

Figure 2.18 *Force-Time* and *Displacement-Time* curves for a one degree-of-freedom spring damper model of a ball impact on a rigid surface (ball impact velocity = 20m/s)

Pratt (2000) illustrated another weakness of this model by way of the obtained *Force-Time* curve. A similar plot is shown in Figure 2.18. In the last 0.5ms of the restitution phase the force F_B acting on the ball is negative, implying a tensile force which is not physically possible. During this period the ball centre-of-mass displacement x_B is still positive. However, the magnitude of the damping force exceeds that of the stiffness force resulting in a negative force.

(b) The Ball and Racket

Leigh & Lu (1992) determined a visco-elastic model for an impact between a ball and a handle clamped racket. The model was constructed in three stages, the first being to model the impact

between a ball and rigid surface. This model contained a spring and damper in parallel, as in Dignall & Haake (2000b), but it was assumed that the stiffness parameter was a function of the ball COM displacement, and defined using

$$k_B = k_0 + n_B x_B^{\ 2} \qquad [2.53]$$

where k_0 is 18.44kN/m and n_B is 23860kN/m^3.

Equation [2.53], and the coefficients k_0 and n_B, were determined from quasi-static compression data. This data was modified to account for the different shapes of the deformed balls found in a static compression test between two flat plates compared to a dynamic impact. This modification was based on the assumption that the ball only deforms on one side during a dynamic impact, and therefore the measured quasi-static deformation should be halved. No data is presented to validate this assumption.

It was assumed that the damping was linear and also the force due to gravity was accounted for. Many authors, for example Brody (1984), have shown that the gravitational force is negligible. The governing equation for a vertically moving ball hitting a rigid surface is,

$$m_B \ddot{x}_B + c_B \dot{x}_B + k_0 x_B + n_B x_B^{\ 3} - m_B g = 0 \qquad [2.54]$$

There is no analytical solution for this equation and therefore a numerical method, utilizing the Newton-Raphson iteration procedure, was required. This calculation method was used to determine the value of the damping coefficient c_B for an experimentally determined coefficient of restitution for the impact between a ball and rigid surface. An impact velocity of 7m/s gave a value of c_B equal to 6.7Ns/m, comparable with Dignall & Haake.

The next stage of the investigation was to model the impact between a ball and head clamped racket. The stringbed was modelled as a spring with no damping. Research by the authors showed that the energy losses in the stringbed were negligible. The stiffness of the stringbed was found from a quasi-static compression test of the stringbed in which the force was applied by the ball. The details of the complete model of a ball impact with a stringbed are covered in detail in Leigh & Lu. The model was solved by numerical methods as before. Good correlation was found between the model and experimental ball rebound velocities, although the maximum ball impact velocity was only 7m/s.

The final stage of the work was to model the impact between a ball and handle clamped racket, and this is shown in Figure 2.19. The racket was modelled as an equivalent lumped mass supported by a linear spring and linear damper in parallel. The values of k_R and c_R were taken from other researcher's work, and the mass m_R was determined using the assumption that the racket was a uniform beam. By equating the natural frequency of a uniform beam with that of a lumped mass the reduced mass m_R was determined. Typical values of m_R, k_R and c_R were 0.225kg, 10kN/m and 0.94Ns/m respectively.

The full equations of motion for this model are covered in Leigh & Lu but are considered too lengthy to present here. The equations were solved using numerically integration with acceptable error of less than 0.01%. A major criticism of this work was that the final model of the complete

ball-racket impact was not experimentally verified in terms of the ball rebound velocity. The model does however illustrate some well documented findings such as reducing string tension increases ball velocity. It also illustrated less-established findings such as an increase in ball velocity can be obtained by increasing the damping in the racket.

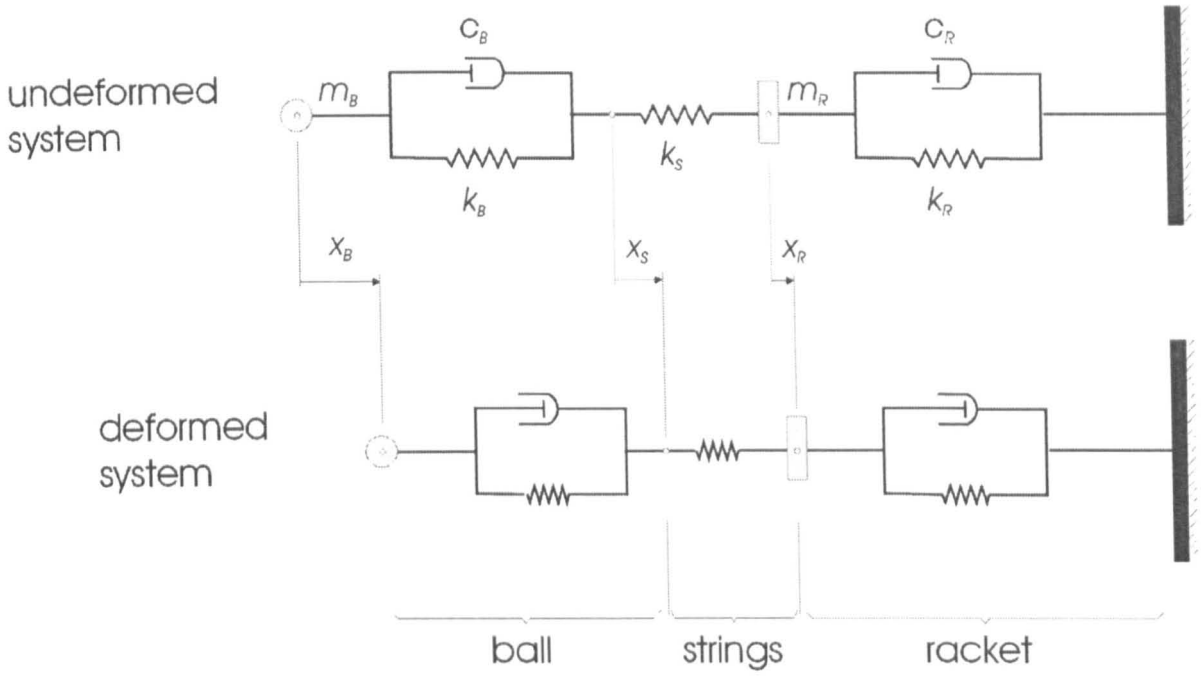

Figure 2.19 A visco-elastic model of an impact between a ball and grip clamped racket (reproduced from Leigh and Lu (1992))

Pratt, Dignall & Haake and Leigh and Lu have all generated models for the impact of a ball on a rigid surface. It has been shown that this model determines the acceleration, velocity and displacement of the ball COM during impact. Recent data, published by Cross (1999a, 1999b, 2000a), has used a force platform to determine the experimental data for the acceleration, velocity and displacement of the ball COM. This could be used to verify the 1-DOF models generated for the impact between a ball and rigid surface.

2.5.4 Finite Element Analysis (FEA)

There is a limited number of papers published in the field of tennis racket modelling which have used FEA. However, it is likely that this method is used heavily in the commercial development of tennis rackets due to the latest developments in PC software. These have lead to the availability of three dimensional CAD packages which act as the pre-processor for finite element solvers, reducing the time and cost of using FEA in product development (Yoxall 2002).

Widing & Moeinzadeh (1990) used linear curved elements to model the frame and nonlinear cable elements to model the strings. The strings were modelled discretely and therefore the pattern, tension and characteristics could easily modified. The handle was clamped which has been proved by other authors to be unrepresentative of a players grip (Brody (1987)). This assumption had to be made because the complexity of the model meant that only a static analysis could be conducted. A load is applied to the racket and the resulting stress and strain distribution was calculated. This

data is useful to designers who are attempting to stiffen the racket frame, but does not necessarily help increase the knowledge of the ball-racket interaction during impact. In this paper it is quoted that increasing string tension also stiffens the racket frame and thus decreases racket deformation. This contradicts the findings of Cross (2001c) who stated that increasing string tension reduces the stiffness of the racket frame.

2.6 Field data

Field data for tennis has been published at many different levels, all very useful for their intended purpose. Brody (1993) published a simple chart which gave the relationship between the ball velocity and the time taken for a ball to travel from one player to the other. Although this method was subject to simplification errors, it allowed coaches to determine the ball velocity simply from VCR or camcorder footage.

A more comprehensive field study has been coordinated by UC Davis (2001) who have obtained typical ball velocities and spins in a range of tournaments including the US Open. They used two high speed digital video cameras which operated at 250fps, with a shutter speed of 1/2000s. A summary of the data is given in Table 2.1.

Table 2.1 Data for a range of professional tennis player first serves from the US Open (reproduced from UC Davis (2001)).

Player	*Average service velocity (mph)*		*Ball spin range (rpm)*		*Average ball spin (rpm)*	
	1st serve	2nd serve	1st serve	2nd serve	1st serve	2nd serve
Jim Courier	108	91	2500-4054	3571-4167	2842	3810
Todd Martin	98	89	1667-3947	3000-4284	2798	3370
Tomas Muster	105	71	1667-4284	3750-4998	2754	4374
Pete Sampras	120	85	2100-4260	3900-5357	2699	4623
Petr Korda	101	88	1579-3750	3750-4284	2688	4017
Andre Agassi	102	74	1200-4284	4054-4998	2449	4650
Mark Philippousis	123	99	1765-2830	2830-4546	2198	4018
Michael Chang	112	77	1000-3750	3125-4284	1677	3928
Tim Henman	120	85	1429-1667	4284-4998	1548	4641

UC Davis (2001) measured the speed throughout the entire flight of the ball using the high speed video system. The maximum velocity of the ball during flight, at the point it leaves the racket, was

compared with the value given by a radar gun. Overall there was an average difference of 3.5% in the results, implying that the radar gun method of obtaining ball service velocities, which is used in many tournaments, is an accurate method.

This study was conducted for both serves and ground strokes. It was found that the fastest serve and ground stroke were approximately 127mph and 82mph respectively. This compares with the fastest recorded serve in the world which is currently 149mph (Rusedski) on the male tour and 127mph (Williams) on the female tour (Guinness (2000)). UC Davis determined that a serve of approximately 127mph slowed down to approximately 58mph when it reached the receiver. Table 2.1 shows that players reduce the speed of their 2nd serve, but increase the amount of spin. The data is quoted to an accuracy of 1rpm yet no error analysis is given to justify this high level of confidence.

Table 2.2 Summary of the data for male and female tennis players performing a serve (reproduced from Elliott *et al.* (1986)).

Parameter	Mean value	Standard Deviation
Ratio of vertical impact position and standing height	1.51	0.02
Maximum resultant velocity at tip of racket before impact	33.3m/s	4.1m/s
Angular velocity of the racket at impact	38.2rad/s	9.9rad/s
Resultant ball velocity at impact (downwards)	2.16m/s	0.7m/s
Resultant ball rebound velocity	38.4m/s	5.2m/s
Direction of racket vector at impact, relative to horizontal	4.0°	2.0°

Elliott *et al.* (1986) recorded tennis players of state or national level using two phase-locked high speed video cameras operating at 200fps. The direct linear transformation method (King (2000)) was used to obtain a three dimensional reconstruction of the tennis serve. A mean square error of 6mm is quoted for the accuracy of the X, Y and Z values of the known points in space. Table 2.2 summarises the data which was obtained from the digitised points on the player and racket. It shows that the ball was struck from a mean vertical position equal to 151% of a player's standing height, representing 2.7m for a player who is 1.8m (6ft) tall. The velocity of the racket prior to impact was 33.3m/s and this resulted in a ball service velocity of 38.4m/s.

Groppel *et al.* (1983) described an experiment which used a 16mm Locam camera operating at 500fps to record the spin for two varsity tennis players hitting forehand drives (Groppel 1975). The maximum top and back spin obtained in this experiment was 195 and 235rad/s respectively. The quoted error range in the spin calculation was ±24.1 rev/s (152rad/s), which highlights the difficulty in obtaining spin from high speed video images.

Mitchell *et al.* (2000) used a three-dimensional active marker system which sampled at 400Hz to measure the motion of a tennis racket during a serve for 6 county standard players. The maximum velocity of the impact point on the racket was approximately 38m/s and the maximum angular velocity of the racket was 65rad/s. It was found that these values generally dropped by ~10% for an increase of ~12% in the racket moment of inertia. It was found that the instantaneous centre of rotation at impact was approximately 330mm from the butt end of the racket. All this data contributed to the conclusion that the velocity of the impact point was primarily due to the angular velocity of the racket as the hand is moving relatively slowly at this point.

Schleihauf *et al.* (2000) used two cameras operating at 60fps to conduct a three dimensional analysis of tennis serves, for 25 professional players. The mean ball rebound velocity was measured as 46.8, 41.6 and 37.6m/s for flat, slice and topspin serves respectively. The standard deviations quoted for this data sample was ~5m/s. This data shows that a flat serve gives the highest ball rebound speed, followed by a slice and then a topspin. The racket head velocity was measured as 35.8, 36.1 and 36.4m/s for the flat, slice and topspin serves respectively. This shows that the racket head velocity is not strongly affected by the types of serve. This paper also shows that all serves are never purely 'flat', 'slice' or 'topspin' but always contain a combination of components.

2.7 Summary

This review has highlighted the typical equipment used by players in the game of tennis. There are two main constructions of tennis ball which are defined as *Pressurised* and *Pressureless*. It has been shown that the *Pressurised* ball is structurally stiffer than the *Pressureless* ball, and has a higher coefficient of restitution for an impact with a rigid surface. The review has highlighted that many types and diameters of string are available to the player, and these are used at tensions of between 40 and 70lbs.

A review of existing 'Field data' has ensured that any experimental or theoretical analysis is conducted using realistic velocities, angles and spins, for the ball and racket. For example, the literature shows that the maximum recorded ball speed, in the men's and women's game, is 149mph and 127mph respectively.

The main aim of this current study is to model the impact between a tennis ball and a racket. It has been shown that a player's hand provides little support to the racket, for impacts located on the longitudinal axis. Therefore it is generally excepted that the racket can be considered to be 'freely suspended', for impacts at these locations. This assumption will be used throughout this current study.

Numerous authors have modelled the impact between a ball and racket using rigid body dynamics. This type of model can be used as a first approximation to understand the fundamental dynamics which occur during impact. However, due to the nature of this model it is not capable of simulating the deformation of the ball, stringbed or racket during impact. It therefore is of limited use when attempting to realistically model the impact.

Several authors have superseded this simple rigid body model and simulated a tennis racket as a one-dimensional flexible beam. The literature shows that the modes of vibration and node locations for this simple flexible beam are very similar to those for a tennis racket. The main weakness of this published material is that the accuracy of the derived model has not been experimentally quantified. Also, the model properties of the ball and stringbed have generally been assumed and, therefore, may not be physically representative of the actual objects.

This current study aims to advance the models which have been discussed in this review. The current study aims to derive a model which is (1) verified using experimental data, and (2) contains components which are physically representative. This type of model will enable the impact to be accurately simulated and also can be used to increase the level of understanding of the impact.

3. Tennis Ball Properties - Experiment Apparatus and Methods

3.1 Introduction

The overall aim of this study is to develop a model and understanding of the impact between a tennis ball and racket, as was expanded upon in the introduction in Chapter 1. This impact involves a complex interaction of four physical bodies, which are,

1. The Ball
2. The Stringbed
3. The Racket frame
4. The Human body

A detailed understanding of each of these parameters is required in order to construct the overall model. For example, the model must be able to predict the effect of changing the mass, stiffness or damping of the ball on the impact. This would be used to determine the differences between different ball types. The completed model will therefore contain some component which corresponds to the ball, and this element can be assigned the relevant mass, stiffness and damping properties for the impact that is being simulated. This component may take the form of a single or multi degree-of-freedom visco-elastic model, a 3D finite element model or an analytical solution based on shell theory.

Clearly the model of the ball must be verified using experiment data. For example, high speed video cinematography could be used to determine the deformation of the ball for an impact between a ball and a swinging racket. The obvious problem with this type of experiment is the potential lack of repeatability as the player is unlikely to swing the racket at a control speed. A solution to this would be to build a robotic device which simulated the grip forces that a player applies to a tennis racket. However, in section 2.4.3 it was shown that a racket can be considered to be freely-suspended for impacts along the longitudinal axis. By changing the frame of reference, a typical ball/racket impact can easily be simulated by propelling the ball at a stationery freely suspended racket. The main difficulty in this experiment is that the ball properties must be isolated from those of the string bed and racket frame which themselves combine to form a complex non-linear system. For example, to develop a relationship between ball compression and impact velocity, the properties of the stringbed must also be fully understand.

An alternative approach to the development of a model for the ball component in a ball/racket impact involves the determination of a ball model for a much simpler impact. For example, it would be much easier to develop a model for an impact between a ball and rigid surface, and then attempt to modify this so that it is suitable for an impact on a deformable surface.

In this, and the subsequent two chapters, a model of a tennis ball impacting perpendicular to a rigid surface is developed. An understanding of the physical properties of the ball can be gained by performing a range of suitable experiments. The data obtained from these experiments can also be

used to verify the accuracy of the model of an impact between a ball and rigid surface. These experiments include both quasi-static compression tests and dynamic impact tests to determine various physical properties such as the structural stiffness of the ball. This chapter discusses the apparatus used in these experiments which include high speed video systems and force platforms, as well as the standard equipment used for the International Tennis Federation approval tests (ITF 2001).

Ultimately, a model of the complete ball, stringbed and racket frame system will be developed. It is not claimed that the model of a ball impact on a rigid surface can be used directly to define the ball component for an impact with a racket. However, the understanding of ball's physical properties which is gained during the development of this simple ball model can be used to give a first approximation of a model for the ball in an impact with a racket.

Chapters 3 to 5 form a trilogy which aims to develop a model of a ball impact on a rigid surface. The aim of this chapter is only to introduce the relevant experimental apparatus. The data obtained using this apparatus is presented in Chapter 4, and the model is developed in Chapter 5.

3.2 Quasi-Static Ball Stiffness

3.2.1 Overview

It is widely accepted that the structural stiffness of the ball will affect the impact between a ball and rigid surface; the magnitude of ball deformation being inversely proportional to the stiffness. In section 2.2.3 it was shown that the quasi-static structural stiffness can be determined by compressing the ball between two plates and sampling the force and resulting deflection. The deflected form of the tennis ball in this compression test is different to that which occurs in a dynamic impact with a surface. However, it still gives a measure of the difference in stiffness between different ball types, and has been used by many authors (Leigh and Lu 1992, Kawazoe 1997a) to aid the development of an impact model.

3.2.2 Experimental Apparatus

A MecMesin uniaxial test machine was used to determine the quasi-static stiffness of the ball. This is the same device as that used in the International Tennis Federation compression test, and is shown in Figure 3.1. This test specifies the rate and magnitude of the ball compression and is designed to ensure that all approved tennis balls have the same structural stiffness. The ball is compressed at a rate of 2.5mm/sec (0.1in/sec) throughout the test. A schematic diagram of the loading sequence is shown in Figure 3.2. Two different compression readings are taken for an 80N (18lbs) load; these are defined as the forward and return deformation. The measured values of these two parameters must fall within the range specified in the Rules of Tennis. A full description of this test is given in Section 2.2. In brief, the test involves loading the ball up to 80N (18lbs) and then maintaining the load for 5 seconds before reading the forward deformation. Then the load is

then increased to 25.4 mm and then reduced back to 80 N. The load is held at this value for 10 seconds before the return deformation is recorded. Finally the load is returned to zero.

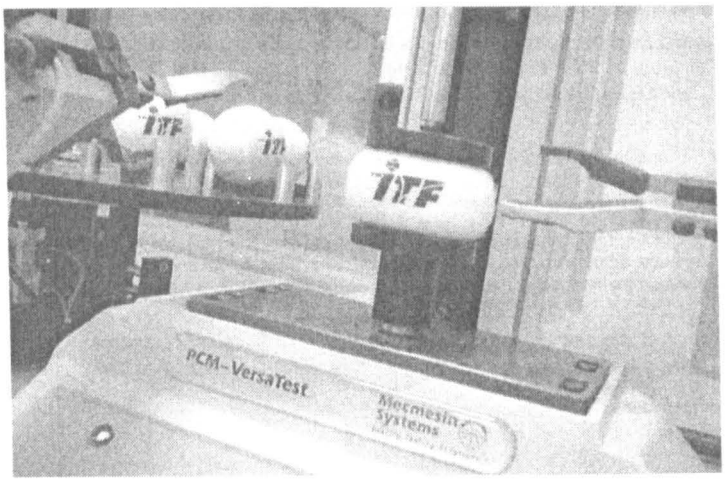

Figure 3.1 MecMesin machine used for ITF compression test.

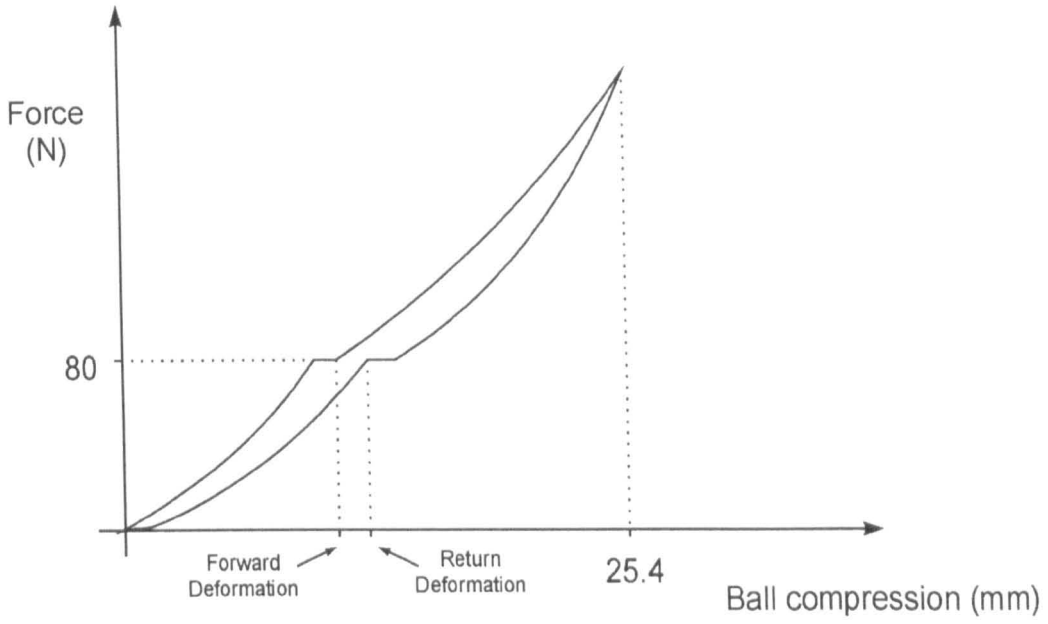

Figure 3.2 Schematic of a force-deformation plot from MecMesin machine.

The forward deformation gives a true indication of the stiffness of the ball, neglecting any damping effects. This is achieved by maintaining the 80 N load for 5 seconds to allow the deformation to settle before the value is recorded. This is necessary because rubber is a visco-elastic material and its stiffness is thus rate dependent. As the loading is not truly static the deformation must be allowed to settle in order to determine the actual stiffness.

The return deformation is read in a similar manner but, due to the extra deformation, the load is maintained for 10 seconds to allow the value to settle. The return deformation is always greater than the forward deformation because the rubber exhibits hysteresis loss during compression. The difference between the forward and return deformation is a measure of how much energy has been recovered by the ball.

Groppel *et al.* (1987a) and Williams (2000) have shown that a typical ball deformation for a ground stroke was in the order of 20 mm. The ITF test simply determines if the ball passes or fails the approval test based upon whether the measured values of forward and return compression lie within predefined limits. Therefore this test only regulates the stiffness of the balls for a deformation of approximately 8 mm. However, the MecMesin device exports the force-deformation data for the complete load cycle shown in Figure 3.2. Therefore, in this current investigation the quasi-static stiffness will be determined for ball deformations up to 25.4 mm (1 inch). The results of this testing are discussed in section 4.2.

3.3 Analysing normal ball impacts on a rigid surface using a high speed video system

3.3.1 Overview

In the introduction it was stated that the aim of Chapters 3 to 5 was to develop a model of an impact between a ball and rigid surface. This requires experimental data for this impact which will be used to both increase the understanding of the ball properties and to verify the model results. In this section, a method is discussed which uses a high speed video system to record the impact between a ball and rigid surface. The objectives of this work are listed as follows,

1. Determine the contact time for the impact
2. Determine the magnitude and form of the ball deformation during impact.

This testing will be performed for a range of ball impact velocities that are typical in the game of tennis.

3.3.2 Experiment Apparatus

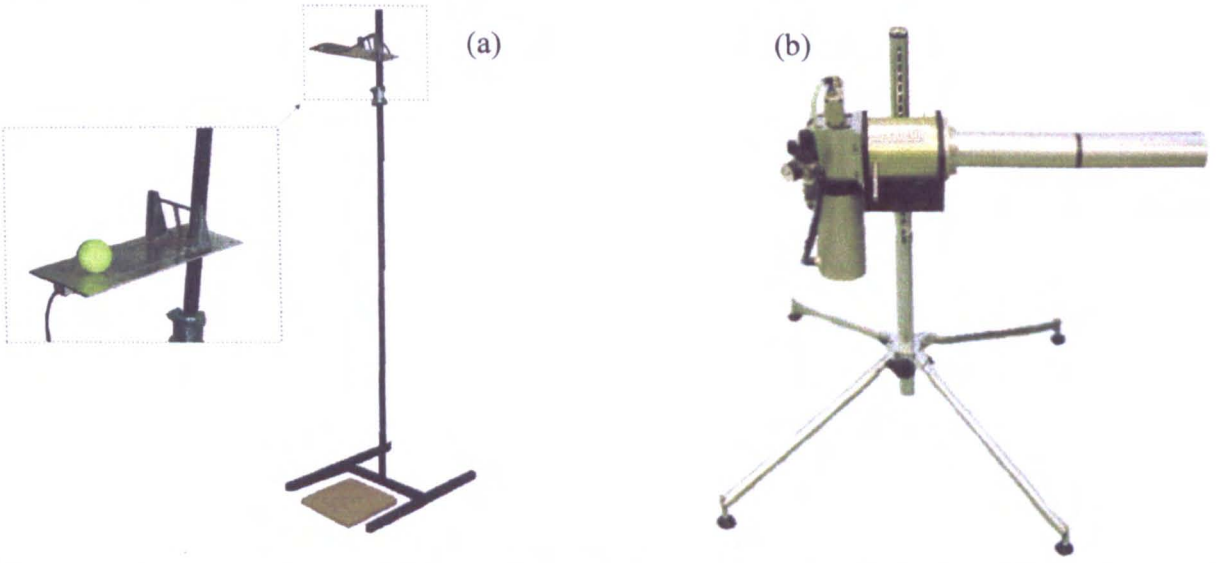

Figure 3.3 (a) Dropper used to release the ball vertically with no spin, and (b) Air cannon used to propel the ball horizontally with no spin.

In this study, balls were projected normal to a flat surface at a range of speeds. For low speed impacts, the balls were dropped vertically onto the surface using a dropper device developed by Goodwill (1997) and shown in Figure 3.3(a). This device was designed so that the ball is released with no spin. This was achieved by using a trapdoor which rapidly accelerated away from the ball once triggered.

Due to obvious height constraints, the highest velocity obtainable by dropping the ball is approximately 7m/s. For speeds greater than this value the ball is propelled horizontally at the rigid surface using the air cannon shown Figure 3.3(b). Compressed air is stored in an chamber then rapidly exhausted through the cannon. High speed video analysis has shown that the ball leaves the cannon with no spin. The minimum speed for the cannon to work reliably is approximately 13m/s. There is therefore a range of velocities between 7 and 13m/s where no results could be obtained as neither projection device is suitable.

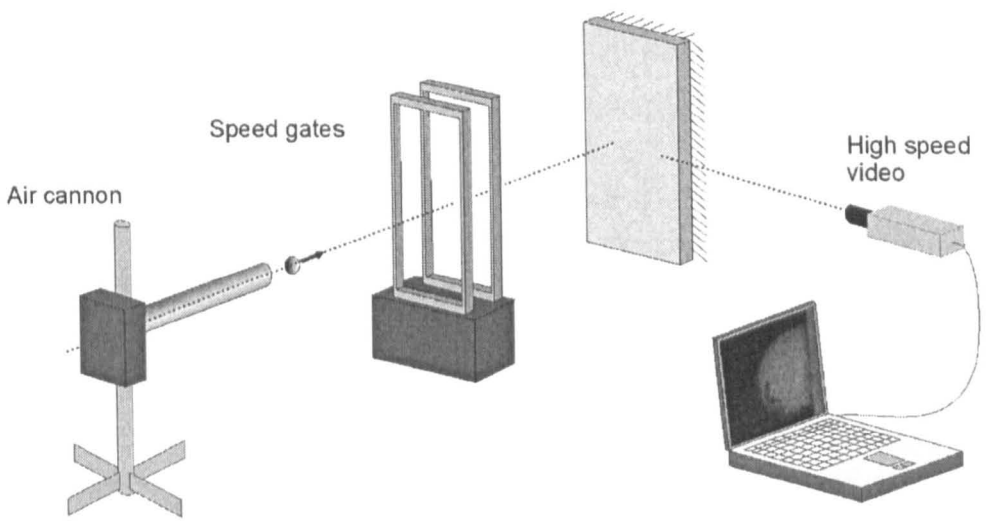

Figure 3.4 Experiment layout showing ball projected at rigid surface using an air cannon (for ball impact velocity > 13m/s)

The objectives of this study are to measure the ball deformation and contact time for an impact between a ball and rigid surface. The equipment used to perform this task is illustrated in Figure 3.4. Speed gates were used to measure the ball impact and rebound velocity. These gates used two beams of light, two photo-sensors and a sampling unit to calculate the ball velocity. Figure 3.4 shows the arrangement for ball impact velocities above 13m/s. For the drop tests (velocities < 7m/s) the rigid surface was rotated so that it was orientated horizontally, and the speed gates were removed as they can not operate reliably at velocities less than approximately 10m/s.

A *Phantom HIAAA* high speed video system was used to record the impact. This camera is capable of recording at up to 30,500 frames per second, and has a maximum resolution of 512 x 512 pixels. It was important to ensure that the focal axis of the camera was perpendicular to the flight of the ball and in the same plane as the surface to minimise perspective errors during image analysis. The high speed video system was controlled using *Phantom v4* software on a PC laptop and the images were stored in the native *Cine* file format.

Two different camera settings were used in this experiment depending on the ball impact velocity.

1. The camera was operated at 6,000 frames per second at a resolution of 256 x 128 pixels for the drop tests. For these low speeds the speed gates could not operate reliably therefore the impact and rebound velocities were determined using the high speed video images. This required a relatively large field of view to ensure that sufficient images were captured for the velocity and ball deformation to be calculated accurately.

2. The camera was operated at 11,000 frames per second at a resolution of 128 x 128 pixels for the impact tests which used the cannon. For these tests the speed gates were used to determine the velocity of the ball so a smaller field of view was allowable to capture the necessary information to determine the ball deformation during impact.

3.3.4 Analysis of high speed video images

The *Cine* video images were converted into the Microsoft AVI file format to allow analysis to be conducted in *Vidimas v1*. *Vidimas v1* is dedicated image analysis software which was written by the Sports Engineering Research Group at the University of Sheffield. It is based on *Richimas v1* software (Carré 2000) but has been modified by the author to allow the importing of Microsoft AVI files. *Vidimas v1* has a circular mouse cursor which is used to select the co-ordinates of the ball, as shown in Figure 3.5. The co-ordinates are exported into *MS Excel 2000* for analysis. These co-ordinates are in screen pixel units, and therefore have no physical dimension. In this experiment, the pixel-to-mm conversion factor was obtained by placing a grid with a line spacing of 40mm in the same plane as the ball trajectory, perpendicular to the focal axis of the camera. An image of this grid was recorded by the camera; the camera being located at the same position as shown in Figure 3.4. The intersect points on the grid were sampled in *Vidimas v1*, and the relevant pixel-to-mm conversion factor was calculated. To optimise the accuracy of the calibration, the intersect points were obtained over the entire field-of-view.

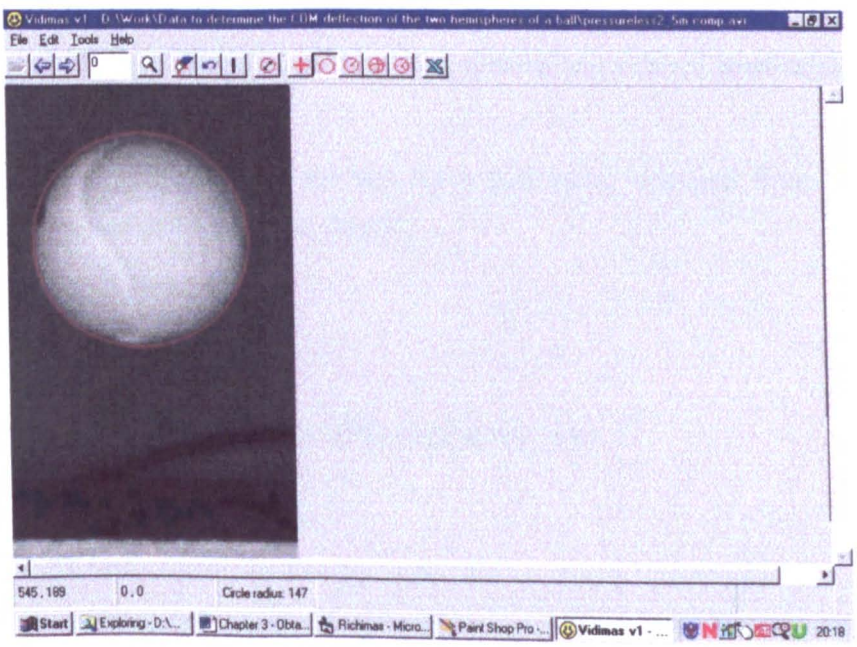

Figure 3.5 Illustration of the *Vidimas v1* user interface, showing a high speed video image of the ball prior to impacting on a rigid surface, during a drop test.

(a) Determining the ball impact and rebound velocity

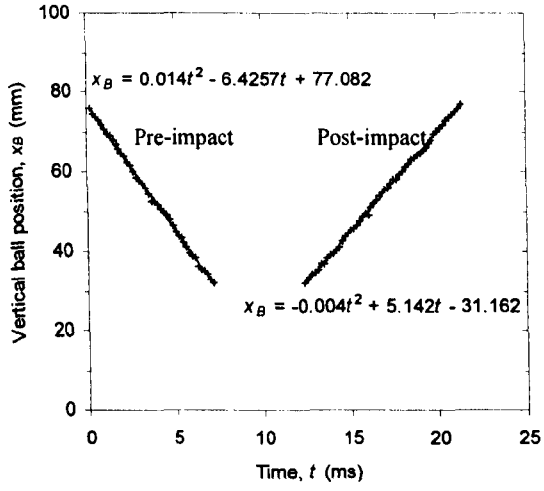

Figure 3.6 Illustration of the vertical motion of the ball before and after impact, for a ball dropped from 2.54m (100inchs)

For the tests that used the cannon to propel the tennis ball (ball impact velocity >13m/s), the velocity of the ball was measured using the speed gates. However, for the drop tests (ball impact velocity <7m/s) the impact and rebound velocity of the ball was determined from these high speed video images. The ball velocity was determined by plotting the vertical position of the ball at a number of discrete time intervals. The distance (and time) over which the ball position was sampled was maximized as this minimized errors when determining the ball impact velocity (Goodwill 1997). The camera was operated at a relatively high frame rate to ensure that a sufficient number of images were captured to accurately determine the deformation of the ball during impact. This meant that there were approximately 50 frames available to determine the ball impact and rebound velocity. During this short time (approximately 8ms) the ball will accelerate due to gravity and therefore if an average velocity for this period was used then the velocity would be underestimated (Thomson 2000). An alternative method involves plotting a 2nd order polynomial trendline through the position time data, determined using a least-squares regression in *MS Excel 2000.*

Figure 3.6 shows an example of this method for a ball being dropped from 2.54m. The ball position was only sampled prior and post impact.

The 2nd order polynomial of the form,

$$x_B = at^2 + bt + c \qquad [3.1]$$

[3.1] is differentiated to give the velocity of the ball at any time, t,

$$\frac{dx_B}{dt} = 2at + b \qquad [3.2]$$

The parameters a, b and c can easily be determined using the least-squares regression method. Therefore the velocity $\frac{dx_B}{dt}$ at time t can be found using [3.2]. This analysis is conducted for both

the impact and rebound phase, and the time *t* at which the ball impacts and leaves the surface can easily be determined from the high speed video images. A more detailed description of this method can be found in Thomson (2000).

(b) Determining ball compression and contact area

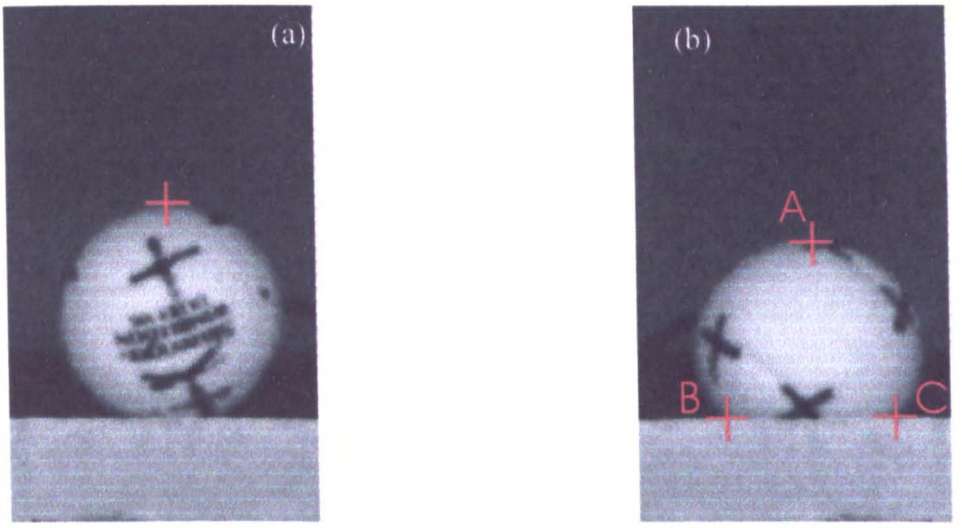

Figure 3.7 (a) Image of ball resting on surface used to accurately define uncompressed ball position, and (b) positions sampled on compressed ball during impact.

Before the impact tests were conducted, an image of the ball resting on the surface was captured, as shown in Figure 3.7a. This was used to define the uncompressed ball position. The images of the ball, during contact with the surface, were analysed in *Vidimas v1* to determine the magnitude of the ball compression and contact area diameter, as illustrated in Figure 3.7b. The diameter of the ball/surface contact area is defined as the length BC. The data obtained from this experiment was also used to measure the contact time for the impact. In this experiment, the definition of measured contact time was the time taken for the ball deformation to return to zero. The results for this experiment are shown in section 4.4.3.

A simple repeatability study was conducted to determine the accuracy of the manual method for obtaining the magnitude of ball compression and contact area diameter. In this study, an individual image was imported into *Vidimas v1* and the points A, B and C were sampled. The image was then unloaded and the co-ordinates of the points were stored. This process was repeated 50 times to generate sufficient data to conduct a valid statistical analysis. The standard deviations for the obtained values of ball compression and contact area diameter were 1mm and 2mm respectively.

3.4 Normal ball impacts on a Force Platform

3.4.1 Overview

One of the aims of this chapter was to generate experimental data which could be used to verify a model for an impact between a ball and rigid surface. The exact form of this required experimental data will depend on the nature of the model. If the model simulates the structural shape of the ball deforming on the surface, for example the finite element method, then the experimental data in section 3.3 may be sufficient. However, if the model simulated the force acting between the ball and surface, for example a visco-elastic model, then the experiments conducted in section 3.3 would be insufficient as no forces have been measured.

In this section an experimental method is discussed which uses a force platform to measure the force acting between the ball and surface, during impact. Thomson (2000) showed that this data can be analysed to give the motion of the ball centre of mass during impact. This data can also be used to determine the contact time for the impact and thus an effective stiffness for the ball.

3.4.2 Experiment Apparatus

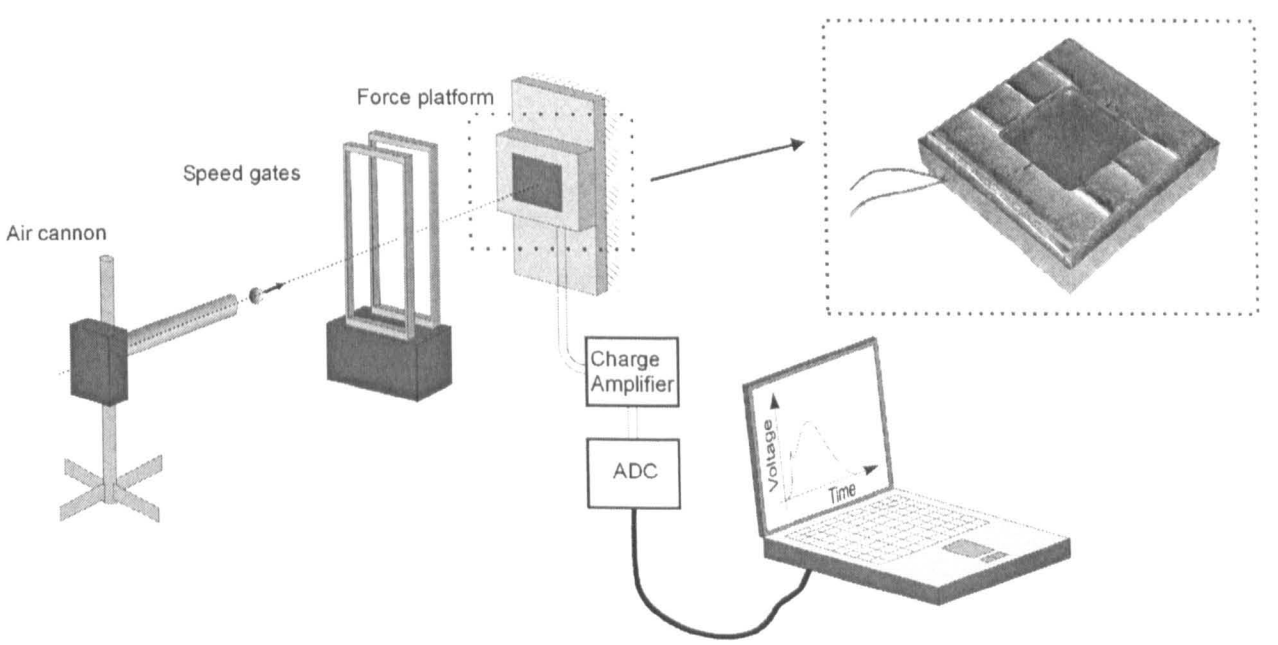

Figure 3.8 Experiment layout showing ball projected at force platform using an air cannon (for ball impact velocity > 13m/s).

The equipment used in this experiment is shown in Figure 3.8, and is very similar to that described in section 3.3. The balls were projected at the piezoelectric force platform using either the cannon or the dropper, depending on the impact speed used. The speed gates were used to determine the impact/rebound speed of the ball when it was propelled using the cannon, and a *Phantom HIAAA* high speed video camera was used for this purpose during the drop tests. The platform was capable of withstanding impacts of up to 30m/s, so this was the maximum speed that was tested. The force platform is shown in Figure 3.8, and detailed construction details for this platform are given in both

Cross (2000a) and Thomson (2000). A ×10 probe was used to connect the piezoelectric platform to a charge amplifier to increase the time constant of the circuit, as explained in more depth by Thomson (2000). The voltage output from the charge amplifier was sampled by an analogue-to-digital converter (ADC) and laptop PC, at a rate of approximately 67kHz.

3.4.3 Calibration of Force Platform

The force platform outputs a voltage V and this was sampled by the ADC and PC to give a voltage-time plot. Thomson (2000) used the same equipment and verified that the voltage was linearly proportional to the force. However, there is known to be a degree of scatter in the actual calibration value which has been assigned to the ball not impacting in a consistent position on the platform. To account for this a separate calibration factor, k_{cal}, was determined for each impact. The integral of the voltage-time signal $\int_0^{T_C} V dt$ is proportional to the impulse applied to the ball $m(V'_B - V_B)$. The ADC samples at a sufficiently high frequency for the trapezium rule to be used to integrate the voltage data with negligible error; the time step Δt between samples is only 0.0149ms. The calibration factor, k_{cal} is defined as,

$$k_{cal} = \frac{m(V'_B - V_B)}{\int_0^{T_C} V dt} \qquad [3.3]$$

The force F_B acting on the ball at any time t can therefore be determined from the voltage V_t using

$$F_B = k_{cal} . V_t \qquad [3.4]$$

The acceleration of the ball centre-of-mass $\ddot{x}_B$ can easily be determined from the *Force-Time* plot. The velocity $\dot{x}_B$ and displacement x_B of the ball COM during impact can be determined from successive numerical integration of the *Acceleration-Time* data. As the time step of the sampled data is so short, it was assumed that in the time period from (t-Δt) to t the acceleration acting on the ball was constant and equal to the average of $(\ddot{x}_B)_{t-\Delta t}$ and $(\ddot{x}_B)_t$. The enforced boundary constraints were $(\dot{x}_B)_{t=0} = V_B$ and $(\dot{x}_B)_{t=T_C} = V'_B$, where V_B and V'_B were the experimentally measured impact and rebound velocities of the ball respectively. The velocity of the ball COM at time t can be calculated using,

$$(\dot{x}_B)_t = (\dot{x}_B)_{t-\Delta t} + \left(\frac{(\ddot{x}_B)_{t-\Delta t} + (\ddot{x}_B)_t}{2} \right) . \Delta t \qquad [3.5]$$

A similar method was used to determine the displacement of the ball COM, x_B, during impact.

3.5 Summary

In this chapter, two main experimental methods have been discussed which had the collective aim of increasing the understanding of the physical properties of a tennis ball. The two experiments described were,

1. Quasi-static compression between two rigid plates.
2. Normal impact between a ball and rigid surface.

The experimental methods can be used to obtain the following parameters from these two tests,

a) Quasi-static ball stiffness.

b) Ball impact and rebound velocity.

c) Ball compression and contact area during impact.

d) Contact time for impact.

e) Force acting on ball during impact.

f) Ball centre-of-mass motion during impact.

4. Tennis Ball Properties – Experimental Data

4.1 Introduction

The aim of this overall study is to obtain a model for an impact between a tennis ball and racket. In Chapter 3 it was noted that this study must be split into a number of finite stages due to the high number of variables involved in the ball-racket impact. The logical first stage is to develop an understanding of a much simpler impact in which a tennis ball lands perpendicular to a rigid surface. This smaller study requires a range of experimental parameters to be measured for this impact, such as contact time, ball impact/rebound velocity and ball compression. The experimental methods which are suitable for measuring these parameters are described in sections 3.3 and 3.4 In this chapter, data is obtained using these experimental methods. The two main objectives of this chapter are to generate experimental data which can be used as follows,

1. To increase the understanding of the mechanism involved in an impact between a ball and rigid surface.
2. To generate experimental data to verify a model of this impact.

A supplementary objective of this work is to identify how the structural stiffness of the ball influences the dynamic impact between a tennis ball and racket. This requires a further experiment to be performed to determine the quasi-static stiffness of the ball for a compression between two flat plates. This experiment is described in section 3.2.

In this chapter, experimental data is obtained for a range of ball types which encompass all those typically used in a game of tennis.

4.2 Ball Types used

In this chapter, the experiments are conducted on the following three standard production tennis balls which are defined as,

1. *Pressurised* – Dunlop Wimbledon Slazenger.
2. *Pressureless* – Tretorn TXT.
3. *Oversize* – Wilson Rally.

and one non-standard ball which is

4. *Punctured* – a *Pressurised* ball which has been punctured repeatedly around the seam using a paperclip to release the pressure.

These balls were chosen to illustrate the influence of different constructions on the physical properties of the ball. Table 4.1 summarises the nominal ball constructions. The *Pressurised* and

Pressureless balls are representative of the range of ball properties exhibited by Type 2[1] balls. The *Pressurised* ball is typical of a ball which is considered to have the best playing properties. This is deduced from evidence of its popularity with players of professional and club standard. The *Pressureless* ball has a thicker wall thickness to compensate for the internal air being at atmospheric pressure. The *Pressureless* ball is typical of a ball which is popular, according to its manufacturers, with recreational level players who appreciate its durability; this ball does not lose its stiffness unlike *Pressurised* balls which suffer from air pressure leakage.

Table 4.1 Summary of nominal ball construction properties.

Ball definition	Diameter (mm)	Shell thickness (mm)	Internal pressure (gauge) (bar)
Pressurised	67	3	0.827
Pressureless	67	4	0
Oversize	71.5	2.7	0.827
Punctured	67	3	0

The *Oversize* ball is typical of a Type 3 ball which has recently been approved by the ITF to be used in competitions of any level. This ball is approximately 6% larger than a Type 2 ball and has the same internal air pressure but a thinner wall thickness compared to the *Pressurised* ball.

Anecdotal evidence from players suggests that *Pressureless* balls, and to a lesser extent *Oversize* balls, feel 'heavier' than *Pressurised* balls. The *Punctured* ball is a gauge of a tennis ball with 'poor' playing properties, and is also known to feel 'heavy' and 'lifeless' according to players. It is intended that the results in this chapter can be used to explain these differences.

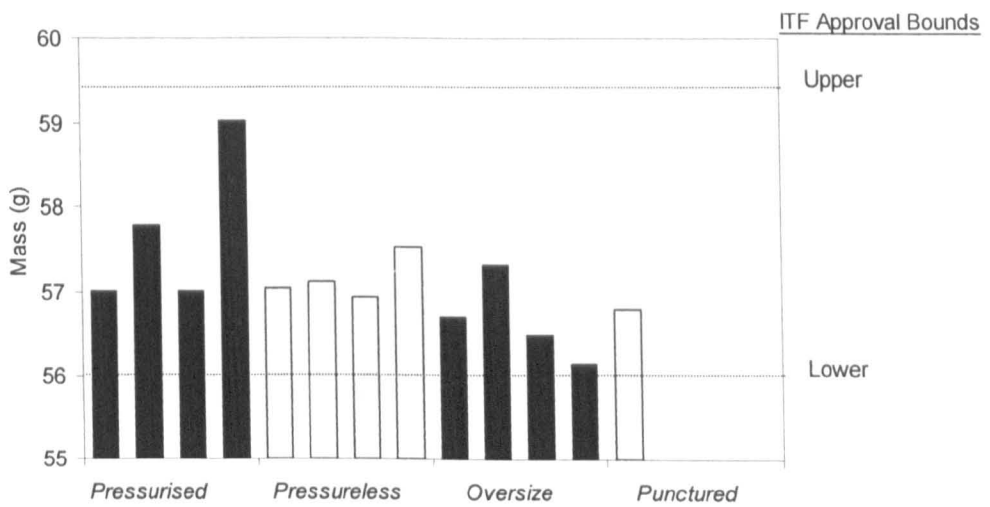

Figure 4.1 Mass of four balls of each type, showing the bounds of acceptance for ITF Approval.

The *Punctured* ball is a *Pressurised* ball with no internal air pressure. It is assumed that very little air can escape out of the punctured holes during impact, due to its short duration. This ball would not pass the ITF regulations due to its low stiffness, but was tested to help understand the contribution that the internal pressurisation of a tennis ball has on its quasi-static stiffness and impact behaviour.

[1] In December 2000 the ITF brought in a rule change which classified balls into three categories based on the diameter and stiffness. The definitions of these categories are given in Chapter 2.

In this study, four balls of each type are used (except for the *Punctured* ball); the mass of each ball is shown in Figure 4.1. This figure also shows that all the balls lie within the upper and lower bounds of acceptance for ITF Approval. There is some scatter in the values which can be assigned to manufacturing tolerances. It should be noted that the majority of the balls have a mass of 57.0±0.5g, which corresponds to a variation in the order of only ±1%.

4.3 Quasi-static compression testing

4.3.1 Force-Deformation results

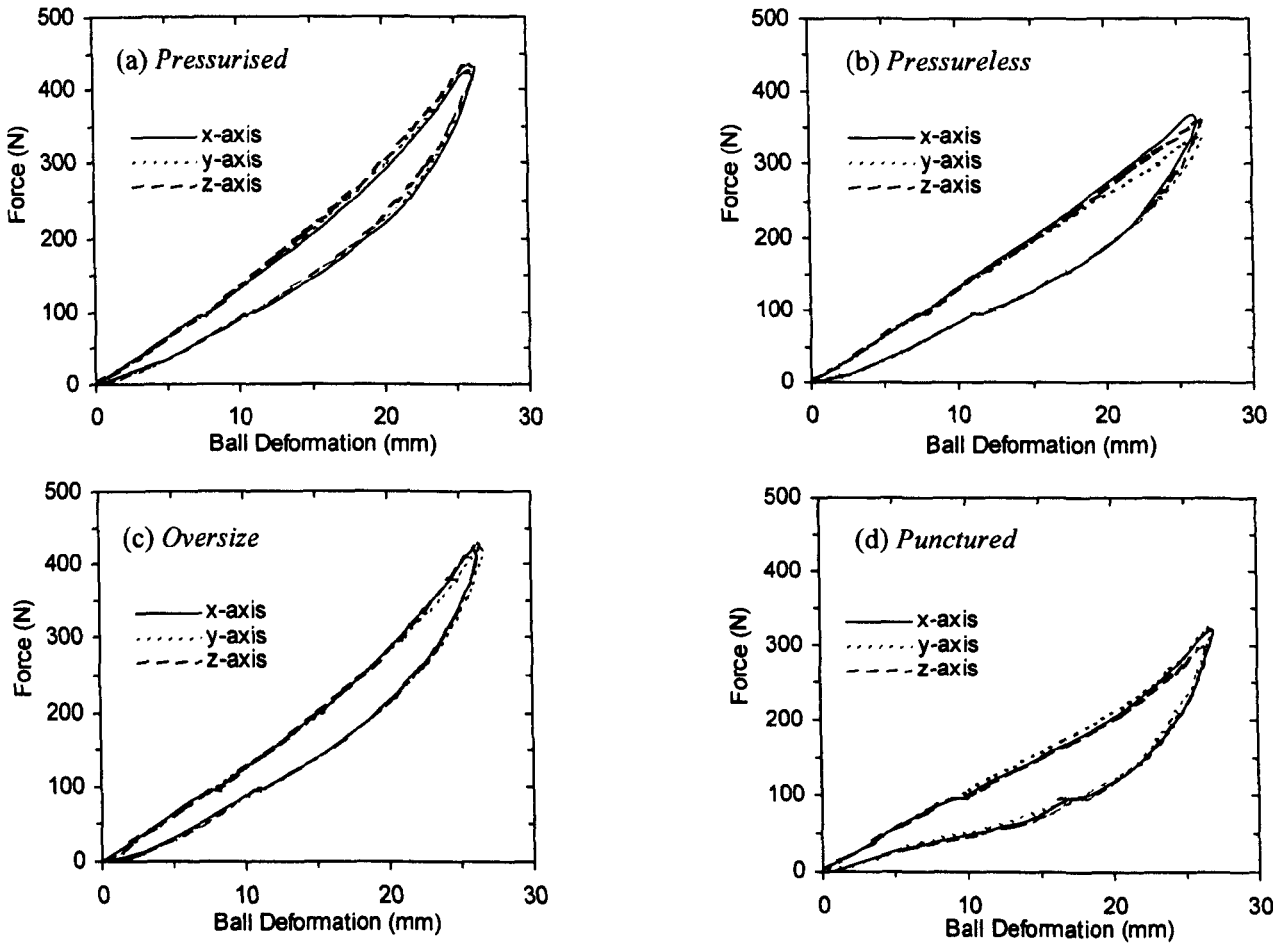

Figure 4.2 Quasi-static *Force-Deformation* plots for the three mutually perpendicular axes of the balls. The data is presented for four ball types.

In section 3.2.2, a test was described which involved the ball being compressed between two rigid plates in a MecMesin test device. This is the same test procedure as used in the ITF Approval test (ITF 2002). Before each test, the balls are pre-compressed to remove the 'set' in the rubber. The MecMesin test device compresses the balls by approximately 25.4mm (1 inch). Figure 4.2 (a)-(d) show the results for the quasi-static compression tests for one ball of each type. The plots for the other balls of each type are shown in Appendix B.2.

It was found that there was very little scatter in the results for the three mutually perpendicular axes of all of the *Pressurised, Oversize* and *Punctured* balls. However, for the *Pressureless* ball, it was found that the maximum force measured for the *y-axis* was consistently lower than for the other

axis's. (It should be noted that the *y-axis* simply corresponds to the second axis that was tested, and not any specific orientation of the ball.) The variation of the ball stiffness in each axis should give an indication of the homogeneity of the ball. The results therefore imply that the *Pressurised, Oversize* and *Punctured* balls can be considered homogenous, whereas the *Pressureless* ball can not. However, the fact that the 'rogue' orientation is always along the *y-axis* could be a coincidence but it is more likely to be due to a systematic error in the experiment. More balls would need to be tested to further investigate this phenomenon.

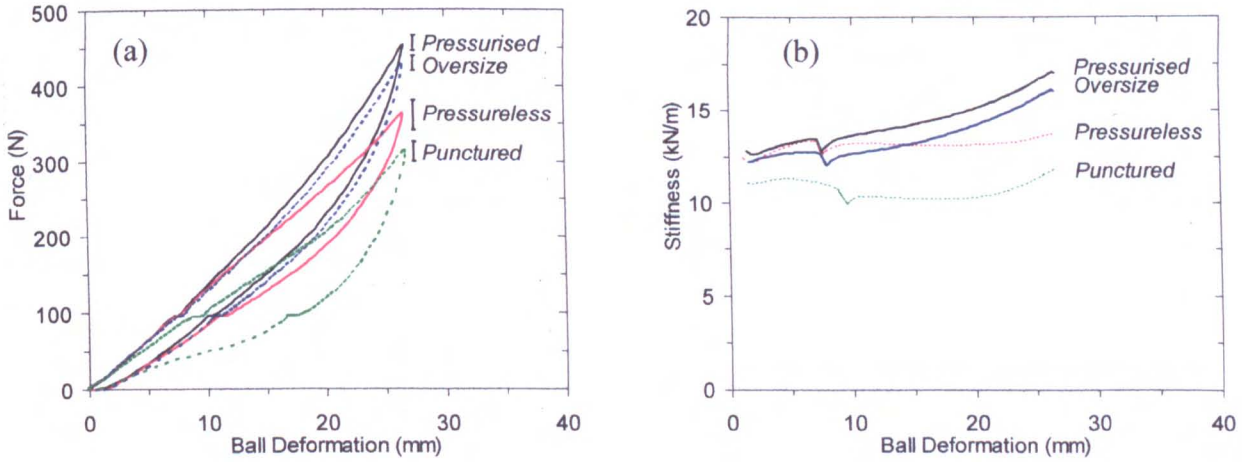

Figure 4.3 (a) Mean *Force-Deformation* plot for each ball type, with error bars illustrating the scatter in the data for the individual axes, and (b) forward stiffness calculated using the mean force-deformation plots.

To enable comparisons to be made between the different ball types, the mean result for the three axes of the four balls of each type was calculated (12 compressions in total); this is defined as the *mean axis* data. A comparison of the *mean axis* data for each ball type is shown in Figure 4.3 (a). Figure 4.3(a) shows a force-deformation plot of the *mean axis* data with error bars. Insufficient data was obtained to conduct a full statistical analysis of the results so the error bars simply represent the absolute scatter in the raw data for the individual axes. Figure 4.3(a) shows that the differences between the ball types are of greater magnitude than the scatter represented by the error bars.

Figure 4.3(b) shows the ball stiffness for the *mean axis* data of each ball type; the stiffness being defined as the ratio of the force and deformation during the loading phase of the test. The ITF Approval test (described in detail in section 2.2) ensures that all the balls deform within a specified range for a load of 80.0N (18lbf). This load corresponds to a ball deformation of ~7mm. The approval test specifies that the MecMesin machine pauses at this load for five seconds before the deformation is recorded. This explains the discontinuity in the plots in Figure 4.3(b) at a ball deformation of ~7mm. This figure shows that all the standard production tennis balls have a similar stiffness for ball deformations of this value. This can be explained by the fact that all these balls passed the ITF Approval test for compression. The measured stiffness of the *Punctured* ball is likely to be influenced by air leaking through the 'puncture' holes, and therefore may not be a true value for this ball. However, the results do give an indication of the contribution of the internal air pressure on the ball structural stiffness.

Figure 4.3(b) shows that the Pressurised ball is consistently stiffer than all the other ball types. For a ball compression of ~7mm, the Pressureless ball is stiffer than the Oversize ball. However, at higher ball deformations the Pressureless ball is less stiff compared to the Pressurised and Oversize balls. The Punctured ball is significantly less stiff than all the three standard production balls. It is interesting to note that the stiffness of the two balls which are internally pressurised (Pressurised and Oversize) increases appreciably with ball deformation, whereas the other two balls, which are not internally pressurised, have a stiffness which is relatively independent of ball deformation. Figure 4.3(a) and (b) also show that, at high ball deformations, the Pressureless ball acts more like a Punctured ball than a Pressurised ball. If the holes in the Punctured ball could be sealed then this would act to increase the stiffness of this ball. This confirms that the Pressureless and Punctured balls have a similar stiffness at high ball deformations.

4.3.2 Hysteresis loss results

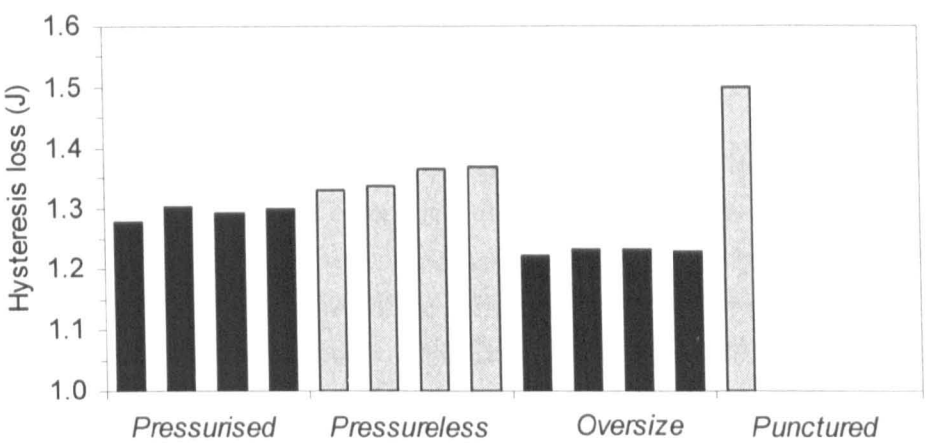

Figure 4.4 Hysteresis losses obtained from the *Force-Deformation* plots for each ball type.

In section 4.3.1, data is presented for a compression of a tennis ball between two rigid plates. The ball is loaded to a compression of 25.4mm, at a rate of approximately 2.5mm/sec, and then unloaded. Figure 4.2(a)-(d) show that the ball exhibits a large hysteresis loss during this compression cycle. The magnitude of this hysteresis loss can easily be calculated by integrating the data using the trapezium rule. The mean loss for the three individual axes of each ball (of each type) is presented in Figure 4.4. This figure shows that the *Punctured* ball exhibits the largest hysteresis loss, followed by the *Pressureless*, *Pressurised*, and then the *Oversize* balls.

A reason for the *Oversize* ball having the lowest hysteresis loss was suggested by Goodwill & Haake (2000). The *Oversize* ball has a larger diameter and therefore the angle θ through which the wall is deformed during compression is smaller (see Figure 4.5). Also, the wall of the rubber core is thinner for an *Oversize* ball compared to a *Pressurised* ball. Both these characteristics lead to lower stresses in the rubber during compression, so the hysteresis losses are lower for a specific deformation magnitude. An analogous argument can be used to illustrate why the *Pressureless* ball has a higher hysteresis loss compared to the other two standard production tennis balls. The *Pressureless* ball has a much thicker wall thickness and therefore the stresses in the rubber are much higher, for a specific deformation, resulting in a higher hysteresis loss. The high value of

hysteresis loss measured for the *Punctured* ball is likely to be a combination of air leaking through the holes during compression and the lack of structural stiffness during the recovery phase.

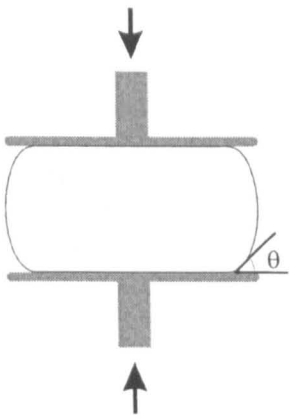

Figure 4.5 Illustration of the angle through which the ball wall is deformed when compressed between two plates.

4.3.3 Summary

In this section a collection of four types of tennis ball were tested in a MecMesin test device. This machine compressed the ball at a rate of approximately 2.5mm/sec, to a distance of 25.4mm. It was found that the stiffness of all the production tennis balls was very similar for deformations of approximately 7mm. This was because all the balls were designed to pass the ITF approval test which regulates the stiffness of a tennis ball for a deformation of ~7mm. At higher ball deformations the *Pressurised* ball was stiffest, followed by the *Oversize*, *Pressureless* and then the *Punctured* ball. The results highlighted that two types of tennis ball can have an identical stiffness at a low deformation, but vastly different stiffness at higher deformations. For example, at high deformations the *Pressureless* ball had a similar stiffness as a *Punctured* ball.

The hysteresis loss which the balls exhibited during the compression test was measured by integrating the *Force-Deformation* data. It was found that the *Oversize* ball had the lowest hysteresis loss, followed by the *Pressurised*, *Pressureless* and then the *Punctured* ball. It was concluded that the *Oversize* ball exhibited the lowest losses due to its geometry and reduced wall thickness which both acted to reduce the bending stresses in the rubber wall.

The results presented in this section give a good comparison of the physical properties of the different types of tennis ball. They are only directly relevant to a quasi-static compression of the ball, between two rigid plates. However, they may be used at a later stage to help explain results obtained for a dynamic impact between a ball and surface.

4.4 Normal ball impacts on a rigid surface

4.4.1 Introduction

In section 3.3 an experiment is described which involves a ball being projected towards a flat, rigid surface; impacting perpendicular to the plane of the surface. The ball impact and rebound velocity was measured using either a set of speed gates or a high speed video system. The video system was also used to determine the magnitude of the ball deformation and ball/surface contact area during impact.

The following section illustrates and discusses the results for this impact test. Four different ball types are used, as in the previous section. The objectives of this experiment were,

1. To determine the energy loss in an impact between a ball and rigid surface by measuring the ball impact and rebound velocities.
2. To determine the magnitude of the ball deformation and the contact time.

The acquired data can then be used to understand the differences in the physical properties of the different ball types, and also to identify how these properties vary with the ball impact velocity.

4.4.2 Ball rebound velocity – Results and Discussion

Figure 4.6(a) illustrates the relationship between the ball impact and rebound velocity for four different ball types. It shows that all the standard production balls (*Pressurised*, *Punctured* and *Oversize*) exhibit a similar rebound velocity for an impact speed of ~6m/s. This is likely to be because the ITF regulations ensure that all approved tennis balls must rebound to a specified height, for a drop on a rigid flat surface. In this approval test, the ball is dropped from 100inch which corresponds to a ball impact velocity of ~6m/s.

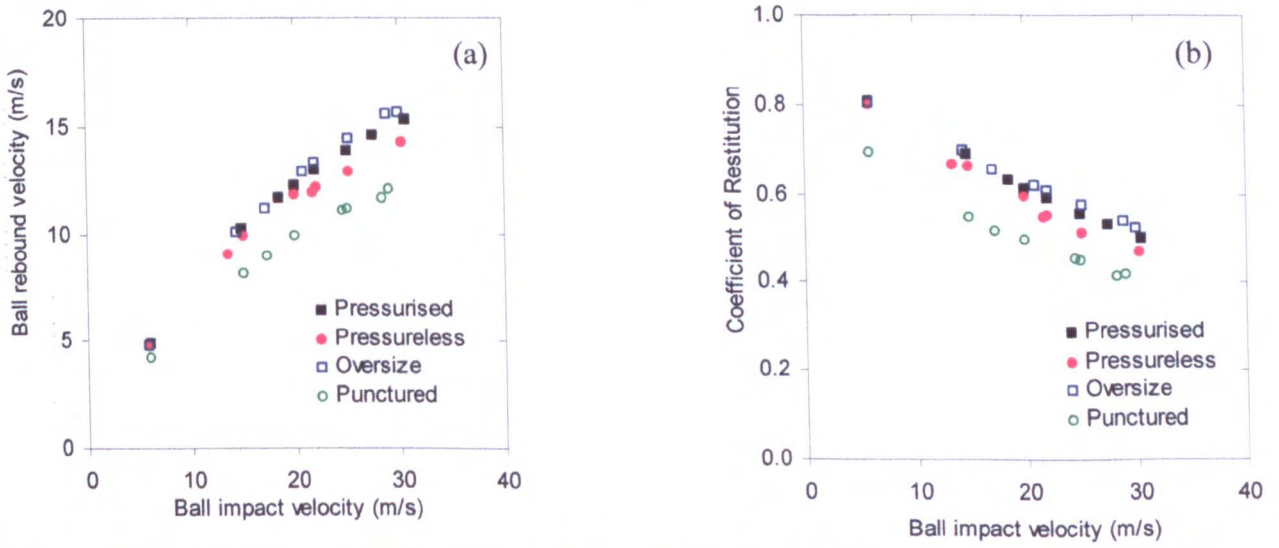

Figure 4.6 (a) Ball rebound velocity, and (b) Coefficient of restitution, for an impact between a ball and rigid surface, for four different ball types.

The *Pressurised* and *Oversize* balls rebounded faster than the other two balls for the full range of ball impact velocities. At the highest ball impact velocities, the *Oversize* rebounded fractionally

faster than the *Pressurised* ball. The *Pressureless* ball rebounded slower than the other two production balls, by ~7%. The *Punctured* ball rebounded the slowest of all the production balls; it is generally 20% slower than the *Pressurised* ball. This result illustrates that the internal pressurisation of the *Pressurised* ball contributes to approximately 20% of the rebound speed, for an impact on a rigid surface.

Figure 4.6(b) shows the coefficient of restitution plotted against the ball impact velocity; the coefficient of restitution *COR* is defined as the ratio of ball impact and rebound velocity. This is an alternative illustration of the same results that are shown in Figure 4.6(a). The ratio of the energy lost during impact and the initial energy can be defined as $\left(1-COR^2\right)$. Therefore the results in Figure 4.6(b) show that a tennis ball loses an increasing fraction of its energy as the impact velocity increases. A simple calculation can be performed to show that the *Pressurised* ball loses 36% and 75% of its initial energy for impacts at 6m/s and 30m/s respectively. By comparison, a *Punctured* ball loses between 51% and 84% of its initial energy for impacts between 6m/s and 30m/s, respectively.

The results in Figure 4.6(a) and (b) show that the *Oversize* and *Pressurised* balls dissipate a similar amount of energy during impact. This energy is dissipated in the form of heat which is produced by the deformation of the rubber core. The *Pressureless* ball dissipates more energy during impact than the other two production balls. This ball has a thicker core and therefore the volume of rubber which is deformed is larger compared to the other two balls. The *Punctured* ball loses the most energy during impact which is probably due to its low stiffness resulting in higher deformations of the rubber core. A tennis ball dissipates an increasingly large fraction of its initial energy as the impact velocity is increased. This is likely to be due to a combination of both the increased magnitude and rate of deformation for the higher speed impacts.

4.4.3 Ball Deformation during impact – Results and Discussion

The method used to determine the magnitude of the ball deformation during an impact with a rigid surface is described in section 3.3. Figure 4.7(a)-(d) illustrates the ball deformation, as a function of time. The results are presented for four nominal impact velocities which are 6m/s, 15m/s, 20m/s and 30m/s. All the production tennis balls have similar deformation-time plots for an impact velocity of 6m/s, as shown in Figure 4.7(a). At this impact velocity, the maximum ball deformation is approximately 10mm. This is of a similar order of magnitude as the compression that balls are subjected to in the ITF approval test. Therefore, this may account for the similarity in the results for all production tennis balls when the ball impact velocity is 6m/s. The *Punctured* ball deforms more than the production balls, which is likely to be due to its lower structural stiffness.

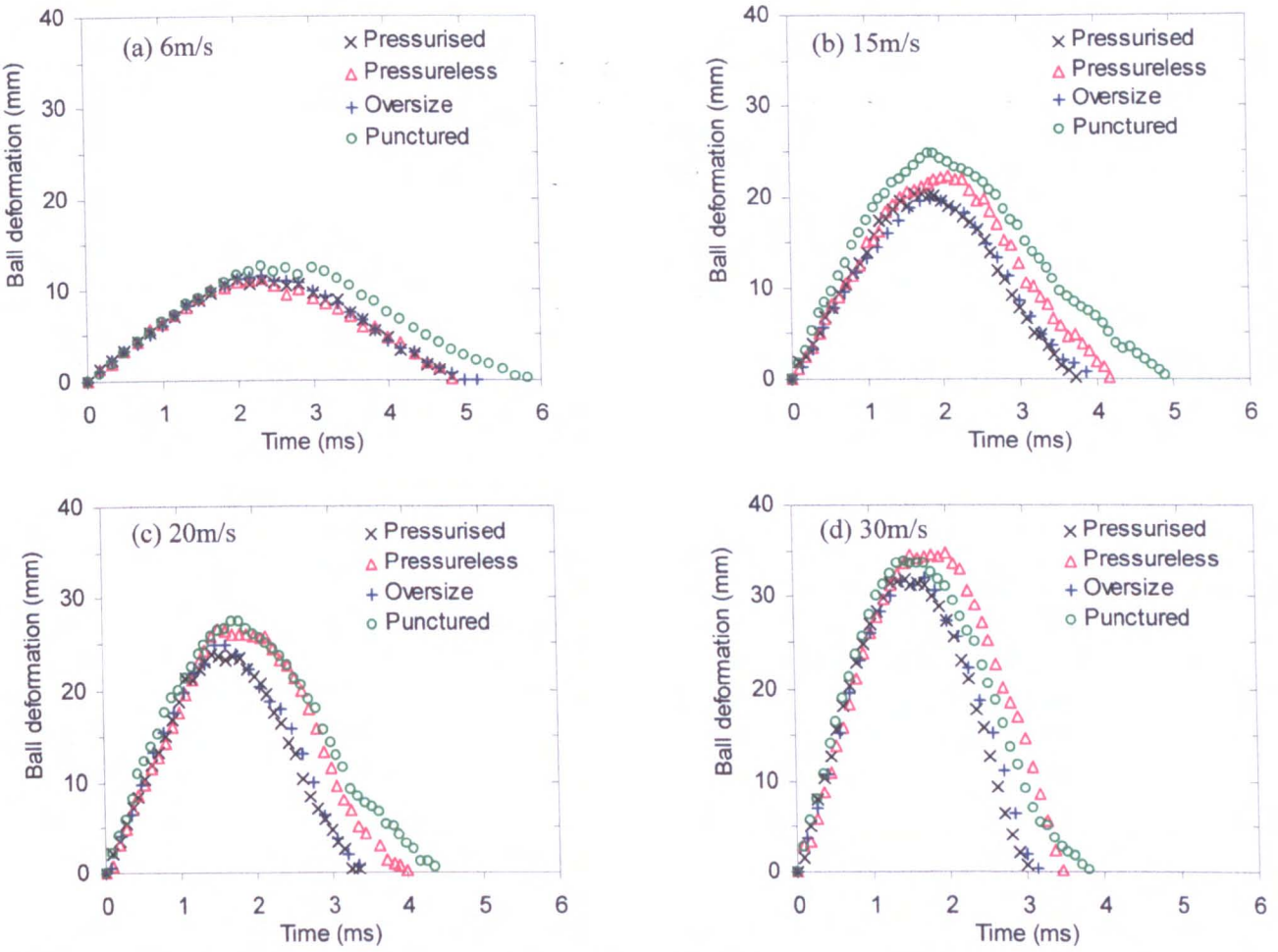

Figure 4.7 Ball deformation during an impact between a ball and rigid surface, for a range of nominal impact velocities, (a) 6m/s, (b) 15m/s, (c) 20m/s and (d) 30m/s.

Figure 4.7(a)-(d), and other similar plots for different impact velocities, can be used to determine the maximum ball deformation during impact $\delta_{BALL(max.)}$ and the contact time T_C. In this experiment, T_C is defined as the time taken for the ball to regain its original, undeformed shape i.e. the time at which the ball deformation returns to zero.

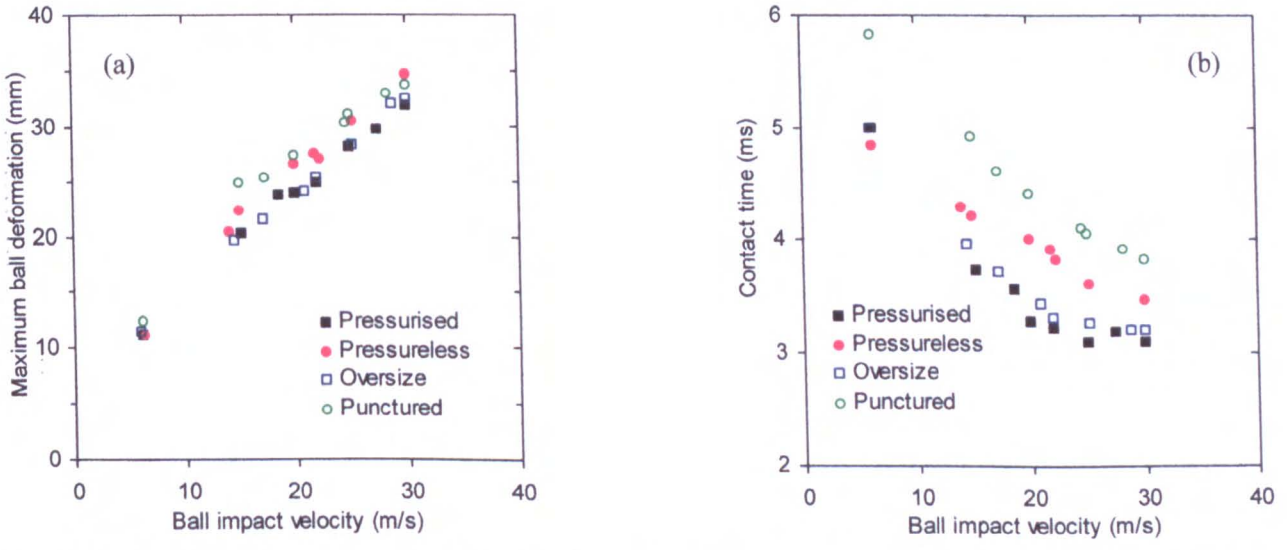

Figure 4.8 (a) Maximum ball deformation $\delta_{BALL(max)}$ during impact, and (b) Contact time T_C for an impact between a ball and rigid surface.

Figure 4.8(a) illustrates the relationship between impact velocity and maximum ball deformation for the four different ball types. It shows that the *Pressurised* and *Oversize* balls deform by similar amounts for all ball impact velocities. The *Pressureless* ball consistently deforms more than these two balls, for impact velocities above 15m/s. The *Punctured* ball generally deforms more than all the other balls, except at high impact velocities when it deforms by a similar amount as the *Pressureless* ball.

Figure 4.8(b) shows that the contact time for the all the standard production balls is similar at the lowest impact velocity; the *Pressureless* ball having a fractionally lower T_C than the other two balls at this velocity. However, at all other impact velocities the *Pressureless* ball has a higher contact time than the other two balls. The *Punctured* ball exhibits a considerably longer contact time than all standard production balls, for all ball impact velocities. The *Pressurised* and *Oversize* balls have very similar contact times over the full range of velocities.

The data in Figure 4.7 and 4.8 shows that the *Pressurised* and *Oversize* balls deform by comparable amounts during impact, and exhibit similar contact times. Simple modelling of an impact between a deformable object and rigid surface shows that the ball deformation and contact time are a function of the structural stiffness of the ball. Therefore, this data suggests that the *Pressurised* and *Oversize* balls have a similar stiffness and the *Pressureless* and *Punctured* balls are less stiff than the other two balls; the *Punctured* ball being the least stiff. Also, the results in Figure 4.8(b) suggest that the balls act stiffer at higher ball impact velocities.

In section 3.3.4 a method of determining the diameter of the ball/surface contact area is discussed. This diameter is defined as the length of the ball that is in contact with the surface. This length is measured from the high speed video images. Figure 4.9(a)-(h) illustrate the relationship between the contact area diameter and the ball deformation for the four ball types, for a range of impact velocities. For clarity, this data is plotted separately for the compression and restitution phases of impact, on the left and right hand side of Figure 4.9, respectively. This figure shows that, during the compression phase, the relationship between contact area diameter and ball deformation is relatively independent of the ball impact velocity. For each ball type, there is a single function to describe the relationship between the contact area and the ball deformation. However, in the restitution phase there is no single function to describe this relationship, and there are no apparent trends evident between the four ball types. Interestingly, a comparison of Figure 4.9 (d) and (h) shows that the *Punctured* ball is the only ball type that acts similarly in the restitution and compression phases. However, the significance of this can not be obtained from this data alone.

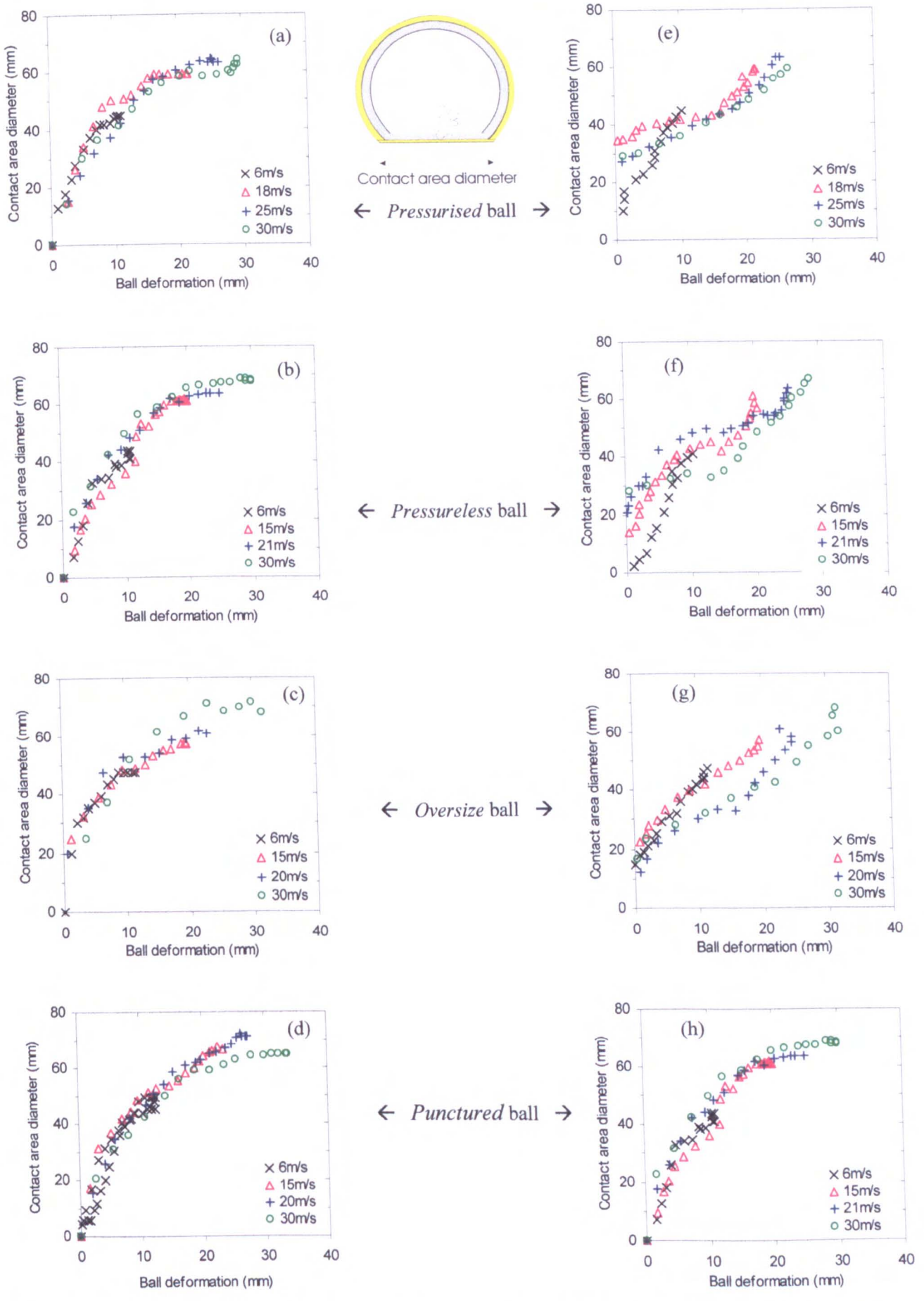

Figure 4.9 Diameter of the ball/surface contact area during an impact between a ball and rigid surface. The data is plotted for four different ball types and four different ball impact speeds. (a)-(d) illustrate data for the compression phase of impact, and (e)-(h) illustrate data for the restitution phase.

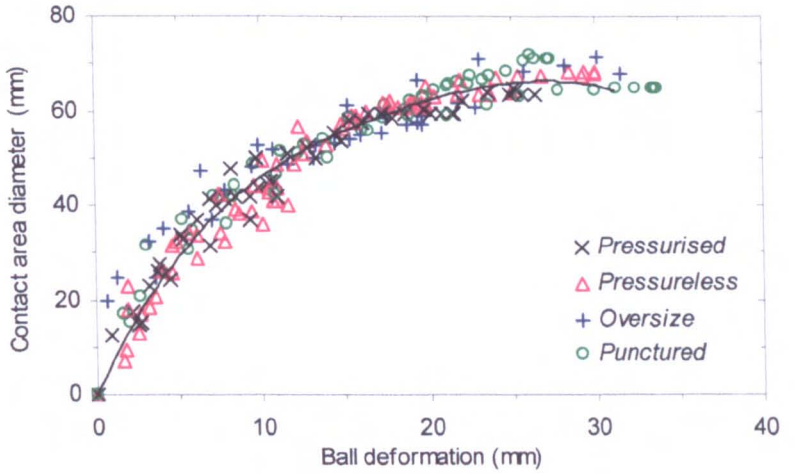

Figure 4.10 Relationship between diameter of ball/surface contact area and ball deformation during the *compression* phase of impact. A single fourth order polynomial trendline is plotted through the combined data set of all the ball types.

Figure 4.10 shows the data for the contact area diameter d_{CONT} plotted as a function of the ball deformation δ_{BALL}, for all four different ball types. This data is only plotted for the compression phase of impact. The equation for the 4th order polynomial trendline which is plotted in this figure (converted into SI units) is,

$$d_{CONT} = -1.66\times10^{5}\,\delta_{BALL}^{4} + 1.27\times10^{4}\,\delta_{BALL}^{3} - 4.13\times10^{2}\,\delta_{BALL}^{2} + 7.6\,\delta_{BALL} \qquad [4.1]$$

There appears to be no significant differences between the four ball types, and therefore [4.1] gives an approximate relationship between d_{CONT} and δ_{BALL} for all ball types.

There is considerable scatter in the data which was quantified by conducting a simple statistical analysis. The standard deviation of the raw data from the trend line was calculated as 4mm. In Chapter 3 it was quoted that the standard deviation associated with the accuracy of the manual sampling method was 2mm. This implies that the scatter in the data in Figure 4.10 is not solely due to inaccuracies in the analysis method. A possible reason for the scatter is that the relationship between contact area diameter and ball deformation is a subtle function of the ball type and impact velocity. However, this subtle function can not be quantified using this data.

An equation similar to [4.1] cannot be determined for the restitution phase of impact because there is too much scatter in the data for this phase, as is evident in Figure 4.9(e)-(h). This implies that, during the restitution phase, there is no simple function to describe the relationship between contact area diameter and ball deformation.

4.4.4 Summary

In this section, data is presented for a normal impact between a tennis ball and rigid surface. Four different types of ball were tested which covered the range of balls used in the game of tennis. For the lowest impact velocity of 6m/s, it has been shown that all the standard production balls exhibit the same maximum ball deformation, contact time and rebound speed. This is most likely to be

due to the fact that the ITF approval tests regulate the bounciness and quasi-static stiffness of the ball for an impact at a similar velocity/deformation. The *Punctured* ball has a lower rebound velocity and deforms more than the other balls, but obviously this ball would not pass the ITF approval test.

The *Oversize* and *Pressurised* balls rebound with a similar velocity, for the full range of impact velocities. The measured values of contact time and ball deformation for the impact are also similar for these two balls. The *Pressureless* ball rebounds approximately 7% slower than these two balls, at higher velocities. This ball also deforms more during impact and has a longer contact time at these velocities, which implies that it is less stiff in comparison to the other two production balls. The *Punctured* ball deforms the most; approximately 15% more than the other balls. It also exhibits a considerably longer contact time which confirms that it is less stiff.

These results correlate qualitatively with the quasi-static compression test results in the previous section. In that section it was shown all the standard production balls have a similar quasi-static stiffness for ball deformations of approximately 7mm. In this section it has been shown that all these balls deform by a similar amount in a dynamic impact which involves a deformation of ~7mm. At higher ball deformations the quasi-static stiffness of the *Pressureless* ball is lower than that for the *Pressurised* ball. An analogous finding was made in this section where a *Pressureless* ball exhibited a larger deformation and contact time compared to a *Pressurised* ball, for high impact velocities. Any subtle differences that existed between the *Pressurised* and *Oversize* balls could not be concluded in this section. The larger deformation exhibited by the *Pressureless* and *Punctured* balls result in a greater volume of rubber being deformed during impact. Therefore the energy losses will be higher and so the rebound velocity will be lower.

The diameter of the ball/surface contact area is an increasing function of the ball deformation. However, it is not dependent on the ball impact velocity or the ball type for the compression phase of the impact. A single function was obtained to describe the relationship between ball/surface contact area and ball deformation for this phase of impact. No definite correlation could be found between these parameters during the restitution phase of impact.

4.5 Ball impacts on a Force Platform

4.5.1 Overview

In section 4.4, a high speed video system was used to determine the ball deformation during impact, contact time and ball rebound velocity for an impact between a ball and rigid surface. These results can be used to define the required stiffness and damping properties of the ball which give realistic values of contact time and energy loss. The main weakness of the method used in the previous section is that the force which acts on the ball can not be calculated. Therefore the force which is calculated in the model can not be verified experimentally.

In this section the rigid surface was replaced with a force platform and the ball was propelled perpendicularly towards it. The details of this experiment are given in section 3.4. In brief, the piezo-electric force platform outputs a voltage which is proportional to the force applied, and this

voltage is sampled at approximately 67kHz. This signal is multiplied by a calibration factor to determine the magnitude of the force at each time increment. The *Force-Time* data from the force platform was used to determine the acceleration, velocity and displacement of the ball centre-of-mass during impact.

The balls were propelled at a velocity of between 4 and 30m/s (10 and 70mph) which exceeds the speeds used by other authors who have performed a similar experiment (Neville 2001, Thomson 2000). The impact velocities were chosen in an attempt to simulate the magnitude of ball deformation which occurs in a professional serve. Mitchell *et al.* (2000) showed that the relative ball/racket impact speed for a college standard serve was up to 35m/s. Professional serves are likely to involve a larger relative impact speed but this data has not yet been published to date. In a later chapter of this study, the magnitude of ball deformation which occurs in a ball/racket impact during a professional serve is presented.

Neville (2001) and Thomson (2000) tested a range of tennis balls for impact velocities between 2 and 20m/s. Each researcher tested three balls of each type and it was universally found that there was no significant differences between the results for all the balls of one type. Therefore, in this study it was concluded that only one ball of each type needed to be used. The same four types of ball are tested in this section as were used in section 4.4; *Pressurised*, *Oversize*, *Pressureless* and *Punctured* balls.

4.5.2 Results

(a) Ball rebound velocity

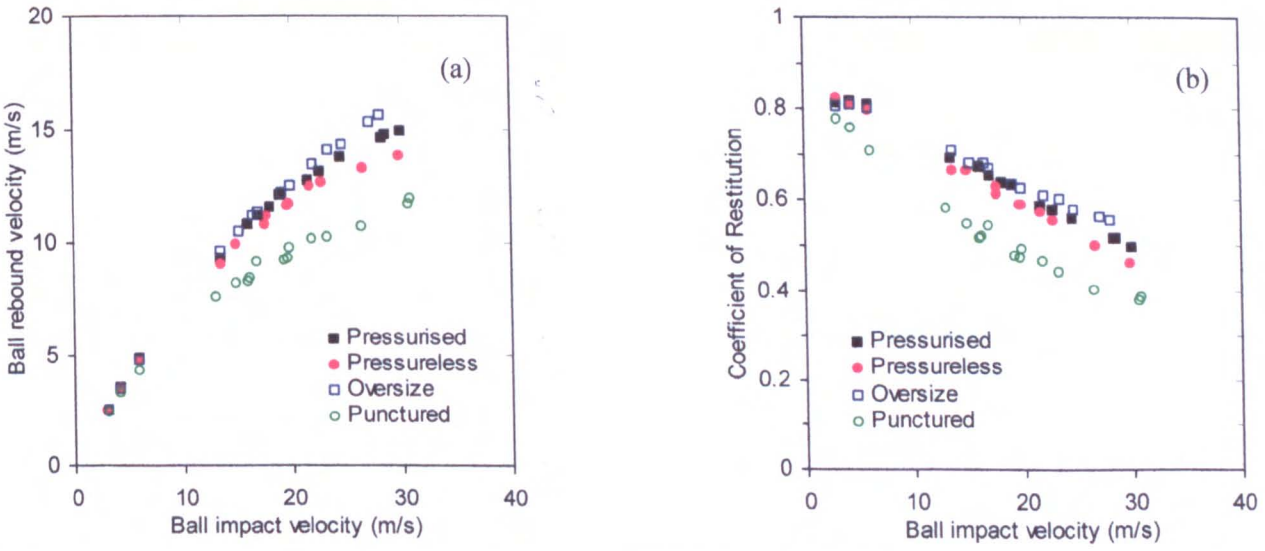

Figure 4.11 (a) Ball rebound velocity, and (b) coefficient of restitution plotted against impact velocity for normal impacts on the force platform.

Figure 4.11(a) and (b) show the results for ball rebound velocity and coefficient of restitution respectively, for impacts on a force platform. In section 4.4, these two parameters were obtained for an impact on a rigid surface and the results are shown in Figure 4.6 (a) and (b). A simple visual comparison of these two sets of figures shows that the results are very similar for both experiments.

All production balls have a similar rebound velocity for low speed impacts. For higher impact velocities, the *Oversize* ball rebounds fractionally faster than the *Pressurised* ball, and significantly faster than the *Pressureless* ball. The *Punctured* ball rebounds considerably lower than the production balls, for all ball impact velocities. These results confirm the data and conclusions which were presented in section 4.4.

(b) Force platform data

Figures 4.12 (a)-(h) show the force platform results for impacts using the four balls types and a range of impact velocities. Figures 4.12 (a)-(d) show the *Force-Time* data and Figures 4.12 (e)-(h) show the *Force-Displacement* data (the *Displacement* parameter referred to here is the displacement of the ball centre-of-mass). These results are very similar to those found by Thomson (2000) and Cross (1999, 2000), although all these authors only used impact velocities of approximately 20m/s or less. The figures show that the maximum force and ball COM displacement increases with the impact velocity.

For impact velocities of 6m/s and below, Figures 4.12 (a)-(d) show that the *Force-Time* plot is an approximate sine curve for all ball types. Figures 4.12 (e)-(h) show that the hysteresis loss in the ball, defined by the area enclosed within the *Force-Displacement* curve, is relatively small for these low speed impacts. The exception to this is the *Punctured* ball which exhibits a significant hysteresis loss.

For impact velocities above 6m/s, all the *Force-Time* plots have an asymmetrical shape with a variable number of oscillations that are super-imposed onto a smooth curve. The *Force-Displacement* data in Figures 4.12 (e)-(h) show that the ball initials experiences a very low load which is due to the compression of the cloth on the ball. As the cloth has a much lower stiffness than the ball (Cross 1999b) the load in this section of the impact is very low. In general, the force then rises sharply, followed by a sudden dip, then continues rising at a lower rate. The force rises along an almost vertical path and the load magnitude at which the dip occurs is proportional to the impact speed. During the restitution phase, Figures 4.12 (e)-(h) show that the force values lie on a path which is relatively independent of impact velocity. This implies that the measured force value is primarily a function of the ball centre-of-mass displacement and not the instantaneous speed of the ball.

The data for the coefficient of restitution, described in section 4.4.2, showed that the fraction of initial energy that is lost during impact increases with ball impact velocity. The *Force-Displacement* plots in Figures 4.12 (e)-(h) illustrate this finding in an alternative manner; the hysteresis loss being defined as the area enclosed by the *Force-Displacement* curve.

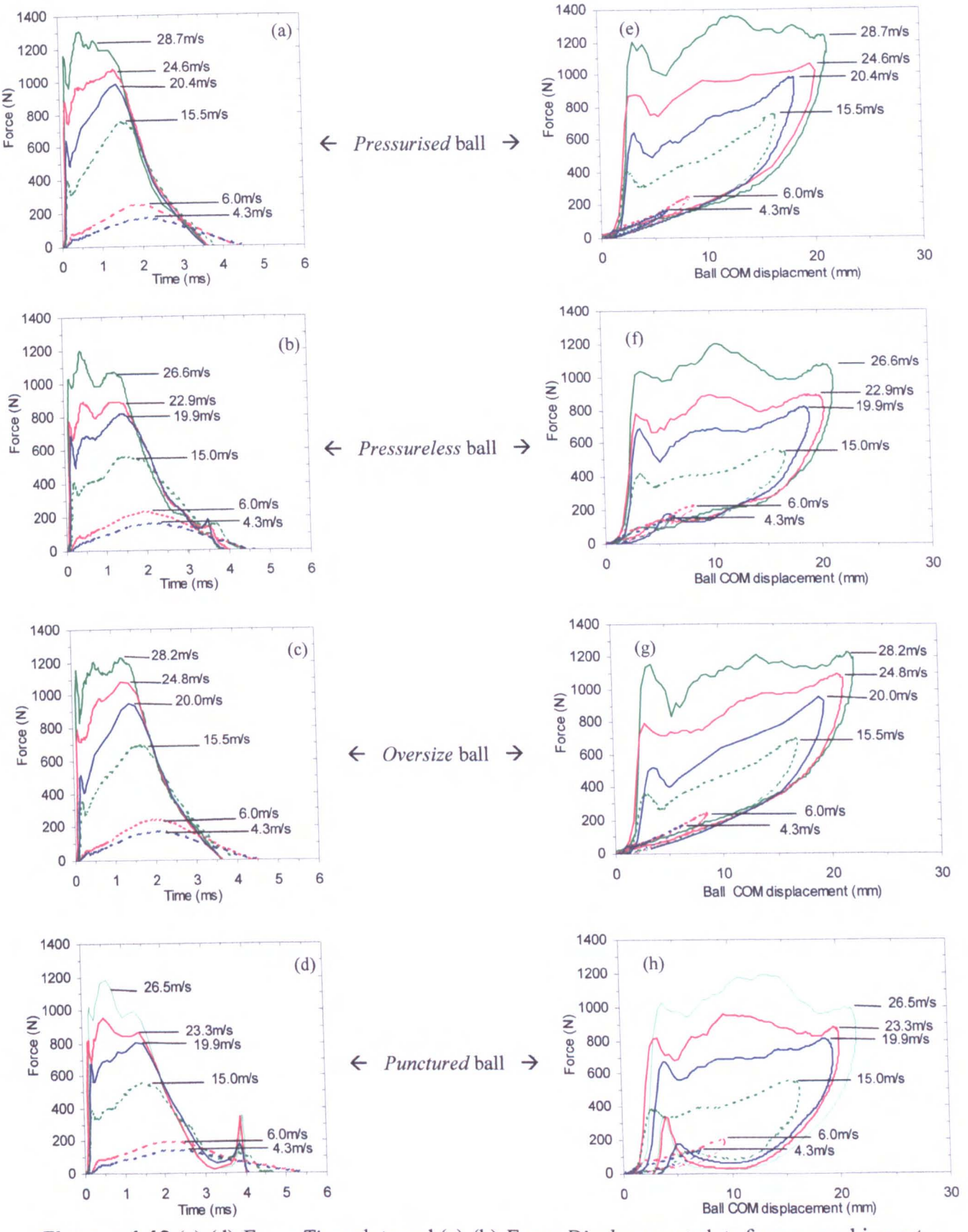

Figures 4.12 (a)-(d) *Force-Time* plots and (e)-(h) *Force-Displacement* plots for a normal impact between a tennis ball and force platform. The data is presented for each ball type separately, for a range of ball impact velocities.

Figures 4.12(e)-(h) show that the maximum force always occurs at the point of maximum ball centre-of-mass displacement, for impact velocities below 20m/s. For impact velocities of 20m/s and above there is a secondary peak in the force which occurs at approximately 50% of the

maximum deformation. This secondary peak is generally most noticeable for the two unpressurised balls (*Pressureless* and *Punctured*) and is of equal magnitude to, or greater than, the force which occurs at maximum deformation for these two balls. This second peak is least prominent in the data for the *Oversize* ball. The presence of a peak in the force which is not at the point of maximum deformation implies that the force acting on the ball is not solely due to its structural stiffness. If this had been the case then the force would consistently be at a maximum at the point of maximum deformation. Therefore it can be concluded that there must be other components which make up the load on the ball.

The *Force-Displacement* plots show that the ball centre-of-mass returns to zero displacement when the force returns to zero. This may appear obvious, but it confirms that the ball COM returns to its original, undeformed position at the end of impact.

Figures 4.13 (a)-(h) illustrate the same data as that presented in Figures 4.12(a)-(h) but is categorised by the ball impact velocity so that comparisons can be made between the four different ball types. For a low speed impact velocity of 6m/s, Figures 4.13(a) and (e) show that the three production balls (*Pressurised*, *Pressureless* and *Oversize*) exhibit very similar *Force-Time* and *Force-Displacement* responses for an impact on a rigid surface. The *Oversize* ball deforms slightly more, and the *Pressureless* ball is subjected to a fractionally lower force, compared with the *Pressurised* ball. When compared to the three production balls, the *Punctured* ball (i) deforms significantly more, (ii) has a longer contact time, (iii) is subjected to a lower maximum load, and (iv) has a higher hysteresis loss.

At the higher impact speeds (15m/s-24m/s) the two internally pressurised balls (*Pressurised* and *Oversize*) act very similarly, with two exceptions. The *Oversize* ball generally deformed slightly more and had a lower load throughout impact, especially during the compression phase. Also, the peak load which occurs at approximately 0.2ms after initial impact is generally the lower for the *Oversize* ball. The force always rises to a peak at the maximum deformation for these two internally pressurised balls and the restitution phase is very similar for both balls, for all impact velocities.

The two unpressurised balls (*Pressureless* and *Punctured*) act very similarly during the compression phase, for impact velocities between 15 and 24m/s. For the initial 0.5ms of impact, they have a *Force-Time* trace similar to the *Pressurised* ball. During the remainder of the compression phase the force initially drops and then rises steadily until maximum COM displacement. The maximum force is very similar for both balls, and the *Punctured* ball deforms fractionally more than the *Pressureless*. They both deform by about the same amount as the *Oversize* ball, but have a considerably lower force. In the restitution phase, the force acting on the *Pressureless* ball is similar to that of the pressurised balls but slightly lower. The force in the *Punctured* ball is considerably lower than all the others, which is likely to be due to the very low stiffness of this ball. The force acting on the *Punctured* ball almost drops to zero when the ball COM displacement returned to a value of approximately 10mm. Towards the end of impact it rose significantly before dropping back to zero. This sudden rise is probably due to the ball 'flipping back' to its original shape after compression. This occurs to a lesser extent in the *Pressureless* ball trace, but generally not in the pressurised balls.

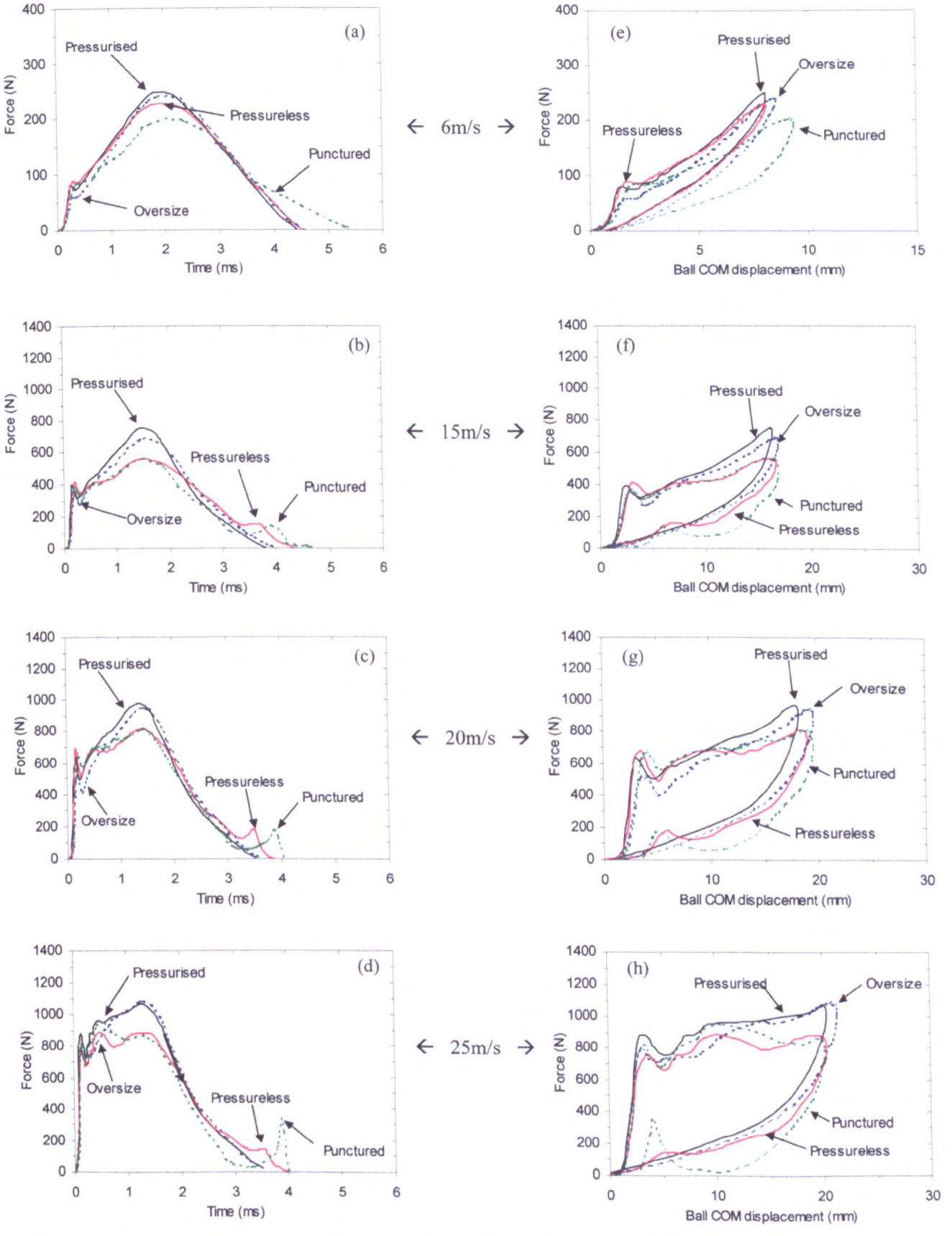

Figures 4.13 (a)-(d) *Force-Time* plots and (e)-(h) *Force-Displacement* plots for a normal impact between a tennis ball and force platform. The data is categorised for each impact velocity, for a range of ball impact velocities.

(c) Contact Time

The *Force-Time* plots, shown in Figures 4.12(a)-(d), were used to determine the contact time; the contact time being defined here as the time at which the force returns to zero. This data is presented in Figure 4.14(a) and shows that the contact time decreases with ball impact velocity. For low speed impacts, all the production balls have a similar contact time. At higher speeds, the *Pressurised* ball has the lowest contact time, only fractionally shorter than the *Oversize* ball. The *Pressureless* ball has a contact time which is approximately 0.3ms longer than that of the *Pressurised* ball, for impact velocities between 13 and 30m/s. The *Punctured* ball has a significantly longer contact time compared with all the other balls; the contact time is approximately 0.8ms longer than that for the *Pressurised* ball.

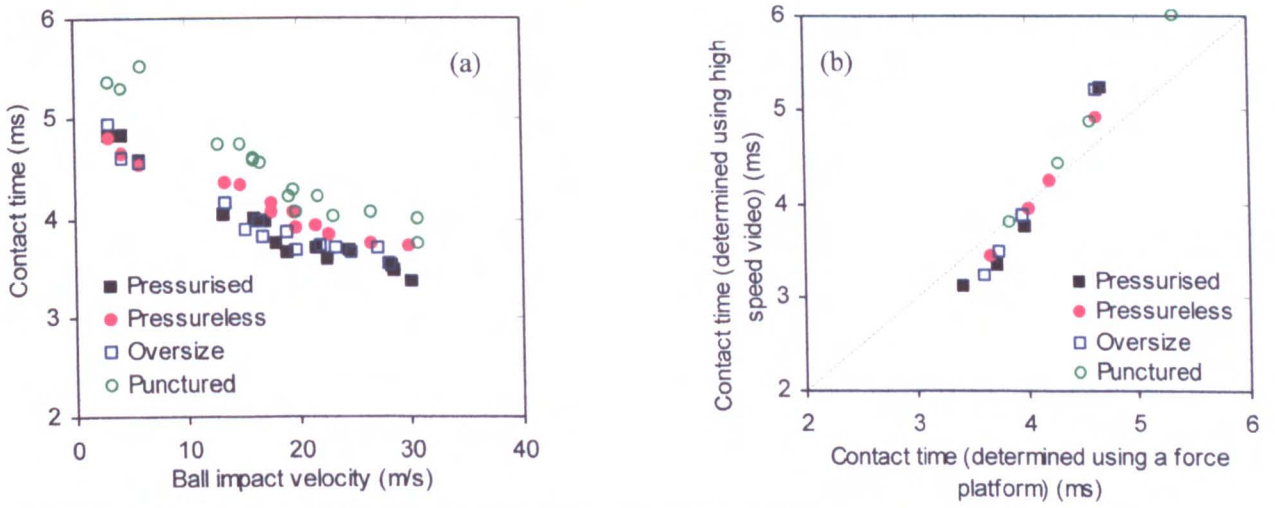

Figure 4.14 (a) Contact time plotted against ball impact velocity determined from the force platform, and (b) comparison of contact times determined using the force platform and the high speed video system for impact velocities ranging between 6m/s and 30m/s.

The differences in the contact times for the four ball types which have been determined here are similar to the findings in section 4.3. In that section, the contact time was measured using a high speed video system; the contact time being defined as the time taken for the ball to return to its undeformed shape. Comparison of the values of contact time determined using the two methods reveals that the different methods give different values of contact time. A comparison of the data collected using the two methods is shown in Figure 4.14(b). Each data point in this figure represents the contact time at one of four discrete impact velocities; 6, 15, 20 and 30m/s. The value of contact time at each discrete velocity was determined by plotting a 2nd order polynomial trend line for each dataset in Figure 4.8(b) and Figure 4.14(a). The diagonal line in Figure 4.14(b) represents the 1:1 relationship between the two values of contact time. Figure 4.14(b) shows that the contact time determined using the high speed video is higher, for large contact times (lower speed impacts). For the shorter contact times (higher speed impacts) the force platform gives the higher values of contact time.

The reason for the differences in the two sets of contact time data can easily be assigned to the fact that different definitions are used in the two cases. Figure 4.15 shows a collection of high speed images which illustrate the ball deformation throughout impact. This figure shows that a ball can

have a negative deformation (-7mm in this case) yet still be in contact with the surface. Using the high speed video method, the contact time would have been determined as 3.3ms. However, clearly the ball is still in contact with the surface and therefore may be applying a force which is registered by the force platform. This explains why the force platform may give different contact times than the those obtained using the high speed video system.

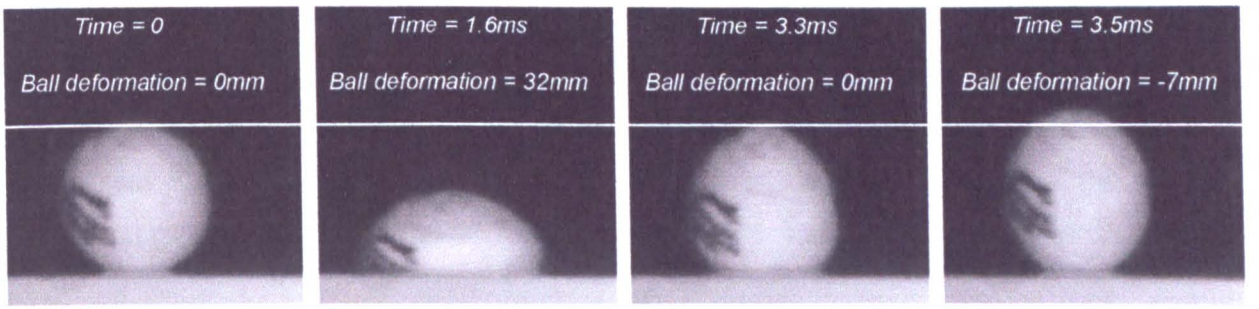

Figure 4.15 High speed video images showing an impact between a ball and rigid surface (ball impact velocity = 25m/s)

(d) Ball deformation

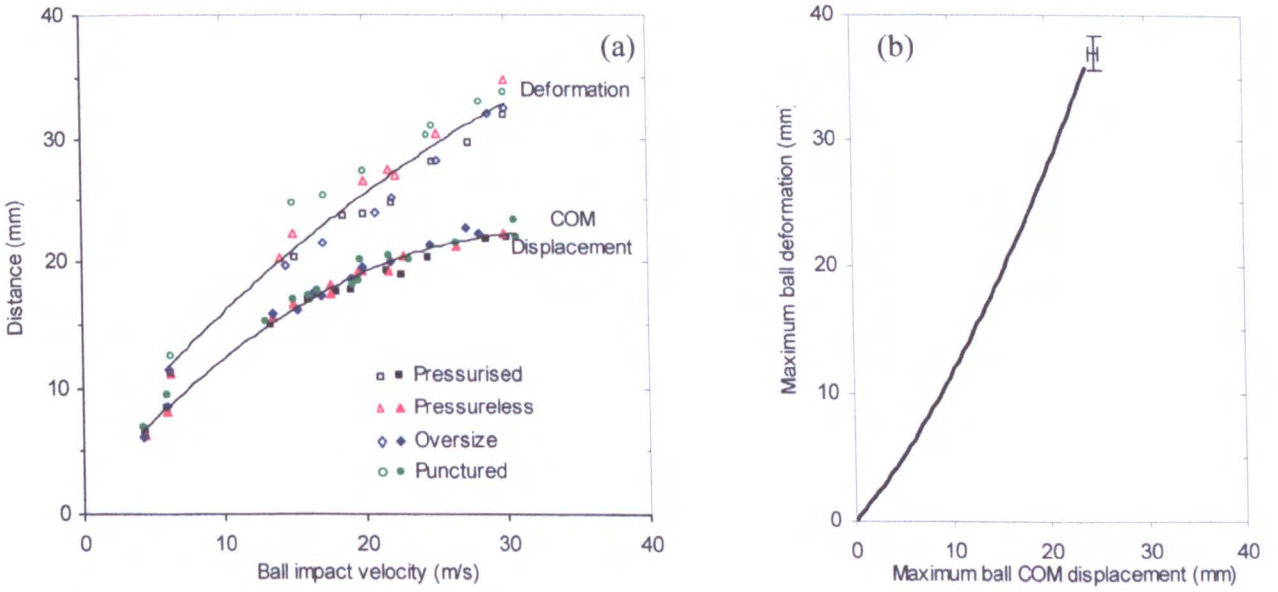

Figure 4.16 (a) Maximum ball COM displacement and maximum ball deformation, plotted against ball impact velocity. The trendlines represent the best-fit line for the combined data for all ball types. (b) Approximated relationship between maximum ball COM displacement and maximum ball deformation. The error bars represent one standard deviation of each variable.

Figures 4.12 (e)-(h) show the magnitude of the ball centre-of-mass displacement during impact for impact velocities between 4 and 30m/s. The maximum ball COM displacement for each of these impacts is shown in Figure 4.16(a). For comparative purposes, the magnitude of the maximum ball deformation is also shown in this figure. This is the same data that is shown in Figure 4.8(a) and was determined using the high speed video system. Figure 4.16(a) shows that the *Punctured* and *Pressureless* balls deform significantly more than the *Pressurised* and *Oversize* balls. However, it

also shows that the *Oversize* ball exhibits the largest maximum centre-of-mass displacement, and the *Pressurised* ball the least. This relationship is difficult to identify in Figure 4.16(a) but can be seen more clearly in the *Force-Displacement* plots such as those in Figures 4.13(e)-(h).

In Figure 4.16(a), trendlines are plotted which have been obtained by performing a least squares regression of the combined data for all ball types. It is assumed that the uncertainty of each data point is equal and therefore the standard deviation of the measured data can be calculated using the method described in Appendix A. The standard deviations were calculated as 0.5mm for the maximum ball COM displacement trend line, and 1.4mm for the maximum ball deformation data.

Figure 4.16(b) gives a quantification of the relationship between the maximum ball COM displacement and maximum deformation. This relationship was determined using trendlines which are plotted in Figure 4.16(a). The error bars on this figure represent one standard deviation of each variable. The relationship between these two variables has been estimated by many authors (Leigh & Lu 1992, Thomson 1999) as it is a useful tool to relate the quasi-static structural stiffness of a ball with its behaviour during impact.

4.5.3 Discussion

In this section, four types of tennis ball were projected at a force platform for a range of ball impact velocities. The ball rebound velocity was measured and the results were identical to those presented in the previous section. In that section, the ball was propelled at a rigid surface and the differences between the four ball types have been presented and explained.

At the lowest impact speed (6m/s), the *Force-Time* plots for the three production balls are very similar and approximate a sine curve. Figure 4.16(a) shows that all of these balls deform by approximately 12mm during this low speed impact. Figure 4.3 shows that all the ball types have a similar quasi-static stiffness for ball deformations up to 12mm. The stiffness of the *Punctured* ball is considerably lower than that of the three production balls and this would explain why this ball deforms more and has a longer contact time; contact time being an inverse function of the stiffness of the ball.

For impact velocities of between 15m/s and 25m/s, the *Pressurised* and *Oversize* balls act very similarly. The data in Figure 4.8 shows that the balls deform by between 20 and 30mm at these impact velocities. At these high deformations, the results in Figure 4.3 show that the *Pressurised* ball has the highest quasi-static stiffness, closely followed by the *Oversize* ball. The *Pressureless* and *Punctured* balls have a lower stiffness and both these balls exhibit a longer contact time and lower peak forces during impact, compared to the other two balls. The *Punctured* and *Pressureless* balls dynamically act very similarly to one another, with similar peak loads and centre-of-mass displacements. This is probably explained by them having similar a quasi-static stiffness at high deformations. At low deformations, the *Pressureless* ball is definitely stiffer and this may explain why the *Pressureless* ball has a slightly shorter contact time than that for the *Punctured* ball for low speed impacts. This may also explain why the *Pressureless* ball always exhibits a higher load than the *Punctured* ball during the restitution phase.

A very noticeable feature of the *Force-Time* and *Force-Displacement* plots is the sharp rise in the force at the initial stage of impact. This is followed by a sudden dip before the force begins to rise again. In Thomson (1999) and Cross (1999a) this dip has been accounted for by the instability of the ball core during the initial stages of impact. Cross (1998) used a two-piece force platform to prove that the dip coincides with the ball core buckling, and Dignall (1999) arrived at a similar conclusion using a finite element model of the ball. These researchers have all assigned the sharp rise before the dip to the high structural stiffness of the shell prior to the buckling. However, an alternative explanation can be given by considering the work done by Hubbard & Stronge (2001). This work has been discussed in detail in Chapter 2 and involved the modelling of table tennis ball impacts on a rigid surface. In brief, it was assumed that the section of the ball in contact with the surface was at rest, and the remainder of the ball was a truncated sphere in which all elements of this sphere were moving with an identical group velocity. An analogous analysis can be conducted for a tennis ball impacting on a force platform. If it is assumed that a section of the tennis ball is being brought to rest (from the group velocity) in a specific time interval, then this will exert a force on the platform, separate to any force due to the stiffness of the ball. Therefore the total force applied to the platform is a combination of this momentum flux, the wall stiffness and the internal air pressure, for the period during compression. At the initial stage of compression, the ball is moving at its maximum velocity and therefore, in any specific time interval, the magnitude of the section that is being brought to rest is largest at this initial stage. This would result in a large force during this period contributed mainly by the momentum flux.

There are alternative explanations for the high initial force which is exerted on the ball. Neville (2001) and Thomson (2000) assumed that the sudden initial rise in the force was due to the high structural stiffness of the ball, before buckling occurs. Although it is appreciated that the stiffness of the ball will be higher before buckling, compared to post-buckling, a simple one degree of freedom spring model can be used to show that the stiffness must be very large to achieve this rapid rise in force (Neville 2001). Also, a one degree-of-freedom spring-damper model, which is summarised in section 2.5.3., shows that the high rise in initial force could be due to the damping properties of rubber. If the damping in the core is modelled as a dashpot damper then the damping force is proportional to the rate at which the ball rubber is being deformed, which is proportional to the instantaneous velocity of the ball. This is obviously highest at the initial stage of compression which may explain the high initial force.

To summarise, there are three possible reasons for the high initial force which are,

1. High structural stiffness - the ball will have a higher structural stiffness before buckling occurs.
2. Momentum flux - the force due to a section of the moving ball being brought to rest on the surface, which is largest at the initial stage of impact
3. Material damping - the rubber core exhibits high levels of damping which are proportional to the rate of deformation, which is largest at the initial stage of impact.

The definitive explanation of the high initial force probably involves a combination of all three factors. The work in Chapter 5 considers all the three factors individually in an attempt to derive a

model for the impact. The aim of the model is to further the understanding of the impact mechanism. The results presented in this section will be referred to in Chapter 5 in order to verify the model and explain the differences between ball types further.

4.5.4 Conclusions

In this section it was found that all production tennis balls exhibit similar *Force-Time* plots for normal impacts between a ball and force platform, for impact velocities of approximately 6m/s. It was concluded that this was due to them all having a similar structural stiffness for deformations of this magnitude. The *Punctured* ball deforms considerably more than these three production balls, which is due to the lower quasi-static stiffness of this ball.

During the initial stage of the compression phase of impact, the measured force rises sharply, followed by a sudden dip, then continues rising at a lower rate. It has previously been shown that the dip is due to the buckling instability of the ball wall. The two main possible explanations for this sudden rise in force (i) high structural stiffness of the ball prior to buckling, and (ii) momentum flux force due to finite sections of the ball being brought to rest on the surface during the compression phase. During this first 0.5ms of impact, the force which acts on the ball is similar for all of the standard sized balls (*Pressurised*, *Pressureless* and *Punctured*) but lower for the *Oversize* ball. It is intended that the model which is to be developed in the following chapter can verify the precise reason for the value of the force in this period.

It has been shown that the maximum force which is measured during impact does not always occur when the ball has reached maximum deformation. This confirms that the force acting on the ball during impact is not solely due to the structural stiffness because, if these were the case, then the force would be an increasing function of the ball COM displacement.

During the restitution phase, the relationship between the measured force and ball centre-of-mass displacement is independent of the ball impact velocity, but does vary between ball types. This information will assist in the development of a model for this phase of impact.

The *Oversize* ball consistently exhibited a larger ball centre-of-mass displacement, compared to the *Pressurised* ball; the *Oversize* ball generally displacing by an equivalent amount to the *Punctured* and *Pressureless* balls. However, the *Oversize* and *Pressurised* balls exhibit similar contact times for the impact.

4.6 Summary

In this chapter, the physical properties of four different types of tennis balls have been obtained. It has been shown that the *Pressurised* and *Oversize* balls have the highest quasi-static stiffness when compressed between two flat plates. The *Pressureless* ball has a similar stiffness to these balls for low deformations, but a much lower stiffness at high deformations. At these high deformations it had a similar stiffness to the *Punctured* ball.

The ball was propelled at a rigid surface and various parameters were measured. It was found that the *Oversize* and *Pressurised* balls rebound with approximately the same velocity. The *Pressureless* ball rebounds slightly slower, and the *Punctured* ball rebounds significantly slower. This indicates that the *Oversize* and *Pressurised* balls exhibit the lowest hysteresis loss during impact. The contact time was generally shortest for the *Pressurised* ball and longest for the *Punctured* ball. This correlates with the quasi-static stiffness results because the contact time is inversely proportional to the structural stiffness.

In a separate experiment, the balls were propelled towards a force platform. The results for this experiment correlated qualitatively with the quasi-static compression test results. For example, in the quasi-static testing the *Pressureless* and *Punctured* balls had a similar stiffness for large ball deformations. Using the force platform, it was found that the *Force-Time* plots for these two balls were very similar for high impact velocities. It was also shown that the force which acts on the ball is not solely due to the structural stiffness and alternative components have been proposed.

One of the main objectives of this section was to experimentally determine the force which acts on the ball during impact. This objective was successfully achieved for a wide range of ball types and impact velocities. This data will be used in the following chapter to quantify the accuracy of a model of the impact.

5. Modelling of a Tennis Ball Impact on a Rigid Surface

5.1 Introduction

Chapters 3 and 4 describe the methods and results of an experimental investigation of a ball impacting on a rigid surface. In these experiments, a range of parameters were measured including the ball rebound velocity, ball deformation and contact time for the impact. Results were obtained for four different ball types, for a wide range of ball impact velocities. In the following chapter a model is developed which simulates this impact and can be used to predict such parameters as the force which acts on the ball during impact. The model will be used to help illustrate and explain the differences between the four ball types which were identified in Chapter 4.

In a later chapter, this model will be developed so that it is applicable for an impact between a ball and tennis racket. This model must not be over complex as it would then be unusable. However, it should correlate with the experiment data within reasonable error bounds. The main requirement is that each component of the model must have a physical significance so that, for example, the effect of a change in ball stiffness can be assessed using the model. Therefore, a numerical model which produces a perfect agreement with the experiment data is of no use.

5.2 General Modelling Procedure

There are many modelling techniques which could be used and the suitability of each of these is discussed in Chapter 2. In this current chapter, a visco-elastic model is used to simulate the ball for an impact with a surface. This technique was chosen as it is a relatively versatile method; the stiffness and damping of the ball can be defined using any function of the ball deformation and velocity. In Chapter 2, methods for modelling a tennis racket were discussed. It was shown that a one-dimensional flexible beam gave a good approximation of the modal response of a tennis racket. A review of previous researcher's work revealed that a visco-elastic model of the ball is an ideal method to simulate the ball, for an impact between a ball and flexible beam. The solution for the flexible beam equation and for the governing equations of the visco-elastic model can both be solved relatively easily using the finite difference method. A more complex method of modelling the ball, such as the finite element method, would be more difficult to combine with the flexible beam model of the racket.

The model that is developed in this chapter is a one degree-of-freedom, visco-elastic model similar to that discussed in Dignall (2000b). The structural stiffness is represented by a spring, and the energy loss in the rubber is simulated using a dashpot damper. Dignall (2000b) showed that the stiffness and damping of the visco-elastic model define the contact time T_C and coefficient of restitution COR respectively, for the model. In Chapter 4, the relationship between T_C, COR, and ball impact velocity was determined experimentally. Using this experimental data for T_C and COR, the coefficients of the spring and damper can be determined using either analytical or numerical

methods, i.e. the value of the spring stiffness was chosen so that the model exhibited the correct value of T_C. The model output included the following,

1. Ball centre-of-mass displacement, velocity, and acceleration.
2. Force acting on ball.

The criteria used to quantify the accuracy of the model involved comparing the *Force-Time* and the *Force-Displacement* plots for the experiment and model. Unless otherwise stated, this comparison was performed using the experimental and model data for all four ball types which were described in detail in section 4.2 and defined as,

1. *Pressurised*
2. *Pressureless*
3. *Oversize*
4. *Punctured*

In this chapter, the simple visco-elastic model which was proposed by Dignall (2000b) is developed with the aim of improving its accuracy and applicability.

5.3 One Degree-of-Freedom Visco-Elastic Model – Constant Parameters

5.3.1 Derivation of Model

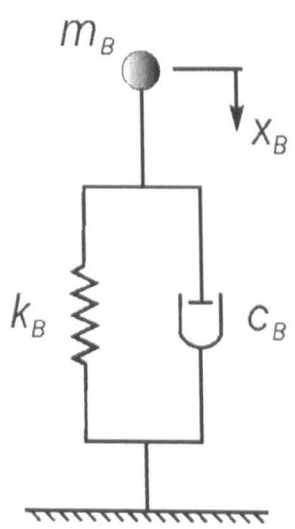

Figure 5.1 Kelvin-Voigt visco-elastic model of a tennis ball impact on a rigid surface.

A suitable one degree-of-freedom (DOF) visco-elastic model for a tennis ball impact on a rigid surface is shown in Figure 5.1 This Kelvin-Voigt model was used by Dignall (2000b) and this work is described thoroughly in section 2.5.3 and, to avoid redundancy, is only briefly discussed here. The model contains a spring in parallel with a dashpot damper. The point mass m_B represents the centre-of-mass (COM) of the ball. In this model the values of k_B and c_B represent the linear

stiffness and damping of the ball respectively and therefore the governing equation for this system is,

$$m_B\ddot{x}_B + c_B\dot{x}_B + k_B x_B = 0 \qquad [5.1]$$

where x_B is the displacement of the mass x_B.

In section 4.3 it is shown that the quasi-static stiffness of the ball increases as the ball deformation is increased, as determined for a compression between two flat plates. This would imply that the value of k_B would not be constant throughout impact. However, any assumed relationship between x_B and k_B would be arbitrary because there is no established link between these two parameters. Dignall (2000b) assumed that the values of the stiffness and damping coefficients, k_B and c_B respectively, remained constant throughout the impact. The values of the stiffness and damping parameters, k_B and c_B respectively, were determined analytically using the following equations,

$$k_B = m_B \frac{\pi^2}{T_C^2} \qquad [5.2]$$

$$c_B = -\frac{2m_B}{T_C}\ln(COR) \qquad [5.3]$$

where T_C and COR were the experimentally measured value of contact time and coefficient of restitution.

The analysis can easily be extended to define the equations required to calculate the displacement, velocity and acceleration of the point mass m_B at any time t during impact. These equations are derived in section 2.5.3 and are therefore not presented here. Also, the force F_B acting on the point mass can be directly calculated using the relationship,

$$F_B = m_B\ddot{x}_B \qquad [5.4]$$

where $\ddot{x}_B$ is the acceleration of the point mass.

5.3.2 Results and Discussion

The spring and damper coefficients, k_B and c_B respectively, were calculated using equations [5.2] and [5.3] along with the experimentally determined data for contact time and COR, shown in Figures 4.11 and 4.14(a). The results for these coefficients are shown in Figure 5.2(a) and (b). It can be seen that the stiffness and damping increase linearly with ball impact velocity, as was found by Dignall (2000b). The figures show that the *Pressurised* and *Oversize* balls have the highest stiffness, followed by the *Pressureless* and then the *Punctured* ball. The damping is highest in the *Punctured* ball, then the *Pressurised* and *Pressureless* which are very similar, and lowest in the *Oversize* ball.

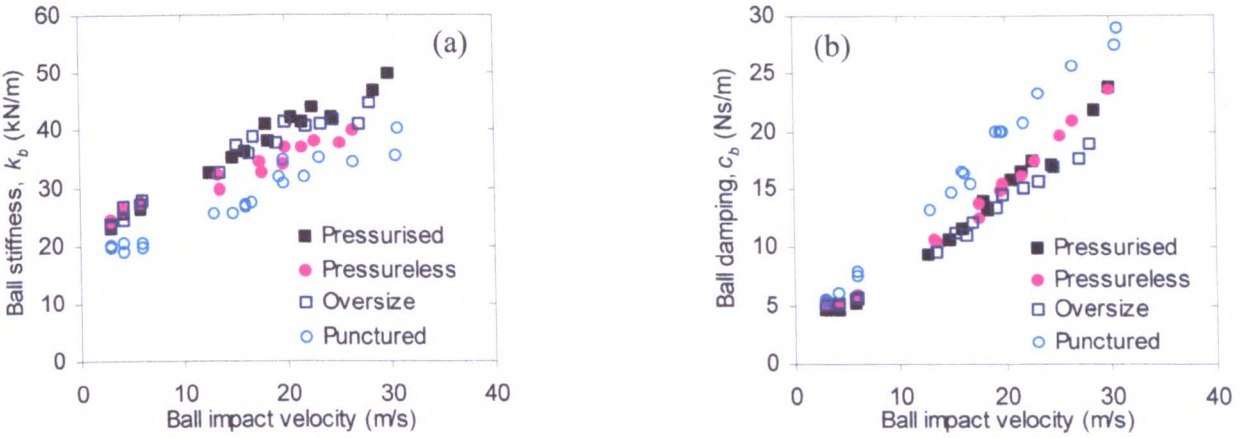

Figure 5.2 Comparison of the (a) ball stiffness and (b) ball damping, plotted against the ball impact velocity.

The main observation from this data is that the parameters k_B and c_B are a function of the ball impact velocity. Clearly the maximum ball deformation increases with the impact velocity and therefore it is not surprising that the effective stiffness is an increasing function of the impact velocity. The magnitude of the rubber which is deformed during impact will also increase as the ball deformation is increased. This may explain why the value of c_B also increases with ball impact velocity. Alternatively, this may be due to the term $c_B\dot{x}_B$ in [5.1] being unsuitable to model the damping in the ball.

The model was used to determine *Force-Time* and *Force-Displacement* plots for the impact, similar to those determined experimentally using a force platform, as described in Chapter 4. Figure 5.3(a)-(f) illustrate a comparison of the experimental and model data, for an impact between a *Pressurised* ball and a rigid surface. A similar comparison of the two sets of data are given in Appendix B.3 for the *Pressureless* ball. Both comparisons reveal a similar pattern between the experimental and model data and therefore the results in Figure 5.3(a)-(f) can be considered typical.

In the model, the contact time is defined as the time at which the ball COM displacement returned to zero. Figure 5.3(a)-(f) shows that the modelled force is negative at the end of the impact which corresponds to a tensile force being applied during this period. This is clearly unrealistic as the ball and surface are not physically attached together. It also highlights that the contact time of the model is a meaningless parameter as the spring and dashpot are not representative of a realistic impact mechanism. The reason for the tensile load at end of the impact can be explained by considering equation [5.1]. The damping force $c_B\dot{x}_B$ has a high negative value in this region, and the stiffness force $k_B x_B$ is relatively low. Therefore, the net load on the ball is negative.

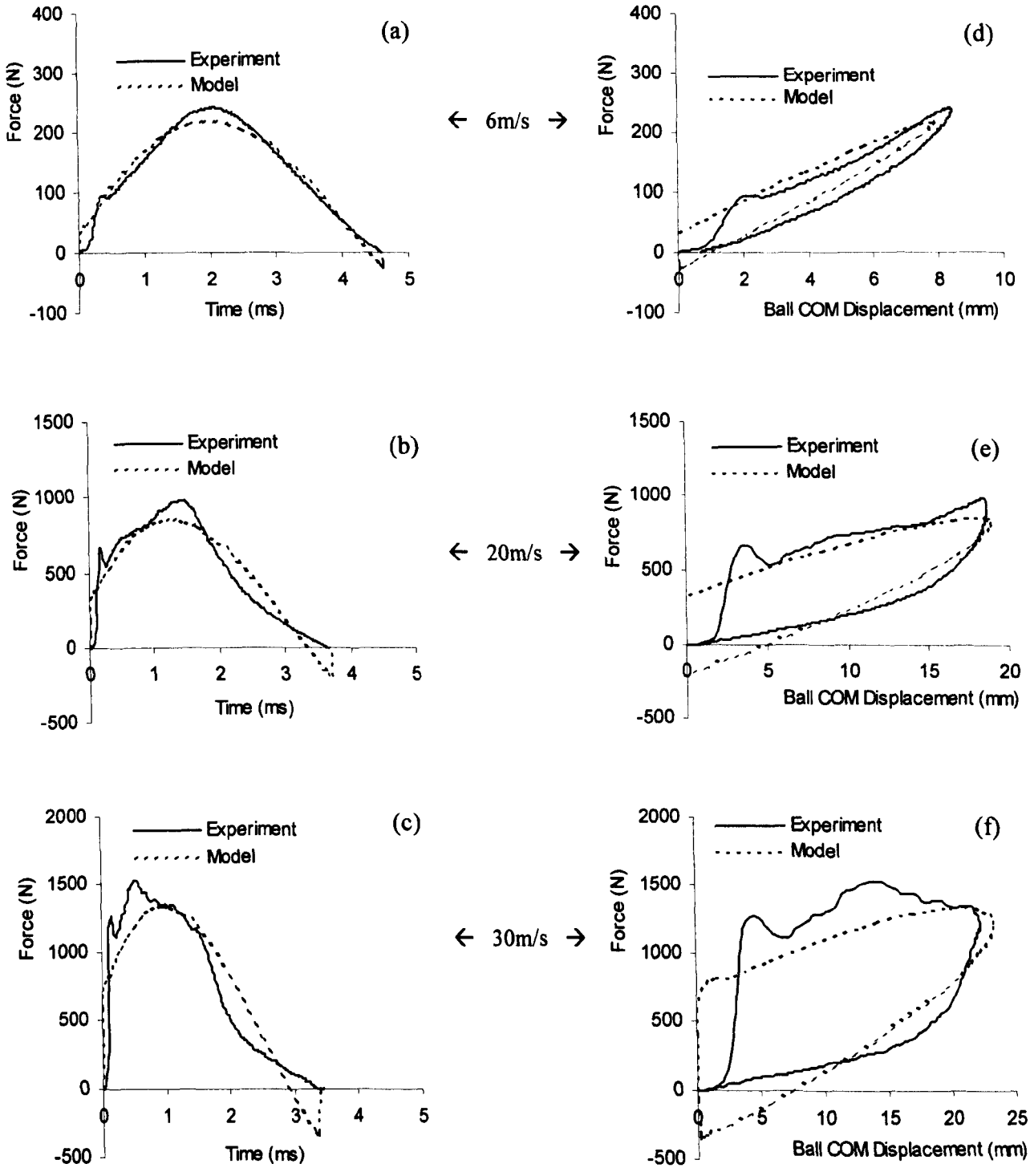

Figure 5.3 Comparison of experimental and *constant parameter* model data for a *Pressurised* ball impacting normal to a rigid surface, for a range of impact velocities between 6 and 30m/s. The force acting on the ball during impact is plotted against, (a)-(c) Time, and (d)-(f) Ball centre-of-mass displacement.

Figure 5.3(a)-(f) give an indication of the correlation between the model and experimental data. These figures shows that, for low speed impacts, the model and experiment values show a high correlation. For these impacts the ball deformation will be low and therefore the assumption that the ball stiffness remains constant is most valid for low speed impacts. At high speeds the model and experiment data generally differs by as much as 20-30%. Figure 5.3(d)-(f) show that, during the compression phase, the experiment force is negligible for ball COM displacements less than

2mm. In section 4.5.2 it was explained that this was due to the compression of the cloth, which has a low stiffness. Clearly the model can not simulate this because it is a *constant parameter* system. This also explains why the model can not simulate the subtle fluctuations in the experiment *Force-Time* plots such as the sudden drop in force after about 0.2ms, which has been assigned to the ball buckling at this point.

Figure 5.3(a)-(c) show that the model and experiment force values rise sharply in the initial stage of impact. In section 4.5.2 it was explained that the sharp rise in the force measured by the platform was due to the high initial structural stiffness of the ball and the relatively large force due to the momentum flux during this period. However, the reason for the sharp initial rise in the modelled force is simply due to the $c\dot{x}_B$ term in equation [5.1] being high because $\dot{x}_B$ is at a maximum value at this point. Therefore, the fact that the force initially rises rapidly both in the model and in the experiment data is purely coincidental, and the model is not a true representation of the actual impact.

5.3.3 Conclusions

The Kelvin-Voigt model returned values for spring stiffness and damping which were dependent on the contact time and coefficient of restitution for the impact. It was found that the *Pressurised* and *Oversize* balls were the stiffest, followed by the *Pressureless* and then the *Punctured.* The damping was highest in the *Punctured* ball, very similar for both the *Pressurised* and *Pressureless* balls, and lowest for the *Oversize* ball.

The experiment *Force-Time* and *Force-Displacement* plots determined by the force platform are very complex shapes and a 1 DOF *constant parameter* visco-elastic model is neither capable or suitable to simulate them. The model only correlates to within about 30% of the experiment results at the highest impact velocity of 30m/s, although it was more accurate at lower impact velocities. There were two main problems with this model. Firstly, both the model and experiment force value rose rapidly in the initial stage of impact but this was for different reasons. Therefore the solution is effectively no more use than a simple numerical solution which did not physically represent the actual impact mechanism. The second failing of this model was that, towards the end of impact, the force value was negative which represented a tensile force that was clearly not realistic.

The main constraint of this model was the assumption that the parameters remained constant throughout impact which was not realistic. It was shown that the *constant* value for stiffness increased with maximum COM displacement which was logical because when a ball is compressed between two flat plates the quasi-static stiffness increases with ball deformation. It was also shown that the value of the damping coefficient increased with maximum COM displacement. This is probably due to the fact that when a ball deforms, the amount of rubber being deformed increases with ball deformation, and this is represented in the value of the damping coefficient.

The main conclusion regarding this model is that it is reasonably accurate for low impact velocities, but very poor for higher impact velocities. This is because the assumption that the parameters

remained constant throughout impact was most valid for low impact velocities where there is little difference between the properties of the ball at zero and maximum deflection. Clearly, at higher impact velocities the ball properties vary considerably between zero and maximum deflection. This implied that the ball stiffness and damping should increase with ball COM displacement. This type of model is defined as a one degree-of-freedom *variable parameter* model as the values of stiffness and damping are allowed to vary during impact. The development of this model is presented in the following section.

5.4 One Degree-of-Freedom Visco-Elastic Model – Variable Parameters

5.4.1 Overview of the model

In section 5.3, a one degree-of-freedom visco-elastic model was developed in which the magnitude of the stiffness and damping remained constant throughout impact. It was shown that this system was a good first approximation of the model, especially at low impact velocities. However, the model was effectively no more use than a numerical solution because the spring stiffness and dashpot damping parameters in the model did not physically represent the structural stiffness and hysteresis losses in the ball. Also, the *constant parameter* model resulted in a tensile load at the end of impact which was not realistic.

In the following section, a one DOF *variable parameter* model is developed which allows the stiffness and damping to vary throughout impact. The model consists of a spring and damper in parallel, identical to that in Figure 5.1, and the governing equation for this system is defined by [5.1].

5.4.2 Model derivation

(a) Spring stiffness

This model assumes that the ball can be simulated using a linear spring and dashpot, and in the previous section it was assumed that the parameters were constant throughout impact. However, it was shown that the values of k_B and c_B increase as the magnitude of the maximum COM displacement increased. Therefore the physical accuracy of the model would be improved by assuming that k_B was a function of x_B throughout impact. The exact form of this relationship is unknown as it is impossible to determine it either mathematically or experimentally. The simplest solution assumes that the relationship between k_B and x_B is linear and the equation to define this function is,

$$k_B = k_{B(0)} + A_K x_B \qquad [5.5]$$

where $k_{B(0)}$ is the initial stiffness at $x_B = 0$, and A_K is the stiffness constant.

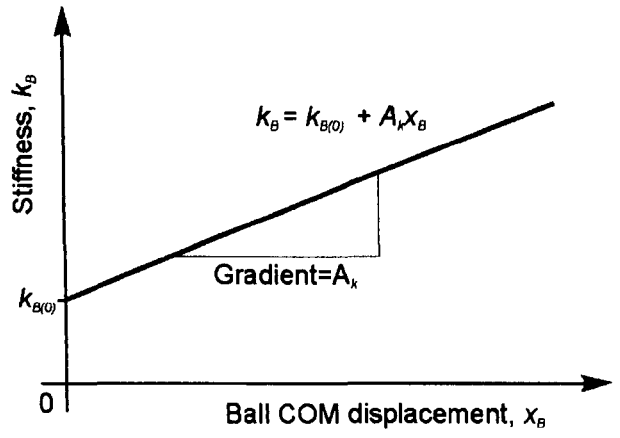

Figure 5.4 Assumed linear relationship between the spring stiffness k_B and the ball COM displacement x_B showing the initial stiffness at zero displacement $k_{B(0)}$.

Figure 5.4 illustrates the assumed linear relationship between the spring stiffness and ball COM displacement, which is defined by [5.5]. The initial value of stiffness $k_{B(0)}$ was obtained by plotting 2nd order polynomial trend lines through the data in Figure 5.2a. These trend lines were extrapolated to the *y-axis*, and it was assumed that the intersect point gave the spring stiffness for an impact with zero ball deformation, which correlates with the definition of $k_{B(0)}$. The values of $k_{B(0)}$ for each ball type are summarised in Table 5.1.

Table 5.1 Summary of initial stiffness values $k_{B(0)}$ for each ball type.

Ball type	$k_{B(0)}$ (kN/m)
Pressurised	21
Pressureless	23
Oversize	21
Punctured	16

(b) Dashpot damping

In the *constant parameter* model, the damping coefficient was constant which caused a steep rise in the force in the initial stage of impact, and also meant that there was a tensile load in the model just prior to the end of contact. This was due to the impact/rebound velocity being at a peak in these phases and therefore the damping force $c_B \dot{x}_B$ was relatively high. It was shown that the damping parameter increases with the impact velocity and this was attributed to the increase in the volume of rubber being deformed as the ball COM displacement increased. Therefore, in this current model it will be assumed the damping parameter is a function of the volume of rubber deformed. This implied that the model should have a damping parameter which was a function of the ball COM displacement.

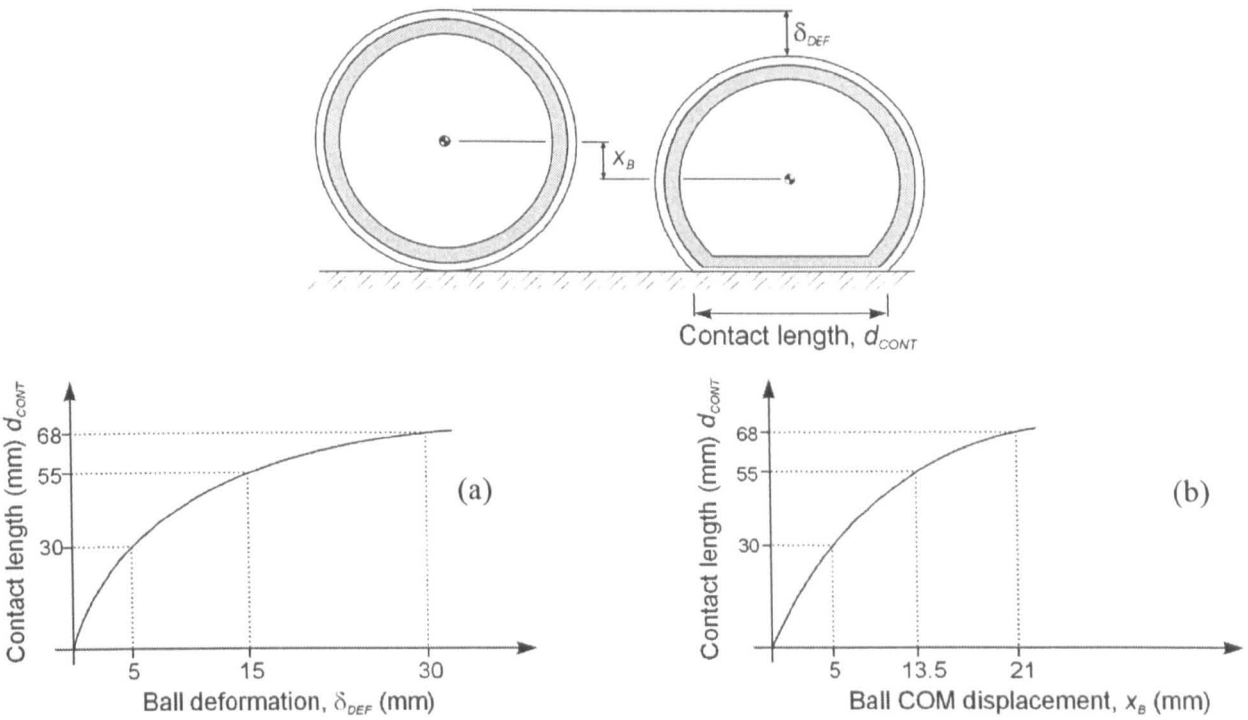

Figure 5.5 (a) Illustration of empirical relationship between contact length and ball deformation, for the compression phase of impact, and (b) interpolated relationship between contact length and ball centre-of-mass displacement.

In this model, a relationship between the damping parameter and the volume of rubber being deformed needs to be determined. In section 4.4.2, the ball deformation δ_{DEF} and the contact length d_{CONT} was measured experimentally for an impact between a ball and rigid surface; the definition of the contact length is illustrated in Figure 5.5. During the restitution phase, the relationship between δ_{DEF} and d_{CONT} was dependent on the ball type and impact velocity. Therefore, there was no single function which could define this relationship. However, during the compression phase, this relationship was independent of ball type and impact velocity, and was defined by a 4th order polynomial trend line (equation [4.1]). A schematic illustration of this trend line is shown in Figure 5.5(a).

In chapter 4 experiments were conducted to measure the relationship between the maximum ball deformation and maximum ball COM displacement, for a normal impact between a tennis ball and rigid surface. Figure 4.16(b) illustrates this empirical relationship. This relationship is strictly only valid for the point of maximum compression, but it is assumed that it can be applied to any stage of the impact. This relationship was used to translate the data in Figure 5.5(a) into Figure 5.5(b). Figure 5.5(b) gives a schematic plot of the contact length d_{CONT} and the ball COM displacement x_B. This relationship could not be obtained directly because the two parameters could not be measured simultaneously using the available apparatus.

The plot in Figure 5.5 (b) (converted into SI units) is defined by,

$$d_{CONT} = -2.77 \times 10^5 x_B^4 + 1.74 \times 10^4 x_B^3 - 453 x_B^2 + 7.66 x_B \qquad [5.6]$$

The contact length d_{CONT} is equal to the diameter of the contact area. As mentioned previously, in this model the damping parameter c_B will be a function of the volume of rubber being deformed. It

is assumed that the volume of rubber is proportional to the contact area and therefore c_B is defined as,

$$c_B = B\pi.(d_{CONT})^2 \qquad [5.7]$$

where B is a constant. Let $A_C = B\pi$, therefore,

$$c_B = A_C.(d_{CONT})^2 \qquad [5.8]$$

where A_C is defined as the damping constant.

Substituting [5.5] and [5.8] into the governing equation [5.1] gives,

$$m_B\ddot{x}_B + \left(A_C(d_{CONT})^2\right)\dot{x}_B + \left(k_{B(0)} + A_K x_B\right)x_B = 0 \qquad [5.9]$$

In the previous model, experimentally determined values of contact time and coefficient of restitution were used to calculate the two unknown variables k_B and c_B. In this model, A_K and A_C need to be determined using the experimental values of T_C and COR. However, unlike in the previous model there is no analytical solution for [5.9] and therefore A_K and A_C can not be calculated directly. Therefore this model required a numerical method to solve these two parameters.

5.4.3 Numerical solution for model

A numerical solution of [5.9] can easily be determined using the finite difference method, using a time step of Δt=0.01ms. Assuming the velocity $\dot{x}_B$ does not change considerably during this time step, the finite difference form of [5.9] at time t is,

$$m_B\left(\frac{(x_B)_{t+\Delta t} - 2(x_B)_t + (x_B)_{t-\Delta t}}{(\Delta t)^2}\right) + \left(\left(A_C(d_{CONT})^2\right)\left(\frac{(x_B)_t + (x_B)_{t-\Delta t}}{\Delta t}\right)\right) + \left(k_{B(0)} + A_K(x_B)_t\right)(x_B)_t = 0 \qquad [5.10]$$

which, rearranged, gives the displacement of x_B at time t+Δt as,

$$(x_B)_{t+\Delta t} = -\left(\frac{(\Delta t)^2}{m_B}\left(\left(k_{B(0)} + A_K(x_B)_t\right)(x_B)_t + \left(A_C(d_{CONT})^2\right)\left(\frac{(x_B)_t + (x_B)_{t-\Delta t}}{\Delta t}\right)\right) - 2(x_B)_t + (x_B)_{t-\Delta t}\right) \qquad [5.11]$$

[5.11] can be used to determine x_B for time steps of Δt using the following two boundary conditions to initialise the solution,

$$(x_B)_{t=0} = 0 \qquad [5.12]$$

and

$$(x_B)_{t=-\Delta t} = -V'_B.\Delta t \qquad [5.13]$$

The following equation is used to calculate the force at time t,

$$(F_B)_t = m_B\left(\frac{(x_B)_{t+\Delta t} - 2(x_B)_t + (x_B)_{t-\Delta t}}{(\Delta t)^2}\right) \quad [5.14]$$

The solution of equations [5.11]-[5.14] was written in *MS Excel 2000* spreadsheet. The value of d_{CONT} was calculated at each time step using [5.6], and substituted into [5.11]. The unknown parameters A_K and A_C were initially given values of 900kN/m^2 and 0.005Ns/m^3 respectively. The end of impact was defined as the point at which x_B equalled zero. At this instant, the contact time T_C and coefficient of restitution *COR* were recorded by the PC. A *Visual Basic Script Macro* was programmed that utilised the *Goal Seek* function to facilitate the iterative process of finding the appropriate values of A_K and A_C which converged to give the same T_C and *COR* as that found experimentally. As in the previous model, the value of T_C was defined as the time taken for the ball COM displacement to return to zero. This iterative process was performed for all the impacts which are discussed in section 4.5 to find the converged solution values of A_K and A_C for each impact and for each ball type. The converged solution was defined as the combination of A_K and A_C which gave model values of T_C and *COR* that were within 0.5% of those found experimentally.

5.4.4 Results and Discussion

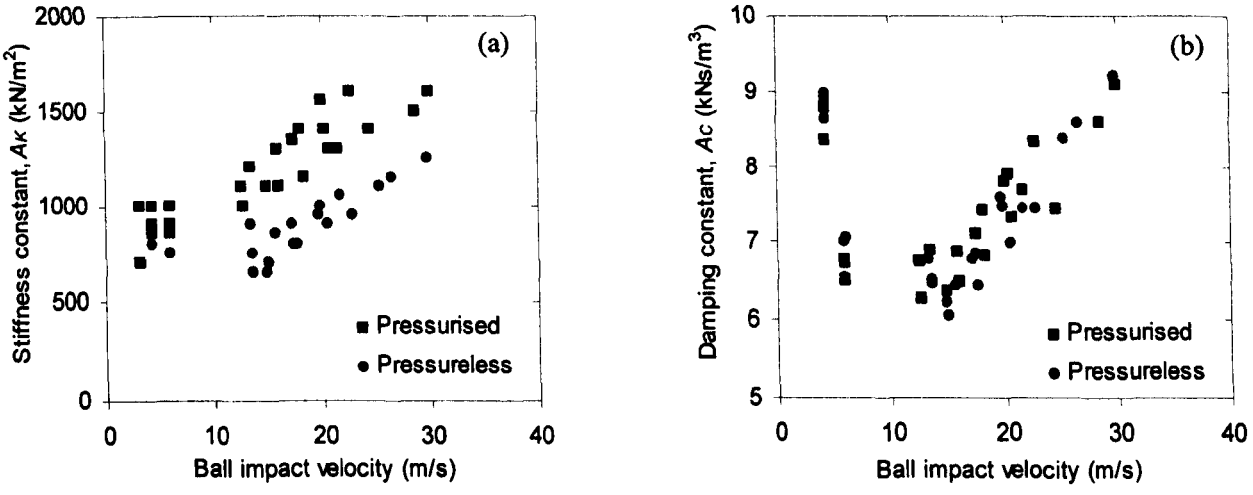

Figure 5.6 (a) Stiffness constant A_K and (b) Damping constant A_C plotted against the ball impact velocity. The data is plotted for two different ball types.

In this section only the *Pressurised* and *Pressureless* balls are used to illustrate the features of the model. Equations [5.5] and [5.8] define the stiffness and damping constants, A_K and A_C respectively. Figure 5.6(a) shows that the stiffness constant is very similar for both balls at low impact velocities, but at higher impact velocities the *Pressureless* ball has a lower stiffness. Figure 5.6(b) shows that the damping constant is similar for both balls. All these observations are consistent with the those from the previous model.

It was assumed that the relationship between the stiffness parameter k_B and the ball COM displacement x_B was linear, as illustrated in Figure 5.4. If this was a correct assumption then the value of A_K would be constant for all impacts. However, Figure 5.6 shows that the value of A_K increases as the ball impact velocity is increased. A similar conclusion can be drawn for the

damping constant A_C. This suggests that the relationship between stiffness/damping and ball COM displacement is non-linear.

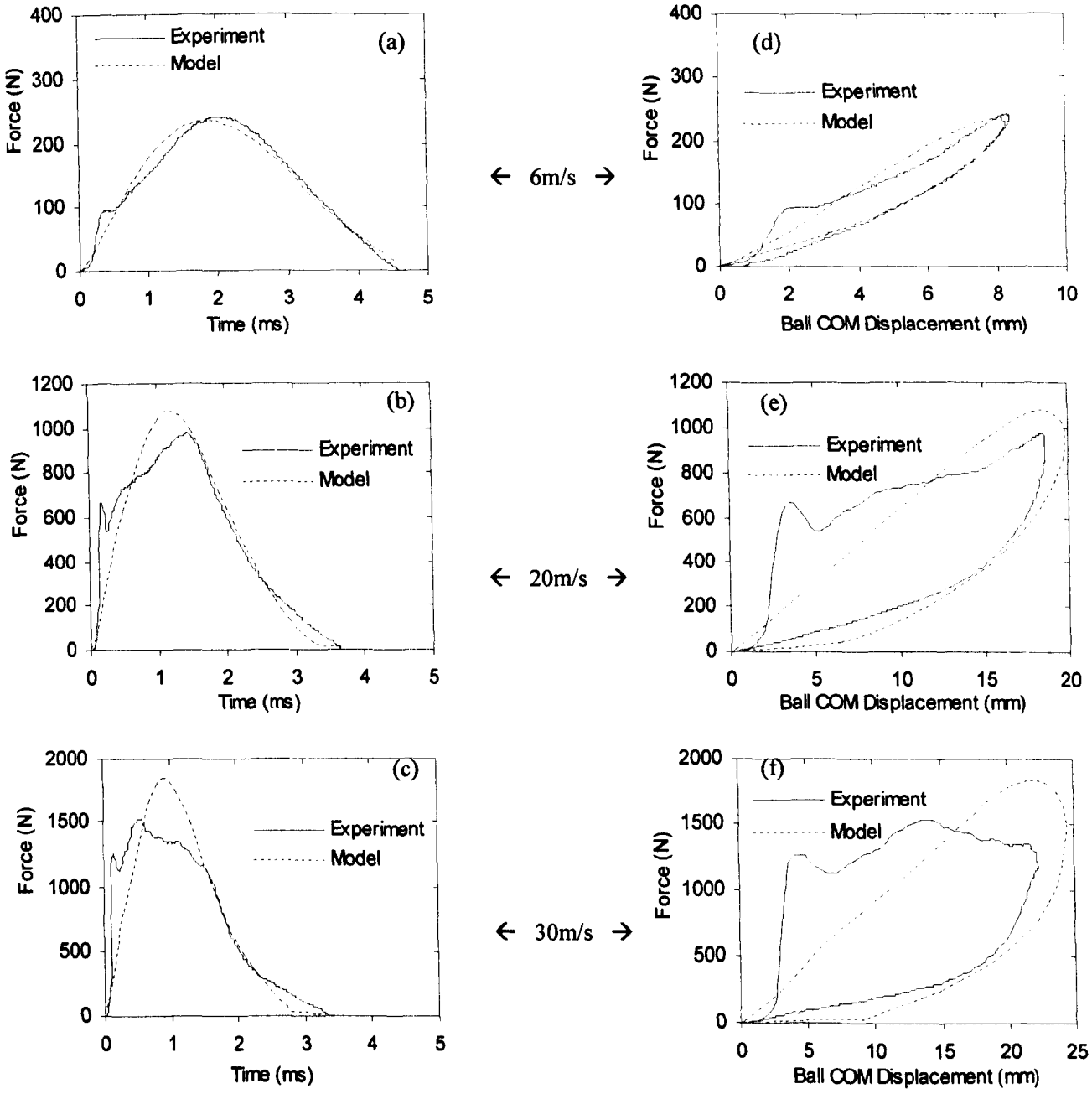

Figures 5.7 Comparison of experiment and model data for a *Pressurised* ball impacting on a rigid surface, for a range of impact velocities.

The model solution, using the converged values of A_K and A_C, was used to determine the *Force-Time* and *Force-Displacement* data. Typical plots of these relationships are shown in Figures 5.7(a)-(f) for a *Pressurised* ball and supplementary comparisons are shown in Figure B.5 for a *Pressureless* ball. These figures show that the model force is lower than that in the experiment, for the first and last 0.5ms period of the impact, which correspond to low COM displacements. The model force is higher than that of the experiment, for the middle part of the impact. Also, the maximum ball COM displacement is generally higher in the model than that in the experiment. It

is important to note that Figures 5.7(a)-(f) show that the model and experiment *Force-Time* data (and *Force-Displacement* data) correlate reasonably well for the restitution phase of the impact.

The most noticeable differences between the model and experiment results are evident in Figures 5.7(d), (e) & (f). The figures show that the two traces generally vary by up to 40%. By comparison, the *constant parameter* model was generally accurate to within about 20%. This initially implies that the *variable parameter* model is less accurate than the model which it was supposed to supersede. However, in the previous section it was shown that the *constant parameter* model did not physically represent the ball impact. Therefore, the *constant parameter* model is fundamentally flawed and should not be used.

The reasons for the differences between the *constant parameter* and *variable parameter* models are most easily illustrated by comparing Figure 5.8(a) & (b). These figures show the individual contribution of the stiffness and damping parameters, for an impact velocity of 20m/s, for the two models. These figures also show the overall force value (the sum of the stiffness and damping forces). It can be seen that, during the first 0.5ms of impact the overall force is smaller in the *variable parameter* model than in the *constant parameter* model. After this time the force is generally greater in the *variable parameter* model, especially in the last 0.5ms of impact.

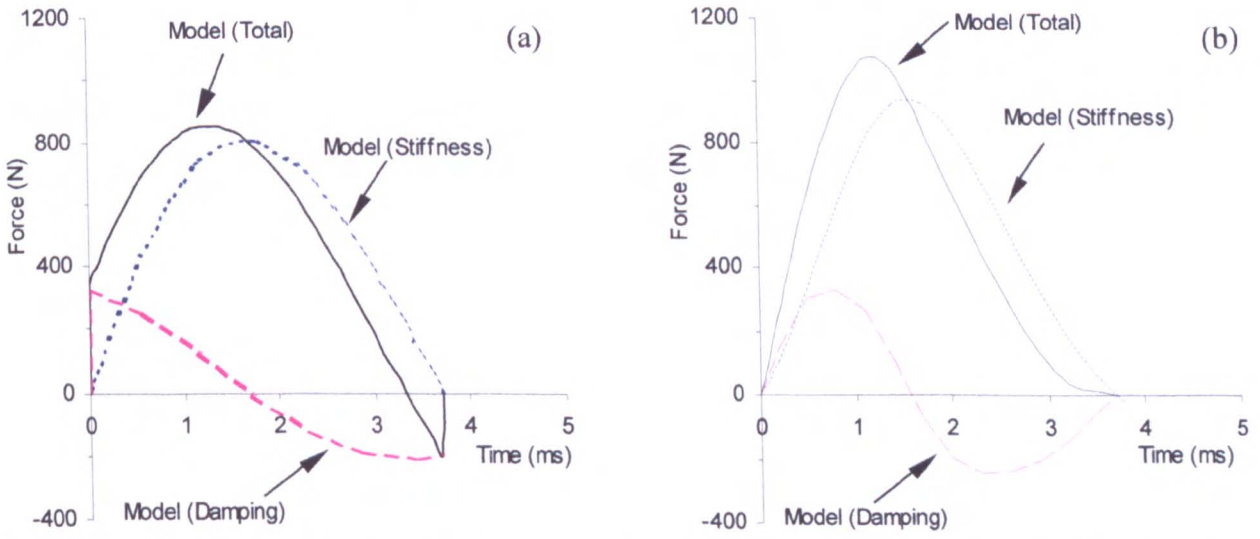

Figure 5.8 Illustration of the typical contribution of the stiffness and damping parameters to the overall force for an impact velocity of 20m/s, (a) *Constant parameter* model and (b) *Variable parameter* model.

In the *constant parameter* model it was assumed that the stiffness parameter was constant, whereas in the *variable parameter* model the stiffness parameter increased with COM displacement. This meant that the stiffness force in the *variable parameter* model was relatively low at the start and end of impact, and high during the period of maximum compression. This is evident in Figure 5.8(a) & (b) where the peak stiffness force is higher in the *variable parameter* model. It is for this reason that the overall peak force is higher in this model compared to the *constant parameter* model.

In the *constant parameter* model the damping parameter was constant which meant that the modulus of the damping force, $|c_B\dot{x}_B|$, was high at the start and end of impact, as illustrated in Figure 5.8a. This lead to the relatively high and low overall model force at the start and end of impact respectively. In the *variable parameter* model the damping parameter increased with COM displacement so the modulus of the damping force, $|c_B\dot{x}_B|$, was lower at the start and end of impact in the *variable parameter* model compared to the *constant parameter* model. A consequence of this was that there was no tensile load during the final phase of impact, which is an improvement on the *constant parameter* model. This occurs because the value of the term $|c_B\dot{x}_B|$ was lower than that of the stiffness force during this final phase of impact so the overall force that was plotted in Figure 5.8b remained positive throughout.

The comparisons made between the models and the force platform data have shown that the *constant parameter* model correlates better with the experiment data in the initial stage of impact; the force value in the *variable parameter* model is too low. However, in the previous section it was mentioned that the *constant parameter* model was not realistically modelling the impact in this period. Therefore the *variable parameter* is actually a better model but it needs to be modified to account for a higher load in this period. Implementing such a change will inherently reduce the maximum load because the total impulse acting on the ball remains constant. It has been noted that the *variable parameter* model *Force-Time* data correlates well with the experiment data in the restitution phase so no major modifications need to be made in this period.

5.4.5 Conclusions

Modifications were made to the existing *constant parameter* model to allow the stiffness and damping properties to vary during impact. The resulting system was termed a *variable parameter* model. It was assumed that the stiffness and damping parameters varied linearly with the ball COM displacement and ball-surface contact area respectively; the ball-surface contact area was itself a function of the ball COM displacement. An iterative process was used to determine the values of the stiffness and damping constants in the linear relationships for a range of impacts. This method determined the appropriate values for these constants which gave the same contact time and coefficient of restitution for the model as that found experimentally for a range of impact velocities up to 30m/s. It was found that the value of the stiffness constant increased as the impact velocity increased, and therefore there was no single value that could be used to model the entire range of velocities. The implication of this was that the assumption of a linear relationship between stiffness and ball COM displacement was incorrect. A similar conclusion was drawn for the damping constant.

Comparisons made between the *variable parameter* model and the experimental data showed that the model force value was too low in the initial stage of impact. Therefore this model needs to be modified to account for a higher load in this period. The consequence of the low initial load was that the maximum model load was higher than that in the experiment. This was because the total impulse acting on the ball remained constant. During restitution, the model *Force-Time* data

correlates well with the experiment data so no modifications need to be made in this period. This correlation is much improved from that of the *constant parameter* model and is mainly due to the assumption that the damping was a function of the ball COM displacement.

5.5 One Degree-of-Freedom Visco-Elastic – Variable Parameters and Momentum Flux

5.5.1 Overview of the model

The main aim of this chapter is to develop a visco-elastic model of an impact between a tennis ball and a rigid surface. The empirical model parameters are to be determined for a range of tennis balls. It is intended that this model will be used to simulate the ball in a ball-racket impact, which is discussed later in this study. In order to achieve this aim, the model must physically represent the impact mechanism and not just resemble a numerical solution. A numerical solution can not be used to advance the knowledge of a ball impact because the model would not physical simulate the impact mechanism.

The *variable parameter* model was physically representative of the impact but did not give a sufficiently good correlation between the model and experiment results. This model assumed that the stiffness and damping increased with the ball COM displacement. In section 5.4 it was explained that this was a more realistic model compared to the *constant parameter* model. The main weakness of the *variable parameter* model was that the force was considerably lower than that in the experiment during the initial phase of compression. Cross (1999a), Dignall (2000b) and Thomson (2000) all arrived at the conclusion the experimentally determined force was relatively high because of the initial high stiffness of the ball before it buckled. However, if this was the reason for the high load then when the ball buckled the force would drop considerably, which does not happen. This suggests that there is an extra feature in the impact mechanism that has not yet been accounted for.

Hubbard & Stronge (2001) published a study on the analytical modelling of table tennis ball impacts on a rigid surface which was discussed in Chapter 2. This paper ignored the hysteresis losses in the material but showed that the force acting on the ball consisted of two components during the compression phase of the impact; these were the ball stiffness and the momentum flux force. This momentum flux force was not accounted for in either the *constant parameter* or *variable parameter* models, but will be included in the model in this section. The momentum flux force corresponds to the change in momentum for the section of the deformed ball which is being flattened upon impact with the surface.

This new model is defined as a one degree-of-freedom *momentum flux* model. This is a modified version of 1-DOF *variable parameter* model and partly accounts for the fact that the ball is a complex three dimensional highly deformable body, and not a point mass suspended on a spring and damper. A possible solution would have been to use a multi-DOF system to simulate the mass and stiffness distribution, or alternatively use finite element methods (FEM) to model the ball. However, the aim of this work was to develop a simple model which could be used to model a ball-

racket impact. Neither an FEM model or multi-DOF visco-elastic system would be suitable for this task.

5.5.2 The construction of the model

(a) Momentum flux simulation

Hubbard & Stronge (2001) used thin shell theory to define an analytical solution for the shape of the ball during impact. In this paper, it is shown that the wall thickness of a tennis ball is too large for this shell theory to be used to model a tennis ball impact on a rigid surface. Also, this impact involves large, non-linear deformations which are very difficult to model analytically.

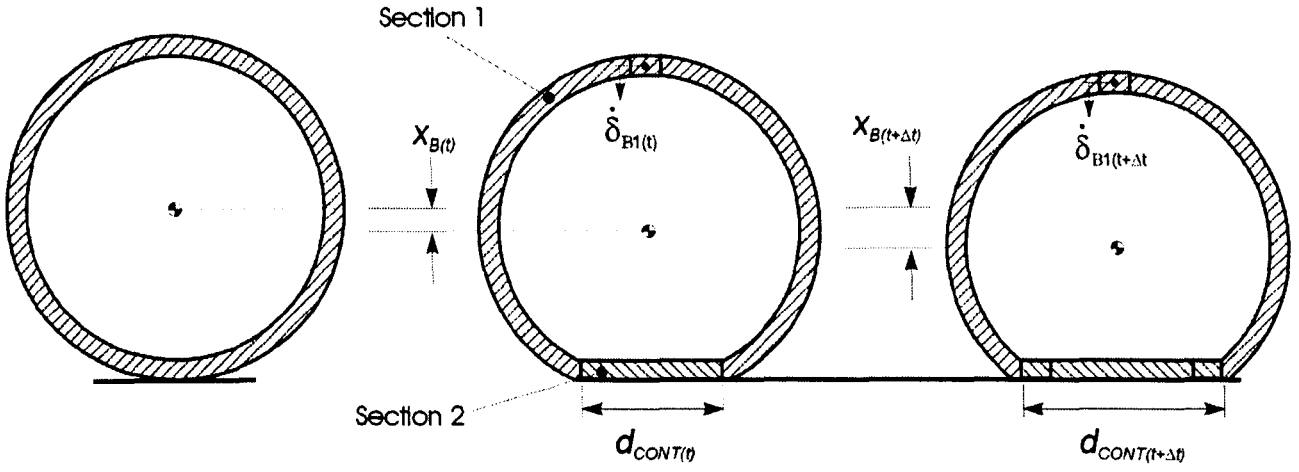

Figure 5.9 Definition of the contact length, and ball COM displacement.

In this current study, an empirical approach is adopted in an attempt to model the resultant force that is due to the momentum flux. During impact, the ball can be considered as two separate sections; section 1 continuing to move towards the surface section and section 2 is at rest in contact with the surface (as shown in Figure 5.9). For simplicity it is assumed that section 2 is flat and stationary and therefore remains in contact with the surface during impact. It is also assumed the section 1 is undeformed and therefore all points on this section move towards the surface with the same velocity $\dot{\delta}_{B1}$. When a segment of section 1 impacts on the surface its velocity changes from $\dot{\delta}_{B1}$ to zero, and the size (and mass) of section 2 increases. The masses of sections 1 and 2 are defined as M_1 and M_2 respectively, and the mass of the ball is defined as m_B. The 'flow' of mass into section 2 is defined as $\dot{M}_2$.

During the compression phase of impact, the momentum flux force is compressive and therefore results in a force being exerted onto the surface, separate to that caused by the stiffness of the ball shell and internal pressure. This momentum flux force at time t $(F_M)_t$ is equal to the change of momentum and is defined using,

$$(F_M)_t = (\dot{M}_2 \dot{\delta}_{B1})_t \qquad [5.15]$$

It is assumed that the flattened section remains approximately flat throughout impact. This assumption has to be made because it is very difficult to predict the exact form of this shape.

Hubbard & Stronge determined the mass M_2 analytically. However, in this current study M_2 is determined from the length of the contact-area diameter d_{CONT} and the mass per unit surface area ρ_{AREA}. The relationship between d_{CONT} and x_B is given by [5.6] and is the same as that used in section 5.3 to determine the volume of rubber that is being deformed during impact. It is assumed that the tennis ball shell is inextensible and therefore the value of ρ_{area} remains constant throughout impact. For a standard size tennis ball with an effective radius of 29.5mm and a mass of 57g, value of ρ_{area} is 5.212kg/m^2. For an oversize ball the value of ρ_{area} is 4.552kg/m^2. [5.15] can be solved to determine the momentum flux force for a unit time interval Δt,

$$(F_M)_t = \frac{\left|\rho_{area}\pi\left((d_{CONT(t)})^2 - (d_{CONT(t-\Delta t)})^2\right)\right|}{4\Delta t}(\dot{\delta}_{B1})_t \qquad [5.16]$$

The centre-of-mass velocity $\dot{x}_B$ is different to the velocity of section 1 $\dot{\delta}_{B1}$, as noted in Hubbard & Stronge (2001). For this simplified model the relationship between these two variables is defined as,

$$(\dot{\delta}_{B1})_t = \left(\frac{m_B}{M_1}\dot{x}_B\right)_t \qquad [5.17]$$

Substituting [5.17] into [5.16] gives

$$(F_M)_t = \frac{m_B\left|\rho_{area}\pi\left((d_{CONT(t)})^2 - (d_{CONT(t-\Delta t)})^2\right)\right|}{4\Delta t(M_1)_t}(\dot{x}_B)_t \qquad [5.18]$$

which is an equation of the form,

$$(F_M)_t = (c_M\dot{x}_B)_t \qquad [5.19]$$

where,

$$(c_M)_t = \frac{m_B\left|\rho_{area}\pi\left((d_{CONT(t)})^2 - (d_{CONT(t-\Delta t)})^2\right)\right|}{4\Delta t(M_1)_t} \qquad [5.20]$$

It is important to reinforce that [5.17]-[5.18] only apply in the compression phase of impact. During the restitution phase, the momentum flux force is tensile and therefore c_M is equal to zero throughout this phase.

The equation for the momentum flux force [5.16] can be rearranged into the form of [5.17] which is analogous to an equation of motion for a dashpot damper, with a damping coefficient defined as c_M. The value of c_M can be determined for any time t by determining the values of d_{CONT} for the relevant value of x_B using [5.6]. As in the previous models, the structural stiffness and material damping will be modelled using a linear spring and damper respectively. The *momentum flux* visco-elastic model is illustrated Figure 5.10.

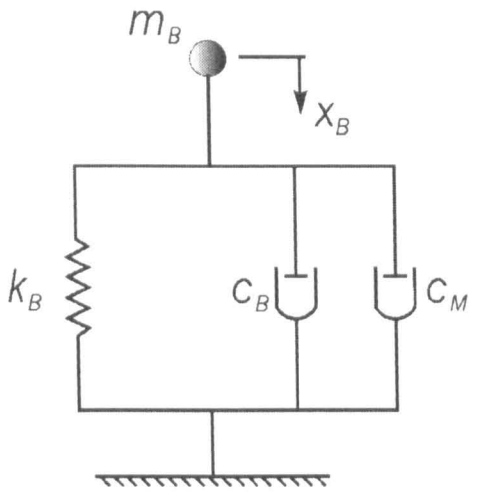

Figure 5.10 Illustration of the 1-DOF *momentum flux* visco-elastic model.

(b) Ball structural stiffness

In section 4.5, a force platform was used to determine *Force-Time* data for an impact between a ball and a rigid surface, for a range of ball types and impact velocities. It was noted that the force increased rapidly for the first ~0.2ms then dropped suddenly. It was concluded that this was due to the relatively high initial structural stiffness of the ball shell, which instantaneously reduced when the shell buckled. In this model it is assumed that the ball stiffness k_B equals a constant value k_{SHELL} for $t < 0.2ms$. The value of k_{SHELL} is chosen arbitrarily as there is no analytical solution.

For $t > 0.2ms$ it was assumed that the structural stiffness of the ball k_B was proportional to the displacement of the ball x_B. In the *variable parameter* model it was assumed that this relationship was linear but it was found that the stiffness constant A_K increased with ball impact velocity. This implied that the true relationship was non-linear and therefore equation [5.5] was not of a suitable form to describe the relationship between ball stiffness and displacement. Other researchers (Carré 2000, Ujihashi 1994) have successfully used a power law relationship between the ball stiffness and displacement. Therefore, in this model [5.5] was modified so that k_B is proportional to a power of x_B,

$$k_B = k_{B(0)} + A_K x_B^{\alpha} \qquad [5.21]$$

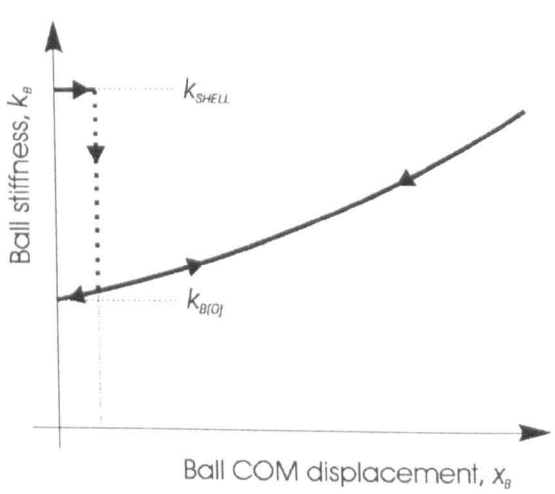

Figure 5.11 Schematic illustration of the assumed relationship between the spring stiffness k_B and ball COM displacement x_B showing the initial high stiffness k_{SHELL} which is valid for $t < 0.2ms$.

Equation [5.21] is applicable for $t > 0.2ms$. An illustration of the relationship between k_B and x_B is shown in Figure 5.11. As before, $k_{B(0)}$ is the effective stiffness of the ball when $x_B = 0$, and the values of this parameter are given in Table 5.1. Equation [5.20] is assumed to be valid for both the compression and restitution phases of impact.

(c) Material damping

In the *variable parameter* model it is assumed that that the force in the linear dashpot damper F_C was only proportional to the magnitude of the contact area, i.e.,

$$F_C = c_B \dot{x}_B = A_C.(d_{CONT})^2 \dot{x}_B \qquad [5.22]$$

where A_C is defined as the damping constant.

In that model it was effectively assumed that the ball deformed at a rate of $\dot{x}_B$; $\dot{x}_B$ being the velocity of the ball centre-of-mass. In this current model, it has been shown that the ball deforms at a rate of $\dot{\delta}_{B1}$. Therefore, the model needs to be modified with the assumption that the damping force is proportional to this deformation rate $\dot{\delta}_{B1}$ rather than the COM velocity $\dot{x}_B$. The relationship between $\dot{x}_B$ and $\dot{\delta}_{B1}$ is defined in [5.17], and therefore [5.22] is modified to become,

$$F_C = c_B \dot{x}_B = \frac{m_B}{M_1} A_C.(d_{CONT})^2 \dot{x}_B \qquad [5.23]$$

and therefore,

$$c_B = \frac{m_B}{M_1} A_C.(d_{CONT})^2 \qquad [5.24]$$

(d) Summary

The *momentum flux* visco-elastic model is illustrated in Figure 5.10. The governing equation for this model is,

$$m_B \ddot{x}_B + (c_B + c_M)\dot{x}_B + k_B x_B = 0 \qquad [5.25]$$

The values of the parameters k_B, c_B and c_M have been fully defined in this section, except for one minor adaptation which will be explained here. The experimental *Force-Displacement* plots, such as that in Figure 4.13 shows that the force is negligible for $x_B < \sim 2$mm (during the compression phase). This characteristic is simplified in the model by assuming that the force is zero for $x_B <$ 2mm (during the compression phase). This is achieved by enforcing the parameters k_B, c_B and c_M to equal zero during this period. After this period the parameters are defined using the equations discussed in this section.

5.5.3 Numerical solution of model

The values of the model parameters k_{SHELL}, A_K, α and A_C were defined so that the contact time T_C and coefficient of restitution *COR* determined by the model were close to those determined experimentally in section 4.5. There is clearly no analytical solution to obtain the four parameters so a similar numerical method is used as that which was adopted in the *variable parameter* model. This method is discussed in the following passage.

Using [5.17]-[5.25], the general equation for the ball COM displacement x_B at time t is,

$$(x_B)_t = 2(x_B)_{t-\Delta t} - (x_B)_{t-2\Delta t} - \left(\frac{(\Delta t)^2}{m_B}\left([k_B(x_B)_{t-\Delta t}]+\left[(c_B + c_M)\left(\frac{(x_B)_{t-\Delta t}+(x_B)_{t-2\Delta t}}{\Delta t}\right)\right]\right)\right) \qquad [5.22]$$

This equation was solved in *MS Excel* using a time step of Δt=0.01ms and the relevant values of k_B, c_B and c_M.

In the *variable parameter* model, the value of A_K was adjusted so that the contact time for the model matched that of the experiment. A similar iterative method was also used to determine the damping parameter A_C which gave the same coefficient of restitution for the model as was found experimentally. In this *momentum flux* model, the combination of the values k_{SHELL}, A_K and α defined the model value of contact time. This meant that there was an infinite number of valid solutions for these two parameters, which all gave the same value of T_C. Clearly, the optimum solution would be a specific combination of k_{SHELL}, A_K and α which gave the correct value of T_C for all ball impact velocities. If this was achieved, then each ball type would have a single function [5.21] that described the value of k_B at any value of x_B. A single value of the damping parameter A_C was determined which minimised the difference between the model and experimentally determined coefficient of restitutions, for all ball impact velocities.

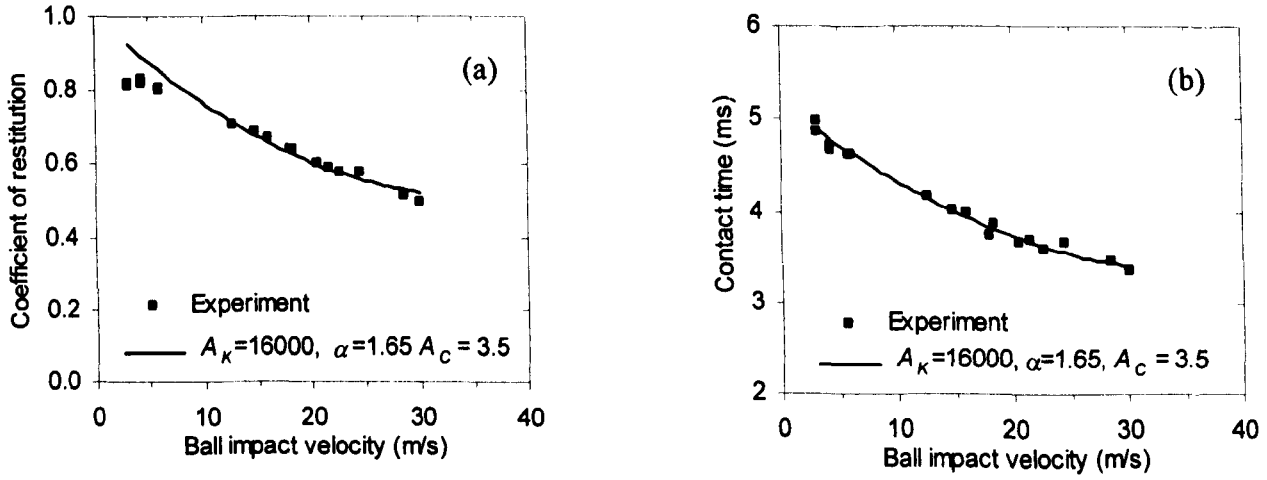

Figure 5.12 Comparison of the experimental and model data for (a) contact time and (b) coefficient of restitution. The results are shown for a *Pressurised* ball and the model parameters used were A_K=16000 kN/m^2, α=1.65, A_C = 3.5 kNs/m^3.

In section 4.5, *Force-Time* data obtained for an impact between a ball and force platform was used to conclude that the ball initially had a relatively high structural stiffness. The magnitude of this stiffness instantaneously dropped when the shell buckled. This feature is simulated in the model by

assuming that the stiffness of the ball was equal to a high constant value k_{SHELL}, for $t < 0.2ms$. Then, after this time, the stiffness was defined using a function of the ball displacement. The value of k_{SHELL} can not be directly measured by either analytical or experimental methods and therefore has to be chosen arbitrarily. In this study, it was assumed that k_{SHELL} was equal to 80kN/m for all ball types, for all ball impact velocities. This single value was chosen as it gave a model *Force-Time* curve which was similar to that determined experimentally. This is confirmed in the figures in the results section.

The iterative method used to determine the combination of A_K, α and A_C for each ball type is most easily explained by way of an example. The example uses the experimental data obtained for a *Pressurised* ball, and this data is shown in Figure 5.12(a) and (b). The model was solved for six discrete impact velocity increments between 5 and 30m/s. For each of these impact velocities the same combination of A_K, α and A_K were used, and the calculated values of contact time and *COR* are plotted in Figure 5.12(a) and (b); the contact time being defined as the time in which the ball COM displacement returns to zero. Different combinations of A_K, α and A_C were input into the model until the model values of contact time and *COR* matched those determined experimentally, as shown in Figure 5.12(a) and (b). When determining the optimum value of A_C, the value was chosen which gave the highest accuracy for ball impact velocities between 13 and 30m/s as these velocities are more relevant for a ball/racket impact. This explains why the model solution in Figure 5.12(b) correlates more closely to the experimental data for impacts in this velocity range. Clearly the value of A_C could have been allowed to vary with ball impact velocity and this would have meant that the model and experiment values of *COR* would be identical. However, a neater solution is obtained if a single value of A_C is used for all impact velocities.

5.5.4 Results and Discussion

(a) Model parameters A_K, α and A_C

Table 5.2 Spring parameters $k_{B(0)}$, A_K and α and damping coefficient A_C for the four ball types.

Ball type	$k_{B(0)}$ (kN/m)	A_K (kN/m^2)	α	A_C (kNs/m^3)
Pressurised	21	16000	1.65	3.5
Pressureless	23	12500	1.70	4.0
Oversize	21	3600	1.30	3.2
Punctured	16	60000	2.00	5.8

The iterative method described in section 5.5.3 was used to determine the combination of A_K and α that gave the minimum difference between the model and experiment contact time, for each ball type, and this data is shown in Table 5.2. The magnitude of this difference is illustrated in Figure 5.12 for the *Pressurised* ball and in Figure B.6(a)-(c) for the *Pressureless*, *Oversize* and *Punctured*

balls. These figures show that the model and experimentally determined contact time exhibit a high correlation.

Included in Table 5.2 is the constant $k_{B(0)}$ which corresponds to the stiffness of the spring for a zero displacement. This was defined in the *variable parameter* model. The parameters in this table can be used to determine the stiffness of the spring at any displacement x_B using,

$$k_B = k_{B(0)} + A_K x_B^{\alpha} \qquad [5.21]$$

An illustration of the relative stiffness of each ball type is shown in Figure 5.13. This figure shows that all the standard production balls have a similar stiffness for a COM displacement of ~10mm and below. The *Pressureless* ball is the stiffest in this range because this ball has the highest value of initial stiffness $k_{B(0)}$. The *Punctured* ball has a considerably lower stiffness than all other balls, for small displacements. At the highest displacements, the *Pressurised* ball is the stiffest, followed by the *Oversize* ball and then the *Pressureless* ball. At these displacements, the *Punctured* and *Pressureless* balls have a similar stiffness.

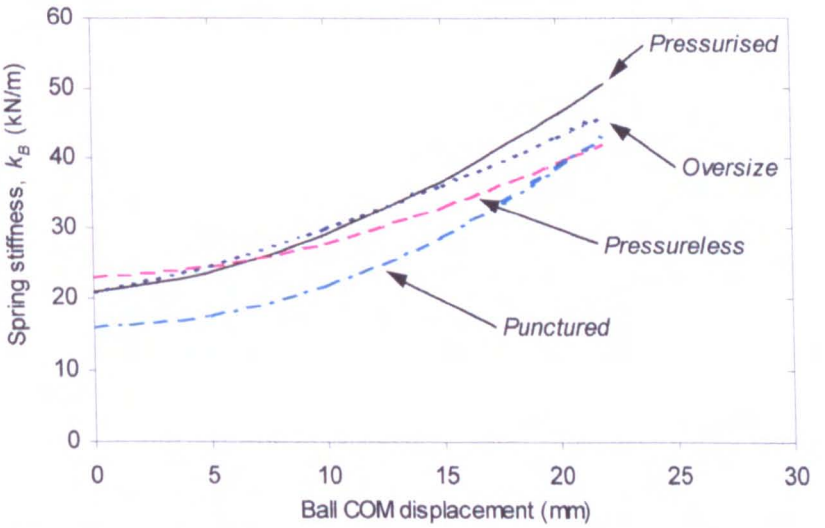

Figure 5.13 Comparison of the model spring stiffness k_B for each ball type.

In this model, the material damping is characterised by the parameter A_C. The value of this parameter, for all ball types, is shown in Table 5.2. The accuracy of the model is assessed by comparing the coefficient of restitution for the model and experiment. This comparison is shown in Figure 5.12(b) for a *Pressurised* ball and in Figures B.7(a)-(c) for the *Pressureless*, *Oversize* and *Punctured* balls. These figures show that the model and experimentally determined values of *COR* exhibit a very high correlation for impact velocities above 13m/s. For velocities below this, the model over predicts the coefficient of restitution.

(b) Force-Time and *Force-Displacement* data

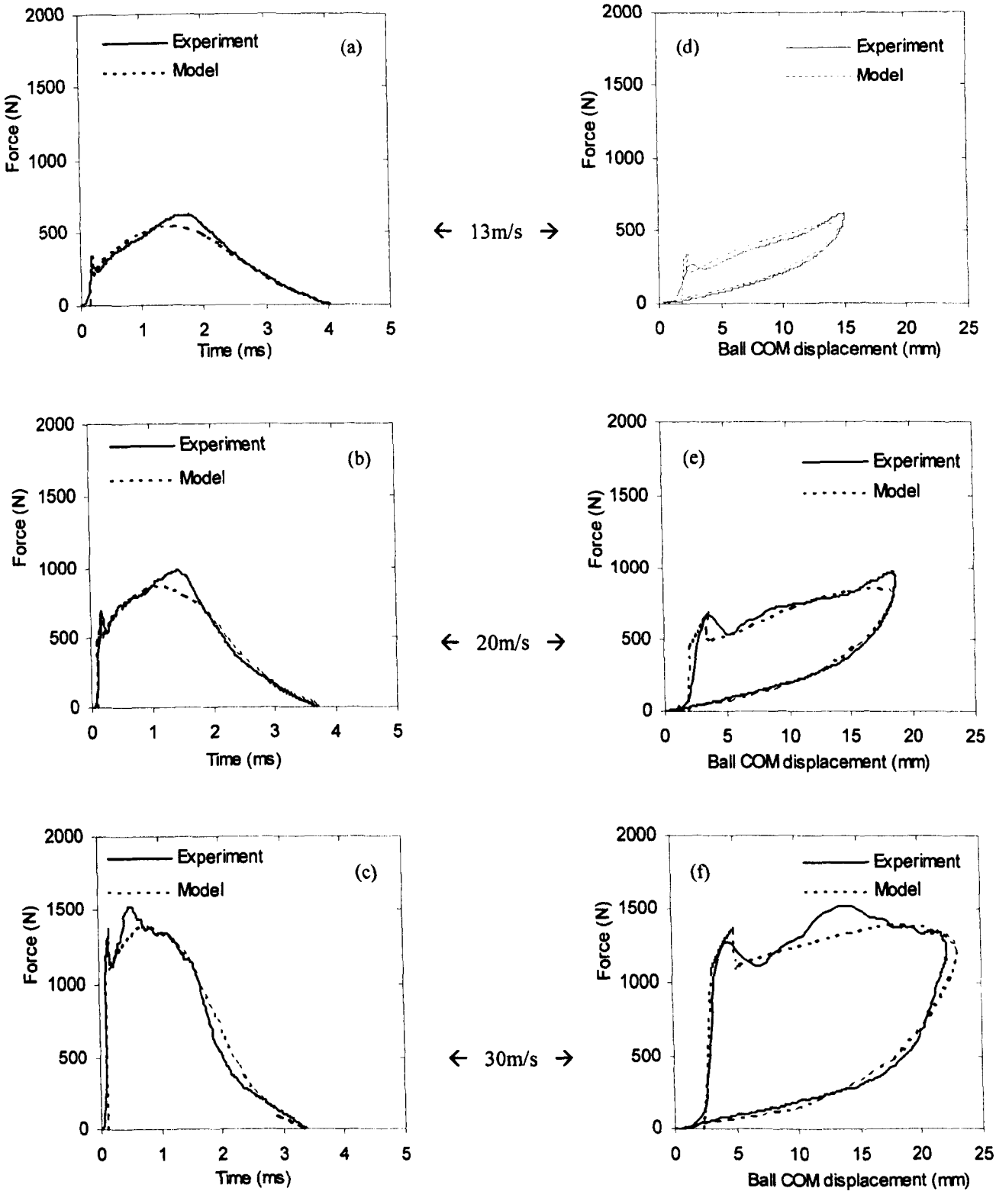

Figures 5.14 (a)-(f) Comparison of 1-DOF *momentum flux* model and experiment results for an impact between a *Pressurised* ball and a rigid surface for three different impact velocities.

Figures 5.14(a)-(f) show a typical comparison between experimental and model results for an impact between a *Pressurised* ball and rigid surface. All these figures show that the model exhibits a good correlation with the experiment data.

Figures 5.14(d)-(f) show that the force initially rises rapidly in both the model and experiment *Force-Displacement* plots. This is followed by a sudden drop in force due to the instantaneous drop in structural stiffness; it is at this point that the spring stiffness changes from the high shell stiffness (k_{SHELL}) to a lower value which is proportional to ball COM displacement $\left(k_{B(0)} + A_K x_B^{\alpha}\right)$. In the remaining part of the compression phase, the model force is very close to that measured experimentally. However, the maximum force is always higher in the experiment than in the model. During the restitution phase, the model and experiment *Force-Displacement* plots exhibit a very close correlation with the two sets of results never differing by more than approximately 10%.

Further comparisons are given in Figures B.8-B.10 for the *Pressureless*, *Oversize* and *Punctured* balls. The results for the *Oversize* ball show a similar, high correlation between the model and experimental results as was found for the *Pressurised* ball.

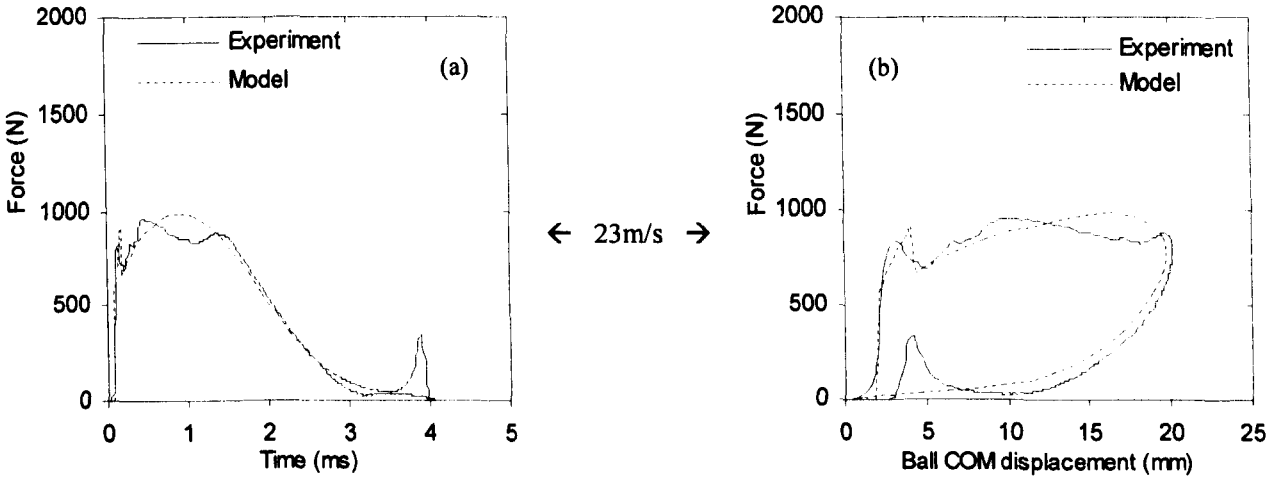

Figure 5.15 Comparison of 1-DOF *momentum flux* model and experiment results for an impact between a *Punctured* ball and a rigid surface for an impact velocity of 23m/s.

The correlation between the model and experiment was found to be generally lower for the *Punctured* and *Pressureless* balls. Comparisons between the model and experiment *Force-Displacement* plots for these two ball types are shown in Figure B.8(c)-(d) and B.10(c)-(d). An example of this lower correlation is given in Figure 5.15 which shows an impact between a *Punctured* ball and a rigid surface, for an impact velocity of 23m/s. During the compression stage, the model predicts the experimental data with a reasonable accuracy of approximately 20%. During the restitution phase, the experimental data shows that the *Pressureless* and *Punctured* balls exhibit a local peak towards the end of impact which has been assigned to the ball suddenly 'flipping' back. The model is unable to account for this and therefore leads to differences between the model and experimental results. This illustrates that there are supplementary components in the impact mechanism, for these ball types, which are not simulated in this visco-elastic model. This explains the lower accuracy of the model for these ball types.

5.5.5 *Discussion of Model*

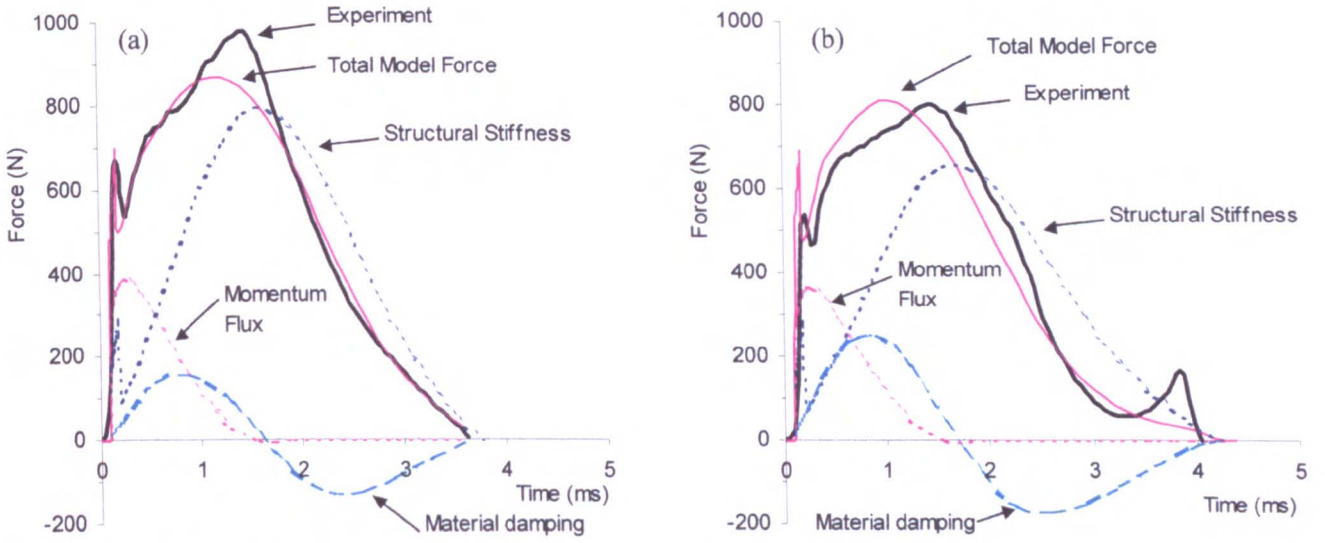

Figure 5.16 Typical comparison of experiment and model *Force-Time* data, showing the contribution of each component on the total model force for an impact velocity of 20m/s. (a) *Pressurised*, and (b) *Punctured* ball.

The *momentum flux* visco-elastic model is composed of three components, (1) structural stiffness, (2) material damping, and (3) momentum flux. Typical contributions for each of these parameters in an impact between a ball and rigid surface at 20m/s are illustrated in Figure 5.16(a) and (b) for a *Pressurised* and *Punctured* ball respectively. Also plotted on these figures is the experimentally obtained force data. These figures can be compared with similar comparisons for the other models in Figure 5.8(a) & (b).

This model is similar to the *variable parameter* model; the main difference being the contribution made by the damper that represented the momentum flux force. In the model it was assumed that this force was proportional to the rate of mass flow into the flattened section of the ball, and is only applicable during the compression phase of impact. This explains the initial sharp rise in the momentum flux force, followed by its steady drop off up until maximum COM displacement. Also, it should be noted that a large fraction of the initial model force ($t<0.5ms$) is due to the momentum flux component. The magnitude of this component is very similar for all ball types as it is essentially a function of the deformation rate. Figure 5.16(a) and (b) compare the momentum flux contributions for the most stiff and least stiff balls respectively and shows that the two magnitudes are very similar.

Another difference between the model which has been discussed in this section and the *variable parameter* model occurs in the initial stage of impact. In this current model it is assumed that no force acts on the ball for COM displacements of below 2mm. This assumption was made to simulate the compression of the cloth; the cloth having a very low stiffness. It could be argued that this assumption should also be made for the final stage of impact, during the period where the ball COM displacement was less than 2mm. However, it was found that such an assumption had negligible effect on the overall model solution and therefore was not implemented.

Figure 5.16(a) and (b) both show that the principal component of the total model force at maximum COM displacement is the structural stiffness force. It can be seen that this is higher for the stiffer *Pressurised* ball compared to the less stiff *Punctured* ball.

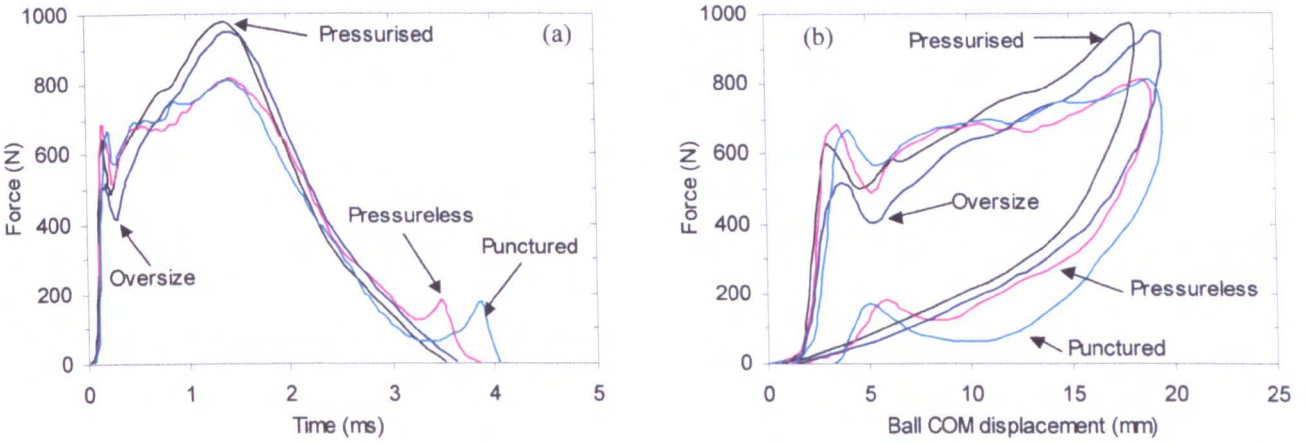

Figure 5.17 Experimental data for (a) *Force-Time* and (b) *Force-Displacement* for a normal impact between a tennis ball and rigid surface, for an impact velocity of 20m/s.

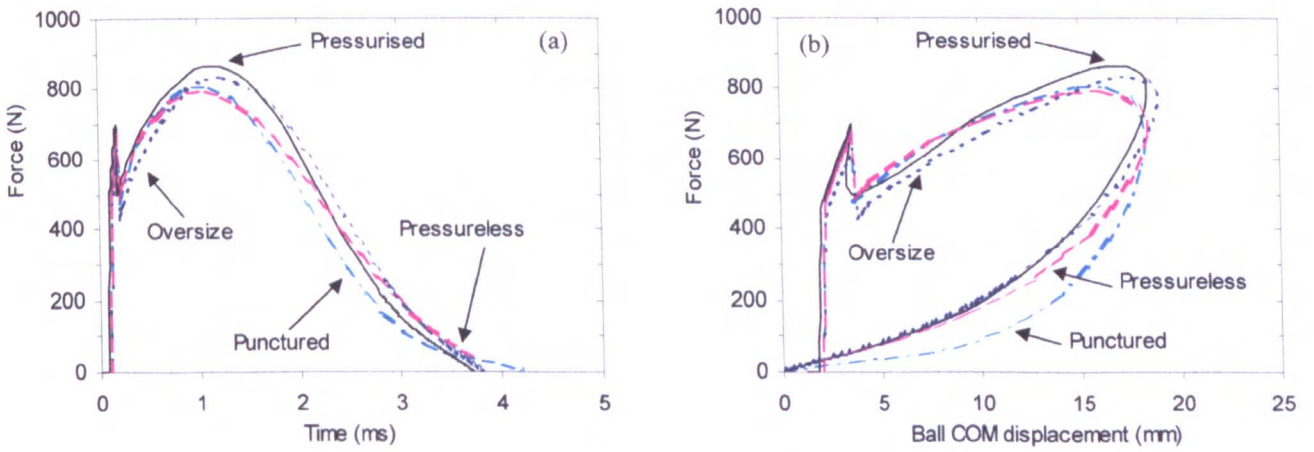

Figure 5.18 Model data for (a) *Force-Time* and (b) *Force-Displacement* for a normal impact between a tennis ball and rigid surface, for an impact velocity of 20m/s.

In Chapter 4, a force platform was used to obtain *Force-Time* and *Force-Displacement* plots for four different ball types; an example of these plots being given in Figure 5.17(a) and (b) respectively. The data in these figures represents impacts for a ball impact velocity of 20m/s. This impact was modelled using the 1-DOF *momentum flux* model and the results are shown in Figure 5.18(a) and (b).

Figure 5.17(a) and (b) shows that all the standard sized balls exhibit a similar experimentally measured force during the first 0.5ms of impact. It has been shown previously that all these balls have a different structural stiffness and wall thickness which implies that the load measured in this phase is not dependent on either of these characteristics. The experimentally measured load for the *Oversize* ball is lower than that for the standard sized balls, during this phase. The model results in Figure 5.18(a) and (b) exhibit a similar trend. The smaller load that is calculated by the model for

the *Oversize* ball is due to the relatively smaller component of momentum flux force for this ball. It has a thinner shell and therefore the density per unit area is lower. Immediately after buckling, the force measured experimentally remains lower than for all the other balls. Therefore this suggests that the lower experimental load is due to the smaller momentum flux force.

In Figure 5.17(a), it can be seen that that the maximum force during impact was lower in the *Punctured* and *Pressureless* balls, compared to the *Pressurised* and *Oversize* balls. A similar trend is evident in the model results shown in Figure 5.18(a) and (b). It was shown previously that the main component of the force at this point is the structural stiffness. Since the two internally pressurised balls have a higher stiffness, these balls exhibit the highest force.

In Figure 5.17(b), and the force platform data in Chapter 4, it can be seen that the *Oversize* ball generally deforms by a similar amount to the *Punctured* ball, even though it is considered stiffer than it. This is due to the *Oversize* ball generally exhibiting a lower force during the initial phase of compression which results in a lower deceleration of the ball centre-of-mass. Interestingly, both balls reach maximum COM displacement at a similar time, to within 0.1ms. The *Oversize* ball, with its higher stiffness and lower damping does, however, exhibit a higher force during the restitution phase which results in a much shorter contact time for this ball. The difference in contact time for these two balls is up to 0.5ms.

The inherent weakness of the model is that the impact between a rigid surface and a tennis ball is very complex and difficult to simulate using a single DOF model. The impact involves structural instabilities, large deformations and high energy losses which would require a more detailed analysis for a more accurate model to be developed. However, an advancement of this current model is beyond the scope of this work. Each of the elements of this visco-elastic model physically represents a component of the impact mechanism. Therefore this model can be used to illustrate the differences noted between the different ball types that have been tested. Also, this model can be adapted for impacts in which the rigid surface is replaced by a deformable surface.

5.5.6 Summary

In this section, a visco-elastic model has been developed which simulates the (1) the structural stiffness, (2) the material damping, and (3) the momentum flux due to the large deformation of the ball. The governing equation of this model is,

$$m_B\ddot{x}_B + (c_B + c_M)\dot{x}_B + k_B x_B = 0$$

The four main features of the model are individually summarised as follows,

1. *High ball stiffness until buckling (for t<0.2ms).* For the first 0.2ms of impact, it was assumed that the ball stiffness was high. This was simulated in the model by assigning a relatively high value to the spring stiffness; this value being constant and defined as k_{SHELL}. It was assumed that k_{SHELL} was equal to 80kN/m for all ball types and ball impact velocities.

2. *Ball stiffness is a non-linear function of the ball deformation (for t>0.2ms).* After the first 0.2ms of impact, the spring stiffness k_B was assumed to be a non-linear function of the ball COM displacement, $\left(k_B = k_{B(0)} + A_K x_B^{\alpha}\right)$. In this equation, $k_{B(0)}$, A_K and α were constants that were dependent on the ball type, but independent of ball impact velocity.

3. *Material damping was a linear function of the volume of rubber being deformed.* The material damping was simulated using a dashpot with parameter c_B, $\left(c_B = \frac{m_B}{M_1} A_C . (d_{CONT})^2\right)$ An empirical equation was derived which estimated the shape of the deformed ball, for a specific ball deformation. This was used to determine the mass of the ball that was not in contact with the surface M_1, and the diameter of the ball/surface contact area d_{CONT}. The damping parameter A_C was dependent on the ball type, but independent of the ball impact velocity.

4. *Momentum flux force.* The momentum flux force is equal to the change of momentum and results from a mass segment, which was initially moving towards the surface, being brought to rest. No analytical solution can be obtained for this internally pressurised, thick walled shell so empirical data was used to define the form of the deformation.

For each ball type, a single function $\left(k_B = k_{B(0)} + A_K x_B^{\alpha}\right)$ was determined that defined the structural stiffness of the ball which gave the same model contact time as that found experimentally. It was found that the *Pressurised* ball was the stiffest, followed by the *Oversize* and then the *Pressureless* balls. The *Punctured* ball was considerably less stiff, for small deformations. However, at higher deformations it had a similar stiffness to the *Pressureless* ball.

For each ball type, a single value for the damping parameter A_C was obtained. This gave a high correlation between the model and experiment values of coefficient of restitution, for impact velocities between 13 and 30m/s. These are representative of the impact speeds for an impact between a ball and racket. For other speeds, the model and experiment values of *COR* could be forced to correlate by determining the relevant value of A_C.

The experimental and model *Force-Time* plots (and *Force-Displacements* plots) exhibit a very strong correlation, especially for the internally pressurised balls. For the other ball types, there are supplementary features of the impact mechanism which are not being simulated by the model and therefore a weaker correlation is obtained. However, it should be noted that, for the majority of the impacts, the model and experiment correlate to within 10%. Therefore this model is a significant improvement on the previous models.

The model has been used to elucidate the differences between the experimentally determined *Force-Time* and *Force-Displacements* plots, for the different ball types. Analysis of the individual contribution of each element of the model has shown that the main component of the force during the first 0.5ms of impact is the momentum flux force. In the model, this is relatively independent of the ball stiffness and wall thickness, and therefore the magnitude of the force is similar all the standard size balls. In the experiment, a similar finding is reached with the *Pressurised*, *Pressureless* and *Punctured* all exhibiting a similar force. Experimentally it was found that this

force is lower in the *Oversize* ball and this ball exhibits a lower momentum flux force in the model as the density per unit area is lower for this ball.

At maximum COM displacement, the magnitude of the model force is primarily a function of the structural stiffness. In the model, the *Pressurised* ball is the stiffest and therefore exhibits the largest force in this phase. The experimental data reveals a similar finding, with the *Pressurised* ball giving the largest force and the *Punctured* and *Pressureless* balls giving the lowest force; these latter two balls being the least stiff.

5.6 Summary

In this chapter, a one degree-of-freedom visco-elastic model of a normal impact between a tennis ball and rigid surface has been developed. This model is used to predict the coefficient of restitution and the *Force-Time* plot for the impact. The accuracy of the model has been quantified by comparing these model results with those determined experimentally. Three models have been discussed in this chapter. Each of these models uses a spring to represent the stiffness of the ball and a dashpot damper to simulate the material damping. These two components act in parallel.

In the first model, it was assumed that the stiffness and damping parameters were constant throughout impact, but varied with ball impact speed. These assumptions are clearly not realistic and lead to a model which predicts a tensile force between the ball and surface towards the end of impact. This results in a low correlation between the model and experiment *Force-Time* plots, for significant proportions of the impact. This model is not physically representative of the impact mechanism and is therefore not a suitable solution.

In the second model, it was assumed that the stiffness and damping parameters were functions of the ball COM displacement. The stiffness of the spring was assumed to be linearly proportional to the ball COM displacement; the gradient of this relationship was defined A_K. However, it was found that the value of A_K increased with impact velocity which implied that the relationship between stiffness and ball COM displacement should be non-linear. The damping parameter was assumed to be proportional to the volume of rubber which is being deformed. The relationship between the magnitude of rubber being deformed and the ball COM displacement was obtained using empirical data. This assumption ensured that no tensile loads could be present in the model solution. A comparison of the *Force-Time* plots for the model and experiment revealed a poor correlation for the compression phase. The model greatly underestimated the force for low displacements, and vice versa for high displacements. Also, the model exhibits a larger COM displacement compared to the experiment. During the restitution phase, the correlation between model and experiment was considerably higher. However, due to the larger ball COM displacement in the model, the model force was significantly lower than that measured experimentally.

Clearly, the second model required a component which acted to increase the model force during the earlier part of the compression phase. The third model includes a second dashpot damper which acts in parallel with the first damper and the spring. This second damper represents the force which

acts on the ball due to the momentum flux. The momentum flux force corresponds to the change in momentum for the section of the deformed ball which is being flattened upon impact with the surface. This force is separate to the stiffness force and only acts during the compression phase. The stiffness of the spring was assumed to be a non-linear function of the ball COM displacement. This function was identical for all ball impact velocities, but varied between ball types. The damping parameter was assumed to be a function of the amount of rubber being deformed and the rate of deformation. It was found that this model could accurately predict the contact time and coefficient of restitution for most impact velocities.

The experimental and model *Force-Time* and *Force-Displacement* plots exhibit a very high correlation, for this *momentum flux* visco-elastic model. However, there are some features of the actual impact mechanism that this model can not account for which leads to some small differences between the two sets of data.

The *momentum flux* model has been used to explain the experimental *Force-Time* plots for the four ball types. The differences and similarities between the balls have been qualitatively accounted for using the model. For example, the model illustrates that the main component of the model force at maximum deformation is due to the structural stiffness; a stiffer ball producing a larger force. This correlates with the experimentally obtained *Force-Time* plots that show the stiffer balls exhibiting a larger force during this phase, compared with the less stiff ball types.

In this chapter, an impact between a ball and rigid surface has been modelled. The model will be referred to in a later chapter when the impact between a ball and racket is investigated.

6. The Racket Stringbed – Quasi-static Compression testing

6.1 Introduction

The aim of this overall study is to determine a model for the impact between a ball and a racket, for a typical tennis stroke. This model involves four distinct, interacting components; the human body, racket frame, stringbed and ball. The technique which has been adopted in this study involves the construction of the overall model in discrete stages. In Chapter 5, a model has been developed for an impact between a ball and rigid surface. This model was verified using experimental data obtained for an impact between a ball and force platform. The logical next stage of this study involves the development of a model of a ball impacting on a stringbed. The stringbed is a discrete component of the impact mechanism and shall be modelled as such. In Chapters 6, 7 and 8, a visco-elastic model of an impact between a ball and head clamped racket will be developed; a visco-elastic model being chosen for its versatility. In this type of impact, the racket frame is rigidly clamped and therefore does not contribute to the impact mechanism. This minimises the number of variables which need to be considered in this model.

It is well established that different string tensions and types result in differences in the impact between a ball and racket. There is both analytical and anecdotal evidence of this in academic journals (Cross 2000f) and commercial publications (Racket Tech 1998). The main finding has been that a lower string tension results in a higher coefficient of restitution. It has also been shown that an increase in string tension results in a decrease in the measured contact time for the impact (Taylor 2002). The explanation for these findings is most easily understood by considering the work by Cross (2000f). In this work, the ball and stringbed are modelled as two springs in series, and the racket as a one dimensional flexible beam. A reduction in string tension was represented in the model as a reduction in the stiffness of the spring which represented the stringbed. This increased the contact time for the system and meant that the maximum force was lower, and so the ball deformed by a smaller amount. The consequence of this was that hysteresis losses in the ball were lower and so it rebounded with a higher velocity. In the work by Cross, the values of the stringbed stiffness were assumed and not experimentally obtained. In this current chapter, estimates of the quasi-static stringbed stiffness are obtained for a range of string tensions. Experiments will be conducted on these head clamped rackets in Chapter 7 to measure the ball rebound velocity, contact time and ball/stringbed deformation. Finally, a model of this impact will be developed in Chapter 8.

The quasi-static stiffness of the stringbed can easily be measured by applying a load, perpendicular to the string plane, and measuring the resulting displacement. Leigh and Lu (1992) experimentally determined a value of approximately 30kN/m which was found by compressing a tennis ball against the stringbed for loads of up to 200N. Kawazoe (1993) also used a tennis ball to apply a load and determined a stiffness of 30kN/m for very small loads, and over 100kN/m at deflections of 20mm (about 1200N load). Brody (1979) applied a distributed force of 480N over a 40mm diameter disc and obtained a deflection of 14.5mm, giving a stiffness of approximately 35kN/m.

In the first part of this chapter, the quasi-static stringbed stiffness is obtained for a selection of rackets which are considered to cover the range that is typical in a game of tennis. In this first section, the displacement is only measured at the load point, as this is all that is required to determine the stringbed stiffness. However, the displacement of the other points on the stringbed are of equal importance in the understanding of the deformation mechanism. Therefore, in the second part of this chapter, the shape of the deformed stringbed will also be measured.

6.2 Measuring the quasi-static stiffness of a stringbed

6.2.1 Introduction

In this section, the quasi-static stiffness of the stringbed is measured. In this test, the head of the racket frame is clamped so that the measured deformation is solely due to that of the stringbed. The load will be applied at the geometric string centre of the racket, in a direction which is perpendicular to the plane of the stringbed. The load could have been applied by compressing a tennis ball into the stringbed. However, one weakness of this method is that the force is applied over a continually varying area which is difficult to measure. It is common practise to minimise the number of variables in an experiment and therefore it would be more appropriate to apply the load over a fixed area. A standard device which can be used to perform such an experiment is called the Babolat RDC (Babolat 2002). The racket is placed onto a circular support and a load is applied to the stringbed using a rigid disc with a diameter of 51mm. The Babolat RDC machine applies a specific force and measures the resulting displacement. This displacement is converted to a number between 0 and 100, which is then shown on the LCD display. This number is only meant to give a guide to the relative stiffness of the stringbed, and therefore is not measured in physically significant units. This feature makes this apparatus unsuitable for the current study as the measured stringbed stiffness could not be compared with that used in a visco-elastic model of the stringbed.

In this section, a machine is discussed that is based upon the Babolat RDC machine but which measures the actual load that is applied to the stringbed. The device also measures the displacement of the load point on the stringbed.

6.2.2 Experiment Apparatus

Figure 6.1 shows the rig which was used to determine the quasi-static stiffness of the deformed stringbed. The rig supports the racket below a rigid lower plate (labelled A). A threaded rod, attached to an S-type strain gauge load cell, was attached to a rotating handle (labelled B) which was supported on a bearing on the upper plate (labelled C). At the other end, the rod passes through the geometric string centre of the racket and a rigid circular disc, of diameter ϕ_{DISC}, was attached to the end. Rotating the handle clockwise causes the rod, and disc, to traverse upwards which results in a distributed load being applied to the stringbed across the area of the disc. The displacement of the stringbed at the load point was determined from the number of revolutions of the handle N_H; each revolution of the handle corresponding to a displacement of 1.75mm. The displacement of the load point on the stringbed is referred to as δ_{LOAD} and is equal to $1.75N_H$.

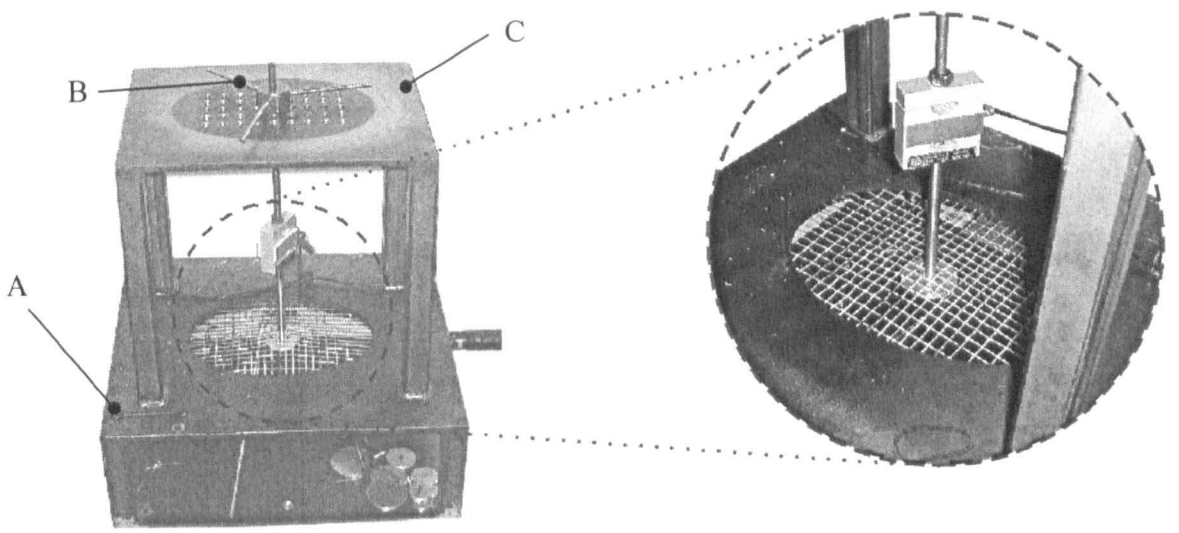

Figure 6.1 Rig used to determine the stiffness of the stringbed.

The load cell has been calibrated for compressive loads of up to 2500N. A pre-load of 10N was applied to the stringbed to ensure that the racket head was positioned properly in the rig before the measured loading commenced. The handle was rotated at a steady rate of one rotation per second, up to a maximum of 12 rotations ($N_H = 12$) or a load of 1200N, whichever was reached first. The load was then removed, at the same rate as for the loading phase. The output of the load cell was sampled using a strain indicator unit, for each increment N_H, for both the loading and unloading phase. At each increment of N_H there was a delay of five seconds before the load value was recorded. During the loading cycle the reading on the load cell would reduce during this five second period. This occurred due to stress relaxation taking place in the string. A delay was employed in an attempt to obtain a true, settled value for the actual stiffness of the stringbed which was not dependent on the rate of loading. In practise, the load value actually continued to decrease after the five second delay although the rate of this decrease was relatively small. This highlights the difficulty in measuring a value for the quasi-static stiffness of the stringbed because the recorded value is time dependent. Indeed, holding the load for five seconds may not be giving a true reading of the static stiffness of the stringbed because the load may be 'damaging' the strings. However, it does give a repeatable method which can be used to test the range of rackets used in this section.

Four identical racket frames were used in this section, each having a head size of 630cm^2 (98in^2). The four rackets were all strung at different tensions using the same 15 gauge (1.4mm diameter) nylon string. The string tensions T_S used in the rackets were 40lbs, 50lbs, 60lbs and 70lbs. These cover the range of tensions typically used in the game of tennis.

Four different sized discs were used to apply the load to the stringbed. These discs had diameters of 35mm, 45mm, 55mm and 65mm. The Babolat machine applies the load onto the stringbed using a circular disc with a diameter of 51mm. For interest, high speed video footage, such as that discussed by Goodwill & Haake (2001), shows that the diameter of a typical contact area of the ball on the racket was in the region of 30-50mm, depending on the magnitude of ball deformation.

Before the main testing commenced, a short investigation was conducted to identify whether the properties of the stringbed change during testing. This simple repeatability study involved cyclically loading and unloading the stringbed 8 times; the load and displacement being measured throughout each cycle. The results for this repeatability study are discussed in the following section.

Before any testing was conducted, the stringbed was compressed to full deflection and then unloaded. This was conducted to ensure that the racket was correctly sat beneath the main plate, and the loading disc was correctly located on the stringbed.

6.2.3 Results and Discussion

(a) Repeatability study

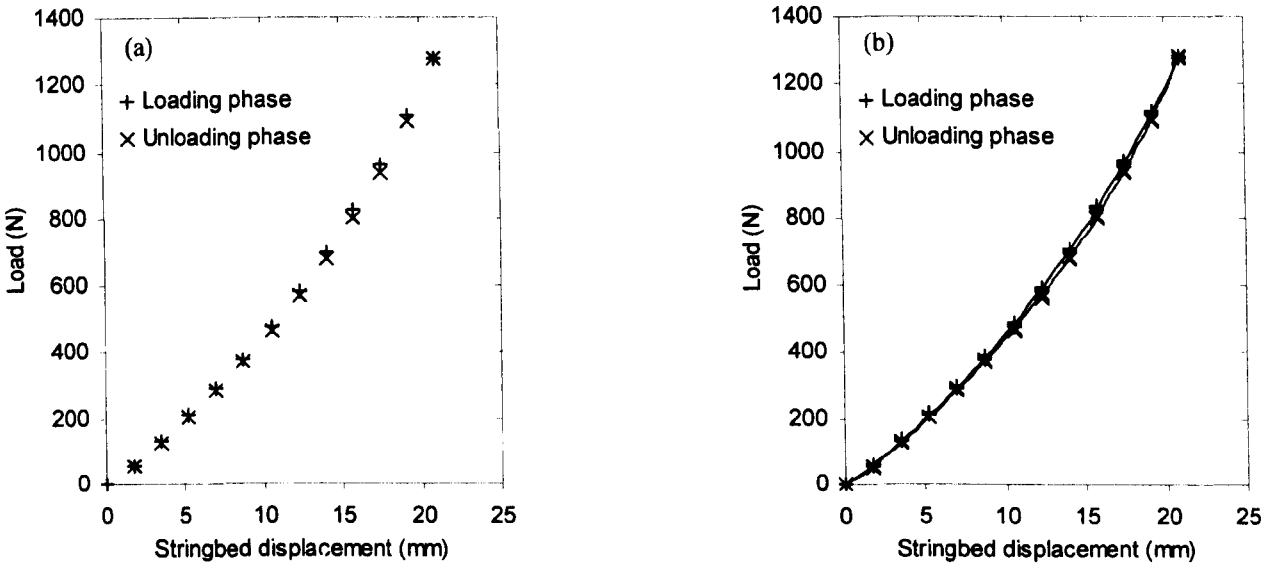

Figure 6.2 (a) Single quasi-static loading and unloading of the stringbed and (b) Eight quasi-static cyclic loadings of the stringbed.

In this section of the experiment, a racket with a string tension of 60lbs was placed in the rig. The stringbed was loaded and unloaded eight times, using a disc diameter of 35mm. Figure 6.2(a) shows the data for a single quasi-static compression of the stringbed, and Figure 6.2(b) shows the data for eight cyclic compressions of the stringbed. In these figures the load is plotted separately, as two data sets, for the loading and unloading phases. In Figure 6.2(b), two separate fourth order polynomial trend lines are plotted through these two sets of data. The difference in the two data sets is largest for stringbed displacements of between 10 and 20mm; the magnitude of this difference being 4%.

The repeatability of the experiment can be quantified by measuring the uncertainty in the data, for the eight cyclic compressions, with respect to the trendline. It is assumed that the level of uncertainty is equal for all data points and therefore the standard deviation of the data can be found using the method described in Appendix A. It was found that the standard deviation of the loading and unloading phases was 3.7N and 2.8N respectively. This relatively small deviation implies a high level of confidence can be assigned to the test results.

The data has shown that the stringbed exhibits a small level of hysteresis, even for this quasi-static deformation. However, in the following section only the data that was measured for the compression phase of the impact is presented. Whilst it is accepted that the magnitude of hysteresis loss is of some interest, it has been omitted here for the sake of clarity.

(b) Stringbed displacement

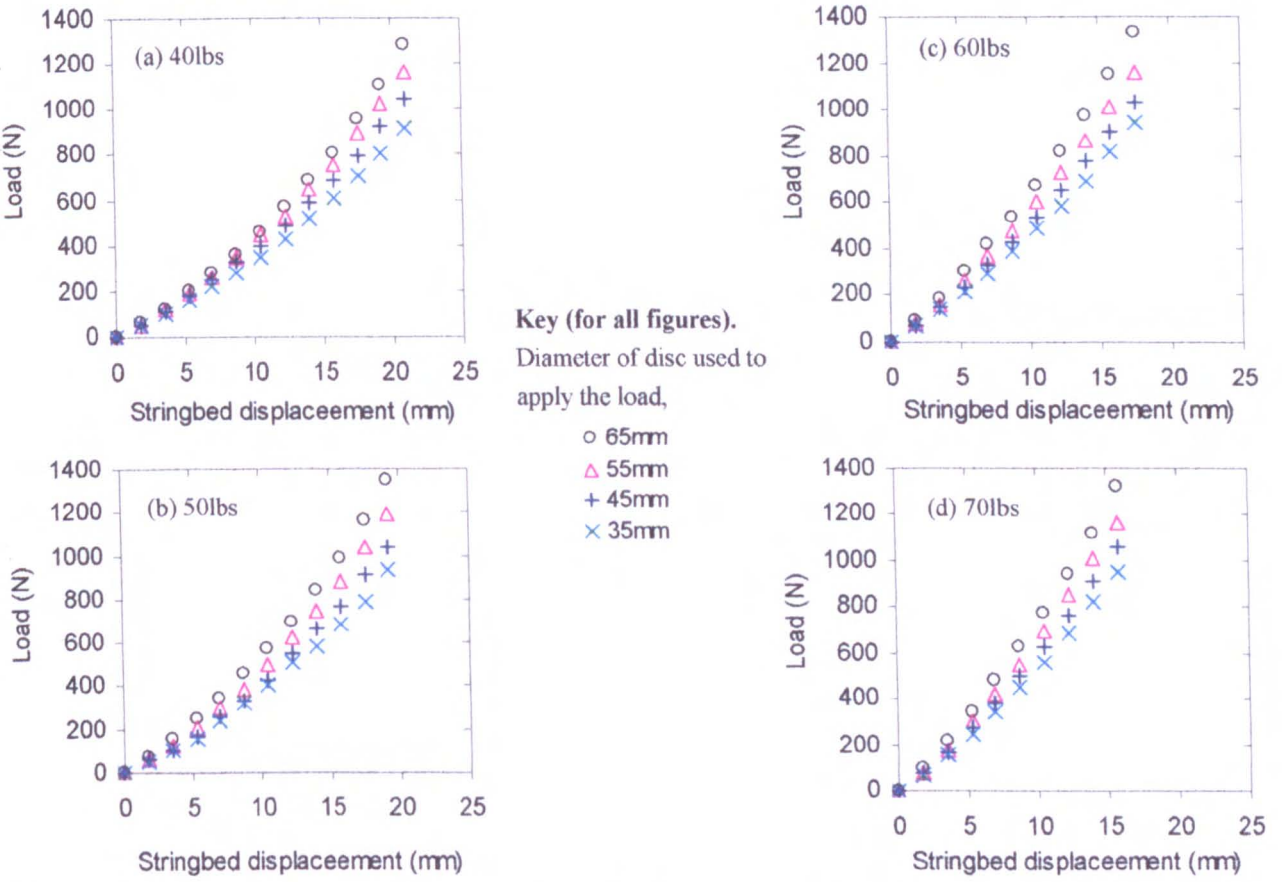

Figure 6.3 Measured load plotted against the displacement of the load point on the stringbed. The data is plotted for rackets strung with a range of tensions.

Figure 6.3 shows the measured load plotted against the displacement of the stringbed, at the point at which the load is applied. The data is presented for all the string tensions that were tested, and for the four different disc sizes that were used to apply the load. The data shows that the force increases, as the displacement is increased. For each string tension, the stringbed is loaded to the same maximum displacement for each disc diameter. The figures show that the measured force is largest for the tests conducted with the largest disc size; the measured force obtained using a 65mm diameter disc being approximately 35% larger than that obtained using the 35mm disc.

A qualitative comparison of Figure 6.3 (a)-(d) shows that the force in the stringbed, for a specific displacement and disc size, is smallest for the racket strung at a tension of 40lbs and largest for the racket strung at 70lbs. A more accurate comparison of the different string tensions can be performed by plotting the stiffness of the stringbeds directly. In this case, the stiffness is defined as the ratio of the force applied and the resulting displacement.

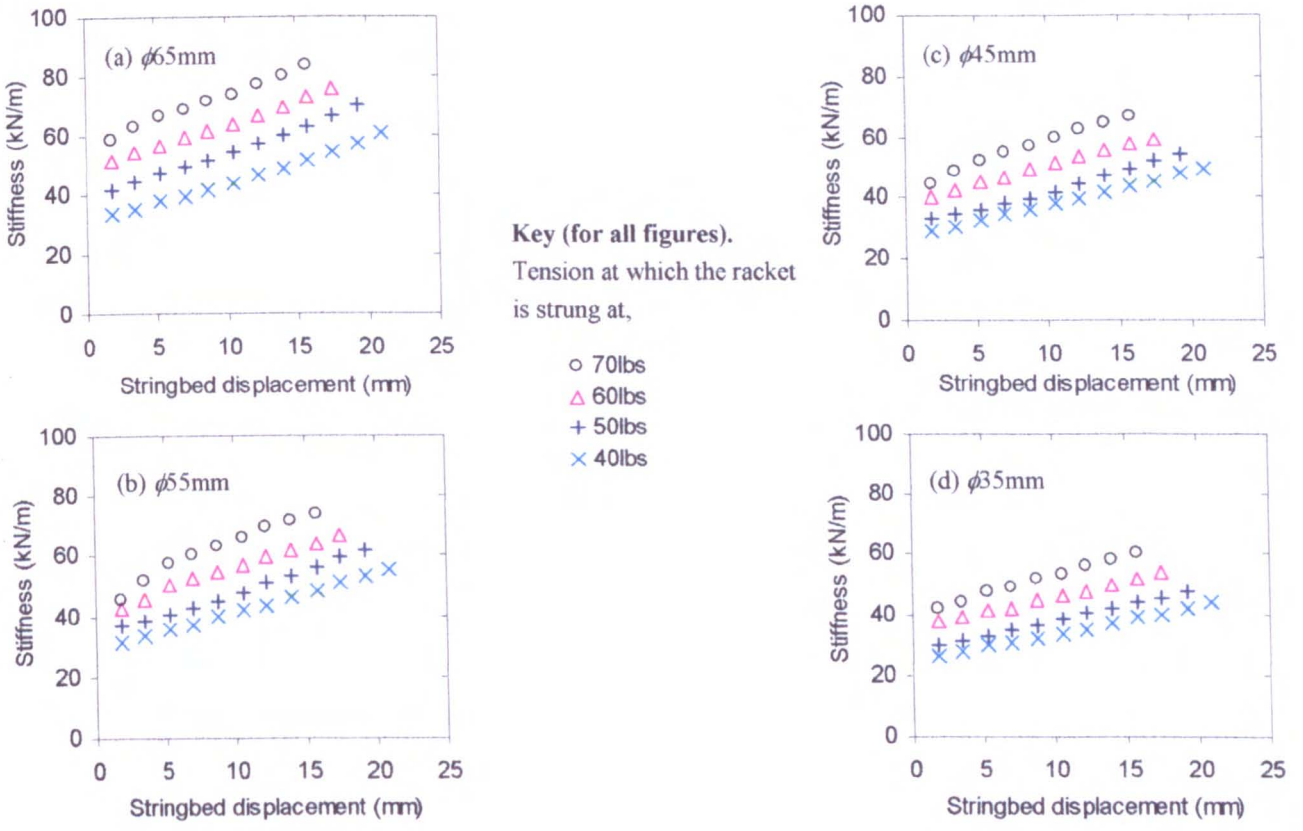

Figure 6.4 Stringbed stiffness plotted against the displacement of the load point on the stringbed. The load was applied via a rigid disc which had a diameter that ranged from 65mm to 35mm.

In Figure 6.4 (a)-(d), the calculated stiffness of the stringbed is shown. In each figure, the data is plotted for the four rackets (strung at different tensions). The diameter of the disc used to apply the load is different in each figure, and ranges from 65mm (Figure 6.4(a)) to 35mm (Figure 6.4(d)).

Figure 6.4 (a) shows that the stringbed of the racket strung at 70lbs is approximately 70% stiffer than for the racket strung at 40lbs. This figure also shows that the stringbed stiffnesses of the rackets strung at 50lbs and 60lbs are 25% and 45%, respectively, stiffer than that strung at 40lbs. In this figure, the load was applied using a circular disc with a diameter of 65mm. In Figure 6.4 (d), the load was applied using a disc with a diameter of 35mm and the data in this figure shows that rackets strung at 50lbs, 60lbs and 70lbs have a stringbed stiffness which is approximately 15%, 40% and 60% stiffer, respectively, than that for a racket strung at 40lbs. Figure 6.4 (b)-(c) exhibit a similar trend as that found in the other two figures.

The data in Figure 6.4 (a)-(d) indicates the relative quasi-static stiffness for the different string tensions. However, in a model it would be useful to have a generic relationship between the stringbed stiffness and the diameter of the disc used to apply the load. Clearly, it is not possible to have a single function that can describe this relationship as the magnitude of the stiffness is a function of the string tension, stringbed displacement and the disc diameter. For example, in this current study, 16 equations are required to define the stiffness of the stringbed at a specific displacement, for the four disc diameters and four string tensions. By selecting a suitable normalising technique, it may be possible to reduce the number of required equations, as shall be discussed below.

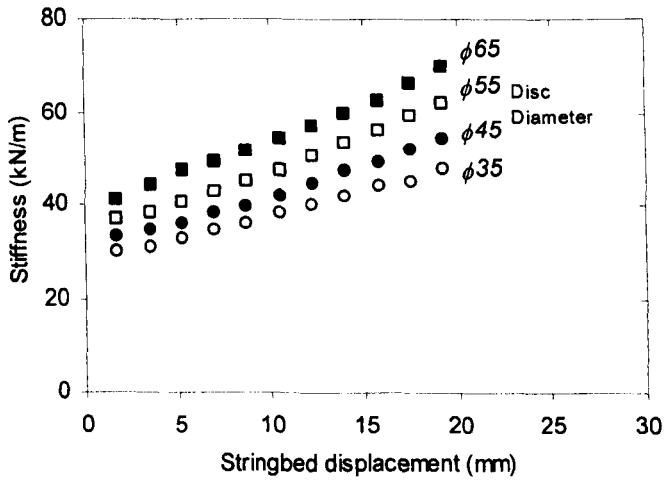

Figure 6.5 Illustration of the variation of stringbed stiffness with displacement and disc diameter (that is used to apply the load). The data is presented for a string tension of 50lbs.

In Figure 6.5, the measured stringbed stiffness data is plotted for a range of different disc diameters that have been used to apply the load. This data has been obtained for four different string tensions, but is only presented here for a string tension of 50lbs. Figure 6.5 confirms that the stringbed stiffness is a function of the disc diameter. However, it also shows that the shape of the curves which define this stiffness are very similar for all disc diameters. It is therefore hypothesised that the stiffness data can be normalised to a specific reference value. In this case, this reference data has been arbitrarily chosen as the stiffness data which was obtained by using a disc with a diameter of 55mm (ϕ_{55}). Therefore, the normalised stiffness $\tilde{k}_S$, for a specific stringbed displacement and a disc diameter of ϕ_D, is defined using [6.1],

$$\tilde{k}_S = \frac{k_S(\phi_D)}{k_S(\phi_{55})} \qquad [6.1]$$

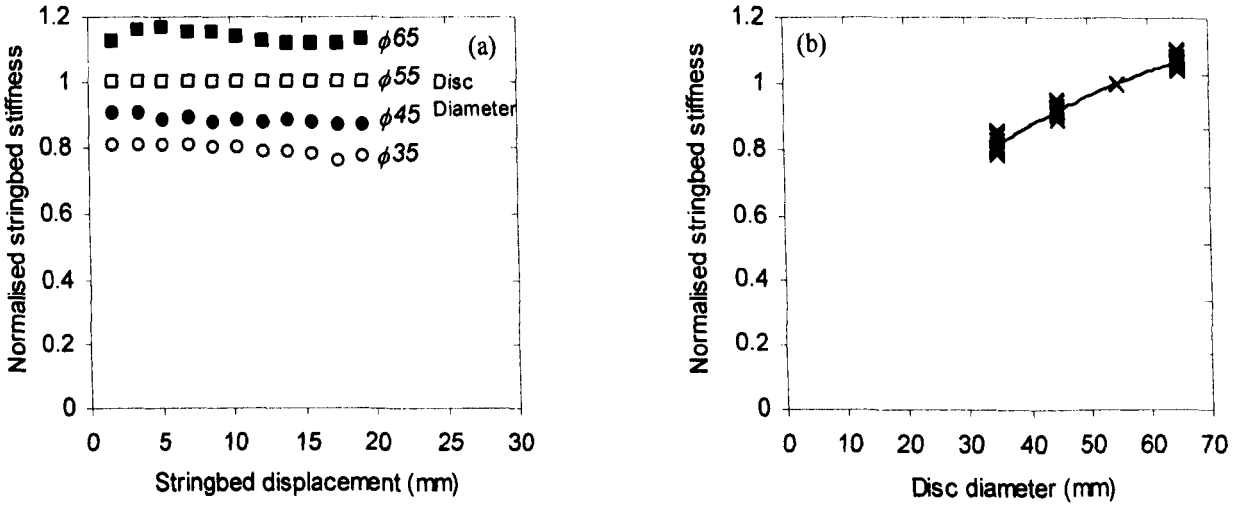

Figure 6.6 (a) Illustration of variation of normalised stringbed stiffness $\tilde{k}_S$ with displacement and disc diameter (that is used to apply the load). (b) Normalised stringbed stiffness $\tilde{k}_S$ plotted against disc diameter, using data for all stringbed displacements. The data is presented for a string tension of 50lbs.

Figure 6.6 (a) illustrates the variation of the calculated normalised stringbed stiffness for the four different disc diameters. This is the same data as is shown in Figure 6.5 but the data has been

normalised to the stringbed stiffness which was obtained for a disc diameter of 55mm and therefore all the normalised data for ϕ_{55} is equal to unity. This figure shows that the normalised stiffness is approximately independent of the stringbed displacement, and is solely a function of the disc diameter.

Figure 6.6 (b) shows the same normalised stringbed stiffness data that is presented in Figure 6.6(a). However, in this figure the data is plotted as a function of the disc diameter ϕ_D. For each disc diameter, the data is presented for all the stringbed displacement increments. A second order polynomial is plotted through this data and the equation of this trendline can be used to estimate the relationship between the normalised stringbed stiffness and the disc diameter. The general form of this equation is,

$$\tilde{k}_S = a\phi_D^2 + b\phi_D + c \qquad [6.2]$$

where a, b and c are constants.

Equation [6.2] can be used to estimate the normalised stiffness $\tilde{k}_S$ for a specific value of ϕ_D; this stiffness being normalised to the stringbed stiffness obtained using a disc diameter of 55mm. A second order trend line can be plotted through the data in Figure 6.5 and be used to define an equation for the stringbed stiffness that was obtained using a disc of this diameter of 55mm. The general form of this equation is,

$$k_S(\phi_{55}) = d\delta_S^2 + e\delta_S + f \qquad [6.3]$$

where d, e and f are constants.

To complete the solution, [6.1] is rearranged into the form,

$$k_S(\phi_D) = \tilde{k}_S \times k_S(\phi_{55}) \qquad [6.4]$$

Using [6.4], the stringbed stiffness at any displacement and for any disc diameter can be calculated by knowing the normalised stiffness for the relevant disc diameter ([6.2]) and the stiffness measured using a 55mm diameter disc, for the specific displacement δ_S ([6.3]).

The above analysis has revealed a possible method of minimising the number of equations that are needed to represent the stringbed stiffness of a racket. The method was illustrated using a tennis racket that was strung at 50lbs tensions. In brief, the method involved the normalisation of the stringbed stiffness data with respect to the data that was obtained using a disc diameter of 55mm. This data was shown in Figure 6.6(b), for a racket strung at 50lbs. The normalised stiffness $\tilde{k}_S$ data for all the rackets that have been used in this section (40lbs, 50lbs, 60lbs and 70lbs), is given in Figure 6.7.

Figure 6.7 shows the normalised stringbed stiffness plotted against the diameter of the disc that is used to apply the load. This figure contains the normalised stringbed stiffness data for all string tensions and for all values of stringbed displacement.

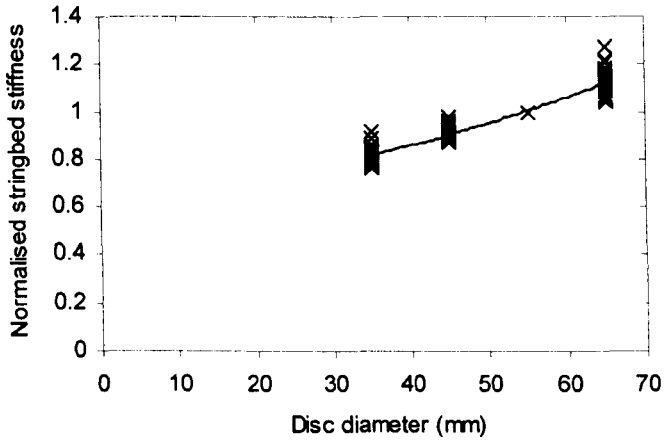

Figure 6.7 Normalised stringbed stiffness $\widetilde{k}_S$ plotted against disc diameter that was used to apply the load. The data is presented for all string tensions and all the stringbed displacements.

A second order polynomial trendline is plotted through the data in Figure 6.7; the coefficients of this equation being obtained using the *least squares regression* method. The equation for the trendline shown in this figure (converted to SI units) is,

$$\widetilde{k}_S = 78.42\phi_D^2 + 2.336\phi_D + 0.6392 \qquad [6.5]$$

Using this equation, along with [6.3] (for the relevant racket) and [6.4], the stringbed stiffness at any displacement and for any disc diameter can be estimated . In Figure 6.7, the scatter in the results, with respect to this trend line, illustrates the uncertainty in the use of the trendline to estimate the relationship. It is assumed that this level of uncertainty is equal for all data points and therefore the deviations form a normal distribution. A statistical analysis of the data, as described in Appendix A, can be used to calculate the standard deviation of the data as 0.03. A visual analysis of the scatter in the data in Figure 6.7 would lead to a conclusion that this value is unrealistically small. However, it should be noted that this graph contains approximately 160 data points. A large proportion of these data points exhibit a very low uncertainty, which leads to the low value of the standard deviation being obtained.

To summarise, [6.3]-[6.5] are very useful equations for estimating the measured values of the stringbed stiffness. The only requirement of the solution is that the stringbed stiffness for a disc diameter of 55mm is known. If this is satisfied, then the actual value of stiffness can be estimated for any value of disc size between 35mm and 65mm.

6.2.4 Summary

In this section it was shown that the quasi-static stiffness of the stringbed can be found by applying a distributed load to the stringbed using a rigid disc. It has been shown that the repeatability of this experiment is very high, with standard deviations of the measured load being only 3N. The cyclic compression tests showed that the stringbed exhibited small, but measurable hysteresis losses.

The experiments were conducted using a range of disc sizes, and four identical rackets that were strung using a tension ranging from 40lbs to 70lbs. It was found that the 70lbs racket was approximately 65% stiffer than the 40lbs racket. It was also found that the measured force was

approximately 35% larger when the 65 mm diameter disc was used, compared with when the 35mm diameter disc was used.

An equation was derived which could be used to calculate the normalised stringbed stiffness, for a specific disc diameter. If the stringbed stiffness was measured for a disc diameter of 55 mm, then the stringbed stiffness for any disc diameter could be estimated using the empirical equation.

6.3 Measuring the shape of a quasi-statically deformed stringbed

6.3.1 Introduction

In section 6.2, the quasi-static stiffness of the stringbed was measured for displacements which are perpendicular to the plane of the stringbed. In that section, the load was applied using a rigid circular disc. The stiffness was measured for four different string tensions and four different diameters of disc.

In this current section, the shape of the quasi-statically deformed stringbed is obtained. More precisely, the displacement of a number of points along the longitudinal axis of the stringbed is to be measured. In the previous section, it was shown that the quasi-static stiffness of the stringbed was dependent on the string tension and size of the disc. In this current section, the effect that these parameters has on the shape of the deformed stringbed is to be determined.

6.3.2 Experiment Apparatus

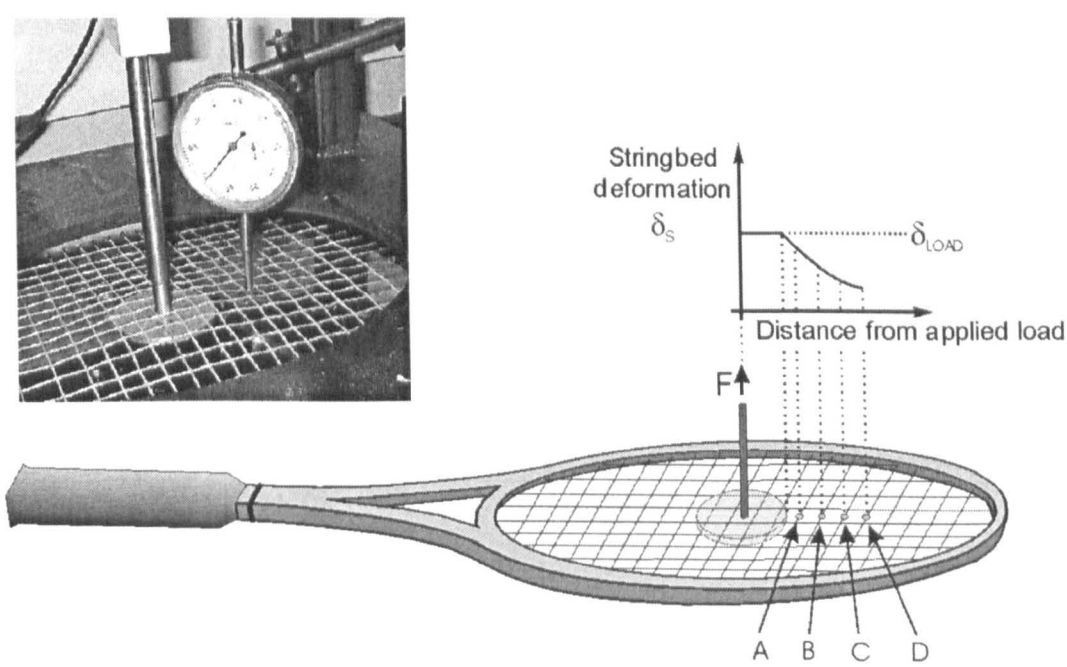

Figure 6.8 Schematic illustration of the four points (A-D) at which the displacement of the stringbed is measured using a dial gauge. The dial gauge is also shown (inset).

In the previous section, the tests were performed on four identical rackets that had been strung at 40, 50, 60 and 70lbs. In this current section, only the rackets strung at 40 and 70lbs are to be tested as this will provide sufficient information as to how the string tension affects the shape of the

deformed stringbed. This testing was conducted approximately three weeks after the testing that was described in section 6.2 was completed. The same two rackets were used in both sections, and were not restrung before this current testing took place.

The load was applied to the stringbed using the same apparatus as that described in section 6.2. A displacement was applied at the geometric string centre using a rigid circular disc. This disc can be seen in Figure 6.8 (inset). This displacement is defined as δ_{LOAD} and is applied in increments of 1.75mm. Two different disc diameters (35mm and 55mm) are used in this study, to assess the effect that the disc size has on the shape of the deformed stringbed.

Figure 6.8 illustrates the four discrete points (*A*, *B*, *C* and *D*) along the longitudinal axis at which the vertical displacement of the stringbed was measured using a dial gauge. These points were located at the intersections between the four cross strings and the longitudinal axis, as illustrated in Figure 6.8. The dial gauge was mounted on the lower plate using a strong magnet. The gauge was used to measure the displacement at point A, for each increment of δ_{LOAD}, up to a load point displacement δ_{LOAD} of 17.5mm. The dial gauge was then moved to point B and the experiment was repeated. The gauge was then moved to point C, and finally point D, resulting in a total of four repeats of this experiment.

6.3.3 Results and Discussion

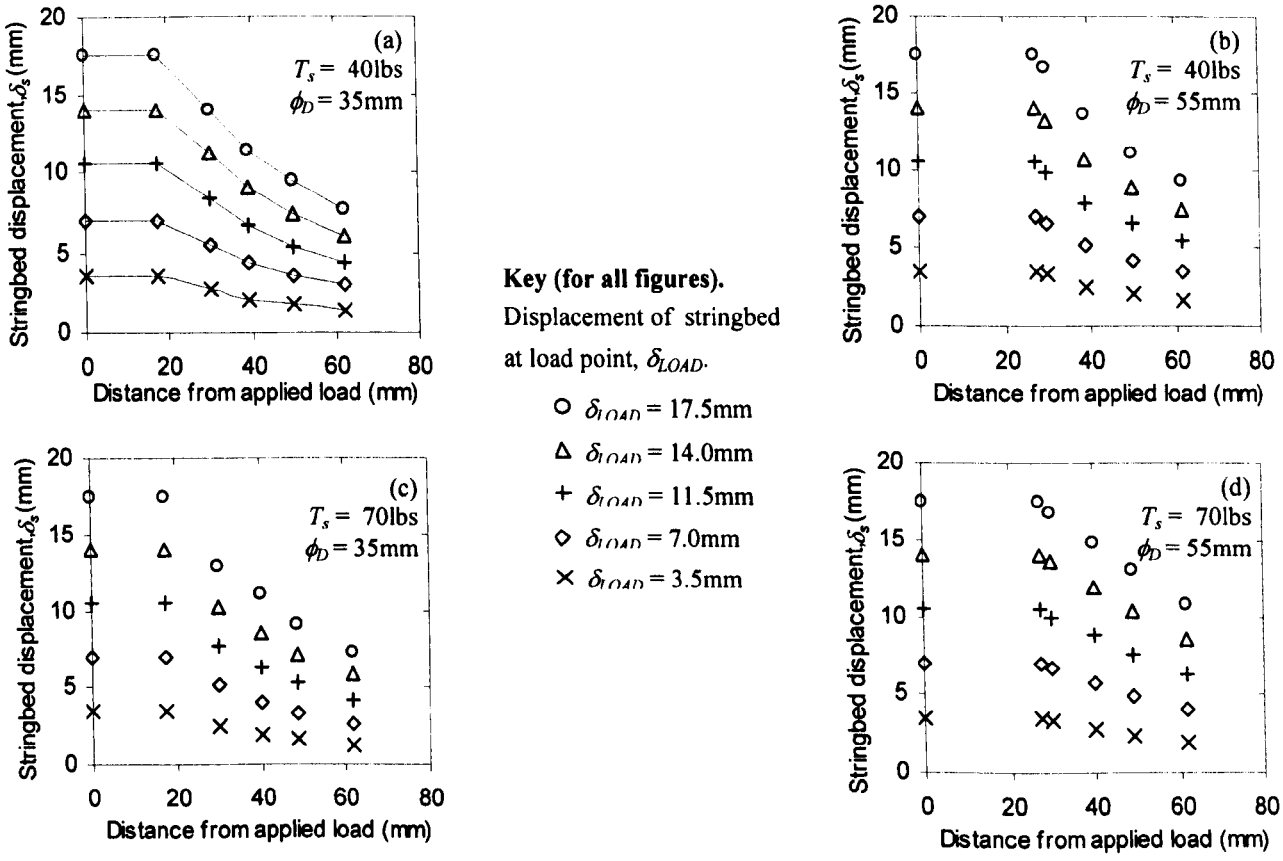

Figure 6.9 The measured displacement of the stringbed at a range of positions from the load point. The data is presented for different combinations of string tension T_S and load disc diameter ϕ_D. The data is categorised by the stringbed displacement δ_{LOAD} at the point at which the load is applied.

Figure 6.9 (a)-(d) show the measured displacement of the stringbed as a function of the distance from the load point; the data is categorised by the displacement of the load point δ_{LOAD}. Figure 6.9 (a)-(b) illustrate the displacement of the stringbed for the racket strung at 40lbs tension. Figure 6.9 (c)-(d) illustrate the data for a racket strung at 70lbs tension. The load was applied using a circular disc with a diameter ϕ_D of either 35mm and 55mm; the value of ϕ_D being specified in each figure. Each data point represents the average of the two values which were sampled; one value being recorded during the loading phase and one for the unloading phase. Lines are plotted through several data sets in Figure 6.9 (a) to give an illustration of the shape of the deformed stringbed. It can be seen that the stringbed displacement is constant over the section of the stringbed that the load is being applied, i.e. for a distance of $\phi_D/2$ from the applied load. The displacement then decreases with distance from the applied load point.

It is difficult to extract any further conclusions from the data in Figure 6.9. An alternative method of plotting this data is given in Figure 6.10. In this figure, the stringbed displacement at each position along the stringbed has been normalised with respect to the displacement δ_{LOAD} at the applied load.

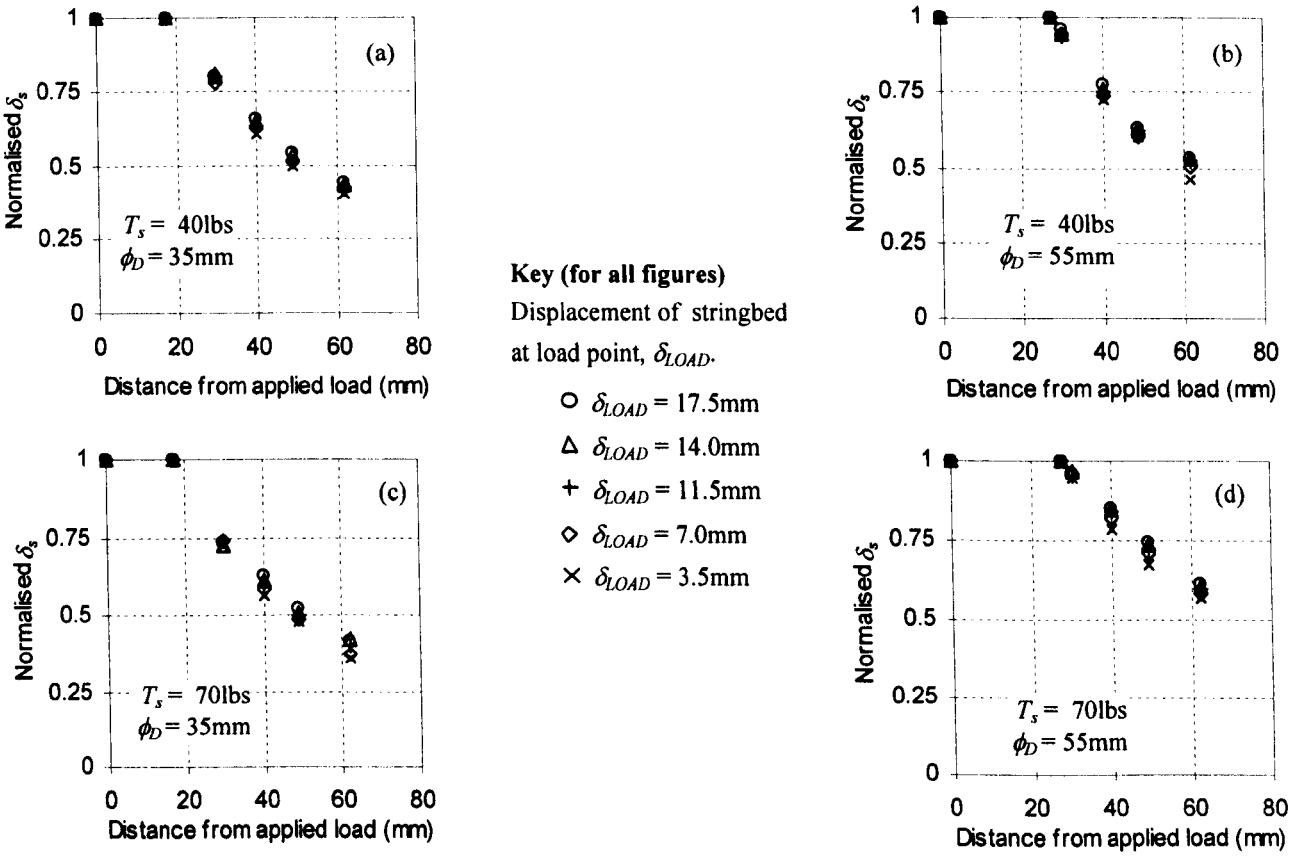

Figure 6.10 The normalised displacement of the stringbed, at a range of distances from the load point. The data is presented for different combinations of string tension T_S and disc diameter ϕ_D. The data is categorised by the displacement of the stringbed δ_{LOAD} at the point at which the load is applied.

Figure 6.10 illustrates that, for a specific combination of string tension and disc diameter, the normalised data is not greatly influenced by the magnitude of the stringbed deformation. The

implication of this is that the shape of the stringbed is effectively constant for all applied forces, for a specific combination of string tension and load area. It could therefore be assumed that a single best-fit line could be plotted through all the data sets in each figure, to represent the shape of the deformed stringbed for the specific tension/diameter combination. These lines are plotted in Figure 6.11.

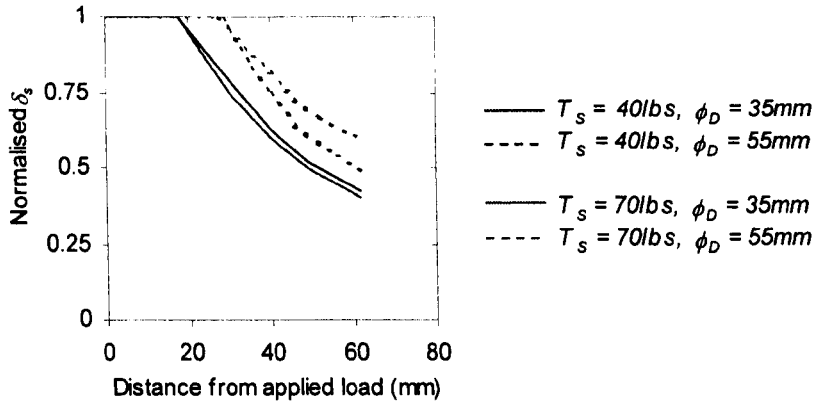

Figure 6.11 The normalised displacement of the stringbed as a function of the distance from the applied load. The data is categorised by the combination of string tension T_S and disc diameter ϕ_D.

Figure 6.11 shows the normalised stringbed displacement data for all of the combinations of the two string tensions and disc diameters, T_S and ϕ_D respectively. This data shows that the shape of the stringbed deformation is a function of the diameter of the disc used to apply the load, especially for the higher string tension. When using a disc diameter of 35mm to apply the load, the shape of the deformed stringbed does not appear to be a function of the string tension. However, when the larger disc was used, the string tension magnitude did affect the shape. The importance of this finding is difficult to quantify because more data would need to be collected to verify this relationship.

6.3.4 Summary

In this section, the deformed shape of the stringbed was measured for a quasi-static loading. In this experiment, the load was applied using a rigid circular disc and the displacement at various points along the longitudinal axis of the racket was measured using a dial gauge. These tests were conducted on two identical rackets that had been strung with two different string tensions, and two different disc diameters were used to apply the load.

It was found that the normalised shape of the deformed stringbed was not a function of the magnitude of the force/displacement which was applied. It was not clear whether this shape was a function of the string tension. However, for a specific string tension, it was found that the shape was dependent on the diameter of the disc.

6.4 General comment about quasi-static stringbed stiffness

6.4.1 Introduction

This section contains a general discussion regarding the measurement of the quasi-static stringbed stiffness of a racket. In sections 6.2 and 6.3, the same rackets were used for the two separate experiments. The differences between the two experiments are clarified as,

1. *Experiment 1.* In this experiment the stringbed stiffness was measured and this testing is discussed in section 6.2.
2. *Experiment 2.* In this experiment the shape of the deformed stringbed was measured, and this testing is discussed in section 6.3.

In both experiments, two identical rackets were used; one racket was strung at 40lbs and the other at 70lbs. The two rackets were first used in *Experiment 1* and then, approximately three weeks later, they were used in *Experiment 2*. The rackets were not restrung during this period. In both experiments, the applied force and displacement of the load point was measured. Initially, it would be expected that the results for the stringbed stiffness would be identical for both experiments. However, during the three week period between the two experiments, the two rackets were subjected to a number of ball impacts, in a separate experiment. This may have affected the properties of the stringbed, and lead to differences in the values of the stringbed stiffness measured in sections 6.2 and 6.3. In this short section, a comparison is made between the measured quasi-static stringbed stiffness for *Experiment 1* and *Experiment 2*.

6.4.2 Results

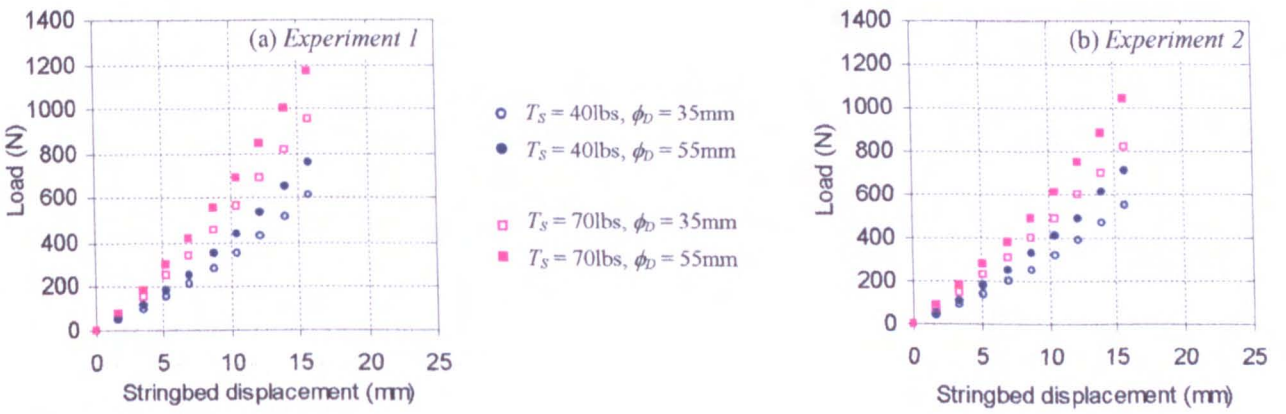

Figure 6.12 The measured force is plotted against the stringbed displacement at the load point δ_{LOAD} for the two experiments. The data is categorised by the combination of string tension and disc diameter T_S and ϕ_D respectively.

Figure 6.12 shows the relationship between the applied force and the displacement of the stringbed at the load point δ_{LOAD}. The data is presented for combinations of two different string tensions and two disc diameters. Figure 6.12(a) shows the results for *Experiment 1* (discussed in section 6.2) and Figure 6.12(b) shows the results for *Experiment 2* (discussed in section 6.3). It can be seen

that the measured force values are consistently higher in Figure 6.12(a) compared with Figure 6.12(b). For the racket strung at 70lbs tension, this difference is approximately 15%. For the racket strung at 40lbs the difference is approximately 10%.

6.4.3 Discussion

This brief comparison has illustrated that the stringbed stiffness has reduced during the three week period between *Experiment 1* and *Experiment 2*. It is not clear whether this reduction is due to the racket being used in the impact tests or if it is simply due to the length of time between tests. It is likely to be a combination of both. For both scenarios, this reduction in stringbed stiffness can be assigned to a reduction in the tension in the strings. The tension loss with time, or stress relaxation, has been measured and discussed thoroughly by Cross (2000b) and therefore shall not be discussed in any depth here. In brief, the loss in tension occurs due to steady breaking of the bonds which connect the polymer molecules together. Cross (2000b) also measured the tension of a single string, before and after an impact with a hammer. During impact, clearly the tension will rise and it was then found that the tension measured after the impact was lower than that measured immediately prior to the impact. This mechanism would also contribute to the tension loss that is found between *Experiment 1* and *Experiment 2*.

This data illustrates that the stringbed stiffness can not be considered to be constant as it is a function of both time and the number of impacts that the racket is subjected to. Ideally, the rackets should be accurately restrung before each experiment. However, this is not always practical and therefore the stringbed stiffness must be measured as frequently as is possible. This allows the properties of the stringbed to be monitored, and highlights another use of a quasi-static compression test.

6.5 Summary

In this chapter, a load was applied at the geometric string centre of a head clamped racket using a rigid circular disc. This load was applied in a direction that was perpendicular to the string plane.

In the first section of this chapter, the magnitude of the applied force was measured along with the displacement of the load point. This experiment was performed using a range of disc sizes, and four identical rackets that were strung using a tension ranging from 40lbs to 70lbs. It was found that the stringbed on the racket that was strung at 70lbs was approximately 65% stiffer than the 40lbs racket. It was also found that the measured force was approximately 35% larger when the 65 mm diameter disc was used to apply the load, compared with when the 35mm diameter disc was used.

In the second section of this chapter, the shape of the deformed stringbed was obtained by measuring the displacement of a number of points along the longitudinal axis of the racket. In this experiment, the load was applied using a circular disc, as done in the first experiment. It was found that the normalised shape of the deformed stringbed was not a function of the magnitude of the force which was applied. It was not clear whether this shape was a function of the string tension. However, for a specific string tension, it was found that the shape of the deformed stringbed was dependent on the diameter of the disc.

This chapter has provided information regarding the stiffness of the stringbed, and the shape in which it deforms. This data will be a valuable resource in a later chapter, when a model of the stringbed is developed for an impact between a ball and racket.

7. Impact between a Ball and Head Clamped Racket

7.1 Introduction

This chapter is the second part of a trilogy which aims to develop a model for an impact between a ball and head clamped racket. In Chapter 6, the quasi-static stiffness of a stringbed was obtained. It was shown that this stiffness increases by approximately 65% for an increase in string tension from 40lbs to 70lbs. Analytical models (Cross 2000f) have illustrated the effect that the magnitude of the stiffness has on the contact time and ball rebound velocity. However, these studies have never been supported by experimental data that has confirmed that the parameters which are used in the models are realistic. In this chapter, experimental data is obtained for an impact between a ball and head clamped racket. In Chapter 8, a model for this impact will be developed and the data in this current chapter will be used to verify this model.

In this chapter, five parameters will be measured for an impact between a ball and head clamped racket. In this impact, the ball lands perpendicular to the plane of the stringbed. The parameters to be measured are as follows,

1. Ball rebound velocity.
2. Contact time.
3. Magnitude of ball deformation.
4. Magnitude of stringbed deformation.
5. Shape of deformed stringbed.

These parameters will be measured using a selection of ball types and string tensions which cover the typical range that is commonly used in the game of tennis.

7.2 Determining the magnitude of stringbed deformation for an impact between a ball and head clamped racket

7.2.1 Introduction

In the introduction to this chapter it was stated that both the magnitude and shape of the deformed stringbed need to be measured. There are two main methods which could be used to determine these parameters during impact which are,

1. Position transducer – attach a transducer to the strings and sample the output signal.
2. High speed cinematography – sample the string motion from still images of the impact.

One of the main problems with the first method is associated with the very short contact time for an impact between a ball and head clamped racket; a typical contact time is between 3 and 5ms (Groppel *et al.* 1987a). During this short time the stringbed will typically deform by approximately 20mm, which inherently results in large accelerations that need to be sampled. For this task to be achieved with a satisfactory accuracy, a low-inertia transducer which is sampled at a very high rate must be used which in many cases is impractical. This is certainly the case if several transducers

needed to be used to sample the shape of the deformed stringbed, as is one of the aims of this chapter. Therefore, it was concluded that a position transducer was not a suitable device to measure the stringbed displacement.

The main difficulty associated with using high speed cinematography is that the strings are not in the field of view when the camera is placed perpendicular to the plane of transverse string motion. However, Groppel *et al.* (1987a) used high speed cinematography to measure the stringbed displacement. The aim of that work was to determine the difference in magnitude of the stringbed displacement motion, for a variety of string tensions, for an impact between a ball and handle clamped racket. The impacts were recorded using a high speed video operating at 3500 frames per second. The optical axis of the camera was positioned at an angle of 8.7°, with respect to the stringbed plane, enabling the entire region of the string face to be viewed during impact. The stringbed deflection at the geometrical string centre was obtained using this method. The main weakness of this solution is associated with the potentially large error associated with this out-of-plane sampling technique.

An alternative high speed cinematography method involves attaching a light, rigid object to the stringbed which is supported in such a way that the motion of the object matches that of the stringbed. This object must be visible in the camera field-of-view. This idea was employed by Johnston (2001) who used hollow tubes of a carbon fibre composite which were defined as trackers. One end of these trackers was fixed to the stringbed and the other end was visible to the high speed camera. The tracker was suitably supported so that the motion of the stringbed was identical to that of the motion of the tip. Johnston used 15 trackers to sample the motion of the stringbed which added approximately 12g to the weight of the stringbed; a typical stringbed weighing approximately 20g. These trackers were attached at increments along the longitudinal axis of the racket. It was concluded that this method could be used to measure the shape and magnitude of the stringbed deformation. However, it was also found that the large additional mass (due to the trackers) acted to reduce the coefficient of restitution for the impact. Therefore, the measured stringbed deformation may not truly represent the motion of a stringbed which does not have 15 'trackers' attached to it.

It was concluded that the high speed cinematography method was the most suitable technique to use to measure the stringbed deformation during impact. It was also concluded that the use of trackers resulted in a more accurate experiment, as it did not involve an out-of-plane sampling method. In this current section, only one tracker was used as the shape of the deformed stringbed was not required at this stage. This experiment enabled the coefficient of restitution, contact time and ball/stringbed deformation to be measured. This tracker has a mass of 0.7g and was therefore assumed to have negligible effect on the impact mechanism.

7.2.2 Experiment Apparatus

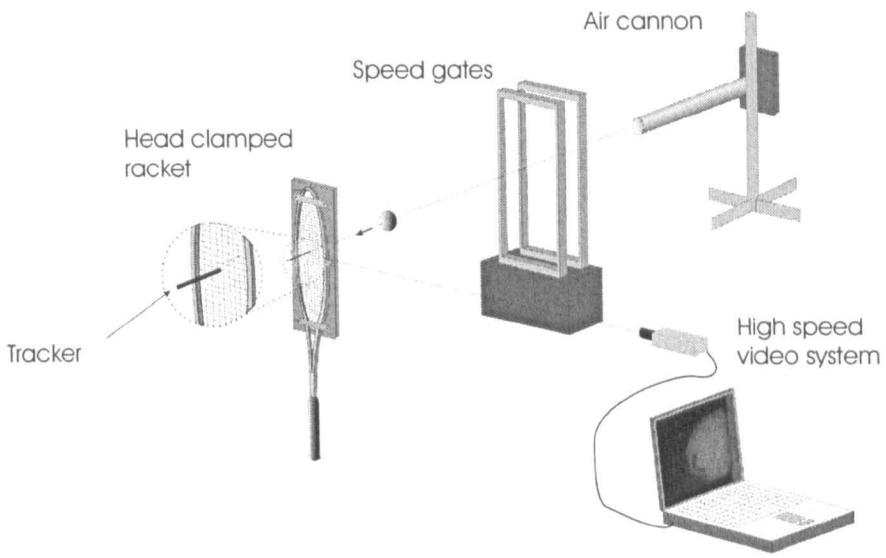

Figure 7.1 Illustration of experimental arrangement showing the tracker attached to the stringbed of a head clamped racket.

Figure 7.1 shows the experiment used to measure the magnitude of the stringbed deformation. The ball was propelled normal to the stringbed plane using an air cannon, identical to that described in Chapter 3. The inbound and rebound velocity of the ball were measured using speed gates. The head of the racket frame was clamped in a rigid structure, with its longitudinal axis vertical. The *Phantom v4* high speed video system was used to record the impact at a rate of 7100 frames per second, and a resolution of 256 x 128 pixels. The focal axis of the camera was aligned perpendicular to the motion of the ball, and therefore the stringbed was not visible.

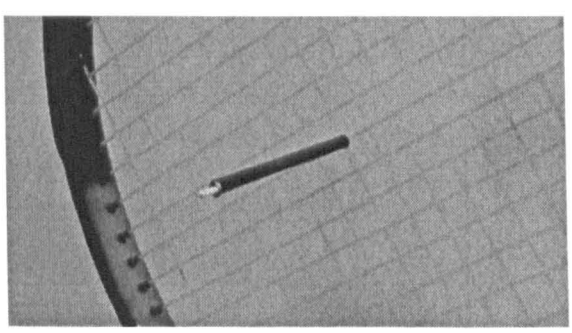

Figure 7.2 Photograph of the hollow carbon fibre 'tracker' which was firmly attached to the stringbed using a thin metal wire.

The tracker, as shown in Figure 7.2, was attached to the stringbed using a light thin wire which was secured at the other end using a metal crimp. The trackers were supported horizontally using a frame (not shown) to ensure that they only moved in a direction perpendicular to the stringbed. The total length of the tracker and crimp was ~70mm. The tip of the tracker was coated in a bright white paint to clearly identify this point.

Two different types of tennis ball were tested in this study; these were a standard *Pressurised* and *Pressureless* ball. These two balls are described in Chapter 4 and are representative of the majority of balls that are used in the game of tennis. The balls were propelled at the racket at a range of impact velocities between 20m/s and 40m/s. The racket used in this section was an *ITF*

Development carbon fibre composite racket with a head size of 630cm^2 (98in^2). This head size is typical of that used by many leisure and professional standard players (Racket Tech 2001). Two rackets were used which were strung at tensions of 40 and 70lbs, using a standard 15 gauge nylon string.

7.2.3 Analysis of high speed video images

(a) Procedure

The operation of the camera is described in detail in section 3.3. In brief, the images were downloaded from the camera in its native *Cine* file format, and converted into the *Microsoft AVI* format to allow the images to be imported into the *Vidimas v1* image analysis software. Typical images are shown in Figure 7.3. Figure 7.3 (a) shows the ball and trackers prior to impact; white paint which was applied to the tips of the trackers is clearly visible in these images. The point at which impact commences is difficult to define because the surface of the stringbed is not visible. This was overcome by recording a high speed video image of the ball resting on the surface of the stringbed, prior to the impact testing. This was used to obtain the x-coordinate of the point P_B at which the ball can be considered to be in contact with the stringbed.

Figure 7.3 (b) shows the deformed ball and tracker during impact. The position of the left edge of the ball P_B and the right edge of the tracker P_T were sampled. The sampled data was exported from *Vidimas v1* and stored in a *MS Excel* worksheet. These coordinates were converted into physical units using a calibration grid, as described in Chapter 3. The tracker was rigid and therefore it was assumed that the motion of the tracker was identical to the motion of the section of the stringbed which it was attached to. The coordinates were then processed to determine the magnitude of the ball and stringbed deformation. The magnitude of the ball deformation was obtained by subtracting the motion of the left edge of the ball with that of the tracker.

The ball impact velocity ranges from approximately 20m/s to 40m/s. The ball and stringbed deformations can easily be determined for the racket which was strung at 70lbs. However, when testing the racket which was strung at 40lbs only the stringbed deformation could be determined at the higher velocities. This was due to the left edge of the ball disappearing from view, during impact, and therefore could not be sampled.

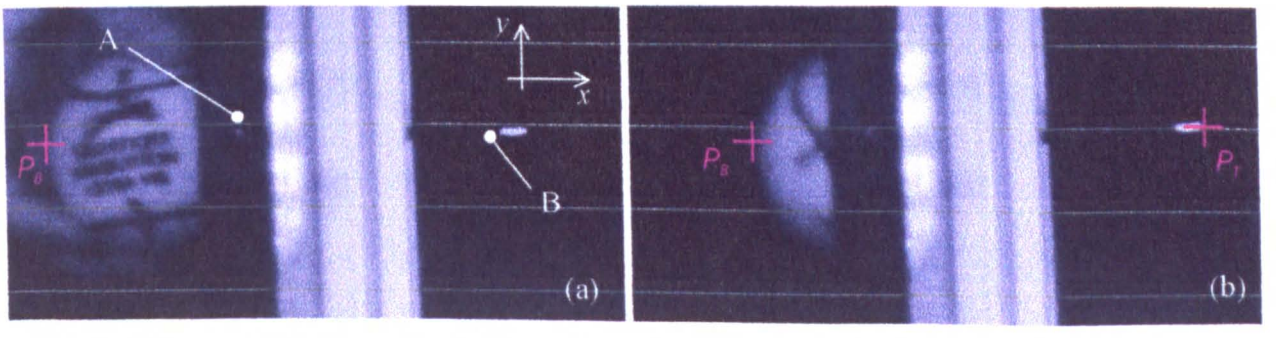

Figure 7.3 (a) Ball held on surface of the stringbed of a head-clamped racket (labelled A), showing the position of the tip of the tracker (labelled B) and (b) image of the ball impacting on the racket showing the two points that were sampled.

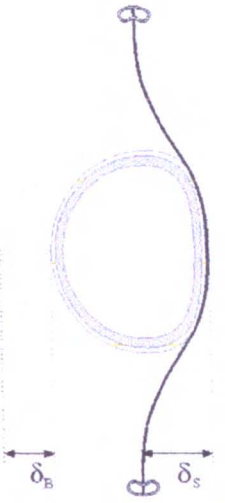

Figure 7.4 Illustration of the definition of the ball and stringbed deformation, δ_B and δ_S respectively.

(b) Comment on the accuracy of the measured coordinates

The *Vidimas v1* image analysis software has been specifically designed to provide an accurate method of sampling co-ordinates; the resolution of the sampled point is equal to one screen pixel. For the image size used in this experiment, this corresponds to a physical resolution of approximately 0.2mm. Therefore a first order approximation of the accuracy of this sampling method is 0.2mm. This is clearly an optimistic estimation of the real accuracy of the measured coordinates as it does not consider the error introduced by the manual point-selection method.

Each point that is being sampled does not always have a well defined edge and this reduces the possible accuracy of the analysis. A simple repeatability study was conducted to quantify the accuracy of the sampling method. In this study the points P_B and P_T, for the image shown in Figure 7.3(b), were each sampled 60 times. This data was used to calculate the mean values of the x co-ordinates for both points, as well as the uncertainty in this co-ordinate for each of the 60 samples. This analysis was repeated for a further four images which were randomly chosen, resulting in a data set of uncertainties that comprised of 300 samples. It was assumed that these uncertainties were normally distributed about the calculated mean x co-ordinate, for the relevant image.

It was found that the standard deviations for the x co-ordinate of points P_B and P_T were 0.9mm and 0.6mm respectively. This gives a good estimate of the realistic accuracy of the manual sampling method. It has been found that the accuracy is higher for the sampling of the x co-ordinate of point P_T, compared with the point P_B. This is due to the tracker tip having a more defined edge, compared with the edge of the ball, resulting in a more consistent sampling of point P_T compared with point P_B.

7.2.4 Results and discussion

In this experiment, a set of speed gates were used to measure the impact and rebound velocity of the ball. The ratio of these two terms is defined as the coefficient of restitution *COR*. Figure 7.5 shows the *COR* plotted against ball impact velocity, for an impact between a ball and head-clamped

racket. In general, *COR* decreases from approximately 0.85 to 0.75 over the ball impact velocity range of 20 to 40m/s. This data correlates qualitatively with that obtained by Johnston (2001) who performed a similar experiment using a racket strung at 60lbs. The coefficient of restitution data presented in Figure 7.5 is considerably higher than that obtained for an impact between a ball and rigid surface. The coefficient of restitution for such an impact ranges from 0.65 to 0.40, as discussed in section 4.4.2, for a similar velocity range as shown in Figure 7.5.

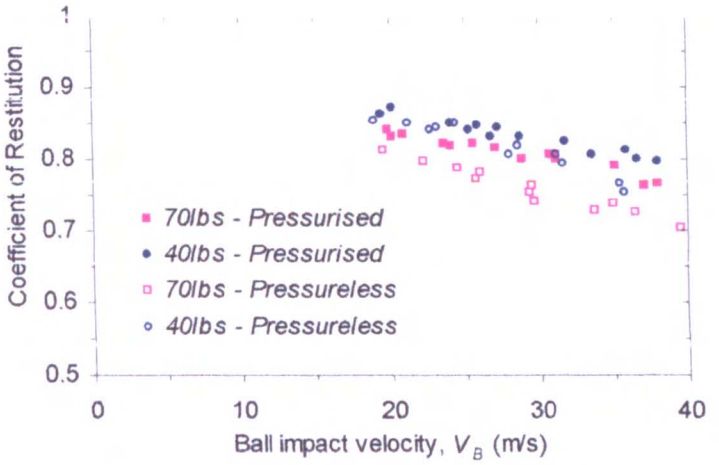

Figure 7.5 Comparison of coefficient of restitution and inbound velocity for four different combinations of string tension and ball type, for the impact between a ball and head-clamped racket.

For a specific string tension, Figure 7.5 shows that the *COR* is generally higher for the *Pressurised* ball, compared with the *Pressureless* ball. More specifically, it can be seen that this difference is most apparent for the impacts on a racket strung at 70lbs. For the racket strung at 40lbs, this difference is only evident for the higher speed impacts, whereas at low speeds the two ball types have identical values of *COR*.

For a specific ball type, the figure shows that the racket strung at 40lbs tension exhibits the higher values of coefficient of restitution. This correlates with anecdotal evidence that a reduction in string tension, increases the 'power' of the racket. Figure 7.5 shows that, for the *Pressurised* ball, the value of the coefficient of restitution is consistently 0.04 higher for the racket strung at 40lbs compared with the data for the 70lbs racket. This difference increases to approximately 0.07 for the impacts involving the *Pressureless* ball. These differences are of a similar order of magnitude measured by Taylor (2002), who also performed impacts using a head clamped racket.

In this experiment, the high speed video images were analysed and the data was processed to give the ball and stringbed deformation throughout impact; the definition of these two terms being illustrated in Figure 7.4. Figure 7.6 shows the ball and stringbed deformation for an impact between a ball and racket at 25m/s, for two different string tensions and ball types. Further comparisons are given in Figures C.1-C.2 for other impact velocities. Using these figures, along with Figure 7.6, it can be seen that the shape of the ball and stringbed *Deformation-Time* curves are consistent for all the impacts.

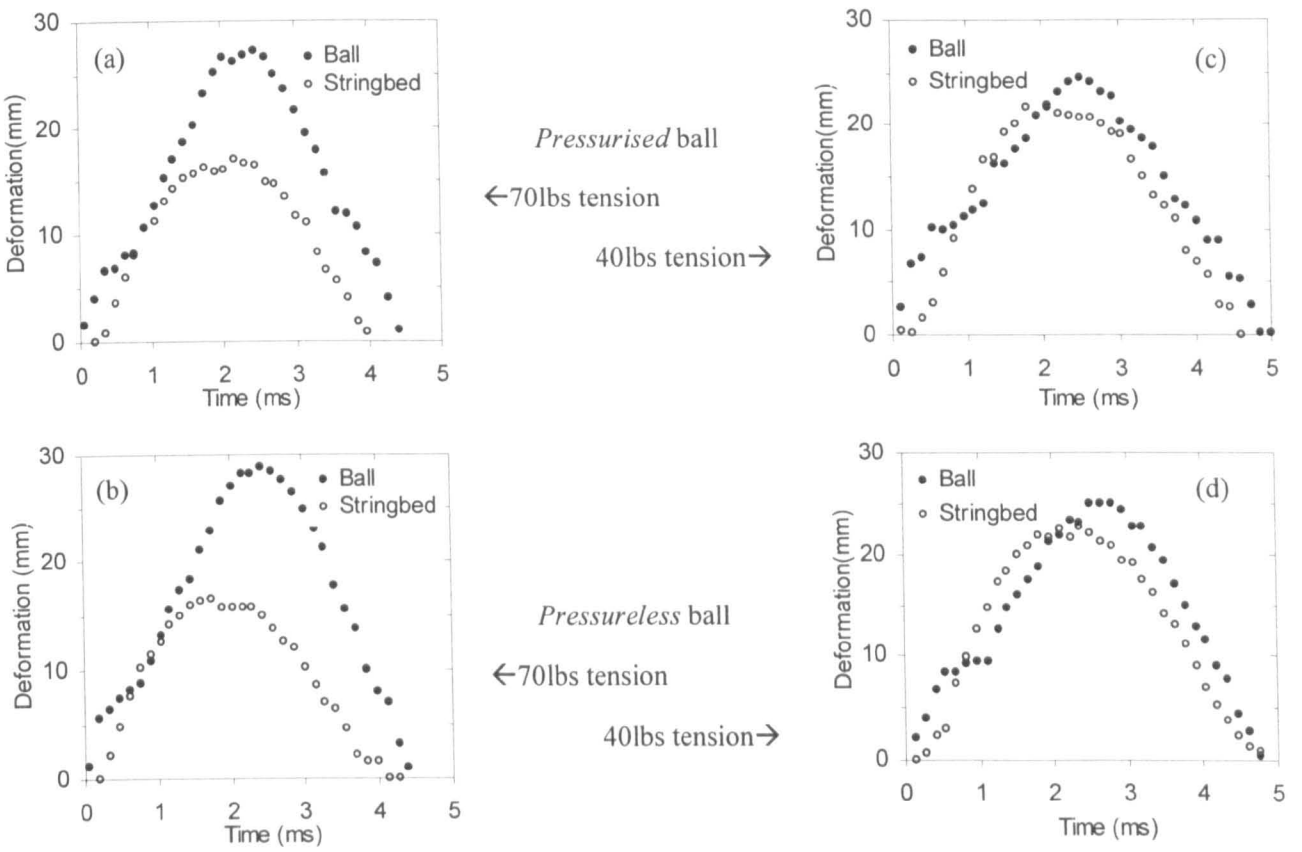

Figure 7.6 Ball and stringbed deformation for an impact between a ball and head-clamped racket, for four different combinations of string tension and ball type, at a nominal impact velocity of 25m/s.

Figure 7.6 shows that the ball compression initially increases rapidly, followed by a temporary reduction in the rate, before continuing to increase at an approximately constant rate. The stringbed does not begin to deform until approximately 0.2ms after initial contact. This is likely to be due the inertia of the tracker and stringbed. It will also be due to the low stiffness of the cloth which will result in a relatively low force acting during the initial stage of impact, as discussed in section 4.4 for an impact on a rigid surface. Figure 7.6 (and Figures C.1-C.2) shows that the maximum deformation of the ball occurs after the point of maximum stringbed deformation. These figures also show that the ball is still compressed even when the stringbed deformation returns to zero.

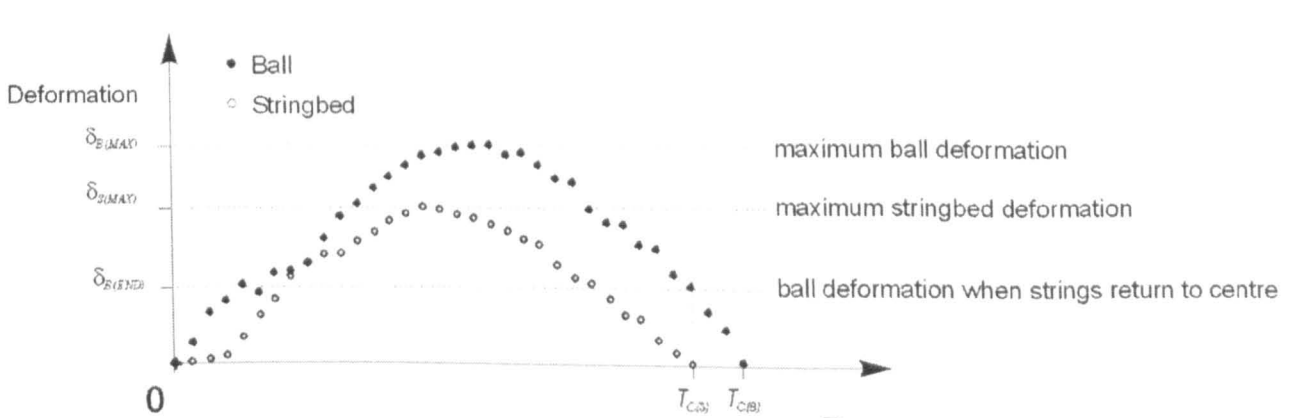

Figure 7.7 Definitions of the measured terms obtained from the force-deformation plots.

Figure 7.7 shows a schematic illustration of the data that is shown in Figure 7.6. Since all the curves shown in Figure 7.6 have a similar shape, the main features can all be defined by the maximum deformation and the time at which the deformation returns to zero. These parameters are defined for both the stringbed and ball deformations in Figure 7.7. The maximum ball and stringbed deformations during impact are defined as $\delta_{B(MAX)}$ and $\delta_{S(MAX)}$ respectively. In Chapter 4, the contact time for an impact between a ball and rigid surface was defined as the time, after initial impact, at which the ball deformation returned to zero. In this current experiment, this contact time is defined as $T_{C(B)}$ as illustrated in Figure 7.7. A further definition of the contact time can be defined as the time taken for the stringbed deformation to return to zero, and this parameter is defined as $T_{C(S)}$. At this time, the ball is still deformed and the magnitude of this deformation has been defined as $\delta_{B(END)}$.

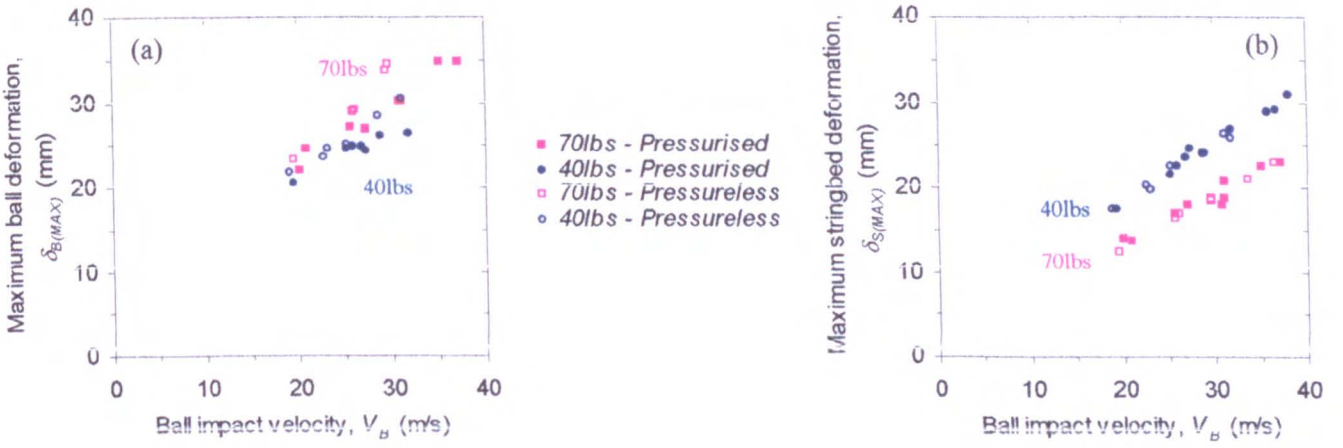

Figure 7.8 (a) Maximum ball deformation and (b) maximum stringbed deformation, plotted against ball impact velocity, for an impact between a ball and head clamped racket.

Figure 7.8 (a) shows the maximum ball deformation $\delta_{B(MAX)}$ during impact plotted against the ball impact velocity. Although the tests were conducted for impact velocities ranging between 20 and 40m/s, it was not always possible to determine the ball deformation at the highest velocities. This was because the left edge of the ball disappeared from view during impact so could not be sampled.

The values of $\delta_{B(MAX)}$ typically vary between 20 and 35mm for the velocity range of 20 to 35m/s. In section 4.4.2, it was shown that the ball deformation increased from 25 to 40mm for a similar velocity range, for an impact on a rigid surface. The maximum ball deformation $\delta_{B(MAX)}$ is generally larger for impacts involving the *Pressureless* ball compared with the *Pressurised* ball. This correlates with the data that has been discussed in Chapters 4 and 5. In these chapters it was shown that a *Pressurised* ball is stiffer than a *Pressureless* ball, for deformations of the same order of magnitude as measured here. Figure 7.8 (a) shows that, for a specific ball type, the ball deforms more for an impact on a racket strung at 70lbs, than a racket strung at 40lbs.

Figure 7.8 (b) shows the maximum stringbed deformation $\delta_{S(MAX)}$ plotted against the ball impact velocity. This figure shows a clear difference between the results for the two string tensions, but no significant difference between the two ball types. It shows that the value of $\delta_{S(MAX)}$ for the racket strung at 40lbs tension is approximately 25% higher than that of the racket strung at 70lbs. This

correlates with the data in Chapter 6 which confirmed that a lower string tension resulted in a lower stringbed stiffness. Comparing Figure 7.8(a) and (b) reveals that, in general, the stringbed does not physically deform as much as the ball during impact.

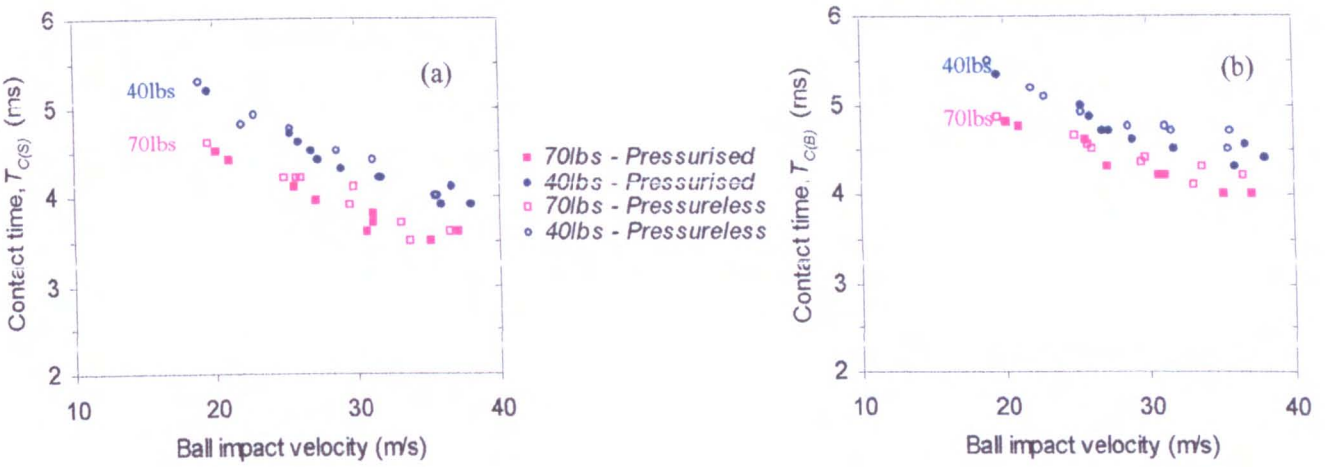

Figure 7.9 The relationship between contact time and ball impact velocity, for two different definitions of contact time. (a) $T_{C(S)}$, which is the time taken for the stringbed to return to its original position, and (b) $T_{C(B)}$, which is the time taken for the ball deformation to return to zero.

Figure 7.7 illustrates the two different parameters which are used to define the contact time; these being $T_{C(S)}$ (time taken for stringbed to return to centre) and $T_{C(B)}$ (time taken for ball deformation to return to zero). Figure 7.9 illustrates the relationship between these two parameters and the impact velocity for the four combinations of ball type and string tension. Figure 7.9(a) shows that the contact time $T_{C(S)}$ is longer for impacts on the racket strung at 40lbs, compared to that strung at 70lbs; this difference being approximately 0.7ms. There is no significant difference in the value of $T_{C(S)}$ for the two ball types, for either string tension. The contact time reduces from 4.4ms to 3.5ms over a velocity range from 20 to 40m/s, for the 70lbs string tension. The contact time parameter $T_{C(S)}$ appears to be a function of the string tension, and not dependent on the ball type.

An alternative description of the contact time is defined as the time taken for the ball deformation to return to zero. This contact time is defined as $T_{C(B)}$ and the results for this parameter are illustrated in Figure 7.9 (b). For impacts on the racket strung at 40lbs tension, there is no significant difference in the value of $T_{C(B)}$ for the two ball types. However, for the impacts on the racket which was strung at 70lbs tension the value of $T_{C(B)}$ is shorter for the *Pressurised* ball, compared to the *Pressureless* ball. This correlates with the data obtained for impacts on a rigid surface, and is likely to be due to the lower stiffness of the *Pressureless* ball compared with that of the *Pressurised* ball.

Figure 7.9(b) shows that the contact time $T_{C(B)}$ is longer for impacts on the racket strung at 40lbs tension. However, the distinction between the values of $T_{C(B)}$ for the two string tensions is not as clear as that which is found in Figure 7.9(a) for the parameter $T_{C(S)}$. This implies that the value of $T_{C(B)}$ is a function of both the ball type and string tension.

Figure 7.9(b) shows that the value of $T_{C(B)}$ reduces from 5.3ms to 4.1ms over the velocity range used in this experiment, for a string tension of 40lbs. This compares to a value of the other

definition of contact time $T_{C(S)}$ reducing from 5.1ms to 3.8ms, for the same velocity range. A similar comparison for the racket strung at 70lbs tension shows that the value of $T_{C(B)}$ ranges from 4.7ms to 3.8ms, whereas the value of $T_{C(S)}$ reduces from 4.3ms to 3.4ms. These comparisons show that the value of $T_{C(B)}$ is generally between 0.2ms and 0.4ms larger than the value of $T_{C(S)}$. This data compares with contact times of between 3.8ms and 3.0ms for an impact between a ball and rigid surface, for a similar velocity range, as discussed in section 4.4.3. In that section, it was shown that a *Pressureless* ball exhibits a longer contact time compared to a *Pressurised* ball (for an impact on a rigid surface). This difference was approximately 0.2ms, which is the same order as the scatter of the data in Figure 7.9(a).

It has been shown above that the time taken for the ball to return to its original shape ($T_{C(B)}$) is longer than that for the stringbed to return to its original position ($T_{C(S)}$). One consequence of this is that the ball is still deformed when the stringbed deformation is zero. The magnitude of this ball deformation, when the stringbed returns to centre, is defined as $\delta_{B(END)}$ and is illustrated in Figure 7.7. Figure 7.10 shows the relationship between the ball impact velocity and the end ball deformation $\delta_{B(END)}$ for all the ball type and string tension combinations. This figure shows that the value of the ball deformation is consistently larger, when the stringbed returns to centre, for the racket strung at 70lbs tension compared with that strung at 40lbs tension, for all ball impact velocities. It also shows that the *Pressureless* ball generally has a higher value of $\delta_{B(end)}$ compared to the *Pressurised* ball, especially at higher ball impact velocities. This is probably due to the *Pressureless* ball being less stiff and will take longer to reform, compared to the *Pressurised* ball.

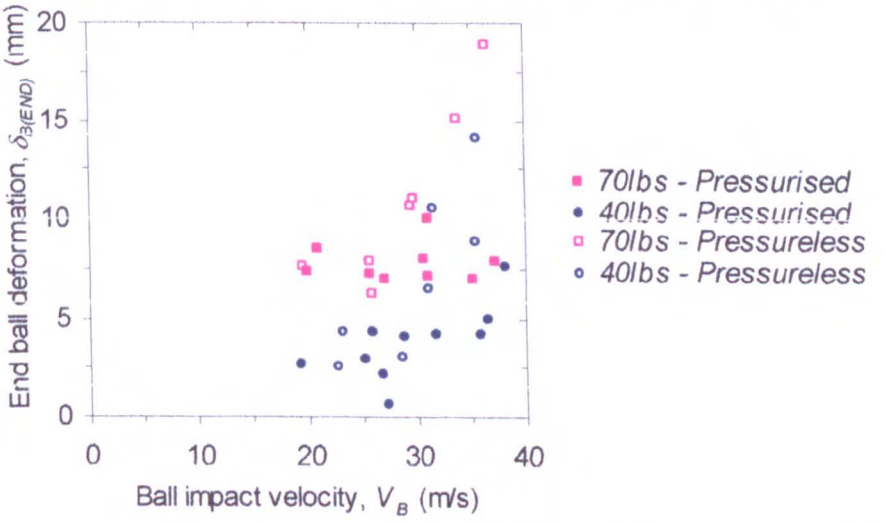

Figure 7.10 Comparison of the ball impact velocity and the ball deformation at time $T_{C(S)}$ i.e. when the stringbed deformation to centre.

7.2.5 Estimating the ball centre-of-mass displacement from ball deformation data

In the previous section the deformation of the ball, during impact, was measured experimentally and presented for a range of ball impact velocities. In a later chapter, a visco-elastic model of the impact will be developed. This type of model is used to calculate the motion of the ball centre-of-mass and therefore it would be useful to compare those model results with experimental data for this displacement. For an impact with a force platform, the ball COM displacement was obtained

directly. However, the motion of the ball COM can not be obtained directly for an impact with a head-clamped racket.

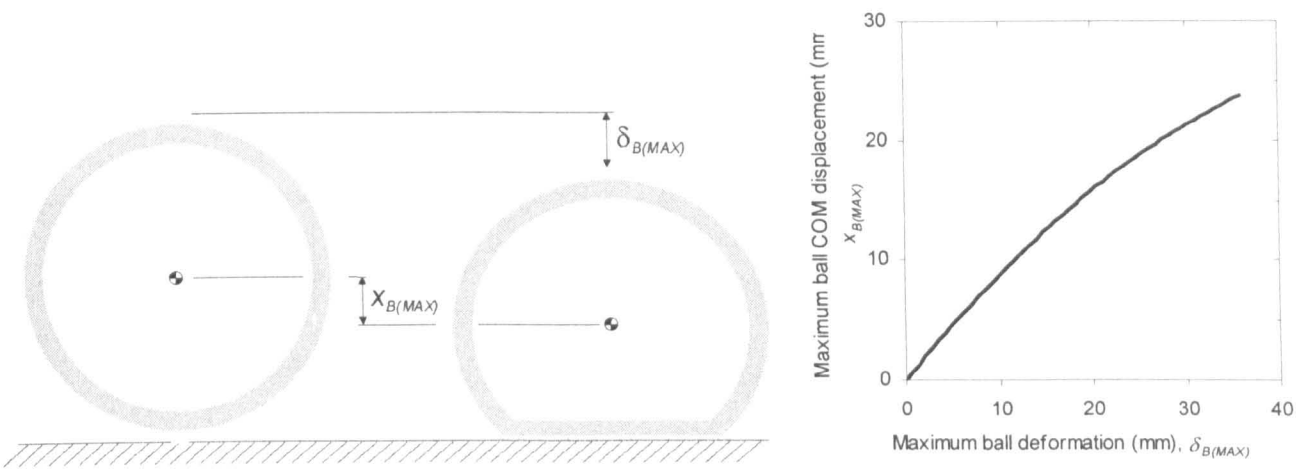

Figure 7.11 Empirical relationship between maximum ball deformation and ball centre-of-mass displacement, for a normal impact between a ball and rigid surface.

In Chapter 4 an empirical relationship was found between the maximum ball deformation and maximum ball COM displacement, for an impact on a flat surface, and this is shown in Figure 7.11. It is appreciated that the form of a deformed ball may be different for an impact on a head clamped racket, compared with that for a rigid surface. However, it is assumed that this relationship shown in Figure 7.11 is a valid first order approximation for an impact on a stringbed. The function which describes the curve in Figure 7.11 (converted to SI units) is,

$$x_{B(MAX)} = -8.184(\delta_{B(MAX)})^2 + 0.954270\delta_{B(MAX)} \qquad [7.1]$$

where $x_{B(MAX)}$ is the calculated maximum ball COM displacement, and $\delta_{B(MAX)}$ is the measured maximum ball deformation.

The relationship defined by [7.1] is only strictly valid for the point of maximum ball deformation. However, it is assumed that it is valid for all stages of the impact and therefore it can be used to convert the ball deformation δ_B values (from the previous section) into ball centre-of-mass displacement x_B values. Therefore, equation [7.1] can be modified to describe the general relationship,

$$x_B - x_S = -8.184(\delta_B)^2 + 0.954270\delta_B \qquad [7.2]$$

where $(x_B - x_S)$ is the ball COM displacement with respect to the stringbed displacement x_S.

Equation [7.2] can be used to translate the *Ball Deformation-Time* plots, such as those in Figure 7.6 into *Ball COM Displacement-Time* plots. Typical plots are given in Figure 7.12, which also shows the magnitude of the stringbed displacement. It should be noted that the stringbed displacement is identical to the stringbed deformation which was discussed in the previous section. Figure 7.12 shows that the ball centre-of-mass displacement is generally higher than the stringbed displacement for a string tension of 70lbs, but lower for a string tension of 40lbs. This figure illustrates the findings for an impact velocity of 25m/s. Further data is given in Appendix C.3, for other impact velocities.

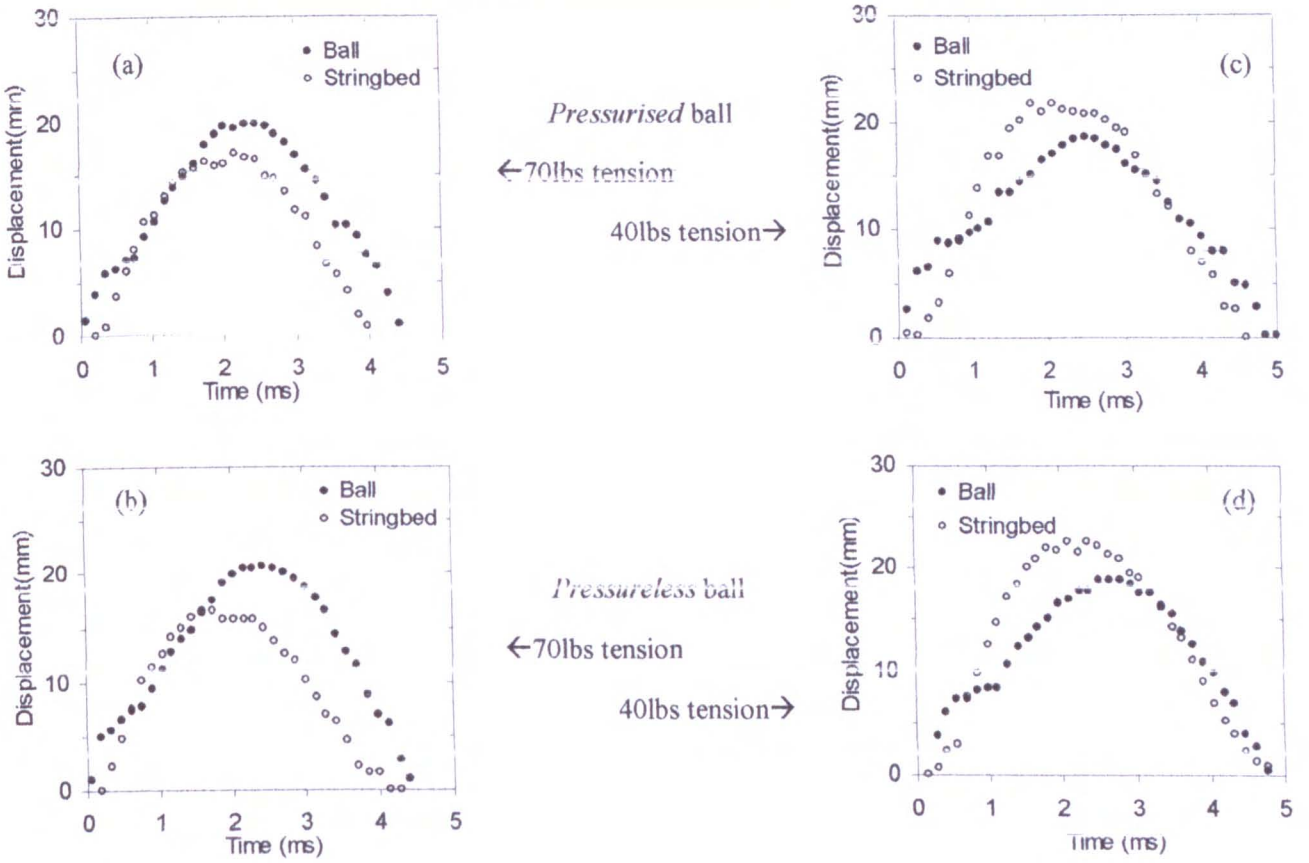

Figure 7.12 Ball centre-of-mass displacement and stringbed displacement for an impact between a ball and head-clamped racket, for four different combinations of string tension and ball type. The ball impact velocity is 25m/s.

The data collected in this section can be used to determine the maximum ball COM displacement, for the full range of ball impact velocities, and this data is given in Figure 7.13. In Figure 7.8, it was shown that the maximum stringbed displacement was a function of the string tension (and ball impact velocity). This stringbed data, for the two string tensions, is superimposed on the plot in Figure 7.13 for comparative purposes.

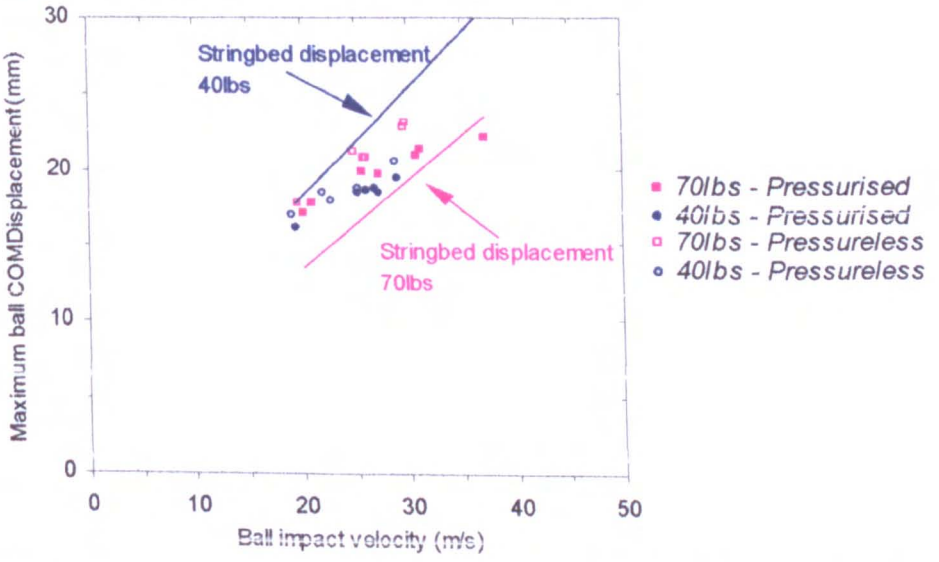

Figure 7.13 Calculated maximum ball centre-of-mass displacement plotted against the ball impact velocity. Values of the measured maximum stringbed displacement are superimposed on this plot.

A comparison of the data in Figure 7.13 reveals that the ball centre-of-mass displaces by approximately the same amount as the stringbed which is strung at 40lbs, for low impact velocities. At higher impact speeds, the ball COM displaces by approximately the same amount as the stringbed with a tension of 70lbs. This implies that the ball has a similar stiffness to the stringbed which is strung at 40lbs, for low speed impacts which result in maximum ball COM displacements of approximately 18mm. The stiffness seemingly then increases to that which is comparable to the stringbed that is strung at 70lbs, for the higher speed impacts.

7.2.6 Conclusions

In this section, a ball was propelled towards a head clamped racket with the ball impacting perpendicular to the string plane. Two different ball types were tested, and the racket was strung at two different string tensions. It was shown that the coefficient of restitution for the impact was highest for the racket strung at 40lbs, compared with that strung at 70lbs. This difference was larger for the *Pressureless* ball compared with the *Pressurised* ball. The *Pressurised* ball generally rebounded faster than the *Pressureless* ball. However, at low impact speeds the difference between the two balls is considerably smaller than at the higher speeds.

It has been shown that the maximum ball deformation is greater for the *Pressureless* ball, compared to the *Pressurised* ball, for the higher string tension. At the lower tension, there is no significant differences between the two ball types. It was also shown that the maximum deformation of the stringbed during impact is a function of the string tension, but not the ball type.

It was consistently found that the contact time reduces with impact velocity, and is longer for the racket strung at 40lbs. The magnitude of the contact time for the impact is dependent on the definition used for this parameter. If it is assumed to be the time taken for the stringbed deformation to return to zero, then the contact time is a function of the string tension and not the ball type. An alternative definition of the contact time corresponds to the time taken for the ball deformation to return to zero. The results show that this parameter is a function of both string tension and ball type.

For interest, the data presented here for an impact on a head clamped racket was compared with that for an impact on a rigid surface. It has been shown that the coefficient of restitution is typically between 0.85 and 0.75 for an impact on a head clamped racket. For an impact on a rigid surface the coefficient of restitution is much lower and typically equals a value between 0.65 and 0.40. For the impacts studied here, the maximum deformation of the ball was between 20 and 35mm, for an impact on a racket. In section 4.4 it was shown that the ball deformation, for an impact on a rigid surface, increased from 25 to 40mm, for a similar impact velocity range. In this current section it was shown that the time taken for the ball to reform to its original shape $T_{C(B)}$ was between 5.5 and 4.0ms, for impacts on a head clamped racket. By comparison, the contact time for an impact on a rigid surface has been measured as between 3.9 and 3.0ms, for a similar range of impact velocities.

7.3 Determining the shape of a deformed stringbed for an impact between a ball and racket

7.3.1 Introduction

In section 6.2, the stringbed stiffness was measured for a quasi-static compression test in which the load was applied perpendicular to the string plane. In section 6.3, the shape of the deformed stringbed was also measured, for a similar quasi-static loading. It was found that the stringbed stiffness and the shape of the deformed stringbed were both dependent on the diameter of the circular disc which was used to apply the load. This data could effectively be used to find the relationship between these two measured variables; the shape of the deformed stringbed and the stiffness.

When a ball impacts on a tennis racket, it deforms considerably and the area over which the force is applied to the stringbed varies throughout impact. Therefore it can be concluded that the stringbed stiffness will also vary during this period. It has been stated that a visco-elastic model of the ball impacting on the stringbed will be developed in a later chapter. This model must be able to predict the magnitude of the stringbed stiffness throughout impact. It would be very difficult to measure the effective contact area of the ball on the stringbed because the stringbed surface is not visible during impact. However, it would be possible to measure the shape of the deformed stringbed using a similar method as that described in section 7.2. In this current section, the shape of the deformed stringbed will be measured for an impact between a ball and racket. The data will then be compared with the shape obtained for a quasi-static deformation.

7.3.2 Experiment Apparatus

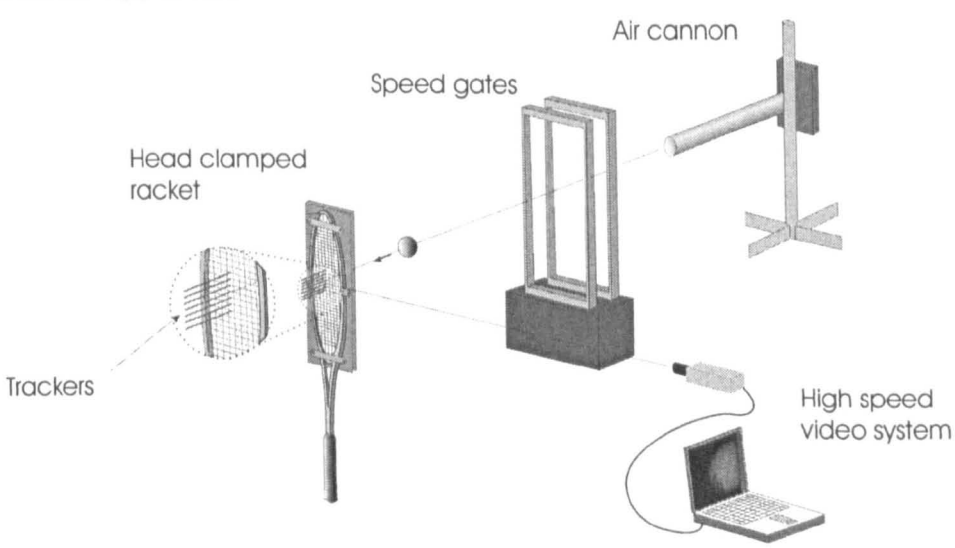

Figure 7.14 Illustration of experiment arrangement showing the eight trackers attached to the stringbed of the head clamped racket.

Figure 7.14 shows the experimental apparatus which was used to measure the shape of the stringbed deformation. This is a similar arrangement as that described in section 7.2.2 except that eight trackers are attached to the longitudinal axis of the racket; four either side of the geometric

string centre (GSC). The spacing of the trackers was approximately 11mm which meant that the stringbed deformation was being measured over a length of ~77mm, along the longitudinal axis.

The total mass of the trackers was 5.6g, which compares with a total string mass of approximately 20g. The same rackets are used in this section as were used in section 7.2. A *Pressurised* ball was propelled at these rackets at impact velocities ranging between 15m/s and 30m/s.

7.3.3 Analysis of high speed video images

A typical high speed image is shown in Figure 7.15. The position of the left edge of the ball (P_B) and the right edge of each of the eight trackers (P_{T1} to P_{T8}) were sampled. The trackers were rigid and therefore it was assumed that the motion of the trackers was identical to the motion of the section of the stringbed which they were attached to. The coordinates were then processed to determine the shape of the stringbed deformation.

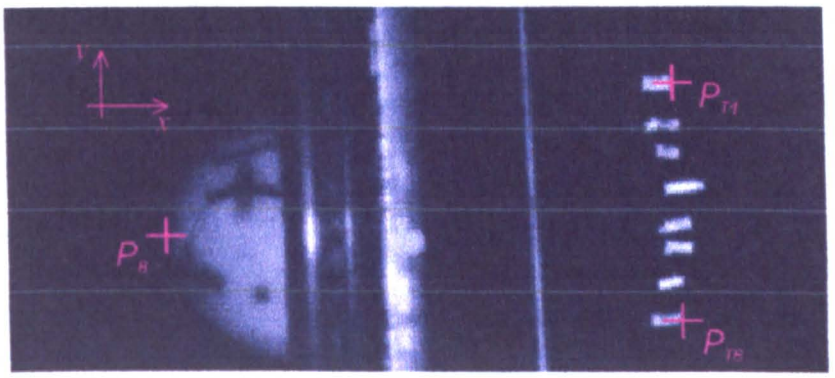

Figure 7.15 High speed video image of the ball impacting on the head-clamped racket, showing the positions of three of the nine points on the image which were sampled during impact.

7.3.4 Results and Discussion

The impact was recorded using the high speed video system which operated at a rate of 4000 frames per second giving a time step Δt between images equal to 0.25ms. This recording rate resulted in approximately 20 frames being recorded that showed the ball in contact with the stringbed. During impact, the displacement of each tracker was measured. The ball was nominally aimed at the geometric string centre of the racket, i.e. at a point mid-way between trackers 4 and 5. However, the actual impact position was generally up to 20mm either side of the intended position. To accommodate for this, all stringbed positions are referenced to the impact point.

Figure 7.16 (a)-(f) illustrate the deformed shape of the stringbed during impact, for a range of time intervals. The data shown here was obtained for impacts on the racket that was strung using a tension of 70lbs. Figure 7.16(a) shows the measured data points which were used to generate the curves; each data point corresponding to the displacement of one of the trackers. For clarity, the data is plotted separately for the compression and restitution phases. Data was collected for several impact velocities but is only plotted here for three impact velocities; these results being typical of the data collected.

Figure 7.16 shows that the stringbed displacement increases for the first 2.0ms-2.5ms of the impact; the maximum displacement increasing with impact velocity. This maximum displacement consistently occurs at the impact point. During restitution, the curves have a similar shape to those determined for the compression phase. At the mid-point of the impact, the displacement of the stringbed at the impact point is approximately 25% larger than that at a point only 40mm away, along the longitudinal axis. However, there is considerable scatter in this magnitude. Impact tests were also conducted on a head clamped racket that was strung at 40lbs tension. The results for this experiment exhibit similar trends as those shown in Figure 7.16. Therefore this data is not presented here and can be found in Appendix C.4.

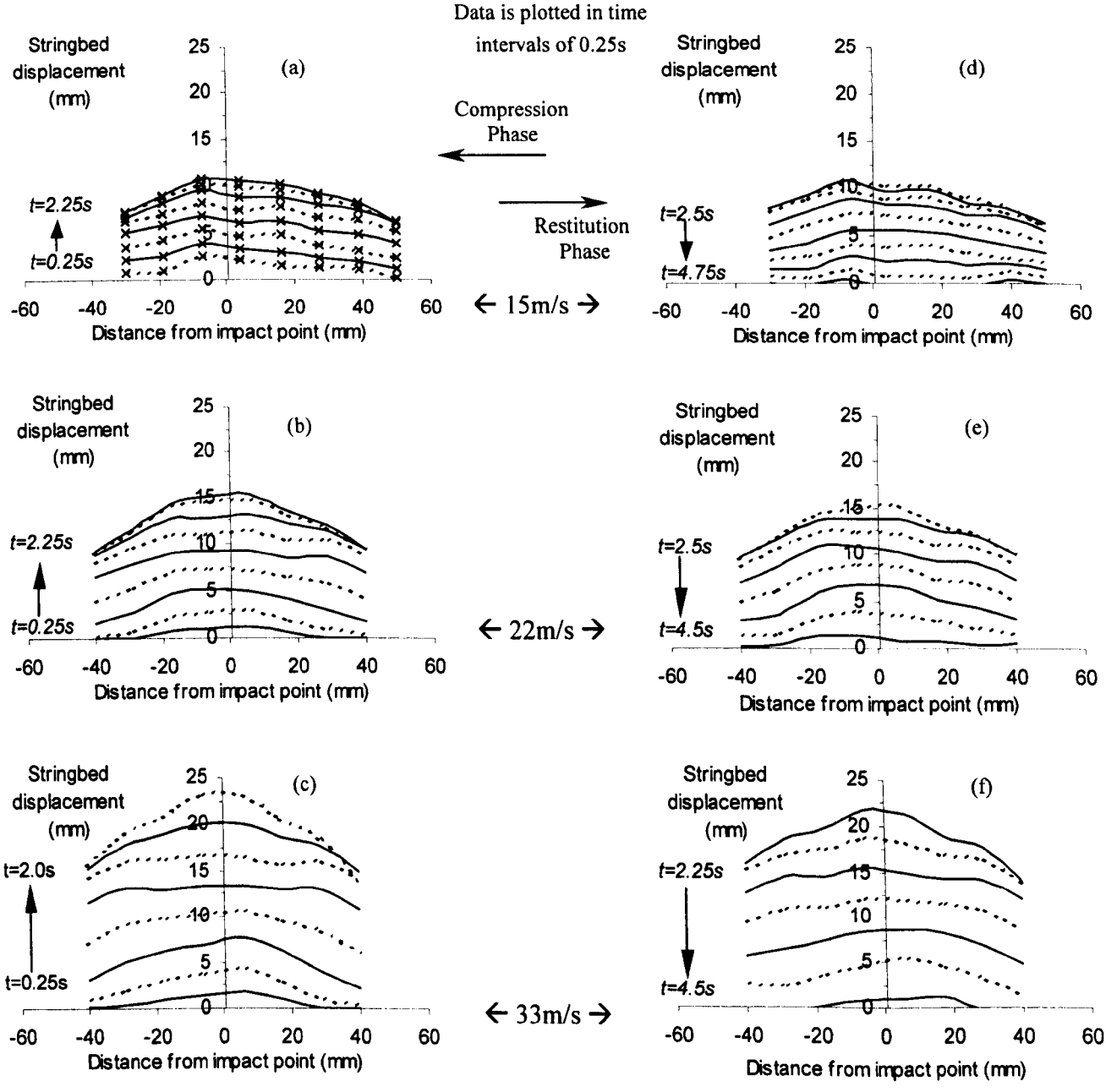

Figure 7.16 Stringbed displacement plotted as a function of the position along the longitudinal axis of a racket (70lbs tension). The data is shown for three different impact velocities and presented individually for the, (a)-(c) compression phase and (d)-(f) restitution phase.

The data in Figure 7.16 (and Figure C.5) gives a good indication of the motion of the stringbed during impact but does not give a clear indication of the shape of the stringbed, which was the main aim of this section. A technique used in section 6.3 to determine the general shape of the deformation involved normalising the results, with respect to the stringbed displacement at the load point. A similar, normalising analysis was conducted in this section which involved normalising the results with respect to the stringbed displacement at the impact point. This stringbed displacement is termed $\delta_{S(IP)}$ and is defined schematically in Figure 7.17. The normalised stringbed displacement is defined as the ratio of the actual stringbed displacement and the value of $\delta_{S(IP)}$ at that time increment. Normalising the data does not give a perfect physical representation of the shape of the deformed stringbed. This is because the actual shape is dependent on the absolute magnitude of the deformation at each point on the stringbed, and not just the relative magnitude. However, it can be used as a valid method of comparing the data in this section with the normalised data obtained for a quasi-static compression.

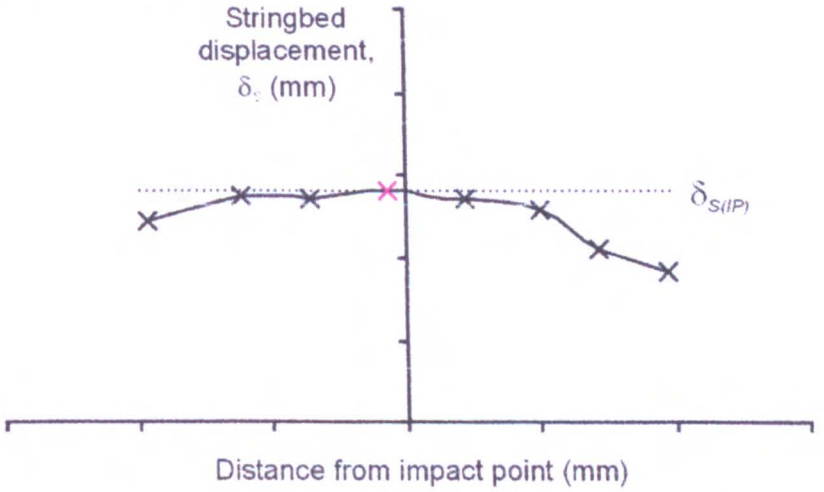

Figure 7.17 Definition of $\delta_{S(IP)}$ which is the displacement of the tracker that is closest to the impact point.

The normalised stringbed displacements for an impact between a ball and head-clamped racket are presented in Figure 7.18, for ball impact velocities between 15 and 30m/s. This normalised data has been categorised by the value of the stringbed displacement $\delta_{S(IP)}$ because it is assumed that the shape of the deformed stringbed will be a function of the magnitude of $\delta_{S(IP)}$. In Figure 7.18 the normalised data is presented separately for the two different string tensions.

Figure 7.18 (a) & (d) show the normalised results for the 70lbs and 40lbs string tension, respectively, for stringbed displacements $\delta_{S(IP)}$ of less than 5mm. These figures show that, for these small stringbed displacements, there is a considerable amount of scatter in the normalised data. However, it was assumed that the data could be approximated using a 2nd order polynomial trend line which was plotted through the data using the *least squares regression* method. It was assumed that the uncertainty in the data was equal for all positions along the longitudinal axis of the string bed. Therefore the level of scatter in the data can be quantified by calculating the standard deviation of the data, from the trend line, using the method described in Appendix A. The standard deviations of the data shown in Figure 7.18 (a) & (d) are 0.35 and 0.40 respectively. Figure 7.18

(b) & (e) show the normalised results for the 70lbs and 40lbs string tension respectively, for stringbed displacements of between 5mm and 10mm. In these figures the magnitude of scatter in the results is lower than in Figure 7.18 (a) & (d) which is confirmed by the calculated standard deviation values of 0.12 and 0.13, for Figure 7.18 (b) & (e) respectively. Figure 7.18 (c) & (f) show the normalised results for the 70lbs and 40lbs string tension for stringbed displacements of more than 10mm. These figures show that the magnitude of the scatter in the results is considerably lower than for the other values of $\delta_{S(IP)}$, with standard deviations of 0.07 and 0.06 for Figure 7.18 (c) & (f) respectively.

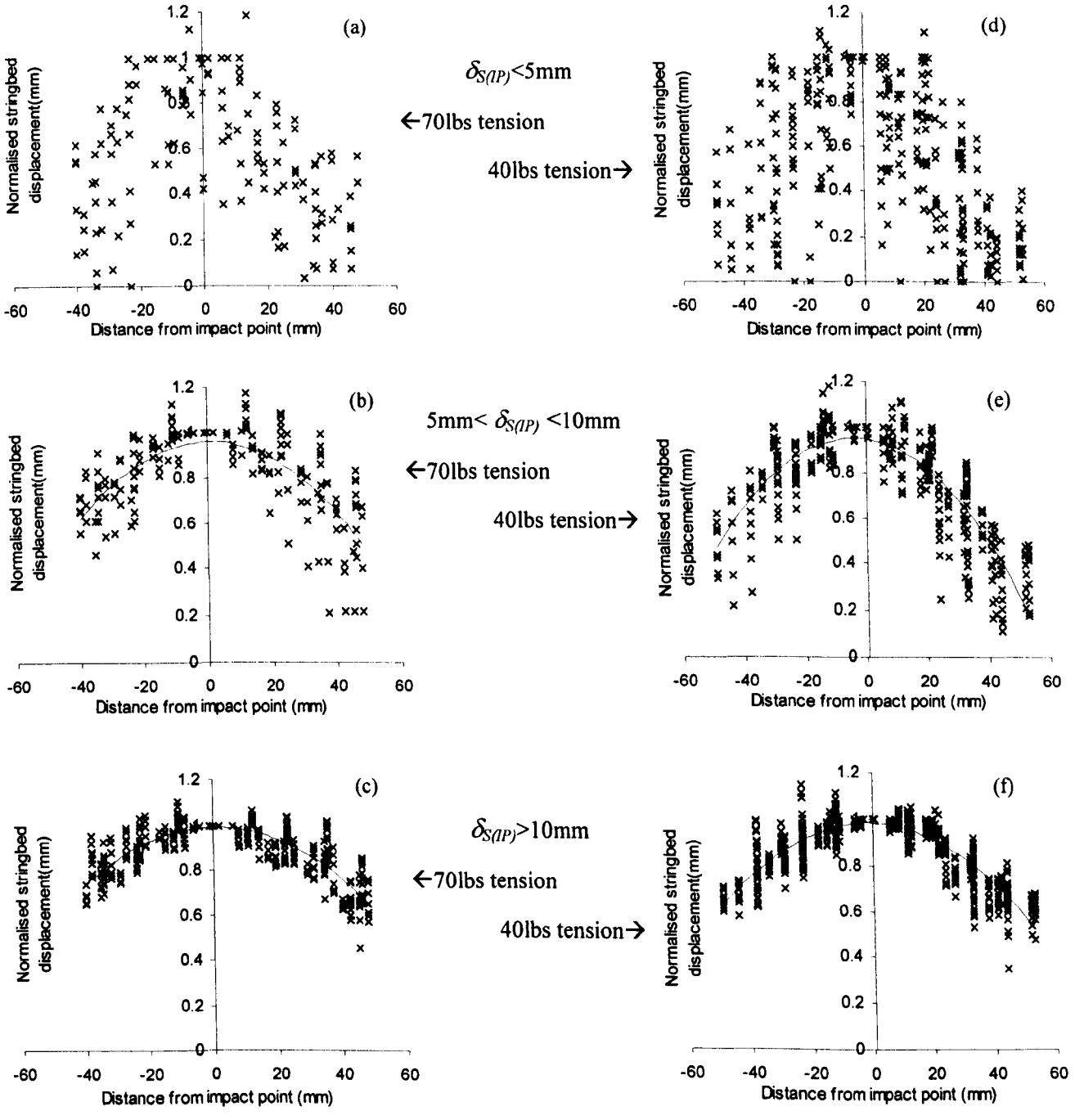

Figure 7.18 Relationship between normalised stringbed displacement and position along the longitudinal axis of the racket for an impact between a ball and head clamped racket. The data is presented for two rackets with different string tensions. The results have been categorised into three datasets, depending on the value of the stringbed displacement at the impact point $\delta_{S(IP)}$.

The trend lines plotted in Figure 7.18 give an indication of the shape of the deformed stringbed. The calculated value of the standard deviation, for this trend line, quantifies the level of confidence in using the trend line to estimate the measured data. In this study it has been found that the magnitude of the standard deviation is relatively high, especially for $\delta_{S(IP)} < 5mm$, and therefore it is difficult to make any definite conclusions regarding the shape of the stringbed. Any conclusions which are made about this shape are subject to an error with a magnitude similar to that of the calculated value of the standard deviation.

For stringbed displacement values $\delta_{S(IP)}$ of between 5mm and 10mm (Figure 7.18 (b) & (e)) the trend lines show that the normalised displacement of the stringbed which is 40mm from the impact point is approximately 60% of $\delta_{S(IP)}$. For values of $\delta_{S(IP)}$ which are greater than 10mm (Figure 7.18 (c) & (f)), the trend lines show that the normalised displacement at this same point is approximately 70% of $\delta_{S(impact)}$. This is implying that an increase in the value of $\delta_{S(IP)}$ results in the normalised shape of the deformed stringbed becoming relatively 'flatter'. However, it should be remembered that there is considerable scatter in the data.

The calculated values of standard deviation give a good indication of the level of confidence in the data. However, in calculating these values of standard deviation it has been assumed that the level of uncertainty is equal for all of the normalised data. A consideration of the source of this uncertainty can be used to assess the validity of this assumption. The scatter in the measured data is probably due to inaccuracies in the manual sampling method. This would lead to an absolute error which has a length dimension, for example 1 mm. When the measured data is normalised, the magnitude of this error will no longer be equal for all stringbed displacements. Therefore the standard deviations that have been calculated can only be considered to be mean estimates of the confidence level in the data.

7.3.5 Comment on errors caused by adding weight to the stringbed

The eight trackers which are attached to the stringbed have a total mass of 5.6g, compared to a string mass of approximately 20g. This is clearly a relatively significant addition of mass to the stringbed and therefore its influence should not be neglected. Johnston (2001) used a similar method to determine the deformation of a stringbed and found that the trackers caused a significant decrease in the coefficient of restitution for the impact. Johnson used fifteen trackers, which had a total mass of over 10g, and found that the coefficient of restitution for an impact between a ball and head clamped racket was reduced by 5% when these markers were attached. Johnson compared the maximum stringbed displacement when measured with only one marker attached, and compared it with that obtained when 15 markers were attached. It was concluded that the stringbed displacement was 2% larger when the 15 markers were attached, compared to the value measured using the single marker. This data suggests that the use of trackers does effect the impact, but this effect is likely to be small for the eight trackers used in this experiment.

A method of deducing the effect of the adding weight to the stringbed involves a comparison of the measured results for the two different experiments in which a different number of markers have been used in each. In *Experiment 1* (discussed in section 7.2) only one tracker was attached to the

stringbed, and in *Experiment 2* eight trackers were used (discussed in section 7.3). This comparison is made for the coefficient of restitution and maximum stringbed displacement during impact, similar to that made by Johnston (2001).

Figure 7.19 (a) gives a comparison of the measured coefficient of restitution *COR* for two different experiments in which either 1 or 8 trackers are attached to the stringbed. The data is presented for impacts on rackets which have been strung using two different string tensions. It can be seen that the measured *COR* does not appear to be a function of the number of trackers which are attached to the racket. More precisely, any differences in the results of the two experiments are of the same order of magnitude as the uncertainty in the data. Unfortunately the data was collected using a different range of ball impact velocities for the two experiments, and therefore it is not possible to conclusively confirm this finding.

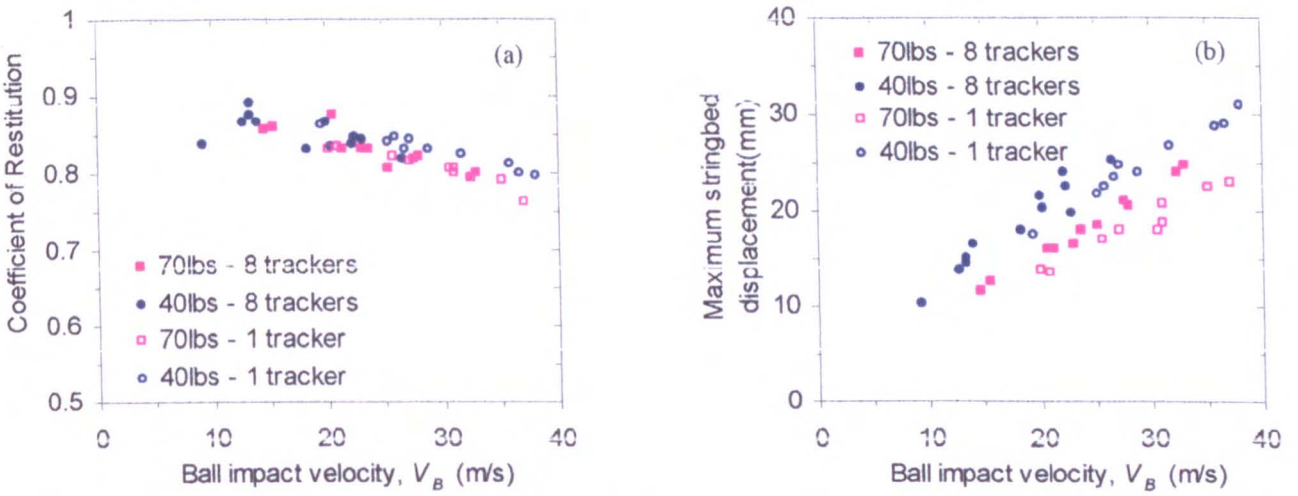

Figure 7.19 (a) Coefficient of restitution and (b) Maximum stringbed displacement for an impact between a ball and head clamped racket. The data is presented for two different string tensions and either 1 or 8 trackers attached to the stringbed. A *Pressurised* ball was used for all tests.

Figure 7.19 (b) shows that the magnitude of stringbed displacement is larger for impacts on the racket which has eight trackers attached to it, compared to the data for the racket with only one tracker. The difference is approximately 15% and is consistent for both string tensions and all impact velocities. This may be due to a systematic experimental error or it may be a true difference between the two experiments. A possible systematic error would be due to an inaccurate calibration of the field-of-view; the calibration performed to determine the relationship between a displacement measured on the PC screen and a physical displacement measured in SI units (explained further in section 3.3.4). However, the calibration was always performed twice; immediately before and after the testing. The difference between the two calibrations was always negligible and therefore this is unlikely to be causing a systematic error.

A more likely cause of the increased stringbed displacement which was measured when eight trackers were attached is due to a drop in the string tension of the rackets for this test. The same rackets were first used for the tests in which one tracker was attached (*Experiment 1*), and then they were used for the tests with 8 trackers attached (*Experiment 1*). The rackets were not restrung between the two experiments and *Experiment 2* was conducted approximately one calendar month

after *Experiment 1* was completed. The drop in tension may explain the higher stringbed deformations which were found for the tests which used eight trackers.

To verify this hypothesis, the stiffness of the stringbed was measured after *Experiment 2*; the stiffness being measured using the method described in Chapter 6. This data showed that the stiffness had reduced by 15% and 10% for the rackets strung at 70lbs and 40lbs, respectively. This change in stiffness can not be quantitatively compared with the results obtained for dynamic stringbed deformation but does highlight that the racket would have had to be restrung for a 'true' comparison to be made between *Experiment 1* and *Experiment 2*.

To summarise, it is not possible to conclude whether the mass of the trackers affects the deformation of the stringbed. The data implies that the coefficient of restitution is not altered, but the maximum deformation increased by approximately 15% when 8 trackers are attached to the stringbed. However, some of this increase in deformation will be due to the stringbed being less stiff in *Experiment 2* compared to *Experiment 1*. Also, the change in the stiffness of the stringbed may affect the coefficient of restitution for the impact. Therefore it can not be concluded whether the addition of the eight trackers affects this parameter.

7.3.6 Summary

In this section, the shape of a deformed stringbed has been measured for an impact between a ball and head clamped racket. The shape was measured for a length of approximately 80mm along the longitudinal axis of the racket. Experiments were conducted for two different string tensions and a range of ball impact velocities. The measured values of the stringbed displacement were normalised to the displacement of the stringbed at the impact point. This allowed conclusions to be drawn regarding the shape of the stringbed. It was found that this normalised shape was not a function of the string tension, but was dependent on the magnitude of the stringbed displacement at the impact point. It was assumed that the shape of the deformed stringbed could be simplified by a 2^{nd} order polynomial trend line that was plotted through the experiment data. The maximum stringbed displacement occurred at the impact point and this displacement was defined as $\delta_{S(IP)}$. The displacement of the stringbed which is 40mm from this point, along the longitudinal axis, is approximately 60-70% of the displacement $\delta_{S(IP)}$. It was also found that the normalised shape of the deformed stringbed became relatively 'flatter' as the magnitude of the displacement $\delta_{S(IP)}$ increased.

7.4 Comparison between quasi-static and dynamic stringbed deformation shape

7.4.1 Introduction

In section 7.3, the shape of a deformed stringbed was measured for an impact between a ball and head clamped racket. It was found that that the normalised shape of a deformed stringbed is a function of magnitude of the stringbed deformation. In section 6.3, the stringbed was deformed

quasi-statically using a force that was distributed over a circular area. In that experiment, it was shown that the normalised shape of the stringbed was not dependent on the magnitude of the displacement (or force), but importantly was a function of the size of this area. In an impact between a ball and head clamped racket it was found that the shape of the deformed stringbed became 'flatter' as the stringbed deformation increased. Comparing this with the quasi-static data, this finding corresponds with an increase in the area over which the force is applied. Therefore, it can be deduced that, in a ball/racket impact, the area over which the force is applied to the stringbed increases with increasing stringbed deformation. This is logical because the magnitude of ball deformation will be increasing and therefore so will the contact area.

In this section, the shape of the quasi-statically and dynamically loaded stringbed will be compared in an attempt to further the understanding of the impact mechanism. This understanding will be used in Chapter 8 when the impact will be modelled.

As mentioned above, it has been found that the shape of the deformed stringbed is not a function of the string tension, for an impact between a ball and head clamped racket. Therefore, in this section only the data for the racket which was strung at 70lbs tension is discussed.

7.4.2 Results and Discussion

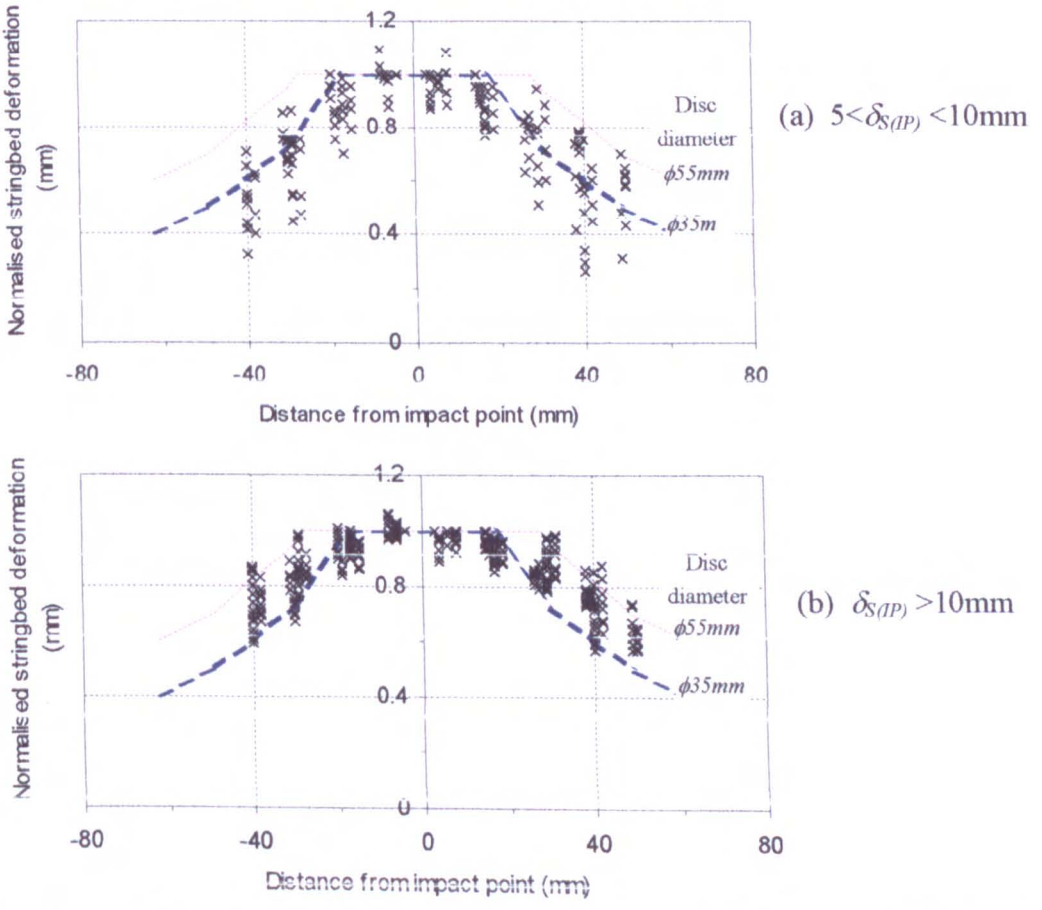

Figure 7.20 Comparison of dynamic and quasi-static normalised stringbed deformation, for two different ranges of the stringbed displacement at the impact point $\delta_{S(IP)}$. The data points represent measurements taken during an impact between a ball and a racket. The quasi-static data is presented for two different disc diameters. All data was obtained using a racket strung at 70lbs.

In section 7.3 it was shown that the shape of the deformed stringbed is dependent on the magnitude of deformation. Figure 7.20 shows the normalised data for two different ranges of stringbed displacement $\delta_{S(IP)}$, for an impact between a *Pressurised* ball and head clamped racket; $\delta_{S(IP)}$ representing the displacement of the stringbed at the impact point. The normalised shape of the deformed stringbed which was measured for a quasi-static compression is also plotted in these figures. This data was obtained in section 6.3 for two different circular areas over which the distributed load was applied; the diameters of these circular areas being 35mm and 55mm.

Figure 7.20 (a) shows that, for values of $\delta_{S(IP)}$ between 5 and 10mm, the dynamic data correlates most closely with the quasi-static data obtained using a circular disc with a diameter of 35mm. Figure 7.20 (b) shows that, for values of $\delta_{S(IP)}$ greater than 10mm, the dynamic data is distributed between the curves obtained using the discs with diameters of 35mm and 55mm.

Due to the large scatter in the data obtained for an impact between a ball and racket, it is difficult to precisely relate the quasi-static and dynamic results. Indeed, it is not even clear whether it is valid to directly compare the two sets of normalised data. The main weakness of the work is that the stringbed has been loaded using two different methods, for the quasi-static and dynamic cases. However, these results illustrate that the 'effective' contact area diameter increases from approximately 35mm at low stringbed displacements to almost 55mm at the highest displacements. This finding will be useful when the impact is modelled in Chapter 8, providing the limitations of this work are considered.

7.5 Summary

In this chapter, the impact between a ball and head clamped racket is investigated. In the first part of this chapter, the coefficient of restitution was measured for combinations of two different ball types and two different string tensions. It was found that, for a specific string tension, the coefficient of restitution is higher for the *Pressurised* ball, compared with the *Pressureless* ball. This difference is generally in the order of 0.05 for the racket strung at 70lbs and 0.02 for the racket strung at 40lbs. For a specific ball type, it was found that the coefficient of restitution is higher for the racket strung at 40lbs, compared with the racket strung at 70lbs.

The magnitude of the maximum ball and stringbed deformation, during impact, has been measured using a high speed video system. It was found that the ball deformation increased as the impact velocity was increased, but it did not appear to be a function of the ball type or string tension. The maximum stringbed deformation, during impact, was consistently 25% larger for the racket strung at 40lbs, compared to that strung at 70lbs. The magnitude of this stringbed deformation was very similar for both ball types.

In this experiment, the contact time for the impact was measured; the contact time being defined using two different methods. The first definition of the contact time is equal to the time taken for the stringbed deformation to return to zero and this is defined as $T_{C(S)}$. The second definition is equal to the time taken for the ball deformation to return to zero and is defined as $T_{C(B)}$. It was consistently found that the second definition yielded a longer contact time, for all combinations of

ball type and string tension. This implies that the stringbed deformation returns to zero, before the ball deformation does so.

The value of the contact time $T_{C(S)}$ decreased as the ball impact velocity increased. It was found that $T_{C(S)}$ was consistently 0.6ms longer for impacts on the racket strung at 40lbs, compared with impacts on the racket strung at 70lbs. It was concluded that the parameter $T_{C(S)}$ was not dependent on the ball type.

The value of the contact time $T_{C(B)}$ decreased as the ball impact velocity increased. It was found that $T_{C(S)}$ was approximately 0.4ms longer for impacts on the racket strung at 40lbs, compared with impacts on the racket strung at 70lbs. For impacts on the racket strung at 40lbs, it was found that $T_{C(B)}$ was not a function of the ball type. However, for impacts on the 70lbs racket, the value of $T_{C(B)}$ was larger for the *Pressureless* ball compared with the *Pressurised* ball.

The measured values of the ball deformation, during impact, was used to estimate the motion of the ball centre-of-mass. This data will be used in the following chapter to help verify a visco-elastic model of the impact.

In the second part of this chapter, an experiment was conducted to measure the shape of the deformed stringbed, during impact. The experiments were conducted using two different string tensions and a range of ball impact velocities. It was found that the normalised shape of the deformed stringbed was not a function of the string tension, but was dependent on the magnitude of the stringbed displacement at the impact point. It was found that the normalised shape of the stringbed became relatively 'flatter' as the magnitude of the stringbed displacement increased. This is logical because, as the stringbed displacement increases, the magnitude of ball deformation will also increase, resulting in a larger contact area between the ball and stringbed. This will lead to a relatively 'flatter' stringbed.

A comparison was made between the shape of the stringbed for a dynamic and quasi-static loading. The dynamic loading refers to an impact between the ball and head clamped racket, and the quasi-static loading is applied via a rigid circular disc. It was found that, for stringbed displacements between 5mm and 10mm, the dynamically deformed stringbed has a similar shape to a stringbed that has been loaded quasi-statically using a rigid disc with a diameter of 35mm. For stringbed displacements greater than 10mm, the dynamically deformed stringbed has a similar shape to a quasi-statically loaded stringbed using a disc with a diameter of between 45mm and 55mm. This comparison will be referred to in the following chapter as it will aid in the development of the visco-elastic model of the impact.

8. Modelling an Impact between a Ball and Head Clamped Racket

8.1 Introduction

In Chapter 7, results are presented for an experimental investigation of an impact which involved a tennis ball being propelled perpendicularly towards a head clamped tennis racket. In that experiment, a number of parameters were measured, which included the following,

1. Ball rebound velocity.
2. Contact time.
3. Magnitude of ball deformation.
4. Magnitude of stringbed deformation.

These parameters were measured for impacts that involved two rackets which had been strung with different string tensions, and two different ball types. It was noted in Chapter 7 that this covered a wide range of typical ball types and tensions used in the game of tennis.

In this chapter, a visco-elastic model of the impact between a ball and head-clamped racket is to be developed. Whilst it is accepted that a head clamped racket is not representative of a player's grip, this type of impact does involve the interaction between the ball and stringbed. The head is clamped and therefore it can be considered rigid. This simplifies the required model as the racket frame does not need to be modelled.

A visco-elastic model has been chosen as a suitable simulation method for this type of impact for two main reasons. Firstly, a visco-elastic model of a ball impact on a rigid surface was successfully developed in Chapter 5. Therefore, it would be logical to utilise the understanding gained in that work to help develop a model of the ball for an impact with a stringbed. Secondly, a visco-elastic model has been chosen for its versatility. In this type of model the stiffness and damping can be defined as functions of any number of parameters (e.g. the stringbed displacement).

The developed model will be used to calculate the four parameters which are listed above. The accuracy of the model will be assessed by comparing the model results, for these four parameters, with the experimental data obtained in Chapter 7.

8.2 Generic model for an impact between a ball and head clamped racket

8.2.1 Introduction

In section 5.5, a visco-elastic model of a tennis ball impacting perpendicular to a rigid surface was developed. This model accounted for the forces that acted on the ball due to the structural stiffness, material damping and momentum flux. Each ball type had a unique set of parameters that defined the model components (e.g. spring stiffness), and these parameters were valid for any impact

velocity. The model results were compared with experimental data that had been obtained for an impact between a ball and force platform. It was shown that the *Force-Time* and *Force-Displacement* plots for the two sets of data correlated very closely. In this section, the model which was developed in section 5.5, is to be developed to enable it to be used to simulate the impact between a ball and head clamped racket.

8.2.2 The model

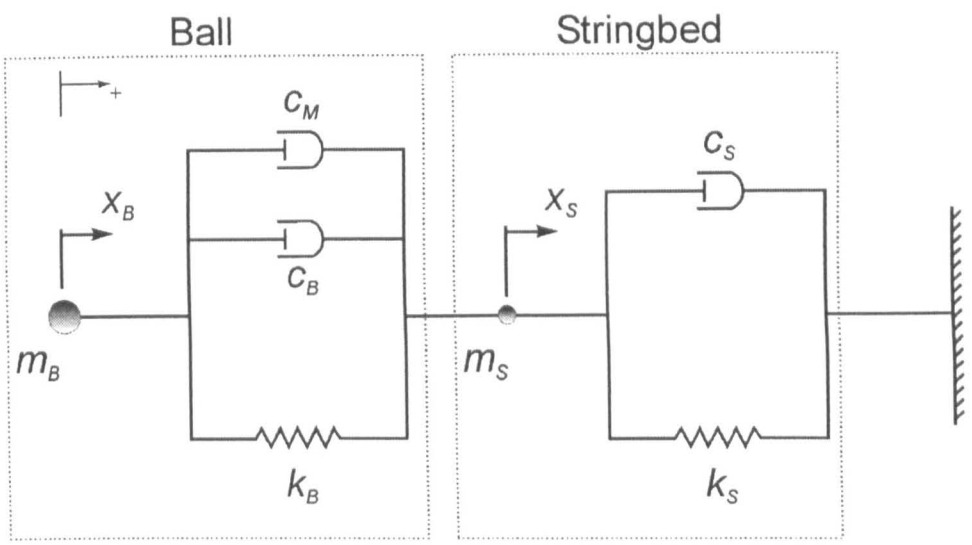

Figure 8.1 Illustration of a visco-elastic model of a ball impact on a head-clamped racket.

In this section, the ball and stringbed are to be modelled as a series of springs and dashpot dampers. The ball will be simulated using the same one degree-of-freedom model as that developed in section 5.5. The stringbed will be simulated as a simple one DOF model, as it has initially been assumed that only the displacement of the impact point is required. The visco-elastic model of an impact between a ball and head-clamped racket is shown in Figure 8.1. The stringbed is represented by a spring and dashpot in parallel. The spring is used to represent the stiffness of the stringbed, in a direction perpendicular to the plane of the stringbed. The dashpot is used to simulate the energy loss for an impact in this same direction. Many authors (Cross 2000b, Leigh and Lu 1993) have shown that the energy losses in a stringbed are approximately 5% and therefore the value of c_S is likely to be small.

The displacements x_S and x_B represent the motion of the stringbed at the ball impact position and the ball centre-of-mass respectively. The mass m_B is equal to the mass of the ball, and can easily be measured using an electronic balance. The mass m_S represents the effective mass of the stringbed that is displaced by a distance x_S during the impact. This can not be measured directly and therefore must be chosen arbitrarily. The total mass and surface area of a stringbed is typically 20g and 0.063m^2 (98in^2), respectively. In section 7.3, the shape of the deformed stringbed was measured. Using this data, it is estimated that the effective mass of the stringbed can be represented by a circular section of the stringbed, with a diameter of 130mm. This disc has an area of 0.014m^2 and therefore the assumed value of m_S was 5g. This value has clearly been chosen arbitrarily and the actual value could actually lie anywhere between the two bounds of 0 and 20g. In Appendix C.7, the sensitivity of the model solution to the magnitude of this value is quantified

to assess the validity of this assumption. The findings of that analysis shall be referred to later in this chapter.

The equation that is used to define the force F_B which acts on the ball mass m_B is,

$$F_B = m_B\ddot{x}_B = -[(c_B + c_M)(\dot{x}_B - \dot{x}_s) + k_B(x_B - x_s)] \quad [8.1]$$

The force acting on the stringbed mass m_S is,

$$F_S - F_B = m_S\ddot{x}_S = -[c_S\dot{x}_S + k_S x_S] - F_B \quad [8.2]$$

The motion of the points x_B and x_S was evaluated numerically using the finite difference method. The time step Δt used in this solution is $5\mu s$. The finite difference equation which defines the displacement of x_B at a time $t+\Delta t$ is,

$$(x_B)_{t+\Delta t} = \Delta t^2(\ddot{x}_B)_t + 2(x_B)_t - (x_B)_{t-\Delta t} \quad [8.3]$$

A similar finite difference equation can be used to determine the value of x_S at time $t+\Delta t$,

$$(x_S)_{t+\Delta t} = \Delta t^2(\ddot{x}_S)_t + 2(x_S)_t - (x_S)_{t-\Delta t} \quad [8.4]$$

Assuming that the values of x_B and x_S (and $\dot{x}_B$ and $\dot{x}_S$) are known at time t, then $(\ddot{x}_B)_t$ and $(\ddot{x}_S)_t$ can be calculated using [8.1] and [8.2]. The values of $(x_B)_{t+\Delta t}$ and $(x_S)_{t+\Delta t}$ can then be calculated using [8.3] and [8.4]. As the time step used in this solution is very small, it was assumed that the velocity change during this period was negligible. Therefore the velocities $(\dot{x}_B)_{t+\Delta t}$ and $(\dot{x}_S)_{t+\Delta t}$ can be calculated using,

$$(\dot{x}_B)_{t+\Delta t} = \frac{(x_B)_{t+\Delta t} - (x_B)_t}{\Delta t} \quad [8.5]$$

$$(\dot{x}_S)_{t+\Delta t} = \frac{(x_S)_{t+\Delta t} - (x_S)_t}{\Delta t} \quad [8.6]$$

The accelerations $(\ddot{x}_B)_{t+\Delta t}$ and $(\ddot{x}_S)_{t+\Delta t}$ were then calculated using [8.1] and [8.2], and the solution was then repeated for this new time step.

Table 8.1 The displacement, velocity and acceleration of the ball and stringbed at time when $t=0$ and $t = -\Delta t$.

At time, $t = -\Delta t$	At time, $t = 0$
$x_B = -V_B\Delta t$, and $x_S = 0$	$x_B = x_S = 0$
$\dot{x}_B = V_B$, and $\dot{x}_S = 0$	$\dot{x}_B = V_B$, and $\dot{x}_S = 0$
$\ddot{x}_B = \ddot{x}_S = 0$	$\ddot{x}_B = \ddot{x}_S = 0$

To commence this type of solution the displacement, velocity and acceleration of the ball and stringbed need to be defined for the time when $t = 0$ and $t = -\Delta t$. For an impact with initial ball

velocity V_B, these values are given in Table 8.1. These values have been obtained using the assumptions that the stringbed is initially stationary and the ball is not accelerating prior to impact.

A more powerful numerical solving technique, such as the Runge-Kutta method, could have been used to solve a numerical solution of the model. However, it was found that the simple finite difference method only gave an maximum error in the order of ~0.2%, due to the relatively small time step being used. The solution was written in *MS Excel 2000* and could be solved for each time step of the impact, provided that the values of the parameters k_B, k_S, c_B, c_M and c_S are all known.

In this section, a generic visco-elastic model of a ball impact on a head clamped racket has been developed. In the next section, the methods used to define the parameters k_B, k_S, c_B, c_M and c_S is described.

8.3 Modelling Technique – 1st Attempt

8.3.1 Determining the visco-elastic model parameters

In the model in section 8.2, an equation has been derived which can be used to define a visco-elastic model of an impact between a ball and head clamped racket. In this model, the value of a number of parameters are required in order to solve the equation. As stated previously, this model considers the two components separately, and therefore the methods used to obtain the values of the parameters shall also be described individually.

(a) The ball

The ball has been modelled as a spring in parallel with two dashpot dampers, as illustrated in Figure 8.1. The spring is used to simulate the structural stiffness of the ball and this parameter is defined as k_B. A dashpot damper is used to simulate the hysteresis loss in the material, and this parameter is defined as c_B. A second dashpot damper is used to simulate the force which acts on the ball due to the momentum flux, and this parameter is defined as c_M. A detailed explanation of this model can be found in section 5.5. However, a brief résumé is given here to illustrate the method which is used to define the parameters k_B, c_B and c_M.

In section 5.5, the ball model was used to simulate an impact with a rigid surface. In this type of model, the ball deformation is analogous to the displacement x_B. It was found that the ball stiffness k_B was a function of x_B, as defined in [5.21]. In the model of a ball impact on a stringbed, it is assumed that the parameter $(x_B - x_S)$ is analogous to the ball deformation. Therefore in [5.21], the term x_B is replaced by $(x_B - x_S)$ and this equation becomes,

$$k_B = k_{B(0)} + A_K (x_B - x_S)^{\alpha} \qquad [8.7]$$

In the model of a ball impact on a rigid surface, the parameters $k_{B(0)}$, A_K and α were found to be constants for a specific ball type. In this current model, it is assumed that these parameters are valid for an impact between a ball and head clamped racket. A minor addition to this model is that it was found that the ball has a very high structural stiffness during the first 0.2ms of impact. In the

model this is simulated by assuming that k_B=80kN/m for this period. For the remainder of the impact, the stiffness of the spring is defined by [8.7].

For the model of an impact on a rigid surface, it was assumed that the magnitude of the material damping was proportional to the volume of rubber being deformed, and also the ball deformation rate. In that model, the dashpot parameter c_B which represented the material damping is defined using,

$$c_B = \frac{m_B}{M_1} A_C . (d_{CONT})^2 \qquad [8.8]$$

where m_B is the mass of the ball, and the other parameters are defined below.

To derive this equation, a number of assumptions were made regarding the shape of the deformed ball. The parameter d_{CONT} refers to the diameter of the circular area of the ball that is in contact with the surface. The empirical relationship between d_{CONT} and the ball COM displacement x_B, for an impact between a ball and rigid surface, was given in [5.6]. In this current model, the analogous parameter to x_B is $(x_B - x_S)$. It is not possible to empirically obtain the relationship between d_{CONT} and $(x_B - x_S)$, for an impact on a stringbed. Therefore, it is assumed that the relationship derived in [5.6] for an impact on a rigid surface is valid for an impact on a stringbed. The modification of [5.6] is therefore,

$$d_{CONT} = -2.77 \times 10^5 (x_B - x_S)^4 + 1.74 \times 10^4 (x_B - x_S)^3 - 453 (x_B - x_S)^2 + 7.66 (x_B - x_S) \qquad [8.9]$$

The term M_1 in [8.8] refers to the mass of the section of ball that is not in contact with the surface. This value clearly varies throughout impact, and is a function of the ball deformation. It is assumed that M_1 is equal to the difference between m_B and the mass of the ball that is in contact with the surface M_2. The value of M_2 is estimated using,

$$M_2 = \rho_{area} \pi \left(\frac{d_{CONT}}{2} \right)^2 \qquad [8.10]$$

where ρ_{area} is the mass per unit surface area density of the ball and is equal to 5.212kg/m^2 for a standard size ball.

The parameter A_C was defined as a constant for each ball type, for an impact between a ball and rigid surface. This constant value was arbitrarily chosen with the aim of defining a value that gave a model ball rebound velocity that was similar to that measured experimentally.

The values of the parameters $k_{B(0)}$, A_K, α and A_C, for a typical *Pressurised* and *Pressureless* ball, are given in Table 8.2. These parameters will be used in the current model.

Table 8.2 Spring parameters $k_{B(0)}$, A_K and α and damping coefficient A_C for the four ball types.

Ball type	$k_{B(0)}$ (kN/m)	A_K (kN/m^2)	α	A_C (kNs/m^3)
Pressurised	21	16000	1.65	3.5
Pressureless	23	12500	1.7	4.0

For an impact between a ball and rigid surface, the work in section 5.5 showed that the force due to the momentum flux can be simulated using a dashpot damper with coefficient c_M, as defined by [5.19]. In that model, the force due to the momentum flux is effectively proportional to the mass (and velocity) of the ball being brought to rest in a unit time interval Δt. The equation used to define c_M at time t is,

$$(c_M)_t = \frac{m_B\left[\rho_{area}\pi\left((d_{CONT(t)})^2 - (d_{CONT(t-\Delta t)})^2\right)\right]}{4\Delta t(M_1)_t} \qquad [8.11]$$

In [8.11], it is assumed that the mass of the ball being brought to rest can be calculated from the empirically measured ball/surface contact area diameter at time t and t-Δt which are defined as $d_{CONT(t)}$ and $d_{CONT(t+\Delta t)}$ respectively.

In the model of an impact between a tennis ball and stringbed, the section of the ball that comes into contact with the surface in a unit time interval is not brought to rest. Instead the velocity of this section instantaneously changes to that of the stringbed. This is simulated in the model by assuming that the force acting on the ball due to the momentum flux $F_{B(M)}$ is equal to,

$$F_{B(M)} = c_M(\dot{x}_B - \dot{x}_S) \qquad [8.12]$$

The equations which have been discussed in this section can be used to define all the ball parameters that are required to solve the model which was given in section 8.2.

A minor modification is made to this model to simulate the contribution of the cloth on the ball, during impact. In Chapter 4, it was shown that the cloth has a relatively low stiffness, compared with the rubber core. In Chapter 5 it was shown that this characteristic could be modelled by assuming that the force which acted on the ball was equal to zero during the initial stage of impact, when only the cloth was being compressed. This same assumption shall be used in this current model, and therefore it is assumed that the force which acts on the ball is equal to zero, for ball COM displacements of less than 2mm (during the compression phase only), regardless of the values of the ball model parameters

(b) The stringbed

The stringbed of a head clamped racket is to be modelled as a spring and damper in parallel. The stiffness of the spring is clearly analogous to the stiffness of the stringbed for a compression that is perpendicular to the plane of the stringbed. In section 6.2, a force was applied to a stringbed and

the resulting displacement was measured. This data was converted to a linear quasi-static stiffness which is defined as the ratio of the applied force and stringbed displacement. In that section, the quasi-static stiffness was measured for rackets which have been strung at different tensions. The load was applied using a rigid circular disc, and data was obtained for a range of different disc sizes.

It is to be assumed that the quasi-statically measured stiffness can be used to define a 1st order approximation of the spring stiffness in the model, for the specific string tension of the racket that is being modelled. The stringbed stiffness increased with the magnitude of stringbed displacement which could easily be accounted for in the model. However, the stiffness of the stringbed was also dependent on the size of the circular disc that is used to apply the load. The effective contact area over which the ball applies the load onto the stringbed is not known. Therefore it is not possible to directly define the stiffness of the stringbed for an impact with a ball, from the quasi-static stiffness data.

Initially, let it be assumed that the effective contact area diameter of the ball on the surface be known; this diameter being defined as ϕ_D. In section 6.2, a technique was discussed which could be used to minimise the number of equations that were required to define the stiffness of the stringbed. This technique involved the concept of a normalised stringbed displacement. This normalised stringbed stiffness $\tilde{k}_S$ is defined using,

$$\tilde{k}_S = \frac{k_S(\phi_D)}{k_S(\phi_{55})} \qquad [8.13]$$

The parameter $k_S(\phi_D)$ is equal to the stiffness of the stringbed at a specific displacement x_S, measured using a disc diameter of ϕ_D. The parameter $k_S(\phi_{55})$ is equal to the stiffness of the stringbed at the same displacement x_S, measured using a disc diameter of 55mm.

In section 6.2, it was shown that an empirical approximation can be used to define the relationship between the normalised stringbed stiffness and the size of the disc diameter. This equation is,

$$\tilde{k}_S = 78.42\phi_D^2 + 2.336\phi_D + 0.6392 \qquad [8.14]$$

To complete the solution, the stiffness of the stringbed must be known, for a quasi-static loading applied using a rigid disc with a diameter of 55mm. This quasi-static stiffness is a constant function of x_S and is defined as $k_S(\phi_{55})$ using an equation of the form,

$$k_S(\phi_{55}) = a.x_S^2 + b.x_S + c \qquad [8.15]$$

In Chapter 6, the quasi-static stiffness of the rackets strung at 40 and 70lbs tension was measured for a compression using a 55mm circular disc, and the parameters of equation [8.15] are shown in Table 8.3.

Table 8.3 The coefficients of the second order trendline which defines the stiffness of the stringbed, for two different string tensions.

String tension	a (kN/m^3)	b (kN/m^2)	c (kN/m)
40lbs	4785	1147	29.02
70lbs	-30140	2519	43.07

To summarise, the parameter which will be input into the model is defined as $k_S(\phi_D)$. This parameter describes the stiffness of the stringbed at a specific displacement, for a specific disc diameter. Therefore,

$$k_S(\phi_D) = fn(x_S, \phi_D) \qquad [8.16]$$

The equations which are required to determine $k_S(\phi_D)$ have been discussed above. However, they require a value of ϕ_D to be defined. In the quasi-static test, ϕ_D was simply equal to the diameter of the disc used to apply the load. However, in the model, the value of ϕ_D needs to describe the effective contact area of the ball and stringbed. An initial discussion of this was given in section 7.5, in which the shape of a quasi-statically deformed stringbed, was compared with that of a dynamically deformed one. This discussion is continued below.

In an impact between a tennis ball and stringbed, the ball does not apply a load on the stringbed in the same way that the load is applied by a rigid disc; a tennis ball being a highly deformable body. The shape of the deformed stringbed for a quasi-static and dynamic loading was compared in section 7.4. The quasi-static loading was applied by a rigid disc and the dynamic loading referring to an impact between a ball and head clamped racket. In that section, a qualitative relationship between the magnitude of stringbed displacement and the effective contact area of the ball was obtained. In this current section, a quantitative relationship is required which can be used in the model to estimate the value of the stiffness parameter k_S.

The relationship that needs to be obtained is that which relates the stringbed displacement x_S with the effective contact area diameter that the ball is applying the load over. This is obtained using the data in section 7.4. It is shown that, for stringbed displacements of between 5 and 10mm, the dynamically deformed stringbed has a similar shape to that of a stringbed which was deformed quasi-statically using a disc diameter of 35mm. For all stringbed displacements of more than 10mm, the shape of the dynamically deformed stringbed is similar to that of a quasi-statically deformed stringbed that used a disc diameter of between 45mm and 55mm to apply the load. Using this information as a guide, the assumed relationship between the stringbed displacement and the effective area over which the ball imparts a load on the stringbed can be obtained. This assumed relationship is shown in Figure 8.2. The two points that are used to define this arbitrary relationship are the stringbed displacements for contact area diameters of 35mm and 55mm. It has been assumed that the stringbed displacement for a contact area diameter of 35mm is 7.5mm. This has been arbitrarily chosen by the fact that the shape of the quasi-statically deformed stringbed, using a contact area diameter of 35mm, is similar to that for a dynamically deformed stringbed for

displacements of between 5 and 10mm. The stringbed displacement for a contact area of 55mm was chosen to be 20mm. This was deduced from the fact that, for stringbed displacements between 10mm and 25mm, the effective contact area diameter lies somewhere between 35mm and 55mm. A displacement of 20mm was arbitrarily chosen as the limit.

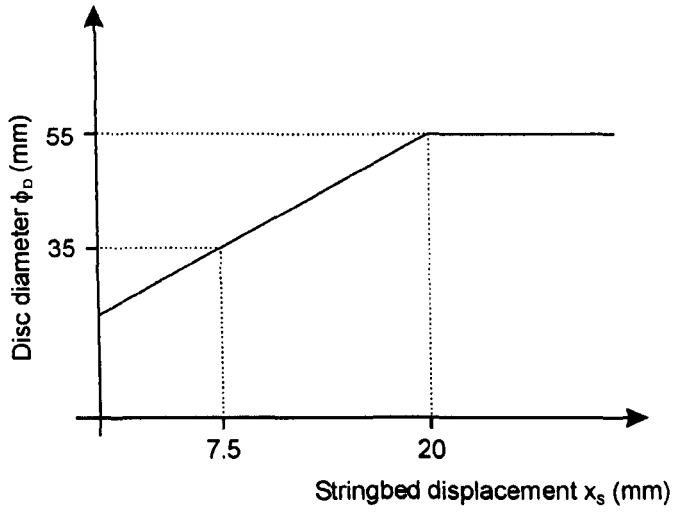

Figure 8.2 Assumed relationship between the disc diameter and the stringbed displacement.

The relationship shown in Figure 8.2 has been chosen arbitrarily. In Appendix C.7, the sensitivity of the model solution to the form of this relationship is discussed. This relationship shows that, for displacements of up to 20mm, the contact area diameter is a continuingly varying function of the stringbed displacement x_S. For stringbed displacements x_S of less than 20mm, the equation that defines the curve in Figure 8.2 (converted into SI units) is,

$$\phi_D = 1.6x_S + 0.023 \qquad [8.17]$$

and for $x_S > 0.020$m the value of ϕ_D is equal to 0.055m.

This information defines the value of ϕ_D for any stringbed displacement x_S. Previously it was shown that equations have been derived which define stringbed stiffness for a specific combination of the values of x_S and ϕ_D. However, it has been described that the solution required the relationship between the two variables, x_S and ϕ_D, to be known. This has been defined in [8.17] and therefore the solution can be completed.

The parameter ϕ_D can be substituted in [8.14], so that the equation to define the normalised stiffness becomes,

$$\tilde{k}_S = 78.42(1.6x_S + 0.023)^2 + 2.336(1.6x_S + 0.023) + 0.6392 \qquad [8.18]$$

[8.18] is valid for stringbed displacements x_S of less than 20mm. For $x_S > 20$mm, the value of ϕ_D is equal to 55mm, and therefore the normalised stiffness $\tilde{k}_S$ is equal to unity.

Using the example of a racket strung at 70lbs, the equation to define the quasi-static stringbed stiffness for a loading with a disc diameter of 55mm is,

$$k_S(\phi_{55}) = -30140000x_S^2 + 2519000x_S + 43070 \qquad [8.19]$$

Rearranging [8.13] gives

$$k_S(\phi_D) = \tilde{k}_S \cdot k_S(\phi_{55}) \qquad [8.20]$$

Using equations [8.18]-[8.20], the stringbed stiffness $k_S(\phi_D)$ can be calculated for any value of x_S. This stringbed stiffness $k_S(\phi_D)$ is substituted for the spring stiffness k_S that is shown in Figure 8.1, and therefore this parameter has now been defined in the model. Clearly, the values of the coefficients in [8.19] are dependent on the string tension. These parameters are determined from a *least squares regression* analysis on data collected for a quasi-static compression of a stringbed, using a disc diameter of 55mm.

In Figure 8.1, it can be seen that there is also dashpot damper, with value c_S, that is used to represent the damping of the stringbed. Cross (2000b) showed that the damping, or material energy losses, in the stringbed are both small and not dependent on the age of the strings or on string tension. In this study, the energy loss which occurs in an impact between a head clamped racket and a 760g rigid sphere was measured. Cross (2000b) found that ball rebounded at 95±2% of the incident speed, regardless of the drop height, string type or string tension.

Clearly, an empirical solution for c_S could be obtained via a simulation of the experimental impact that was conducted by Cross (2000b). This simulation uses the same generic model of a ball impacting on a stringbed as that described in section 8.2. A rigid ball is assumed to exhibit no energy losses and therefore the value of the dashpot damper parameters c_B and c_S are both equal to zero. The ball will clearly be very rigid and to simulate this the spring stiffness k_B was assigned a relatively high, constant value of 400kN/m. The mass of the ball m_B and the stringbed m_S were equal to 760g and 5g respectively. The stringbed stiffness k_S was defined using the equations described above.

The model was then solved using the equations derived in section 8.2. The value of the stringbed damping c_S was initially equal to zero. This value was then increased until the model calculated a ball rebound velocity that was equal to approximately 95% of the incident speed, using an iterative process. It was found this result was achieved using a stringbed damping value c_S that varied between 1.5 and 2.5Ns/m for the range of impact velocities that were used (3m/s to 7m/s). It was therefore concluded that, for simplicity, the value of c_S will be assumed to be equal to 2Ns/m for all impacts in this section, unless otherwise stated.

(c) Summary of model parameters

In this section, the methods that are used to determine the values of the model parameters k_B, k_S, c_B, c_M and c_S are described. In this section, it was assumed that a ball can be modelled using the same technique as was used in Chapter 5 to simulate a ball in an impact with a rigid surface. Therefore, the ball parameters k_B, c_B, and c_M are the same as those used that chapter. A number of assumptions had to be made to allow this to be possible. For example, it was assumed that the relationship between the shape of the deformed ball and the ball centre-of-mass displacement, is the same for both an impact on a rigid surface and on a stringbed.

The model stringbed stiffness k_S was assumed to be equal to the quasi-static stiffness that has been measured in Chapter 6. It was shown that the quasi-static stringbed stiffness is dependent on the size of the circular disc that is used to apply the load. Therefore, assumptions have been made which specify the effective size of the ball-surface contact area for a specific stringbed displacement, for a dynamic impact. The damping parameter c_S is assumed to be equal to 2Ns/m to account for the small hysteresis losses in the stringbed for a dynamic impact.

8.3.2 Results and Discussion

(a) Force-Time plot

In section 8.2, a generic visco-elastic model was derived for an impact between a tennis ball and head clamped racket. In that section, the techniques that are required to solve the model are given. In section 8.3.2, the assumptions are discussed which are needed to determine the values of the model parameters k_B, k_S, c_B, c_M and c_S. As mentioned previously, a numerical solution for the model was calculated in *MS Excel 2000*. This solution calculated the displacement, velocity and acceleration of the ball and stringbed masses, at time intervals Δt of 2μs, for the entire impact. The forces which act on the two masses were also calculated at each time interval, and this data can be used to determine a *Force-Time* curve for the force which acts on the ball.

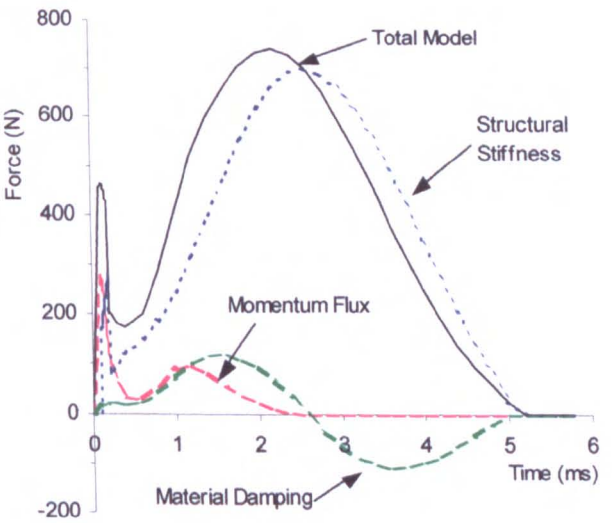

Figure 8.3 Typical *Force-Time* data, showing the contribution of each component of the total model force which acts a *Pressurised* ball during an impact with a racket stringbed that is strung at 70lbs.

Figure 8.3 shows the individual components of the force which acts on the mass m_B, for a simulated impact between a *Pressurised* ball and a head clamped racket that has been strung at 70lbs. These forces were calculated for a ball impact velocity of 20m/s. The major component of the total model force which acts on the ball is that which is due to the spring stiffness (structural stiffness). This accounts for approximately 80% of the total force. Both the momentum flux force and the structural stiffness force are relatively high during the initial stage of impact, which leads to a high value of the total force. The momentum flux force is high during this period because the ball

centre-of-mass is moving relatively quickly at this point and the stringbed is almost stationary. The structural stiffness force is relatively high because the spring stiffness has been assigned a high value of 80kN/m, during the first 0.2ms of impact. The material damping force is a function of the ball velocity, and therefore has a positive value during the compression phase, and a negative value during the restitution phase.

The model solution can also be used to determine the following parameters,

1. Ball rebound velocity.
2. Contact time for the impact.
3. Ball centre-of-mass displacement during impact.
4. Stringbed displacement during impact.

In Chapter 7, these parameters have been experimentally determined for an impact between a head clamped racket and ball. These results have been obtained for rackets strung with two different string tensions (40lbs and 70lbs) and two different ball types (*Pressurised* and *Pressureless*). The required model parameters for the two stringbeds (k_S, c_S) and for the two ball types (A_K, $k_{B(0)}$, α, A_C) are given in section 8.3.1. In the following section, a comparison is made between the model and experiment values of the four parameters shown above.

(b) Comparison of Model and Experiment Results

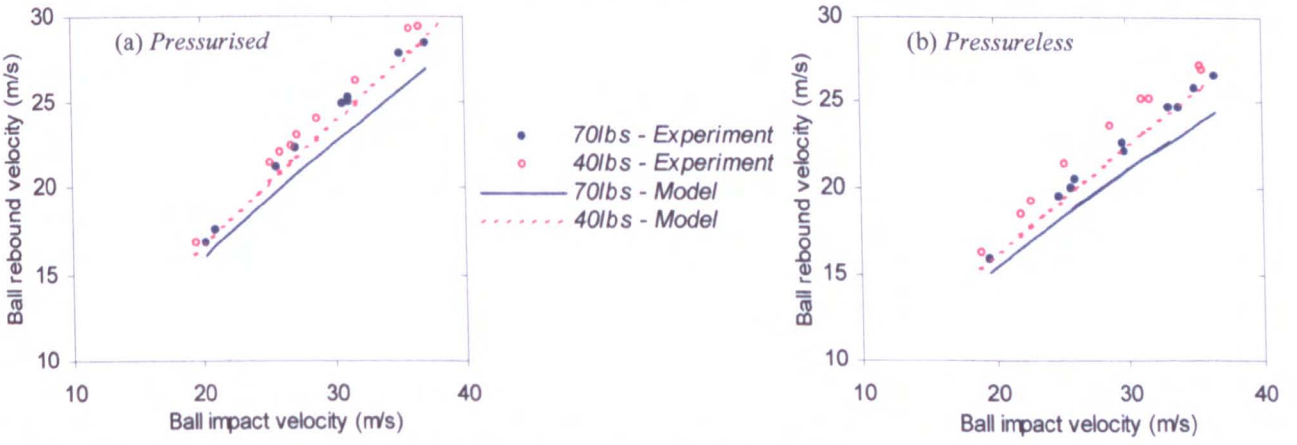

Figure 8.4 Comparison of the ball rebound velocity measured for the experiment and model. The data is presented separately for two different ball types.

Figure 8.4 shows a comparison of the ball rebound velocity data that was obtained using the model and that obtained experimentally. This data is presented separately for the *Pressurised* and *Pressureless* balls. It can be seen that the model consistently calculates a ball rebound velocity which is lower than that which has been measured experimentally. This difference is generally between 5 and 10%.

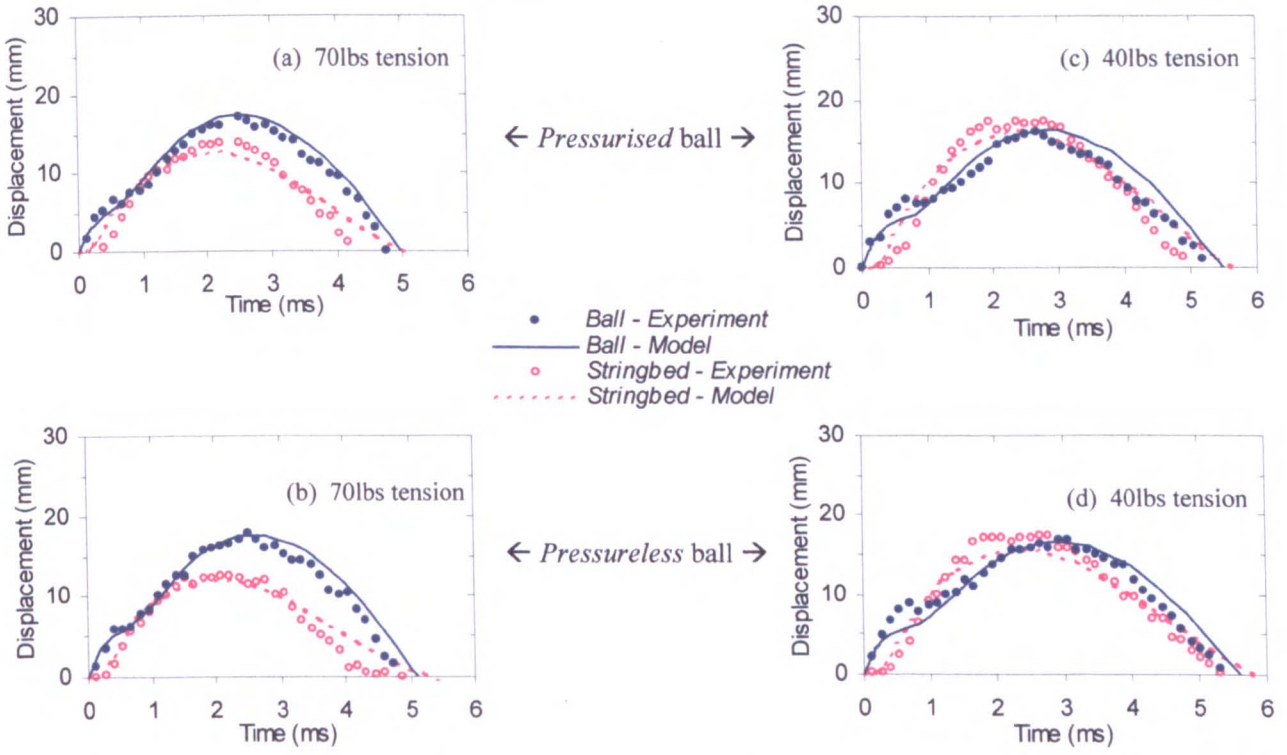

Figure 8.5 Ball centre-of-mass displacement and stringbed displacement for an impact between a ball and head-clamped racket, for four different combinations of string tension and ball type. The ball impact velocity is 20m/s, and both the model and experiment data are presented.

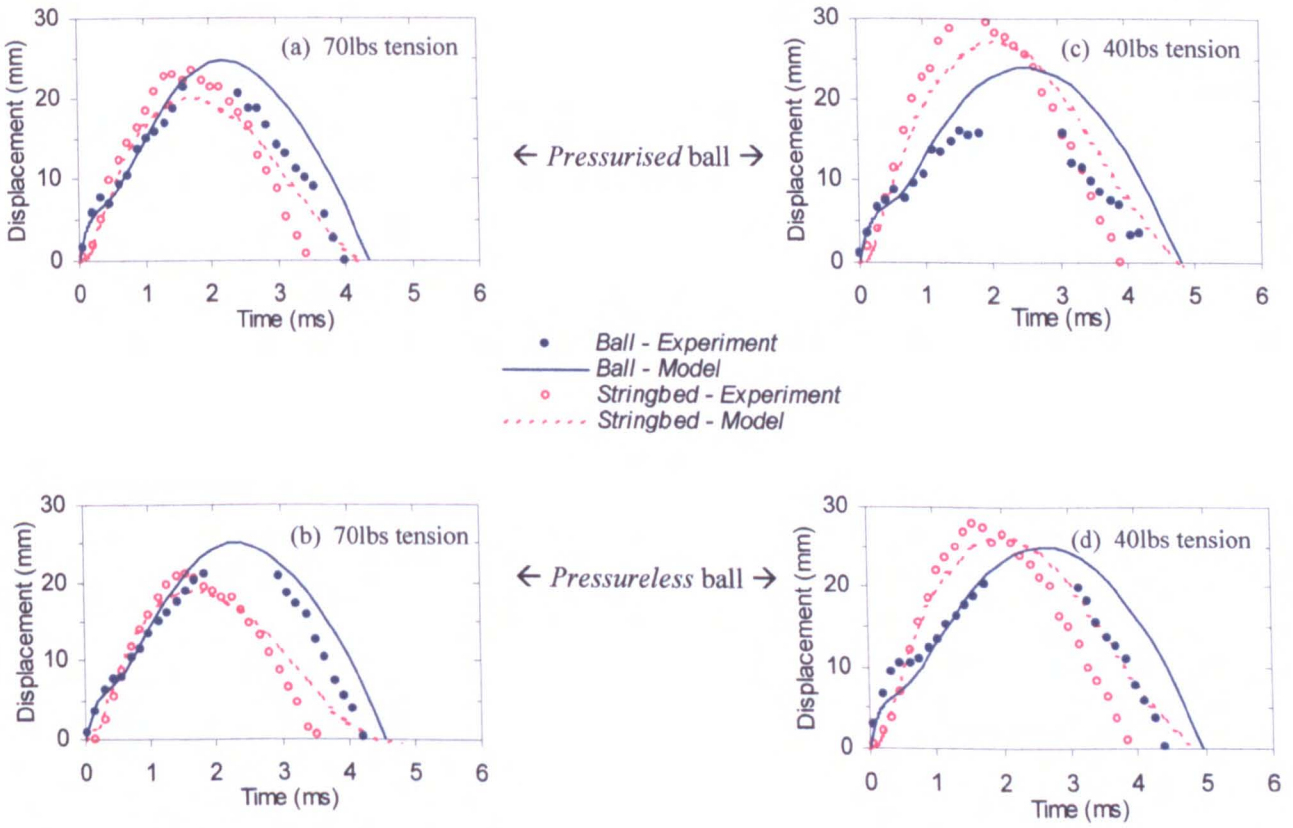

Figure 8.6 Ball centre-of-mass displacement and stringbed displacement for an impact between a ball and head-clamped racket, for four different combinations of string tension and ball type. The ball impact velocity is 35m/s, and both the model and experiment data are presented.

In Chapter 7, high speed video analysis was used to estimate the displacement of the ball centre-of-mass during impact, for a range of ball impact velocities. In these experiments, the magnitude of the stringbed displacement was also measured. These experimental values of ball COM and stringbed displacement are plotted in Figure 8.5 and Figure 8.6, along with the model results that have been discussed earlier in this section. These figures contain data for an impact between a ball and head clamped racket at nominal impact velocities of 20m/s and 35m/s respectively. Data is presented in these figures for the two different ball types and two different tensions. It is noted that some data is 'missing' for the ball COM displacement in Figure 8.6. This data was collected for a relatively high speed impact velocity (35m/s), and the ball could not be viewed during maximum compression for such high speed impacts. Data for other impact velocities is given in Appendix C.

Figure 8.5 and Figure 8.6 show that the model and experiment plots both exhibit a characteristic kink in the curve which represents the ball COM displacement data. This occurs at a time of between 0.5-1.0 ms. Also, both the experiment and model plots show that the stringbed does not start to displace at the instant that contact occurs. There is generally a delay of approximately 0.3ms before the stringbed starts to move. In the model, this is due to the fact that the ball does not exert a force on to the stringbed until a ball COM displacement of 2mm is achieved. This feature of the model is employed to simulate the relatively low stiffness of the cloth. The delay in motion will also be due to the finite mass of the stringbed m_S which must be accelerated .

The kink in the ball COM displacement curve may also be due to this delay in the motion of the stringbed because, initially, the ball will deform rapidly due to the inertia of the stringbed. Then the stringbed will start to move due to the high force which acts on it. This may result in instability in the solution, and the stringbed may overshoot its equilibrium position, causing the ball deformation to momentarily reduce and create a kink in the curve.

The model and experimental results for the magnitude of the ball COM and stringbed displacement correlate for most of the compression phase of impact. However, it is generally found that the model ball COM displacement is greater than that which is measured experimentally, especially during the restitution phase. The figures above show that the maximum value of the model stringbed displacement (during impact) is generally smaller than that measured experimentally. However, during the restitution phase the value of the model stringbed displacement is generally higher than that measured experimentally. Even more evident is the fact that both the model stringbed and ball COM displacement both take longer to return to zero compared to their experimentally determined values. This is implies that the contact time in the model is longer than that obtained experimentally.

A significant feature of the experimentally obtained data that is shown in Figure 8.5 and Figure 8.6 is that the stringbed displacement often returns to zero before the ball COM displacement returns to zero. This characteristic has been discussed in section 7.2.4 and leads to the requirement that there are two different definitions for the contact time of the impact. These two separate definitions are termed $T_{C(S)}$ and $T_{C(B)}$ and the definitions of these two terms are illustrated in Figure 8.7.

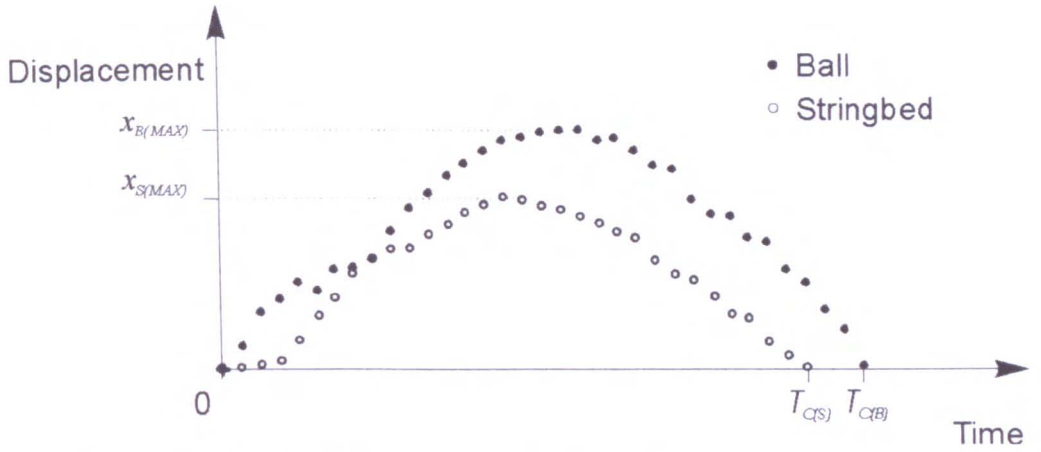

Figure 8.7 Definitions of the measured terms obtained from the *Displacement-Time* plots.

The parameter $T_{C(S)}$ refers to the time taken for the stringbed displacement to return to zero. Figure 8.5 and Figure 8.6 show that the model consistently calculates a shorter value of $T_{C(S)}$ than that which was measured experimentally. This difference between the values obtained by the model and experiment is in the order of between 0.5ms and 1.0ms. These figures also showed that the model consistently calculated a shorter value of $T_{C(B)}$ than that which was measured experimentally; $T_{C(B)}$ being the time taken for the ball displacement to return to zero.

It has been commented that the magnitude of the ball COM displacement (and stringbed displacement) which is calculated by the model during impact, is different to that measured experimentally. Also, the contact times which were calculated by the model were different to those obtained experimentally. This comparison has so far only been made for the two impact velocities shown in Figure 8.5 and Figure 8.6. However, data was collected for many other impact velocities. A method of summarising this data so that it can be neatly presented involves a consideration of only the important measurements of the *Displacement-Time* curves. The four important measurements are defined in Figure 8.7. Since all the curves shown in Figure 8.5 and Figure 8.6 have a similar shape, they can all be defined by the maximum displacement and the contact time; these parameters being defined for both the stringbed and ball COM displacements.

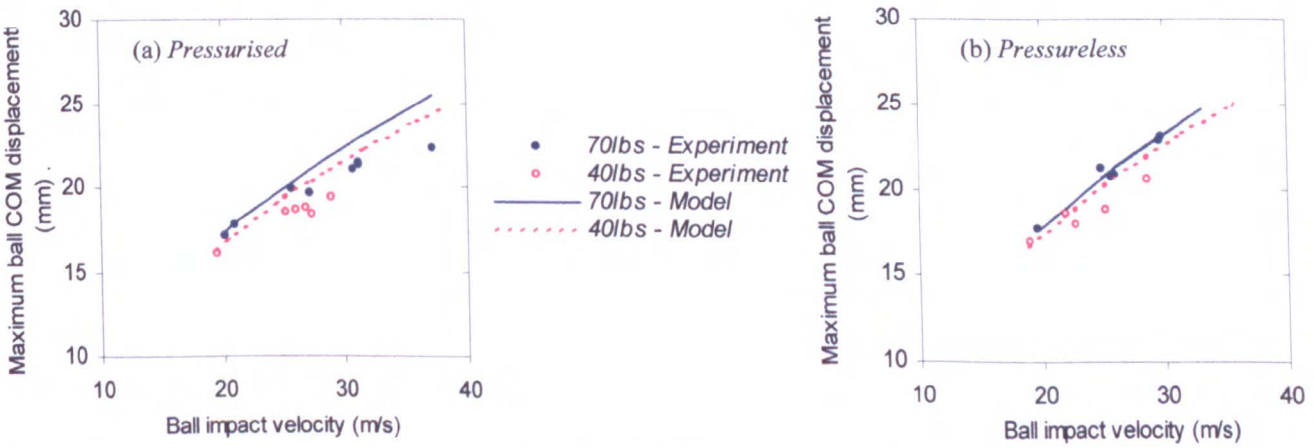

Figure 8.8 The maximum ball centre-of-mass displacement $x_{B(MAX)}$, which occurs during an impact between a ball and head clamped racket. The model and experiment data is plotted for two ball types.

Figure 8.8 (a) and (b) show the maximum ball centre-of-mass displacement $x_{B(MAX)}$ plotted against the ball impact velocity, for the *Pressurised* and *Pressureless* balls respectively. These figures show that the maximum ball COM displacement, which is calculated by the model, is generally larger than that which is measured experimentally.

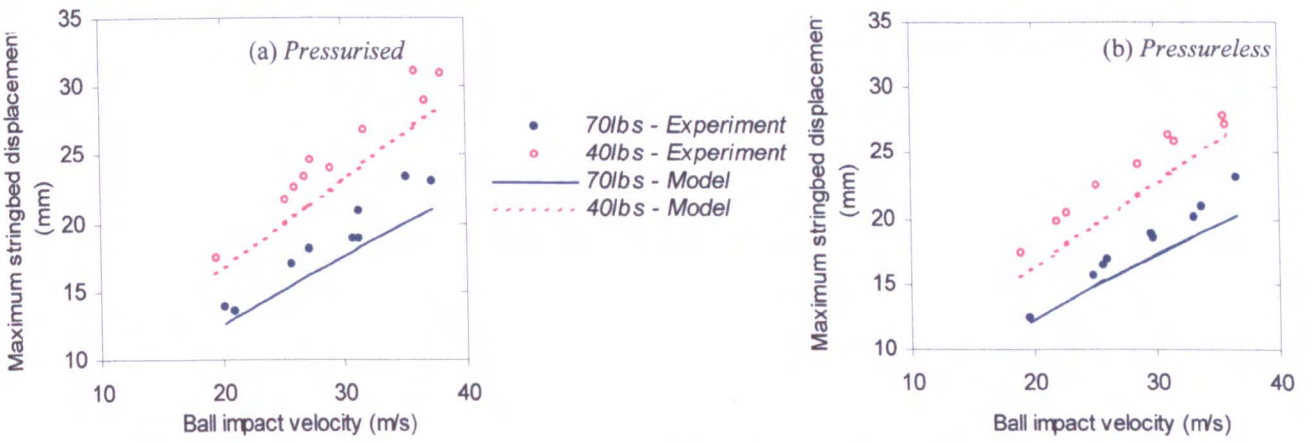

Figure 8.9 The maximum stringbed displacement $x_{S(MAX)}$, which occurs during an impact between a ball and head clamped racket. The model and experiment data is plotted for two different ball types.

Figure 8.9 (a) and (b) show the maximum stringbed displacement $x_{S(MAX)}$ plotted against the ball impact velocity, for the *Pressurised* and *Pressureless* balls respectively. These figures show that the stringbed displacement which is calculated by the model is consistently lower than that measured experimentally. The magnitude of this difference ranges from 1mm to approximately 4mm.

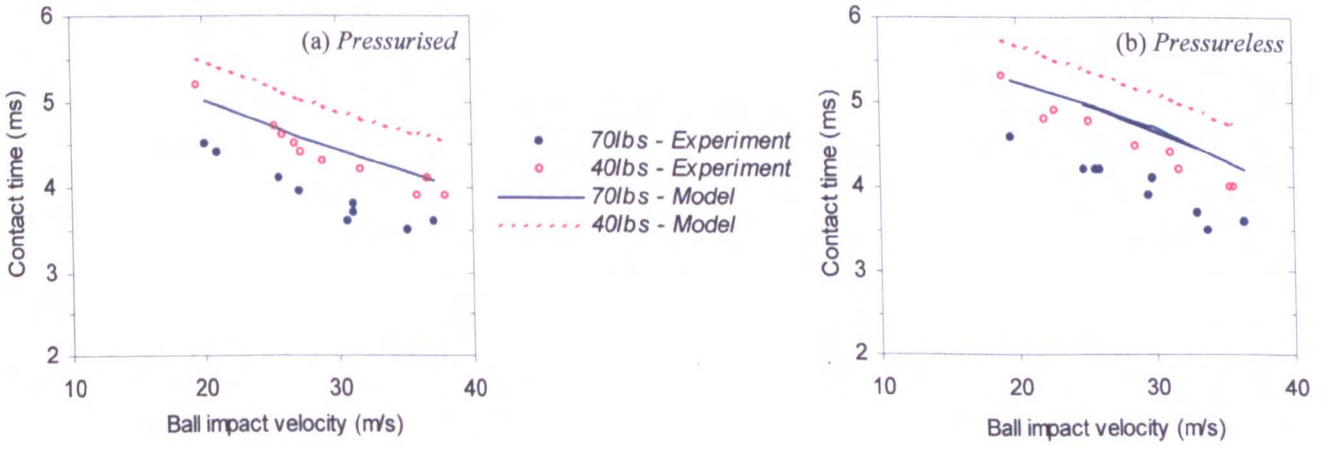

Figure 8.10 The contact time $T_{C(S)}$ for an impact between a ball and head clamped racket; $T_{C(S)}$ being defined as the time taken for the stringbed displacement to return to zero. The model and experiment data is plotted for two different ball types.

Figure 8.10(a) and (b) illustrate the data for the contact time $T_{C(S)}$, for *Pressurised* and *Pressureless* balls respectively. In these figures, both the model and experiment data is presented. The term $T_{C(S)}$ is defined in Figure 8.7, and corresponds to the period of time from initial contact until the

stringbed displacement returns to zero. It can be seen the values of contact time which are calculated by the model are consistently larger than those which have been measured experimentally. The difference between the model and experiment data is generally between 0.4 and 0.8ms, for both ball types and string tensions.

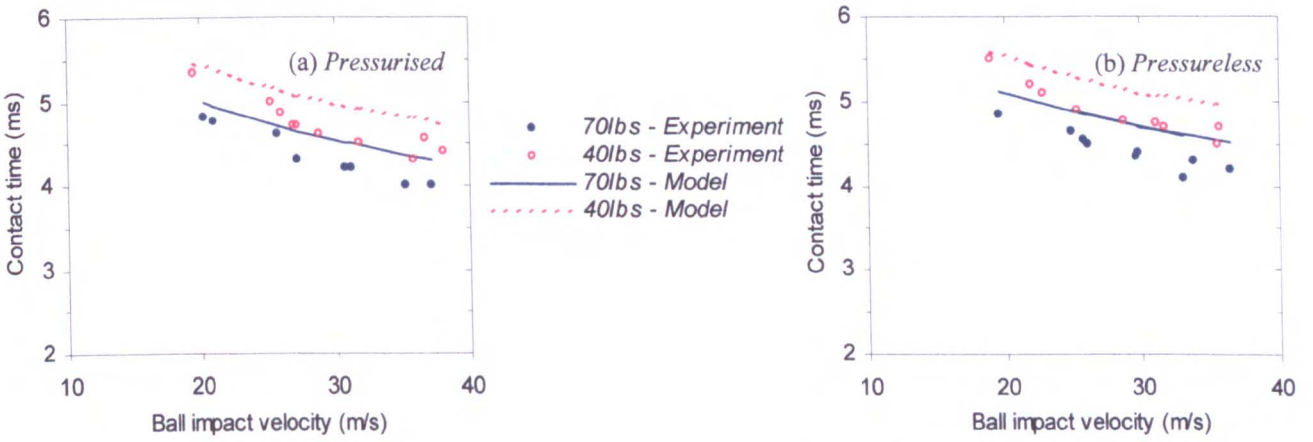

Figure 8.11 The contact time $T_{C(B)}$ for an impact between a ball and head clamped racket; $T_{C(B)}$ being defined as the time taken for the ball COM displacement to return to zero. The model and experiment data is plotted for two different ball types.

Figure 8.11 (a) and (b) illustrate the data for the contact time $T_{C(B)}$, for both the model and experiment data. The term $T_{C(B)}$ corresponds to the length of time from initial contact until the ball COM displacement returns to zero. It can be seen that the values of contact time which are calculated by the model are consistently larger than those which have been measured experimentally. The difference between the model and experiment data is generally between 0.2 and 0.6ms, for both ball types.

(c) Discussion

It can be seen that there are two definitions for contact time ($T_{C(S)}$ and $T_{C(B)}$) and these have different magnitudes. It has been found that the model consistently exhibits a longer contact time than that measured experimentally, for both definitions. It is well established that a longer contact time corresponds to a relatively lower stiffness for the system. This implies that the model stiffness of the ball and/or stringbed is lower than that of the actual ball and stringbed. In the model, the ball and stringbed form a complex interacting system and therefore the properties of one component influences the properties of the other. However, to further the understanding of the impact, the two components will be briefly investigated separately.

Let it be initially proposed that the model stringbed k_S is not as stiff as the actual stringbed. This assumption would explain the longer contact times which have been calculated by the model. However, the calculated value of the stringbed displacement (in the model) is smaller than that which is measured experimentally. This observation implies that the model stringbed is stiffer than the actual stringbed, and thus contradicts the previous assumption. Therefore, it can not be

unanimously concluded whether the model stiffness of the stringbed is higher or lower than the actual stiffness.

The ball stiffness k_B shall now be considered. Again, it is initially assumed that the model stiffness of the ball is lower than that of the actual ball, because of the longer model contact times. The data in Figure 8.8 supports this because it shows that the ball centre-of-mass displacement which is calculated by the model is larger than that which is measured experimentally. This implies that the model ball stiffness is lower than that of the actual ball.

This brief analysis of the stiffness of the ball and stringbed has revealed that the accuracy of the model would be improved by increasing the stiffness of the ball. This would act to decrease both the contact time and the ball COM displacement which are calculated by the model, improving the correlation between the model and experimental data for these parameters. The current values of the ball stiffness parameter are defined using the data obtained for a ball impact on a rigid surface (as described in section 8.3.1). Therefore, it can be concluded that the results in this section imply that the structural stiffness of a tennis ball may be dependent on the nature of the surface that it is impacting on. More specifically, it is suggesting that a ball is effectively 'stiffer' for an impact on a stringbed, compared with an impact on a rigid surface.

The magnitude of the increase in ball stiffness that is required to improve the accuracy of the model is not known. However, a possible reason for this effective increase in the ball stiffness can be illustrated by considering the high speed video image in Figure 8.12.

Figure 8.12 shows a sequence of images that were captured using a high speed video system, in a separate experiment to that which has been described previously. The ball was propelled perpendicularly towards a head clamped racket (strung at 65lbs), and the impact was viewed obliquely, from the rear, using the camera. The displayed images were captured at intervals of 1.0 ms. This sequence shows that the entire surface of the ball stays in contact with the stringbed throughout impact. By contrast, for an impact between a ball and rigid surface, many authors (Cross 1999b, Dignall 2000b) have shown that the ball wall buckles during impact, and the central section of the ball losses contact with the surface. This buckling results in a rapid reduction in the stiffness of the ball, which is confirmed by *Force-Time* data obtained for an impact between a ball and force platform. This has been expanded upon in Chapter 4.

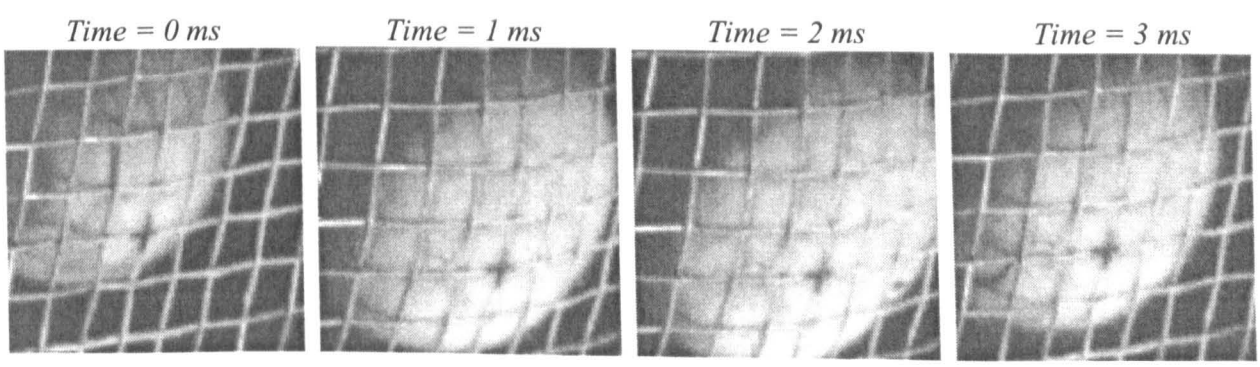

Figure 8.12 A sequence of high speed video images of a *Pressurised* ball impacting perpendicularly on a head clamped racket (viewed obliquely, from rear). The ball impact velocity was 25m/s.

Using the images in Figure 8.12 alone, it is not possible to define the mechanism which may be preventing the ball wall from buckling. However, it can be hypothesised that it is linked to the surface of the deformed stringbed, which is significantly different to that of a flat, smooth rigid surface. Firstly, the shape of the stringbed may act to 'cradle' the ball, supporting it around its perimeter thus making it more stable and less prone to buckling. Alternatively, the buckling may be inhibited by the high frictional force which acts due to the imbedding of the strings into the surface of the ball. It is very difficult to quantify the effect that friction will have on the ball stiffness. A theoretical study by Hubbard & Stronge (2001) confirmed that friction will increase the stiffness of a table tennis ball impacting on a rigid surface. Hubbard found that the stiffness increased by approximately 10% when the coulomb friction was increased from $\mu = 0$ to $\mu = 0.47$. However, clearly it is difficult to quantifiably relate those results to the model being discussed in this section.

Let it be assumed that the ball does not buckle during an impact with a head clamped racket. If this assumption is valid, then it would be reasonable to assume that the stiffness of the ball would be larger for an impact with a head clamped racket, compared with its stiffness during an impact with a rigid surface.

In this section, it has been assumed that the ball stiffness k_B was equal to that obtained empirically for an impact on a rigid surface. However, it was then shown that this stiffness appeared to be too low. This conclusion was based on the observation that the values of the contact time and ball centre-of-mass displacement which were calculated by the model were greater than those measured experimentally. This discussion has hypothesised that the ball stiffness k_B should be increased to improve the accuracy of the model. A possible reason to justify an increase in stiffness has been given. However, this analysis has not generated a method of quantifying the magnitude of the increase in stiffness.

8.3.3 Summary

In this section, a visco-elastic model of an impact between a ball and head clamped racket has been discussed. This model can be used to calculate a number of variables for the impact, including the ball rebound velocity and the contact time. The model of the ball component was the same as that used to simulate a ball impact on a rigid surface. The stringbed stiffness was effectively equal to that which had been experimentally obtained for a quasi-static compression of the stringbed. The stringbed was assigned a damping parameter which was based upon data collected by other researchers.

In this section, the output from the model was compared with the experimental data for an impact between a ball and head clamped racket. The observations are summarised as follows,

1. The ball rebound velocity that was calculated by the model was lower than that measured experimentally.
2. The stringbed displacement that was calculated by the model was lower than that measured experimentally.

3. The ball centre-of-mass displacement of the ball which was calculated by the model was larger than that which was measured experimentally.
4. The contact time which was calculated by the model was longer than that which was measured experimentally.

It was concluded that the model ball stiffness k_B was lower than the stiffness of the actual ball. In this section, the model ball stiffness k_B was defined using the data collected for an impact on a rigid surface. However, it was then proposed that the same ball will be effectively stiffer during an impact with a head clamped racket because the ball wall does not buckle.

In the following section, the model solution is modified to assess the effect of increasing the ball stiffness k_B.

8.4 Modelling Technique – 2nd Attempt

8.4.1 Introduction

In section 8.2, a visco-elastic model of an impact between a ball and head clamped racket was derived. This model contains a collection of springs and dampers which represent the structural stiffness and material damping of the ball and stringbed. The ball was represented by a spring in parallel with two dashpot dampers. The spring stiffness was defined as k_B and the two dampers were defined using the parameters c_B and c_M. The stringbed was represented using a spring in parallel with a damper that were defined as k_S and c_S respectively. A numerical analysis is used to solve the model and therefore the magnitude of each parameter can vary throughout impact.

The model can be used to calculate a number of variables for the impact, including the ball rebound velocity and the contact time. However, to obtain this solution, the magnitude of the parameters k_B, c_B, c_M, k_S and c_S need to be defined using realistic values. In section 8.3, a possible method was discussed in which the ball parameters (k_B, c_B, c_M) were the same as those which were derived for an impact between a ball and rigid surface. The stringbed stiffness was equal to that which had been experimentally obtained for a quasi-static compression of the stringbed. The stringbed was assigned a damping parameter which was based upon data collected by other researchers. In section 8.3, the output from the model was compared with the experimental data that is presented in section 7.2. In brief, it was concluded that the model ball stiffness k_B was effectively smaller than that of the actual ball. Therefore, in this current section, the model solution shall be repeated using higher values of the ball stiffness parameter k_B to assess whether such a modification will improve the accuracy of the model. The same combination of springs and dampers are used to model the impact between a ball and head clamped racket, as was described in section 8.2. Also, the same assumptions are to be used to define the stiffness and damping of the stringbed as were discussed in section 8.3. The only difference between the model in this current section, and that in section 8.3, is that a modified assumption is to be made in regard to the ball stiffness k_B.

8.4.2 Determining the visco-elastic model parameters

In this current section, the generic model which was discussed in section 8.2 is to be used to model the impact between a ball and head clamped racket. The stringbed stiffness and damping parameters (k_S and c_S) are to be defined in the same way as they were in section 8.3, and therefore the details are not repeated here. The definitions described in section 8.3 for the material damping and momentum flux forces which act on a deformed ball during impact (c_B and c_M) are also to be used in this section. The only difference between the work in this section and that in section 8.3, is in regard to the ball stiffness, defined as k_B.

In the section 8.3, it was assumed that the ball stiffness k_B was very high during a short period at the start of the impact. The parameter k_B was assigned a value of k_{SHELL} for the first 0.2ms of impact; k_{SHELL} being arbitrarily chosen as 80kN/m. After the first 0.2ms of impact, the parameter k_B is defined using,

$$k_B = k_{B(0)} + A_K\left(x_B - x_S\right)^{\alpha} \qquad [8.21]$$

These assumptions had been made in the derivation of the model for a ball impacting on a rigid surface, which is discussed in Chapter 5. In that work, experimental data obtained using a force platform was used to illustrate that the ball buckles at an instance of ~0.2ms after initial contact. This was simulated in the model by assuming a high initial stiffness, followed by a sudden transition to a lower stiffness. In section 8.3, it has since been shown that the ball may not buckle in the same way for an impact on a head clamped racket, as it does for a similar impact on a rigid surface. Therefore, the assumption of a transition in the stiffness is not necessarily valid, and may simply be adding an unnecessary complication to the model. Thus, in the model in this current section, the stiffness of the ball is to be defined using 8.21, for the entire impact. For interest, it should be noted that the this modification has negligible effect on the overall model solution, as the high stiffness only acts for a relatively short length of time.

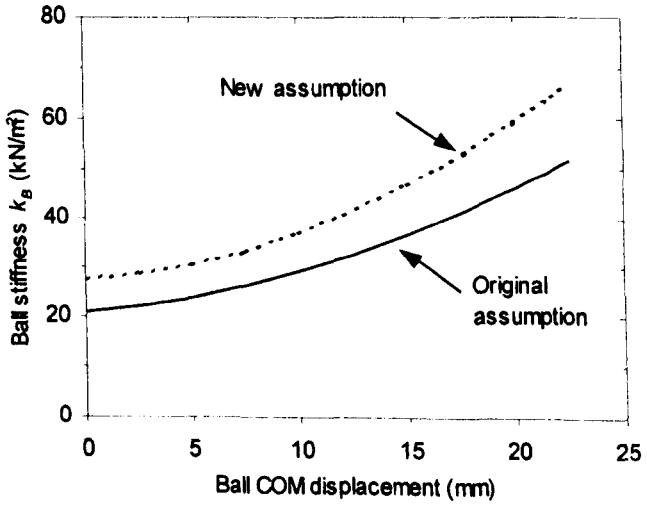

Figure 8.13 Illustration of a possible new function to describe the ball stiffness in the model.

Table 8.2 shows the value of the spring parameters ($k_{B(0)}$, A_K and α) which were used in section 8.3 to define the stiffness of the spring k_B, using [8.21]. An informative way of illustrating the physical significance of these parameters involves the use of graph of the ball stiffness k_B plotted as a

function of the ball COM displacement x_B. In Figure 8.13, such a plot is presented for a *Pressurised* ball. In this figure, the ball stiffness is plotted for two different assumptions; these being defined as (1) 'original assumption' and (2) 'new assumption'. The 'original assumption' plot was calculated using [8.21] and the same values of $k_{B(0)}$, A_K and α that had been originally assumed in section 8.3. Also shown in Figure 8.13 is an arbitrary plot of a proposed 'new' ball stiffness k_B. This is shown merely to illustrate a possible alternative function to define the value of k_B, and the method used to obtain this curve is described below.

The 'new' function which describes the ball stiffness k_B that will be used in the model in this section is assumed to take the form of [8.21]. Also, for simplicity, it is assumed that the 'new' stiffness will be equal to a constant factor K_{MOD} multiplied by the original stiffness, for all values of x_B. The ball stiffness for the 'original' and 'new' assumption are defined as $k_{B(original)}$ and $k_{B(new)}$ respectively. Therefore, the assumed relationship between the two can be defined as,

$$k_{B(new)} = K_{MOD} \times k_{B(original)} \qquad [8.22]$$

It was arbitrarily assumed that the value of K_{MOD} was equal to 1.3; this implying that the ball is effectively 30% stiffer for an impact on a head clamped racket compared with such an impact on a rigid surface.

The value of $k_{B(new)}$, at any value of $(x_B\text{-}x_S)$, could simply be obtained by determining the relevant value of $k_{B(original)}$, using [8.21] and the value of $k_{B(0)}$, A_K and α from section 8.3, and then multiply this value by K_{MOD}. However, a neater solution would be obtained by determining a new set of values of $k_{B(0)}$, A_K and α which give a stiffness that is 30% larger than that obtained previously. The value of $k_{B(new)}$ could then be obtained directly from [8.21], using the new parameters. The value of the new parameters can easily be obtained by multiplying $k_{B(0)}$ and A_K each by 1.3 (α remaining unchanged). These parameters give an increased ball stiffness equal to 30% compared to the original set of values of $k_{B(0)}$, A_K and α.

Table 8.4 The new assumptions for the spring parameters $k_{B(0)}$, A_K and α for the two ball types. The damping coefficient A_C is also shown.

Ball type	$k_{B(0)}$ (kN/m)	A_K (kN/m^2)	α	A_C (kNs/m^3)
Pressurised	27.3	20800	1.65	3.5
Pressureless	29.9	16250	1.70	4.0

The spring parameters shown in Table 8.4 can be used in conjunction with [8.21] to define the ball stiffness k_B throughout impact. The other features of the model are identical to those described in section 8.3, and therefore the solution is complete. As before, it is assumed that the force which acts on the ball is zero for ball COM displacements of less than 2mm, during the compression phase. This accounts for the low stiffness of the cloth and is the same assumption as that used in section 8.3.

As in section 8.3, the model was solved for *Pressurised* and *Pressureless* balls, for impacts on head clamped rackets with two different string tensions (40lbs and 70lbs). The values calculated by the model are compared with experimental data.

8.4.3 Results - Comparison of Model and Experiment results

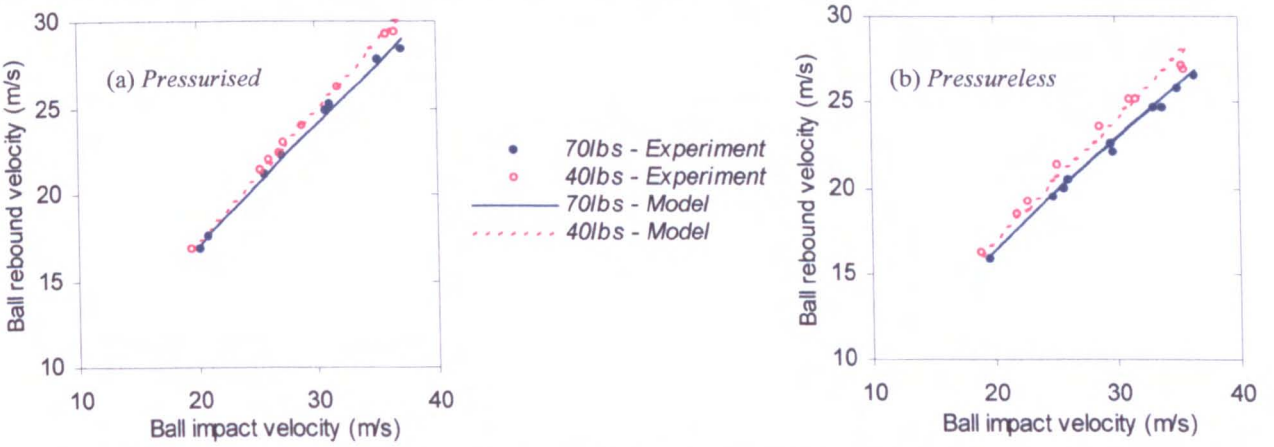

Figure 8.14 Comparison of the ball rebound velocity measured for the experiment and model.

Figure 8.14 shows a comparison of the ball rebound velocity calculated by the model and that measured experimentally. This data is presented separately for the *Pressurised* and *Pressureless* balls. It can be seen that the model predicts the experimentally obtained ball rebound velocity to within approximately 0.5m/s for all combinations of ball type and string tension. This difference is of the same order of magnitude as the scatter in the experimental data.

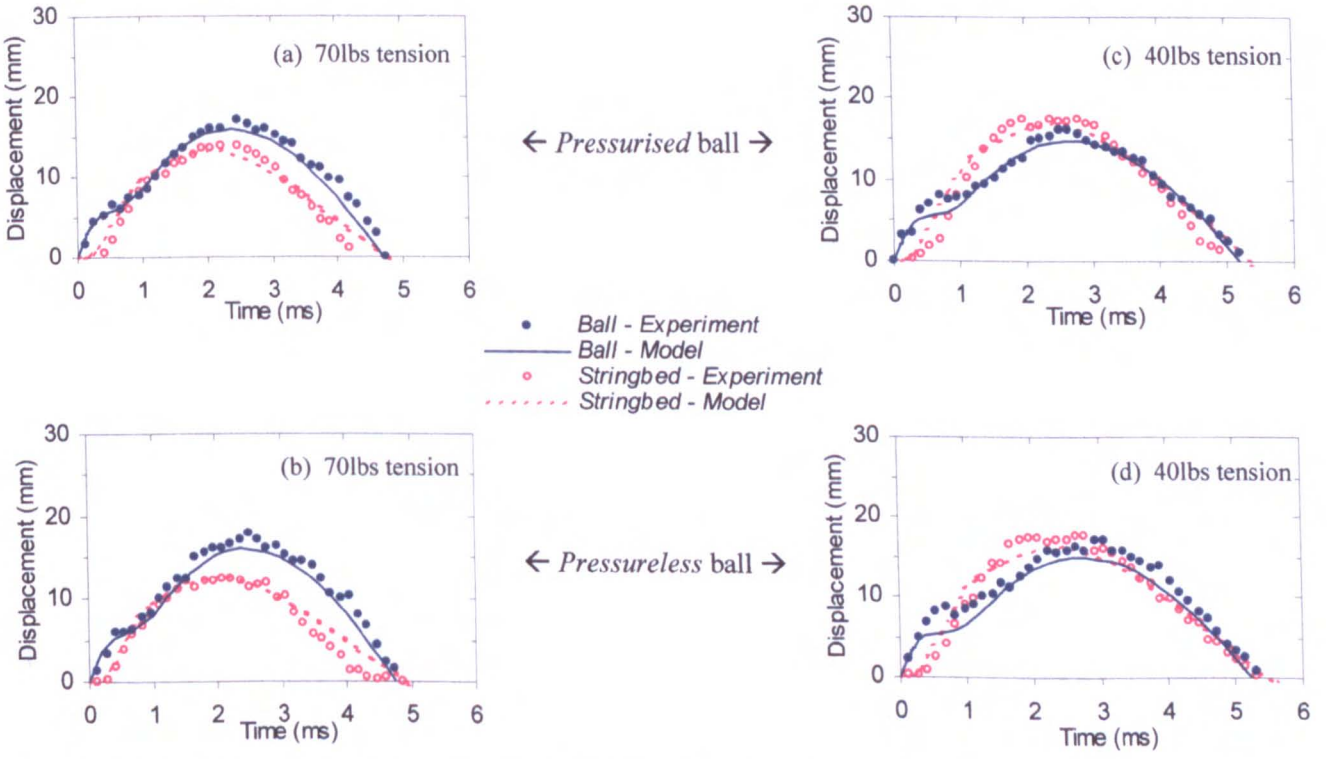

Figure 8.15 Ball centre-of-mass displacement and stringbed displacement for an impact between a ball and head-clamped racket, for four different combinations of string tension and ball type. The ball impact velocity is 20m/s, and both the model and experiment data are presented.

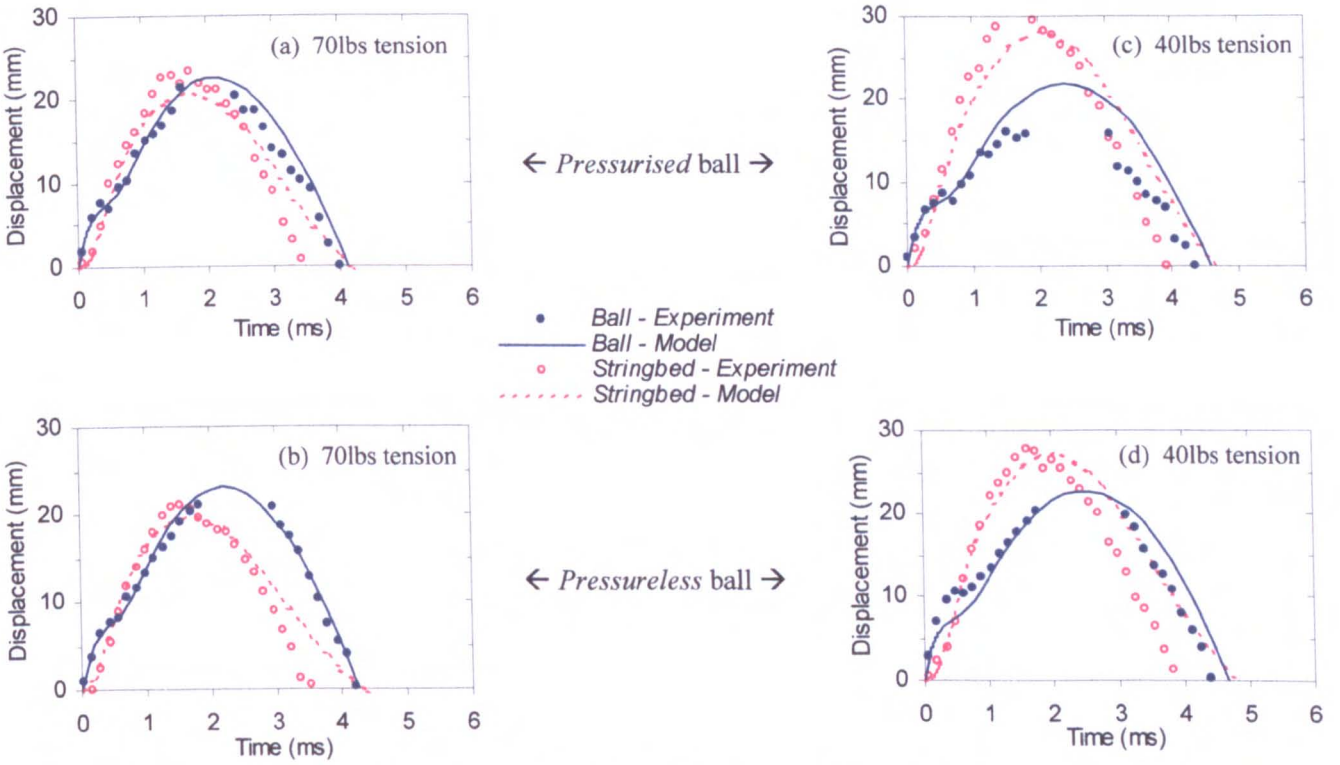

Figure 8.16 Ball centre-of-mass displacement and stringbed displacement for an impact between a ball and head-clamped racket, for four different combinations of string tension and ball type. The ball impact velocity is 35m/s, and both the model and experiment data are presented.

In Chapter 7, experiments were conducted to measure the stringbed and ball centre-of-mass displacement during impact. The experimental values of ball COM and stringbed displacement are plotted in Figure 8.15 and Figure 8.16, along with the results calculated by the model. These figures contain data for an impact between a ball and head clamped racket, at nominal impact velocities of 20m/s and 35m/s respectively. Data is presented in these figures for the two different ball types and two different tensions. The data for other impact velocities is given in the Appendix C.6.

The main characteristics of the plots have been discussed in section 8.3, and therefore the details are not repeated here. In general, the displacement data calculated by the model correlates with that measured experimentally, to within approximately 3mm, for most of the impact. The main point at which a poor correlation is found between the two sets of data occurs towards the end of the impact, for the values of stringbed displacement. It can be seen that the experimentally measured stringbed displacement consistently reaches zero before that calculated by the model.

A method of summarising the above data so that it can neatly be presented is performed by only considering the important measurements of the *Displacement-Time* curves. As discussed in section 8.3, all the plots in Figure 8.15 and Figure 8.16 have a similar shape, and can therefore all be defined by the maximum displacement and contact time. These parameters are defined for both the stringbed and ball COM displacements; the respective contact time being defined as the time at which the displacement returns to zero. Therefore the data can be summarised by just four parameters.

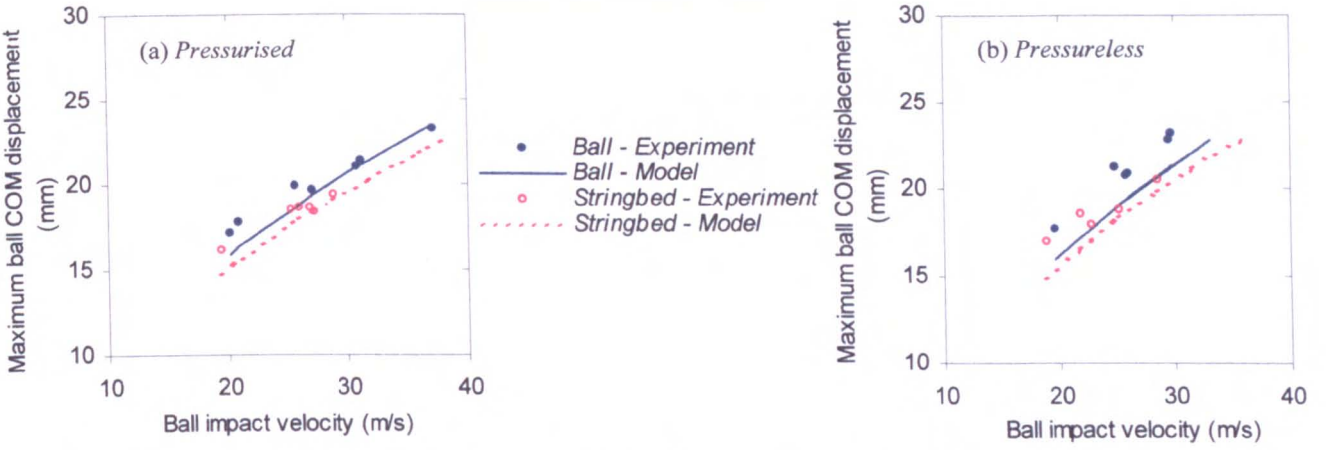

Figure 8.17 The maximum ball centre-of-mass displacement, which occurs during an impact between a ball and head clamped racket. The data is plotted for two different ball types.

Figure 8.17 (a) and (b) show the maximum ball centre-of-mass displacement $\delta_{B(MAX)}$ plotted against the ball impact velocity, for the *Pressurised* and *Pressureless* balls respectively. These figures show that the model ball COM displacement is generally smaller than that which is measured experimentally. However, it is noted that the maximum difference is only in the order of approximately 1 mm for the *Pressurised* ball and between 2 and 3 mm for the *Pressureless* ball. This data is implies that the model calculates a fractionally lower value of ball deformation compared with that which actually occurs.

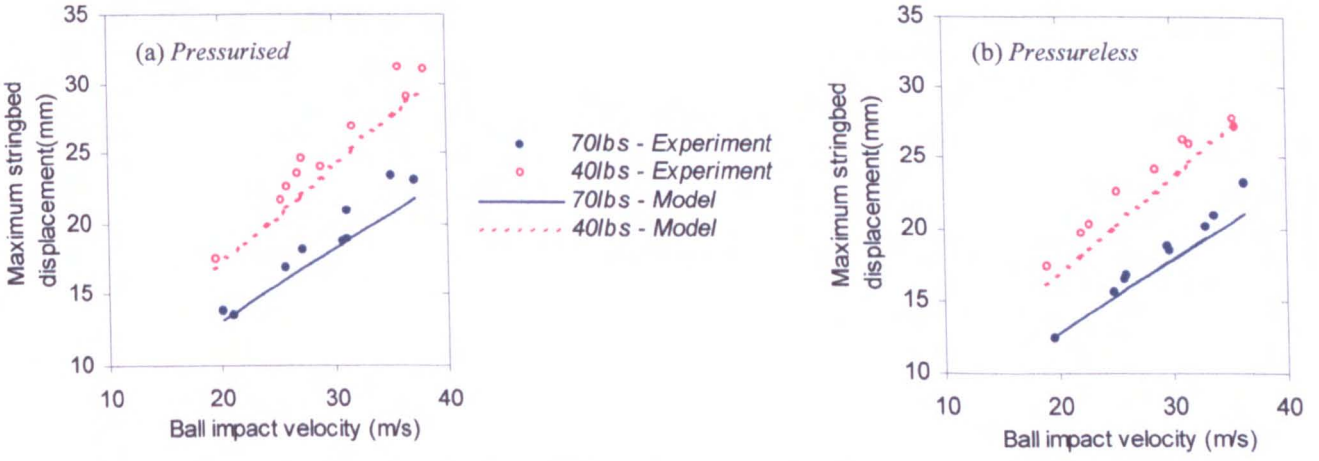

Figure 8.18 The maximum stringbed displacement, which occurs during an impact between a ball and head clamped racket. The model and experiment data is plotted for two different ball types.

Figure 8.18 (a) and (b) show the maximum stringbed displacement $\delta_{S(MAX)}$ plotted against the ball impact velocity, for the *Pressurised* and *Pressureless* balls respectively. These figures show that, for both string tensions, the model stringbed displacement is consistently lower than that measured experimentally. The magnitude of this difference is generally between 1 and 2mm, which is clearly small, and is less than that which was found in the previous modelling attempt in section 8.3.

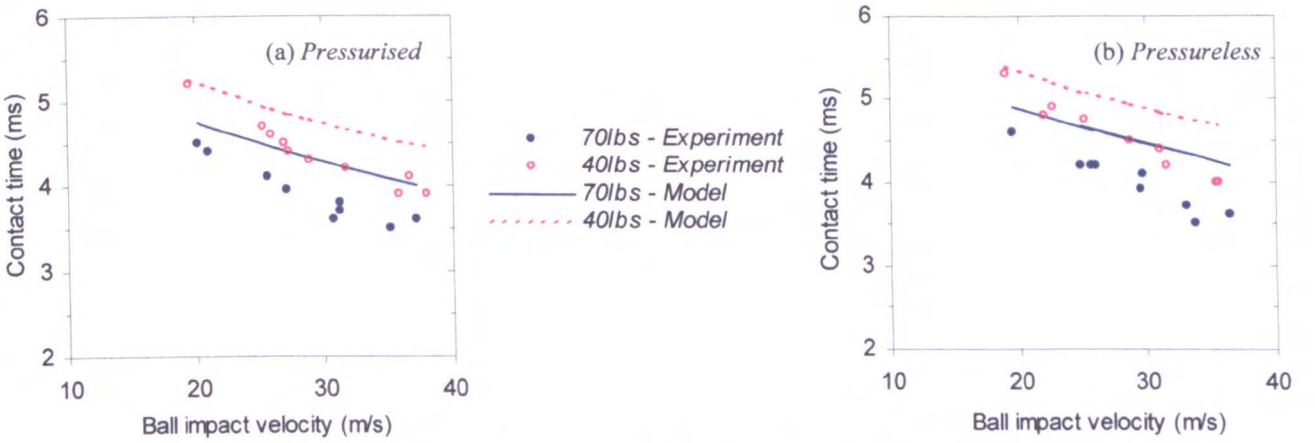

Figure 8.19 The contact time $T_{C(S)}$ for an impact between a ball and head clamped racket; $T_{C(S)}$ being defined as the time taken for the stringbed displacement to return to zero. The model and experiment data is plotted for two different ball types.

Figure 8.19 (a) and (b) illustrate the data for the contact time $T_{C(S)}$, for *Pressurised* and *Pressureless* balls respectively. In these figures, both the model and experiment data is presented. The term $T_{C(S)}$ corresponds to the length of time from initial contact until the stringbed displacement returns to zero. It can be seen the values of contact time which are calculated by the model are between 0.2 and 0.6ms longer than those which have been measured experimentally; the difference being largest for the higher speed impacts. This compares with a difference of between 0.4 and 0.8ms which was found in section 8.3 (for the first modelling attempt) and therefore this data implies a small improvement in the accuracy of the model.

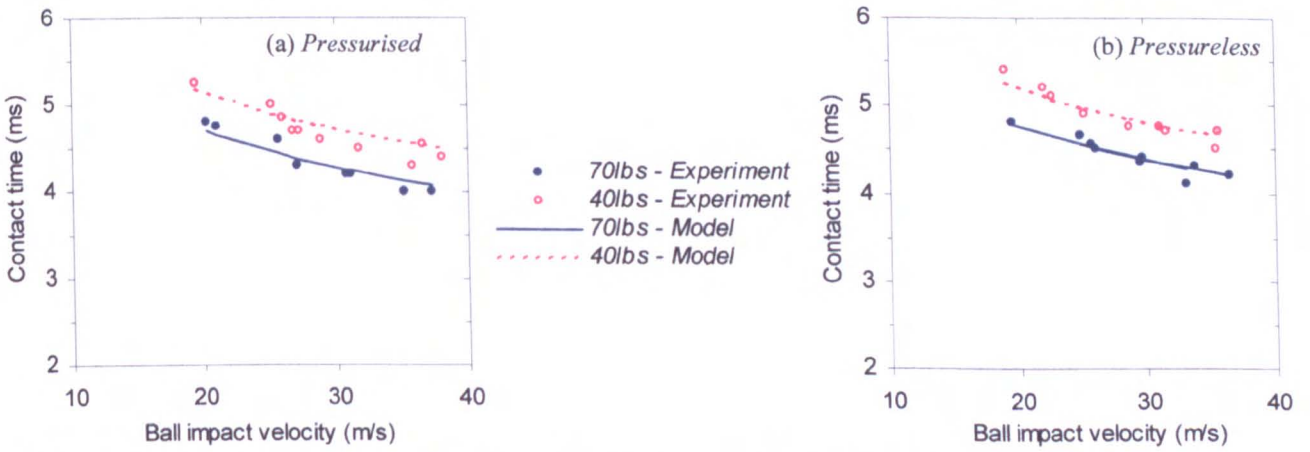

Figure 8.20 The contact time $T_{C(B)}$ for an impact between a ball and head clamped racket; $T_{C(B)}$ being defined as the time taken for the ball COM displacement to return to zero. The model and experiment data is plotted for two different ball types.

Figure 8.20 (a) and (b) illustrate the data for the contact time $T_{C(B)}$, for both the model and experiment data. The term $T_{C(B)}$ corresponds to the length of time from initial contact until the ball COM displacement returns to zero. It can be seen that the values of contact time which are calculated by the model exhibit a good correlation with the values that were measured experimentally, to within 0.2ms. It should be noted that this difference between the two sets of data is of the same order of magnitude as the scatter for the experimental values. In the previous

modelling attempt, discussed in section 8.3, a difference of between 0.4 and 0.8ms was found between the model and experiment data. This signifies a clear improvement in the modelling method.

8.4.4 Discussion

In this section, a visco-elastic model of a ball impact on a head clamped racket has been discussed. This model is identical to that which was described in section 8.3, except the model ball stiffness has been increased by approximately 30%. This value had to be arbitrarily chosen as there is no analytical solution to define the correct value.

It has been found that this modification significantly improves the correlation between the model results and those which were measured experimentally. For example, the ball rebound velocity which was calculated by the model correlates to within approximately 2.5% of the values obtained experimentally. This compared with a difference between the two sets of data of 5-10% which was found in section 8.3 for the previous modelling attempt.

Similarly, the model predicted the contact time $T_{C(B)}$ to within approximately 0.2ms of the experimental data; the variable $T_{C(B)}$ being defined as the time for the ball centre-of-mass displacement to return to zero. This is a significant improvement compared with the data shown in section 8.3.

The comparison between the model and experimental data for the other calculated/measured parameters exhibited a slightly poorer correlation than that for the ball rebound velocity and $T_{C(B)}$. It has been shown that the model consistently underestimates the maximum displacement of both the ball centre-of-mass and the stringbed, during impact. This initially implies a weakness in the model but a consideration of the validity of this comparison can be used to illustrate an alternative reason for this difference. The experimentally measured ball COM displacement is generally between 1 and 2mm larger than that calculated by the model. It should be noted that this displacement is not measured directly in the experiment, and is actually calculated from the measured values of ball deformation, using an empirical formula. It is likely that this empirical formula is subject to errors and therefore, the difference between the model and experiment data may simply be due to an error in the calculation of the experimental values of ball COM displacement. An alternative reason for the difference in the two sets of data can be proposed from a consideration of the limitations of the model. A tennis ball is a complex, multi degree-of-freedom (DOF) object which deforms considerably during impact. It is being modelled as a one DOF system which is capable of simulating a first order approximation of the structural stiffness of the object, but may not be able to model the higher order modes of vibration which will clearly have some influence on the results.

Another consistent difference between the model and the experimental data is that the value of $T_{C(S)}$ which is calculated by the model is consistently smaller than that determined experimentally; the variable $T_{C(S)}$ being defined as the time for the stringbed displacement to return to zero. Again, this can most likely be assigned to the simplification of the multi-DOF ball and stringbed structures as two 1-DOF visco-elastic models. These types of models can not simulate the complex modes of

vibration of these two structures, and therefore differences between the model and experimental data must be excepted.

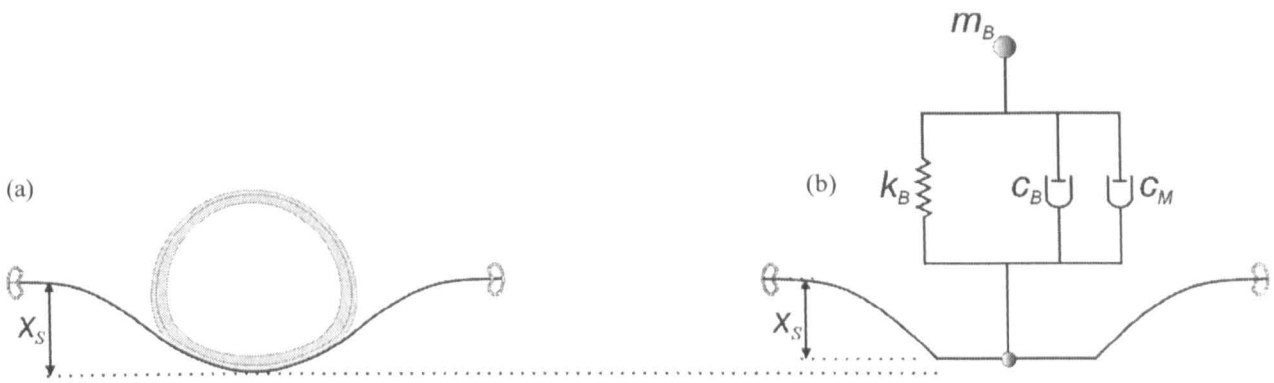

Figure 8.21 Schematic definition of the stringbed displacement x_S which is (a) measured experimentally and (b) calculated by the model.

The value of the experimentally measured stringbed displacement is between 1 and 2mm larger than that calculated by the model. However, an evaluation of this comparison reveals that the two methods are measuring subtly different parameters, as illustrated in Figure 8.21. A schematic illustration of the actual and modelled impacts are given in Figure 8.21 (a) and (b) respectively. The definition of the stringbed displacement x_S is given in each figure. In section 7.3, the shape of a deformed stringbed was measured experimentally, and this approximated shape is shown in Figure 8.21 (a). The key observation being that the displacement of the stringbed is not uniform across the contact area. However, the model has only one degree of freedom to describe this shape, and therefore the stringbed displacement for this case is effectively constant along the contact area. Therefore, the displacement calculated by the model effectively represents the 'average' displacement of the stringbed across its contact area. Thus it is not surprising that the stringbed displacement calculated by the model is less than that measured experimentally.

To conclude, the modification which has been implemented in the model in this section has resulted in an improvement in the accuracy of the model. Any small differences between the model and experimental can be assigned to the inherent weakness of using a simple two degree-of-freedom visco-elastic model to simulate the complex impact mechanism.

8.5 Applications of the model

8.5.1 Introduction

In section 7.2, a comparison between model and experiment data was made for the ball rebound velocity, contact time, stringbed displacement and ball deformation, for the different ball types and string tensions. As mentioned previously, the force which acts on the ball for an impact on a head clamped racket can not be measured experimentally. However, it can be calculated using the model which has been developed in section 8.4.

In this section the model will be used to calculate the forces which act on a range of ball types and string tensions to assess the effect that these two parameters have on the force which acts on the ball.

8.5.2 Calculated Force-Time curve

Figure 8.22 (a)-(d) show the force which is calculated by the model, for two different ball types and string tensions, for an impact velocity of 26m/s. The total force which acts on the ball is presented, along with the magnitude of the individual components of this force. It can be seen that the total force is very similar in all figures, for the first 0.1ms of impact. The only difference, during this period, is that the 'material damping' and 'momentum flux' forces are higher for the impacts on a racket strung at 70lbs. This can be explained by the fact that the racket strung at 70lbs has a higher stringbed stiffness, and therefore the ball is brought to rest faster, during this period. This means that the ball deforms faster, thus leading to higher values of these components. Also, the maximum 'material damping' force is higher for impacts on a racket strung at 70lbs, compared with a racket strung at 40lbs.

It can be seen that, for an impact on a racket with a specific string tension, the calculated maximum force is approximately 50N higher for the *Pressurised* ball compared with the *Pressureless* ball. This increased force is effectively due to the higher 'structural stiffness' component of the *Pressurised* ball. For a specific ball type, the maximum force which acts on the ball is approximately 100N higher for the racket strung at 70lbs, compared with that strung at 40lbs. The data also shows that the contact time is approximately 0.5ms shorter for the racket strung at 70lbs. These two differences can both be assigned to the higher stiffness of the racket strung at 70lbs.

The data in Figure 8.22 can not be experimentally verified. However, it should be noted that this model is (1) based upon the experimentally verified model of a ball impact on a rigid surface, and (2) gives approximately the same ball rebound velocity, contact time, stringbed displacement and ball centre-of-mass displacement as that which has been measured experimentally. Therefore, the magnitude of the impulse which acts on the ball and the duration of the force must be approximately equal to that which actually occurs in the real impact.

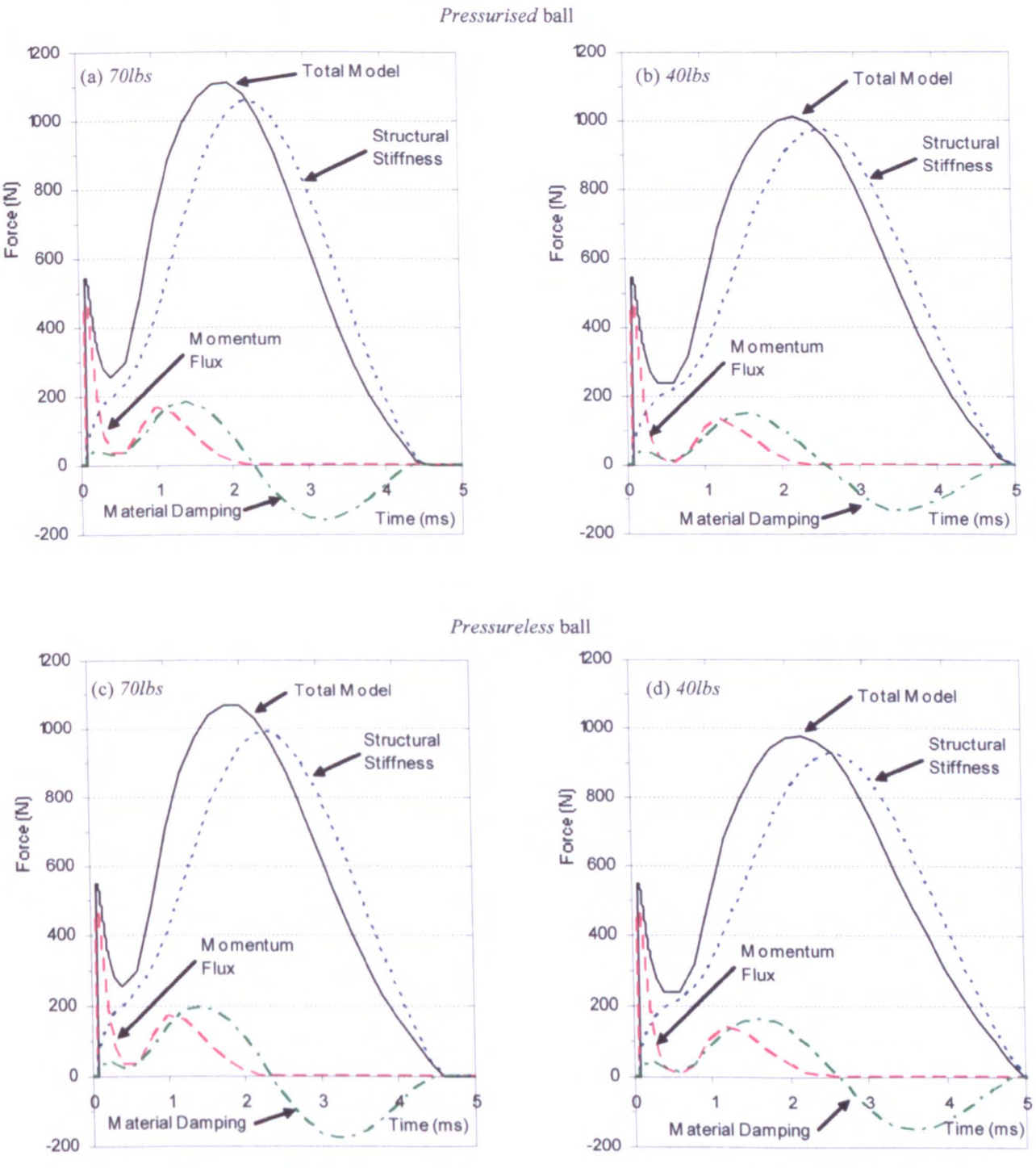

Figure 8.22 Force that acts on the ball for an impact with a head clamped racket. This force is calculated using the model, and the individual components of the model are presented separately. The impact velocity is 26m/s.

In section 7.2.6, a comparison was made between the experimentally measured ball deformation, contact time and ball rebound velocity for impacts on a rigid surface and on a head clamped racket. This comparison showed that the ball deformed more, rebounded slower and exhibited a shorter contact time for impacts on a rigid surface. A similar comparison can be made for the force values which are calculated by the models of the two different types of impacts. Figure 8.23 (a) shows the calculated forces for a model of a *Pressurised* ball impacting on a head clamped racket that has been strung at 40lbs. Figure 8.23 (b) shows the calculated forces for a model of a *Pressurised* ball impacting on rigid surface. The impact velocity is 26m/s for both impacts.

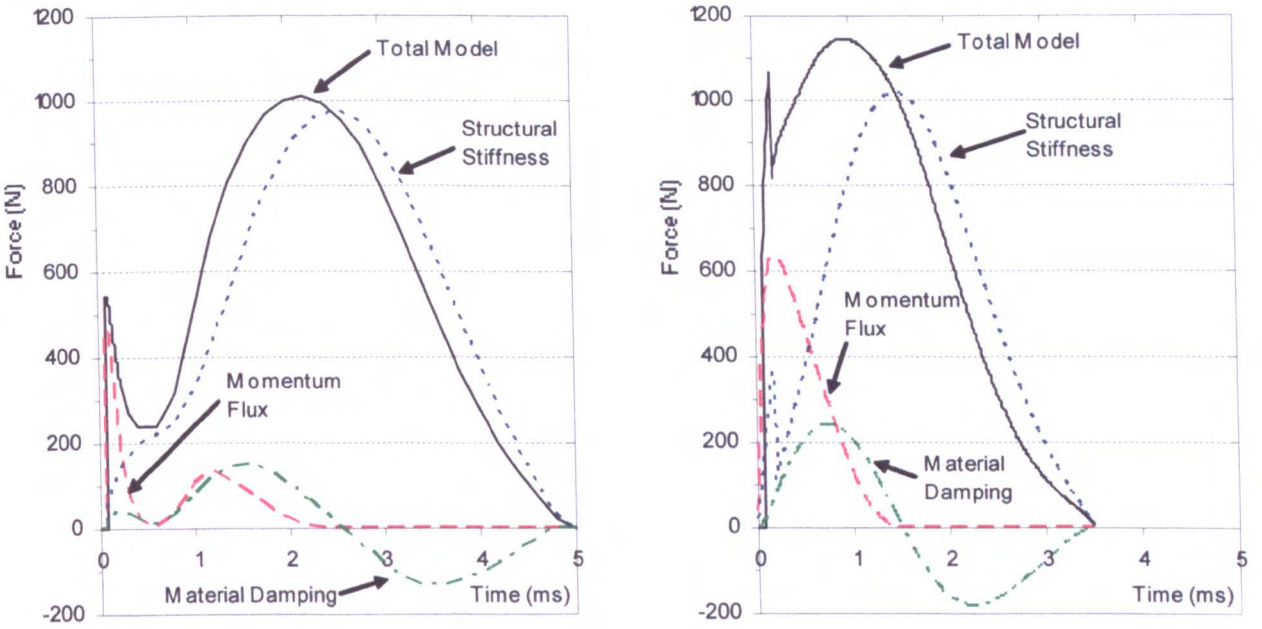

(a) Head clamped racket (b) Rigid surface

Figure 8.23 Force that acts on the ball for (a) an impact with a head clamped racket, and (b) an impact with a rigid surface. This force is calculated using the model, and the individual components of the model are presented separately. The impact velocity is 26m/s for both impacts.

The figures show that, during the initial 0.7ms of the impact, the force which acts on the ball during an impact with a rigid surface is considerably higher than that for the impact on a head clamped racket. During this period, the main component of the force is that due to the momentum flux and this component is considerably larger for the impact with a rigid surface, due to the higher ball deformation rate occurring in this type of impact. The 'material damping' component is also considerably higher during this period, for this type of impact. It is noticeable that the total model force exhibits a distinct drop in both models, at a time of approximately 0.2ms. However, it is interesting to note that this feature occurs for different reasons. In the rigid surface impact, it occurs due to the simulated 'buckling' of the ball wall and in the head clamped impact it is due to the momentum flux force rapidly reducing after initial contact. The maximum structural stiffness component of the force is similar for both types of impact, but the point at which this peak occurs is considerably later for the impact on a head clamped racket. The figures show that the contact time is considerably longer for an impact on a stringbed. This is due to the lower 'effective' stiffness of the system for an impact of this type.

8.5.3 Summary

It has been shown that the model can be used to calculate the force which acts on the ball during impact. The results showed that the maximum force which acts on a *Pressurised* ball, during impact, is approximately 5% higher than that which acts on a *Pressureless* ball. It was also shown that the force which acts on a tennis ball during an impact with a racket strung at 70lbs tension is 10% larger than for an impact with a 40lbs racket.

This model can be used to determine the force which acts on the stringbed, for an impact between a ball and head clamped racket. This model will developed in the later chapters of this study to simulate a ball impacting on a tennis racket which is not head clamped. In this type of impact, clearly the racket frame will deform during impact and this will need to be modelled by some suitable method. The magnitude and form of this frame deformation will be a function of the force applied to the frame by the stringbed. In this current chapter, a method of obtaining the force acting on a ball/stringbed during an impact between a ball and head clamped racket has been obtained. The next stage of the modelling procedure would clearly involve a development of this model to allow the simulation of an impact between a tennis ball and a racket that was supported using a method which was representative of a player's grip.

8.6 Discussion of model

8.6.1 Introduction

In this chapter, a model of a tennis ball impact on a head clamped tennis racket has been developed. In this model, the stringbed was simulated by a spring and damper in parallel, which were attached to a mass m_S. The stringbed was assigned a finite mass so that the model was physically representative of the actual impact mechanism. In this chapter, it has been assumed that the mass m_S is equal to an arbitrarily chosen value of 5g. In this section, this assumption will be investigated.

8.6.2 Assumption of the stringbed mass magnitude

Table 8.5 Comparison of the parameters calculated by the model for three different values of the stringbed mass m_S.

	Ball impact velocity = 15m/s			*Ball impact velocity = 30m/s*			*Ball impact velocity = 40m/s*		
	m_S = 5g	m_S = 0.2g	m_S = 20g	m_S = 5g	m_S = 0.2g	m_S = 20g	m_S = 5g	m_S = 0.2g	m_S = 20g
Ball rebound velocity (m/s)	13.0	13.2	12.4	24.1	24.1	23.3	31.0	30.9	30.3
Maximum stringbed displacement (mm)	10.3	10.3	11.5	18.2	18.1	19.2	23.2	23.0	24.1
Maximum ball centre-of-mass displacement (mm)	12.8	13.0	12.6	20.6	20.9	20.0	24.3	24.5	23.4
Contact time $T_{C(B)}$	4.98	4.96	5.15	4.28	4.21	4.52	4.01	3.92	4.27

The total mass of the strings in a tennis racket is typically 20g but only a fraction of the stringbed actually displaces during impact. The correct mass m_S could actually be equal to any value between 0g and 20g. Therefore, in this section the model solution is calculated using these two extreme values (m_S = 0.2g and m_S = 20g), as well as the value m_S = 5g. It should be noted that a stringbed mass m_S = 0g does not provide a valid solution of the model). The solution was calculated and the effect of the different magnitudes of the masses was quantified by comparing the model output for several parameters (e.g. ball rebound velocity). The parameters were obtained for a model of an impact between a *Pressurised* ball and a racket strung at 70lbs. Three different ball impact velocities were tested which were 15, 30 and 40m/s, and the model results for a range of parameters are given in Table 8.5. Table 8.5 gives the model output for four of the main parameters, as listed in the first column. It can be seen that the ball rebound velocity is very similar for impacts where a stringbed mass m_S of either 0.2g or 5g is assumed. Furthermore, both these stringbed masses give very similar values of values of the other three parameters given in the table. However, if a value of m_S = 20g is assumed then the ball rebound velocity is reduced by approximately 0.7m/s (2-6%). This is clearly due to the extra energy stored in the stringbed which is not recovered by the ball. Also, the maximum stringbed displacement is larger, and the maximum ball COM displacement is smaller, for the assumed mass m_S = 20g. The contact time for the impact is also increased due to this larger mass.

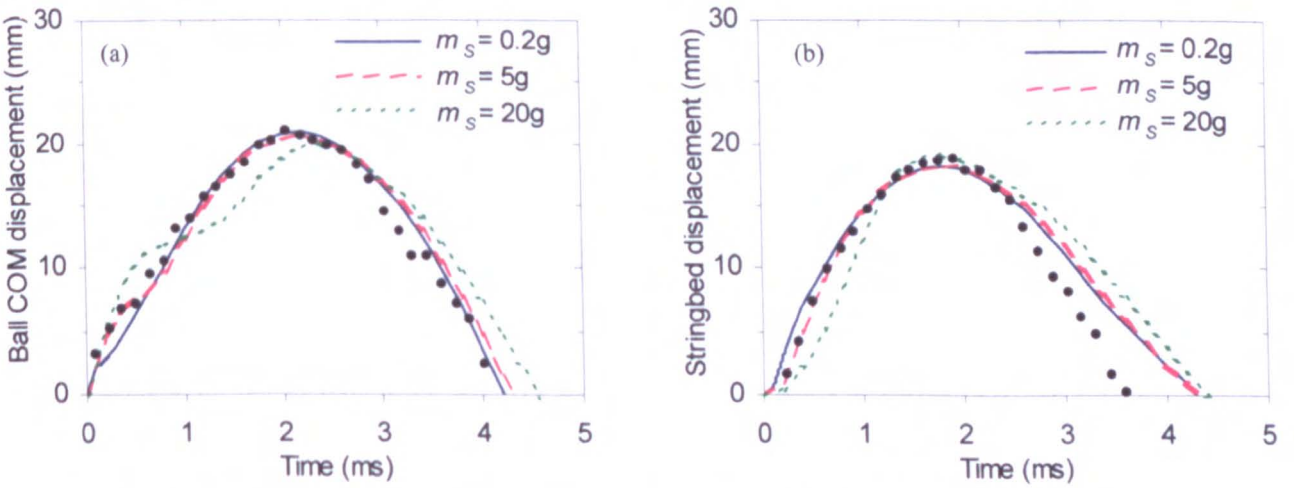

Figure 8.24 (a) Ball centre-of-mass displacement and (b) stringbed displacement for an impact between a ball and head-clamped racket, for three different values of stringbed mass m_S. The ball impact velocity is 30m/s. The data points in these figures represent typical experimental data.

Figure 8.24(a) shows the magnitude of the ball centre-of-mass displacement during impact, for three different values of the model stringbed mass m_S. It can be seen that the experimental data corresponds most closely with the model that assumes a stringbed mass m_S of 5g. The model solution which assumes a stringbed mass m_S of 0.2g is very similar to that with m_S = 5g, except that the characteristic kink at the start of the impact is not evident for the lower stringbed mass. The model solution which assumes m_S = 20g is vastly different to that of the experimental data.

Figure 8.24(b) shows the magnitude of the stringbed displacement during impact, for three different values of the model stringbed mass m_S. Similar trends were found in this figure, as were found in Figure 8.24(a); the most accurate model being that which uses a stringbed mass of 5g.

8.6.3 Discussion

In this section it has been shown that the model solution, for a visco-elastic model of a ball impacting on head clamped racket, is very similar for stringbed masses of 0.5g and 5g. If a stringbed mass of 20g is assumed, then the model solution typically differs by approximately 5-10%, compared with that which assumes a mass of 5g. In the previous work in this chapter (sections 8.3-8.5) it has been assumed that the stringbed mass m_S is equal to 5g. In this section, it has been shown that the assumed magnitude of this mass only effects the model solution by a maximum of 5-10%. This suggests that it was reasonable to assume the arbitrary value of 5g for the stringbed mass.

8.6.4 Application of the results

In the following chapter, a model of an impact between a tennis ball and freely suspended racket is to be developed. This model will be a development of the work which has been discussed in Chapters 6, 7 and 8, for an impact between a ball and head clamped racket. In these chapters, the model has included a component which simulates a finite stringbed mass. However, in this section it has been shown that the model solution is very similar for stringbed masses of 0.2g and 5g. Therefore, it can be concluded that the inclusion of a stringbed mass in the model adds an unnecessary complexity. The modelling work which has been discussed in this chapter could easily be repeated, using a model which does not include a stringbed mass. However, similar conclusions would be found as have been discussed in this chapter and therefore it is concluded that this work was not necessary. However, in the model of a ball impacting on a freely suspended tennis racket, which is discussed in the following chapter, it is to be assumed that the stringbed mass is zero. This assumption is made to simplify the required model.

8.7 Summary

In this chapter, a two degree-of-freedom visco-elastic model has been developed which can calculate the force that acts on the ball during an impact with a head clamped racket. The ball component of the model was identical to that derived for a model of a ball impact on a rigid surface. The stringbed component was assumed to have the same stiffness as that which was measured experimentally for a quasi-statically applied load. A small damping factor was incorporated into the stringbed model to account for the low level of hysteresis loss which has been empirically determined by other researchers.

The values calculated by the model were compared with data measured experimentally. It was found that the model underestimated the ball rebound velocity and the magnitude of the stringbed displacement during impact. It was also found that the magnitude of the ball centre-of-mass displacement and the contact time for the impact were consistently larger for the model compared with the experimental data. Using the comparisons made in this section it was concluded that the accuracy of the model would be improved by increasing the model ball stiffness k_B. The justification for such an increase was proposed based on observations of the shape of the ball surface that was in contact with the stringbed. It was concluded that the stringbed acted to 'cradle' the ball wall, inhibiting the onset of buckling which is known to reduce the structural stiffness during an impact with a rigid surface. Therefore the stiffness of the ball will be higher for an impact with a stringbed, compared to a similar impact with a rigid surface.

It was assumed that the ball stiffness should be increased by 30% and the model solution was repeated using this assumption. It was found that this modification resulted in the ball rebound velocity data that was calculated by the model correlating to with in 2.5% of the experimentally measured values. Similarly the model calculated values of contact time that were with in 5% of those measured experimentally. The values of the stringbed and ball COM displacement which were calculated by the model correlated to within approximately 2mm of those values measured experimentally. This small difference was accounted for by the inherent weakness of a simple two degree-of-freedom model being used to simulate a complex system that involves the interaction of two highly deformable objects.

It is not claimed that this visco-elastic model of a ball impacting a head clamped racket perfectly represents the real impact mechanism. Indeed, the assumption made regarding the magnitude of the increase in the ball stiffness was merely implemented to improve the correlation between the model and experiment results. However, it has been shown that the contact time, ball centre-of-mass displacement, stringbed displacement, and ball rebound velocity which are calculated by the model correlate very closely with the experimentally measured data. Therefore the calculated force which is exerted on the ball during impact, which can not be measured experimentally, should be of a similar magnitude to that which actually occurs in the real impact. This model can also be used to accurately quantify the differences between different ball types and string tensions.

9. Impact between a Ball and Freely Suspended Racket – Modelling Techniques

9.1 Introduction

In the previous chapter, a model of a ball impacting on a head clamped racket was derived. The racket was restrained in this way to simplify the required model as the deformations of the frame did not need to be simulated. However, in the game of tennis a racket is held at the handle by a player and is therefore not rigidly clamped along its length. A thorough discussion of the simulation of a player's grip is presented in section 2.4.3, and is therefore not repeated here. To summarise, many researchers have concluded that a freely suspended racket is the most suitable method of replicating a player's grip for both experimental and modelling work. It should be noted that this assumption is only valid for the duration of the impact, which is acceptable since the motion of the racket after impact is not of immediate importance.

In this chapter, a model of a tennis ball impacting on a freely suspended racket is to be derived. In this model it is to be assumed that all the balls impact perpendicular to the stringbed, and the impact is located at a discrete point along the longitudinal (main) axis of the tennis racket.

The aims of this work are similar to those of the other chapters in this study in which a model of an impact has been derived. This work is sponsored by the International Tennis Federation and their main requirement for this model is that it can be used to simulate a typical impact between a ball and racket, in a game of tennis. Clearly this study could diversify into many fields of research (e.g. biomechanical science), however, this study is focused on the impact mechanism which occurs between the ball and racket. Therefore, the main aim of this work is to derive a model which can quantify the effect of, for example, ball mass or racket frame stiffness, on the displacement of the ball and racket during impact. For example, the model should have the ability to calculate the following parameters,

1. Ball rebound velocity.
2. Contact time.
3. Vibrations of the racket frame which are induced by the impact.

The derived model will be verified in a later chapter using experimental data, similar to the comparisons which have been conducted in previous chapters. This is not discussed further at this stage as it shall be presented in full in Chapter 10.

The model of an impact between a ball and freely suspended tennis racket involves three discrete components; these being the ball, stringbed and racket frame. The ball and stringbed are to be simulated using a visco-elastic model similar to that discussed in Chapter 8. This will be solved, as before, using a numerical analysis which can be used to calculate the time-dependent force that acts on the racket. In this chapter, the racket is to be modelled using two different techniques which

have been utilised by other authors and offer different degrees of complexity. The two different techniques are described separately, as follows.

(a) Rigid beam model of a tennis racket frame

The frame of the racket will be modelled as a rigid beam that has the same inertial properties as the racket. The inertial properties referred to here are the mass, balance point and mass moment of inertia. In this model, the time-dependent force is applied to the rigid beam as a point loading. The rigid beam/racket does not deform and therefore simple Newtonian mechanics can be used to determine the displacement of the beam, at any time interval, for the relevant time-dependent force. This modelling technique does not allow the vibrations of the racket frame to be calculated, but does offer a simple 1st order approximation of the impact mechanism.

(b) One dimensional, flexible beam model of a tennis racket frame

The second modelling technique discussed in this chapter attempts to calculate the deformation of the racket frame during, and immediately after, impact. This is to be performed by modelling the racket frame as a one dimensional flexible beam. The reasons for choosing this method have been discussed thoroughly in section 2.5.2 and therefore will only be summarised here. Many authors (Brody (1987), Kawazoe (1997a), Cross (1998)) have shown that the transverse vibration modes and location of the respective nodes for a freely suspended racket are very similar to those of a simple one-dimensional beam. It should be noted that this is only valid for impacts along the longitudinal axis because off-centre impacts induce torsional vibrations which are not simulated by a one dimensional beam.

The one dimensional beam will clearly be assigned the inertial properties of the racket that is being modelled. The beam will also be assigned a stiffness, or flexural rigidity, for a transverse loading which is equivalent to that of the racket frame. In this chapter, a method will be presented which enables the displacement of the beam to be calculated, for a time-dependent force. Initially it shall be assumed that the force exerted on the beam by the ball/stringbed system acts as a point loading. The model will then be developed to simulate a more realistic distributed loading of the beam.

The numerical solutions of the two racket modelling techniques (rigid and flexible beams) are presented in this following chapter.

9.2 Rigid body model of a tennis racket

9.2.1 General model

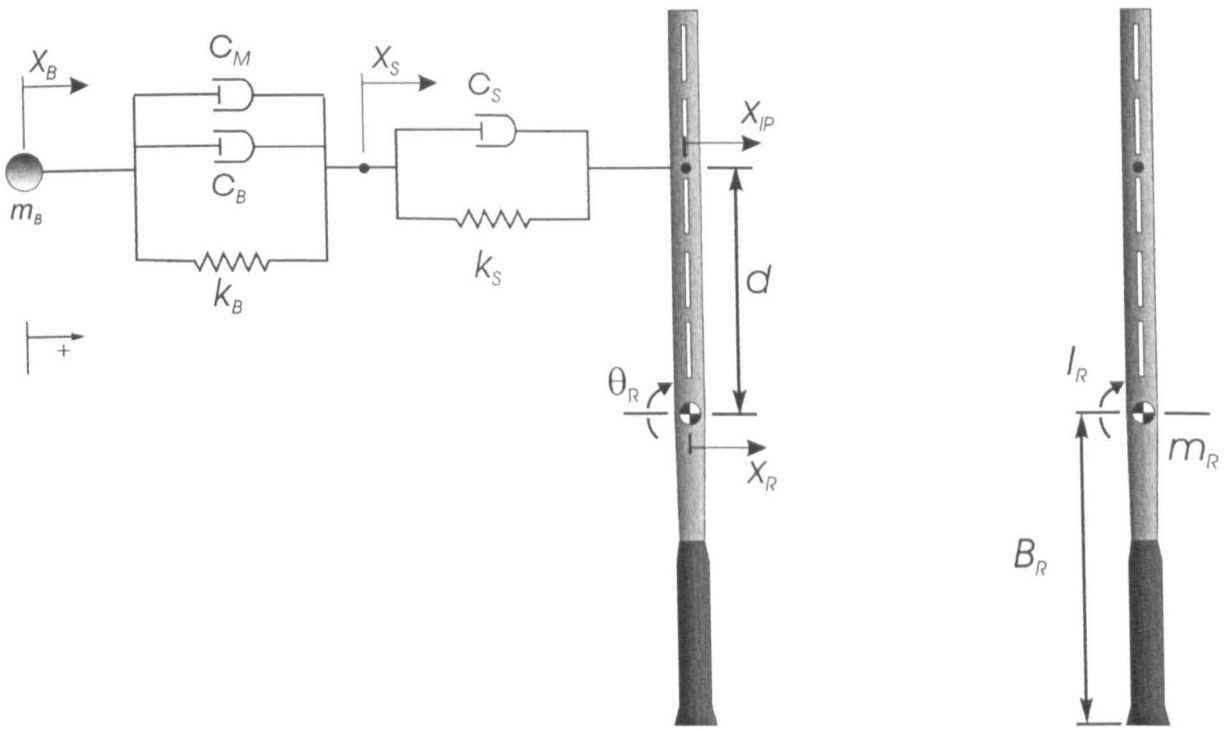

Figure 9.1 Illustration of a visco-elastic model of a ball impact on a freely suspended racket.

The ball and stringbed are to be modelled using a similar technique as that discussed in Chapter 8 for a model of an impact between a ball and head clamped racket, except for a couple of minor simplifications. The ball has been modelled as a spring in parallel with two dashpot dampers, as illustrated in Figure 9.1. The spring is used to simulate the structural stiffness of the ball and this parameter is defined as k_B. A dashpot damper c_B is used to simulate the hysteresis loss in the material. A second dashpot damper is used to simulate the force which acts on the ball due to the momentum flux, and this parameter is defined as c_M. The stringbed is represented by a spring and dashpot in parallel. The spring is used to represent the stiffness of the stringbed, in a direction perpendicular to the plane of the stringbed, and this parameter is defined as k_S. The dashpot damper c_S is used to account for the energy loss for an impact in this same direction.

In this section, the frame of the racket will be modelled as a rigid body that has the same inertial properties (mass, balance point and mass moment of inertia) as the racket. The ball impacts at a distance d from the centre-of-mass (COM) of the racket. It is assumed that the stringbed applies a point load on the rigid body, located at the impact point. The location of the racket centre-of-mass is defined as the balance point and is at a distance B_R from the butt end. The mass moment of inertia, around the racket COM, is defined as I_R.

The displacement x_B represents the motion of the centre-of-mass of the ball. The displacements x_S and x_{IP} represent the motion of the stringbed and frame at the ball impact position, respectively. The parameters x_R and θ_R represent the linear and angular displacements of the racket COM respectively. The parameters m_B and m_R are equal to the mass of the ball and racket respectively. It shall be assumed that the mass of the stringbed is negligible, as done in section 8.4.

The equation that for the force F which acts in the ball/stringbed system in the model is,

$$F = -[(c_B + c_M)(\dot{x}_B - \dot{x}_s) + k_B(x_B - x_s)] = -[c_S(\dot{x}_S - \dot{x}_D) + k_S(x_S - x_D)] \quad [9.1]$$

The acceleration of the point x_B which corresponds to the ball COM displacement, is defined using,

$$\ddot{x}_B = \frac{F}{m_B} \quad [9.2]$$

The acceleration of the point x_R which corresponds to the racket COM linear displacement, is defined using,

$$\ddot{x}_R = \frac{F}{m_R} \quad [9.3]$$

and the angular acceleration of the racket COM is defined using,

$$\ddot{\theta}_R = \frac{Fd}{I_R} \quad [9.4]$$

The acceleration of the racket frame at the impact point x_{IP} can be defined using,

$$\ddot{x}_{IP} = \ddot{x}_R + \ddot{\theta} d \quad [9.5]$$

As explained in previous chapters, the motion of the points x_B, x_S, x_R, x_{IP} and θ_R will be evaluated numerically using the finite difference method. It is noted that the finite difference technique relies on the values of all parameters being known at time t. The finite difference equation which defines the displacement x_B at a time $t+\Delta t$ is,

$$(x_B)_{t+\Delta t} = \Delta t^2(\ddot{x}_B)_t + 2(x_B)_t - (x_B)_{t-\Delta t} \quad [9.6]$$

Similar equations can be used to calculate the values of the racket displacements at time $t+\Delta t$ which are defined as $(x_R)_{t+\Delta t}$ $(x_{IP})_{t+\Delta t}$ and $(\theta_R)_{t+\Delta t}$. The time step Δt used in this numerical solution is $5\mu s$. As the time step used in this solution is very small, it is assumed that the velocity change during this period was negligible for all five parameters. Therefore the velocity of the centre-of-mass of the ball at time t, $(\dot{x}_B)_t$ can be calculated using,

$$(\dot{x}_B)_t = \frac{(x_B)_t - (x_B)_{t-\Delta t}}{\Delta t} \quad [9.7]$$

The three components of the racket velocity $(\dot{x}_D)_t$, $(\dot{x}_R)_t$ and $(\dot{\theta}_R)_t$ can be defined using equations of a similar form. Also, the velocity of the stringbed at time t, $(\dot{x}_B)_t$ can be calculated using,

$$(\dot{x}_S)_t = \frac{(x_S)_t - (x_S)_{t-\Delta t}}{\Delta t} \quad [9.8]$$

Equation [9.8] can be substituted into [9.1]. Equation [9.1] can then be rearranged to define the stringbed displacement at time t, $(x_S)_t$,

$$(x_S)_t = \frac{k_S(x_{IP})_t + k_B(x_B)_t + c_S\left(\frac{(x_S)_{t-1}}{\Delta t} + \dot{x}_{IP}\right) + (\dot{x}_B)_t(c_B + c_M) + \frac{(x_S)_{t-1}}{\Delta t}(c_B + c_M)}{k_S + k_B + \left(\frac{c_S + c_B + c_M}{\Delta t}\right)} \quad [9.9]$$

The equations ([9.7]-[9.9]) can be used to define all the five parameters, at time t. To commence the finite difference solving technique, the displacement and acceleration of the ball and racket need to be known at the times $t = 0$ and $t = -\Delta t$. It is assumed that, prior to impact, the ball velocity is V_B and the racket velocity can be defined by the linear and angular components V_R and ω_R respectively. The velocity of the racket frame at the ball impact position V_{IP}, prior to impact, can be calculated using,

$$V_{IP} = V_R + \omega_R d \quad [9.10]$$

Let it also be assumed that neither the ball or racket are accelerating immediately prior to impact, i.e. at times when $t = 0$ and $t = -\Delta t$. The displacements of the parameters x_B, x_S, x_{IP}, x_R and θ_R at time $t = 0$ are assumed to be all equal to zero. The displacements of these parameters at time $t = -\Delta t$ are $x_B = -V_B.\Delta t$, $x_S = x_{IP} = -V_{IP}.\Delta t$, $x_R = -V_R.\Delta t$ and $\theta_R = -\omega_R.\Delta t$.

The solution was written in *MS Excel 2000* and could be solved for each time step of the impact, provided that the values of the parameters k_B, k_S, c_B, c_M, c_S, B_R, m_R and I_R are all known, along with the impact position and the velocity of the ball and racket prior to impact.

In this section, a generic visco-elastic model of a ball impact on a freely suspended racket has been developed. The racket has been modelled as a rigid body. In the next section, the methods used to define the parameters (k_B, k_S etc) are described.

9.2.2 Defining the model parameters

(a) The ball

The ball has been modelled as a spring in parallel with two dashpot dampers, as illustrated in Figure 9.1. It is assumed that the method used to define the parameters k_B, c_B and c_M is the same as that discussed in Chapter 8 for an impact between a ball and head clamped racket, with a minor modification. A detailed explanation of the general method which is used to define these parameters is given in Chapter 8 and therefore is not repeated here. However, a brief résumé is given here, along with an explanation of the minor modification that is made to the model.

In this model, the deformation of the ball is analogous to the model parameter $(x_B - x_S)$. Using the findings from Chapters 5 and 8, it is assumed that the model ball stiffness k_B is defined as a function of $(x_B - x_S)$ using,

$$k_B = k_{B(0)} + A_K(x_B - x_S)^{\alpha} \quad [9.11]$$

The parameters $k_{B(0)}$, A_K and α are constants for a specific ball type and the values were derived in Chapter 8. The values of these two parameters are given in Table 9.1 for four different ball types.

Table 9.1 Spring parameters $k_{B(0)}$, A_K and α and damping constant A_C for the four ball types.

Ball type	$k_{B(0)}$ (kN/m)	A_K (kN/m^2)	α	A_C (kNs/m^3)
Pressurised	27.3	20800	1.65	3.5
Pressureless	29.9	16250	1.70	4.0
Oversize	27.3	4680	1.30	3.2
Punctured	20.8	78000	2.00	5.8

It is assumed that the magnitude of the material damping was proportional to the volume of rubber being deformed, and also the ball deformation rate. Therefore, the dashpot parameter c_B which represents the material damping is defined using,

$$c_B = \frac{m_B}{M_1} A_C.(d_{CONT})^2 \qquad [9.12]$$

where m_B is the mass of the ball. The parameter A_C is defined as the damping constant and its value is shown in Table 9.1.

The parameter d_{CONT} refers to the diameter of the circular area of the ball that is in contact with the surface. It is assumed that the empirical relationship between d_{CONT} and the relative ball COM displacement $(x_B - x_S)$ is,

$$d_{CONT} = -2.77\times10^5(x_B - x_S)^4 + 1.74\times10^4(x_B - x_S)^3 - 453(x_B - x_S)^2 + 7.66(x_B - x_S) \qquad [9.13]$$

The term M_1 in [9.12] refers to the mass of the section of ball that is not in contact with the surface. This value clearly varies throughout impact, and is a function of the ball deformation. It is assumed that M_1 is equal to the difference between m_B and the mass of the ball that is in contact with the surface M_2. The value of M_2 is estimated using,

$$M_2 = \rho_{area}\pi\left(\frac{d_{CONT}}{2}\right)^2 \qquad [9.14]$$

where ρ_{area} is the mass per unit surface area of the ball and is equal to 5.212kg/m^2 for a standard size ball.

The force which acts on the ball due to the momentum flux is simulated using the dashpot damper c_M. This force only acts during the compression phase of impact and the value of c_M is a function of the mass (and velocity) of the section of ball being brought to rest in a unit time interval Δt. The equation used to define c_M, at time t, is,

$$(c_M)_t = \frac{m_B\left|\rho_{area}\pi\left((d_{CONT(t)})^2 - (d_{CONT(t-\Delta t)})^2\right)\right|}{4\Delta t(M_1)_t} \quad [9.15]$$

Equation [9.15] completes the set of equations which are used to define the parameters k_B, c_B and c_M, throughout the impact. The methods used to define these parameters are identical to those used in the model of a ball impacting on a head clamped racket, as discussed in Chapter 8. However, in that chapter a further assumption was made in regard to the ball component of the model to simulate the contribution of the cloth on the ball, during the compression phase. It was assumed that the force which acted on the ball (and stringbed) was equal to zero, for ball COM displacements of less than 2mm, regardless of the values of the ball model parameters. However, it can be shown that this has negligible effect on the values which are calculated by the model (e.g. ball rebound velocity) and only adds an unnecessary complexity to the model solution. Therefore, in this current model of a ball impacting on a freely suspended racket, it is not assumed that the force is equal to zero for ball COM displacements of less than 2mm. Therefore the equations discussed above are used to define the model parameters throughout the impact.

(b) The stringbed

The stringbed of the freely suspended racket is to be modelled as a spring and damper in parallel. The magnitude of the parameters k_S and c_S is to be determined using the same methods as were described in Chapter 8. It is to be assumed that the stringbed stiffness parameter k_S for the racket is equal to that which is measured experimentally for a quasi-static loading. This assumption is complicated by the fact that the measured quasi-static stiffness is dependent on the diameter of the rigid circular disc that is used to apply the load. Also, the relationship between the diameter of the rigid disc and the equivalent area over which the ball applies the load onto the stringbed, during impact, is difficult to determine. A detailed explanation of the assumptions which were made to define the model stringbed stiffness parameter k_S is given in section 8.3.1. A summary of this work is given here.

The solution is based upon a concept of a normalised stiffness parameter $\tilde{k}_S$. In brief, this parameter defines the diameter of the ball/surface contact area that is equivalent to the diameter of the rigid disc that is used to apply the quasi-static loading. This diameter is then normalised to the arbitrarily chosen maximum diameter of 55mm. Using empirical data, it was found that $\tilde{k}_S$ was dependent on the stringbed displacement x_S. The general equation to estimate the value of $\tilde{k}_S$, for any combination of ball type and string tension, has been defined as,

$$\tilde{k}_S = 78.42(1.6x_S + 0.023)^2 + 2.336(1.6x_S + 0.023) + 0.6392 \quad [9.16]$$

Equation [9.16] is valid for stringbed displacements x_S of less than 20mm. For x_S > 20mm, the value of the normalised stiffness $\tilde{k}_S$ is equal to unity.

The next stage of the solution required the definition of the quasi-static stringbed stiffness obtained when the load was applied using a rigid disc with a diameter of 55mm. The general form of this equation is,

$$k_S(\phi_{55}) = a_S.x_S^2 + b_S.x_S + c_S \qquad [9.17]$$

where a_S, b_S and c_S are empirically determined coefficients of a second order polynomial trendline that was plotted through the experimentally obtained quasi-static stiffness data. The values of a_S, b_S and c_S are given in Table 9.2 for four different string tensions. This data was experimentally obtained using an *ITF Carbon Fibre* tennis racket with a head size of 632cm^2 (98in^2)

Table 9.2 Second order polynomial trendline coefficients a_S, b_S and c_S for four string tensions.

String tension	a_S (kN/m^3)	b_S (kN/m^2)	c_S (kN/m)
40lbs	4785	1147	29.02
50lbs	20790	1044	34.50
60lbs	-17810	1873	39.05
70lbs	-30140	2519	43.07

To complete the solution, the value of the stringbed stiffness k_S, is determined using,

$$k_S = \widetilde{k}_S.k_S(\phi_{55}) \qquad [9.18]$$

To summarise, the stringbed stiffness k_S for a specific stringbed displacement x_S can be obtained by determining the relevant values of $\widetilde{k}_S$ and $k_S(\phi_{55})$ using [9.16] and [9.17] respectively. These two parameters are then input into [9.18] to determine the required value of k_S.

In Figure 9.1 , it can be seen that there is a dashpot damper, with value c_S, that is used to represent the damping of the stringbed. In Chapter 8 a brief analysis was conducted and it was concluded that the value of c_S will be assumed to be equal to 2Ns/m for all impacts. This same assumption will be used for the model presented in this section.

(c) The Racket Frame

In this section, the racket frame is to be modelled as a rigid body with the same inertial properties as the racket. As the model is only to be used to simulate impacts along the longitudinal axis, the only mass moment of inertia (MMI) which is of interest in this case is the transverse MMI, which is defined as I_R in Figure 9.1. This is a measured experimentally using the same technique as that described by Brody (1985). This method is presented in Appendix D.1 along with the measured values of mass moment of inertia for a selection of rackets. The only other parameters which are required for this component of the model are the mass of the racket m_R and the distance d between the racket centre-of-mass and the impact position.

(d) Summary of model parameters

In this section, the methods that are used to determine the values of the model parameters k_B, k_S, c_B, c_M and c_S are described. It was assumed that ball and stringbed can be modelled using the same technique as was used in Chapter 8 to simulate a ball impacting on a head clamped racket. Therefore, the ball parameters k_B, c_B, and c_M and the stringbed parameters k_S and c_S are the same as those used in that chapter.

9.2.3 Summary

In this section, a model of an impact between a ball and a freely suspended racket has been derived. The ball and stringbed have been modelled using the same method as was used in Chapter 8, for a simulation of an impact between a ball and head clamped racket. Therefore the methods used to determine the values of the model parameters have already been defined.

The racket frame is modelled as a rigid body with the same inertial properties as the racket. These properties can easily be obtained using standard techniques.

9.3 One dimensional, flexible beam model – point loading

9.3.1 Introduction

In this section, a model of a ball impacting on a freely suspended tennis racket will be developed which is similar to that described in section 9.2. The major difference in this model however, is that the racket is to be modelled as a flexible beam, instead of a rigid beam. The ball and stringbed will be modelled using the same visco-elastic model as that described in section 9.2. This model defines the force which acts on the flexible beam, as a function of time.

In the first part of this section, a numerical solution is derived which can be used to calculate the displacement of a one dimensional beam for a time-dependent loading. This technique was introduced in section 2.5.2, but is presented more thoroughly in this current section. In the next part of this section, the actual process of determining the one dimensional beam which is equivalent to a tennis racket is discussed. This process involves the simplification of the complex three-dimensional geometry of a tennis racket into a simple one dimensional beam. The errors associated with this simplification process are also discussed in this section.

9.3.2 *One dimensional flexible beam subjected to a time-dependent force*

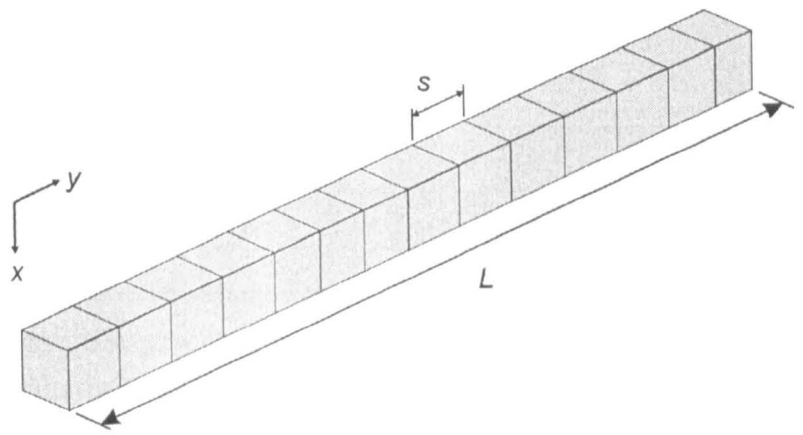

Figure 9.2 A one-dimensional flexible beam, split into N equal length segments.

The equation of motion for a one dimensional beam subjected to an external distributed force, F_0 per unit length, which acts perpendicular to the longitudinal axis of beam, has the form (Goldsmith (1960)),

$$\rho A \frac{\partial^2 x}{\partial t^2} = F_0 - \frac{\partial^2}{\partial y^2}\left(EI \frac{\partial^2 x}{\partial y^2} \right) \qquad [9.19]$$

where ρ is the density of the beam, A is its cross-sectional area, E is the Young's modulus, I is the area moment of inertia and x is the transverse displacement of the beam at coordinate y along beam, as defined in Figure 9.2.

Equation [9.19] neglects the shear force which is of negligible significance for the low frequencies of vibration which are of most interest in this work (Van Zandt 1992). The beam has a mass M_B and a length L_B.

In this study, it is to be initially assumed that the flexural rigidity was constant along the length of the one-dimensional beam, as was done by Cross (2001b). The suitability of this assumption will be discussed in a later section of this chapter. It is assumed that the beam may have a non-uniform mass distribution. A numerical solution of [9.19] can be obtained by splitting the beam into N equal sized segments. The length of each segment is constant and defined as $s=L_B/N$ but the segment mass m_n may vary along the beam. This segmented beam is illustrated in Figure 9.2. The equation of motion for the nth segment is obtained by multiplying all terms in [9.19] by s, which gives,

$$m_n \frac{\partial^2 x_n}{\partial t^2} = F_0 s - \left(EIs \frac{\partial^4 x_n}{\partial y^2} \right) \qquad [9.20]$$

The force exerted by the ball may act over a number of segments, each segment n being subjected to a time-dependent force F_n. The equation of motion for each of these segments is given by,

$$m_n \frac{\partial^2 x_n}{\partial t^2} = F_n - \left(EIs \frac{\partial^4 x_n}{\partial y^4} \right) \qquad [9.21]$$

and for all other segments,

$$m_n \frac{\partial^2 x_n}{\partial t^2} = -\left(EIs \frac{\partial^4 x_n}{\partial y^4} \right) \qquad [9.22]$$

In this current section it is to be assumed that the stringbed applies a point load on the beam and so the force only acts on one segment of the beam. Consequently, the value of F_n is simply equal to the force acting in the ball/stringbed visco-elastic model. It is assumed that the racket is freely suspended during impact, and the relevant boundary conditions for this assumption are, $\left(\frac{\partial^2 x}{\partial y^2} = 0 \right)$ and $\left(\frac{\partial^3 x}{\partial y^3} = 0 \right)$.

The subsequent motion of the beam was evaluated numerically using finite difference forms of [9.21] and [9.22]. The procedure used to solve these equations is based on that presented in Cross(1999c). The method used to obtain the magnitude of the time-dependent force F, which is applied to the beam, is a relatively trivial feature of the model and will therefore not be discussed in this section. The following analysis gives an overview of the numerical solution that is used to determine the motion of the beam which is subjected to a time-dependent force.

(a) Numerical solution for the displacement of the beam

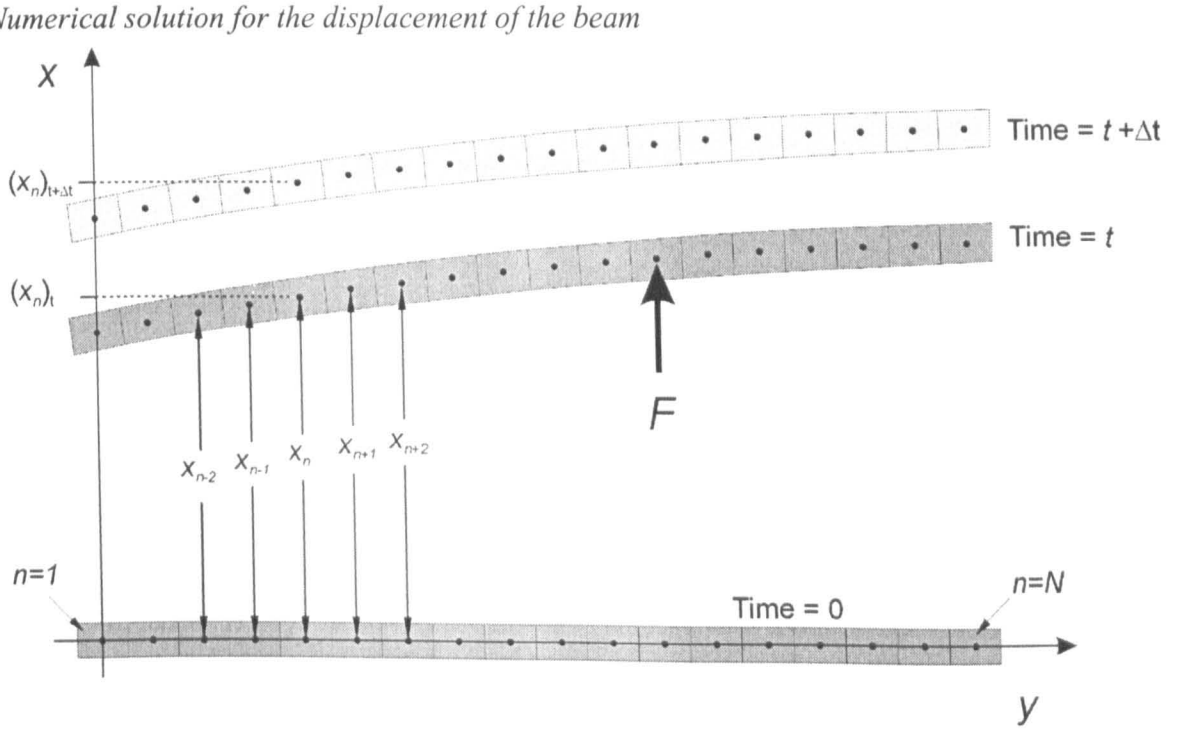

Figure 9.3 Illustration of the definition of the beam displacement at times t and $t+\Delta t$.

Substituting for the finite difference form of $\frac{\partial^2 x_n}{\partial t^2}$ into [9.21], at time t, gives,

$$m_n\left(\frac{(x_n)_{t+\Delta t}-2(x_n)_t+(x_n)_{t-\Delta t}}{\Delta t^2}\right)=F-\left(EIs\left(\frac{\partial^4 x_n}{\partial y^4}\right)_t\right) \qquad [9.23]$$

Rearranging this equation to determine the displacement of the *nth* segment, at time $t+\Delta t$ gives

$$(x_n)_{t+\Delta t}=2(x_n)_t-(x_n)_{t-\Delta t}+\frac{F\Delta t^2}{m_n}-\left(\frac{EIs\Delta t^2}{m_n}\left(\frac{\partial^4 x_n}{\partial y^4}\right)_t\right) \qquad [9.24]$$

The magnitude of the force F which acts on each segment will be discussed later in this section. The magnitude of the product EI, which is termed the flexural rigidity, will also be discussed later.

Equation [9.24] requires the term $\left(\frac{\partial^4 x_n}{\partial y^4}\right)_t$ to be evaluated. The finite difference form of this term is,

$$\left(\frac{\partial^4 x_n}{\partial y^4}\right)_t=\frac{(x_{n+2})_t-4(x_{n+1})_t+6(x_n)_t-4(x_{n-1})_t+(x_{n-2})_t}{s^4} \qquad [9.25]$$

To calculate the fourth derivative of x_n with respect to y, using [9.25] requires the displacement of the two segments either side of the *nth* segment to be known, as illustrated in Figure 9.3. Therefore [9.25] is valid for all segments except the two segments at either end of the beam. For these four segments, alternative finite difference forms of $\left(\frac{\partial^4 x_n}{\partial y^4}\right)_t$ are required, as described by Cross (1999c). These equations are determined using the boundary conditions for a freely supported beam.

The fourth derivative of x_1, the left-hand end segment of the beam in Figure 9.3, is defined as,

$$\left(\left(\frac{\partial^4 x_n}{\partial y^4}\right)_t\right)_{n=1}=\frac{(x_1)_t-2(x_2)_t+(x_3)_t}{s^4} \qquad [9.26]$$

and the fourth derivative of x_2, which is adjacent to the end segment, is defined as,

$$\left(\left(\frac{\partial^4 x_n}{\partial y^4}\right)_t\right)_{n=2}=\frac{-2(x_1)_t+5(x_2)_t-4(x_3)_t+(x_4)_t}{s^4} \qquad [9.27]$$

Analogous equations can be determined for $\left(\left(\frac{\partial^4 x_n}{\partial y^4}\right)_t\right)_{n=N}$ and $\left(\left(\frac{\partial^4 x_n}{\partial y^4}\right)_t\right)_{n=N-1}$, which completes the necessary parameters for [9.24]. For convenience, [9.24] is written in a matrix form to define the motion of the entire beam,

$$[x]_{t+\Delta t} = 2[x]_t - [x]_{t-\Delta t} + \Delta t^2[M][F]_t - \frac{EI\Delta t^2}{s^3}([M][DX4]_t)[x]_t \qquad [9.28]$$

where $[x]_{t+\Delta t}$, $[x]_t$ and $[x]_{t-\Delta t}$ are all column matrices with N rows and have the general form,

$$[x] = \begin{bmatrix} x_1 \\ x_2 \\ x_3 \\ \\ \text{---} \\ \text{---} \\ x_{N-2} \\ x_{N-1} \\ x_N \end{bmatrix} \quad N \text{ rows} \downarrow$$

The force matrix $[F]_t$ is also a column matrix, with N rows, and contains all zeros, except for the row number which corresponds to the segment on which the force acts. The number of the segment on which the force is applied is defined as IP. For example, if IP is equal to two then the force matrix will be of the form,

$$[F] = \begin{bmatrix} 0 \\ F \\ 0 \\ 0 \\ \text{---} \\ \text{---} \\ 0 \\ 0 \\ 0 \end{bmatrix}$$

The mass matrix $[M]$ is an $N \times N$ matrix with the general form,

$$[M] = \left[\begin{array}{cccccc:cccccc} 1/m_1 & 0 & 0 & 0 & 0 & 0 & 0 & 0 & 0 & 0 & 0 & 0 \\ 0 & 1/m_2 & 0 & 0 & 0 & 0 & 0 & 0 & 0 & 0 & 0 & 0 \\ 0 & 0 & 1/m_3 & 0 & 0 & 0 & 0 & 0 & 0 & 0 & 0 & 0 \\ 0 & 0 & 0 & 1/m_4 & 0 & 0 & 0 & 0 & 0 & 0 & 0 & 0 \\ 0 & 0 & 0 & 0 & 1/m_5 & 0 & 0 & 0 & 0 & 0 & 0 & 0 \\ \hdashline 0 & 0 & 0 & 0 & 0 & 0 & 0 & 1/m_{N-4} & 0 & 0 & 0 & 0 \\ 0 & 0 & 0 & 0 & 0 & 0 & 0 & 0 & 1/m_{N-3} & 0 & 0 & 0 \\ 0 & 0 & 0 & 0 & 0 & 0 & 0 & 0 & 0 & 1/m_{N-2} & 0 & 0 \\ 0 & 0 & 0 & 0 & 0 & 0 & 0 & 0 & 0 & 0 & 1/m_{N-1} & 0 \\ 0 & 0 & 0 & 0 & 0 & 0 & 0 & 0 & 0 & 0 & 0 & 1/m_N \end{array}\right] \quad N \text{ rows} \downarrow$$

N columns $\longrightarrow$

where m_n is the mass of the nth segment.

For a freely suspended beam, $[DX4]$ is an $N \times N$ matrix of the general form,

$$[DX4] = \left[\begin{array}{ccccccccc:ccccccccc}
1 & -2 & 1 & 0 & 0 & 0 & 0 & 0 & 0 & 0 & 0 & 0 & 0 & 0 & 0 & 0 & 0 & 0 \\
-2 & 5 & -4 & 1 & 0 & 0 & 0 & 0 & 0 & 0 & 0 & 0 & 0 & 0 & 0 & 0 & 0 & 0 \\
1 & -4 & 6 & -4 & 1 & 0 & 0 & 0 & 0 & 0 & 0 & 0 & 0 & 0 & 0 & 0 & 0 & 0 \\
0 & 1 & -4 & 6 & -4 & 1 & 0 & 0 & 0 & 0 & 0 & 0 & 0 & 0 & 0 & 0 & 0 & 0 \\
0 & 0 & 1 & -4 & 6 & -4 & 1 & 0 & 0 & 0 & 0 & 0 & 0 & 0 & 0 & 0 & 0 & 0 \\
0 & 0 & 0 & 1 & -4 & 6 & -4 & 1 & 0 & 0 & 0 & 0 & 0 & 0 & 0 & 0 & 0 & 0 \\
0 & 0 & 0 & 0 & 1 & -4 & 6 & -4 & 1 & 0 & 0 & 0 & 0 & 0 & 0 & 0 & 0 & 0 \\
\hdashline
0 & 0 & 0 & 0 & 0 & 0 & 0 & 0 & 0 & 1 & -4 & 6 & -4 & 1 & 0 & 0 & 0 & 0 \\
0 & 0 & 0 & 0 & 0 & 0 & 0 & 0 & 0 & 0 & 1 & -4 & 6 & -4 & 1 & 0 & 0 & 0 \\
0 & 0 & 0 & 0 & 0 & 0 & 0 & 0 & 0 & 0 & 0 & 1 & -4 & 6 & -4 & 1 & 0 & 0 \\
0 & 0 & 0 & 0 & 0 & 0 & 0 & 0 & 0 & 0 & 0 & 0 & 1 & -4 & 6 & -4 & 1 & 0 \\
0 & 0 & 0 & 0 & 0 & 0 & 0 & 0 & 0 & 0 & 0 & 0 & 0 & 1 & -4 & 6 & -4 & 1 \\
0 & 0 & 0 & 0 & 0 & 0 & 0 & 0 & 0 & 0 & 0 & 0 & 0 & 0 & 1 & -4 & 5 & -2 \\
0 & 0 & 0 & 0 & 0 & 0 & 0 & 0 & 0 & 0 & 0 & 0 & 0 & 0 & 0 & 1 & -2 & 1
\end{array}\right]$$

Equation [9.28], and the matrices which are defined above, form the numerical solution which can be used to solve the displacement of each of the N segments at sequential time intervals of Δt. Equation [9.28] is firstly used to determine the displacement of each of the N beam segments at $t = \Delta t$, which forms the column matrix $[x]_{\Delta t}$. This is done using the relevant displacements for the two preceding time steps which are $[x]_{t=0}$ and $[x]_{-\Delta t}$. It is assumed that the displacement of the beam at $t=0$ is equal to zero, as shown in Figure 9.3 The displacement of the beam segments at $t = -\Delta t$ can be calculated from the initial velocity of the beam/racket, as was discussed in section 9.2.

The process is repeated for the remaining time steps for the required time period T; the number of time steps required being $NStep = T/\Delta t$ The ball/stringbed system will apply a force F on the IPth segment for a period of approximately 5ms, as explained in more detail later in this section. When impact ceases, the value of F will be equal to zero, but the induced vibrations of the beam can be calculated using the same technique as described above. The only exception being that the force matrix contains all zero values.

In this study, it has been assumed that the beam is freely suspended at either end and this assumption was used to define the terms in the $[DX4]$ matrix; this matrix corresponding to a numerical approximation of the fourth derivative of x with respect to y. For interest, this matrix is the only part of the model which would need to be adjusted if different end conditions were to be modelled.

The completed solution generated a column matrix $[x]$ for each time interval Δt, in the range $t=0$ to $t=T$. It was assumed that the velocity of each segment $\dot{x}_n$ did not change significantly during the time period Δt and therefore the velocity, at time t, $(\dot{x}_n)_t$ can be determined using,

$$(\dot{x}_n)_t = \frac{(x_n)_t - (x_n)_{t-1}}{\Delta t} \qquad [9.29]$$

(b) Numerical computation of Fourier Series coefficients

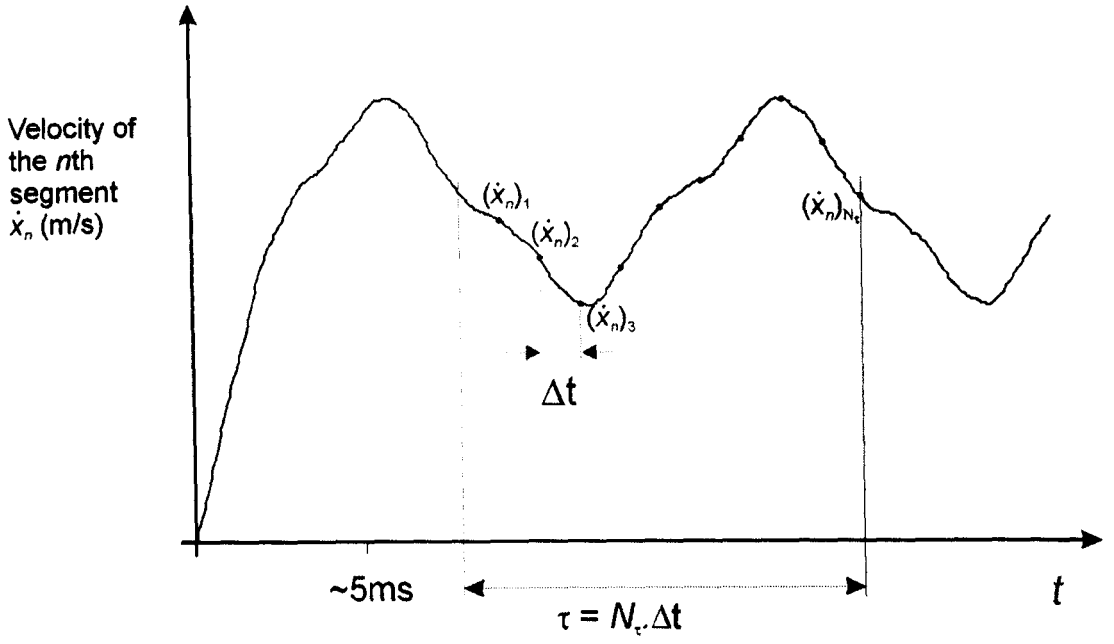

Figure 9.4 Illustration of the velocity of the *n*th beam segment as a function of time.

Figure 9.4 gives a schematic illustration of the typical velocity of the *n*th segment of the beam. The duration of the time-dependent force F is approximately 5ms and after this period the beam oscillates freely. Cross (1999c) noted that, due to this impact duration, the only modes of vibration that are significantly excited are those with a frequency of up to approximately 300Hz. This generally means that only the fundamental frequency of the beam/racket is excited as the next highest mode has a frequency which is greater than 300Hz. In this work it is assumed that the fundamental frequency f_F of the beam is known.

In this section, a numerical harmonic analysis is conducted to obtain the mean velocity of each segment. This analysis can also be used to calculate the amplitude of the fundamental mode of vibration. This is useful as the calculated amplitude illustrates the amount of energy that is stored in the racket due to this mode of vibration, and it can also be used to determine the node points on the beam. This harmonic analysis of the time-dependent velocity data, such as that shown in Figure 9.3, involves the numerical computation of the Fourier series coefficients which are assumed to describe the calculated data. This is a standard method which is described in detail in Rao (1995), and therefore only summarised here.

The time period τ for one cycle of the fundamental mode of vibration is,

$$\tau = \frac{1}{f_F} \qquad [9.30]$$

This time period corresponds to N_τ time intervals, each of length Δt. In this solution the value of f_F must be defined such that N_τ is an integer. The mean velocity $\bar{\dot{x}}_n$ of the *n*th beam segment, over this period τ, is calculated using,

$$\bar{\dot{x}}_n = \frac{1}{N_\tau}\sum_{i=1}^{N_\tau}(\dot{x}_n)_i \qquad [9.31]$$

The amplitude of vibration $\hat{x}_n$ for the fundamental frequency, for the nth beam segment is defined as,

$$(\hat{x}_n)_{amplitude} = \sqrt{a_n^2 + b_n^2} \qquad [9.32]$$

where a_n and b_n are Fourier coefficients defined as,

$$a_n = \frac{2}{N_\tau}\sum_{i=1}^{N_\tau}(\dot{x}_n)_i \cos\frac{2\pi t_i}{\tau} \qquad [9.33]$$

$$b_n = \frac{2}{N_\tau}\sum_{i=1}^{N_\tau}(\dot{x}_n)_i \sin\frac{2\pi t_i}{\tau} \qquad [9.34]$$

Using the above equations, the mean and amplitude of the velocity for each of the N segments can be calculated.

It is evident from Figure 9.4 that the numerical solution for the free oscillations of the beam must continue for a significant period after impact has ceased, to ensure that this numerical harmonic analysis can be conducted. The fundamental frequency of a tennis racket, for transverse vibration, is known to range from approximately 70Hz and 200Hz. This gives a time period τ for one cycle which ranges from 14ms to 5ms. It was therefore concluded that the solution should be obtained for 25ms after the commencement of the impact, to ensure that the harmonic analysis can be conducted.

(c) Numerical computation of the beam fundamental frequency

In the above analysis, it was assumed that the fundamental frequency f_F of the beam was known for a beam with a specific mass distribution and flexural rigidity. There is no analytical solution for this fundamental frequency f_F for a beam with a non-uniform mass distribution. However, a numerical solution can be obtained using a similar technique as that used to determine the displacement of the beam for a known time-dependent force.

Earlier in this section, it was mentioned that the flexural rigidity EI is assumed to be uniform along the length of the one-dimensional beam. The motion of a vibrating one-dimensional beam subjected to no external forces can be determined by substituting,

$$\frac{\partial^2 x_n}{\partial t^2} = -\omega^2 x_n \qquad [9.35]$$

into,

$$m_n\frac{\partial^2 x_n}{\partial t^2} = -\left(EIs\frac{\partial^4 x_n}{\partial y^4}\right) \qquad [9.36]$$

to give,

$$\omega^2 x_n = \frac{EIs}{m_n}\left(\frac{\partial^4 x_n}{\partial y^4}\right) \qquad [9.37]$$

Equation [9.37] can be written in matrix form to describe the motion of the entire beam,

$$EI[k_n]\times[x]=\lambda\times[x] \qquad [9.38]$$

where $[x]$ is a column matrix with N columns. For a freely suspended beam, $[k_n]$ is an $N\times N$ matrix of the form,

$$[k_n]=\frac{1}{s^3}[M][DX4] \qquad [9.39]$$

where $[M]$ and $[DX4]$ are matrices that define the mass distribution and the fourth derivative of x with respect to y for the entire beam respectively. The definitions of these matrices has already been presented.

The parameter λ corresponds to the set of *eigenvalues* for the matrix defined by $EI[k_n]$. However, to generate a more general solution, the *eigenvalues* are only initially calculated for the $[k_n]$ matrix, and these *eigenvalues* were defined by the parameter λ_{kN}. For completeness,

$$\lambda = EI.\lambda_{kN} \qquad [9.40]$$

The values of λ_{kN} were determined using the *eig* function in *MATLAB v5.2*. The fundamental frequency f_F of the beam corresponded to the first real, non-zero *eigenvalue* and was determined using,

$$f_F = \frac{\sqrt{EI}}{2\pi}\sqrt{\lambda_{kN}} \qquad [9.41]$$

The analysis which is described above can be used to determine the fundamental frequency of a freely suspended model beam, for specified values of the mass matrix $[M]$, the flexural rigidity EI and the segment length s. It can be seen that, for a beam with a specific length and mass distribution, the fundamental frequency is proportional to the square-root of the flexural rigidity EI.

(d) Summary

In this current section, a numerical solution for the displacement of this flexible beam, for a time-dependent point loading, has been presented. In this solution, the beam is split into a finite number of segments and the displacement of each of these segments is calculated, at discrete time intervals. It has been assumed that this beam has a uniform value of flexural rigidity along its entire length, but the mass of each segment is not constant.

The velocity of each segment can be calculated for the free vibration of the beam, after impact has ceased. A method has been presented which allows the mean and amplitude of the beam segment

velocity to be calculated, using a numerical harmonic analysis. This harmonic analysis requires the fundamental frequency of the beam to be known, and a method for calculating this parameter has been given.

9.3.3 Using a one dimensional flexible beam to model a tennis racket

(a) Introduction

It has been proposed that a one dimensional beam should be used to model a tennis racket frame, for an impact with a tennis ball. In section 9.3.2, an algebraic solution was presented to illustrate the numerical technique which can be used to solve for the displacement of a flexible beam that is subjected to a time-dependent force F; this force being applied as a point loading. In this current section, the method which is used to incorporate this one dimensional beam into a model of a ball impact on a freely suspended racket is discussed. It should be noted that this model is only applicable for impacts along the longitudinal (main) axis of the racket.

(b) The model

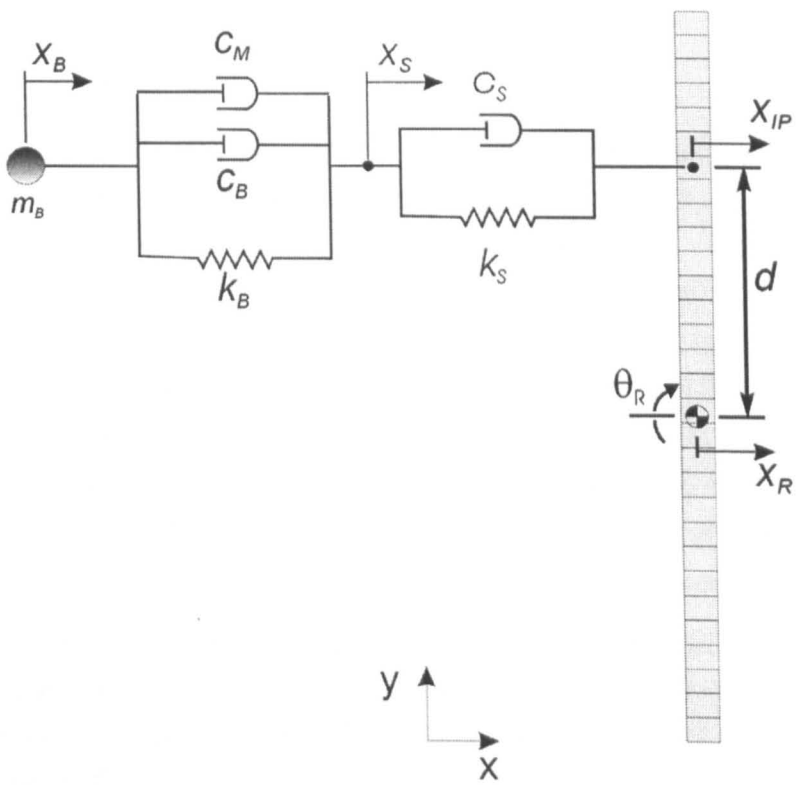

Figure 9.5 Illustration of a visco-elastic model of a ball impact on a one dimensional flexible beam (tennis racket).

The model which is to be discussed in this section is very similar to that which is presented in section 9.2. In that section, the ball/stringbed system was simulated as a visco-elastic model and the racket was assumed to be a rigid beam with the same inertial properties as the racket that was being modelled. In this current section, the rigid body beam is replaced by a one dimensional beam with a finite bending stiffness or flexural rigidity, and the overall model is shown in Figure 9.5.

This figure illustrates that the ball impact position must coincide with the centre of one of the beam segments, as mentioned in the previous section. The segment number that the impact point corresponds to is defined as IP, and the displacement of this point on the beam is defined as x_{IP}.

The visco-elastic model of the ball/stringbed system is identical to that described in section 9.2. Therefore, to avoid repetition, the method used to determine the force F which acts in the ball/stringbed system is not repeated here. To summarise,

$$F = -\left[(c_B + c_M)(\dot{x}_B - \dot{x}_s) + k_B(x_B - x_s)\right] = -\left[c_S(\dot{x}_S - \dot{x}_{IP}) + k_S(x_S - x_{IP})\right] \qquad [9.42]$$

The magnitude of F, at time t, can be calculated using [9.42] provided the value of all the parameters are known at this instant. The displacement of the beam at the impact point x_{IP} can be obtained from the relevant row of the displacement matrix $[x]$. The displacement of the ball centre-of-mass x_B and the stringbed x_S can be obtained using the same methods as described in section 9.2.

The spring and damper values k_S, k_B, c_S, c_B and c_M are all assumed to be functions of the ball centre-of-mass displacement x_B, the stringbed displacement x_S and the racket impact point displacement x_{IP}. For example, the ball stiffness k_B is determined using,

$$k_B = k_{B(0)} + A_K\left(x_B - x_S\right)^{\alpha} \qquad [9.43]$$

The parameters $k_{B(0)}$, A_K and α are constants for a specific ball type and the values were derived in Chapter 8. The values of these three parameters are given in Table 9.1 for a range of ball types. The other functions, which define k_S, c_S, c_B and c_M, are all defined in section 9.2.2 and are therefore not repeated here. These functions, and equation [9.42] above, are used to determine the force F at a discrete time interval t. This force value is applied to the beam on a single segment, as described in section 9.3.2. The new displacement of the beam, ball, and stringbed, at the following time interval $t+\Delta t$, can then be evaluated. The new value of the force which acts on the beam can then be evaluated, and the process is repeated until the end of impact. The end of impact is defined as the instance when the ball deformation, or in this case (x_B-x_S), returns to zero. After this point, the beam continues to vibrate and translate freely until the solution is terminated.

In this numerical solution, the beam is split into a finite number of segments and is solved for finite time intervals. In theory, both the segment length and time steps should be infinitesimally small for the beam to simulate the infinite number of modes of vibration of the racket. However, as mentioned previously, Cross (1999c) noted that the only modes of vibration that are excited with a significant amplitude are those with a frequency of up to approximately 300Hz. It was also stated that the division of the beam into discrete segments eliminated modes which had a wavelength that was shorter than the segment length s. Therefore, an infinitely small time step was not required.

In this study, the beam was split into 51 segments (N=51) and the time step Δt used was 5μs. Using this value of N, the first three real, non-zero *eigenvalues* for a uniform beam were calculated numerically using the procedure in section 9.3.2(c). These *eigenvalues*, for the uniform beam, were also determined analytically using equations defined in Goldsmith (1960). In practise it was found that this value of N gave a good correlation between the *eigenvalues* which were determined

numerically and those determined analytically. The difference between the two sets of data was generally less than 0.2%, for all combinations of beam mass and beam flexural rigidity that are typical of a tennis racket. Furthermore, it was found that the two sets of *eigenvalues* correlate to within 0.3% for values of flexural rigidity which are considerably higher than those typical of a tennis racket model.

This analysis confirmed that the chosen value of N was sufficient to model tennis rackets which had fundamental frequencies that covered the full range of typical values. An increase in the value of N would only act to increase the number of calculations which need to be performed to solve the model.

A further investigation was conducted to verify that the time step Δt used in this solution was satisfactorily small to model the magnitude of beam deformation and the modes of vibration which were excited in this type of impact.

(c) Deriving a beam model of a tennis racket

In the previous section, it has been stated that a one dimensional beam can be used to model a tennis racket frame. In this current section, the method which is used to determine the equivalent one dimensional beam model of a tennis racket is discussed.

Clearly, the modelling of a tennis racket as a one-dimensional beam is a significant simplification. However, it should be remembered that in this model, the main aim is to replicate the inertial and vibrational properties of the racket. To be geometrically consistent, the beam and racket must also have the same length. Therefore, in an ideal model, the following properties should be identical for the beam and racket,

1. Length
2. Mass
3. Balance Point
4. Mass Moment of Inertia
5. Fundamental Frequency
6. Node points of fundamental frequency

In this section, three different techniques are to be discussed which can be used to generate a model beam that is equivalent to the relevant tennis racket. The list above shows the properties that the model beam must match with those of the tennis racket. More specifically, the technique is used to determine the values of the mass segments which form the mass matrix $[M]$, and the value of the uniform flexural rigidity EI. If these two properties can be obtained for the beam, then the displacement of the beam can be calculated using the numerical analysis in section 9.3.2, for specified ball/stringbed properties.

In the first part of this section, the investigation is focused upon matching the inertial properties of the racket and beam. In the latter part, the method used to determine the flexural rigidity EI is presented.

1. Uniform beam

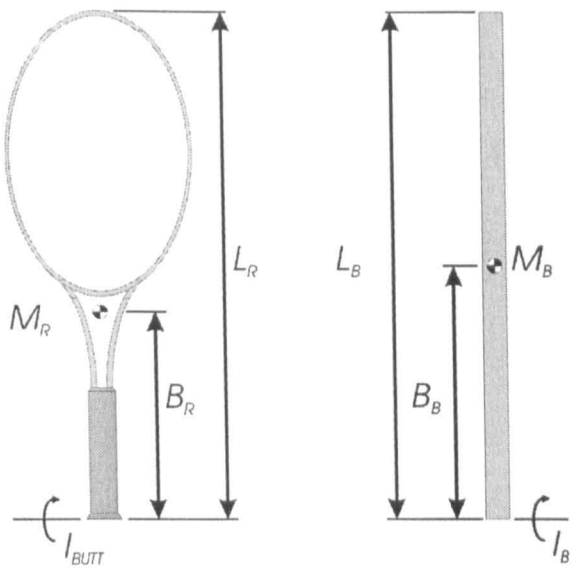

Figure 9.6 Tennis racket and equivalent uniform beam model.

The simplest, one-dimensional beam has a uniform mass distribution and this is illustrated in Figure 9.6. This beam can be assigned the same mass and length properties as the tennis racket. For example the beam parameter M_B can be assigned the value of M_R. A minor, yet very important, point should be raised at this stage. It can be inferred from Figure 9.5 that the stringbed and racket frame are modelled discretely, and indeed this section concentrates solely on developing a beam model which is equivalent to the frame. However, it should be remembered that the stringbed is being modelled as having a zero mass. To compensate for this, the parameter mass M_R is actually equal to the combined mass of the frame and strings.

The balance point B_B and the mass moment of inertia around the butt end I_B for a one section uniform beam are functions of the beam length and the beam mass, and are defined using,

$$B_B = 0.5L_B \qquad [9.44]$$

and

$$I_B = \frac{M_B L_B^{\,2}}{3} \qquad [9.45]$$

It can be seen that the balance point B_B of a uniform beam is always located at the geometric centre, whereas many tennis rackets are generally either 'head-heavy' or 'head-light'; these terms being used to define whether the racket centre-of-mass is positioned closer to the head or butt respectively. The mass moment of inertia of the beam I_B is a 'fixed' function of the beam mass and length. Therefore, both B_B and I_B cannot be assigned the same values as B_R and I_{BUTT} respectively. This highlights the inherent weakness in using a uniform beam as a model to simulate the inertial properties of a tennis racket. This type of beam is referred to as the *uniform section* beam in the remainder of this chapter.

2. Two uniform sections

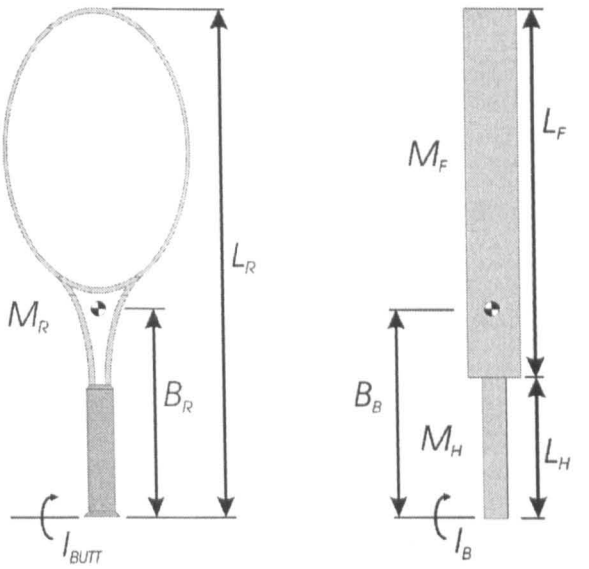

Figure 9.7 Tennis racket and equivalent two section beam model.

Cross (2001b) used a beam consisting of two uniform sections to improve the correlation between the inertial properties of the beam and racket. In that work, it was assumed that the two sections had an equal length, but had different masses. In this current work, it is assumed that one section is equal to the length of the handle, and the other section equal to the remainder of the racket, as illustrated in Figure 9.7. The three inertial properties of the beam for a two section uniform beam are defined using,

$$M_B = M_H + M_F \qquad [9.46]$$

$$B_B = \frac{M_H\left(\frac{L_H}{2}\right) + M_F\left(L_H + \left(\frac{L_F}{2}\right)\right)}{M_B} \qquad [9.47]$$

$$I_B = \frac{M_H L_H^{\,2}}{3} + \left(\frac{M_F L_F^{\,2}}{12} + M_F\left(L_H + \left(\frac{L_F}{2}\right)\right)^2\right) \qquad [9.48]$$

In this solution, the beam could be assigned the same length and mass as the racket, as was possible for the uniform beam. However, it was also possible to define the balance point of the beam to be equal to that of the racket. The value of B_R is substituted for B_B in [9.47], and M_R is substituted for M_B in [9.46], and the combination of M_H and M_F can be determined which satisfies both equations. It is not possible to directly define the mass moment of inertia of the beam I_B to be equal to that of the racket I_{BUTT}, because I_B is a function of M_H, L_H, M_F and L_F, which have already been defined to give the correct balance point for the beam. However, Cross showed that the mass moment of inertia is primarily determined by the mass and location of the balance point. Therefore, the calculated value of I_B for the beam should be approximately equal to that of the racket mass

moment of inertia I_{BUTT}. This type of beam is referred to as the *two section* beam in the remainder of this chapter.

3. Five uniform sections

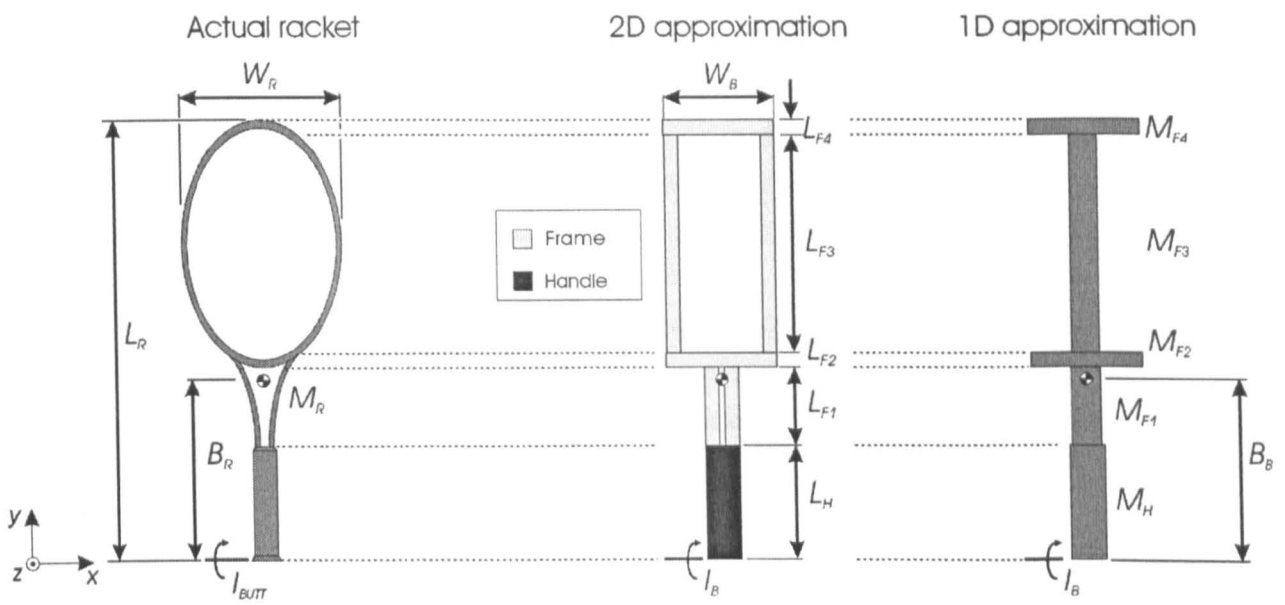

Figure 9.8 A two dimensional approximation of a tennis racket, along with the one dimensional beam which is equivalent to the 2D approximation.

A tennis racket is clearly a three dimensional object and, therefore, has a complex mass distribution which is a function of the geometry and material density. In the derivation of the *uniform section* beam, no consideration of this geometry was made. In the discussion of the *two section* beam model, it was assumed that the handle had a uniform mass distribution, and the rest of the racket had a different uniform mass distribution. In the development of this current beam model, defined as the *five section* model, a more detailed evaluation of the geometry is presented, in an attempt to derive a more accurate one dimensional approximation of the three dimensional mass distribution. Firstly, due to the nature of the assumption that a racket can be approximated as a one dimensional beam, the mass distribution in the z-axis does not influence the one dimensional beam model. Therefore, this mass distribution is not considered here. One of the simplest two dimensional approximations of a tennis racket mass distribution is shown in Figure 9.8. This two dimensional approximation is essentially constructed from two different uniform sections; these being defined as the *handle* and the *frame*. The handle section is a single, straight section which has the same length as that of the racket handle. The throat of the racket is modelled in the 2-D approximation as two straight, vertical sections which extend from the handle to the head, as illustrated in Figure 9.8. The head of the racket is modelled as a rectangle with a width of W_B. This rectangle is simply meant to replicate the mass distribution of the head. Most racket heads have a shape that is more comparable to an ellipse than a rectangle but, for simplicity, a rectangular shape is assumed. This assumption is made because it is easier to obtain a one dimensional equivalent of a rectangle than it is to obtain for an ellipse. However, it is not assumed that the width of the racket head W_R is equal to that of the model rectangle W_B. It has been assumed that the relationship between these two

parameters is $W_B = 0.75W_R$. This relationship was determined by assuming that the perimeter of the rectangle was equal in length to that of the racket head, assuming that the racket head was elliptical.

The translation of the two dimensional approximation to the one dimensional beam is relatively trivial; the one dimensional beam simply giving the equivalent mass distribution as the two dimensional shape. The resulting one dimensional beam has five discrete sections as shown in Figure 9.8.

In this model, all the lengths L_H to L_{F4} can easily be defined by simply measuring the appropriate sections on the racket. However, the masses of each section are not known. Clearly, it would be valid to assume that the mass density of the handle is constant along its section. It is also to be assumed that the density of the frame is constant along its section, in the two dimensional approximation. Therefore, the density of each of the two straight sections of the throat and head are numerically equal to that of the horizontal sections of the rectangular head. The mass densities of the handle and frame are to be defined as ρ_{HANDLE} and ρ_{FRAME} respectively; the density being defined here with units of kgm^{-1}. Using the two dimensional approximation in Figure 9.8 it can be shown that,

$$M_H = \rho_{HANDLE}.L_H \quad [9.49]$$

$$M_{F1} = 2.\rho_{FRAME}.L_{F1} \quad [9.50]$$

$$M_{F2} = \rho_{FRAME}.W_B \quad [9.51]$$

$$M_{F3} = 2.\rho_{FRAME}.L_{F3} \quad [9.52]$$

$$M_{F4} = \rho_{FRAME}.W_B \quad [9.53]$$

The three inertial properties of the one dimensional beam can be defined using,

$$M_B = M_H + M_{F1} + M_{F2} + M_{F3} + M_{F4} \quad [9.54]$$

$$B_B = \frac{M_H\left(\frac{L_H}{2}\right) + M_{F1}\left(L_H + \left(\frac{L_{F1}}{2}\right)\right) + M_{F2}\left(L_H + L_{F1} + \left(\frac{L_{F2}}{2}\right)\right)}{M_B} + \frac{M_{F3}\left(L_H + L_{F1} + L_{F2} + \left(\frac{L_{F3}}{2}\right)\right) + M_{F4}\left(L_H + L_{F1} + L_{F2} + L_{F3} + \left(\frac{L_{F4}}{2}\right)\right)}{M_B} \quad [9.55]$$

$$I_B = \frac{M_H L_H^{\,2}}{3} + \left(\frac{M_{F1} L_{F1}^{\,2}}{12} + M_{F1}\left(L_H + \left(\frac{L_{F1}}{2} \right) \right)^2 \right) + \left(\frac{M_{F2} L_{F2}^{\,2}}{12} + M_{F2}\left(L_H + L_{F1} + \left(\frac{L_{F2}}{2} \right) \right)^2 \right)$$

$$+ \left(\frac{M_{F3} L_{F3}^{\,2}}{12} + M_{F3}\left(L_H + L_{F1} + L_{F2} + \left(\frac{L_{F3}}{2} \right) \right)^2 \right) + \left(\frac{M_{F4} L_{F4}^{\,2}}{12} + M_{F4}\left(L_H + L_{F1} + L_{F2} + L_{F3} + \left(\frac{L_{F4}}{2} \right) \right)^2 \right) \quad [9.56]$$

The two equations that are used to solve for ρ_{HANDLE} and ρ_{FRAME} are [9.54] and [9.55]. Substituting [9.49]-[9.53] into these two equations gives,

$$\rho_{FRAME} = \frac{B_B M_B - \dfrac{M_B L_H}{2}}{2L_{F1}\left(L_H + \dfrac{L_{F1}}{2} \right) + W_B\left(L_H + L_{F1} + \dfrac{L_{F2}}{2} \right) + 2L_{F3}\left(L_H + L_{F1} + L_{F2} + \dfrac{L_{F3}}{2} \right)}$$

$$+ \frac{B_B M_B - \dfrac{M_B L_H}{2}}{W_B\left(L_H + L_{F1} + L_{F2} + L_{F3} + \dfrac{L_{F4}}{2} \right) - L_H\left(L_{F1} + W_B + L_{F3} \right)} \quad [9.57]$$

$$\rho_{HANDLE} = \frac{M_B - 2\rho_{FRAME}\left(L_{F1} + W_B + L_{F3} \right)}{L_H} \quad [9.58]$$

The two parameters ρ_{HANDLE} and ρ_{FRAME} can be solved using [9.56] and [9.57], and then the relevant value of the mass moment of inertia I_B for the beam can be calculated using [9.56].

(d) Comparison of the three types of beam model

In the above section, three different types of one dimensional beam models have been derived; these being defined as *uniform section*, *two section* and *five section*. In this section, the three models will be generated for a specific tennis racket, to illustrate the procedure. The details of an *ITF Carbon Fibre* racket are given in Table 9.3. The details of six other rackets are given in Appendix D.3.

Table 9.3 Measured properties of an *ITF Carbon Fibre* tennis racket.

Length L_R (m)	Mass M_R (kg)	Balance Point B_R (m)	Mass Moment of Inertia I_{BUTT} (kgm^2)	Handle length L_H (m)	Racket width W_R (m)	Frame Length (m)			
						L_{F1} (m)	L_{F2} (m)	L_{F3} (m)	L_{F4} (m)
0.683	0.348	0.325	0.05337	0.228	0.265	0.094	0.027	0.308	0.027

Table 9.4 Properties for a beam model of an *ITF Carbon Fibre* tennis racket.

Total number of segments N	Segment length s (m)	Number of segments in each of the sections of the *two section* beam		Number of segments in each of the sections of the *five section* beam				
		N_H	N_F	N_H	N_{F1}	N_{F2}	N_{F3}	N_{F4}
51	0.0134	17	34	17	7	2	23	2

The *uniform section* beam model for the *ITF Carbon Fibre* tennis racket will have the same length and mass as that quoted in Table 9.3. It will be split into 51 segments each having a length s equal to 0.0134m. This number of segments is used for the reasons given earlier in this section.

The mass of each segment m_n will be equal to $M_R/51$ which gives $m_n = 0.00683$kg, for the *uniform section* beam. The beam balance point B_B is equal to $L_R/2$ for this beam, which gives $B_B =$ 0.342m. The actual balance point on the racket B_R is equal to 0.325m and therefore the two points do not coincide.

The other two beam models require the lengths of one or more features of the racket to be measured. These measurements are relatively trivial to execute but it should be remembered that the beam models will be split into 51 segments. Therefore, the measurements must be in discrete length units that allow the beam to be segmented. Therefore, for example, the length of the handle L_H is equal to,

$$L_H = N_H.s$$

where N_H is the number of segments which are used to model the handle, and s is the segment length as defined in Figure 9.2. (N_H must be an integer). The lengths of the various sections of the *ITF Carbon Fibre* tennis racket are quoted in Table 9.3. For completeness, the number of segments for each of the sections in the beam models is given in Table 9.4.

In the derivation of the *two section* and *five section* beam models, equations were derived to calculate the total mass of each of the sections. The mass of each segment in the relevant section can easily be calculated using the value of the total mass, and the number of segments in that section. For example, the segment mass m_n of each of the N_H segments in the handle of the *two section* beam is equal to M_H/N_H. The segment masses for each of the seven rackets are given in tabulated form in Appendix D.3, for each of the three types of model. A sample of these results is illustrated in Figure 9.9, for the *ITF Carbon Fibre* racket. Figure 9.9 illustrates typical mass distributions for a *two section* and a *five section* beam model respectively. Figure 9.9 (b) highlights the relatively large segment mass which is associated with extremities of the racket head. Interestingly, the mass distribution given in this figure is similar to that determined by Brannigan and Adali (1981). In that work, the mass distribution was measured experimentally.

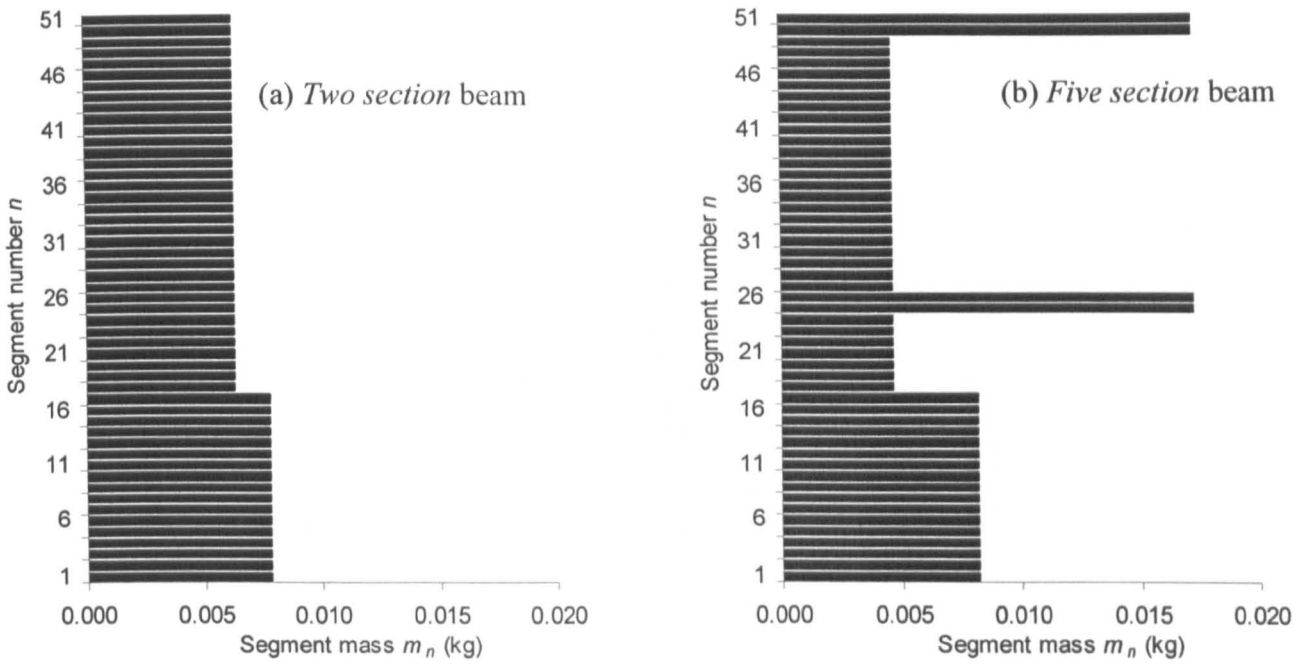

Figure 9.9 Illustration of the mass of each segment for a beam model of an *ITF Carbon Fibre* tennis racket.

To summarise the work discussed above, an example has been given to illustrate the method used to determine the details of the three different models, for an *ITF Carbon Fibre* tennis racket. The details of the models, for several other rackets, are given in Appendix D.3. Equations are presented in the derivations of three model beams which can be used to determine the beam mass moment of inertia I_B., This mass moment of inertia was calculated for the three different types of model beam, for each of the seven rackets which are being studied in this chapter, and this data is presented in Figure 9.10. In Appendix D.1, the mass moment of inertia I_{BUTT} was measured experimentally for these racket types, and this data is also shown in Figure 9.10.

This figure shows that the mass moment of inertia I_B of the *uniform beam* does not correlate very closely with that which was measured experimentally, for all racket types. An improved correlation is found for the mass moment of inertia for the *two section* beam, but the *five section* beam exhibits the best correlation. It can be seen that the value of I_{BUTT} and I_B (calculated using the *five section* beam) generally correlate to within 2%. It should be noted that generally this difference is less than 1%. For completeness, the data in Figure 9.10 is shown in tabulated form in Appendix D.3.

It can therefore be concluded that the *five section* beam model gives the closest correlation between the inertial properties of the beam and those of the tennis racket. The mass and balance point of the *five section* beams are identical to those of the racket, and the mass moment of inertia values correlate to within 2%.

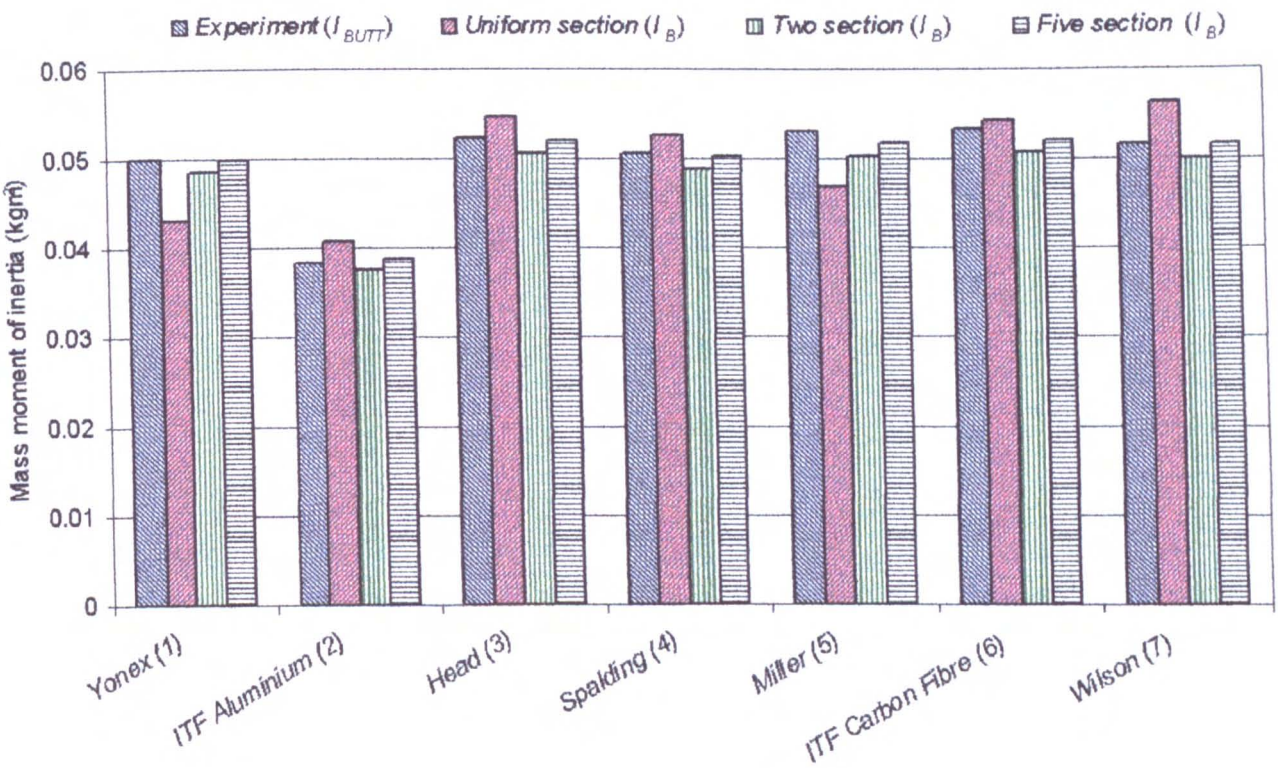

Figure 9.10 Mass moment of inertia for seven different tennis rackets. The data is presented for the value measured experimentally (I_{BUTT}), and the three model beams (I_B) for each racket.

(e) Determining the flexural rigidity of the one dimensional beam

The stiffness of the beam for a perpendicular loading is defined as the flexural rigidity EI. The flexural rigidity EI is the product of the Young's modulus of the material E and the second moment of area for the cross-section I. Clearly, the value of E could be estimated from a knowledge of the material used to construct the frame. The second moment of area could be measured by cutting the racket into segments, as done by Missavage *et al.* (1984). However, there are many disadvantages of this type of solution. Firstly, it is a time-consuming, destructive method and therefore is not suitable if a large number of rackets are to be modelled. Also, due to the high level of uncertainty in the definition of E and I, it is likely that the resulting model beam will have a different stiffness compared with the actual racket.

A more suitable method of obtaining the value of the flexural rigidity EI can be derived from a consideration of what the aim of the actual model is. It is remembered that the aim of the model is to replicate the inertial and vibrational properties of the racket. The former requirement has already been discussed in the previous section where it was shown that a *five section* model could be assigned very similar inertial properties as that of the racket. The vibrational properties refer to the fundamental frequency and the node points of this mode of vibration. Therefore, the discrete measurement of the terms E and I, although valid for certain circumstances, may not actually be the most suitable method in this case.

The ideal solution for this problem would be to derive a method of obtaining the value of EI which gives the beam the same fundamental frequency as that which was experimentally measured for the

tennis racket. In this work, it is assumed that the flexural rigidity EI is constant along the length of the one-dimensional beam. This assumption is required as it is difficult to define the magnitude of the parameter EI as a function of the distance along the longitudinal axis (y-axis). Also, a racket is generally constructed using a beam which has a uniform cross-section with minor additions to construct the handle and to shape the head. Therefore, to a first order approximation, it is assumed to be valid to consider that the flexural rigidity is constant.

In the previous section, it was shown that the fundamental frequency of the beam can be calculated using,

$$f_F = \frac{\sqrt{EI}}{2\pi}\sqrt{\lambda_{kN}} \qquad [9.59]$$

The *eigenvalue* parameter $\sqrt{\lambda_{kN}}$ is a function of the mass distribution, beam length and the method used to support the beam. Therefore, this parameter is constant for each beam, regardless of the value of EI, and can be evaluated using the methods described in the previous section. Equation [9.59] can be rearranged to give,

$$EI = \frac{(2\pi f_F)^2}{\lambda_{kN}} \qquad [9.60]$$

The fundamental frequency of the actual tennis racket, for transverse vibrations, can easily be measured using the method described in full in Appendix D.2. In brief, the vibrations of a tennis racket are sampled for an impact along the longitudinal axis using a soft hammer. The fundamental frequency was determined for a range of tennis rackets, and these experimentally determined values are given in Table 9.5.

Table 9.5 Experimentally measured fundamental frequency of the racket and the beam flexural rigidity for the three beam models.

Racket Type	Fundamental frequency of racket (Hz)	Flexural rigidity of beam EI (units)		
		Uniform section	*Two section*	*Five section*
Yonex (1)	161	186	183	218
ITF Aluminium (2)	103	70	73	81
Head (3)	138	169	167	197
Spalding (4)	127	138	137	186
Miller (5)	143	155	155	184
ITF Carbon Fibre (6)	134	156	156	185
Wilson (7)	142	184	180	212

Clearly, it is intended that the beam model will have the same fundamental frequency f_F as that measured experimentally for the racket. Therefore the experimentally measured values of f_F are input into [9.60] to enable the flexural rigidity EI of the beam to be calculated.

The calculated values of *EI* which are presented in Table 9.5 can be seen to represent the average properties of the tennis racket frame. When this is coupled with the assumption that the inertial properties of the beam are very similar to those of the racket, then it can be concluded that the beam will act very similarly to the racket, in vibration.

It is interesting to note that the calculated values of the flexural rigidity are considerably larger for the *five section* beam compared with the other two beam models. This is likely to be due to the fact that the *five section* beam has a large mass concentration at the tip of the beam. This may require a larger stiffness for a given fundamental frequency, compared with the *uniform beam*.

The evidence that the flexural rigidity can vary by up to 20%, depending on the assumed mass distribution, highlights a weakness of this modelling technique. The relevance of this weakness will be commented on further, later in this study. However, it should be remembered that all the beam models have the same fundamental frequency as that of the racket, which was the initial aim of this study. The finding that different flexural rigidity values are needed to achieve this aim must simply be excepted at this stage.

(f) Comparison of node positions on the model beam and the racket

In this section, a comparison is to be made between the node points for the racket and beam model, to quantify the correlation between the two. When a racket is excited by some external impulse, the resulting vibration of each point on the beam is a collection of an infinite number of modes of vibration. The amplitude of each of these modes is dependent on the duration of the impulse. It has been shown that, for a typical impact between a ball and racket, the duration is sufficiently long that only the fundamental mode of vibration is excited with any significant amplitude. For a given impulse, the amplitude of this mode will vary along the length of the beam/racket. The node point of vibration corresponds to the point on the racket/beam at which this amplitude is zero.

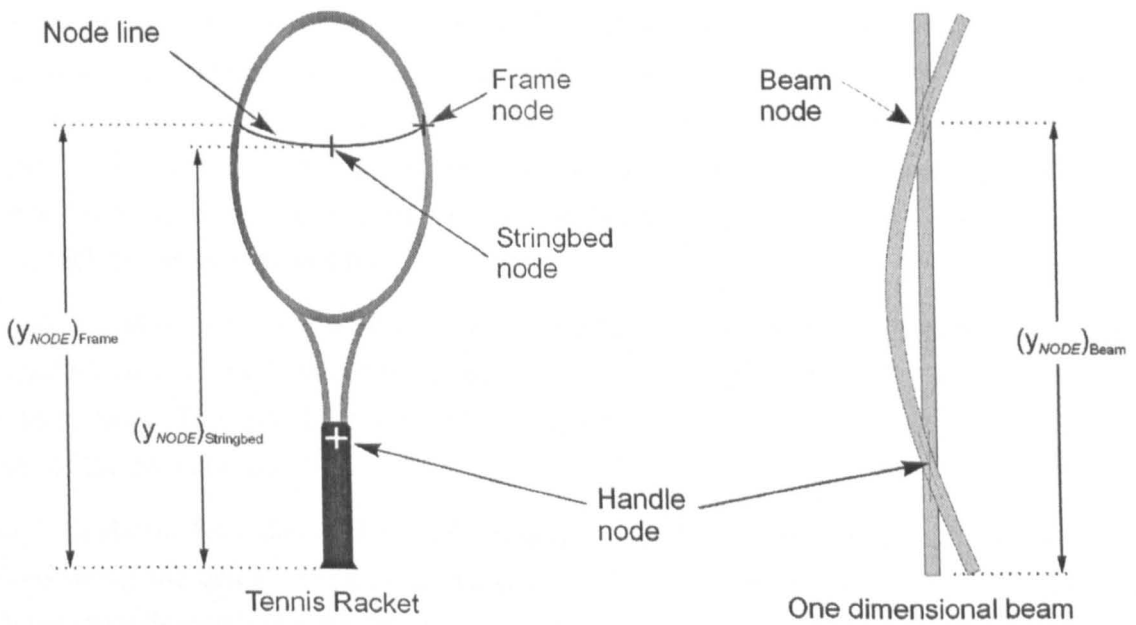

Figure 9.11 Definition of the nodes points for the fundamental mode of vibration for the racket/beam.

The correlation between the beam model and a tennis racket is to be assessed by comparing the node positions for the fundamental mode of transverse vibrations. For this mode, there is a node towards the tip of the racket, and one node towards the butt end. The latter node is defined as the *handle node* in Figure 9.11 and is not investigated in this study as all impacts occur on the head of the tennis racket.

Work by previous researchers (Cross 2001b and Kawazoe 1997a) has shown that the node position along the longitudinal axis (stringbed node) was in a different location to that of the node on the frame (frame node). A schematic illustration of these two node positions is shown in Figure 9.11. The single node point for a one dimensional beam is also shown in this figure. A comparison of the racket and beam node points highlights an inherent weakness of a one dimensional beam model; there is a unique node point on the beam compared with a two-dimensional node line on the tennis racket.

Cross (2001b) showed that the beam node for a *uniform beam* generally coincides with the stringbed node. However, this comparison was only made for one racket type. In this study, the frame node and stringbed node on the racket will be compared with the beam node for the three different beam models, for all seven racket types.

In the previous section, a numerical harmonic analysis was presented that could be used to calculate the amplitude of vibration for the fundamental mode of vibration, for each point along the beam. This analysis can be used to determine the position of the beam segment which has a negligible amplitude of the fundamental mode. This point is defined as the beam node point and is located a distance $(y_{NODE})_{Beam}$ from the butt end.

The details of the beam, such as the mass matrix $[M]$ and the flexural rigidity *EI*, were input into the model using the data which has been presented in the previous sections. To excite typical vibrations in the beam, the model of a ball impacting on the beam, as described in section 9.3.3(b) is used. In this case, the ball impacted close to the centre-of-mass of the beam as this was known to be near to an anti-node of vibration for the fundamental mode, and thus will excite a significant amplitude of vibration. The impact velocity of the ball was 20m/s and the racket was initially stationary. The ball type was a *Pressurised* ball and a stringbed stiffness equivalent to that measured for a racket strung at 70lbs was used, although it should be noted that these parameters do not effect the beam node position.

The model solution was calculated and the amplitude of vibration for the fundamental mode was evaluated for each of the N segments, using the harmonic analysis method that was described in a previous section. This information was then analysed to determine the node point for this mode, for each of the beam models.

Figure 9.12 shows the calculated velocity amplitude of the fundamental mode for the a range of positions along the beam. Data is presented for the three different model beams. The point at which the velocity amplitude for this mode equals zero corresponds to the node point for the beam. The position of the stringbed and frame nodes, for the *ITF Carbon Fibre (6)* tennis racket which is being modelled, are also shown in this figure.

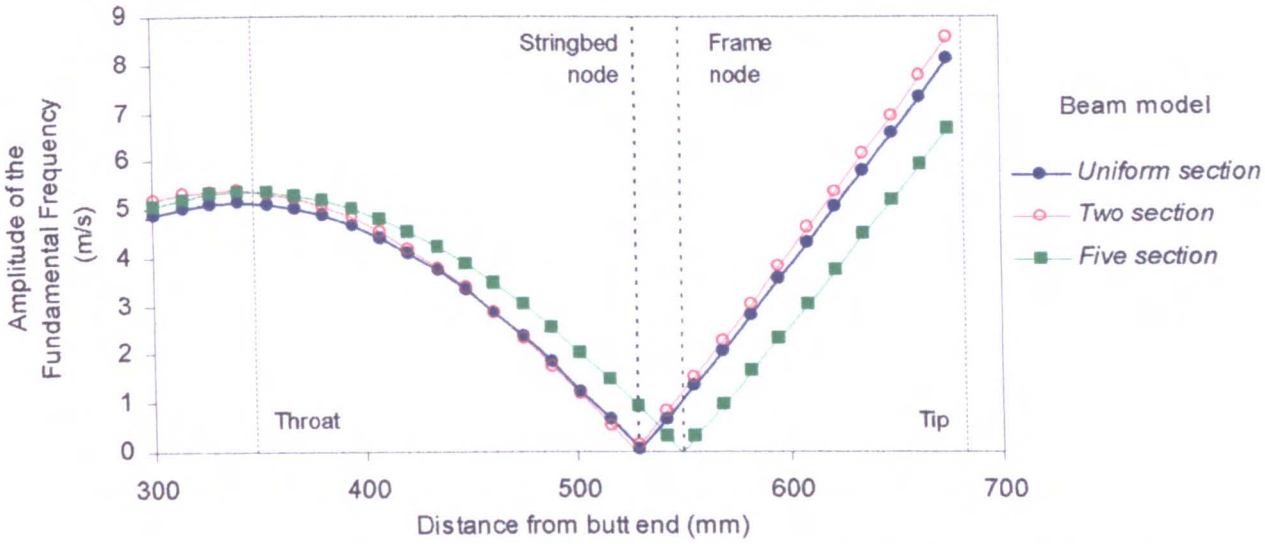

Figure 9.12 Modelled amplitude of vibration for the fundamental frequency for an impact on three different beam models that are simulating an *ITF Carbon Fibre (6)* tennis racket. The positions of the throat, tip, stringbed node and frame node for the tennis racket are also shown. The ball impact velocity was 20m/s. The impact position was at a distance of 328mm from the butt end.

These racket node points were determined using a standard experimental technique which is described fully in Appendix D.2. A brief summary of this method is given here. Impacts at the node point of the racket do not excite vibrations of the relevant mode in any part of the racket. Therefore, the node point of a tennis racket can be experimentally obtained by sampling the vibrations which result from an impact between a soft hammer and the racket, at a variety of locations. The location of the impact is moved until minimum vibrations of the fundamental mode are measured. A schematic illustration of the approximate node locations, for a tennis racket, are given in Figure 9.11.

The node point for *uniform section* beam is located at a distance 529mm from the butt end, as shown in Figure 9.12. The analytical solution for the node point of a uniform beam of length L_B is $0.776L_B$ (Cross 2001b). This gives an analytical node position equal to 530mm which clearly corresponds very closely to the numerically obtained value of 529mm. This confirms that the numerical and analytical solutions correlate very closely.

It can be seen that the location of the beam node point, for the *uniform section* and *two section* beams correspond closely with the stringbed node. This means that impacts at this point on the beam will not excite the fundamental mode of vibration. Correspondingly, impacts at this point on the longitudinal axis of the racket will not excite this mode of vibration either. This would initially suggest that these two beam models suitably simulate the transverse vibrational properties of a tennis racket. However, this is purely coincidental because the actual frame node is located at a different position. The frame node corresponds very closely to the node for the *five section* beam, and is located at a distance of approximately 550mm from the butt end. This implies that this type of beam model is a more suitable technique for modelling the vibrational properties of the racket frame. However, if this *five section* beam was used to model an impact on the longitudinal axis at a

point ~530mm from the butt, a vibration of the fundamental mode would be established. By contrast, an identical impact on the longitudinal axis of the racket tennis racket would not have excited any vibrations of this mode. This discrepancy is discussed later in this chapter.

Table 9.6 Stringbed and frame nodes for the tennis rackets. Beam nodes for the three model beams.

Racket Type	Stringbed Node $(y_{NODE})_{Stringbed}$ (mm)	Frame Node $(y_{NODE})_{Frame}$ (mm)	Beam node $(y_{NODE})_{Beam}$ (mm)		
			Uniform section	*Two section*	*Five section*
Yonex (1)	547	579	552	549	575
ITF Aluminium (2)	524	551	528	529	549
Head (3)	523	557	529	529	551
Spalding (4)	534	554	531	529	556
Miller (5)	538	561	531	534	559
ITF Carbon Fibre (6)	528	549	529	529	551
Wilson (7)	523	558	531	525	549

The comparison between the model beam and racket node points has thus far only being made for an *ITF Carbon Fibre (6)* racket. In Table 9.6 this comparison is extended to cover the other six racket types. It can be seen that the all the rackets exhibit the similar trend that was found for the *ITF Carbon Fibre (6)* racket. As before, the stringbed node generally corresponds most closely with beam node for the *uniform section* and *two section* beams; the frame node being closer to the beam node for the *five section* beam model.

In Appendix D.2 it was quoted that the accuracy of the measurements of $(y_{NODE})_{Stringbed}$ and $(y_{NODE})_{Frame}$ was only in the order of ±5mm. Therefore, the location of the experimentally obtained node point on the racket corresponds with the respective beam node, within the bounds of the experimental error.

(g) Summary

In this section, it has been shown that the inertial properties (mass, balance point and moment of inertia) of a tennis racket can most closely be simulated by using a one-dimensional beam which is composed of five uniform sections. It was then shown that the node point on this *five section* model beam correlates very closely with the frame node of the corresponding tennis racket, implying that this is the most suitable model of the three which have been developed in this section.

However, the weakness of this model can be identified from a consideration of the positions of the node points on the racket. The node point on the frame is at a different position to the stringbed node on the longitudinal axis of the racket. As this study is only concerned with impacts along the longitudinal axis, it can be deduced that impacts at the stringbed node of the racket will excite no vibrations, whereas impacts at this same point on the *five section* beam will excite vibrations because this is not the node point. This weakness in the model is due to the simplification of a

complex three dimensional object as a one dimensional beam. This discrepancy will be discussed later in this chapter.

9.4 One dimensional, flexible beam model – distributed loading

9.4.1 Introduction

In section 9.3, a numerical method was discussed which can be used to solve for the displacement of a one dimensional flexible beam that is subjected to a time-dependent loading. This numerical method involves the division of the beam into N segments. In that section, it was assumed that the force was applied over a single segment to simplify the solution. However, it was noted that the same solving method is valid for distributed load cases.

Clearly, in an impact between a ball and racket, the ball/stringbed does not impart a point load on the racket frame. Instead, the force will be distributed, in some way, across the head of the racket. Therefore, in a model of a ball impacting on a one-dimensional beam, the force should be distributed over the beam segments that are representative of the racket head. The exact form of the distributed load is not easily defined but can be approximated using a suitable function. Also, the definition of a continuous distributed load case over a finite number of discrete load points is not a trivial problem and therefore the derivation of this load case is given a thorough explanation in this section.

9.4.2 The beam model

In this section, the resultant force $(F)_t$ acts on the beam at the ball impact position; this position being located at a distance y_{IP} from the butt end of the beam. It is assumed that this force is applied as a distributed load across the beam segments that represent the head of the racket. Clearly, this distributed load must be equivalent to the force $(F)_t$.

The form of this distributed loading must be representative of the mechanism that acts to apply the load to the racket frame, via the stringbed. To understand this mechanism fully would require a two dimensional analysis of the frame/stringbed system, which is beyond the scope of this work. Various authors have commented upon this mechanism (Brannigan & Adali (1981) and Cross (1999c)). Cross (1999c) assumed that the loading could be simulated using a point load, similar to the method discussed in section 9.3. Furthermore, Cross (1999c) stated that the propagation of the force through the stringbed was of a comparable speed to that through the beam (due to bending) and therefore a point loading was a satisfactory 1st order approximation. Brannigan & Adali (1981) conducted a two dimensional analysis of the frame/stringbed system. In this analysis, the impact was located at the geometric string centre, to simplify the solution procedure. This publication does not a present a generic solution for impacts located at other positions along the longitudinal axis.

In this current study, the general form of the distributed loading will be determined by considering several simplifications of the stringbed/frame interaction. Furthermore, a number of assumptions

are defined. These assumptions are required because a two dimensional analysis of the frame/stringbed system is not conducted in this study. In this analysis, it should be noted that the distributed loading is only to be defined in one dimension; this being parallel to the longitudinal axis.

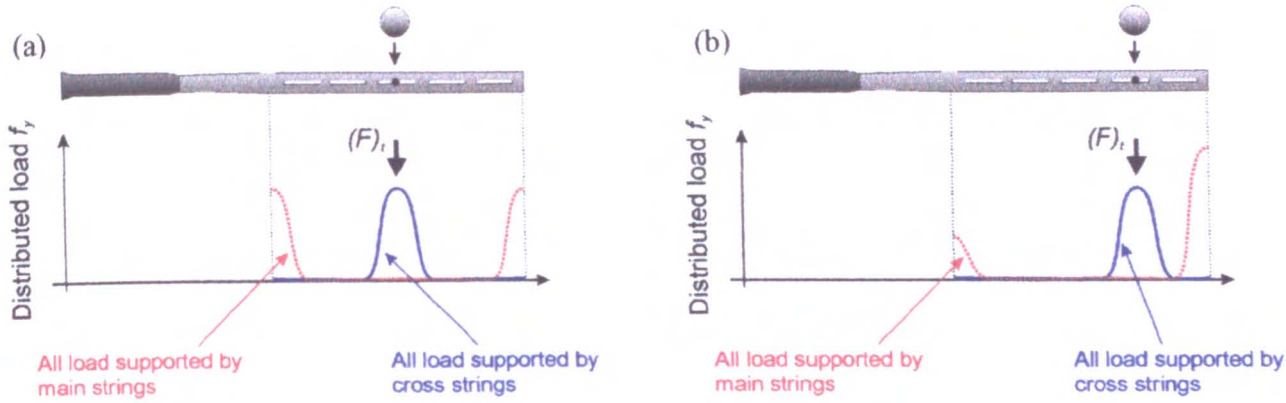

Figure 9.13 Simplified distributed loading if the load is taken solely by either the main or cross strings, (a) for an impact at the geometric string centre of the head of the racket, and (b) for an impact towards the tip of the racket.

The simplest impact to consider is that which is located at the geometric string centre of the racket. If it is assumed that the racket head is approximately symmetrical in both the longitudinal and transverse axes, then the distributed loading will also be symmetrical along its one dimension. If all the load was supported by the cross strings, and the main strings were subjected to zero loading, then the distributed loading would have a form similar to that shown in Figure 9.13(a). Also plotted in this figure is the form of the distributed loading for the case where all the load is supported by the main strings. These two simple load forms are not representative of the actual loading mechanism. Furthermore, a simple superposition of the two forms would not be realistic as the two sets of strings interact, thus distributing the load to all parts of the frame, not just those implied by the plots in Figure 9.13(a). However, using the two simple curves illustrated in this figure, and the knowledge that the load will be distributed to all parts of the frame, it is assumed that the load will be uniformly distributed along the longitudinal axis of the frame, for impacts at the geometric centre of the head. This uniform loading will only act on the beam segments which represent the head of the racket.

A similar analysis can be conducted for impacts located at other positions along the longitudinal axis. Figure 9.13(b) illustrates an impact which is located towards the tip of the tennis racket. In this figure, the two simplified loadings are plotted which represent the assumptions that all the load is either supported by the main or cross strings. If the load is supported by the main strings, it is assumed that the force which acts at the tip is larger than the force acting at the throat to ensure that the resultant loading is equivalent to the point load $(F)_t$. As before, the two load cases in Figure 9.13(b) can not simply be superimposed to find the form of the resultant distributed loading because the two sets of strings are do not move independently and they physically interact during impact. Clearly, there are many possible forms of the distributed loading but in this study only two main examples are investigated. These two general shapes are illustrated in Figure 9.14.

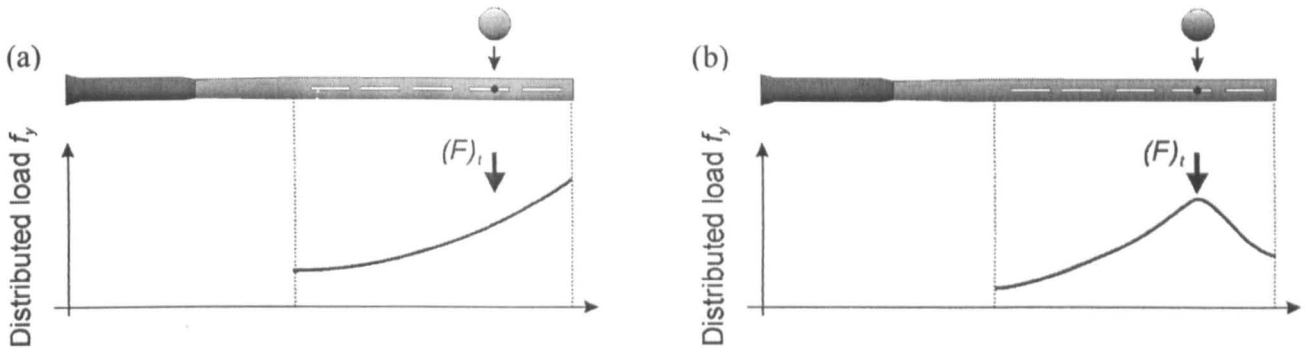

Figure 9.14 Two general examples of distributed loadings which are equivalent to a point load of $(F)_t$. (a) A function which is maximised at the edge of the racket head, and (b) a function which is maximised at the impact location.

The distributed loadings shown in Figure 9.14 are not associated with specific functions that describe their shape but are merely meant to represent two different general forms of the distributed loading. Both of these general shapes are deduced using the two discrete load forms shown in Figure 9.13(b), along with the knowledge that the load will be distributed to all points on the racket frame.

Figure 9.14(a) shows a distributed loading which is maximised at the edge of the racket head, whereas Figure 9.14(b) illustrates the distributed loading which is maximised at the impact location. The form shown in Figure 9.14(a) is based on the assumption that the load which is supported by the main strings dominates the mechanism. For example, in this case the peak load acts at the tip of the racket. The form shown in Figure 9.14(b) assumes that the load which is supported by the cross strings dominates the mechanism, and therefore the load is maximised at the impact location.

Intuitively, the actual distributed loading is likely to be an amalgamation of the two forms shown in Figure 9.14. A two dimensional analysis of the stringbed system is required to obtain the details of this amalgamated distributed loading. However, as mentioned previously, this is beyond the scope of this current study. Therefore, it is assumed that a first order approximation of the distributed loading could be achieved by using one of the two forms in Figure 9.14. It is also assumed that both these shapes exhibit an equal correlation with the actual distributed loading. This assumption was made because it is not possible for the validity of either form to be quantified.

Initially, it would appear that both shapes are equally suitable to be used to model the load which acts on the beam. However, it is considerably simpler to define a function which is of a similar form to that of the continuous curve in Figure 9.14(a), compared with that required to define the curve in Figure 9.14(b). Therefore, it is concluded that the distributed load, with the form that is shown in Figure 9.14(a), should be used in the model.

There are many functions which could define a curve similar to that in Figure 9.14(a), e.g. a second order polynomial. However, some of these functions are more suitable than others. For example, it must be possible to uniquely calculate the coefficients of the distributed loading function which gives the required magnitude and location of the resultant force $(F)_t$. Generally, this requires the equation to have two non-zero coefficients for a unique solution to be obtainable. Furthermore, an

important feature of the function is that it must produce a valid distributed loading, for all impact locations. For example, a second order polynomial is not suitable as it may define a loading which has a negative value at some points along the beam.

An alternative function, which is of a similar form to that shown in Figure 9.14(a), is defined as a general spandrel (*Efunda* 2002). This is a suitable function as the coefficients can be uniquely determined by the magnitude and location of the resultant force. Also, the solution remains valid (positive) at all locations along the beam, for any impact position. Furthermore, for impacts at the geometric string centre, the general spandrel curve represents a uniform loading, which is the assumed shape for these impacts. Therefore, it was concluded that a general spandrel was a suitable first order approximation of the distributed loading.

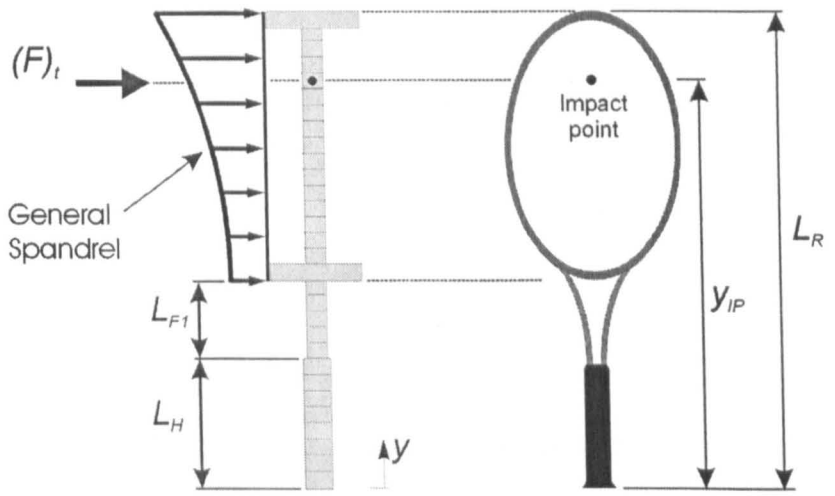

Figure 9.15 Illustration of a distributed loading which acts over the beam segments that represent the racket head.

Figure 9.15 illustrates the distributed loading that is defined using the general spandrel function. In this figure, it can be seen that the loading only acts on the beam segments which represent the head of the tennis racket. The magnitude and location of the resultant of this distributed loading is equivalent to that of the force $(F)_t$ being located at a distance y_{IP} from the butt end of the beam.

The form of a general spandrel, for this co-ordinate system is,

$$f_y = \frac{h}{b^\beta}\left(y - \left[L_H + L_{R1}\right]\right)^\beta \qquad [9.61]$$

for $\left[L_H + L_{R1}\right] < y < L_B$

The parameter b is equal to the length of the base of the general spandrel curve which is equal to,

$$b = L_B - \left[L_H + L_{R1}\right] \qquad [9.62]$$

The parameter β is a function of the position at which the force is applied y_{IP} and the base b,

$$\beta = \frac{2c_y - b}{b - c_y} \qquad [9.63]$$

where,

$$c_y = \left(y_{IP} - \left[L_H + L_{R1}\right]\right) \qquad [9.64]$$

The parameter h, which is equal to the height of the general spandrel curve, can be calculated using,

$$h = \frac{A_{GS}}{b}(\beta + 1) \qquad [9.65]$$

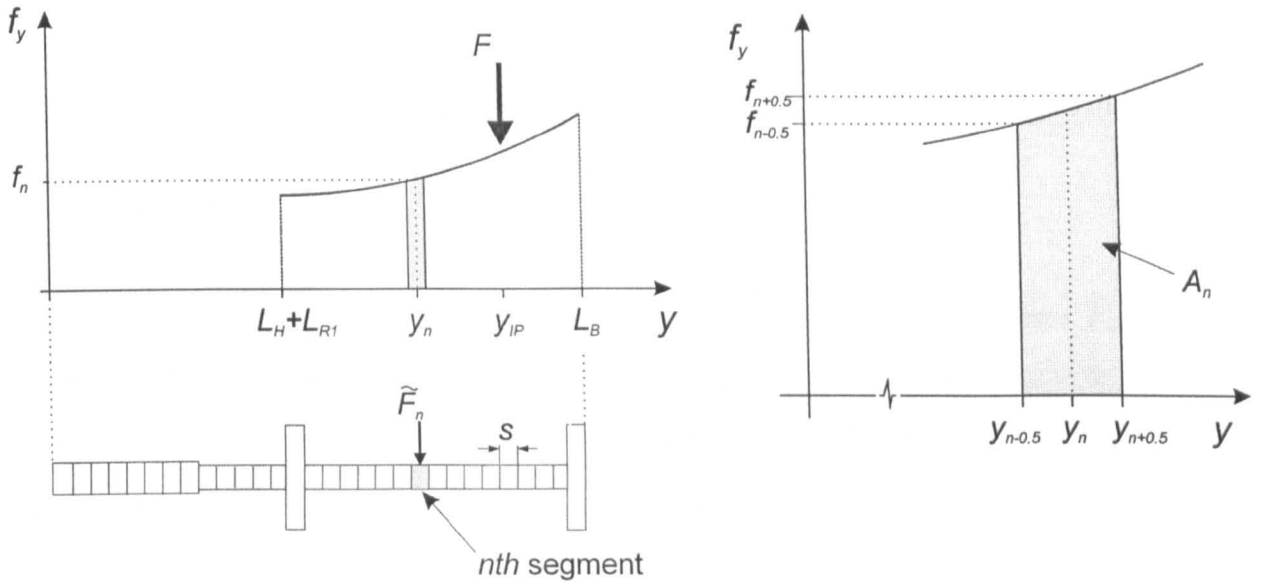

Figure 9.16 Illustration of the distributed loading f_y and the discrete loading $\widetilde{F}_n$ which acts on each segment.

The parameter f_y is equal to the magnitude of the distributed load, as a function of the distance along the beam y. Therefore, the area enclosed by the general spandrel curve is numerically equal to the total force applied to the beam. To generate a normalised solution, the force F is assumed to be unity, and thus the area A_{GS} under the general spandrel curve is also equal to unity. For this normalised solution, [9.65] becomes,

$$h = \frac{1}{b}(\beta + 1) \qquad [9.66]$$

The above analysis has generated equations to define the continuous function that gives a normalised distributed loading which is equivalent to the load F, applied at a distance y_{IP} from the butt end. The magnitude of each of the parameters b, β, c_y and h can therefore be defined for the relevant beam model and impact position. However, for the beam model, the load must be applied at a finite number of discrete points, at the centre of the segments; each discrete load being defined as $\widetilde{F}_n$ as illustrated in Figure 9.16. The total sum of the discrete loads $\widetilde{F}_n$ will be equal to unity.

The continuous loading f_y acts over a finite number of segments of the beam which are analogous to the head of the racket. The discrete load $\widetilde{F}_n$ which acts on the *nth* segment must be equivalent to the continuous loading which acts over the length of this segment. The area A_n enclosed by this

continuous loading over the nth segment is shown in Figure 9.16. The position along the beam y_n is defined using,

$$y_n = ns - s/2$$

where n is the segment number.

The area A_n can be approximated using,

$$A_n = \frac{s}{2}\left(\frac{f_{n-0.5} + f_n}{2}\right) + \frac{s}{2}\left(\frac{f_n + f_{n+0.5}}{2}\right) \quad [9.67]$$

The area A_n is equivalent to the force which acts on this segment $\widetilde{F}_n$ and therefore,

$$\widetilde{F}_n = \frac{s}{4}\left(f_{n-0.5} + 2f_n + f_{n+0.5}\right) \quad [9.68]$$

This equation, along with those discussed above, can be used to determine the force $\widetilde{F}_n$ which acts on each of the segments, for an overall equivalent loading F; the force F being equal to unity in this case. The values of the normalised force $\widetilde{F}_n$ for each of the N segments can be collated to form a column matrix with N rows $\left[\widetilde{F}_n\right]$.

$$\left[\widetilde{F}_n\right] = \begin{bmatrix} 0 \\ 0 \\ 0 \\ \cdots \\ \cdots \\ \cdots \\ \widetilde{F}_{N-2} \\ \widetilde{F}_{N-1} \\ \widetilde{F}_N \end{bmatrix}$$

where the value of $\widetilde{F}_n$ is non-zero for the segments which represent the head of the tennis racket, and zero for all other segments.

The force matrix $[F]$, which is used in the numerical solution for determining the displacement of the beam (equation [9.28]), can be calculated using,

$$[F] = (F)_t\left[\widetilde{F}_n\right]$$

The magnitude of the scalar force $(F)_t$ which acts during the impact is determined using the visco-elastic model of the ball and stringbed, shall be discussed in the following section.

9.4.3 Modification to the spring-damper model for a distributed loading.

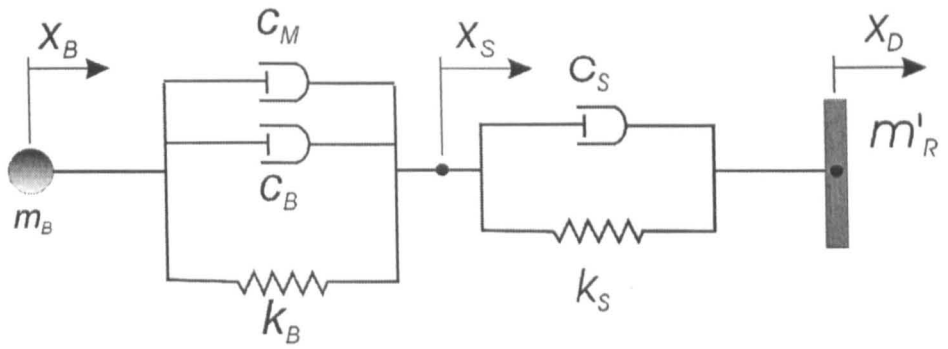

Figure 9.17 Visco-elastic model of the ball/stringbed system, for a ball impact on a tennis racket.

As discussed previously, the ball is simulated as a point mass m_B and the stringbed was assumed to have zero mass. The ball and stringbed were both individually modelled as springs and dampers in parallel as illustrated in Figure 9.17 The parameters m'_R and x_D represent the 'effective' mass and displacement of the impact point on the racket frame, respectively. The force acting in the spring damper system at any time t is defined as $(F)_t$.

The displacement x_D is not simply equal to the displacement of the beam segment at that point x_{IP}. This assumption would disobey the law of energy conservation, for a distributed loading of the beam. The displacement x_D is equal to the 'weighted' average displacement of all the beam segments which are subjected to an excitation force (those segments which represent the racket head). The data is 'weighted' by multiplying the displacement of each segment by the force which acts on that segment. The equation used to define the value of x_D at time t is,

$$(x_D)_t = \left(\frac{1}{(F)_t N_{HEAD}}\right) \sum_{n=(N+1)-N_{HEAD}}^{N} (F_n \times x_n)_t \qquad [9.69]$$

where N_{HEAD} is the number of segments over which the force $(F)_t$ is distributed over.

Apart from this minor modification, the solution of the visco-elastic model is identical to that described in section 9.2. The force $(F)_t$ which acts on the beam can be calculated using [9.42], where x_{IP} is replaced with x_D.

9.4.4 Comparison of a point load and a distributed loading of a beam.

(a) Introduction

In section 9.3, a numerical solution was given that can be used to determine the displacement of a one-dimensional beam which is subjected to a time dependent point load. It was shown that the model required certain parameters to be defined which were dependent on the ball type, stringbed stiffness and racket type. To complete the required model inputs, the velocity of the ball and racket

were specified for the instance immediately prior to impact. The output of the model included the ball rebound velocity and the motion of the freely oscillating beam.

In section 9.4.2, it was shown that it was possible to modify the model so that the force is applied as a distributed loading. The model was otherwise identical to that described in section 9.4. The distributed load case is more physically representative of the actual mechanism which loads a tennis racket during an impact with a ball; the load being applied to the racket frame via the stringbed. However, the distributed load case leads to a more complicated force matrix $[F]$ and it may be introducing an unnecessary complication into the model. In this section, this is to be evaluated by comparing the model solutions for the point load case with those of the distributed load case. Clearly, if there is no significant difference in the results for the two loading conditions, then the simpler point load case should be used in the model.

The two main outputs of the model are (1) ball rebound velocity and (2) the amplitude of beam vibrations after impact. Therefore, these are the two parameters which are to be compared for the two models which use (a) a point load case and (b) a distributed load case. The comparison is to be conducted using the model parameters for a *Pressurised* ball and stringbed strung at 70lbs, as shown in Tables 9.1 and 9.2. The ball velocity for all the tests in this section is 20m/s and the impact is located at a range of points which stretch across the longitudinal axis of the head of the racket/beam. These locations are in increments of the segment length s as the impact must be located at the centre of one of the N segments of the one dimensional beam. The model solution is to be calculated using the *five section* beam for the *ITF Carbon Fibre (6)* tennis racket. The parameters for this racket have been described in Tables 9.3 to 9.5, and in Table D.7.

(b) Results

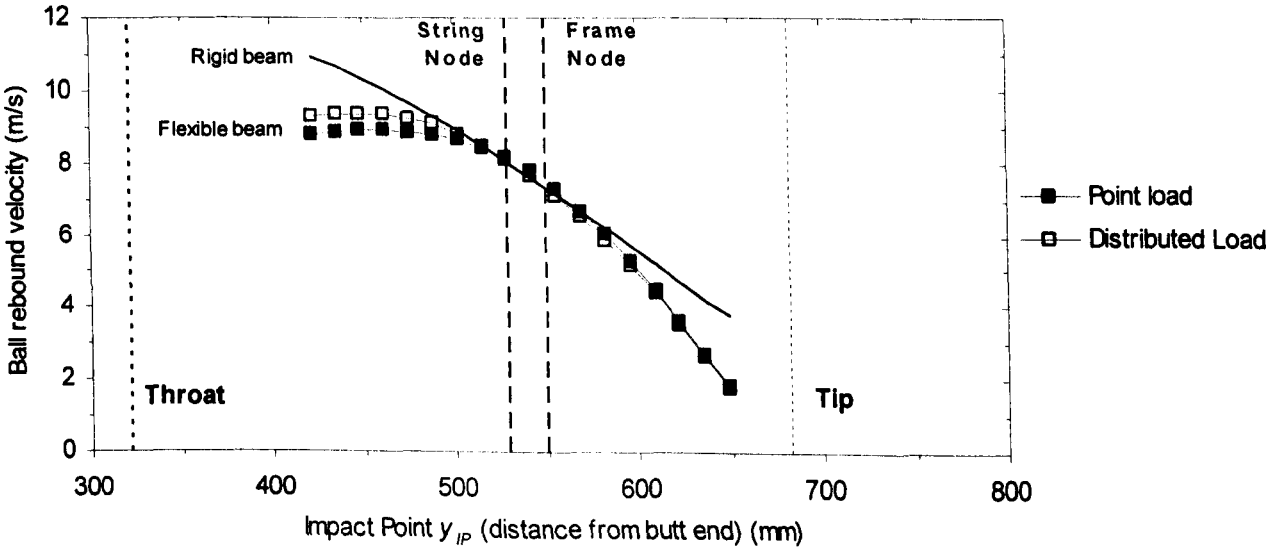

Figure 9.18 Calculated ball rebound velocity for a range of ball impact positions on a freely suspended beam. Data is presented for both a point loading and distributed loading on a flexible beam, and also for a point loading on a rigid beam. The beam model represents an *ITF Carbon Fibre (6)* tennis racket. The positions of the throat and tip on the head of the racket, and the string and frame nodes are also given.

Figure 9.18 shows the ball rebound velocity which has been calculated by the model of a freely suspended racket, for a range of ball impact positions. The two sets of data points which represent impacts on a flexible beam are presented for the two different assumptions regarding the method of loading; these two methods being a point and a distributed loading. Also, plotted in each figure is a data line which represents the rigid beam solution which was calculated using the same method as that described in section 9.2. The data is presented in Figure 9.18 for the *ITF Carbon Fibre (6)* tennis racket.

Figure 9.18 shows that the two different loading mechanisms yield different values of ball rebound velocity for impacts towards the throat end of the head. Also, both sets of data for a flexible beam model yield considerably lower ball rebound velocities than those exhibited for impacts on a rigid beam, for impacts towards the throat end of the head. At an impact point y_{IP} of approximately 540mm, the rigid and flexible beam models exhibit very similar ball rebound velocities. This position corresponds closely with both the string and frame node points of the racket; the definitions of these two points being given in Figure 9.11. At impact positions which are close to the tip of the racket, the two flexible beam models (point loading and distributed loading) both give similar results, which are considerably lower than those exhibited by the rigid beam model.

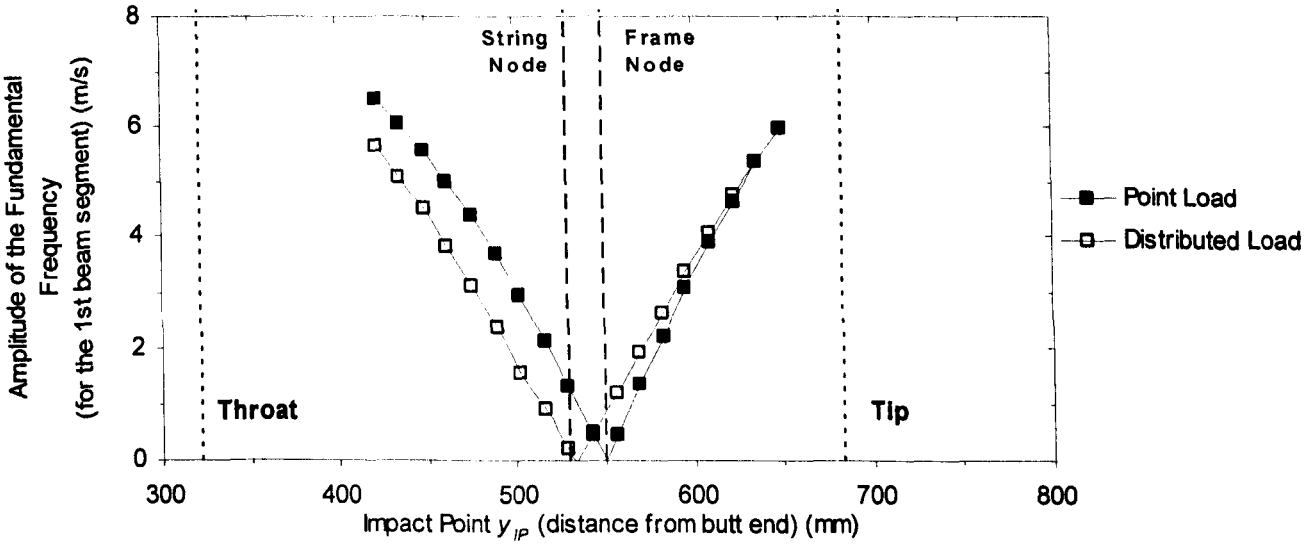

Figure 9.19 Calculated amplitude of vibration of the fundamental frequency for a range of ball impact positions on the beam, for the vibration of the 1st beam segment (closest to the butt end). Data is presented for both a point loading and distributed loading on a flexible beam, and also for a point loading on a rigid beam. The data is presented for the *ITF Carbon Fibre (6)* tennis racket. The positions of the throat and tip on the head of the racket, and the string and frame nodes are also given.

The beam model which has been discussed in sections 9.3 and 9.4 calculates, amongst other parameters, the displacement of the beam after impact. During the period after impact, the model beam vibrates freely and the displacement of each beam segment is calculated for a period of approximately 25ms. The numerical harmonic analysis which was described in section 9.3.2, was used to determine the amplitude of the fundamental mode of vibration, for each of these segments. Figure 9.19 shows the amplitude of this mode for the segment at the butt end of the beam, for a

range of different ball impact positions. The string and frame nodes are also plotted on these figures.

An impact on the flexible beam with a point load which is located at approximately 550mm from the butt produced minimum vibrations of the fundamental frequency. This point corresponds with the node point for this beam which has been determined previously and is shown in Figure 9.12 and Table 9.6. Also, as mentioned earlier, this point corresponds very closely with the frame node for the racket. This data confirms that the beam and racket frame exhibit very similar node locations, which was one of the aims of this work.

An impact on the beam with a distributed load at approximately 530mm from the butt produced minimum vibrations of the fundamental frequency, for this load case. However, it should be noted that this does not mean that the beam node has moved because this is not physically possible without the beam being modified in some way. Instead, it is illustrating that the point of minimum vibrations does not coincide with the beam node point, for impacts involving a distributed load. This impact position corresponds very closely to the racket string node.

A supplementary comparison of the beam and racket nodes is presented for a *Yonex (1)* racket in Appendix D.4. This comparison exhibits a similar correlation as was found for the *ITF Carbon Fibre (6)* racket.

(c) Discussion

It has been shown that the frame node and string node, on a tennis racket, do not coincide. Typical locations of these two nodes are shown in Figure 9.19. The string node is the point on the longitudinal axis of the stringbed which excites minimal vibrations in the frame. An impact of this nature will involve some kind of complex distributed loading being applied to the racket frame, although the precise form of this loading is not known. The frame node corresponds to the point on the frame which excites minimum vibrations. By contrast, this kind of impact involves a point loading of the frame. Clearly, these two different kinds of loading yield different locations at which minimal vibrations are excited.

Intuitively, it would have been expected that any impact which is located at the node point would not excite vibrations of the fundamental mode. However, it was found that a distributed loading of the beam, which has a resultant that acts at this node, excites vibrations of this mode. It is beyond the scope of this study to fully explain this mechanism but the differences in the induced vibrations of a beam, for different loading methods, can be illustrated using a simple example. If a one dimensional, uniform beam is subject to a point load which acts at its mid-point, for a short duration, significant vibrations of the fundamental mode will be excited. However, if this same beam is subjected to a uniform loading along its full length, equivalent to the point loading, then no vibrations of this mode are excited. This example confirms that a point load and distributed load do not necessarily excite the same vibrations in a beam.

In this current section, the beam model has been used to show that a point loading and a distributed loading yield different locations at which minimal vibrations are excited, for an impact on a simple

one dimensional beam. The distributed load case induces minimal vibrations at a location which is close to the experimentally measured string node. Clearly, both the model and experimental cases involve a distributed loading and therefore it is consistent that these two locations coincide. This is supported by the observation that the locations of the beam node (minimal vibrations for a point loading) and the frame node also coincide.

(d) Conclusions

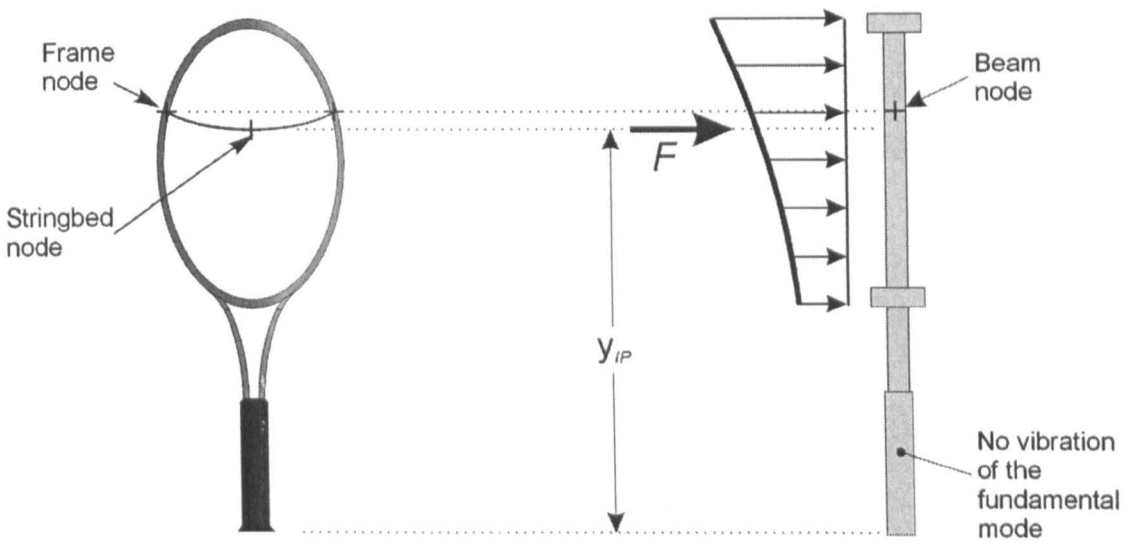

Figure 9.20 Illustration of an impact involving a distributed loading of the beam. The resultant of the distributed loading, force F, does not act on the beam node. A qualitative comparison of the frame, stringbed and beam nodes is also presented.

The important findings from this short study are illustrated in Figure 9.20, which shows a tennis racket and a *five section* beam model. It can be seen that the racket frame node correlates very closely to the beam node. The beam is subjected to a distributed loading, with a resultant force F located at a distance y_{IP} from the butt end. This loading results in minimal excitation of the fundamental mode of vibration, even though the resultant does not coincide with the beam node. Figure 9.20 illustrates that this impact location corresponds with the experimentally measured stringbed node on the racket.

For the beam model, the location y_{IP} does not represent a node point, but instead can be considered to be an impact point which excites minimum vibrations of the fundamental mode. Extending this concept to a tennis racket, the stringbed node can simply be considered as an impact point which excites minimal vibrations. This can not be proven and therefore the analysis of this finding is not continued further.

9.4.5 Summary

In section 9.3, a model was developed for a ball impact on a freely suspended tennis racket. In that section, the racket was modelled as a one dimensional beam which was subjected to a point loading. In this current section, the model was modified so that the force was applied as a

distributed loading. It has been shown that the visco-elastic model, which is used to simulate the ball/stringbed system, has to be modified to account for the load being distributed over the beam. This visco-elastic model is used to calculate the overall resultant force F which acts on the beam. It is assumed that this overall force acts over the beam segments that represent the head of the racket. A method has been presented which can be used to determine the time-dependent forces which act on each of the segments of the beam, that give the equivalent loading as that of the overall resultant load F. The displacement of the beam, for this distributed loading, can be determined using the same methods described in section 9.3.

A comparison was made between the model solutions obtained for (a) a point loading, and (b) a distributed loading. It was shown that, for impacts close to the throat end of the head, the ball rebound velocity was larger for the distributed loading, compared with the point loading. However, for all other impact points, the ball rebound velocity was very similar for both loading methods.

The main finding from this model is that the impact location which excites minimal vibrations of the beam does not coincide with the node point, for a distributed loading. Furthermore, this impact location correlates very closely with the measured stringbed node for a tennis racket. It can therefore be concluded that a distributed loading, as opposed to a point loading, is a more suitable method of applying the load. This is because the nodal properties of the beam are most closely simulated using this loading method.

9.5 Computer software used to solve the model

9.5.1 Introduction

In section 9.3, algebraic equations have been defined which can be used to calculate the displacement of a beam for a time-dependent force. In section 9.4, it was shown that this beam could be used to represent a freely suspended tennis racket in an impact with a tennis ball. In that section, the model parameters are defined for a range of ball types, stringbed stiffnesses and racket types which allow the model to be solved for any input combination of initial ball and/or racket velocities, and any impact location along the longitudinal axis. In sections 9.3 and 9.4 it has been shown that the load can be applied onto the beam as either a point load or a distributed load. Both these loading methods involve the same numerical solving method, which was given in section 9.3. However, it was concluded that a distributed loading was the most suitable method of applying the load.

The equations and parameters which were defined in sections 9.3-9.4 are sufficient to allow the reader to repeat the model calculations which were performed in those sections. Although all the necessary equations are given, it is estimated that a typical impact requires more than six million calculations to be performed (based on $N = 51$ and $\Delta t = 5\mu s$). Therefore, the method used to perform the calculations is not trivial and shall be discussed in this section.

There are many PC software packages available which are capable of efficiently performing the required calculations. Cross(1999c) used an MS-DOS BASIC routine to solve the equations. This

was sufficient for the scope of the work covered in that publication. However, in this current work, a model with a user-friendly graphical interface was required to allow a trained user to simulate different types of impact, without the required knowledge that is needed to apply the equations given in sections 9.3-9.4. A suitable software development package for such a task is *MS Visual Basic v6*. This software development tool allows the production of an executable *MS Windows* program with a suitable graphical interface. It also possesses an efficient numerical processing ability which is necessary due to the large number of calculations involved. The desired program would have a function which allowed different ball types, stringbed stiffnesses and racket types to be entered into the model, along with the initial velocity of the ball and racket. The program must then be capable of solving the model equations which were given in the previous section, and giving a suitable output, such as ball rebound velocity. The features of the developed program, which will be referred to as *Racket Impact v1.1*, will be discussed in this section.

9.5.2 Definition of Ball and Stringbed type

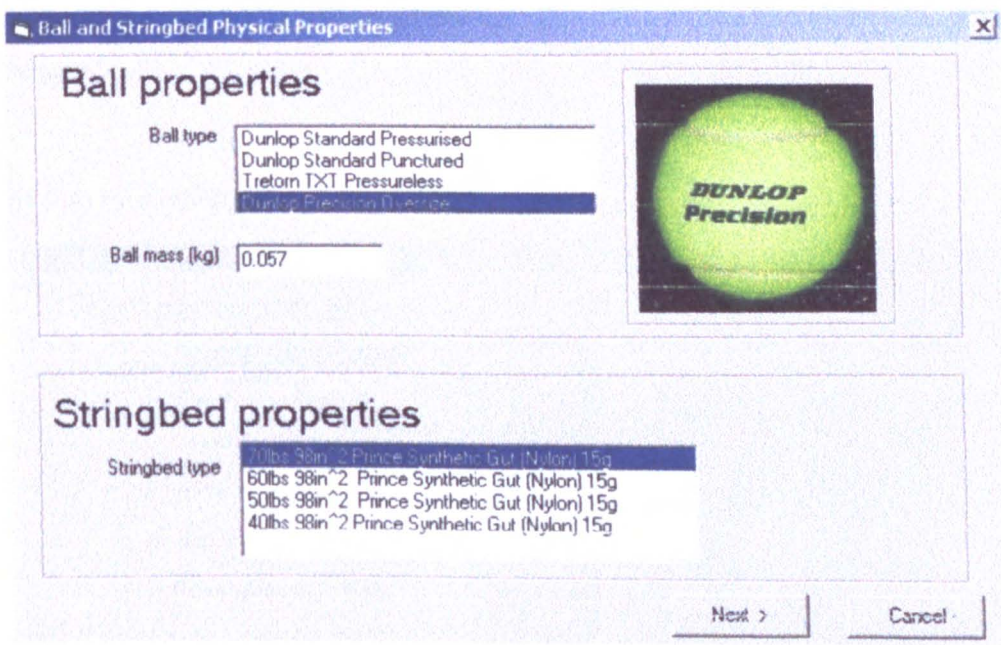

Figure 9.21 Illustration of the *Racket Impact v1.1* form which is used to select the ball/stringbed type.

Before the model solution can be calculated, the values of the ball, stringbed and racket parameters must be entered into the *Racket Impact v1.1* software. This is commenced by selecting the 'Input Parameters' option in the menu of the *Racket Impact v1.1* software. Figure 9.21 shows the *Visual Basic* form which allows the user to select the ball and stringbed type which is to be used in the model. This figure shows that the user can choose one of a selection of four different ball types; the picture of the chosen ball being shown on the form. The ball parameters $k_{B(0)}$, A_K, α and A_C, which are shown in Table 9.1, are stored in an *MS Access 2000* database and the relevant values for the selected ball type are retrieved by the *Racket Impact v1.1* program and stored as appropriate variables. New ball types can easily be modelled by entered into the relevant values of the ball

parameters into the *MS Access 2000* database; these parameters being obtained using the procedures already discussed in earlier chapters.

The method used to define the stiffness of the stringbed is similar to that described above for the ball type selection. Figure 9.21 shows a selection of four different options which refer to four identical rackets with a head size of 98in^2, strung using a 15gauge nylon string at four different string tensions. The stringbed stiffness of these rackets was discussed in Chapter 6. Each of these selections has a unique combination of the stringbed parameters a_S, b_S and c_S, as shown in Table 9.2, which are stored in the *MS Access 2000* database. These parameters apply to the equation,

$$k_S(\phi_{55}) = a_S . x_S^2 + b_S . x_S + c_S \qquad [9.70]$$

The parameter $k_S(\phi_{55})$ refers to the quasi-static stiffness of the stringbed for a load applied perpendicular to the string plane, using a rigid disc of diameter of 55mm. The experimentally obtained values of $k_S(\phi_{55})$ are plotted against the stringbed displacement x_S, and a second order trendline is plotted through this data. The coefficients of this trendline are then input into the database. This procedure can be conducted for any new stringbed, and the relevant values entered into the database.

9.5.3 Definition of Racket type

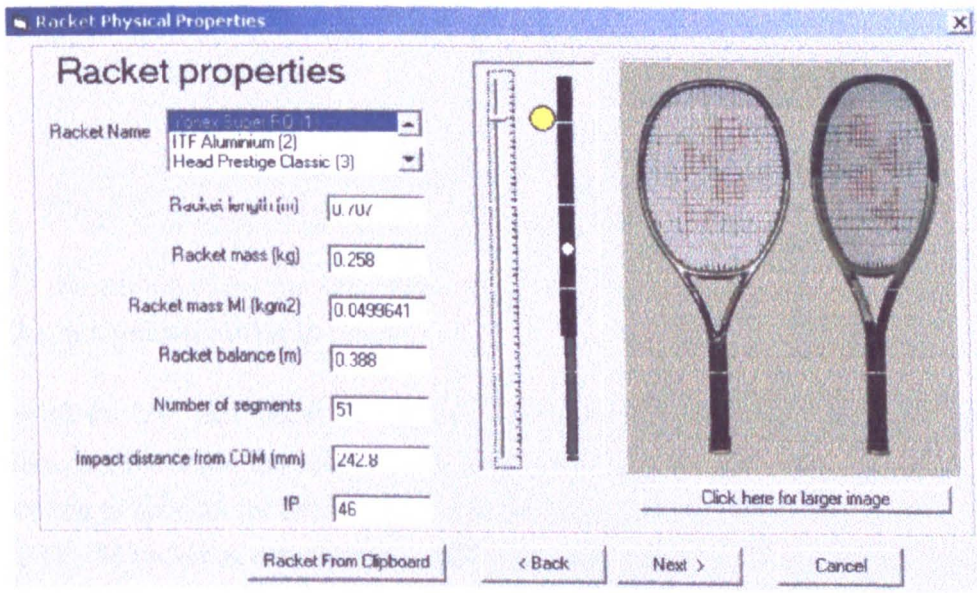

Figure 9.22 Illustration of the *Racket Impact v1.1* form which is used to select the racket type.

Figure 9.22 shows the *Visual Basic* form which allows the user to select the desired racket type. This figure shows that the user can choose one of a selection of seven different rackets from a scroll-down menu; the picture of the chosen racket being shown on the form. In section 9.3 it was shown that the *five section* beam model was the most accurate method of simulating a tennis racket. Therefore, this is the type of beam model that is used in the *Racket Impact v1.1* program. The racket parameters which are required for the model, such as those given in Figure 9.9 and Table 9.3-9.5 for the *ITF Carbon Fibre (6)* racket, are stored in the *MS Access 2000* database and the

relevant values for the selected racket type are retrieved by *Racket Impact v1.1* program. The parameters are stored as variables in the program, and some of these are displayed on the form in Figure 9.22. A slider-bar is used to allow the user to easily select the impact position, relative the centre-of-mass of the racket/beam. New racket types can easily be modelled by entered into the relevant values of the racket parameters into the *MS Access 2000* database; these parameters being obtained using the procedures already discussed in this chapter.

It has been stated that the ball, stringbed and racket parameters are all stored in an *MS Access 2000* database. The three sets of parameters are stored in three separate tables. The field names for each of the tables, and an accompanying description of these fields, is given in Appendix D.5.

9.5.4 Definition of Ball and Racket speed before impact

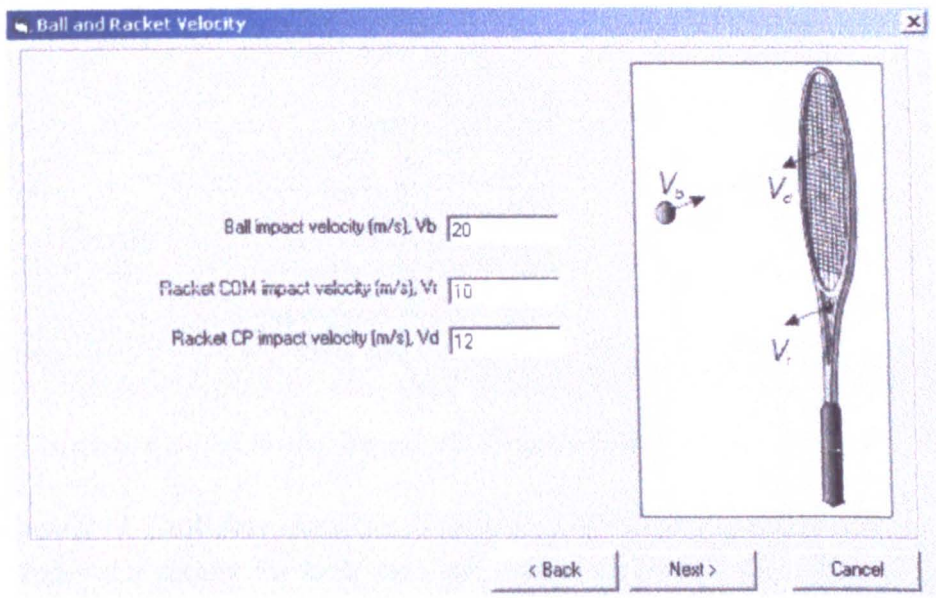

Figure 9.23 Illustration of the *Racket Impact v1.1* form which is used to select the velocity of the ball and racket immediately prior to impact.

The velocity of the ball and racket immediately prior to impact must be specified. Figure 9.23 shows the form used to input the velocities of these two objects. The velocity of two points on the racket is required to account for the rotation of the racket around its centre-of-mass. The velocity is specified for (1) the racket centre-of-mass and (2) the impact position on the racket, as illustrated in Figure 9.23.

After the velocity of the ball and racket has been entered, the *Racket Impact v1.1* software can perform the calculations which are required for the numerical solution. This numerical method is described in detail in sections 9.3-9.4 and therefore is only summarised here. The displacement of the N beam segments is calculated at time t, along with the displacement of the other parameters in the visco-elastic model of the ball/stringbed system. The force which acts in this system is then calculated by the *Racket Impact v1.1* software. The displacement of all the relevant parameters can then be determined at the time $t+\Delta t$. The process is then repeated for the required time period.

The *Racket Impact v1.1* software also performs the calculations for a modelled impact between a ball and rigid beam. The equations for this model are given in section 9.2. The only difference between this model and the flexible beam model is that the racket does not deform. Therefore all the required parameters have already been entered from the *MS Access 2000* database.

The automated calculating procedure is commenced by selecting the 'Run Rigid/Flexible Beam Solver' option in the menu.

9.5.5 Output from the model.

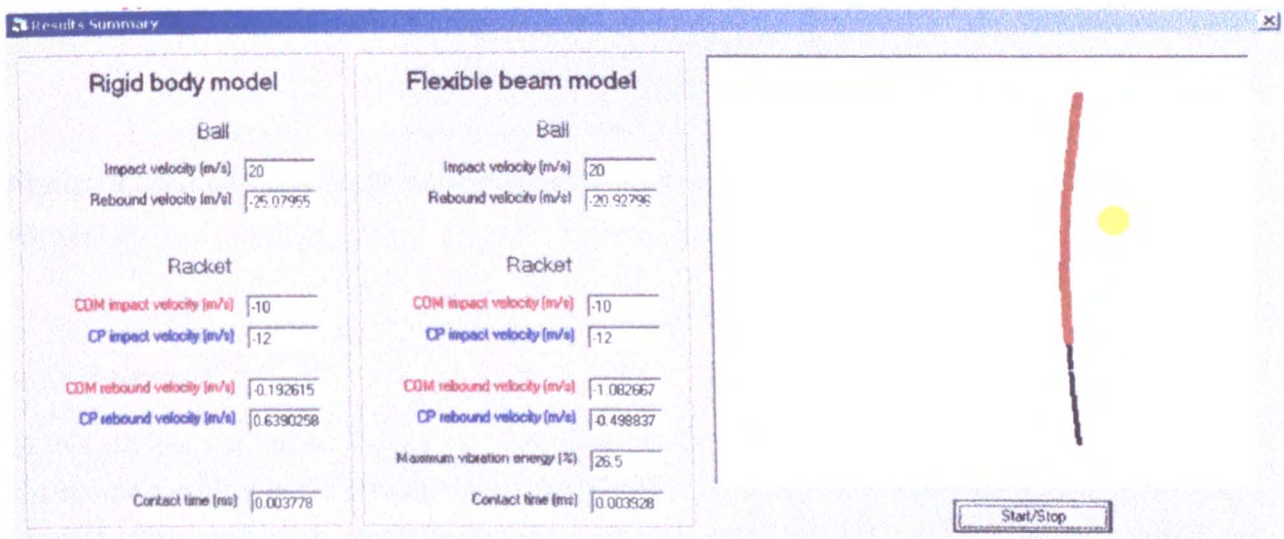

Figure 9.24 Illustration of the *Racket Impact v1.1* form which gives a summary of the results.

The *Racket Impact v1.1* software outputs a summary of the results, as shown in Figure 9.24. The summary includes the results for both the rigid beam model and the flexible beam model to illustrate the effect that the racket deformation has on the model output (e.g. ball rebound velocity). An animation of the ball and racket before, during and after impact is also given in this results summary, as shown in Figure 9.24. This is merely intended to give the user a illustration of the motion and vibration of the ball and racket. If the user requires the actual displacement of each segment of the beam, then a separate set of functions is required. These functions are built-in to the *Racket Impact v1.1* program and the relevant form is shown in Figure 9.25.

The 'Data Transfer' form that is shown in Figure 9.25 allows the user to export the data for a wide range of parameters into a software package such as *MS Excel 2000* for post-analysis. For example, the 'Fourier Analysis' function performs a numerical harmonic analysis on the data to determine the amplitude of the fundamental mode of vibration, for each beam segment. This analysis also determines the zero frequency response of each of the beam segments. As with all the 'Data Transfer' functions, the relevant data is temporarily stored on the *MS Windows Clipboard* until the user chooses the location that the data should be exported to.

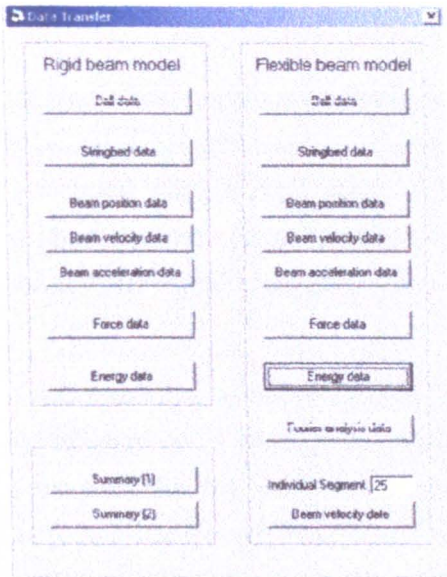

Figure 9.25 Illustration of the *Racket Impact v1.1* form which allows the user to export the relevant data.

9.5.6 Summary

In this section, the *Racket Impact v1.1* software has been described. This software was written by the author specifically for solving the models that have been derived in this chapter. The software simplifies the method of inputting the required ball, stringbed and racket parameters which are needed to solve the model. The calculations are performed without any user input. This gives a trained user the ability to use the software, with out requiring a thorough knowledge of the numerical solution that is needed to determine the required model output.

The software produces a graphical results summary which shows the main output of the model. Furthermore, a function is provided which allows the user to export the required data into a different software package for analysis.

9.6 Summary

In this chapter, two different models of a ball impact on a freely suspended tennis racket have been developed. In both models, the ball and stringbed are simulated using a visco-elastic model. In the first model, the racket was simulated using a rigid beam. This beam was assigned the same inertial properties (mass, balance point and moment of inertia) as the racket that it was modelling. The inherent weakness of this model is the inability of the beam to model the vibrations of a tennis racket.

In the second model, the racket was modelled as a one dimensional flexible beam. A numerical solution was derived for the displacement of a beam which was subjected to a time-dependent loading. In this solution, it was assumed that the beam had a uniform flexural rigidity but a non-uniform mass distribution. It was found that a beam which was comprised of five uniform sections could be assigned inertial and vibrational properties which were very similar to those of the racket. The vibrational properties referred to here are (1) the fundamental frequency of the beam and (2) the node locations for this mode. More specifically, the beam was assigned the relevant flexural rigidity which gave the same fundamental frequency as that measured experimentally for the racket. Also, the beam node correlated very closely with the frame node of the racket; the frame node referring to the node point for hammer impacts directly on the frame. It was found that, for impacts on the longitudinal axis of the stringbed, the stringbed node was located in a different position compared with the frame node.

The force was applied to the one dimensional beam by the visco-elastic model of the ball/stringbed system. It was initially assumed that this force should be applied as a point loading. This lead to the predictable result that an impact at the beam node point excited no vibrations of the fundamental mode. However, it was subsequently assumed that the force should be applied as a distributed loading. Using this assumption, it was found that the impact point which excited minimum vibrations did not correlate with the beam node. Furthermore, this impact point correlated very closely with the stringbed node.

It was concluded that a distributed loading, on a *five section* beam model, is the most suitable method of simulating the inertial and vibrational properties of a tennis racket, for an impact with a ball. The position of the node on the beam correlates very closely with that of the frame node. Also, the impact location which excites minimal vibrations of the beam coincides with the measured stringbed node for the tennis racket when a distributed loading is used.

10. Impact between a Ball and Freely Suspended Racket – Experiment Data

10.1 Introduction

In Chapter 9, two different models were developed which simulated an impact between a freely suspended tennis racket and a tennis ball. In that chapter, the methods that were used to determine the model parameters were presented. In the first model, the racket frame was assumed to be a rigid beam and therefore did not deform during impact, whereas in the second model, the racket was simulated as a one dimensional, flexible beam. In this current section, the validity of both of these models will be assessed by comparing the model results with relevant data that has been obtained experimentally.

In Chapter 7, results are presented for an experimental investigation of an impact which involved a tennis ball being propelled perpendicularly towards a head clamped tennis racket. In that experiment, a number of parameters were measured, which included the following,

1. Ball rebound velocity.
2. Contact time.
3. Magnitude of ball deformation.
4. Magnitude of stringbed deformation.

These four parameters will be measured in this chapter, for a range of impacts along the longitudinal (main) axis of the freely suspended racket. In these experiments, the racket is freely suspended and therefore it will recoil and vibrate during, and after, impact. In this chapter, the racket's motion will be determined experimentally.

In this section, five separate experimental arrangements are used to measure the parameters which are discussed above. Each of these experiments involves a different experimental arrangement which has been optimised for the aim of the specific experiment. These five separate experiments are,

1. Measurement of the ball rebound velocity.
2. Measurement of the motion of the ball, stringbed and racket *during* impact.
3. Measurement of the ball and racket velocity *after* impact.
4. Modal analysis of a tennis racket.
5. Measurement of racket vibrations.

These experiments shall be discussed individually in the following sections of this chapter.

10.2 Experiment 1 – Ball rebound velocity

10.2.1 Introduction

One of the most important features of the model is its ability to predict the ball rebound velocity for an impact between a ball and freely suspended tennis racket. In Chapter 9, it is shown that the model is capable of calculating this velocity, but the accuracy of the results has not yet been verified. In this current section, this issue will be addressed. The comparison between the model and experiment results will be made using five rackets with vastly different properties (racket mass, stiffness, etc.) which are assumed to cover the typical range used in the game of tennis. The experiments will be performed for a range of impact locations along the longitudinal axis of the tennis racket.

In this chapter, all impact locations will be generally referenced to the geometric string centre (*GSC*) of the racket, this point corresponding to the centre of the racket head. This is used as a reference position as it is the most tangible method of visualising the impact location.

10.2.2 Experimental Procedure

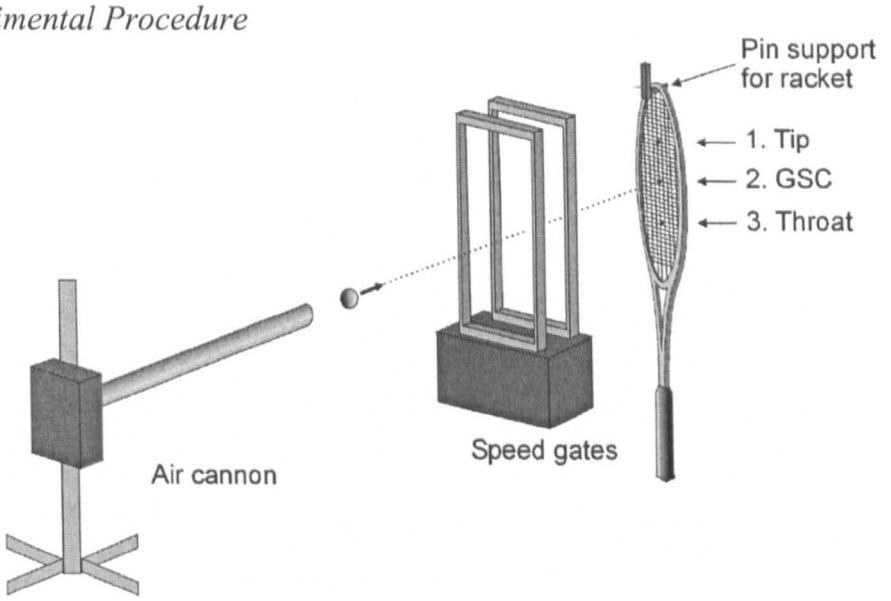

Figure 10.1 Illustration of the experimental layout used to measure the ball rebound velocity for an impact on freely suspended racket. Three nominal impact locations are illustrated.

(a) Introduction

In this experiment, the tennis racket was supported at the tip on a smooth pin with its longitudinal axis orientated vertically, as shown in Figure 10.1. *Pressurised* tennis balls were projected at the longitudinal axis of the racket, perpendicular to the stringbed, at velocities between 15 and 45 m/s (33 and 100mph). Three discrete impact points on the racket were tested and these points are defined as,

1. Tip.
2. *GSC* (Geometric String Centre).
3. Throat.

The inbound velocity of the ball was determined using speed gates. These were positioned approximately 1.0m away from the tennis racket. The ball rebound velocity was also measured using the speed gates, for impacts located at positions *2* and *3*. However, for impacts located at position *1* the ball rebounded with a velocity which was generally too low to be sampled by the speed gates. For these impacts, the rebound velocity was determined using a *Kodak Motioncorder* high speed video system. This camera was positioned perpendicular to the flight of the ball and operated at a frame rate of 240 frames per second. The general operation of this camera is given in Williams (2000).

The location of the three impact positions, for each of the tennis rackets, is given in Figure 10.2. It should be noted that all the distances and racket sizes are drawn using a scale of 13:1. (Only two impact locations are given for the *Head* racket as the strings broke during testing). All the impact locations are referenced to the geometrical stringbed centre (*GSC*). For completeness, the position of the experimentally measured stringbed nodes are also given in this figure; this point corresponding to the experimentally measured node of the fundamental mode of transverse vibrations for the racket.

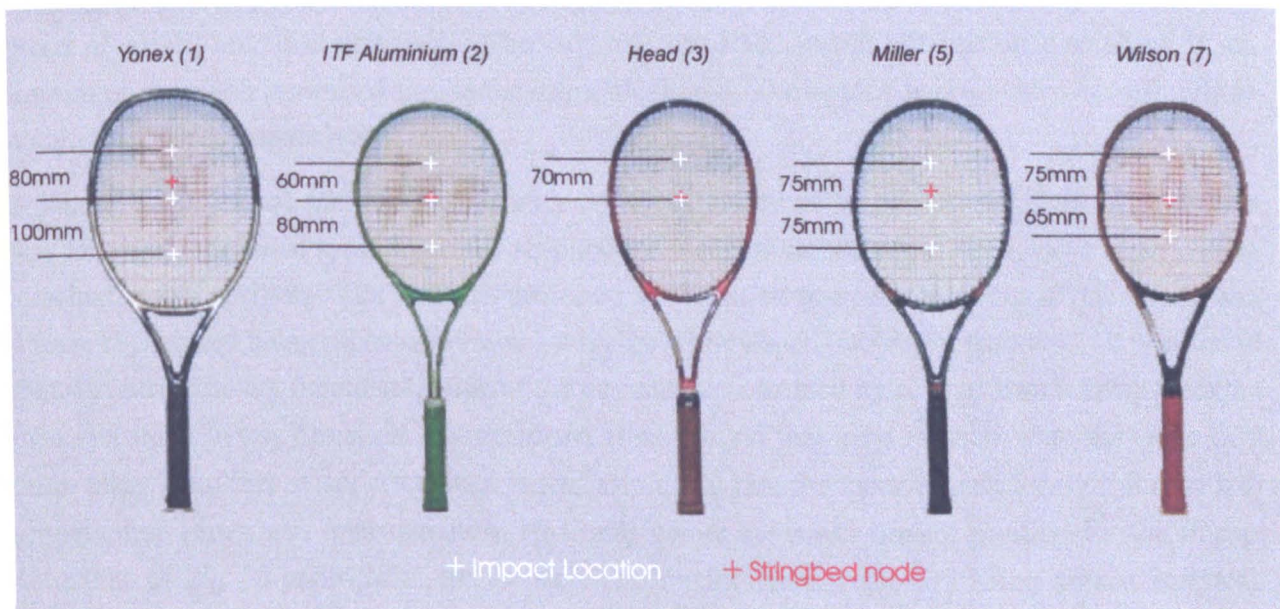

Figure 10.2 Definition of the three impact positions which were tested for each of the five tennis rackets used. The stringbed node location is also illustrated.

The five rackets shown in Figure 10.2 have been chosen to represent the wide range of typical rackets used in the game of tennis. The rackets have been assigned an ID number and this is given next to the name in this figure. The properties of these rackets are given in Chapter 9 and Appendix D. The *Yonex* tennis racket is an example of a very light racket which has a large head and is head heavy (the centre-of-mass is located towards the head). The *ITF Aluminium* racket has a very low stiffness, it is head light and has a relatively low mass moment of inertia. The *Head* and *Miller* rackets are very similar and can be considered to have 'average' racket parameters. The main difference between these two rackets is that the *Head* racket is head-light and the *Miller* racket is head-heavy. The *Wilson* racket is the heaviest racket that is tested in this study, and is also relatively head-light.

(b) Repeatability of impact location

The nominal impact locations for each racket are defined in Figure 10.2, and the air cannon is aimed at the required position. However, due to the nature of the equipment, there will be some level of uncertainty in the actual impact location. It is clearly important that the impact position for each experiment is known, as the ball rebound velocity is a function of this position (Goodwill and Haake (2000)). This could be obtained by recording each impact using a high speed video camera, but this is not practical for the volume of testing being carried out in this section.

In these experiments the ball was propelled towards the racket using an air cannon. It is well-established that this method gives a highly repeatable impact location, compared with that obtained using other propulsion methods. However, it must be accepted that there will be a finite level of uncertainty in the impact location. Several procedures were adopted to minimise this uncertainty. For example, the cannon was positioned at the closest practical distance away from the tennis racket. Also, a supplementary frame was manufactured to provide further support to the end of the cannon and thus minimise the potential for the cannon to move during use.

The impact location was identified by placing a sheet of carbon-copy paper, attached to a blank piece of paper, onto the stringbed. The ball was projected at this arrangement resulting in an imprint on the paper corresponding to the impact location. The cannon was adjusted accordingly to obtain the desired impact point.

A similar arrangement was used to quantify the repeatability of the impact position. The cannon was aimed at a nominal location on the stringbed; a piece of carbon paper (and white paper) being attached at this position. The ball was projected at the racket at nominal speeds of 15, 20, 30 and 45m/s, each speed being repeated 10 times with the white paper frequently replaced. It was found that, for each velocity increment, none of the impacts were located more than 10mm away from the mean position, in any direction. Furthermore, it was found that most impacts were not more than 5mm away from this mean. However, it was also noted that the mean impact location for the ball propelled at 15m/s was approximately 10-15mm below the mean impact position for the impact velocities of 20, 30 and 45m/s; the impact location for these velocities being almost identical. Clearly this was due to the gravitational force which acts on the ball during flight which affects the ball's trajectory for the lower inbound velocities.

In this experiment, the ball is propelled towards the racket at velocities of between 15 and 45m/s. It was concluded that the cannon should initially be positioned for impact velocities between 15 and 20m/s, using the carbon paper to identify the impact location. The cannon was then repositioned for impact velocities above 20m/s. This method ensured that the majority of impacts landed within 10mm of the intended position.

(c) Error associated with the repeatability of the impact location

In this section, the ball rebound velocity will be measured for a range of nominal impact locations. It has been shown that the desired impact location may differ from the actual location by up to 10mm. The actual location will not be measured in each experiment, so the effect in the results must be identified to give an estimation of the potential errors in the experimental data. This involves establishing the relationship between the uncertainty of the impact location and the change in ball rebound velocity that this causes. A short theoretical study is discussed below to estimate this relationship.

The ball rebound velocity for an impact on the longitudinal axis of a freely suspended tennis racket can simply be calculated using the *Racket Impact* software, as described previously. However, this software is not capable of modelling impacts that are eccentric to the longitudinal axis. Williams (2000) presented a model of an impact between a freely suspended racket and a tennis ball, in which the racket was assumed to be a rigid body. The model was derived using simple Newtonian mechanics and the coefficient of restitution (*COR*) parameter was used to represent the energy 'loss' in the system. The model was derived for impacts at any location on the racket, not just along the longitudinal axis. Therefore, this model could be used to assess the reduction in the ball rebound velocity that results from an eccentric impact.

A preliminary study revealed that the relationship between the shift in impact location and the resulting change in ball rebound velocity was not uniform for all impact locations on the longitudinal axis. It was also found that the change in ball rebound velocity was dependent on the inertial properties of the tennis racket. Consequently, in the example below, two different racket types and two different impact locations are used to illustrate the effect that the uncertainty of the impact location has on the ball rebound velocity.

Figure 10.3 gives an illustration of the effect on the ball rebound velocity which results from a shift of 10mm in the impact location. For example, for impacts close to the tip of the *Miller* racket, a shift of 10mm towards the butt end acts to increase the ball rebound velocity by 8%. The data is presented for two different rackets which have vastly different inertial characteristics; the *Miller* racket being head-heavy and the *ITF Aluminium* being head-light. Two nominal impact locations are presented which approximately correspond to the positions labelled *1* and *3* (tip and throat) in Figure 10.1.

The data in Figure 10.3 confirms that a shift of 10mm in the impact location does not effect the ball rebound velocity in a consistent manner. It can be seen that the ball rebound velocity is highly sensitive to the impact position, for impacts located near the tip of the *ITF Aluminium* racket. Conversely, impacts located towards the throat of the *Miller* racket are not sensitive to the ball impact position.

The results of this theoretical error analysis study will be referred to later in this section.

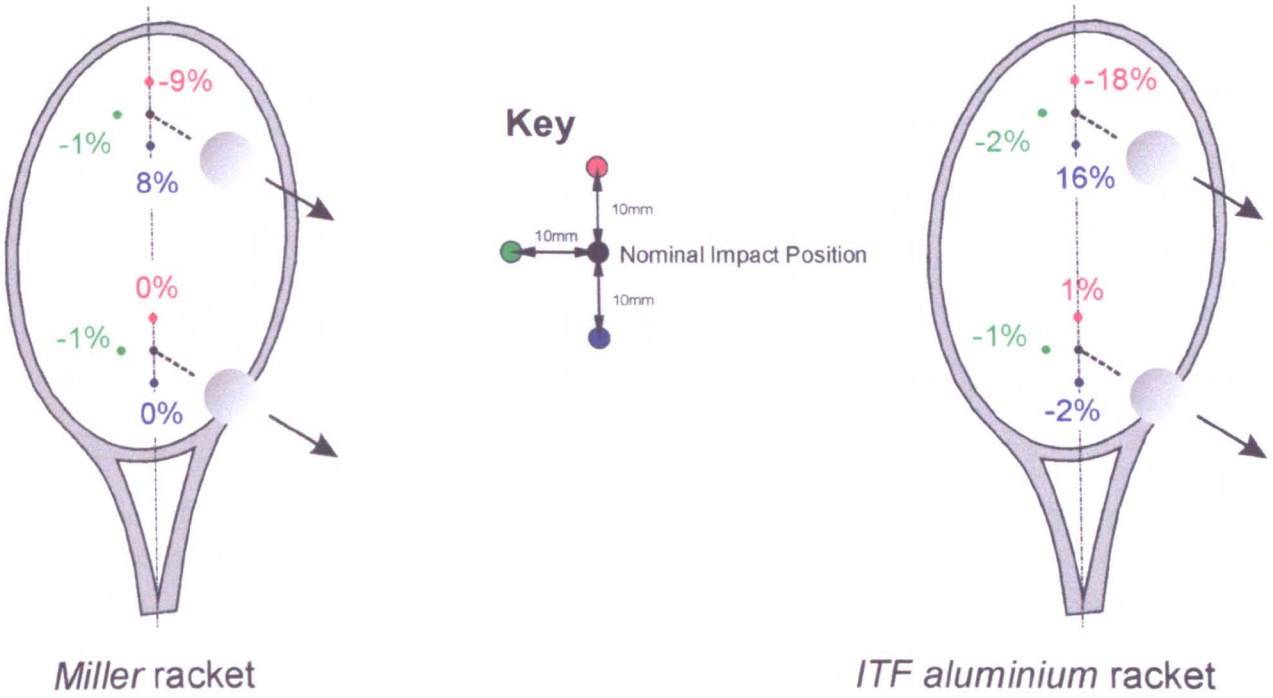

Figure 10.3 Schematic illustration of the difference in the ball rebound velocity that is caused by a shift of 10mm in the impact location. The difference is given as a percentage of the ball rebound velocity which is calculated at the nominal impact position. The examples are given for two different racket types and two impact locations.

(d) Error associated with the determination of the ball velocity

Two different experiment techniques are used in this study to determine the inbound and rebound velocity of the ball; these being the speed gates and the high speed video system. The speed gates are the preferred method of determining the ball velocity as this apparatus gives a direct value of the speed, and does not require any additional analysis procedures to be conducted.

A potential error of this experiment is a function of the position of the speed gates, with respect to the tennis racket. The speed gates are positioned approximately 1.0m away from the tennis racket, in order for them to operate reliably. Using a simple trajectory plot (Haake *et al.* 2000) it can be shown that a ball travelling at 20m/s through the speed gates, towards the racket, will have decelerated by 0.4m/s when it reaches the racket. This represents a 2% variation in the inbound speed of the ball and a similar calculation can be performed for the rebound velocity. Although this difference is small, it highlights the considerations which must be made when using this type of apparatus.

A high speed video system is used to determine the ball rebound velocity for the impacts in which the ball speed was too low for the speed gates to function correctly. The high speed video images are sampled using *Vidimas v1* software using a similar technique to that described in section 7.2.3. The motion of the ball was sampled for a distance of approximately 350mm. A simple repeatability study, similar to that described in section 7.2.3, was used to estimate the accuracy of the manual sampling method which was conducted in *Vidimas v1*. It was found that the standard deviation of the sampled co-ordinate was 2.6mm. This infers a standard deviation of 1.5% in the

calculated value of the ball velocity. This low value is achievable because the motion of the ball is sampled for a relatively long distance/period.

10.2.3 Determining the parameters required by the model

In this section, the model will be used to calculate the ball rebound velocity for an impact between a ball and freely suspended racket. The *Racket Impact* software will be used to determine the model solution. This software already contains the parameters required for the *Pressurised* ball and the beam models of the five tennis rackets. However, it does contain the parameters which define the stringbed stiffness of the rackets.

The rackets were not restrung before this testing commenced and therefore the tension of the strings was not known. However, this is assumed to be unimportant in this testing as the model does not require the tension to be defined; the important parameter being the stringbed stiffness rather than the string tension.

The method used to determine the parameters which define the stringbed stiffness in the model has been given in Chapter 8. To summarise, the quasi-static stiffness of the stringbed is determining by applying a force using a rigid disc (diameter of 55mm) and measuring the resulting displacement.

$$k_S(\phi_{55}) = a_S.x_S^2 + b_S.x_S + c_S \qquad [10.1]$$

where a_S, b_S and c_S are empirically determined coefficients of a second order polynomial trendline that was plotted through the experimentally obtained quasi-static stiffness data. The values of a_S, b_S and c_S are used to define the stiffness of the stringbed in the model.

In this section, three different impact locations are investigated. Williams (2000) confirmed that the stringbed stiffness was not uniform across the stringbed. Therefore, the stringbed stiffness needs to be obtained for each impact location, giving a set of model parameters (a_S, b_S and c_S) for each location. The visco-elastic model of the stringbed was derived using data obtained only for stringbed compressions at the geometric string centre of the racket. However, in this section, it is assumed that this model is valid for impacts at all locations on the stringbed.

Figure 10.4 illustrates the stringbed stiffness for the five rackets. The data is presented for two different locations on the tennis rackets. Figure 10.4(a) and Figure 10.4(b) illustrate the stringbed stiffness measured at the tip and *GSC* respectively. The data for the third location (the throat) is given in Appendix E.1.

The data in Figure 10.4 shows that the stringbed stiffness which is measured at the geometric string centre is significantly lower than that measured at the tip. This confirms that the stringbed stiffness can not be considered to be uniform across the face of the racket. The data in these figures was used to determine the model parameters (a_S, b_S and c_S) for each location, and these values are given in Appendix E.1.

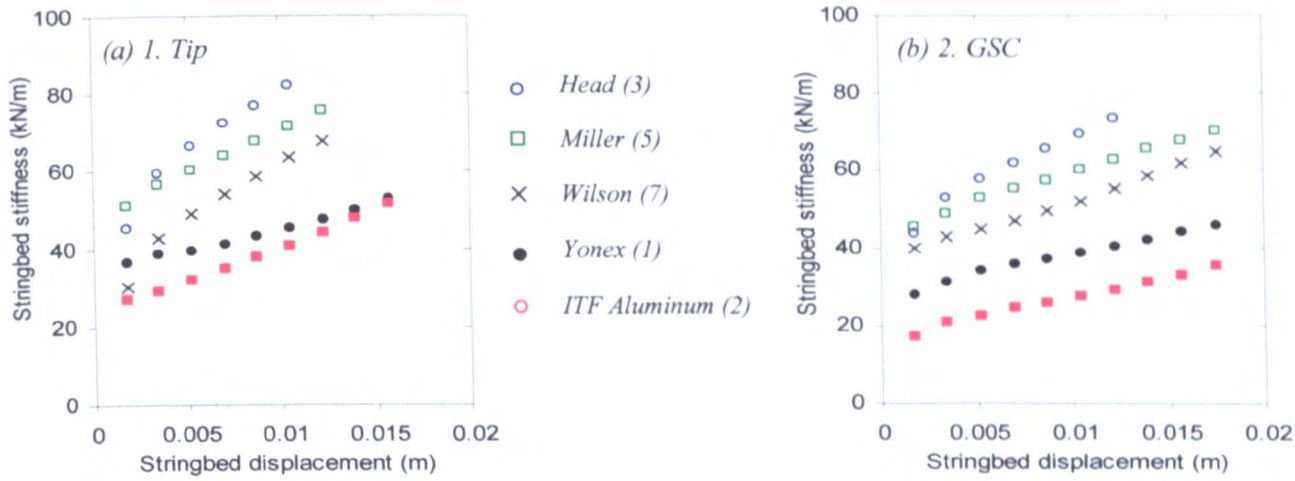

Figure 10.4 Experimentally measured stringbed stiffness at two different locations on the racket.

It is difficult to obtain a generic relationship which could be used to define the relationship between the stringbed stiffnesses which were measured at the *GSC*, at the throat and at the tip. However, it was generally found that the stringbed stiffness was approximately 10-15% higher at the throat position with respect to the stiffness that was measured at the geometric string centre. Also, it was found that the stringbed stiffness measured at the tip location was 15-20% higher than that at the *GSC*.

The model parameters (a_S, b_S and c_S) were added to the *MS Access 2000* database to complete the set of parameters required by the model. The *Racket Impact* software was used to calculate the ball rebound velocity for the impact between a ball and freely suspended racket. Two separate model solutions were obtained. Firstly, the model solution was obtained using the assumption that the racket was a rigid beam. Secondly, it was assumed that the racket could be modelled as a one-dimensional flexible beam using the *five section* beam model that was described in Chapter 9. The *Racket Impact* software assumes that the force is applied to the beam as a distributed load.

The impact locations, for each of the five rackets, are given in Figure 10.2. It has been stated earlier that the *Racket Impact* software can only model impacts which are located at discrete points along the longitudinal racket. This is because the beam/racket is split into 51 segments and the impact must be located at the centre of one of these segments; the distance between these segment centres being approximately 13mm. Generally, the impact locations shown in Figure 10.2 did not coincide with one of these segment centres. A simple linear interpolation method was used to estimate the ball rebound velocity, for impacts at the desired position. This involved the calculation of the ball rebound velocity for impacts on the two segment centres which are located either side of the desired impact position. The ball rebound velocity at the desired impact position can then be interpolated from these two results. This general interpolation method is used throughout this chapter to model impacts which are located at a point which does not coincide with a segment centre.

10.2.4 Results and Discussion

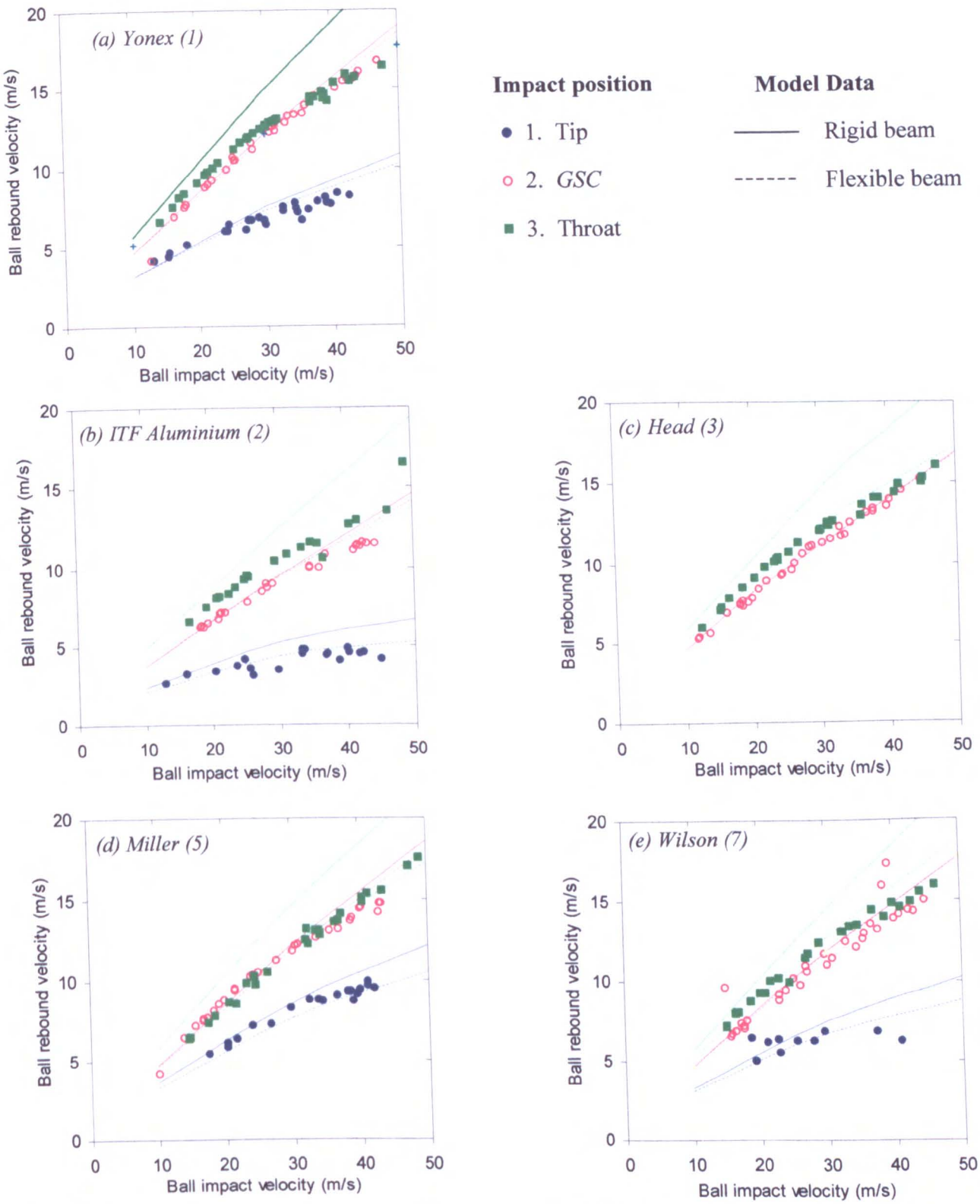

Figure 10.5 Comparison of model and experimental values of ball rebound velocity, for three nominal impact positions on five different racket types. The data points refer to the experimental data, and the curves represent the data for the two different model beams.

The results for this study are given in Figure 10.5, for all five tennis rackets. In each graph, data is presented for the three impact locations (tip, *GSC* and throat). The data points represent the experimental data, and the curves illustrate the data obtained using the *Racket Impact v1.1*

software. The model uses the nominal impact locations to determine the solution, even though the actual impacts do not necessarily land at these points due to the finite accuracy of the ball cannon.

Figure 10.5 shows that the rigid and flexible beam model solutions are almost identical for impacts at the *GSC*. This is because this point coincides very closely with the stringbed node point for each of the rackets, as illustrated in Figure 10.2. Therefore, the flexible beam model acts very similarly to the rigid beam model at this point. Furthermore, it can be seen that there is a very good correlation between the model and experiment data for impacts at the *GSC*, for all five tennis rackets. The results generally correlate to within approximately 5%, with maximum differences in the order of 10%.

For impacts at the tip of the racket, there is a considerable magnitude of scatter in the ball rebound velocity. The two models give different results due to the flexible beam deforming during impact which results in a lower ball rebound velocity. It can be seen that the flexible beam model generally correlates more closely with the experimental data; the difference between the two sets of results being less than 1m/s.

For impacts at the throat position, it can be seen that the rigid beam model calculates a ball rebound velocity which is considerably larger than that which is calculated using a flexible beam model. This is because this impact position is located at the furthest distance from the stringbed node, as illustrated in Figure 10.2. The experimental data generally correlates very closely with the flexible beam model data, for most of the rackets. This illustrates that a rigid beam model is not capable of modelling an impact between a ball and tennis racket.

It is interesting to note that the ball rebound velocity which was measured for impacts at the *GSC* are very similar to those determined for impacts at the throat. Impacts at the throat are closer to the centre-of-mass of the racket and would intuitively result in higher ball rebound velocities, due to the higher 'effective' mass of the racket at this point. However, the data in Figure 10.5 illustrates that this is not the case, experimentally or theoretically. This finding agrees well with the theoretical results in Kawazoe (1997b) and the experimental data in Brody (1997).

In section 10.2.2, it was stated that the ball impact position may vary by up to 10mm, and this leads to a variation in the ball rebound velocity. It was shown that the magnitude of the this variation was a function of both the racket and the impact position. For example, it was found that this variation may be up to 20% for the *ITF Aluminium* racket, but only 9% for the *Miller* racket. It was also shown that the variation was largest for impacts which are close to the tip of the racket, compared with those towards the throat end. A qualitative analysis of the scatter in the plots in Figure 10.5 correlates with the errors predicted using the error analysis. For example, the largest scatter in the experimental data in this figure is that for the *ITF Aluminium* racket, and also for impacts located at the tip of the racket. By comparison, the scatter in the experimental data is minimal for impacts at the throat.

In section 10.2.2, it was also stated that the use of speed gates to determine the ball inbound and rebound velocities introduces an error in the data. For example, it was shown that the speed gates calculate a ball inbound velocity which is approximately 2% larger than the actual speed of the ball

which it impacts on the racket. This error should be taken into account when assessing the correlation between the experimental and model data.

10.2.5 Summary

In this section, it has been shown that the *Racket Impact* software can be used to calculate the ball rebound velocity, for impacts where the ball lands on a range of positions on the longitudinal axis of the tennis racket. This software calculated two different model solutions. In the first model, the racket was assumed to be a rigid body and this model generally over predicted the ball rebound velocity. In the second model, the racket was modelled as a one-dimensional flexible beam. It was found that the ball rebound velocity calculated by this model exhibited a very high correlation with the experimental data. This comparison was made for five different rackets, each with vastly different characteristics.

10.3 Experiment 2 – Measuring the motion of the ball, stringbed and racket *during* impact

10.3.1 Introduction

In the previous section, the experimentally measured ball rebound velocity is compared with that which is calculated by the model, for the impact between a ball and freely suspended racket. A good correlation was found between the two sets of data and therefore it could be concluded that the model represents a good simulation of the impact, in regard to the ball rebound velocity. However, the ball rebound velocity is only one of several components that the model calculates. In this section, the motion of the ball, stringbed and racket will be measured experimentally, and this data will be compared with the appropriate results calculated by the model.

The work conducted in this section is analogous to that presented in section 7.2. In that section, high speed cinematography was used to measure the magnitude of the deformation of the ball and the stringbed, for an impact between a ball and head-clamped racket. The data was then used to verify a model of this impact. In this current section, a similar experiment shall be conducted for an impact between a ball and a freely suspended tennis racket. In this section, the following parameters will be measured throughout the duration of the impact,

1. Ball deformation.
2. Stringbed deformation at the impact point.
3. Racket frame displacement at the impact point.

10.3.2 Experimental Apparatus

Figure 10.6 shows the experimental arrangement used to measure the magnitude of the ball and stringbed deformation, and the displacement of the racket, during impact. The ball was propelled normal to the stringbed plane using an air cannon. The ball was aimed at the geometrical string centre of the racket head. The inbound and rebound velocity of the ball were measured using speed

gates which were positioned approximately 1.0m from the tennis racket. The racket was supported on a small, smooth pin at the tip so that the longitudinal axis was orientated vertically.

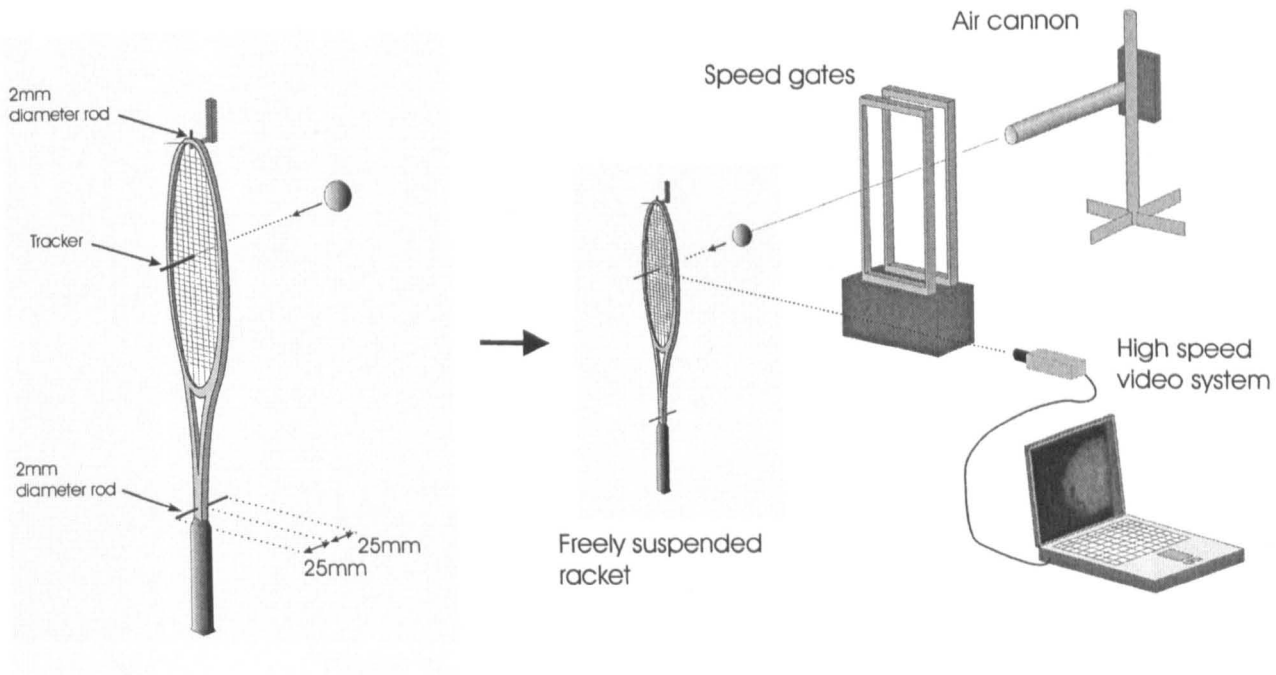

Figure 10.6 Illustration of experimental arrangement showing the tracker attached to the stringbed of a freely suspended racket.

The *Phantom v4* high speed video system was used to record the impact at a rate of 4100 frames per second, and a resolution of 512 x 128 pixels. The focal axis of the camera was aligned perpendicular to the motion of the ball, and therefore the stringbed was not visible.

The motion of the stringbed was sampled using the same technique as described in section 7.2. A rigid, hollow carbon fibre rod, defined as a tracker, was attached to the geometric string centre of the stringbed using a light thin wire and metal crimp. The wire was attached very tightly so that there was sufficient friction acting between the two surfaces to ensure that the axis of the rod remained horizontal throughout impact. The total length of the carbon fibre rod and crimp was approximately 40mm.

A short, light carbon fibre rod, with a diameter of 2mm, was attached rigidly to the tip of the racket. Similarly, a 50mm long carbon fibre rod was inserted through a drilled hole at the top of the handle of the racket. The tips of each of the rods were coated in a bright white paint to clearly identify the ends. The location of the two rods and the tracker is shown schematically in Figure 10.6.

In these experiments, two different types of tennis ball were tested; these being a standard *Pressurised* and *Pressureless* ball. These two ball types are described in Chapter 4 and are representative of the majority of balls that are used in the game of tennis. The balls were propelled at the racket at a range of velocities between 20m/s and 40m/s. The racket used in this section was the *ITF Carbon Fibre* tennis racket. Two rackets were used and these were strung at tensions of 40 and 70lbs, using a standard 15 gauge nylon string.

10.3.3 Analysis of high speed video images

(a) Procedure

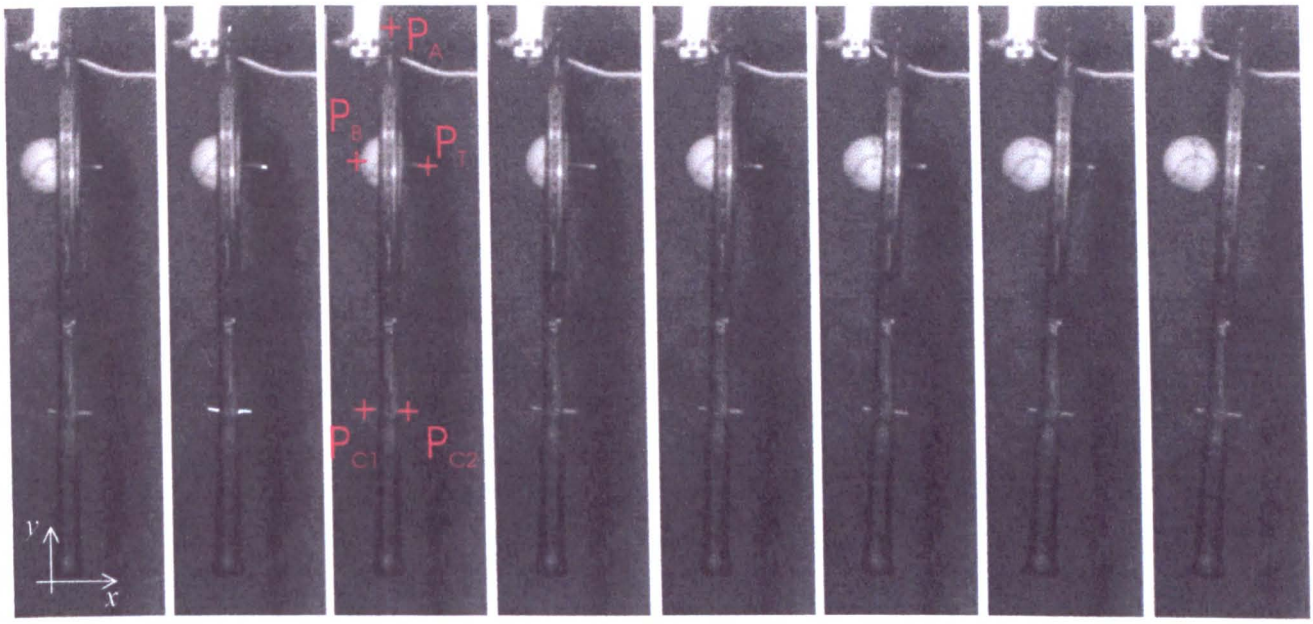

Time = 0ms *Time = 2ms* *Time = 4ms* *Time = 6ms*

Figure 10.7 High speed video images showing an impact between a ball and freely suspended racket (ball impact velocity = 18m/s). The five points which are sampled are illustrated in the third image.

The operation of the camera is described in detail in section 3.3. Typical high speed video images, which were obtained in this study, are shown in Figure 10.7. The second image in the sequence is enhanced to show the white paint on the markers. The third image defines the points which are sampled using the *Vidimas v1* software. The position of the left edge of the ball P_B, the right edge of the tracker P_T, the racket tip P_A and the two points P_{C1} and P_{C2} were sampled. The sampled data was exported from *Vidimas v1* and stored in an *MS Excel* worksheet. These coordinates were converted into physical units using a calibration grid, as described in Chapter 3. The tracker was rigid and therefore it was assumed that the motion of the tracker was identical to the motion of the section of the stringbed which it was attached to.

One of the objectives of this section involves the determination of the displacement of the racket frame at the ball impact position, during impact. This data will then be compared with the model solution which is calculated by the *Racket Impact* software. The displacement of the impact point on the racket (x_{IP}) could have been sampled directly from the high speed video images in Figure 10.7 because the side of the racket frame is clearly visible to the camera. However, this would only constitute a valid procedure if the ball impacted directly on the longitudinal axis. Impacts at any location which is eccentric to the longitudinal axis will cause the racket to rotate around this axis. This rotation is discussed in the analysis below.

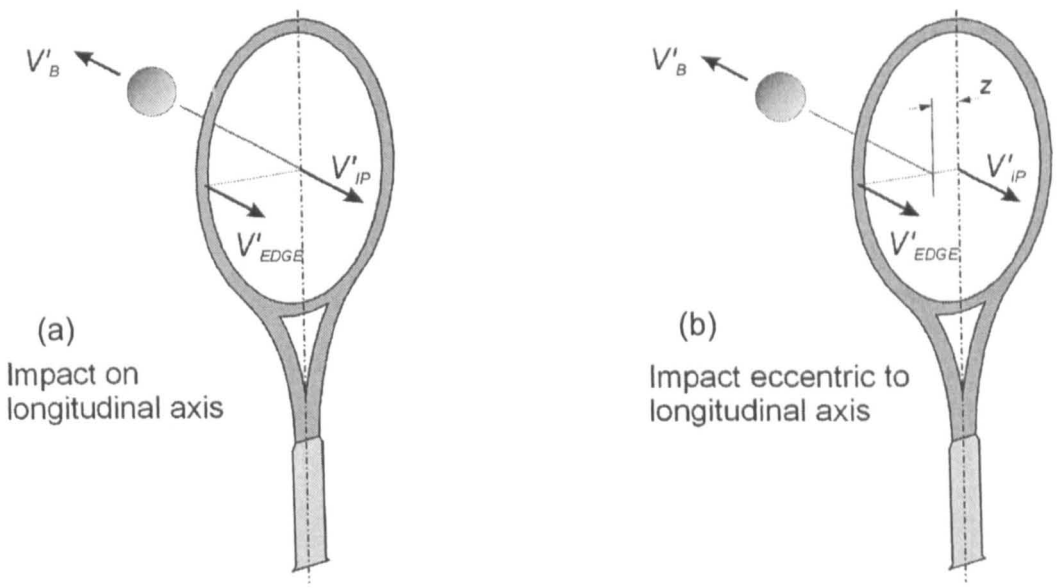

Figure 10.8 Definition of the rebound velocity at the edge of the racket frame for two different impact locations which are, (a) on the longitudinal axis and (b) eccentric to the longitudinal axis.

Figure 10.8 defines the velocity of two points on the racket immediately after the impact with a tennis ball has finished. In this analysis it is assumed that the racket (and stringbed) act as a rigid body, as done by Williams (2000). For the impact in Figure 10.8(a) it can easily be shown that the velocity at the centre of the racket V'_{IP} is equal to that at the edge of the racket V'_{EDGE}. However, for the eccentric impact in Figure 10.8(b), this is not the case. For example, if the eccentricity distance z is equal to 10mm, the velocity V'_{EDGE} is 20% higher than the velocity V'_{IP}. (This example uses the equations defined in Williams (2000), the inertial properties of an *ITF Carbon Fibre* tennis racket and a coefficient of restitution of 0.8.) Furthermore, the model was used to show that, for a specific ball impact velocity, the velocity V'_{IP} (and all other points along the longitudinal axis) was identical for both the impact in Figure 10.8(a) and that in Figure 10.8(b).

In section 10.3 it was found that the ball impact position varied by up to 10mm from the desired position. Although this appears to be a very small eccentricity of impact, it has been shown above that it has a large effect on the rebound velocity of the edge of the racket, using a simple rigid body model of the impact. Therefore, when the high speed video images, such as those in Figure 10.7, are analysed, it is not valid to sample the edge of the racket and assume that the motion of this point is equal to that for an impact in which the ball impacted on the longitudinal axis. Therefore, initially it would appear that it was not possible to accurately determine the displacement of the racket, at the impact point, during impact. However, the utilisation of one of the findings obtained using the rigid body model allows an alternative method to be used. It was found that the velocity of the racket, at all points along the longitudinal axis, is identical for eccentricities of z=0 and z=10mm. Therefore, it can be concluded that the displacement of the racket at any position on the longitudinal axis is not influenced by a small eccentricity in the impact location. This means that this displacement can be measured for eccentric impacts (of up to 10mm) and it can be assumed that this is equal to the displacement measured for an ideal on-axis impact. The application of this finding is described below.

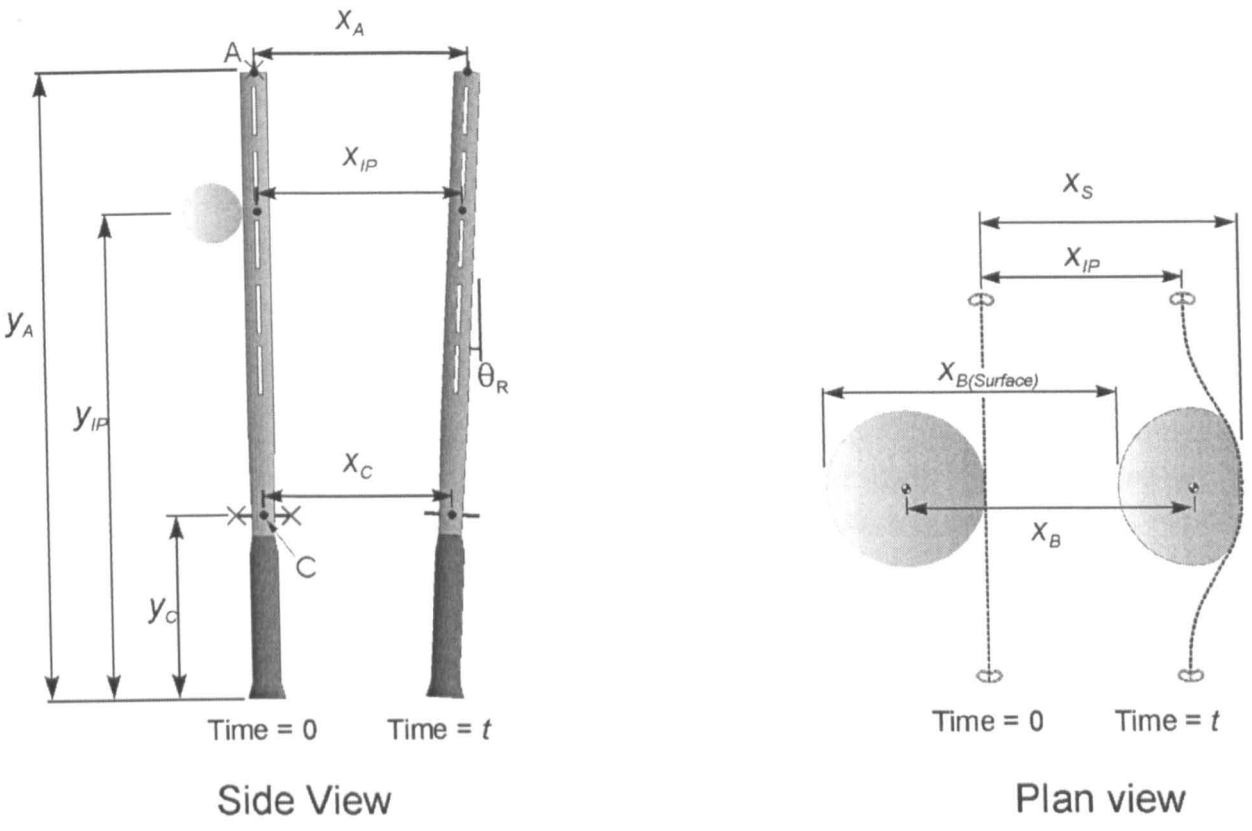

Figure 10.9 Definitions of the ball, stringbed and racket displacements. Two different views of the impact are given.

The definitions of the ball, stringbed and racket displacements are shown in Figure 10.9. A side view of the impact is given to illustrate the displacements of three points on the racket. The point *C* is equivalent to the point located equidistant from *C1* and *C2*; these two points being defined in Figure 10.7. The displacements of the points *A* and *C*, which are defined as x_A and x_C respectively, are determined directly from the high speed video images. However, the displacement which is required in this study is that of the impact point on the racket, defined as x_{IP}. In this analysis, it is assumed that the racket is rigid and also that the angle of rotation θ_R is negligible for the duration of the impact. Therefore the displacement x_{IP} can be calculated from the displacements x_A and x_C using the simple geometrical relationship which relates the points *A* and *C*, and the impact point.

A plan view of the impact is given in Figure 10.9. The stringbed displacement x_S is simply equal to that of the tracker. The deformation of the stringbed δ_S can be calculated using,

$$\delta_S = x_S - x_{IP} \qquad [10.2]$$

Similarly, the deformation of the ball can be determined using,

$$\delta_B = x_{B(Surface)} - x_S \qquad [10.3]$$

The displacement of the ball centre-of-mass x_B is of more interest than the magnitude of the ball deformation δ_B, as discussed in section 7.2.5. The displacement x_B can not be determined directly from the high speed video images. However, in section 7.2.5 it was shown that the empirically

derived equation [7.2] could be used to determine this displacement. It is to be assumed that this equation is valid for impacts on a freely suspended racket and a modified form of [7.2] is,

$$x_B - x_S = -8.184(\delta_B)^2 + 0.954270\delta_B \qquad [10.4]$$

where the term $(x_B - x_S)$ is the relative displacement of the ball centre-of-mass with respect to the stringbed displacement x_S.

(b) Error associated with assumption that the racket frame is rigid

Figure 10.9 illustrates the two points A and C which are sampled in order to determine the displacement of the impact point of the racket frame x_{IP}. The method used to determine x_{IP} involves the interpolation of the displacements of A and C and the assumption that the frame is rigid. Clearly, a racket frame is not rigid and the error induced by this assumption can easily be evaluated using the *Racket Impact* software.

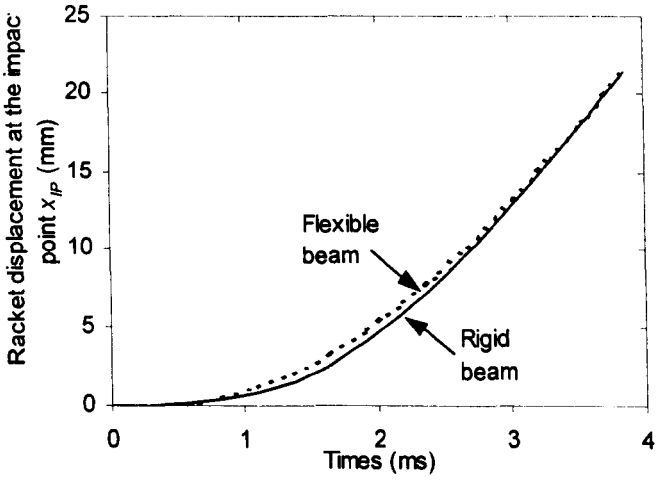

Figure 10.10 Comparison of the displacement of the racket at the impact point calculated using the *Racket Impact* software. The results are presented for two different assumptions regarding the beam used to simulate the racket.

The *Racket Impact* software uses two different assumptions to simulate the racket; these being a rigid beam and a one-dimensional flexible beam. This software was used to determine the displacement of the impact point of the racket, for an impact at the geometric string centre, and these results are given in Figure 10.10. The ball inbound velocity was 25m/s and the racket was an *ITF Carbon Fibre* racket.

Figure 10.10 illustrates the difference between the model solutions for the two different assumptions regarding the beam. It can be seen that the maximum difference between the two curves is less than 1mm and therefore can be considered to be negligible for this study.

The findings of this analysis confirm that it is valid to assume that the racket is rigid, when determining the displacement x_{IP}. However, it should be remembered that this error analysis was only conducted for impacts at the geometric string centre which is close to the node of vibration for the fundamental mode. For other impact locations, it may not be valid to assume that the racket is rigid.

(c) Comment on the accuracy of the measured coordinates

In this section, high speed cinematography is used to determine the motion of the ball, stringbed and racket during the impact between a ball and freely suspended racket. Clearly, there are errors associated with this technique. Many of these potential errors can be minimised simply by following established guidelines for cinematography analysis. For example, it must be ensured that the camera is positioned such that all the sampled points are in the same vertical plane. This can easily be verified by placing a grid with an uniform line spacing into the relevant vertical plane, and subsequently record an image of this grid using the camera. The image can then be analysed using *Vidimas v1* to ensure that the grid spacing on the image is uniform. This procedure was also used to verify that the curvature of the lens was not distorting the image.

The points on the images were sampled using the *Vidimas v1* image analysis software. Each point that was sampled does not always have a well defined edge and this reduced the possible accuracy of the analysis. A simple repeatability study was conducted to quantify the accuracy of the sampling method. In this study the points P_A and P_B on the image shown in Figure 10.7, were each sampled 60 times. This data was used to calculate the mean values of the x co-ordinates for both points, as well as the uncertainty in this co-ordinate for each of the 60 samples. This analysis was repeated for a further two images which were randomly chosen, resulting in a data set of uncertainties that comprised of 180 samples. It was assumed that these uncertainties were normally distributed about the calculated mean x co-ordinate, for the relevant image. It was found that the standard deviations for the x co-ordinate of points P_A and P_B were 0.9mm and 1.2mm respectively. This gives a good estimate of the realistic accuracy of the sampled data in this experiment.

(d) Supplementary measurements

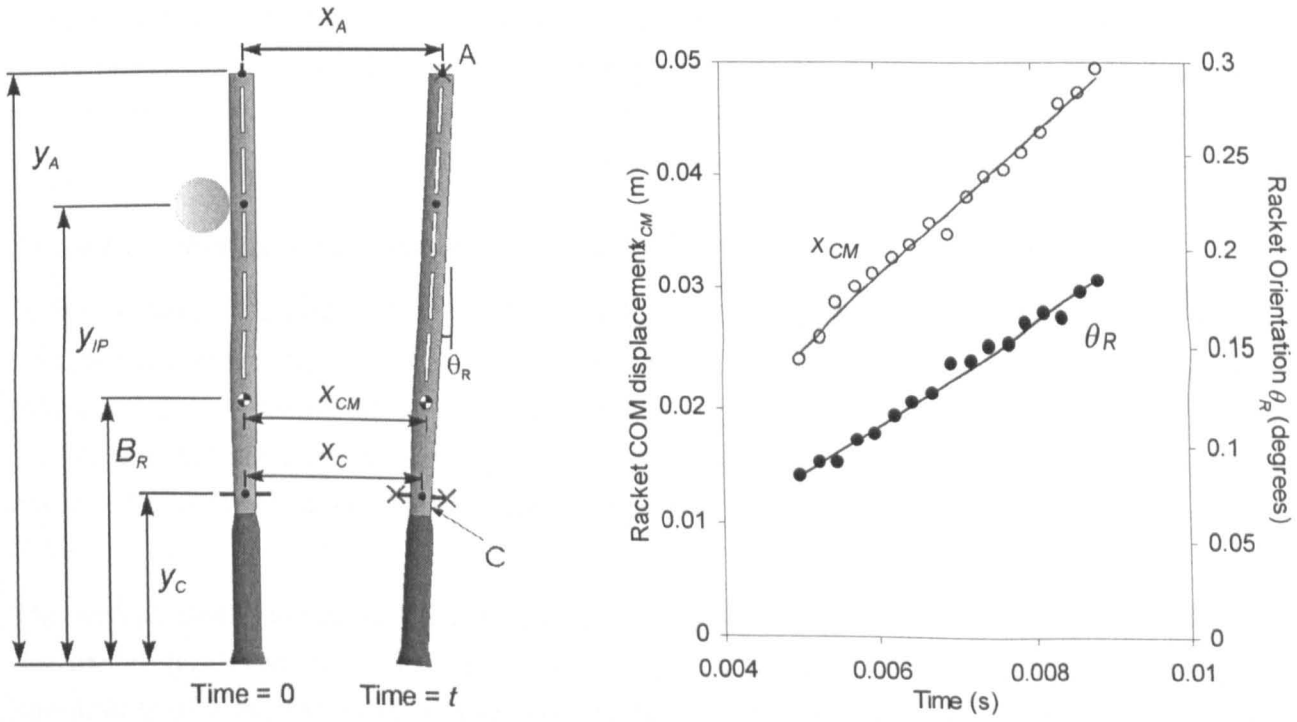

Figure 10.11 Definition of the displacement of the racket, and example data for the racket centre-of-mass displacement x_{CM} and racket orientation θ_R.

Although the main objective of this section involved the determination of the displacement of the ball, stringbed and racket, during impact, other parameters were also measured. The speed gates were used to measure the ball inbound and rebound velocity. Also, the motion of the racket (points *A* and *C*) was sampled during the period immediately after the impact had finished so that the racket rebound velocity could be calculated.

When a ball impacts on the longitudinal axis of a freely suspended tennis racket, the racket will both translate and rotate around its centre-of-mass (COM). The displacement of the racket COM x_{CM} can be determined using the sampled displacements x_A and x_C, as defined in Figure 10.11. The angle of rotation θ_R can also be determined from these two displacements. The displacement x_{CM} and the angle θ_R can be plotted as a function of time, as shown in Figure 10.11. Linear trend lines are plotted through the data in these figures; the gradient of these lines being equal to the respective velocity. For example, the rebound velocity of the racket COM is defined as V'_{CM} and is equal to the gradient of the curve labelled x_{CM} in Figure 10.11. The rebound velocity of the impact point on the racket V'_{IP} was determined using,

$$V'_{IP} = V'_R + d.\dot{\theta}_R \qquad [10.5]$$

where d is the distance between the impact point and the racket centre-of-mass.

In this analysis, the displacement of the racket COM is typically measured over a distance of only 25mm. Earlier in this section it was stated that the sampled points are subject to a standard deviation uncertainty of 1mm. Potentially, this uncertainty in the displacement could result in a standard deviation in the calculated value of the racket COM velocity which is equal to 8%. However, this uncertainty in the calculated velocity will be reduced because the calculation uses the displacement of the racket COM at a number of time intervals, as illustrated in the graph in Figure 10.11. This procedure acts to minimise the errors by the use of a trend line which is plotted through the data. Whilst this analysis does not determine a definite value for the standard deviation of the racket COM velocity, it highlights the potential uncertainties in the data, for this type of experiment.

10.3.4 Determining the parameters required by the model

In this section, the model will be used to calculate the displacement of the ball centre-of-mass, stringbed and racket frame. The *Racket Impact* software will be used to determine the model solution. This software already contains the parameters required for the *Pressurised* and *Pressureless* balls and the beam models of the *ITF Carbon Fibre* tennis racket. However, it does not have the parameters which define the stringbed stiffness for these rackets strung at 40lbs and 70lbs.

The method used to determine the parameters (a_S, b_S and c_S) which define the stringbed stiffness in the model has been given in section 10.2. These parameters are empirically determined coefficients of a second order polynomial trendline that was plotted through the experimentally obtained quasi-static stiffness data. This stiffness data is determined by applying a force using a rigid disc (diameter of 55mm) and measuring the resulting displacement.

In this section, the values of a_S, b_S and c_S were determined for each of the two string tensions, 70lbs and 40lbs. These parameters were obtained for compressions at the geometric string centre, as this corresponded with the location of the ball impact position.

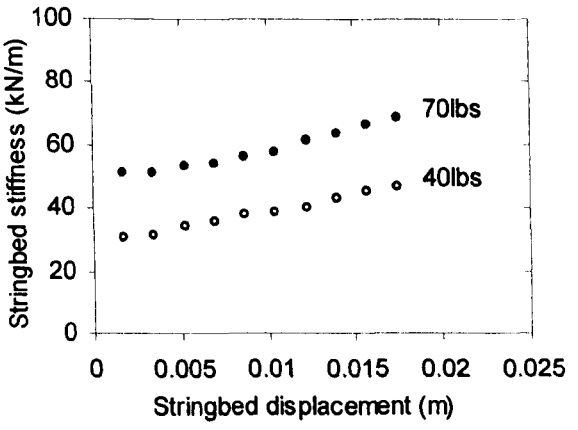

Figure 10.12 Experimentally measured stringbed stiffness for the *ITF Carbon Fibre* which is strung using two different string tensions.

Figure 10.12 illustrates the stringbed stiffness for the *ITF Carbon Fibre* racket which is strung using two different string tensions. The data is presented for a compression at the geometric string centre of the racket. The data in this figure was used to determine the model parameters (a_S, b_S and c_S) for each string tension, and these values are given in Appendix E.2.

The model parameters (a_S, b_S and c_S) were added to the *MS Access 2000* database, and therefore all the required model parameters are now known. The *Racket Impact* software was used to calculate the displacement of the ball centre-of-mass, stringbed and racket for the impact between a ball and freely suspended racket. In the following section, this model data is compared with the experimentally measured data.

10.3.5 Results and discussion – Model and Experiment Data

In this section, the experimental results obtained using the methods described in the previous section, are compared with the results calculated by the model.

Figure 10.13 and Figure 10.14 show the displacement of the ball centre-of-mass, stringbed and racket (at the impact point) for impacts in which the ball inbound speed is 20m/s and 30m/s respectively. The data is presented for both the model and the experiment. Further data is presented in Appendix E.2, for other ball inbound speeds. The model data which is presented here is that which was calculated using the flexible beam model. For interest, it should be noted that the data calculated using the rigid beam model is very similar to obtained using the flexible beam model.

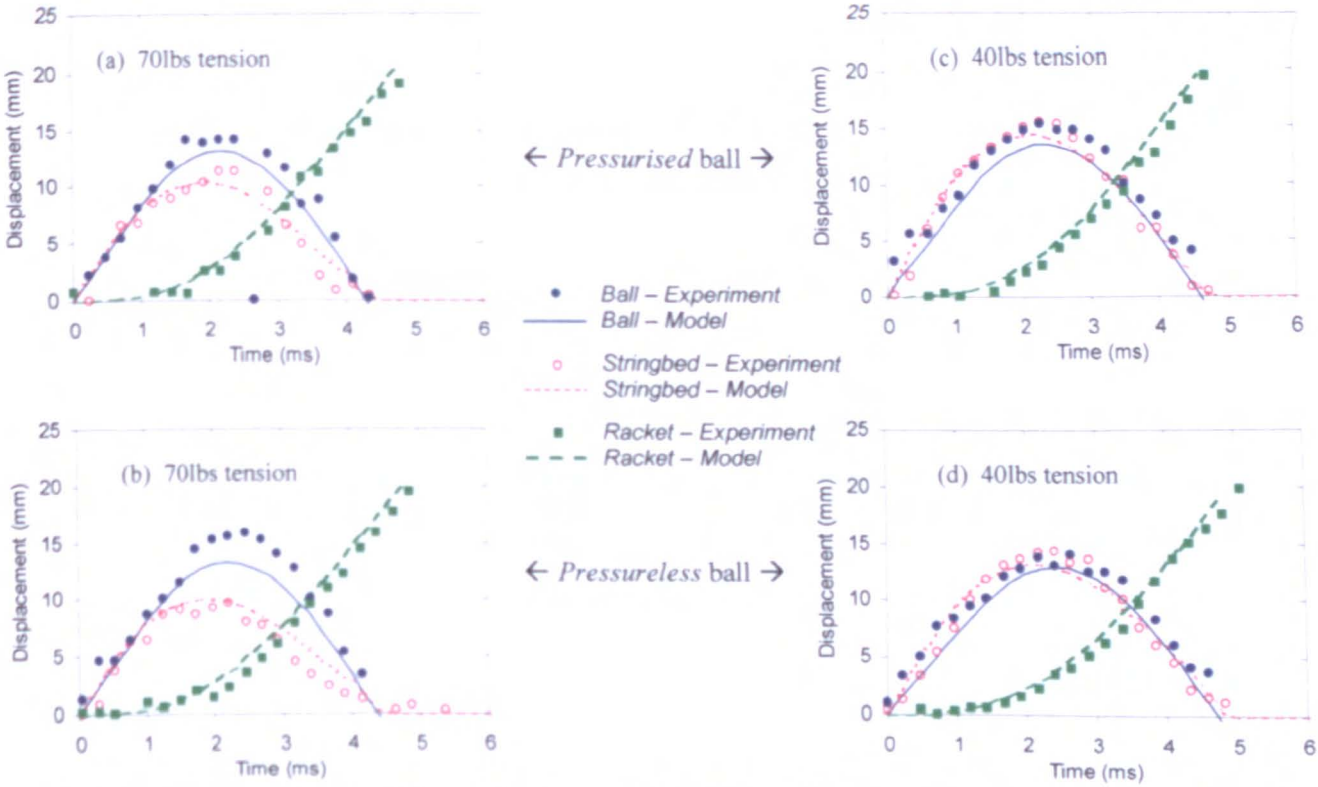

Figure 10.13 Ball centre-of-mass displacement, stringbed displacement and racket impact point displacement for an impact between a ball and freely suspended racket, for four different combinations of string tension and ball type. The nominal ball impact velocity is 20m/s.

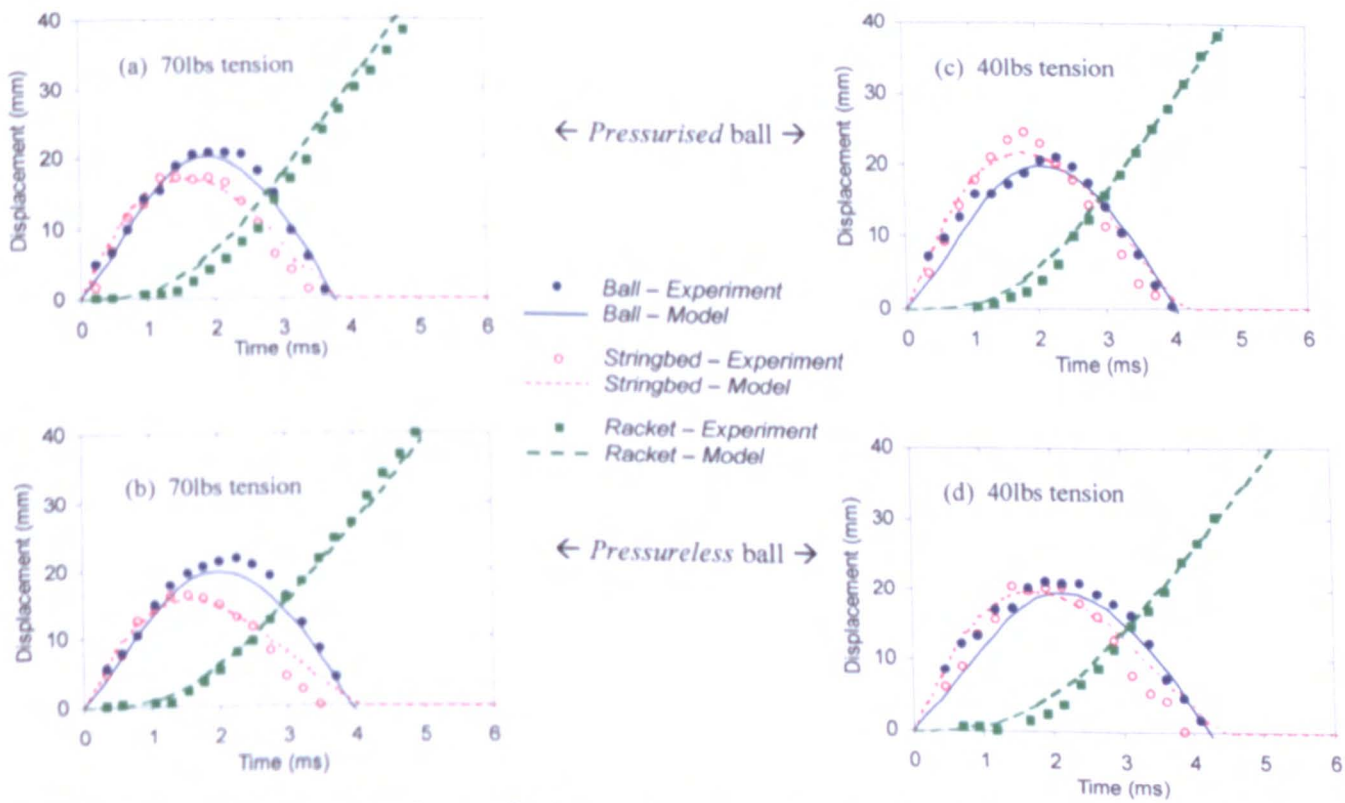

Figure 10.14 Ball centre-of-mass displacement, stringbed displacement and racket impact point displacement for an impact between a ball and freely suspended racket, for four different combinations of string tension and ball type. The nominal ball impact velocity is 30m/s.

These figures show that the model and experiment data generally correlate to within approximately 4mm; the majority of the data exhibiting a higher correlation than this. The main differences which are evident between the two sets of data are analogous to those which were found in Chapter 8. In that chapter, a similar comparison was made as that in Figure 10.13, except the data was determined for an impact on a head clamped racket. Both the maximum ball COM displacement and stringbed displacement are higher for the experiment, compared with the model. This is assigned to the fact that the two sets of data represent subtly different parameters. It can also be seen that, towards the end of impact, the experimentally determined stringbed displacement returns to zero before that which is calculated by the model. Both these differences were essentially assigned to the fact that the ball and stringbed are complex three-dimensional objects and they are being simulated using one degree-of-freedom models. This is expanded upon further in Chapter 8.

Figure 10.13 and Figure 10.14 show the displacement of the racket at the impact point, for both the model and experimental values. It can be seen that the two sets of values generally correlate to within approximately 2mm. It has been shown that the points sampled from the high speed video images have standard deviations of 1mm. Furthermore, the assumption that the racket is rigid results in a maximum error which is also in the order of 1mm.

A supplementary reason for the difference between the model and experiment data lies in the definition of the instant at which the impact commences. The defined time at which impact commences determines the time at which the displacements are plotted in the figures. For example, if the time at which impact commenced was shifted by 0.5ms, then all the data in Figure 10.13 and Figure 10.14 would be shifted by this amount. It is difficult to calculate an estimate of the uncertainty in the definition of the time at which impact commences. However, if one considers that, for example, a ball travelling at 20m/s, takes 0.2ms to travel just 4mm, then it becomes apparent that the definition of the instant at which impact commences is difficult to define with an accuracy of more than approximately 0.2ms. A shift in the data in Figure 10.13 and Figure 10.14 of the order of 0.2ms would significantly change the relative position of the experimental data with respect to the model data, highlighting the dependency of the plot on the definition of the time at which impact commences.

To summarise, the experimental and model data exhibit a high correlation. Any differences between the two can be assigned to the estimated uncertainty in the experimental data and the fact that the complex interaction between the ball, stringbed and racket frame is being simulated using a much simpler model.

Figure 10.15 shows a comparison of the ball rebound velocity calculated by the model and that measured experimentally, for impacts at the geometric string centre of the freely suspended racket. This data is presented separately for the *Pressurised* and *Pressureless* balls. The model data which is presented is that calculated using the flexible beam model.

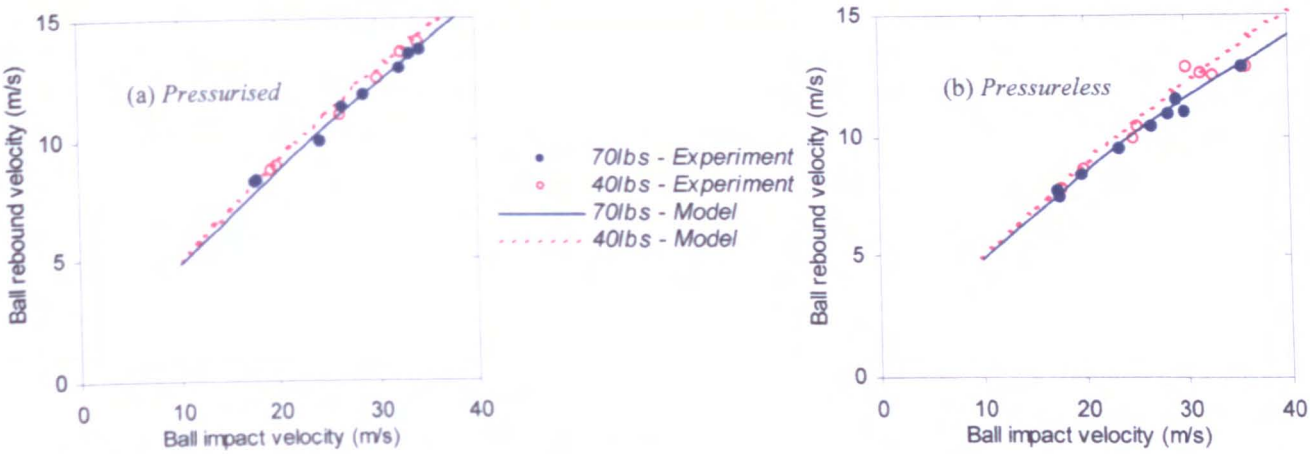

Figure 10.15 Comparison of the ball rebound velocity measured for the experiment and calculated using the flexible beam model. The data is presented for two different string tensions and two ball types.

Figure 10.15 shows that the model correlates with the experimentally obtained ball rebound velocity to within approximately 0.5m/s, for all combinations of ball type and string tension. This difference is of the same order of magnitude as the scatter in the experimental data. For a specific ball type, the model calculates a higher ball rebound velocity for the racket strung at 40lbs, compared with that strung at 70lbs; this difference generally being 5-10%. This difference is not clearly detected in the experimental results due to the low volume of data collected.

In Figure 10.16, the experimentally measured racket rebound velocity is compared with that calculated by the flexible beam model. It can be seen that the two sets of results correlate to within approximately 10%. It is interesting to note that the two model solutions for the rackets strung with the different string tensions are almost identical.

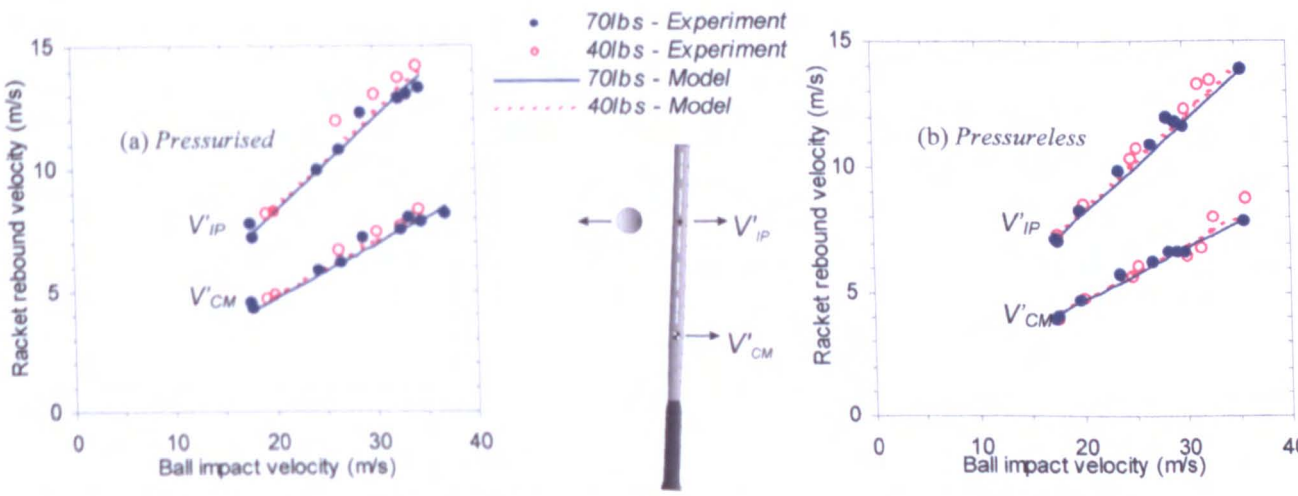

Figure 10.16 Comparison of the racket rebound velocity measured for the experiment and calculated using the flexible beam model. The data is presented for two different string tensions and two ball types.

There is a considerable amount of scatter in the data and therefore it is difficult to determine any further conclusions. In section 10.3.3, the standard deviation in the racket rebound velocity was

calculated as being 8%. This relatively high value was calculated because the velocity was calculated over a very short distance/time, and therefore it was very sensitive to the accuracy of the measured displacements.

10.3.6 Summary

In this section, it has been shown that the displacement of the ball, stringbed and racket calculated by the model, correlate very closely with that measured experimentally. This comparison was made for two different ball types and two different string tensions. Any differences between the model and experimental data can be assigned to the estimated uncertainty in the experimental data and the fact that the complex interaction between the ball, stringbed and racket frame is being simulated using a much simpler model.

10.4 Experiment 3 – Measuring Ball and Racket velocity *after* impact

10.4.1 Introduction

In the previous section, the displacement of the ball, stringbed and racket were experimentally measured for an impact between a ball and freely suspended racket. This experimental data was obtained for a range of impact velocities, string tensions and ball types. It was shown that the experimental data correlates very closely with that calculated by the model. In that section, the ball and racket rebound velocities were also measured, although this was not the main objective of the experiment. The ball rebound velocity was measured using speed gates and the racket rebound velocity was determined from the high speed video images. The measurement of these two parameters was not the main objective of the previous section and, therefore, the experimental technique was not optimised for this purpose. In this current section, a more appropriate experiment is conducted to determine the racket rebound velocity, for an impact between a ball and freely suspended racket. The ball rebound velocity is also determined in this section. This experimental data will be compared with the data calculated by the model. This comparison will be conducted for several impact positions along the longitudinal axis of the racket.

In the previous section (section 10.3), the motion of the racket was only sampled for a relatively short period. This meant that the racket rebound velocity was calculated over a short distance and was very sensitive to the accuracy of the measured displacements. This resulted in a large magnitude of scatter in the calculated values of the racket rebound velocity. The experiment described in this current section is different to that discussed in section 10.3 because the motion of the racket is sampled for a significantly longer period. This improves the accuracy of the calculation that is performed to determine the velocity of the racket *after* impact.

10.4.2 Experimental Apparatus

(a) Procedure

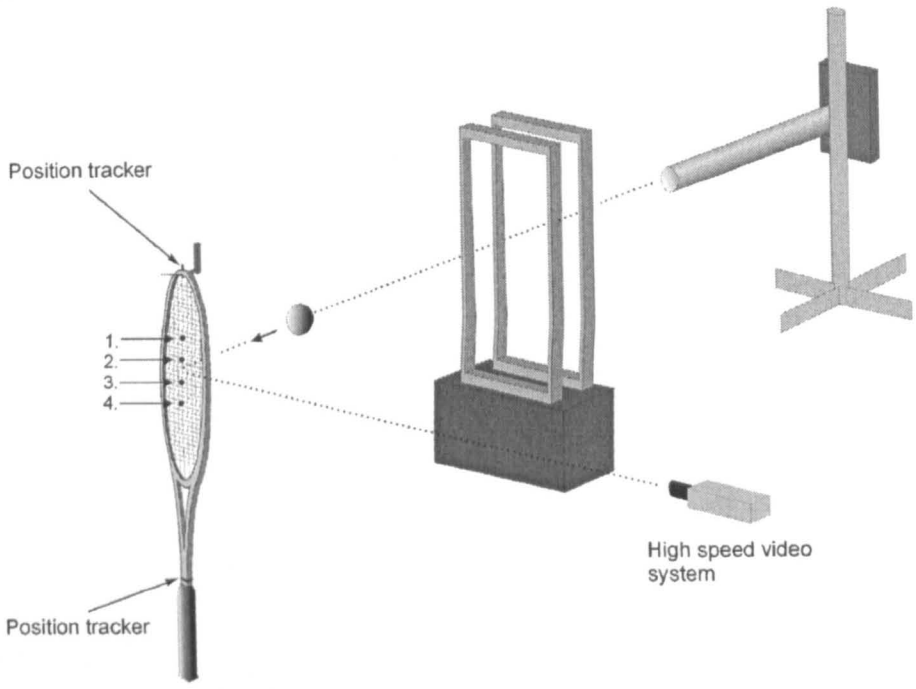

Figure 10.17 Freely suspended racket showing the four nominal impact positions.

The aim of this experiment is to measure the rebound velocity of the ball and racket, for an impact between a ball and freely suspended racket. The experimental layout is very similar to that described in section 10.3, and is shown in Figure 10.17. The impact is recorded using a *Kodak Motioncorder* high speed video system which operated at a frame rate of 240 frames per second (fps). The *Phantom v4* camera is capable of 1000 fps, at the same screen resolution. However, a frame rate of 240 fps is adequate for this current study. Furthermore, the *Motioncorder* is more suitable as it is capable of storing up to 11 impacts in its memory, whereas the *Phantom v4* is only capable of storing one impact.

Pressurised tennis balls were projected at the longitudinal axis of the racket, perpendicular to the stringbed, at velocities between 14 and 35 m/s (30 and 80mph). Two tennis different rackets were used in this study; these being a *Head Prestige Classic 600* and a *Spalding Heat 90*. The full details of these two rackets is given in Chapter 9. To summarise, the *Head* racket is heavier, has a smaller head size and higher mass moment of inertia, compared with the *Spalding* racket.

Four discrete impact points on the racket were tested, as defined pictorially in Figure 10.18. The positions of these impact locations are defined in Appendix E.3, with respect to the geometric string centre of the racket; the position of the *GSC* corresponding to the intersection of the dashed lines in Figure 10.18. For completeness, the distance between the butt end of the racket and the *GSC* is 518mm and 508mm for the *Head* and *Spalding* rackets respectively.

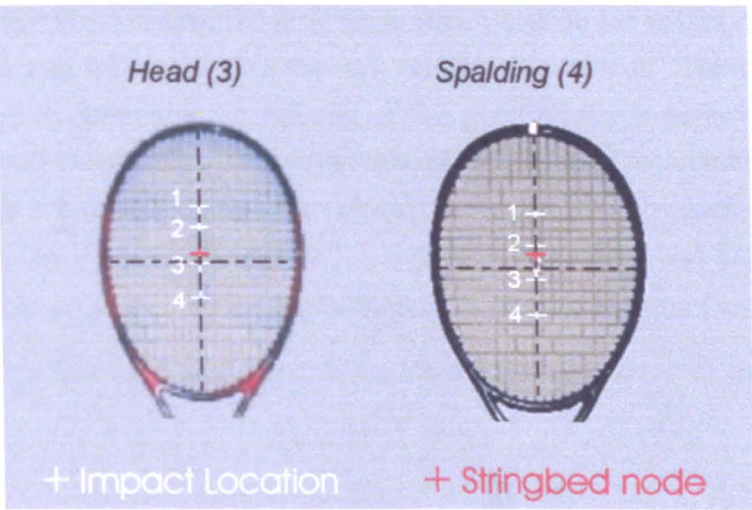

Figure 10.18 Illustration of the four impact positions which were tested for each tennis racket. The stringbed node location and geometrical string centre are also illustrated.

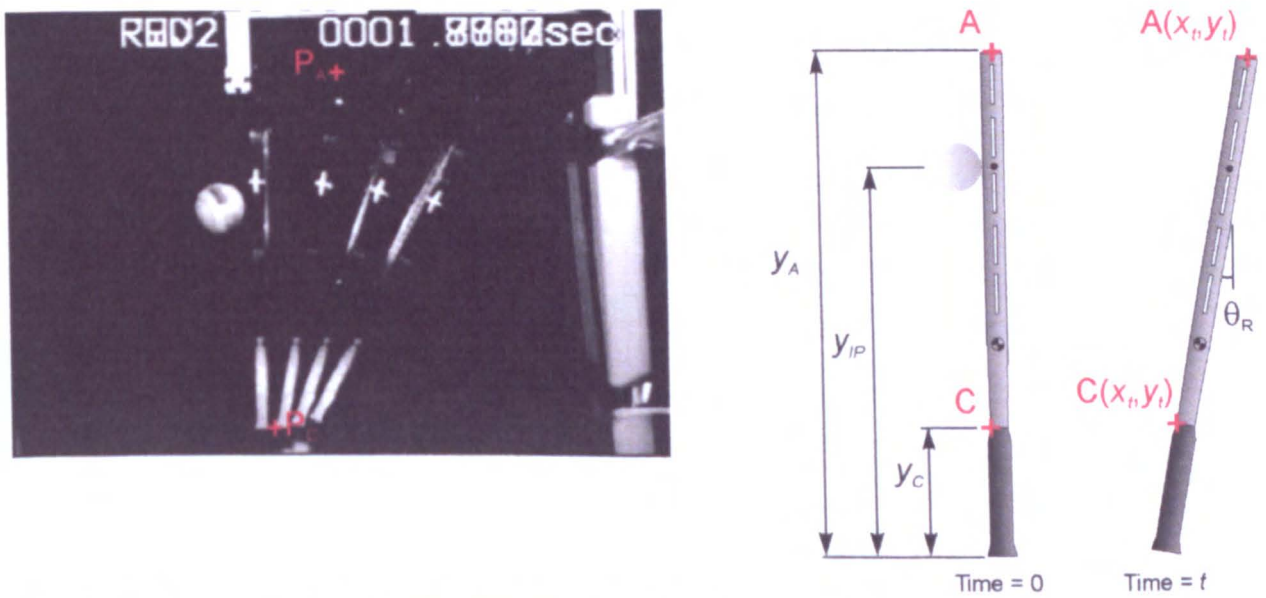

Figure 10.19 Illustration of the motion of the racket after impact.

The *Motioncorder* was used to record the motion of the racket for the period after impact had ceased. A typical high speed video image of the recoiling racket is shown in Figure 10.19. This image is a compiled image which shows the initial position of the racket, along with three images of the recoiling racket. The time interval between these three images is 4.17ms. This figure illustrates the two points on the racket, P_A and P_C, which are sampled to determine the motion of the racket. The top point corresponds to a carbon fibre rod which has been inserted into the racket. The bottom point refers to a white mark which has been painted on the racket, at the top of the handle.

The sampled points were used to determine the linear displacement of the racket centre-of-mass using simple geometrical relationships between the points P_A, P_C and the location of the racket COM, as described in section 10.3. The points P_A and P_C were also used to determine the angular displacement of the racket. In this study, it is assumed that the racket is rigid and the racket rebound velocity is constant for the sampling period; this period lasting approximately 12ms. It

can easily be shown that the aerodynamic drag force which acts on the racket during this period is negligible which validates the assumption that the velocity is constant. The displacement of the racket COM was used to determine the velocity of this point which is defined as V'_{CM} in Figure 10.20. This velocity was simply calculated as the ratio of the distance travelled between frames and the time step for each frame (4.17ms). This velocity was calculated for each pair of frames, and then an average value of V'_{CM} was determined. A similar procedure was used to determine the angular velocity of the racket $\dot{\theta}_R$, as defined in Figure 10.20. The rebound velocity of the impact point on the racket V'_{IP} was calculated using V'_{CM}, the rotational velocity of the racket $\dot{\theta}_R$ and the distance d.

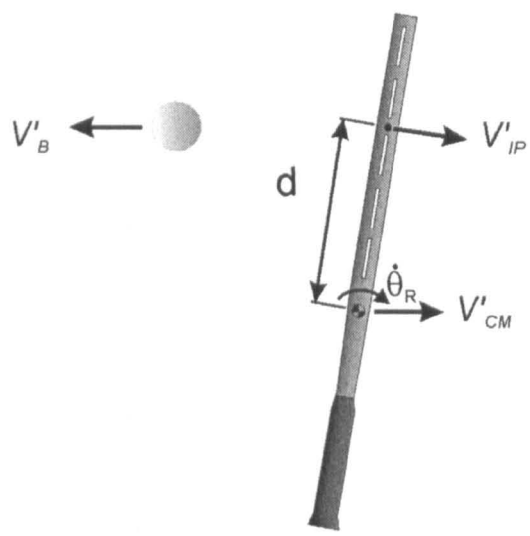

Figure 10.20 Definition of the velocity of the ball and racket after impact.

(b) Error associated with the repeatability of the impact location

In section 10.2.2, it was shown that the ball impact position varied by up to 10mm from the desired position, for balls propelled using the air cannon. The *Racket Impact* software was used to estimate that this uncertainty may cause a variation of up to 9-18% in the ball rebound velocity; the exact value being dependent on the racket and impact location. The full details of the relationship between the ball rebound velocity and impact location can be found in section 10.2.2 and are therefore not repeated here.

A similar analysis can be conducted to estimate the relationship between the uncertainty in the ball impact location and the effect that this has on the racket rebound velocity. For simplicity, this investigation is only conducted for the rebound velocity of the racket at the impact point (V'_{IP}). The *Racket Impact* software was used to calculate that a shift in the impact location of 10mm towards the tip, with respect to an arbitrary impact location on the longitudinal axis, acts to increase the racket velocity V'_{IP} by approximately 3%. This result applies for both rackets and all four impact locations used in this section.

The results of this theoretical error analysis study will be referred to later in this section.

10.4.3 Determining the parameters required by the model

In this section, the model will be used to calculate the ball and racket rebound velocity, for an impact between a ball and freely suspended racket. The *Racket Solver* software will be used to determine this model solution. This software already contains the parameters required for the *Pressurised* ball and the beam models of the two tennis rackets. However, it does not have the parameters which define the stringbed stiffness of the rackets.

The *Head* tennis racket is identical to that which was used in section 10.2. However, this racket was restrung before this testing, at a tension of 65lbs using a standard 15g nylon string. The *Spalding* racket was also restrung before this testing, at a tension of 55lbs using the same string.

The method used to determine the parameters (a_S, b_S and c_S) which define the stringbed stiffness in the model has been given in section 10.2. In this section, the values of a_S, b_S and c_S were determined for each of the two rackets. For simplicity, these parameters were only obtained for the geometric string centre position. In section 10.3, it was found that the stringbed stiffness was approximately 15% higher for locations towards the throat and approximately 20% higher for locations towards the tip (with respect to the stiffness at the geometric string centre). In this current section, it was assumed that these relationships could be used to define the stringbed stiffnesses at the four different impact locations. For example, the stringbed stiffness at the impact point nearest the tip was assumed to be 20% larger than that measured experimentally at the geometric string centre.

Figure 10.21 illustrates both the measured and calculated stringbed stiffness for the two rackets. The stringbed stiffness at the geometric string centre (*GSC*) was assumed to be valid for impact locations labelled *2* and *3* in Figure 10.18. The stringbed stiffness was calculated for the tip position and this was assumed to be valid for the impact location labelled *1* in Figure 10.18. The stringbed stiffness at the throat was also calculated and was assumed to be valid for impact location *4*.

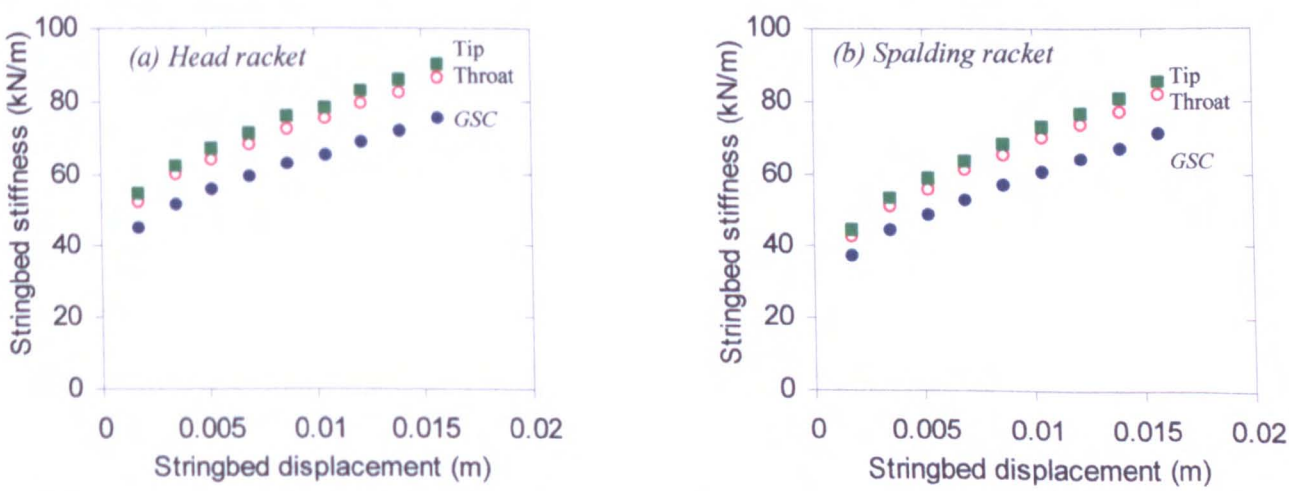

Figure 10.21 Stringbed stiffness of the two tennis rackets at the tip, *GSC* and throat of the racket.

These parameters were added to the *MS Access 2000* database, and therefore all the required model parameters are now known. The *Racket Impact* software was used to calculate the ball and racket rebound velocity for the impact between a ball and freely suspended racket. In this section, the

software was only used to determine the solution for the model which used the flexible beam. The rebound velocity of the racket was calculated at the centre-of-mass and at the impact point, and these were defined as V'_{CM} and V'_{IP} respectively.

10.4.4 Results

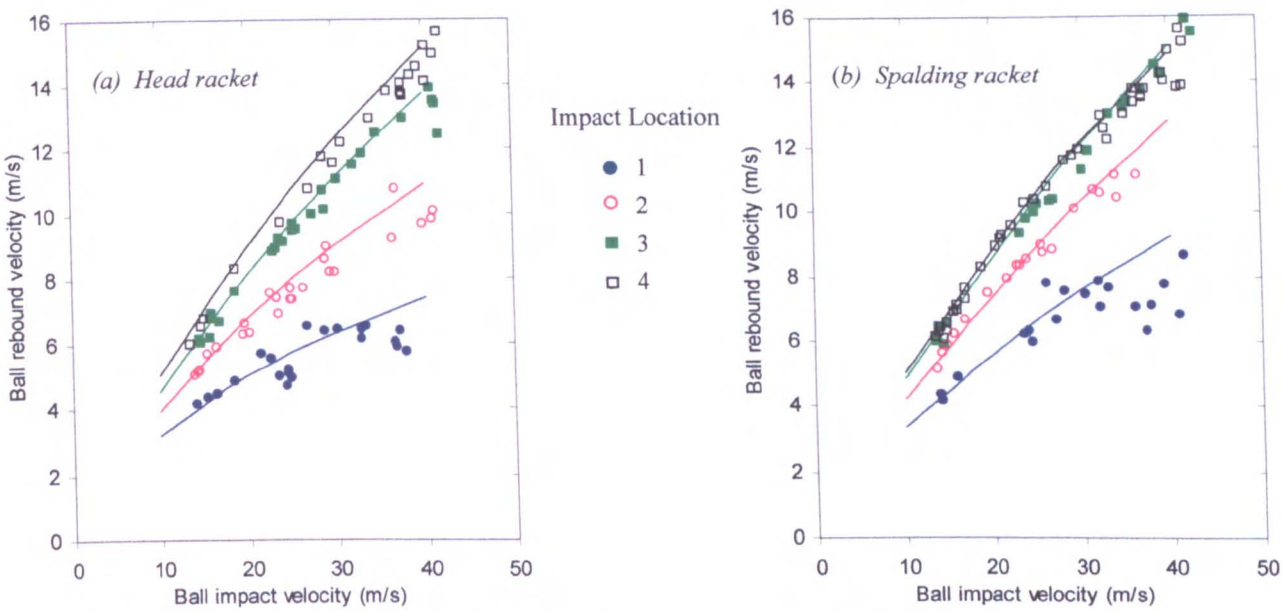

Figure 10.22 The calculated and measured ball rebound velocity for two different tennis rackets. The data points represent experimental data and the curves represent the data calculated by the model.

Figure 10.22 shows the experimental and model values of the ball rebound velocity, for the impact between a ball and freely suspended racket. In this figure the data is presented for two different tennis rackets, and four nominal impact locations.

It can be seen that the model and experimental data correlate to within approximately 5-10%, for all impact locations. There is a considerable amount of scatter in the experimental data, especially for impacts located at position *1* which corresponds to impacts close to the tip of the racket. A similar finding was reported in section 10.2, and in that section it was concluded that the source of this scatter was the variability of the impact location. To summarise, it was found that a shift in the impact location of only 10mm leads to a difference in the ball rebound velocity of approximately 10% for impacts at position *1*. This difference is much smaller for other impact locations.

Figure 10.23 shows the experimental and model values of the racket rebound velocity for the impact between a ball and freely suspended racket. In this figure the data is presented for the velocity of two points on the racket (V'_{IP} and V'_{CM}) and four different impact locations. In Figure 10.23, the data is presented for the *Spalding* racket; the data for the *Head* racket being given in the Appendix E.3. The scatter in the experimental data can be accounted for by the variability of the impact location, as was concluded for the data in Figure 10.22.

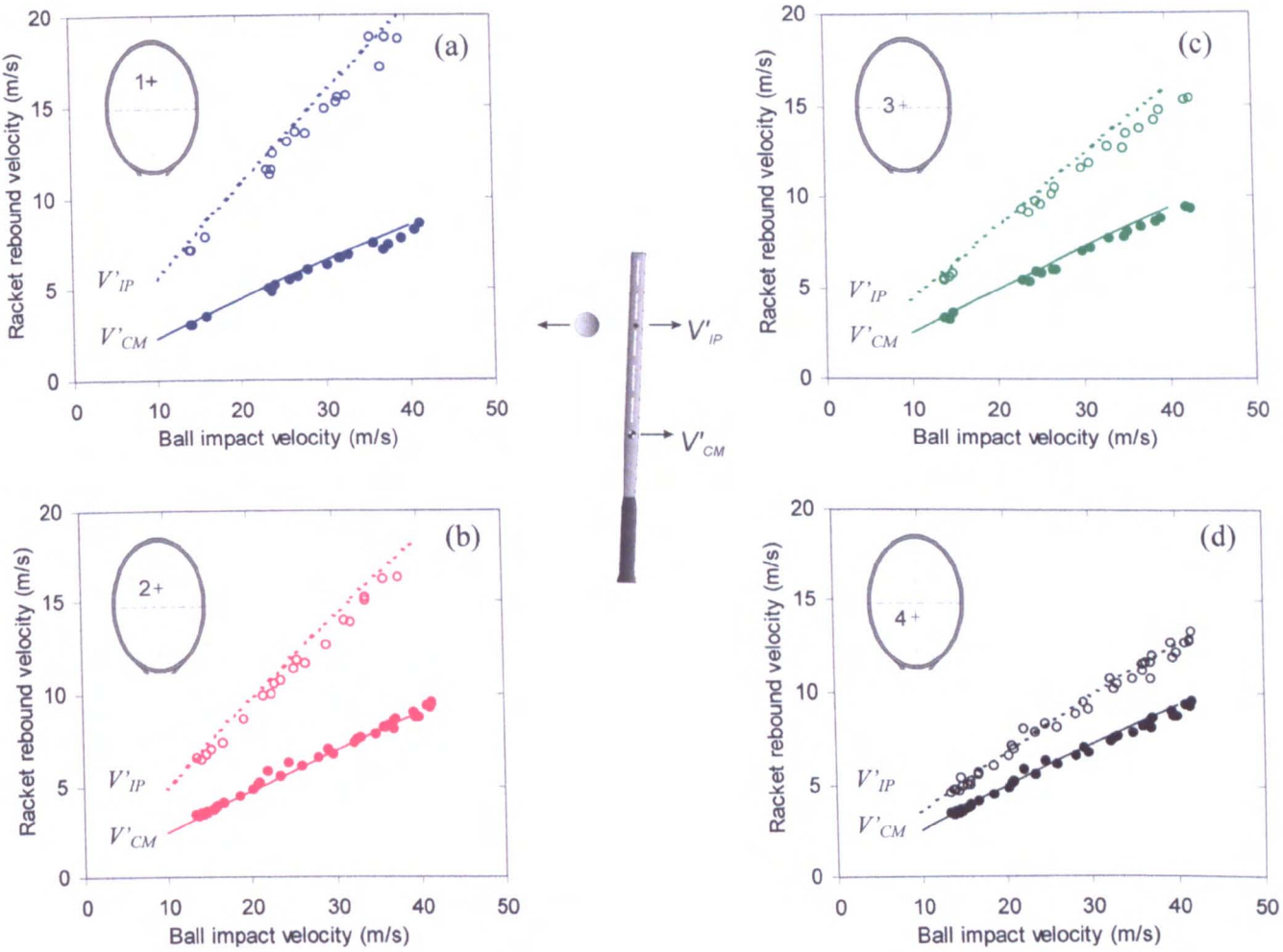

Figure 10.23 The racket rebound velocity for the *Spalding* racket. The data points represent experimental data and the curves represent the data calculated by the model.

Figure 10.23 (and Figure E.4) show that the model and experimental data correlate very closely. The model generally calculates a racket rebound velocity which is larger than that measured experimentally. However, it should be noted that the difference between the two sets of data is in the order of only 5%. This small difference may either be due to a systematic experimental error or a weakness in the model. The experimental errors have been discussed in a previous section and therefore will not be repeated here. A possible weakness of the model, which has not yet been commented upon, is related to the assumption that the stringbed has no mass. This assumption was required to simplify the required solution of the visco-elastic model which represents the ball and stringbed in the *Racket Solver* software. The physical stringbed has a total mass of approximately 20g, but only a fraction of this stringbed deforms significantly during impact. Taylor (2002) showed that a stringbed exhibited large amplitude oscillations which were excited by the impact. Although the energy stored in these oscillations is small compared with that stored in the ball and racket, it will have a finite magnitude which is not accounted for in the model. This weakness of the model may account for a proportion of the difference which has been found between the model and experiment data.

Although differences have been found between the model and experiment values of the racket rebound velocity, this does not render the model worthless. The magnitude of the difference,

which is approximately 5%, can be considered as a guide to the accuracy of the model when it is used to calculate this parameter.

10.4.5 Summary

In this section, experiments were performed to determine the rebound velocities of a ball and racket, for an impact between a ball and freely suspended racket. This data was compared with the model solutions calculated by the *Racket Solver* software. A range of ball impact velocities were tested and the ball was propelled at four different locations on the longitudinal axis of the racket.

It was found that the model and experiment data exhibited a high correlation, especially for the data collected for the ball rebound velocity. However, the model generally calculated a racket rebound velocity which was 5% higher than that which was measured experimentally.

10.5 Vibration Analysis of a tennis racket

10.5.1 Introduction

In sections 10.2-10.4, experiments were conducted in which a tennis ball was propelled at a freely suspended tennis racket. In these experiments, the motion of the ball and racket, during and after impact, was sampled and compared with data that was calculated using a model. The experimental data presented in these sections relates only to the zero frequency response of the racket frame and ball. Therefore, the higher order response (e.g. fundamental mode of vibration) of these two objects has not yet been verified.

The higher order response of the beam, after impact, is calculated by the model (*Racket Impact* software) and will be measured experimentally using two different techniques in section 10.5 and 10.6. This experimental data is compared with the relevant values calculated by the model to verify the accuracy of the model in relation to the higher order response of the beam.

In this current section, the position of the node point for the fundamental mode will be determined, for an impact between a tennis ball and racket. This point corresponds to the ball impact location which does not excite the fundamental mode of vibration of the racket frame. A similar experiment has already been described in section 9.3.3 and section D.2. In these sections, an experiment is presented which was used to measure this node point for the fundamental mode for impacts with a soft hammer. The racket was excited using a soft hammer at various points on the stringbed, along the longitudinal axis, and the resulting vibrations were measured using a piezoelectric transducer that was sampled using suitable PC hardware and software. The amplitude and frequency of the induced vibrations was analysed to determine the location of the node point.

In Chapter 9, the one-dimensional beam model was used to show that the location of the impact point which gave minimal vibrations was different for a point loading and a distributed loading. This effectively showed that this location was a function of the method used to apply the load. If it is assumed that a soft hammer will apply a load to the racket in a different manner to that in which a tennis ball applies the load, then it may be possible that the measured node location is different

for the two experiments. In section 6.2.3, it has been shown that the stiffness of a stringbed increases with deformation and, therefore, the effective stiffness of the stringbed for the hammer strike will be considerably lower than for an impact between the racket and the ball. If it is hypothesised that the stiffness of the stringbed may influence the method in which the load is applied to the frame, then it is conceivable that the stringbed node measured using the soft hammer may be located in a different position to the node for an impact between a ball and tennis racket. This is the motivation for performing the experiments which are conducted in this section.

10.5.2 Experimental Apparatus

In this section, a method is presented which is used to determine the node point for the fundamental mode of vibration of the racket. This node point will be determined for excitations which are induced when a tennis ball impacts on a freely suspended racket. To be consistent with the work in section 9.3.3, the amplitude of vibration will be measured for a point near the butt end. This point is suitable as it is a significant distance from the location of the node of vibration.

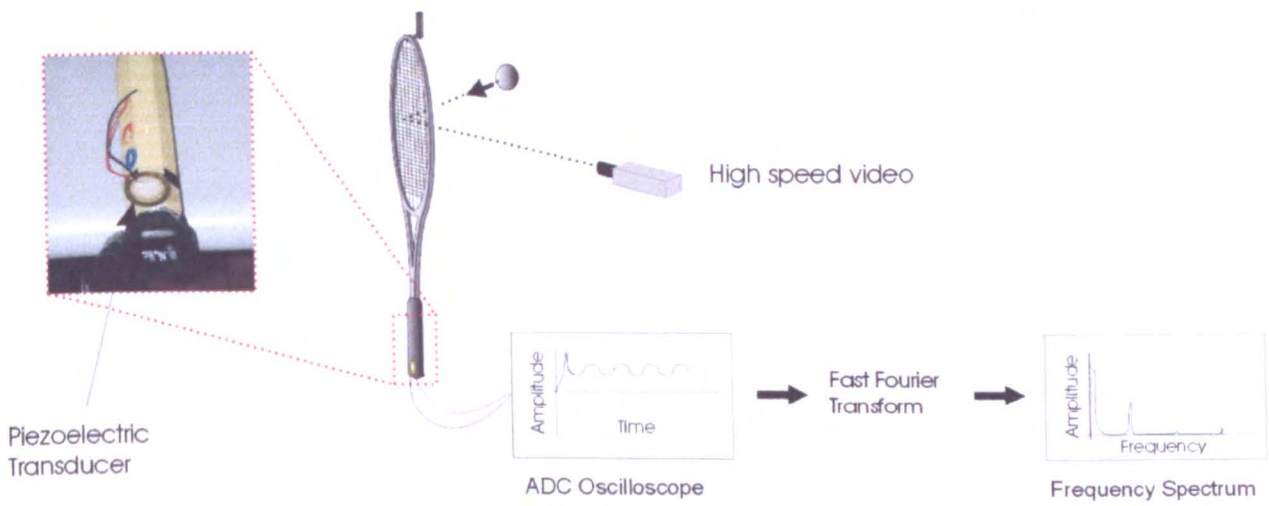

Figure 10.24 Schematic diagram of experiment arrangement used to determine the magnitude of the frame vibrations induced by an impact with a tennis ball.

The ball was propelled at the longitudinal axis of a freely suspended *ITF Carbon Fibre* tennis racket. The *Kodak Motioncorder* high speed video, operating at 240 frames per second, was used to record the impact. These high speed video images were used to determine the impact location of the ball, on the racket. The racket was supported on a small, smooth pin with its longitudinal axis orientated vertically. The ball was propelled at several locations on the longitudinal axis of the racket.

The experimental layout is given in Figure 10.24. In this experiment, the grip on the racket was removed and a small piezoelectric transducer was attached to the rigid surface of the handle, using strong adhesive tape. The strap was then replaced. The ball was propelled at the racket, and the racket was subsequently allowed to recoil freely. The piezoelectric transducer produced a charge (voltage) which was proportional to the acceleration of the racket at that point. However, it should

be noted that this proportionality is non-linear due to the nature of the construction of the piezoelectric transducer.

The signal from the piezoelectric transducer was sampled using an Analogue-to-Digital converter and *Picoscope v5.7.4* software on a PC laptop. A Fast Fourier Transform of this data was performed using the *FFT* function in *MATLAB v5.3* software, to identify the frequency spectrum of the racket vibrations.

The objective of this section is to measure the amplitude of the fundamental frequency for a range of ball impact locations. The fundamental frequency of the *ITF Carbon Fibre* tennis racket has previously been measured in Chapter 9, and is equal to 134Hz. This frequency was determined for small oscillations of the racket. In this current section, the frequency will be determined and compared with the previously obtained value. The amplitude of this mode is easily determined from the calculated frequency spectrum.

10.5.3 Determining the parameters required by the model

In this section, an *ITF Carbon Fibre* tennis racket was strung at 60lbs using a standard 15g nylon string. The quasi-static stringbed stiffness of this racket was tested, using the method described previously, to determine the parameters a_S, b_S and c_S which define the stringbed stiffness in the model. This was only obtained for the point at the geometrical string centre of the racket. For simplicity, in this section it is to be assumed that the stringbed stiffness is uniform along the longitudinal axis. From section 10.2, it can be concluded that this will result in a maximum error of approximately 15%-20% in the value of stringbed stiffness which is being used. This error appears relatively large, however, in practise it was found that a change in stringbed stiffness of 20% had little effect on the resulting vibrations of the racket frame or the ball rebound velocity.

All the parameters required by the *Racket Impact* software have already been defined. The software is used to simulate the experiment described above, for each of the experimentally measured impact locations. The calculated acceleration of the beam segment at the butt end can easily be obtained from the *Racket Impact* software. A Fourier analysis, similar to that described in section 9.3.2, was conducted on this data to determine the amplitude of the acceleration of this segment of the beam.

10.5.4 Results

Figure 10.25 compares the experimentally measured amplitude of the fundamental frequency which was calculated using the sampled signal from the piezoelectric transducer, with that calculated by the model. The units of the experimentally measured vibration are mV because the calibration factor which defines the relationship between the acceleration of the piezoelectric transducer and the resulting voltage is not known. The experiment could be repeated using a calibrated accelerometer, but this is beyond the scope of this study. In Figure 10.25, the location of the stringbed node which was measured using a soft hammer, is also presented; the method used to define this location being given in section 9.3.2.

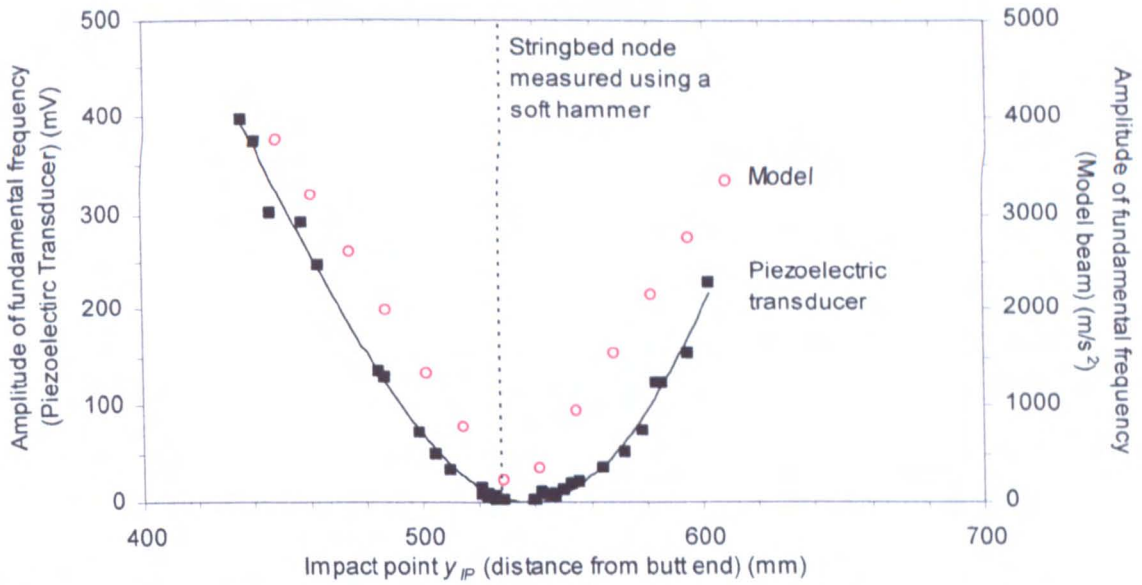

Figure 10.25 Amplitude of vibration measured experimentally using a piezoelectric transducer compared with that calculated by the model, for an impact between a ball and racket. The stringbed node measured for an impact with a soft hammer is also shown.

The main finding from Figure 10.25 is that the amplitude of the fundamental frequency, which is measured by the piezoelectric transducer, is at a local minimum at a distance of 535mm from the butt end. This point corresponds very closely with the stringbed node of the racket that was measured using a soft hammer; these two points corresponding to within 7mm. The accuracy of all location measurements is approximately 5mm and therefore the difference in the location of the two points may be simply accounted for by a measurement error.

These results imply that the location of impact point on the stringbed node which excites minimum vibrations (of the fundamental mode) is very similar for the two methods used in this study to induce the vibrations. The two methods involve a different magnitude of deformation of the stringbed, which results in a different effective stiffness of this component. This implies that differences in stiffness of this order of magnitude do not influence the node location.

The model data, which is presented in Figure 10.25, confirms that the model simulates the vibrational properties of the tennis racket. This can be concluded because the impact point which corresponds to a minimal amplitude of the fundamental mode, for the model, coincides with that measured experimentally using the piezoelectric transducer. This has already been discussed in Chapter 9.

10.5.5 Summary

In this section, an experiment was conducted to measure the racket vibrations induced by a ball impacting on the longitudinal axis of the racket. The impact point which corresponded to the minimum amplitude of these vibrations has been determined. This point coincided very closely with that measured for impacts using a soft hammer. This testing has showed that the node point of vibration is not dependent on the method used to excite the tennis racket, in this study.

10.6 Comparison of racket vibrations in the model and experiment

10.6.1 Introduction

In section 10.2, an experiment was performed to measure the ball rebound velocity for an impact between a ball and tennis racket. In that section, two model solutions were obtained which calculated the ball rebound velocity for this impact. In the first solution, the racket was assumed to be a rigid beam and in the second solution it was assumed to be a flexible beam. It was found the results calculated using the flexible beam model correlated very closely with those measured experimentally. This is assigned to the well-documented finding that the racket deforms during impact and this deformation is only simulated by the flexible beam model.

In the previous section, the vibration of a tennis racket was sampled for the period directly after an impact between a tennis ball and the racket. The impact location which corresponded to the minimum vibrations of the racket was measured experimentally, and calculated using the model. It was found that the two points correlated very closely. Although the work in the previous section studied the vibrations of the racket after impact, and compared them with the model, it did not compare the magnitude of the vibrations for the two cases. In this current section, this issue will be addressed.

The aim of this section is to compare the motion of the racket during and immediately after impact, for the experiment and model. A similar study was done by Cross (1999c) who studied the impact between a ball and an aluminium beam. In that paper the beam was freely suspended using light strings, and a superball impacted on the side of the beam. The motion of the beam was determined experimentally, and also calculated using an equivalent flexible beam model. In that work, a very good qualitative correlation was found between the two traces.

10.6.2 Experimental Technique

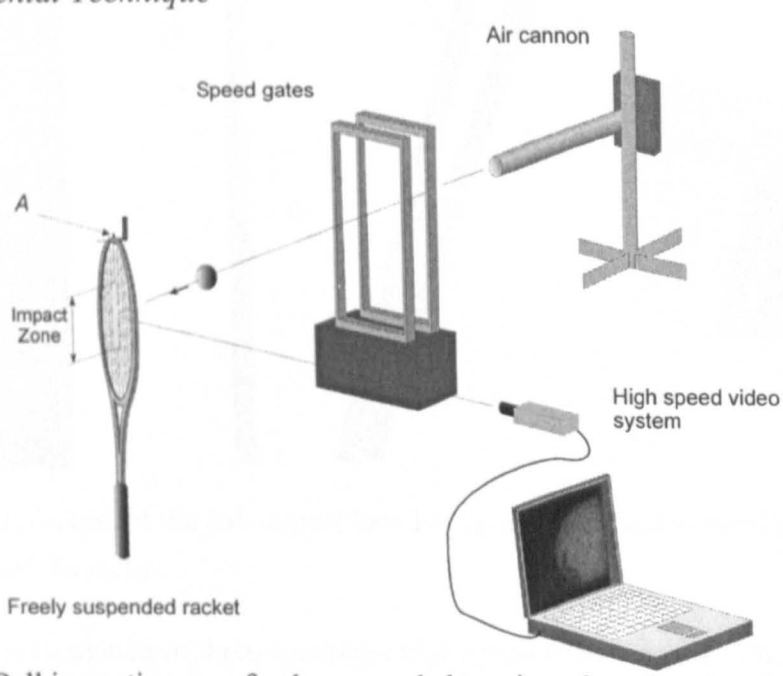

Figure 10.26 Ball impacting on a freely suspended tennis racket, showing the point *A* which was sampled from the high speed video images.

The experimental apparatus used in this section is illustrated in Figure 10.26. The *Phantom v4* high speed video system is used in this experiment and operated at 1908 frames per second with an image resolution of 512 x 256 pixels. *Pressurised* tennis balls were propelled using an air cannon at a nominal velocity of 20m/s. The inbound and rebound velocities of the ball were determined using a set of speed gates; these speed gates being located approximately 0.5m from the racket. The ball impacted normal to the string plane of a freely suspended *ITF Carbon Fibre* tennis racket, at a range of positions along the longitudinal axis, as illustrated by the shaded 'impact zone' in Figure 10.26.. This racket was strung at a tension of 60lbs.

In this section, the amplitude of the transverse vibrations which were induced by the ball impacting on the racket, were measured experimentally and compared with those of the one dimensional beam model as calculated by the *Racket Impact* software. Clearly, it is neither practical nor possible to sample the motion of each point along the racket, for a finite time period and therefore it was concluded that only one point on the racket would be sampled. The point chosen was that at the tip of the racket for two main reasons, which were,

1. This point coincided with an anti-node of vibration of the fundamental mode and therefore vibrated with the largest amplitude for a given excitation force.
2. This point lay on the longitudinal axis and therefore was not subject to errors if the ball landed eccentric to the longitudinal axis, as discussed in section 10.4.

Figure 10.26 defines the point A which corresponds to the tip of the racket. This point was sampled from the high speed video images using the method described in the following section.

10.6.3 Analysis of high speed video images

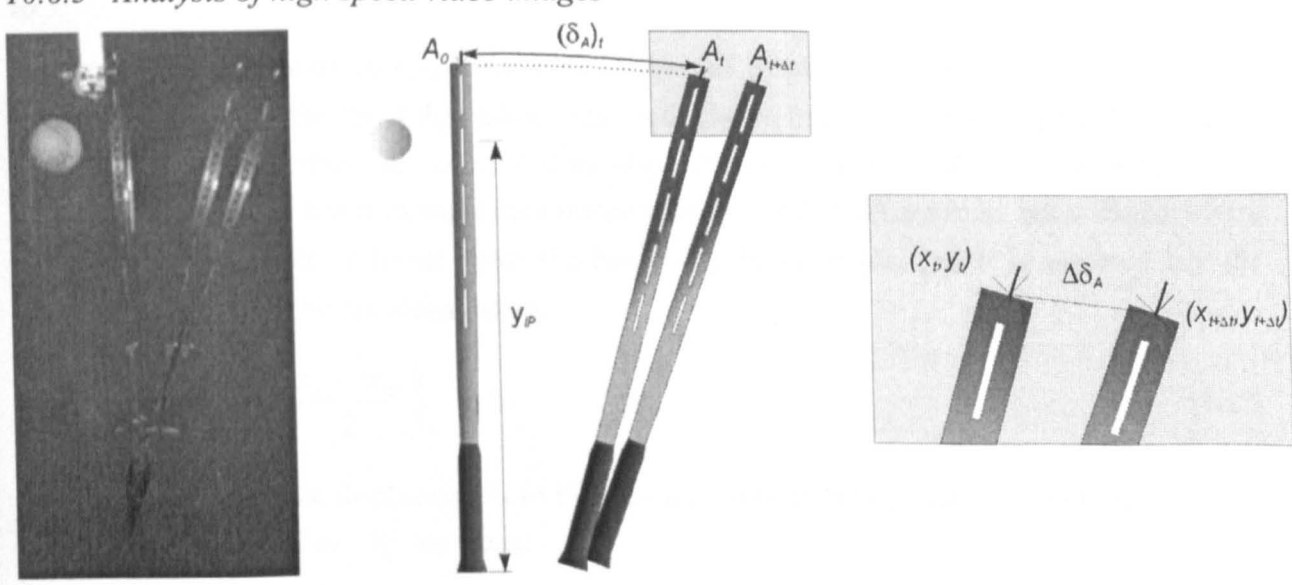

Figure 10.27 Definition of the ball impact location y_{IP} and the displacement $(\delta_A)_t$ of the sampled point A at the tip of the racket.

Figure 10.27 shows a picture of three combined high speed video images. The point A corresponds to the base of the white rod which protrudes from the tip of the tennis racket. This point was

sampled using the *Vidimas v1.1* software using the procedure which has been explained in section 10.3.3.

The motion of the ball was sampled to determine both the impact position on the racket and the instance at which impact commenced. The details of the method used to define the start of impact is explained in section 7.2.3. The high speed images were also used to verify the value of the ball rebound velocity which was measured by the speed gates. This procedure was performed because impacts towards the tip of the racket result in relatively small ball rebound velocities. In section 10.2 it was explained that the speed gates sometimes fail to operate at these low speeds.

The objective of this experiment is to determine the displacement of the point A. The time step Δt between each frame is 0.52ms. During this time interval, the point A typically displaces by only 4-8mm. Therefore, it is assumed that, during the time interval Δt, the motion of the point A can be considered to be linear. The displacement of A during this time interval $\Delta\delta_A$ is defined using,

$$\Delta\delta_A = \sqrt{(y_{t+\Delta t} - y_t)^2 + (x_{t+\Delta t} - x_t)^2} \qquad [10.6]$$

The displacement of A can be determined for each time interval, to obtain the motion of this point.

10.6.4 Determining the parameters required by the model

In this section, an *ITF Carbon Fibre* tennis racket strung at 60lbs was used. This is the same racket as that used in section 10.5, and therefore the *Racket Impact* software already contains the parameters required to determine the model solution. For simplicity, in this section it is to be assumed that the stringbed stiffness is uniform along the longitudinal axis, as was done in section 10.5.

The *Racket Impact* software was used to determine the displacement of the point on the beam which is analogous to the tip of the racket. The model beam displacement at this point can not be determined directly because the point A does not coincide with the centre of one of the beam segments. However, a linear extrapolation method can be used to estimate the beam displacement δ_A. The *Racket Impact* software splits the beam into 51 segments, and it is assumed that the displacement of x_A can be calculated using,

$$\delta_A = x_{51} + \left(\frac{x_{51} - x_{50}}{2}\right) \qquad [10.7]$$

where x_{51} and x_{50} are the displacements of the two segments at the tip end of the beam; both these parameters being calculated by the model.

In the following section, the experimentally determined values of x_A are compared with those calculated by the model.

10.6.5 Results and Discussion

(a) Racket displacement

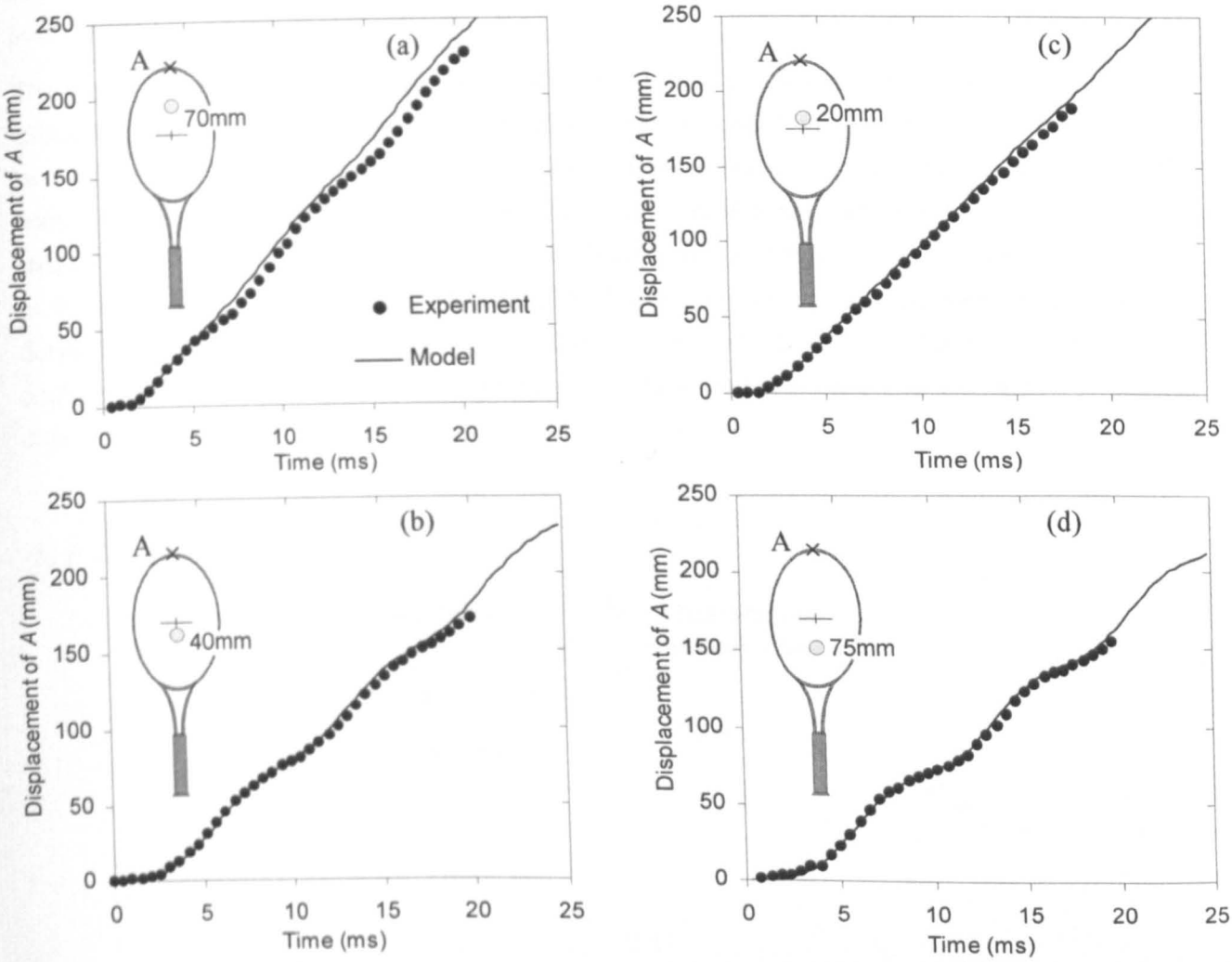

Figure 10.28 The displacement of the tip (point *A*) of the racket/beam for a range of impact locations; the locations are referenced to the geometric string centre. Data is presented for both the experiment and model. In each figure, the nominal ball impact velocity was 20m/s.

Figure 10.28 shows the displacement δ_A of the tip of the racket/beam (point *A* in Figure 10.27), for a range of impact locations. The impact location is given in each figure and is referenced to the geometric string centre (*GSC*) of the *ITF Carbon Fibre* tennis racket. In each figure, the experimentally measured displacement is compared with that determined by the model. Further comparisons are given in Appendix E.4.

Figure 10.28 and Figure E.5 show that the model and experimental results exhibit a very high correlation, for impacts located close to, or below, the *GSC*. The magnitude, phase and frequency of the oscillations are very similar for both sets of data, for the short time period sampled here.

It is generally found that, for impacts towards the tip (Figure 10.28(a) and Figure E.6(a)), the model calculates a larger displacement than that which was measured experimentally. However, it should be noted that the maximum difference in the two sets of data is less than 5%. Differentiating this data, with respect to time, reveals that the racket rebound velocity measured experimentally is

higher than that calculated by the model. It is interesting to note that this corresponds with the data presented in section 10.4. In that section, the racket rebound velocity that was measured experimentally was consistently larger than that which was determined using the *Racket Impact* software.

The experimental data in Figure 10.28(a) and Figure E.6(a) implies that a significant oscillation is excited in the beam, whereas the model calculates a much smaller oscillation. The difference in the two sets of data may be due to the simplification of the method in which the stringbed loads the frame. In a tennis racket, this mechanism involves a complex interaction between the individual strings which will act to disperse the load to each point on the frame, in a time-dependent system. In the model, this mechanism has been simplified and the form of the load distribution has been defined using an arbitrary function. The method in which the load is applied to the model beam could be modified in an attempt to improve the correlation between the model and experimental data. However, this is beyond the scope of this current project.

(b) Ball rebound velocity

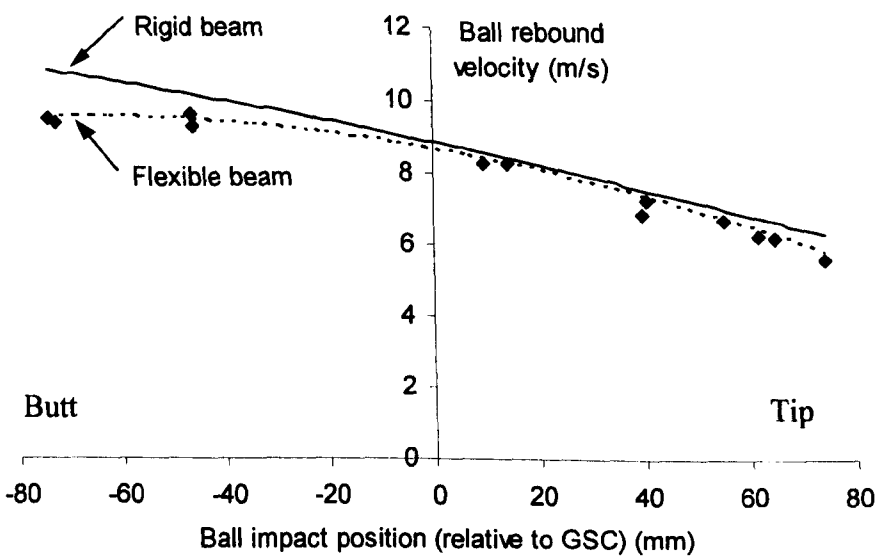

Figure 10.29 Comparison of ball rebound velocity calculated by the experiment and model (rigid and flexible beam), for different impact locations. The data points refer to the experimental data, and the curves represent the data for the two different model beams.

The main objective of this section involves the comparison of the experimentally measured displacement of the racket with that which is calculated by the model, as has been discussed above. However, the ball rebound velocity was also measured in this experiment. The *Racket Impact* software was used to determine the ball rebound velocity for the modelled impacts. Two different model solutions were obtained which assumed either a rigid beam or a flexible beam to simulate the tennis racket. The results for the experiment and the two model solutions are shown in Figure 10.29. this figure shows the model which uses a flexible beam exhibits a very high correlation with the experimental data. The rigid beam model exhibits a very good correlation with the experimental data for impacts which are located between 10 and 30mm from the geometrical string centre, towards the tip. This location coincides with the node point for the fundamental mode and

therefore the model solutions for the rigid beam and flexible beam are very similar, as discussed in section 10.2.

The data in Figure 10.29 offers further evidence to support the high correlation between the flexible beam model and the experimental data. It also illustrates that the inherent weakness of using a rigid beam model to simulate an impact between a tennis ball and racket. Clearly, a rigid beam is not capable of simulating the free vibrations which are plotted in Figure 10.28. The energy stored in these oscillations leads to a reduction in the ball rebound velocity, which is not seen in the model that uses a rigid beam to simulate the racket.

10.6.6 Summary

In this short section, the motion of the tip of the racket has been sampled experimentally, for the period during and after an impact between a ball and racket. The *Racket Impact* software was used to calculate the displacement of the tip, using the assumption that the racket was a flexible beam. A very high correlation was found between the experimental data and the model data, for the majority of impact locations. This comparison supports the assumption that the model predicts the vibration of the tennis racket for an impact between the ball and racket.

The ball rebound velocity was also measured/calculated in this section and a high correlation was found between the experimental data and the model data calculated using the flexible beam, for all impact locations.

10.7 Summary

In this section, a range of different experiments were performed to measure several parameters before, during and after an impact between a ball and freely suspended tennis racket. This measured data was compared with equivalent model data that was calculated using the *Racket Impact* software. This software calculates two different model solutions obtained using two different assumptions regarding the simulation of the tennis racket. The tennis racket is either assumed to be a rigid beam or a flexible beam.

In the first experiment, tennis balls were projected at three different locations on the longitudinal axis of five different tennis rackets. The inbound and rebound velocity of the ball was measured and compared with the two model solutions calculated by the *Racket Impact* software. It was found that the flexible beam model data exhibited a very high correlation with the experimentally obtained ball rebound velocity. However, the rigid beam model generally calculated a ball rebound velocity which was higher than the experimentally obtained data.

In the second experiment, a high speed video system was used to measure the displacement of the ball, stringbed and racket frame during an impact between the ball and racket. In this section, only the model solution for the flexible beam was calculated using the *Racket Impact* software. It was shown that the two sets of data correlate very closely, for all impact velocities. This comparison was made for two different ball types and two different string tensions. Any differences between

the model and experimental data were assigned to the estimated uncertainty in the experimental data and the fact that the complex interaction between the ball, stringbed and racket frame is being simulated using a much simpler model.

In the third experiment, the rebound velocity of the ball and racket was measured, for an impact between a ball and freely suspended racket. This data was compared with the model solution calculated by the *Racket Impact* software (using the flexible beam). A range of ball impact velocities were tested and the ball was propelled at four different locations on the longitudinal axis of the racket. Two different tennis rackets were used which were strung at different tensions. It was found that the model and experiment data exhibited a very high correlation for both the ball and racket rebound velocity. The maximum difference between the two sets of data was approximately 5%.

In the fourth experiment, the transverse frame vibrations were measured which were induced when the ball impacting on the racket. The collected data was used to determine the impact location which corresponded with the minimum amplitude of vibrations for the fundamental mode. This point coincided very closely with that measured for impacts using a soft hammer. It also corresponded very closely with the impact location which induced minimum vibrations of the model beam, as calculated by the *Racket Impact* software.

In the fifth experiment, the motion of the racket tip was sampled for the period during, and after, an impact between a ball and racket. The *Racket Impact* software was used to calculate the displacement of the tip, using the assumption that the racket was a flexible beam. A very high correlation was found between the experimental and model data, for the majority of impact locations. The ball rebound velocity was also measured/calculated in this experiment and a high correlation was found between the experimental and model data calculated using the flexible beam, for all impact locations.

The data collected in this chapter has shown that the *Racket Impact* software is a useful tool for the simulation of an impact between a ball and freely suspended tennis racket. It can be used to calculate the motion of the ball, stringbed and racket during, and after, the impact. The *Racket Impact* software calculates two different model solutions based on two different assumptions regarding the modelling of the tennis racket; these being either a rigid or flexible beam. The data collected in this chapter has highlighted the inherent weakness involved when using a rigid beam model to simulate an impact between a tennis ball and racket. Furthermore, it has been shown that the flexible beam solution correlates very closely with the experimental data. A succinct illustration of this correlation is given in Figures 10.28 and 10.29.

11. Conclusions

11.1 Introduction

In the first part of this chapter, a summary of the important findings which have been obtained in this study is given. This is intended to give the reader an overview of the investigation which culminated in an experimentally verified model of a ball impacting on a tennis racket being derived. This investigation was initially focussed on the static and dynamic properties a tennis ball. This was followed by an investigation of the physical properties of a stringbed, and the dynamic interaction between the ball and stringbed. Finally, a model of a tennis racket frame was developed which was used in a model of a ball impacting on the racket.

This chapter also contains a short section which highlights the conclusions which have been obtained from this work. Finally, suggestions of possible future directions of this study are presented.

11.2 Summary of study

11.2.1 Ball structural stiffness

The structural stiffness of four different tennis balls, which covered the range of balls used in the game of tennis, has been experimentally obtained. It was found that the *Pressurised* and *Oversize* balls have the highest structural stiffness, when compressed quasi-statically between two flat plates. The *Pressureless* ball has a similar stiffness to these two balls for small deformations, but a much lower stiffness at high deformations. Furthermore, at these high deformations it had a similar stiffness to a *Punctured* ball. In this part of the study it was found that the relative structural stiffness of the ball types are not constant for all magnitudes of ball deformation.

11.2.2 Ball impact on a rigid surface

(a) Experimental investigation

Tennis balls were propelled at a rigid force platform and several parameters were measured. It was found that the *Oversize* and *Pressurised* balls rebounded with approximately the same velocity. The *Pressureless* ball rebounded slightly slower, and the *Punctured* ball rebounded significantly slower. This showed that the *Oversize* and *Pressurised* balls exhibit the lowest hysteresis loss during impact.

The force platform was used to determine the dynamic response of the balls for an impact with a rigid surface. It was found that the *Pressurised* and *Oversize* balls exhibited similar dynamic responses for all impact velocities which were tested. The *Pressureless* and *Punctured* balls exhibited similar dynamic responses for high impact velocities.

(b) Theoretical modelling

A simple one degree-of-freedom visco-elastic model of a normal impact between a tennis ball and rigid surface was developed in this study. The model contains three components that correspond to the force contributions made by, (1) the structural stiffness, (2) the material damping and (3) the momentum flux. A set of parameters were determined empirically for each ball type, and these parameters were independent of the ball impact velocity.

This visco-elastic model supersedes previously published models because it includes a component which simulates the force which acts on the ball due to the momentum flux. The momentum flux force corresponds to the change in momentum for the section of the deformed ball which is being flattened upon impact with the surface. This force is distinct to that which is associated with the structural stiffness of the ball, and only acts during the compression phase.

The model can be used to increase the understanding of the dynamic behaviour of tennis balls and interpret the experimental *Force-Time* plots for the four ball types. The differences (and similarities) between the four ball types was qualitatively accounted for using the model.

11.2.3 Ball impact on a head clamped tennis racket

(a) Experimental investigation

Experiments were performed in which a tennis ball was propelled at a head clamped tennis racket. In these tests, the coefficient of restitution was measured for combinations of two different ball types and two different string tensions. For a specific ball type, it was found that the coefficient of restitution was higher for the racket strung at 40lbs, compared with the racket strung at 70lbs.

The magnitude of the maximum ball and stringbed deformation, during impact, was measured using high speed cinematography. The maximum stringbed deformation, during impact, was a function of the string tension, as expected. However, the magnitude of this stringbed deformation was very similar for both the *Pressurised* and *Pressureless* ball types.

It was found that the contact time of the impact was a function of the string tension; the contact time being defined as the time taken for the ball to regain its original shape. The contact times for the impacts on the racket strung at 40lbs were approximately 0.4ms longer than those measured for the racket strung at 70lbs. It is well-documented that there is a qualitative relationship between contact time and string tension. However, this study is an advancement of the published work because it quantifies the relationship.

(b) Theoretical modelling

The impact between a ball and head clamped tennis racket was modelled using a two degree-of-freedom visco-elastic model. The ball component of the model was identical to that derived for a model of a ball impact on a rigid surface. The stringbed component was assumed to have the same stiffness as that which was measured experimentally for a quasi-statically applied load. A small

damping factor was incorporated into the stringbed model to account for the low level of hysteresis loss in the system.

The model was used to determine the ball rebound velocity, and the magnitude of both the ball centre-of-mass and stringbed displacement during impact. This data was compared with that which had been obtained experimentally. Using these comparisons it was found that the accuracy of the model would be improved by increasing the model ball stiffness k_B. The justification for such an increase was based on observations of the shape of the ball surface that was in contact with the stringbed. It was concluded that the stringbed acted to 'cradle' the ball wall, inhibiting the onset of buckling which is known to reduce the structural stiffness during an impact with a rigid surface. Therefore the stiffness of the ball will be higher for an impact with a stringbed, compared to a similar impact with a rigid surface.

It was concluded that the ball stiffness should be increased and it was found that this modification resulted in a very high correlation being achieved between the model and experiment data. For example, the values of the stringbed and ball COM displacement which were calculated by the model correlated to within approximately 2mm of those values measured experimentally. This small difference was accounted for by the inherent weakness of a simple two degree-of-freedom model being used to simulate a complex system that involves the interaction of two highly deformable objects.

It is not claimed that this visco-elastic model of a ball impacting on a head clamped racket perfectly represents the physical impact mechanism. However, the contact time, ball centre-of-mass displacement, stringbed displacement, and ball rebound velocity which are calculated by the model correlate very closely with the experimentally measured data. Therefore, the calculated force which is exerted on the ball during impact should be of a similar magnitude as that which actually occurs in the impact. This model can also be used to predict the differences in the dynamic response of different ball types and string tensions.

11.2.4 Ball impact on a freely suspended tennis racket

The final stage of this study involved the experimental investigation and theoretical modelling of an impact between a tennis ball and freely suspended tennis racket. This study was only conducted for balls which impact on the longitudinal axis of the racket and previous research has verified that a freely supported racket is equivalent to a player's grip, for these kind of impacts.

(a) Theoretical modelling

Two different models of a ball impact on a freely suspended tennis racket have been developed in this study. In both models, the ball and stringbed are simulated using the same visco-elastic model which was developed to simulate a ball impacting on a head clamped tennis racket. In the first model, the racket was simulated using a rigid beam. This beam was assigned the same inertial

properties (mass, balance point and moment of inertia) as the racket. In this model, a point loading was applied to the beam by the visco-elastic model of the ball/stringbed system.

In the second model, the racket was modelled as a one dimensional flexible beam. A numerical solution was derived for the displacement of a beam which was subjected to a time-dependent loading. In this solution, it was assumed that the beam had a uniform flexural rigidity but a non-uniform mass distribution. This beam was assigned the same inertial properties and fundamental frequency as the racket which was being modelled. In this model, a distributed loading was applied to the beam by the visco-elastic model of the ball/stringbed system. This type of loading was used to simulate the mechanism in which the stringbed applies the load to the racket frame. Using this loading method, it was found that the impact point which excited minimum vibrations of the model beam correlated very closely with the stringbed node on a tennis racket. This comparison was conducted for several different rackets.

The advantage of the first, simpler model, in which the racket is simulated as a rigid beam, is that it requires a minimal number of calculations to be performed to obtain the model solution. The inherent weakness of this model is the inability of the beam to model the deformation which a tennis racket is subjected to during, and after, impact. The second, more advanced model, in which the racket is simulated as a flexible beam, involves more than six million calculations being performed to obtain the model solution. These calculations require a significant amount of numerical processing time to be solved.

There are many commercially available PC software packages that are capable of efficiently performing the required calculations in order to obtain the two model solutions. A supplementary requirement of this software is that the graphical interface must be user-friendly so that a trained operator can calculate the two model solutions without possessing the knowledge required to derive the models. The desired software would have a facility for the different ball types, stringbed stiffnesses and racket types to be entered into the two models, along with the initial velocity of the ball and racket. The program must then be capable of solving the numerous model equations and deliver the model solution in a suitable format. It was concluded that the required software needed to be written specifically for this application. This software was written in *MS Visual Basic v6* and is called *Racket Impact*. This software can be used on any *MS Windows* operating system.

(b) Experimental investigation

An experimental investigation was performed to measure several parameters during, and after, an impact between a ball and freely suspended tennis racket.

Tennis balls were projected at several locations on the longitudinal axis of five different tennis rackets. The inbound and rebound velocities of the ball were measured and compared with the two model solutions calculated by the *Racket Impact* software. It was found that the more advanced, flexible beam model data exhibited a very high correlation with the experimentally obtained ball rebound velocity. However, the simpler, rigid beam model generally calculated a ball rebound velocity which was higher than that measured experimentally.

High speed cinematography was used to measure the displacement of the ball, stringbed and racket frame during impact. Equivalent data was calculated using the model and it was found that the two sets of data correlated very closely. This comparison was made for two different ball types and two different string tensions, which cover the range typically used in the game of tennis.

High speed cinematography was used to measure the rebound velocity of the racket, for an impact between a ball and a freely suspended racket. A range of ball impact velocities were tested and the ball was propelled at four different locations on the longitudinal axis of two different rackets. This data was compared with the flexible beam model solution calculated by the *Racket Impact* software. It was found that the model and experiment data exhibited a very high correlation for the racket rebound velocity, with maximum differences between the two sets of data of approximately 5%.

High speed cinematography was used to sample the motion of the racket tip for the period during, and after, an impact between a ball and freely suspended racket. The *Racket Impact* software was used to calculate the displacement of the tip, using the assumption that the racket was a flexible beam. A very high correlation was found between the experimental and model data, for the majority of impact locations.

(c) Application of software

The data calculated by the *Racket Impact* software has been verified by experimental investigation, as explained above. The software is a useful tool for simulating an impact between a ball and freely suspended tennis racket. The software can be used to calculate the motion of the ball, stringbed and racket during, and after, the impact. The user has the ability to adjust many parameters related to the impact including, (1) impact location on the racket, (2) racket stiffness and (3) initial velocity of the racket. This data can be used to assess the influence that these parameters have on the ball rebound velocity. This software will be a useful tool for manufacturers of tennis equipment because it allows them to predict the effect of a change in design, without requiring to build a prototype. It is of even more use to the governing body of tennis because they do not have the facilities to build a prototype, but can use the software to simulate the impact.

11.3 Conclusions

- *Pressurised* and *Oversize* balls have similar physical properties for both quasi-static compressions and dynamic impacts.
- A visco-elastic model is capable of accurately simulating the impact between a tennis ball and rigid surface. The differences (and similarities) between the four ball types tested in this study was qualitatively accounted for using the model.
- A stringbed which is strung at 40lbs deforms approximately 25% more than that which was strung at 70lbs, during an impact with a tennis ball. However, the magnitude of stringbed deformation was not a function of the ball type.

  A rigid beam is not capable of simulating the experimentally measured oscillations which a tennis racket is subjected to during, and after, the impact. Consequently, the model which uses a rigid beam to simulate the racket calculates a ball rebound velocity which is significantly higher than that measured experimentally.

  The model solution which uses a flexible beam to simulate a tennis racket accurately simulates the experimentally measured oscillations of a tennis racket. Furthermore, the model can be used accurately the predict the velocity of the ball and racket, during and after the impact.

11.4 Future research

This study has culminated in a model of a ball impacting on a freely suspended tennis racket being developed. The solution to this model is calculated using the *Racket Impact* software. In this study, experimental investigations have been performed in conjunction with this theoretical modelling to ensure that the final model is valid for the impacts which it is used to simulate. However, the *Racket Impact* software has only been developed to model specific types of impact and therefore can not be used to simulate all shots that are typical in the game of tennis. It would be interesting to extend this work so that the *Racket Solver* software is valid for other types of impact.

(a) Development of the Racket Solver software for other impact locations

The *Racket Solver* software has only been developed to model impacts which land on the longitudinal (main) axis of the tennis racket. In this model, the racket is freely supported because other researchers have verified that this is equivalent to a player gripping the racket, for the duration of impact. However, this assumption is only valid for impacts on the longitudinal axis, and has not been verified for impacts which are eccentric to this axis.

In a game of tennis, the ball can impact on any position on the racket stringbed. The logical development of the model would be to enable impacts which are eccentric to the longitudinal axis to be simulated. Firstly, this would require an experimental investigation of the grip forces that a player exerts onto the racket, during an eccentric impact. The findings of this study will initially be used to determine whether these forces are significant or not. Furthermore, the data will be used to establish a suitable method for simulating a player's grip in the model. This study could be expanded to investigate possible techniques for simulating a player's grip in a laboratory experiment. This would be a useful investigation as it would allow experimental investigations of the player/racket interaction to be conducted in controlled conditions.

(b) Development of the Racket Solver software for impacts in which the ball has initial spin

In this study, the ball was propelled at the racket using an air cannon which delivered the ball consistently at the desired location. However, the main limitation with this type of equipment is that it can not apply spin to the ball and therefore all the experiments conducted in this study involved impacts with zero initial spin.

In the game of tennis, the ball is generally spinning prior to the impact with a tennis racket. Clearly, an important advancement of this study would involve developing the *Racket Solver* software so that it is capable of modelling an impact in which the ball is initially spinning. In order for this software to be validated, an experimental investigation of the equivalent impact must be conducted. This would require a method of propelling the ball, with initial spin, consistently at the desired impact location on the tennis racket. There are currently a number of ball propulsion devices which are capable of applying spin to the ball but initial testing has shown that they do not

propel the ball with sufficient accuracy to be used in this type of experiment. However, it may be possible to develop this apparatus so that it is suitable for the required experiment.

(c) Player testing

One of the uses of the final model which has been developed in this study is to determine the ball rebound velocity for a specified ground stroke or serve. In this simulation, the velocity of the ball and racket must be entered into the *Racket Impact* software. If the example of a serve is considered then, it can be assumed that the ball is stationary, prior to impact, and that the racket is swung with a velocity of 36 m/s (80 mph). The *Racket Impact* software can be used to predict the ball service velocity for any racket in the database. This is a useful exercise as it could be used to give an indication of the 'power' of a tennis racket. However, this analysis is based on a player being able to swing all tennis rackets at the same velocity, which is unlikely to be a realistic assumption. An interesting advancement of this work would involve an investigation of the relationship between racket head speed and racket inertia, for a sample group of tennis players. This study would involve the measurement of the racket head speed, immediately prior to impact, for a range of rackets with different inertias (mass and swingweight). This investigation would need to be performed separately for serves and ground strokes as these two shots involve different techniques. The results of this player testing would become an integral part of the *Racket Impact* software. A study of this nature would further enhance the value of this software as a tool for predicting the dynamic performance of a tennis racket.

References

Babolat (2002) www.babolat.com.

Baker, J.A. & Putnam, C.A. (1979) Tennis racket and ball responses during impact under clamped and freestanding conditions, *Research Quarterly in Exercise Sport*, **50(2)**, 164-170.

Brannigan, M. & Adali, S. (1981) Mathematical Modelling and simulation of a tennis racket, *Medicine & Science in Sport & Exercise*, **13**, 44-53.

Brody, H. (1979) Physics of the tennis racket, *American Journal of Physics*, **47(6)**, 482-487.

Brody, H. (1981) Physics of the tennis racket II : the 'sweet spot, *American Journal of Physics*, **49(9)**, 816-819.

Brody, H. (1984) That's how the ball bounces, *The Physics Teacher*, 494-497.

Brody, H. (1985) The moment of inertia of a tennis racket, *The Physics Teacher*, **5**, 213-216.

Brody, H. (1987) Models of tennis racket impacts, *International Journal of sport Biomechanics*, **3**, 293-296.

Brody, H. (1993) Speed of strokes, *TennisPro*, May/June edition.

Brody, H. (1995) How Would a Physicist Design a Tennis Racket, *Physics Today*, **48**, 26-31.

Brody, H. (1997) The physics of tennis. III. The ball-racket interaction, *American Journal of Physics*, **65(10)**, 981-987.

Brody, H. (2000) A limit on spin, *International Tennis Federation Technical Commission meeting*, Brussels.

Broer, M.R. (1973) *Efficiency of Human Movement*. W.B. Saunders, London, p 245.

Calder, C.A., Holmes, J.G. & Mastry, L.L. (1987) Static and Dynamic Characteristics of Tennis String Performance, *Progs 1987 Sem Conference on Experimental Mechanics, Houston, Bethel Ct. Society of Experimental Mechanics*, pp 613-616.

Carré, M.J. (2000) *The dynamics of cricket ball impacts and the effect of pitch construction*. PhD thesis, University of Sheffield.

Casolo, F. and Ruggieri, G. (1991) Dynamic analysis of the ball-racket impact in the game of tennis. *Meccanica*, **26**, 67-73.

Chadwick, S.G. (2002) *The aerodynamics of tennis balls*. PhD thesis, University of Sheffield.

Coe, A. (2000) The balance between technology and tradition in tennis. In: *Tennis Science and Technology*, London, pp 3-40, (Blackwell Science Ltd, Oxford.).

Cross, R. (1997) The dead spot of a tennis racket, *American Journal of Physics*, **65(8)**, 754-764.

Cross, R. (1998) The sweet spots of a tennis racquet, *Sports Engineering*, **1(2)**, 63-78.

Cross, R. (1999a) Dynamic properties of tennis balls, *Sports Engineering* **2(1)** 23-33.

Cross, R. (1999b) The bounce of a ball, *American Journal of Physics*, **67(3)**, 222-227.

Cross, R. (1999c) Impact of a ball with a bat or racket, *American Journal of Physics,* **67(8)**, 692-702.

Cross, R. (2000a) Dynamic testing of tennis balls. In: *Tennis Science and Technology*, London, pp 175-182, (Blackwell Science Ltd, Oxford.).

Cross, R. (2000b) Physical properties of tennis strings. In: *The Engineering of Sport*, Sydney, pp 213-220, (Blackwell Science Ltd, Oxford.).

Cross, R. (2000c) Dynamic properties of tennis strings. In: *Tennis Science and Technology*, London, pp 119-126, (Blackwell Science Ltd, Oxford.).

Cross, R. (2000d) Effects of friction between the ball and strings in tennis, *Sports Engineering*, **3(2)**, 85-97.

Cross, R. (2000e) The coefficient of restitution for collisions of happy balls, unhappy balls, and tennis balls, *American Journal of Physics*, **68(11)**, 1025-1031.

Cross, R (2000f) Flexible beam analysis of the effects of string tension and frame stiffness on racket performance, *Sports Engineering*, **3**, 111-122.

Cross, R. (2001a) Measurements of string tension in a tennis racket, *Sports Engineering*, **4(3)**, 165-175.

Cross, R. (2001b) Customising a tennis racket, *Sports Engineering*, **4(1)**, 1-14.

Cross, R. (2001c) Why bows get stiffer and racquets get softer when the strings are added, *American Journal of Physics,* **69(8)**, 907-910.

Cross, R. (2002a) Measurements of the horizontal coefficient of restitution for a superball and a tennis ball, *American Journal of Physics*, **70(5)**, 482-489.

Cross, R. (2002b) Optimising the Performance of a Tennis Racket, In press, *Sports Engineering.*

Cross, R., Lindsey C. & Andruczyk D. (2000b) Laboratory testing of tennis strings, *Sports Engineering*, **3(4)**, 219-230.

Daish, C.B. (1972) *The Physics of Ball Games.* English Universities Press, London.

Dignall, R.J. (1999) *The dynamics of tennis ball impacts.* M.Phil transfer report, University of Sheffield.

Dignall, R.J., Haake, S.J. & Chadwick, S.G. (2000a), Modelling of an oblique tennis ball impact on a court surface. In: *The Engineering of Sport*, Sydney, pp 185-192, (Blackwell Science Ltd, Oxford.).

Dignall, R.J., & Haake, S.J. (2000b), Analytical modelling of the impact of tennis balls on court surfaces. In: *Tennis Science and Technology*, London, pp 155-162, (Blackwell Science Ltd, Oxford.).

Efunda (2002) http://www.efunda.com/home.cfm

Elliott, B., Blanksby, B. & Ellis, R. (1980) Vibration and Rebound Velocity Characteristics of Conventional and Oversize Tennis rackets, *Research Quarterly for Exercise Sport*, **51**, 608-615.

Elliott, B.C. (1982) Tennis: the influence of grip tightness on reaction impulse and rebound velocity, *Medicine and science in sports and exercise*, **14(5)**, 348-352.

Elliott, B.C. (1983) Spin and the Power Serve in Tennis, *Journal of Human Movement Studies*, **9(2)**, 97-103.

Elliott, B.C., Marsh, A. & Blanksby, B. (1986) A Three-Dimensional Cinematographic Analysis of the Tennis Serve, *International Journal of Sport Biomechanics*, **2**, 260-271.

Elliott, B.C. (1988) Biomechanics of the Serve in Tennis – A Biomedical Perspective, *Sports Medicine*, **6**, 285-294.

Gobush, W. (1990) Impact force measurements on golf balls, *Golf and Science*, ed. A.J. Cochran, pp219-224.

Goldsmith, W. (1960) *Impact*. Edward Arnold (Publishers), London. pp.22-38.

Goodwill, S.R. (1997) *Dynamic comparison of tennis ball impacts on an artificial surface*. B.Eng Thesis, University of Sheffield.

Goodwill, S.R. & Haake, S.J. (2000) Comparison of standard and oversize tennis balls for normal impacts on a racket. In: *The Engineering of Sport*, Sydney, pp 221-228, (Blackwell Science Ltd, Oxford.).

Goodwill, S.R. and Haake, S.J. (2001) Comparison of flexible and rigid body modelling of a tennis racket. In: *Materials & Science in Sports*, San Diego, California, pp223-236.

Grabiner, M.D., Groppel, J.L. & Campbell, K.R. (1983) Resultant tennis ball velocity as a function of off-centre impact and grip firmness, *Medicine & Science in Sports and Exercise*, **15(6)**, 542-544.

Groppel, J.L. (1975) *A kinematic analysis of Topspin and Backspin techniques in the tennis forehand drive*, Masters thesis. University of Illinois.

Groppel, J.L., Dillman C.J. and Lardner T.J. (1983) Derivation and validation of equations of motion to predict ball spin upon impact in tennis, *Journal of Sports Sciences*, **1**, 111-120.

Groppel, J.L, Shin, I.S., Spotts, J., & Hill, B. (1987a) Effects of Different String Tension Patterns and Racket Motion on Tennis Racket-Ball Impact, *Int. Journal of Sport Biomechanics*, **3**, 142-158.

Groppel, J.L. Shin, I.S, Thomas, J.A., & Welk (1987b) The effects of string type and tension on impact in midsized and oversized tennis racquets, *International Journal of Sport Biomechanics*, **3(1)**, 40-46.

Guinness (2000) *Guinness World Records, Millennium Edition*. Guinness World Records Ltd, Bantam, London, UK.

Haake, S.J. (1989) *Apparatus and test methods for measuring the impact of golf balls on turf and their application in the field*. PhD thesis, University of Aston in Birmingham.

Haake, S.J., Chadwick, S.G., Dignall, R.J., Goodwill, S.R. & Rose P. (2000) Engineering tennis – slowing the game down, *Sports Engineering*, **3(2)**, 131-143.

Hatze, H. (1976) Forces and duration of impact and grip tightness during the tennis stroke, *Medicine and Science in Sports*, **8**, 88-95.

Hatze, H. (1993) The relationship between the coefficient of restitution and energy losses in tennis rackets, *Journal of Applied Biomechanics*, 9, 124-142.

Hatze H. (1994) Impact Probability Distribution, Sweet Spot, and the Concept of an Effective Power Region in Tennis Rackets, *Journal of App. Biomechanics*, **10**, 43-50.

Head, H. (1976) Tennis Racket, *US Patent 3,999,756.*

Hedrick, K., Ramnath, R.V. & Mikic, B. (1979) An authoritative new method of evaluating rackets, *World Tennis*, **27**, 78-81.

Hubbard, M. & Stronge, W.J. (2001) Bounce of hollow balls on flat surfaces, *Sports Engineering*, **4(2)**, 49-61.

International Tennis Federation (2000a) *Rules of Tennis.* Wilton, Wright & Son Limited, London.

International Tennis Federation (2000b) *ITF Approved Tennis Balls.* Wilton, Wright & Son Limited, London.

International Tennis Federation (2001) *ITF Approved Tennis Balls & Classified Court Surfaces.* Wilton, Wright & Son Limited, London.

ICI (1986) Sports racket strings of a synthetic thermoplastic polymeric material, *US Patent 4,586,708*

Johnson, W., Reid, S.W. & Trembaczowski-Ryder, R.E (1972) Impact, rebound and flight of a well-inflated pellicle as exemplified in association football. *The Manchester Association of Engineers*, Session 1972-73, **5**, 1-25.

Johnston, H.F. (2001) *Dynamic characterisation of tennis balls on impact with stringbed.* M.Eng Thesis, University of Sheffield.

Kawazoe, Y., (1993) Coefficient of Restitution between a Ball and a Tennis Racket. *Theoretical & Applied Mechanics*, **42**, 197-208.

Kawazoe, Y. (1997a) Experimental identification of a hand-held tennis racket and prediction of rebound ball velocity in an impact, *Theoretical and Applied mechanics*, **46**, 177-188.

Kawazoe, Y. and Kanda, Y. (1997b) Analysis of Impact Phenomena in a Tennis Ball-Racket System (Effects of Frame Vibrations and Optimum Racket Design), *JSME International Journal*, **40(1)**, 9-16.

King, M. (2000) Three-dimensional Image Analysis, *BASES Biomechanics Workshop*, Loughborough University.

Knudson, D. (1991) Effect of string type and tension on ball vertical angle of rebound in static tennis impacts, *Journal of Human Movement Studies*, **20(1)**, 39-47.

Knudson, D. (1993) Tension and impact on ball rebound accuracy in static tennis impacts, *Journal of Biomechanics*, **9(2)**, 143-148.

Knudson, D. (1997) The effect of string tension on rebound accuracy in tennis impacts, *International Sports Journal*, 108-112.

Kotze, J. (2000) The role of the racket in high-speed tennis serves, *Sports Engineering*, **3(2)**, 67-84.

Koziol, D.L. & Reed, T.F. (1978) Tennis ball, *US Patent 4,098,504.*

Lacoste, F.R (1976) Tennis rackets and similar implements with vibration damper, *US Patent 3,941,380.*

Leigh, D.C. and Lu, W.Y. (1992) Dynamics of the interaction between the Ball, Strings and Racket in Tennis, *Int. Journal of Sport Biomechanics*, **8(3)**.

Lieberman, B.B. (1990) The effect of impact conditions on golf ball spin-rate. In: *Science and Golf: Proceedings of the First World Scientific Congress of Golf* (ed A.J. Cochran), pp. 225-230. E & FN Spon, London.

Lieberman, B.B. & Johnson, S. H. (1994) An analytical model for ball-barrier impact. Part 1: Models for normal impact. In: *Science and Golf II: Proceedings of the World Scientific Congress of Golf* (eds A.J. Cochran & M.R. Farally), pp. 309-314. E & FN Spon, London.

Liu, K.Y. (1983) Mechanical analysis of racket and ball during impact, *Medicine and Science in Sports and Exercise*, **15(5)**, 388-392.

Mish, S.P. & Hubbard, M. (2001) Design of a full degree-of-freedom baseball pitching machine, *Sports Engineering*, **4(3)**, 123-133.

Missavage, R.J., Baker, J.A.W. & Putnam, C.A. (1984) Theoretical modelling of grip firmness during ball-racket impact, *Research Quarterly for exercise and sport*, **55(3)**, 254-260.

Mitchell, S.R., Jones, R. and King, M. (2000) Head speed versus racket inertia in the tennis serve, *Sports Engineering*, **3(2)**, 99-110.

Nathan, A.M. (2000) Dynamics of a baseball-bat collision, *American Journal of Physics*, **68(11)**, 979-990.

Neville, P. (2001) *Dynamic Characterisation of Tennis Balls on Impact with a Solid Surface and their Modelling.* M.Eng Thesis, University of Sheffield.

Penn (2002) www.pennracquet.com/about/how.html

Percival, A.L. (1976) The impact and rebound of a football, *The Manchester Association of Engineers*, Session 1976-77, **5**, 17-28.

Plagenhoef, S. (1970) *Fundamentals of tennis*, Prentice-Hall, Englewood Cliffs, New Jersey

Pratt, G.W. (2000) The interaction of the tennis ball and the court surface. In: *Tennis Science and Technology*, London, pp 163-168, (Blackwell Science Ltd, Oxford.)

Racket Tech (1998) *Tension Contentions*, March **23(3)**.

Racket Tech (2001) *Wimbledon Stringers Journal*, November **26(11)**.

Rao, S.S. (1995) *Mechanical Vibrations*. Addison-Wesley Publishing Company, Reading, Massachusetts.

Reed, T.F. & Thomas G.B. (1988) Know what's inside your tennis ball, *Chemtech*, 48-52.

Rose P., Coe A., & Haake S.J. (2000) The variation of static and dynamic tennis ball properties with temperature, In: *Tennis Science and Technology*, London, pp 49-56, (Blackwell Science Ltd, Oxford.)

Royal and Ancient Golf Club and USGA (2000), *Rules of Golf.* The Programme Publications Group, Liverpool.

Schleihauf, R., Martinez, A., Ahern, G. & Lee, D. (2000) A three dimensional analysis of Flat, Slice and Topspin Serves in Tennis. Internal report.

Shroud, K.A. (1990) *Further Engineering Mathematics.* Macmillan Press Ltd.

Taylor, D. (2002) *The dynamic properties of tennis balls on impact with a racket and their relationship to the subject of 'player feel'.* M.Eng Thesis, University of Sheffield.

Taylor, J.R. (1982) *An Introduction to error analysis.* University Science Books, Oxford University Press.

Thomson, A. (2000) *Dynamic characteristics of tennis Balls and the determination of 'Player Feel'.* M.Eng Thesis, University of Sheffield, pp. 72-80.

Tilmanis (1975) *Advanced tennis for Coaches, Teachers and Players.* Lea Febiger, Philadelphia, Pennsylvania.

Tipton, H. (1955) The Dynamic Tensile Mechanical Properties Of Textile Filaments & Yarns, *Journal of The Textile Institute*, **46**, 322-361.

UC Davis (2001) http://wings.avkids.com/Tennis/Project/motion-02.html

Ujihashi, S. (1994) Measurement of dynamic characteristics of golf balls and identification of their mechanical models. In: *Science and Golf II: Proceedings of the World Scientific Congress of Golf* (eds A.J. Cochran & M.R. Farally), pp. 302-308. E & FN Spon, London.

Van Zandt, L. (1992) The dynamic theory of the baseball bat, *American Journal of Physics*, **60(2)**, 172-181.

Watanabe, T., Ikegami, Y. & Miyashita, M. (1979) Tennis: the effects of grip firmness on ball velocity after impact, **11(4)**, 359-360.

Widing, M.A.B & Moeinzadeh, M.H. (1990) Finite element modelling of a tennis racket with variable string patterns and tensions, *International Journal of Sport Biomechanics*, **6**, 78-91.

Williams, T. (2000) *The dynamic characteristics of impacts between tennis balls and rackets.* M.Eng Thesis, University of Sheffield, pp11-27.

Wilson Sporting Goods Co., (2001) www.wilsonsports.com/tennis/index.asp?content_id=2707

Yoxall, A. (2002) http://www.shef.ac.uk/mecheng/ug/mec209/

A. Statistical analysis methods – least squares regression

A.1 Obtaining the coefficients for a least-square regression

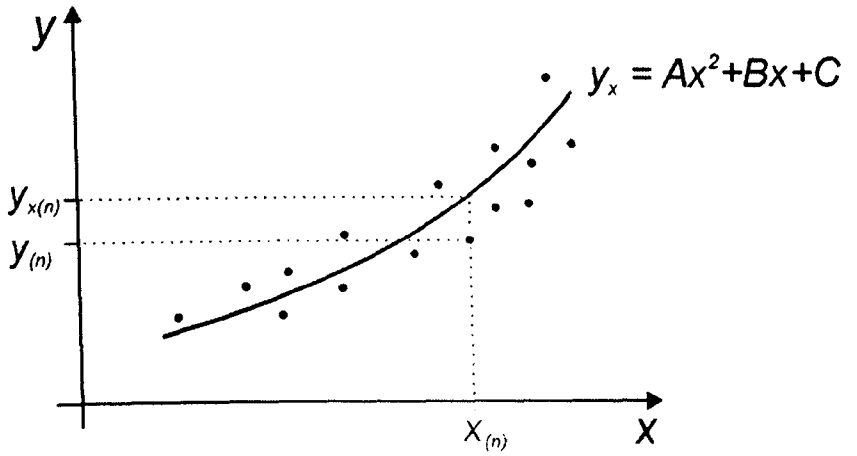

Figure A.1 Second order polynomial plotted through the measured data. The measured and calculated values of the *y-parameter* are shown as $y_{(n)}$ and $y_{x(n)}$ respectively.

There are many examples in this study where a measured quantity is plotted against another variable. It is often useful to be able to plot a best-fit line, or trend line, through this data to define a quantitative relationship between the two variables. This trendline can take one of a variety of forms, for example, linear, polynomial, exponential or logarithmic. An example of a 2nd order polynomial trend line is given in Figure A.1. The analytical method used to find the coefficients A, B and C is called *least-squares regression*. This method is not shown here as it can be found in many text books (Taylor (1982) and Stroud (1990)). The coefficients can be used to define a relationship between the two variables x and y, but do not quantify the quality of the correlation between the measured data and the trend line. The following section concentrates on the calculation of a physically significant parameter that defines the uncertainty of the measured data.

A.1.2 Uncertainty in the measurement of y

This method is an adaptation of that published in Taylor (1982). This method requires a number of assumptions to be made in order to simplify the solution. It is assumed that the uncertainty in the measurement of x is negligible and therefore the only uncertainty that needs to be calculated is that which occurs for y. It is also assumed that the uncertainties in y all have the same magnitude. More specifically, it is assumed that the measurement of y_n is governed by a normal distribution, with the same width parameter for all measurements. This will be valid for most of the experiments in this study, but where it is not valid this error must be noted.

Using the example given in Figure A.1, the value of $y_{x(n)}$ is calculated using,

$$y_{x(n)} = Ax_{(n)}^2 + Bx_{(n)} + C \qquad [A.1]$$

The uncertainty of each y-value can be calculated using,

$$\varepsilon_y = y_{x(n)} - y_n \qquad [A.2]$$

It has been assumed that the measurement of y_n is normally distributed about its calculated value of $y_{x(n)}$ with a common width parameter for the distribution. Therefore, the deviations ε_y are normally distributed, all with the same mean value of zero and the same width parameter. The standard deviation of this normal distribution can be calculated using the standard function *STDEV* in *MS Excel 2000.*

B. Ball properties – Experiment and Model Data

B.1 Introduction

The appendix contains supplementary results which have been referred to in Chapters 4 and 5. The details of the experimental procedures used to obtain this data is given in Chapter 3. There results of the various experiments are generally presented for four ball types; *Pressurised, Pressureless, Oversize* and *Punctured.*

B.2 Quasi-static tests in which the ball was compressed between two rigid plates.

The balls were compressed in a MecMesin test device. The details of this testing are given in section 3.2. Four different ball types were tested and generally four balls of each type were used (only one *Punctured* ball was tested). The results for one ball of each type is given in section 4.3, and the results for the other three balls are given in this section.

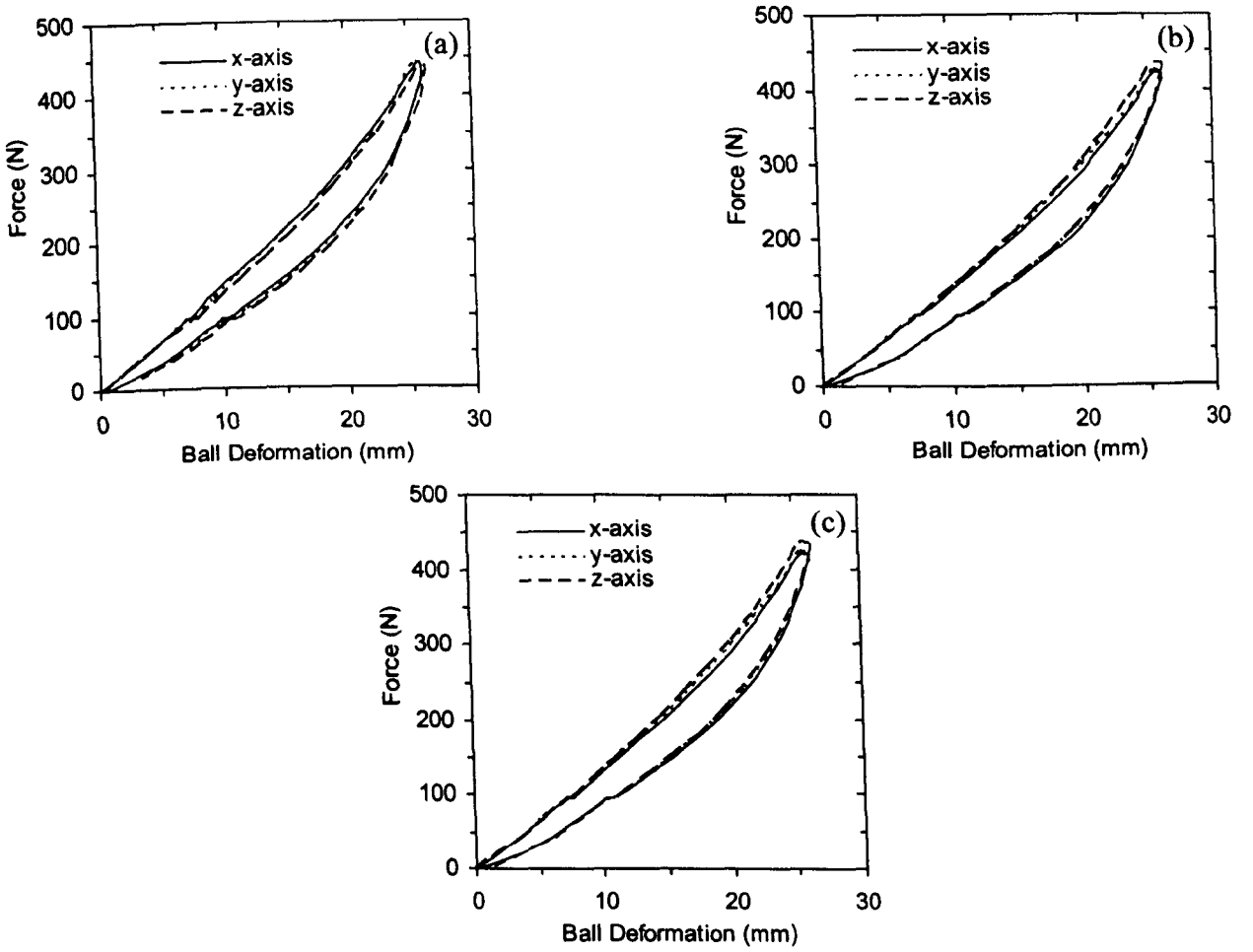

Figure B.1 (a)-(c) *Force-Deformation* results for the individual axes of three *Pressurised* tennis balls.

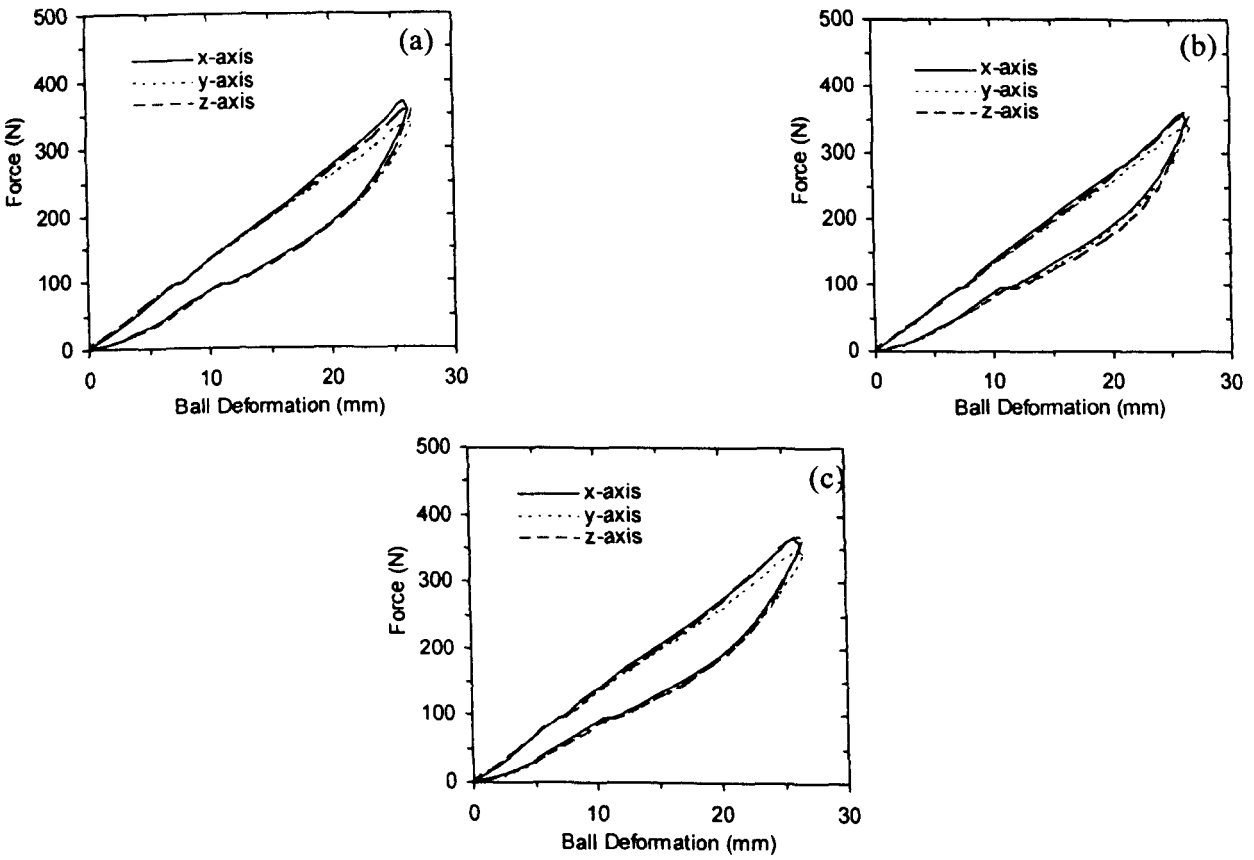

Figure B.2 *Force-Deformation* results for the individual axes of three *Pressureless* tennis balls.

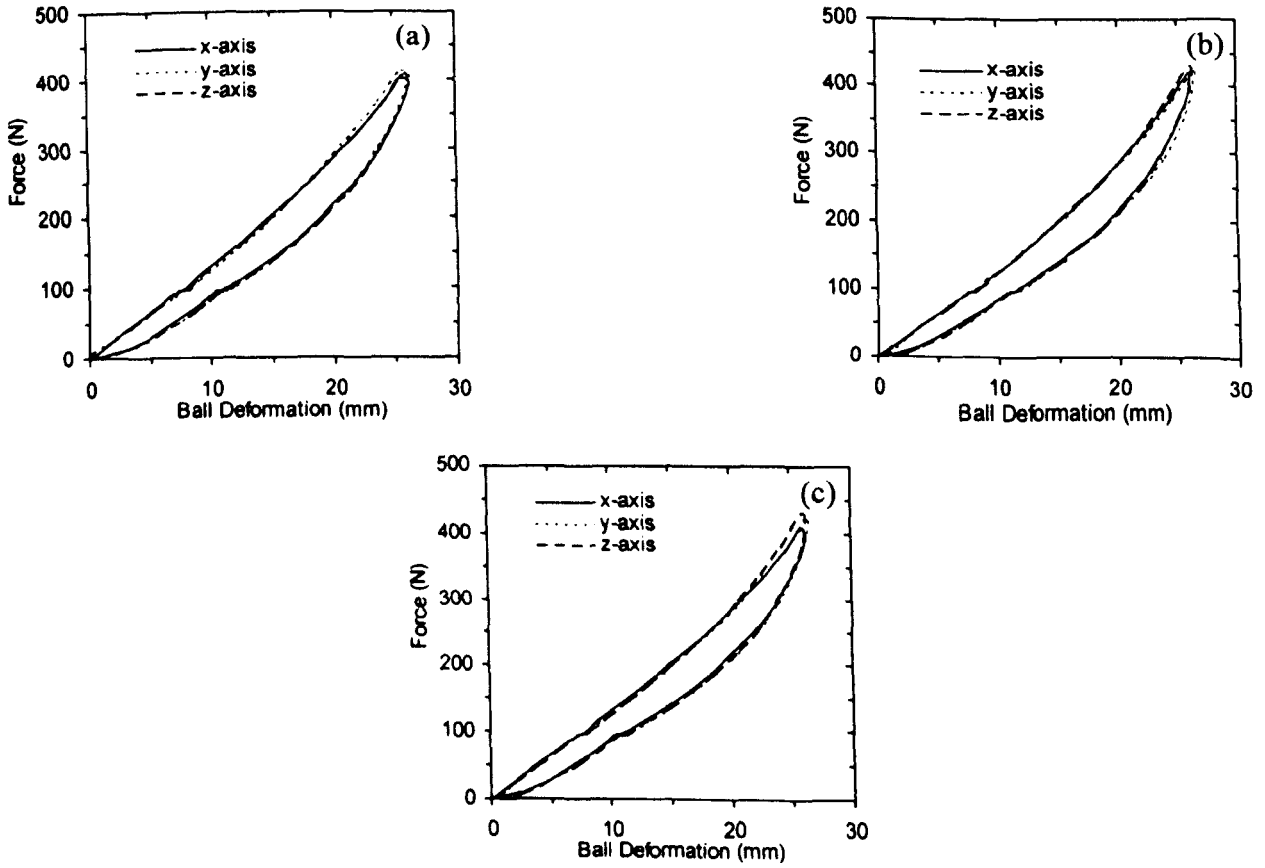

Figure B.3 *Force-Deformation* results for the individual axes of three *Oversize* tennis balls.

B.3 One Degree-of-Freedom Visco-Elastic Model – Constant Parameters

In Chapter 4, a force platform was used to obtain *Force-Time* and *Force-Displacement* plots for a normal impact between a tennis ball and rigid surface. In section 5.3.2 a model was derived to simulate this impact and the accuracy of this model was tested by comparing the model and experiment data. In this visco-elastic model, it was assumed that the stiffness and damping parameters remain constant throughout impact. Figure B.4 shows a comparison of the model and experiment data for a *Pressureless* ball. The data is plotted for two extremes of impact velocity and illustrates the weakness of the model at high impact velocities.

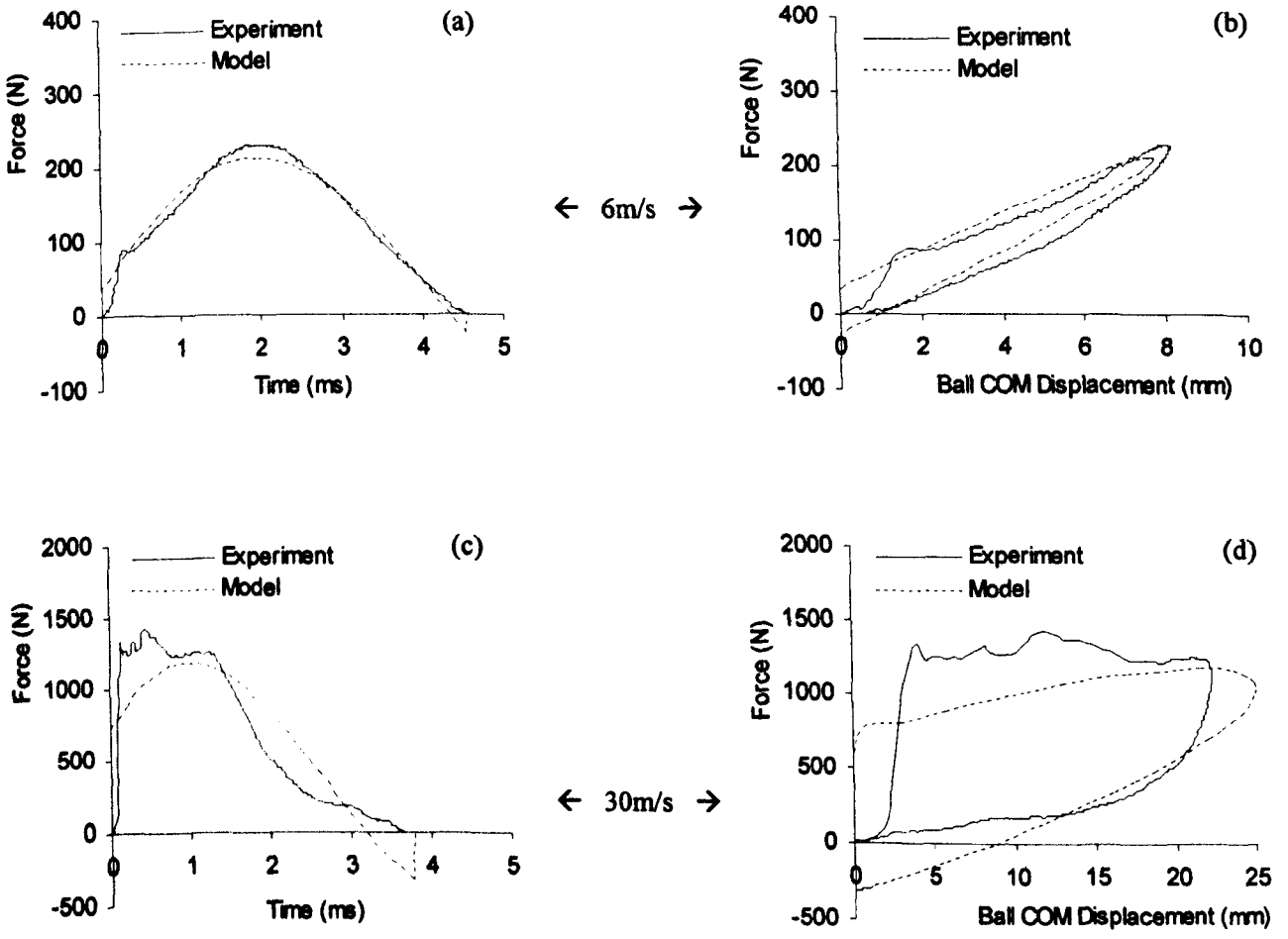

Figure B.4 Comparison of experimental and *constant parameter* model data for a *Pressureless* ball impacting normal to a rigid surface with an impact velocity of (a)-(b) 6m/s and (c)-(d) 30m/s.

B.4 One Degree-of-Freedom Visco-Elastic Model – Variable Parameters.

In section 5.4.2 a model was derived to simulate this impact and the accuracy of this model was tested by comparing the model and experiment data. In this visco-elastic model it was assumed that the stiffness and damping parameters were functions of the ball COM displacement. A comparison between the model and experiment data for a *Pressureless* ball is shown in Figure B.5.

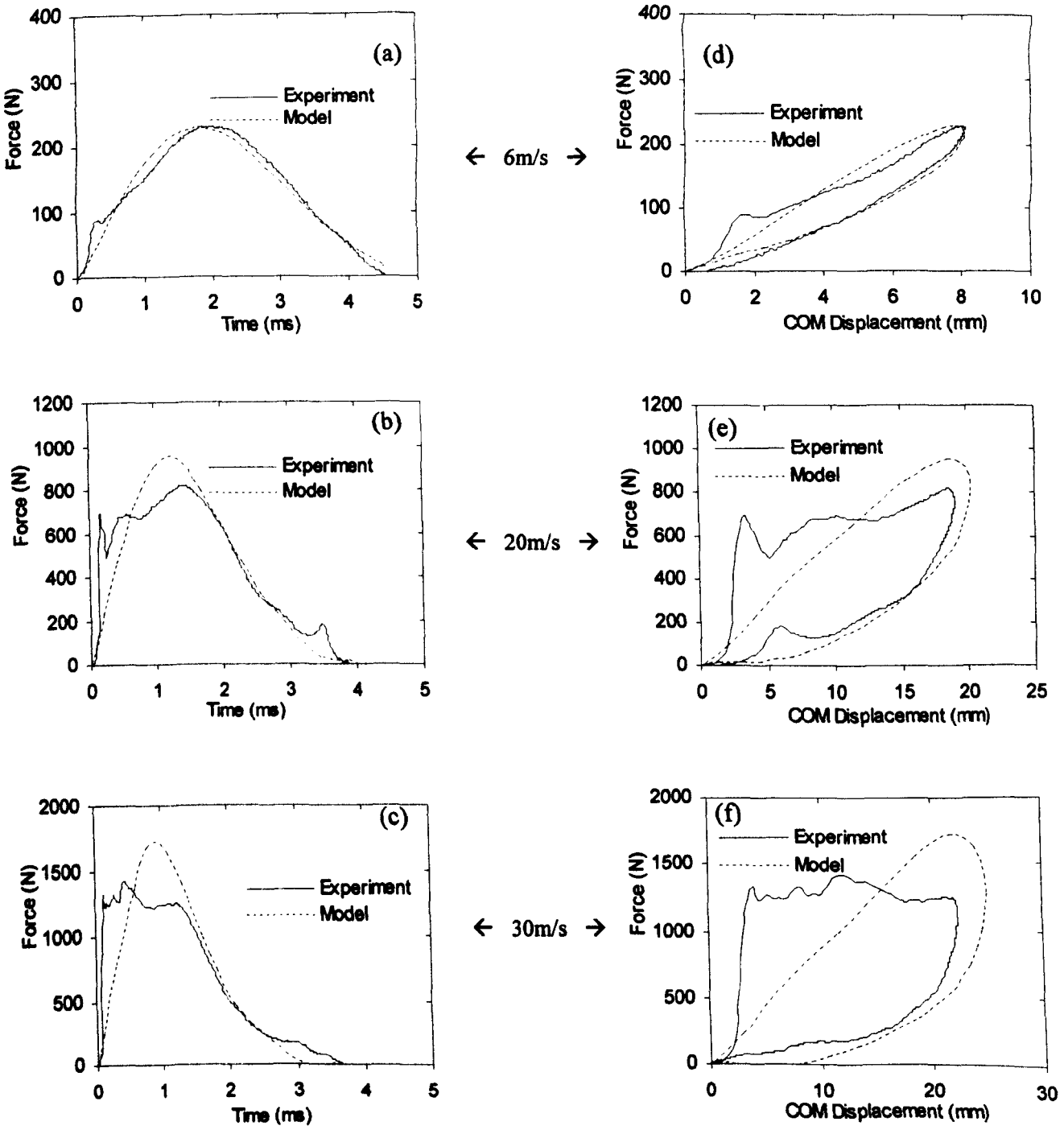

Figure B.5 Comparison of experiment and model data for a *Pressureless* ball impacting on a rigid surface, for a range of impact velocities.

B.5 One Degree-of-Freedom Visco-Elastic – Variable Parameters and Momentum Flux.

In section 5.5.2 a model was derived to simulate this impact and the accuracy of this model was tested by comparing the model and experiment data. In this visco-elastic model, single functions describe the stiffness, damping and momentum flux components. This section contains supplementary comparisons for that study, and illustrate the accuracy of the model for *Pressureless*, *Punctured* and *Oversize* balls.

(a) Contact Time

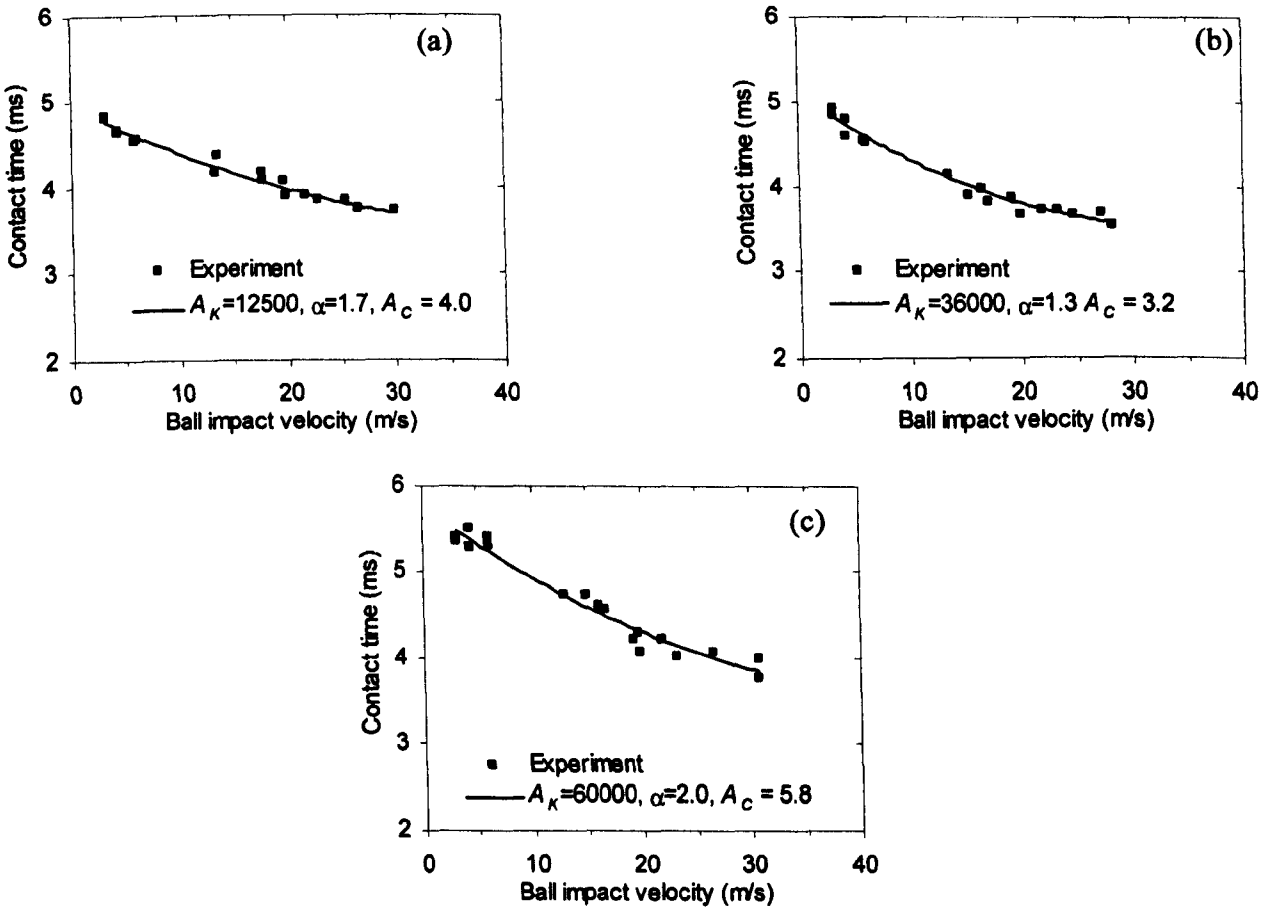

Figure B.6 Comparison between model and experimental contact time for (a) *Pressureless*, (b) *Oversize*, and (c) *Punctured* balls.

In section 5.5.4, the model parameters A_K and α were obtained for all four ball types. The value o these two parameters were chosen so that the model impact had the same contact time as tha determined experimentally. This is confirmed in Figure B.6 for the *Pressureless*, *Oversize* an *Punctured* balls.

(b) Coefficient of restitution

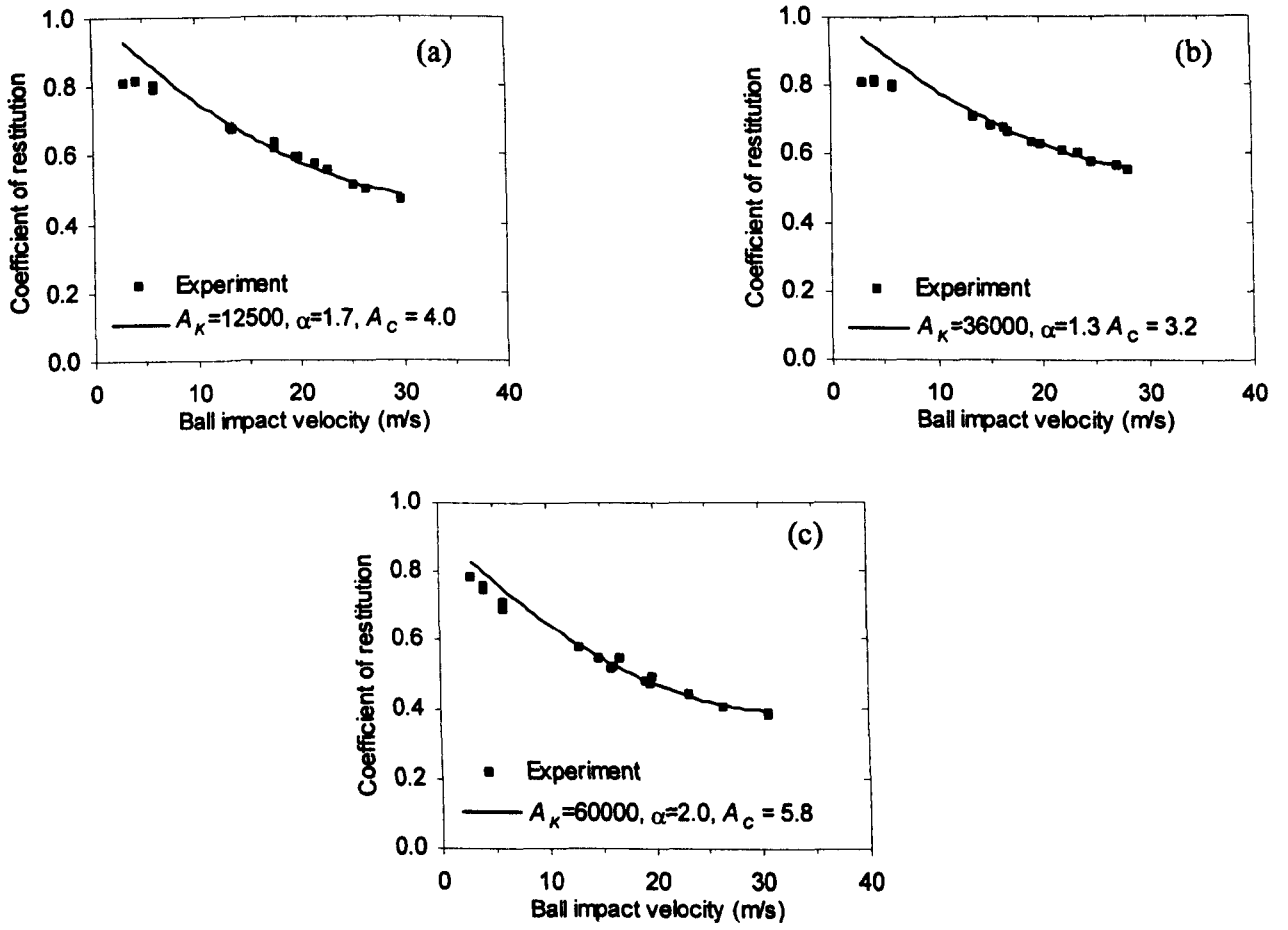

Figures B.7 Comparison between model and experimental coefficient of restitution for (a) *Pressureless*, (b) *Oversize* and (c) *Punctured* balls.

In section 5.5.4, the model parameters A_C was obtained for all four ball types. This value was constant for all ball impact velocities, and the magnitude was adjusted so as to minimise the difference between the model and experiment data. Figures B.7(a)-(c) illustrate the accuracy of the model for the *Pressureless*, *Oversize* and *Punctured* balls. It shows that the model is most accurate for impact velocities above 13m/s.

(c) Force-Time and Force-Displacement data

In section 5.5.4(b), the model *Force-Time* and *Force-Displacement* data is compared with that obtained experimentally for a *Pressurised* ball. In this section, similar comparisons are made for the *Pressureless*, *Oversize* and *Punctured* balls in Figure B.8, Figure B.9 and Figure B.10 respectively.

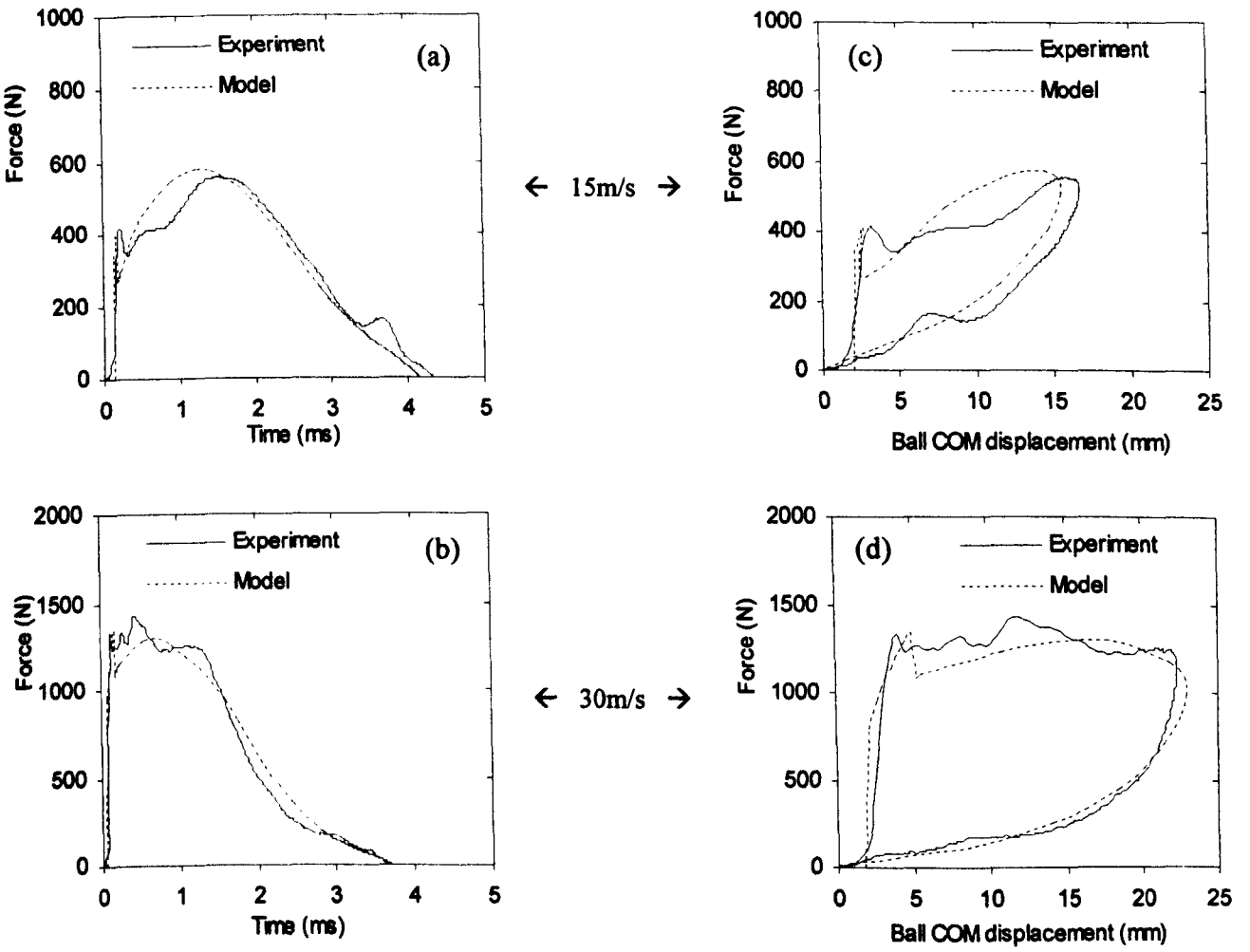

Figure B.8 Comparison of 1-DOF *momentum flux* model and experiment results for an impact between a *Pressureless* ball and a rigid surface for two different impact velocities.

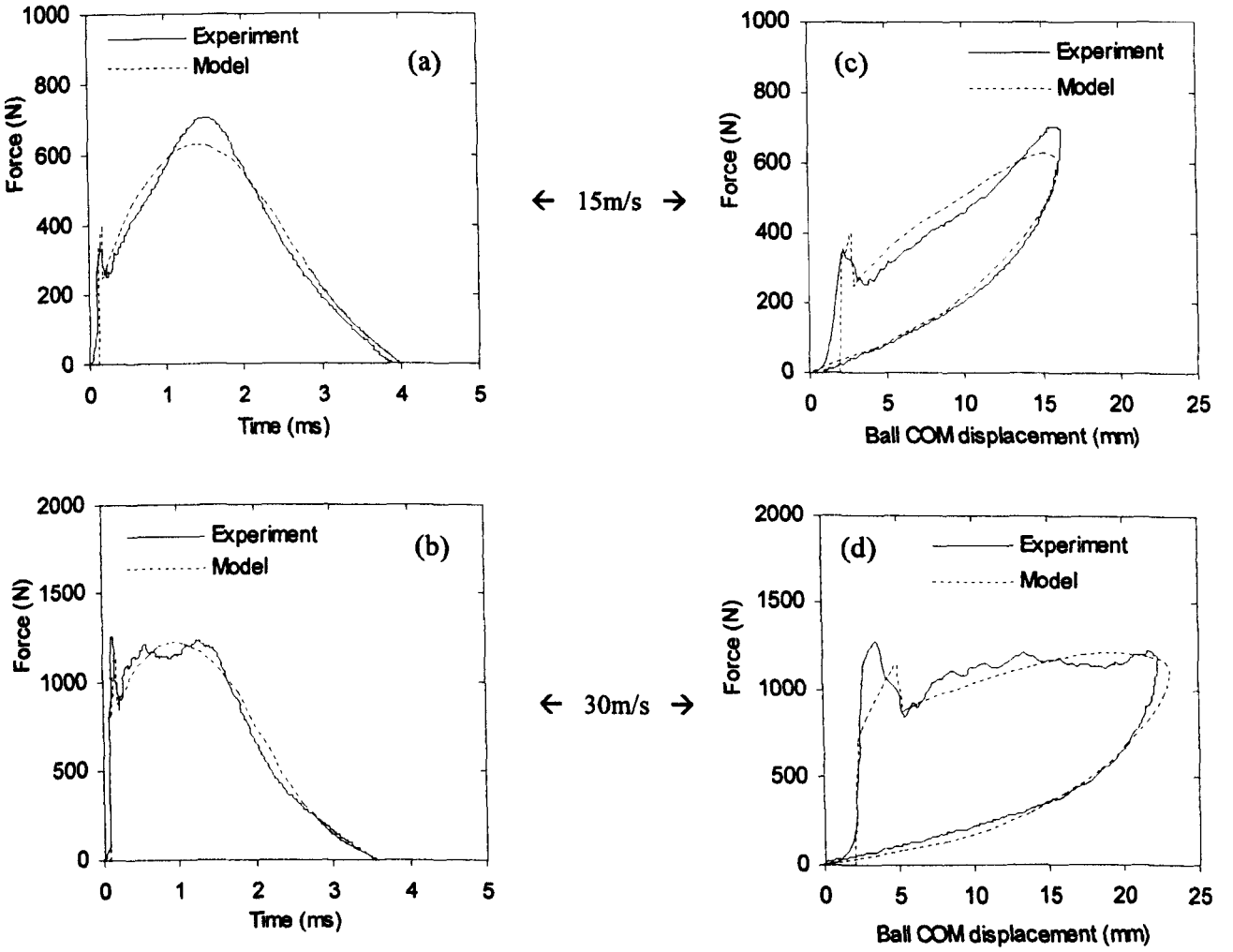

Figure B.9 Comparison of 1-DOF momentum flux model and experiment results for an impact between a Oversize ball and a rigid surface for two different impact velocities.

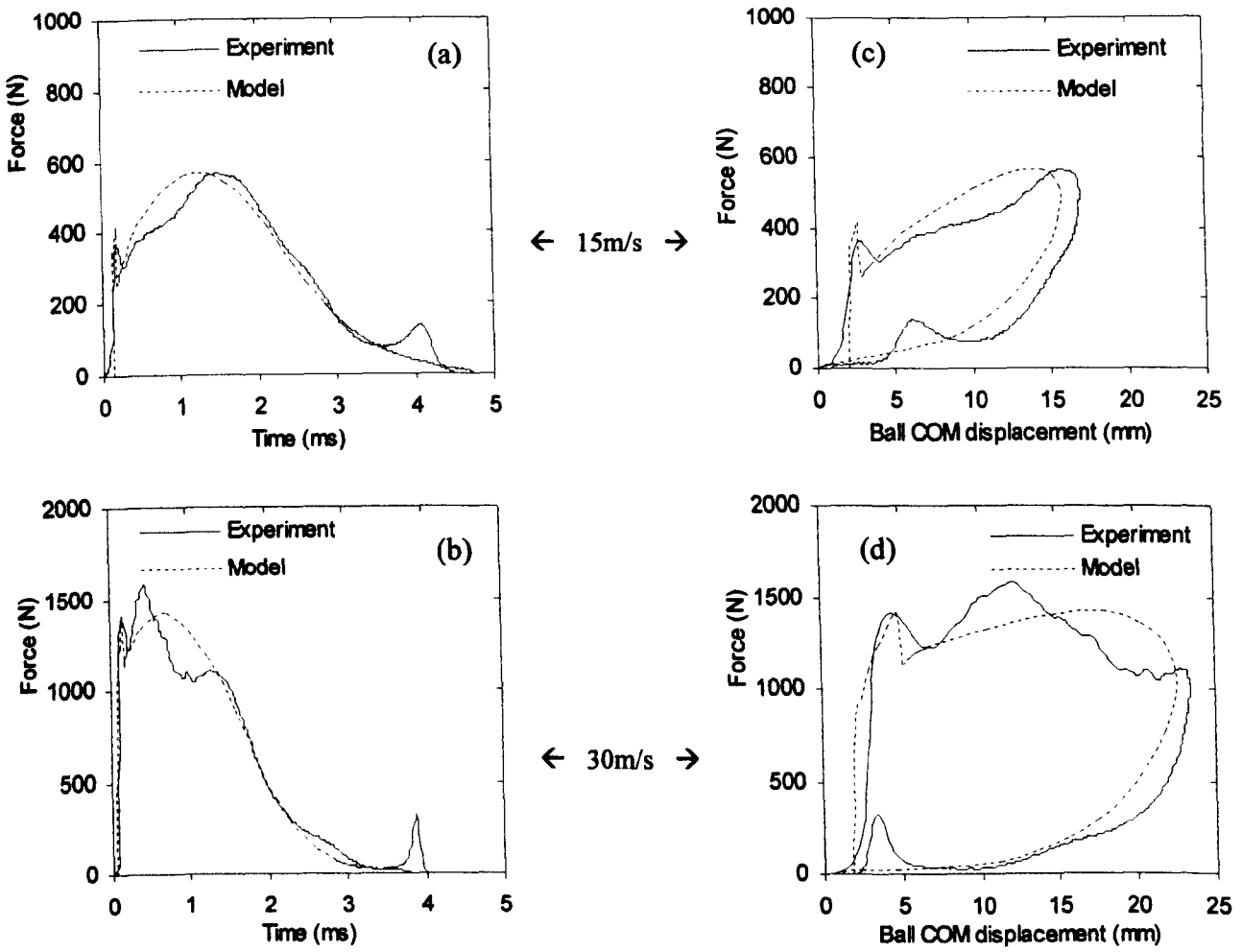

Figure B.10 Comparison of 1-DOF *momentum flux* model and experiment results for an impact between a *Punctured* ball and a rigid surface for two different impact velocities.

C. Impact between a Ball and Head-Clamped Racket

C.1 Introduction

The appendix contains supplementary results which have been referred to in Chapters 7 and 8. The details of the experimental procedures used to obtain this data is given in these chapters. The results of the various experiments are presented for two ball types which are *Pressurised* and *Pressureless* balls.

C2. Stringbed and ball deformation

In section 7.2.2 a method was discussed for determining the ball and stringbed deformation during an impact between a tennis ball and head clamped racket. These tests were performed using *Pressurised* and *Pressureless* tennis balls, and two rackets which had been strung at different tensions (40lbs and 70lbs). The stringbed deformation is defined as the displacement of the stringbed at the impact location. Supplementary data for this experiment is given in this section.

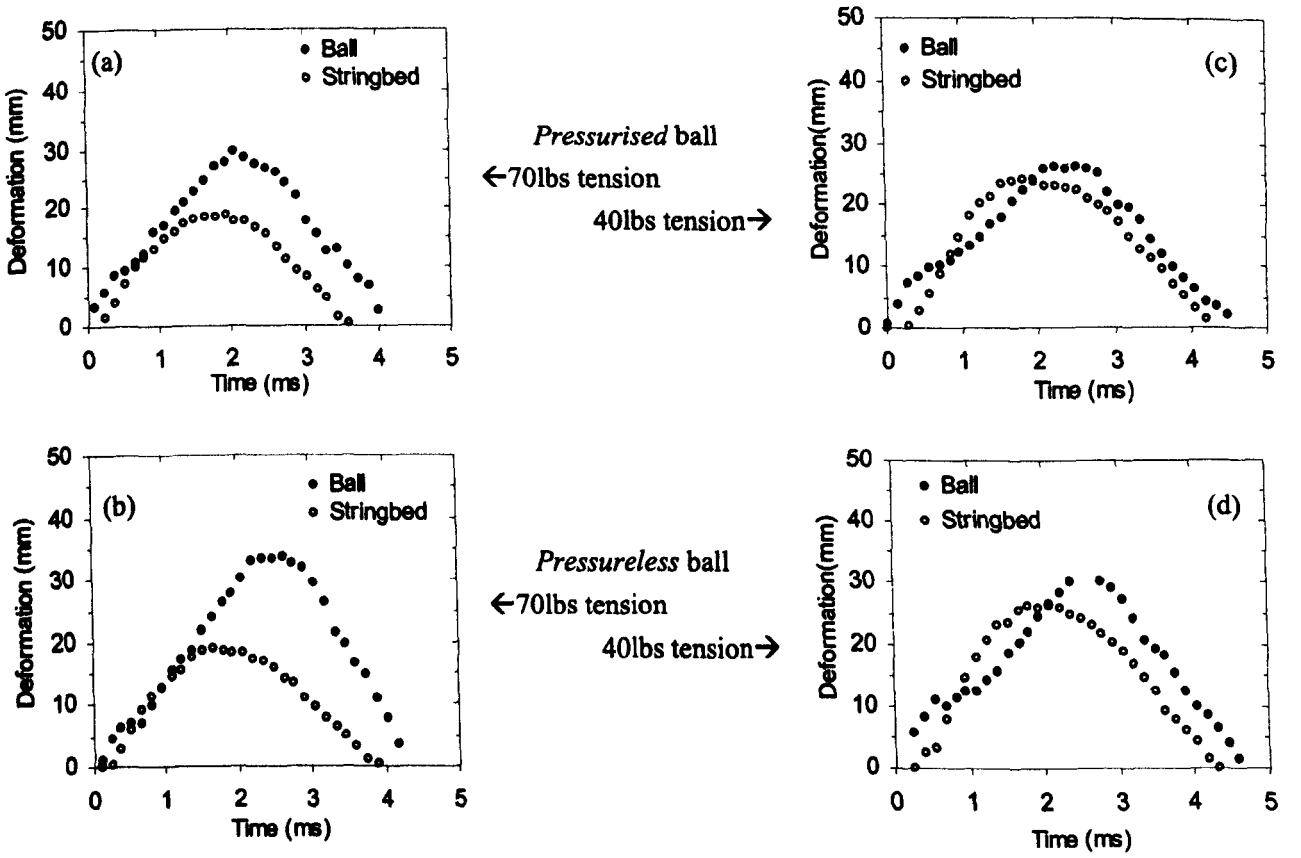

Figure C.1 Ball and stringbed deformation for an impact between a ball and head clamped racket, for four different combinations of string tension and ball type, at a nominal impact velocity of 30m/s.

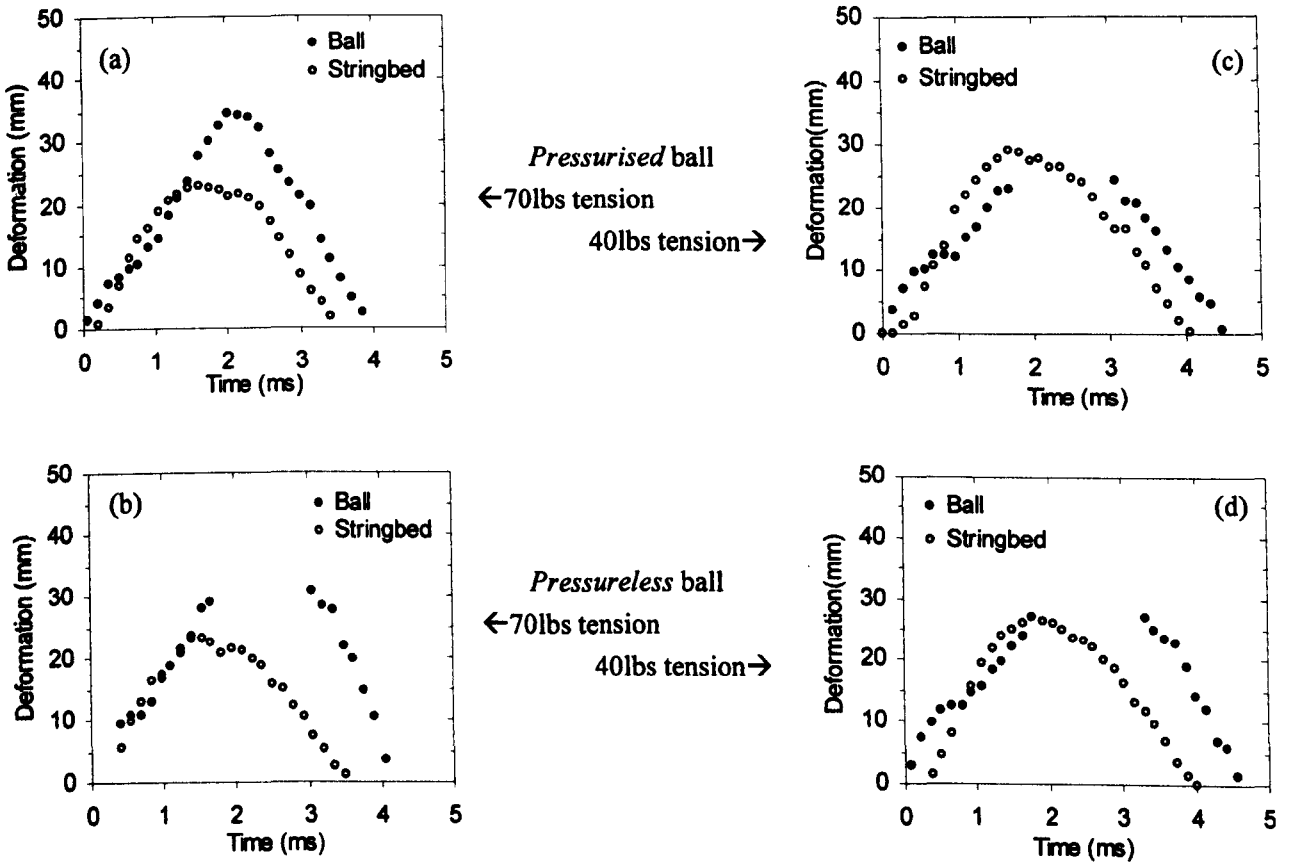

Figure C.2 Ball and stringbed deformation for an impact between a ball and head clamped racket, for four different combinations of string tension and ball type, at a nominal impact velocity of 36m/s.

C3. Stringbed and ball centre-of-mass displacement

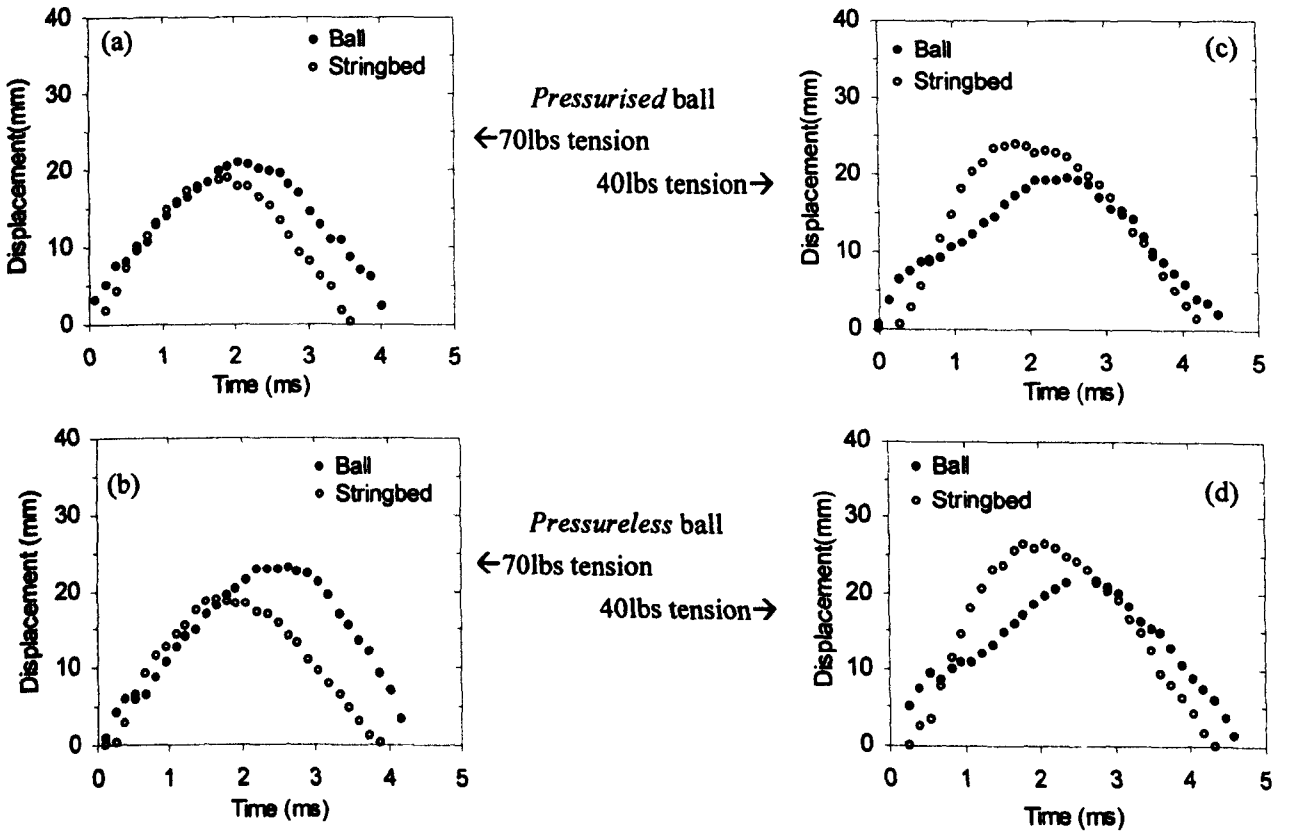

Figure C.3 Ball centre-of-mass displacement and stringbed displacement for an impact between a ball and head-clamped racket. The ball impact velocity is 30m/s.

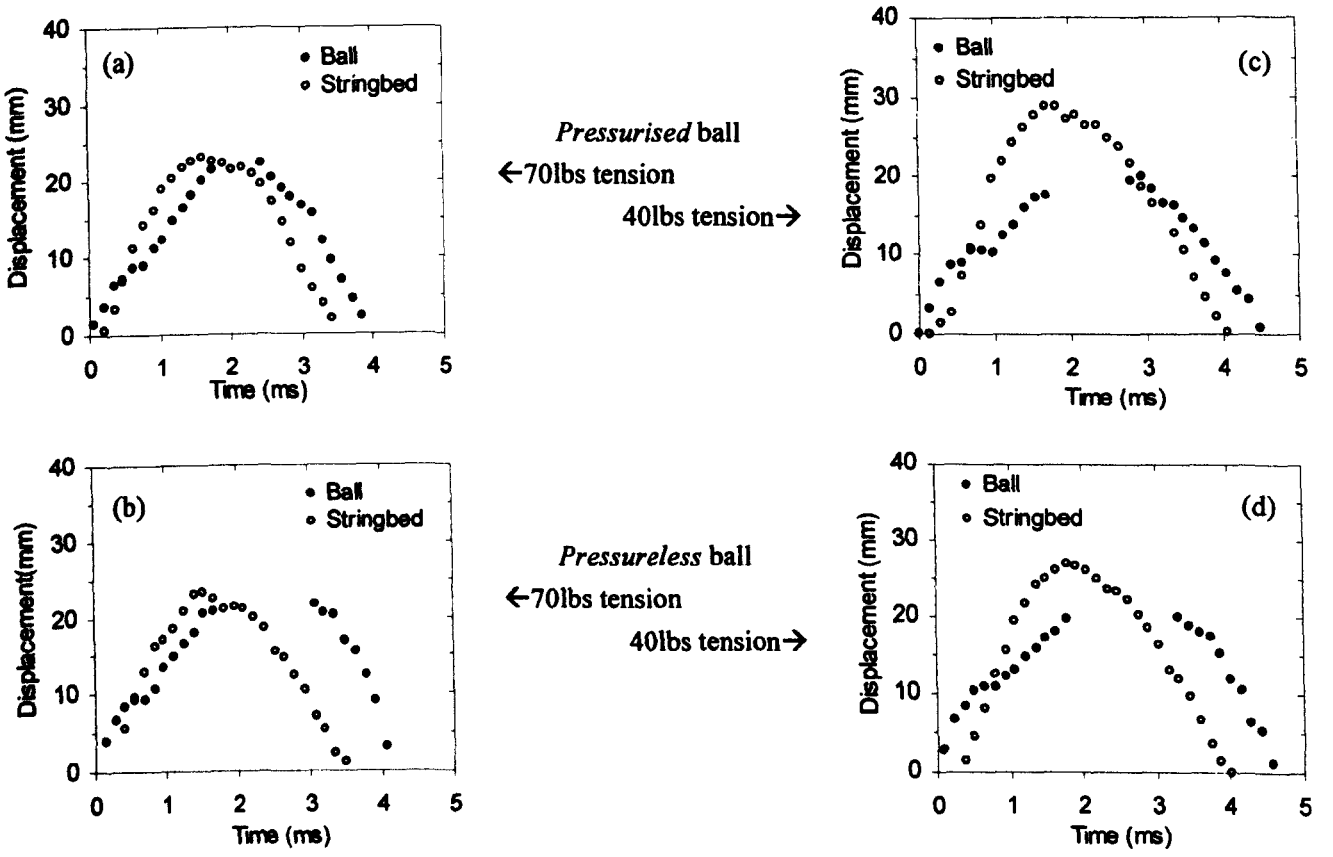

Figure C.4 Ball centre-of-mass displacement and stringbed displacement for an impact between a ball and head-clamped racket. The ball impact velocity is 36m/s.

C.4 The shape of a stringbed for an impact between a ball and racket

In section 7.3.2 a method was discussed for determining the shape of a deformed stringbed during an impact between a tennis ball and head clamped racket. These tests were performed using a *Pressurised* tennis balls, and two rackets which had been strung at different tensions (40lbs and 70lbs). In Figure C.5, data is presented for impacts on the racket which was strung at a tension of 40lbs. The camera operated at a recording rate of 6700 frames per second.

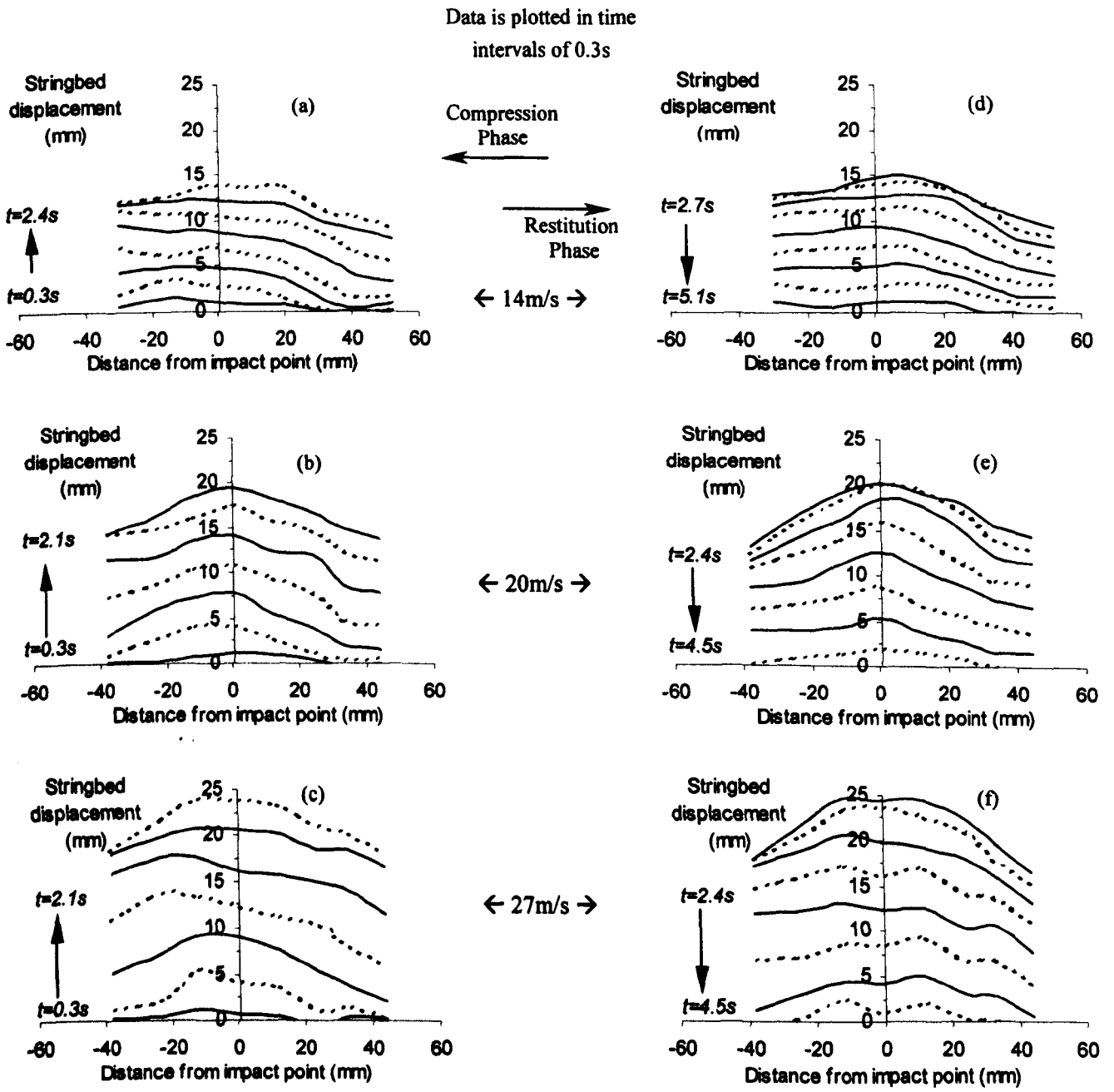

Figure C.5 Stringbed deformation plotted as a function of the position along the longitudinal axis of a racket (40lbs tension), for an impact using a *Pressurised* ball. The data is shown for three different impact velocities and presented individually for the, (a)-(c) compression phase and (d)-(f) restitution phase.

C.5 Comparison of model and experiment data – 1st Attempt

In Chapter 8, a visco-elastic model of a ball impacting on a head clamped racket is developed. A detailed description of the derivation of the generic model is given in section 8.2. This model requires assumptions to be made to enable the definition of the values of the parameters which are input into the model. In section 8.3, a set of assumptions are given which define a first approximation for this model. The main results for this model are given in section 8.3 and supplementary data is given in this current section.

In Chapter 7, high speed video analysis was used to estimate the displacement of the ball centre-of-mass during impact, for a range of ball impact velocities. In these experiments, the magnitude of the stringbed displacement was also measured. These experimental values of ball COM and stringbed displacement are plotted in Figure C.6 and Figure C.7, along with the model results for these parameters.

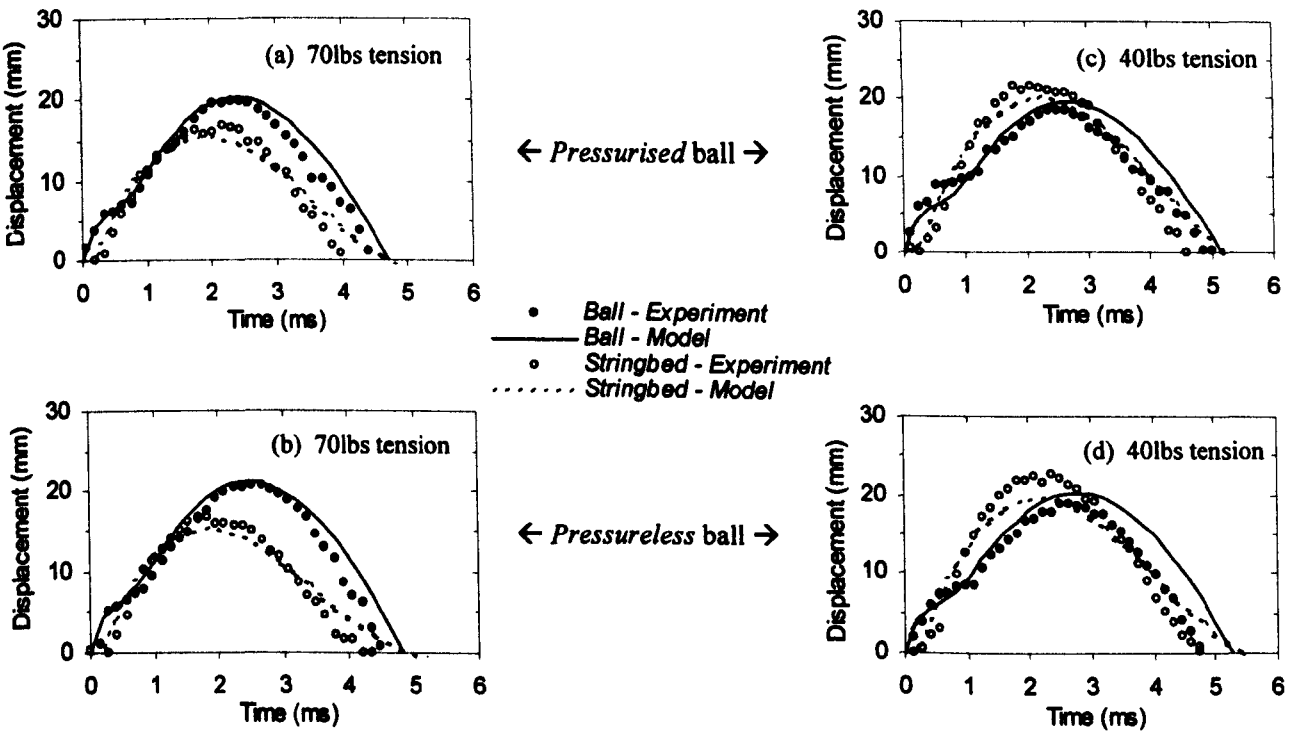

Figure C.6 Ball centre-of-mass displacement and stringbed displacement for an impact between a ball and head-clamped racket, for four different combinations of string tension and ball type. The ball impact velocity is 25m/s, and both the model and experiment data are presented.

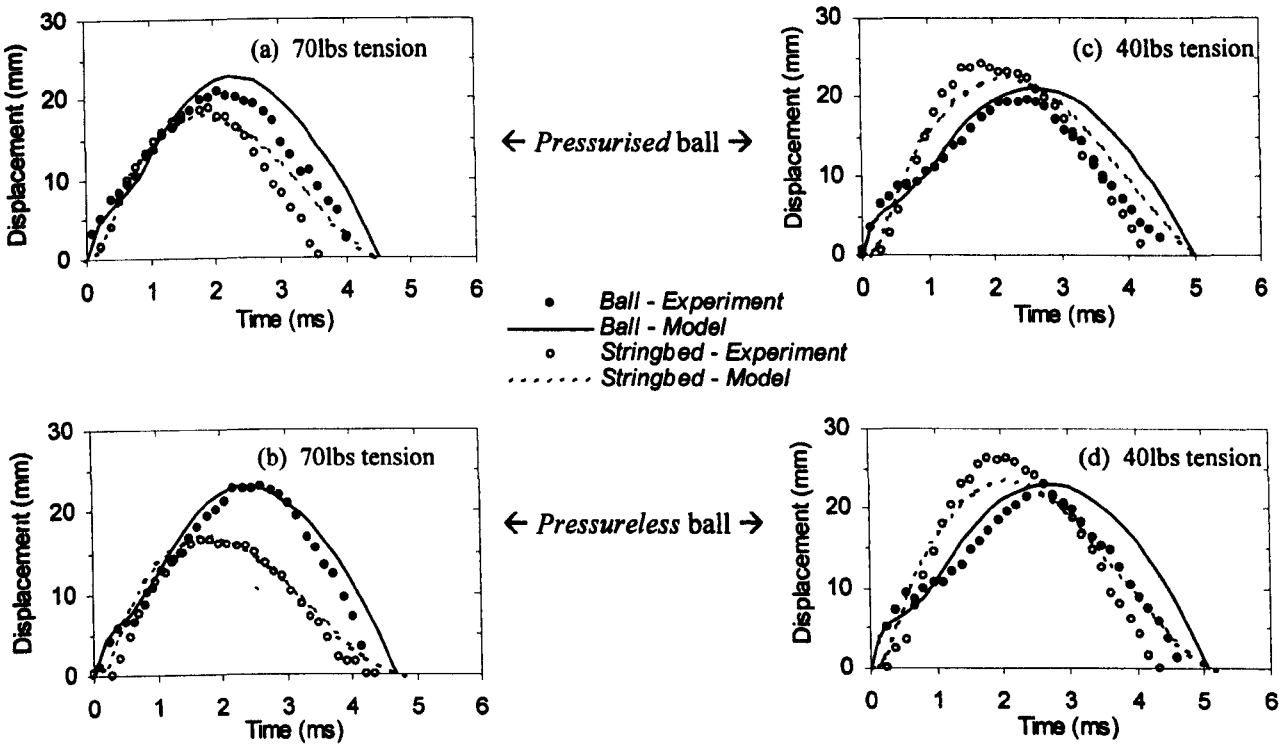

Figure C.7 Ball centre-of-mass displacement and stringbed displacement for an impact between a ball and head-clamped racket, for four different combinations of string tension and ball type. The ball impact velocity is 30m/s, and both the model and experiment data are presented.

C.6 Comparison of model and experiment data – 2nd Attempt

In Chapter 8, a visco-elastic model of a ball impacting on a head clamped racket is developed. A detailed description of the derivation of the generic model is given in section 8.2. This model requires assumptions to be made to enable the definition of the values of the parameters which are input into the model. In section 8.4, a modified set of assumptions are given which define the values of the parameters. The main modification of this model was that the ball stiffness k_B was increased by approximately 30%. Typical results for this model are given in section 8.4 and supplementary data is given in this current section.

As in section C.5, the model results are compared with experimental data. This comparison is conducted for here for both the ball centre-of-mass and stringbed displacement.

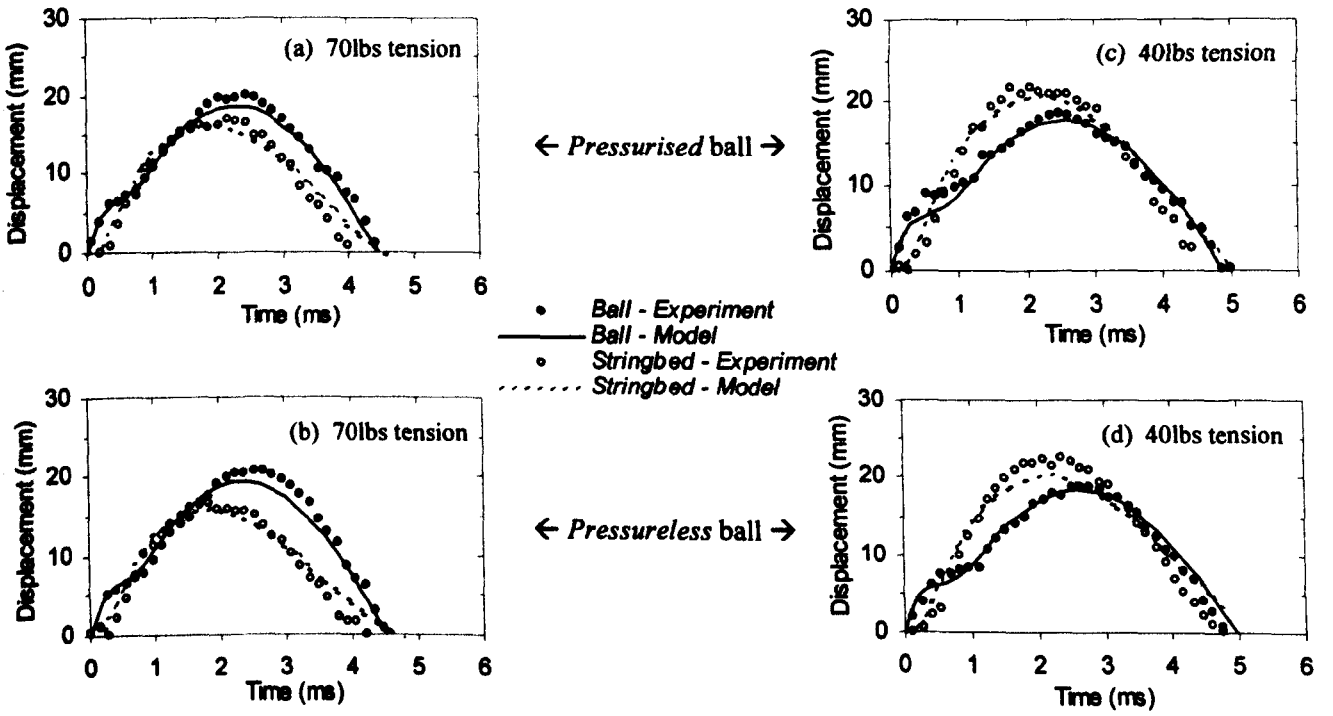

Figure C.8 Ball centre-of-mass displacement and stringbed displacement for an impact between a ball and head-clamped racket, for four different combinations of string tension and ball type. The ball impact velocity is 25m/s, and both the model and experiment data are presented.

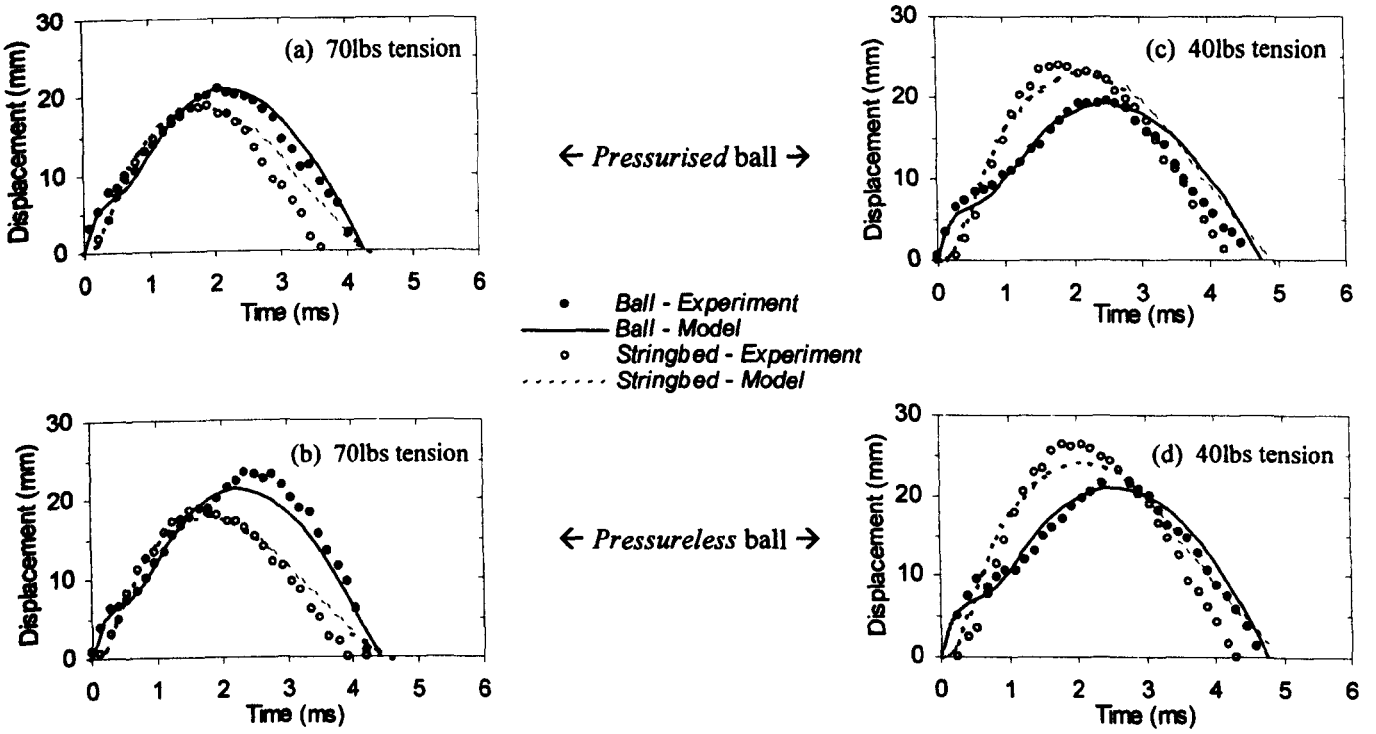

Figure C.9 Ball centre-of-mass displacement and stringbed displacement for an impact between a ball and head-clamped racket, for four different combinations of string tension and ball type. The ball impact velocity is 30m/s, and both the model and experiment data are presented.

C.7 Sensitivity of model solution to the arbitrary assumptions

C.7.1 Results and Discussion

In Chapter 8, a visco-elastic model of a impact between a ball and head clamped racket has been derived and discussed. In this model, the ball and stringbed were treated as two distinct components and numerous assumptions were made to enable the model to be solved. The method used to model the ball component was based upon the findings of a simulation of a ball impact on a rigid surface. It was assumed that the features of this ball model could be applied directly to the simulation of a ball impact on a head clamped racket. It was then assumed that the ball stiffness should be increased by 30% to improve the accuracy of the model. This was a reasonable assumption as the development of the model has always involved the used of empirically determined parameters.

One of the assumptions that was made in regard to the model of the stringbed shall now be considered. The stiffness of the stringbed was assumed to be equal to that which was measured experimentally for a quasi-static loading. However, this assumption is difficult to apply because the quasi-static loading was applied using a rigid circular disc. Clearly, the ball applies a loading to the racket over a continually varying area during impact. An assumption needed to be made to define the diameter of the rigid circular disc which gives an equivalent loading as that applied the ball during the impact. It was assumed that this area will increase as a function of the stringbed displacement, and this function is shown in Figure C.10.

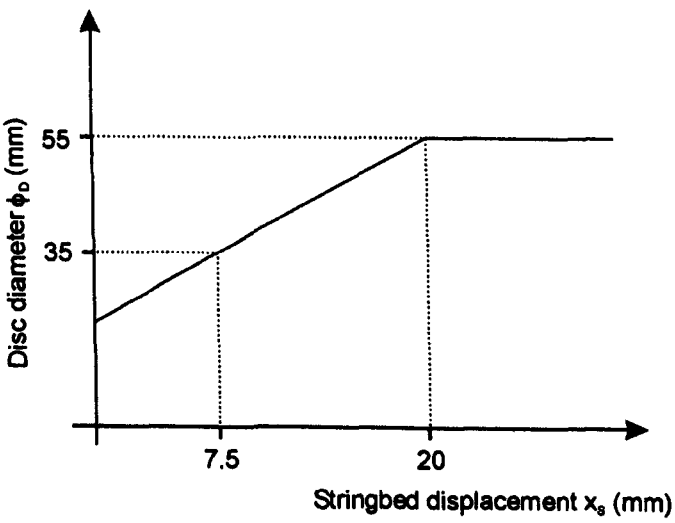

Figure C.10 Assumed relationship between the disc diameter and the stringbed displacement.

The relationship shown in Figure C.10 was obtained by comparing the shape of a deformed stringbed during an impact with a ball with that of a stringbed deformed quasi-statically. This is a subjective analysis because the two shapes are subtly different, and therefore there is a moderate level of uncertainty in the assumed relationship in Figure C.10.

To assess the sensitivity of the model solution to the assumed relationship shown in Figure C.10, two other functions will be used to solve the model. These functions represent the two extreme possibilities for the assumed relationship and are shown in Figure C.11 as 'assumption (a)' and

'assumption (b)'. The definition of these extremes was aided by considering the comparison of shapes of the quasi-statically deformed stringbed and the dynamically deformed stringbed.

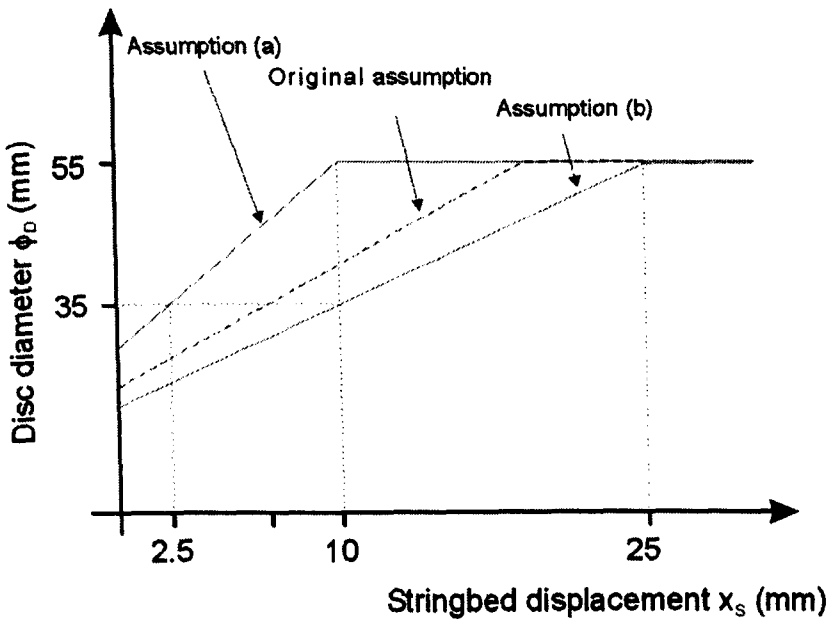

Figure C.11 Assumed relationship between the disc diameter and the stringbed displacement. The 'original assumption' is shown, along with two other arbitrary assumptions.

The solution was calculated and the effect of the different assumptions was quantified by comparing the model output for several parameters as shown in Table C.1. The parameters were obtained for a model of an impact between a *Pressurised* ball and racket strung at 70lbs. The ball impact velocity was 30m/s.

Table C.1 Comparison of the parameters calculated by the model for three different assumptions regarding the stringbed stiffness.

	Original assumption	Assumption (a)	Assumption (b)
Ball rebound velocity (m/s)	24.1	24.0	24.2
Maximum stringbed displacement (mm)	18.2	17.7	19.2
Maximum ball centre-of-mass displacement (mm)	20.6	20.6	20.5
Contact time $T_{C(B)}$	4.28	4.25	4.32

It can be seen from the results in Table C.1 that the choice of function to describe the relationship between the disc diameter and the stringbed displacement does not greatly effect the magnitude of the ball rebound velocity, maximum ball COM displacement or the contact time for the impact.

Assumption (b), which acts to reduce the stiffness of the stringbed, increases the maximum stringbed displacement by 1mm.

C.7.2 Summary

In this section, it has been shown that the arbitrary assumptions made regarding the model of a stringbed do not greatly effect the model output. An assumed relationship between the stringbed displacement and the effective contact area needs to be made to solve the model. Two extreme assumptions were used in this section and it was shown that both assumptions resulted in similar values of the ball rebound velocity, maximum ball COM displacement and the contact time being calculated for the impact.

D. Modelling a tennis racket

D.1 Determination of the Transverse Mass Moment of Inertia

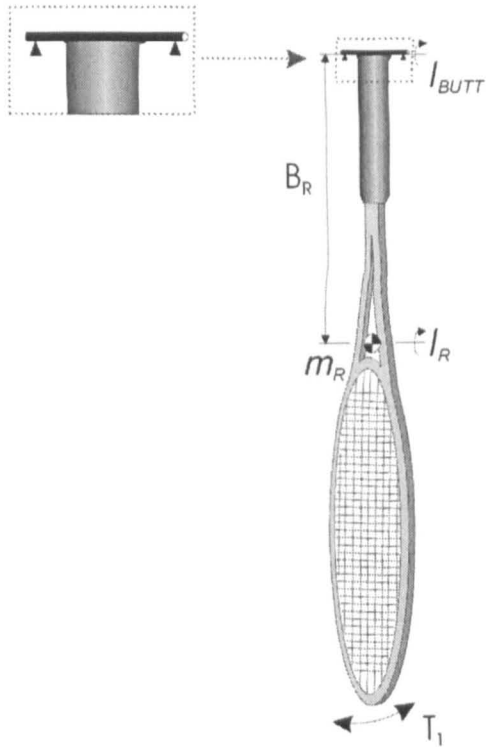

Figure D.1 Illustration of the method used to simply support the racket.

In Chapters 8 and 9, ball impacts on a freely suspended racket are studied, in which the ball impacts on the longitudinal axis of the racket. In these types of impacts, the only mass moment of inertia that is of concern is the transverse moment of inertia. The experimental method which is used to measure this parameter is based on that described in Brody (1985).

A light, thin circular bar was attached to the racket at the butt end as illustrated schematically in Figure D.1. The bar rested on two knife edges and this arrangement acted as a pivot so that the racket could oscillate as a pendulum. The time period of N oscillations was determined using a digital stop clock. The total time which was measured by the stop clock, for N oscillations, is defined as T_N. The time period for one oscillation of the racket is defined using,

$$T_1 = \frac{T_N}{N} \qquad [D.1]$$

The mass moment of inertia of the racket I_{BUTT}, around the butt end, can be determined from the time period of oscillations using,

$$I_{BUTT} = \frac{T_1^2 g M_R B_R}{4\pi^2} \qquad [D.2]$$

for small amplitude oscillations.

For this study, the mass moment of inertia I_{BUTT} was initially only measured for three different racket types. The experiments were repeated for values of N between 10 and 80, and the results are presented in Figure D.2.

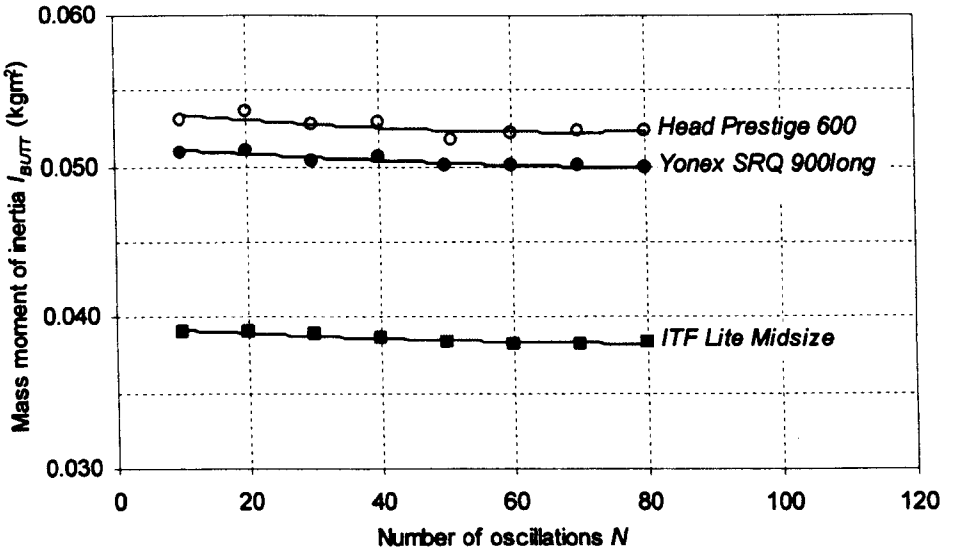

Figure D.2 The experimental mass moment of inertia I_{BUTT} plotted against the number of oscillations N used to obtain this value, for three different rackets.

Figure D.2 compares the mass moment of inertia I_{BUTT} with the number of oscillations N that were used to determine this value of I_{BUTT}; second order polynomial trend lines being plotted through this data. The value of I_{BUTT} should be independent of the number of oscillations yet the trend lines in Figure D.2 show that the value of I_{BUTT} is a function of N. This systematic error, and the scatter in the data, proves that there are inaccuracies in the method which should be investigated. There was insufficient data in this experiment to perform a full statistical error analysis, but the likely source of this error can be discussed by considering the accuracy of the parameters T_1, M_R and B_R which are used in [D.2] to calculate I_{BUTT}.

The mass of the racket was determined independently using two different electronic scales. The mass measured using both scales correlated to within ±0.1 grams. A simple rig was manufactured to aid the accurate measurement of the balance point B_R. This rig was equipped with a set of knife edges to balance the racket and a measurement grid to reference the position of the knife edges with respect to the racket butt. An arbitrary uncertainty of ±1mm was concluded for the accuracy of the measurement of B_R, as the balance point is not a discrete point when measured using this method.

The errors in both m_R and B_R are relatively small and are also independent of the parameter N. Therefore these are not the source of the systematic error for I_{BUTT} which is illustrated in Figure D.2.

The time period T_N for N oscillations is measured using a manual stop watch and is therefore susceptible to human error. If it is assumed that the error in the measured value of T_N is ±0.3 seconds then it can be shown that the relative error ε in the value of T_1 varies between ±2.1% and ±0.26% for values of N equal to 10 and 80 respectively. From [D.2], this causes an error in the order of ε^2 in the value of I_{BUTT} which are between ±4.3% and ±0.52%. This clearly highlights the effect of errors in T_1 on the value of I_H, and confirms the importance of maximising N when performing such experiments. This initially implies that all tests should be run with N equal to, or greater than, 80. However, due to the damping effects in the oscillating system it would be impractical to run a test for more than 80 oscillations. Also, the relationship between N and ε^2 is

non-linear. For example, ε^2 is equal to only ±0.89% for N equal to 50 oscillations. This illustrates that the accuracy of the experiment does not greatly improve as N is increased beyond, for example, 50 oscillations.

It was arbitrarily chosen that the value of I_{BUTT} was determined by calculating a mean of the values of I_{BUTT} that were calculated for N between 50 and 80 oscillations. These results are summarised in Table D.1, along with the values of I_{BUTT} for four other rackets.

Table D.1 The mass moment of inertia I_{BUTT} for a selection of rackets.

Racket Type	I_{BUTT} calculated for N oscillations *(kgm²)*				Mean I_{BUTT} (kgm²)
	$N = 50$	$N = 60$	$N = 70$	$N = 80$	
YONEX Super RQ Ti 900 long	0.05014	0.05003	0.05008	0.04990	0.05004
ITF Dev Court 1 Lite Mid-size	0.03839	0.03827	0.03817	0.03839	0.03830
HEAD Prestige Classic 600	0.05177	0.05227	0.05237	0.05241	0.05220
SPALDING Heat 90	0.05061	0.05066	0.05046	0.05058	0.05058
Miller Twinset	0.05302	0.05297	0.05290	0.05278	0.05292
ITF Dev Carbon Fibre 98	0.05337	0.05340	0.05326	0.05347	0.05337
Wilson ProStaff 6.0 Mid-Size	0.05175	0.05144	0.05164	0.05160	0.05161

Table D.1 shows the mass moment of inertia I_{BUTT} values which were obtained using a different number of oscillations N of the racket. The mean value of I_{BUTT}, calculated from the four individually measured values for $N = 50$ to $N = 80$, is also shown. The level of confidence which can be assigned to this mean value of I_{BUTT} can be quantified by calculating the standard deviation of the difference σ between the mean and the raw data; σ being defined as,

$$\sigma = (I_{BUTT})_N - \bar{I}_{BUTT}$$

where $(I_{BUTT})_N$ is the value of I_{BUTT} calculated using N oscillations, and $\bar{I}_{BUTT}$ is mean value of the mass moment of inertia for the racket.

The standard deviation of the data set of 28 values of σ was calculated to be 0.00013kgm², or approximately 0.3%. This implies that a high level of confidence can be assigned to the value of I_{BUTT} measured using this method.

D.2 Experimental Determination of the Fundamental Frequency and Node Position on the racket

D.2.1 Introduction

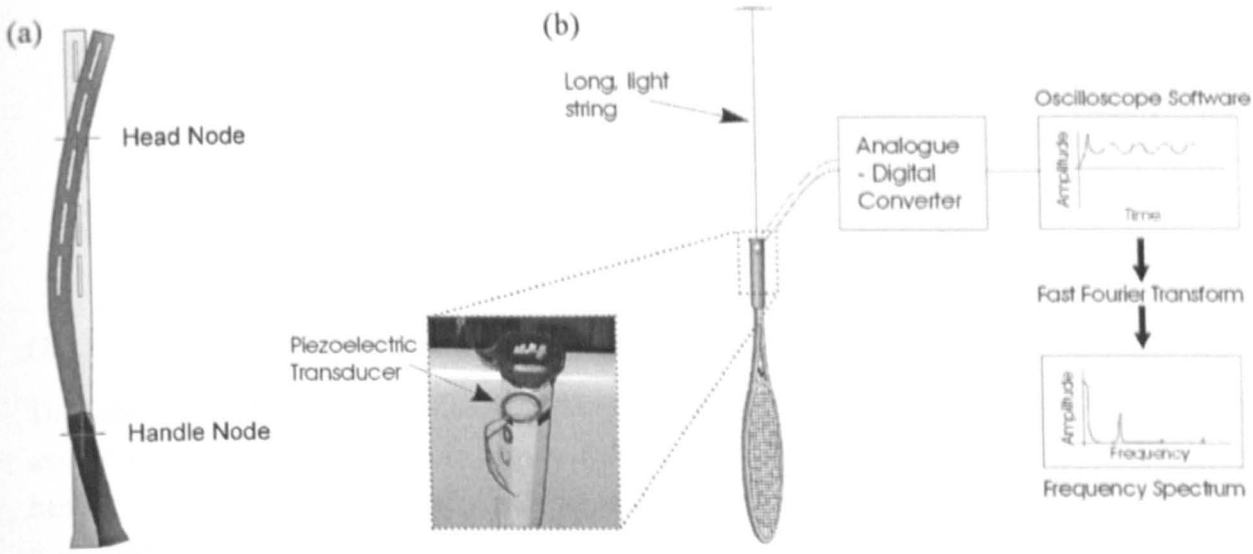

Figure D.3 (a) Definition of Head Node and Handle Node for the fundamental mode of transverse vibrations and (b) The experimental arrangement for determining the fundamental frequency and node positions of transverse vibrations.

In this section, the fundamental frequency of transverse vibrations and the corresponding node points, will be experimentally determined for a freely supported racket. An illustration of this mode of vibration is shown in Figure D.3, along with the definitions of the two nodes for this mode.

In this experiment, the grip on the racket was removed and a small piezoelectric transducer was attached to the rigid surface of the handle, using strong adhesive tape. The strap was then replaced. The racket was supported by a long light string attached to the base of the racket as illustrated in Figure D.3(b). The signal from the piezoelectric transducer was sampled using an Analogue-to-Digital converter and *Picoscope v5.7.4* software on a PC laptop. A Fast Fourier Transform of this data was performed using the FFT function in *MATLAB v5.3* software on a PC, to identify the frequency spectrum of the racket vibrations.

D.2.2 Fundamental frequency of transverse vibrations

The apparatus was set-up as shown in Figure D.3(b). A very soft hammer was used to strike the stringbed near the tip, on the longitudinal axis, to excite the fundamental mode of vibrations. The experiment was repeated several times and the fundamental frequency was determined directly from the frequency spectrum, for each repetition. The resolution of this frequency spectrum was approximately 1Hz, and the calculated value for each repetition exhibited very little scatter.

Table D.2 The experimentally determined values of fundamental frequency.

Racket Type	Fundamental Frequency (Hz)
YONEX Super RQ Ti 900 long	161
ITF Dev Court 1 Lite Mid-size	103
HEAD Prestige Classic 600	138
SPALDING Heat 90	127
Miller Twinset	143
ITF Dev Carbon Fibre 98	134
Wilson ProStaff 6.0 Mid-Size	142

D.2.3 Node location for fundamental mode of transverse vibrations

The fundamental mode of vibration for a tennis racket has two node points along the longitudinal axis of the racket as illustrated in Figure D.3(a); these being defined as the head node and the handle node. As the ball generally only impacts near the head node, this was the only node that was identified in this study. Other researchers have shown that the head node is not actually a unique distance from the tip of the racket, for impacts that are not on the longitudinal axis. This finding is illustrated in Figure D.4, which shows a continuous node line that corresponds to the locus of impact points which result in the minimum excitation of the fundamental mode of vibration.

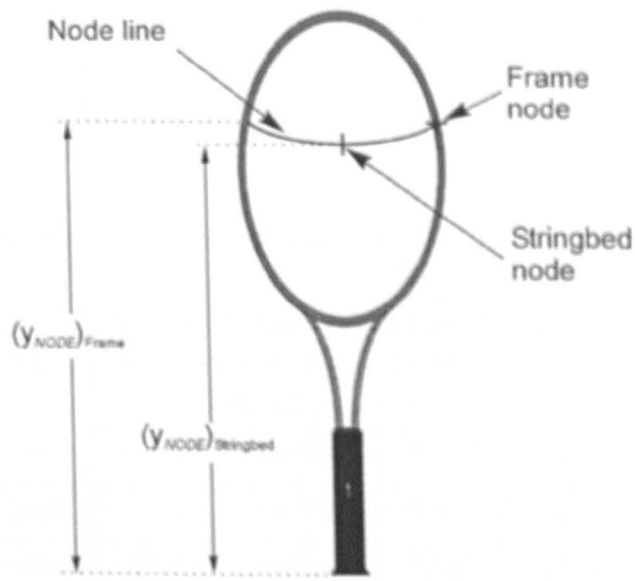

Figure D.4 Definition of the node positions on a tennis racket.

In this study, the stringbed node and frame node were determined for a range of different rackets. The rackets were exited at various points on the stringbed, along the longitudinal axis, and the resulting oscillations were recorded as before. A Fast Fourier Transform was performed on the data to identify the point on the stringbed when the fundamental frequency was not excited. A similar experiment was conducted to find the node position on the frame. The results for the two

node position are shown in Table D.3. Due to the uncertainty in the position that the racket stringbed was excited by the hammer, an accuracy of ±5mm is quoted.

Table D.3 Experimentally measured node locations on a tennis racket.

Racket Type	Stringbed Node Position $(y_{NODE})_{Stringbed}$ (mm)	Frame Node Position $(y_{NODE})_{Frame}$ (mm)
YONEX Super RQ Ti 900 long	547±5	579±5
ITF Dev Court 1 Lite Mid-size	524±5	551±5
HEAD Prestige Classic 600	523±5	557±5
SPALDING Heat 90	534±5	554±5
Miller Twinset	538±5	561±5
ITF Dev Carbon Fibre 98	528±5	549±5
Wilson ProStaff 6.0 Mid-Size	523±5	558±5

D.3 Beam models of a tennis racket frame

D.3.1 Introduction

In Chapter 9, the methods were discussed for determining three different types of one dimensional beam model for a tennis racket frame. In that chapter, an *ITF Carbon Fibre (6)* tennis racket was used to illustrate these methods. In this section, the details of the six other tennis rackets are given, along with the parameters for the three model beams.

Table D.4 Measured properties for range of tennis rackets.

Racket Type	Length L_R (m)	Mass M_R (kg)	Balance Point B_R (m)	Mass Moment of Inertia I_{BUTT} (kgm^2)	Handle length L_H (m)	Racket width W_R (m)	Frame Length (m)			
							L_{F1}	L_{F2}	L_{F3}	L_{F4}
Yonex (1)	0.707	0.258	0.388	0.05004	0.236	0.290	0.097	0.028	0.319	0.028
ITF (2)	0.683	0.262	0.321	0.03830	0.187	0.260	0.161	0.027	0.281	0.027
Head (3)	0.686	0.349	0.323	0.05220	0.215	0.260	0.135	0.027	0.282	0.027
Spalding (4)	0.686	0.335	0.324	0.05058	0.215	0.270	0.121	0.027	0.296	0.027
Miller (5)	0.686	0.298	0.363	0.05292	0.215	0.270	0.121	0.027	0.296	0.027
ITF (6)	0.683	0.348	0.325	0.05337	0.228	0.265	0.094	0.027	0.308	0.027
Wilson (7)	0.686	0.359	0.314	0.05161	0.215	0.255	0.148	0.027	0.269	0.027

Table D.5 Properties of a *uniform section* beam model for a selection of tennis rackets.

Racket Type	Total number of segments N	Segment length s (m)	Mass Moment of Inertia I_B (kgm^2)	Segment mass m_n (kg)	Flexural rigidity EI
Yonex (1)	51	0.0139	0.04295	0.00505	186
ITF (2)	51	0.0134	0.04074	0.00513	70
Head (3)	51	0.0135	0.05475	0.00684	169
Spalding (4)	51	0.0135	0.05255	0.00657	138
Miller (5)	51	0.0135	0.04675	0.00584	155
ITF (6)	51	0.0134	0.05417	0.00683	156
Wilson (7)	51	0.0135	0.05631	0.00703	184

Table D.6 Properties of a *two section* beam model for a selection of tennis rackets.

Racket Type	Total number of segments N	Segment length s (m)	Mass Moment of Inertia I_B (kgm^2)	Flexural rigidity EI	Number of segments in each section		Segment mass m_n (kg) for each section	
					N_H	N_F	$(m_n)_H$	$(m_n)_F$
Yonex (1)	51	0.0139	0.04854	183	17	34	0.00357	0.00579
ITF (2)	51	0.0134	0.03762	70	14	37	0.00626	0.00471
Head (3)	51	0.0135	0.05055	167	16	35	0.00812	0.00626
Spalding (4)	51	0.0135	0.04872	136	16	35	0.00773	0.00604
Miller (5)	51	0.0135	0.05032	155	16	35	0.00476	0.00634
ITF (6)	51	0.0134	0.05068	156	17	34	0.00782	0.00634
Wilson (7)	51	0.0135	0.05005	180	16	35	0.00894	0.00617

Table D.7 Properties of a *five section* beam model for a selection of tennis rackets.

Racket Type	Mass Moment of Inertia I_B (kgm^2)	Flexural rigidity EI	Number of segments in each section					Segment mass m_n (kg) for each section				
			N_H	N_{F1}	N_{F2}	N_{F3}	N_{F4}	$(m_n)_H$	$(m_n)_{F1}$	$(m_n)_{F2}$	$(m_n)_{F3}$	$(m_n)_{F4}$
Yonex (1)	0.04996	218	17	7	2	23	2	0.0040	0.0042	0.0163	0.0042	0.0163
ITF (2)	0.03884	82	14	12	2	21	2	0.0068	0.0034	0.0126	0.0034	0.0126
Head (3)	0.05202	196	16	10	2	21	2	0.0087	0.0046	0.0167	0.0046	0.0167
Spalding (4)	0.05014	160	16	9	2	22	2	0.0083	0.0044	0.0164	0.0044	0.0164
Miller (5)	0.05182	185	16	9	2	22	2	0.0053	0.0046	0.0173	0.0046	0.017
ITF (6)	0.05206	184	17	7	2	23	2	0.0082	0.0047	0.0173	0.0047	0.017
Wilson (7)	0.05158	211	16	11	2	20	2	0.0096	0.0045	0.0167	0.0045	0.017

D.4 Comparison of a point load and a distributed loading of a beam

In section 9.4, a comparison was made between the model results for an impact which involves a point loading, and an impact involving a distributed loading of the beam. A supplementary comparison, for a *Yonex (6)* tennis racket is given in the figures below.

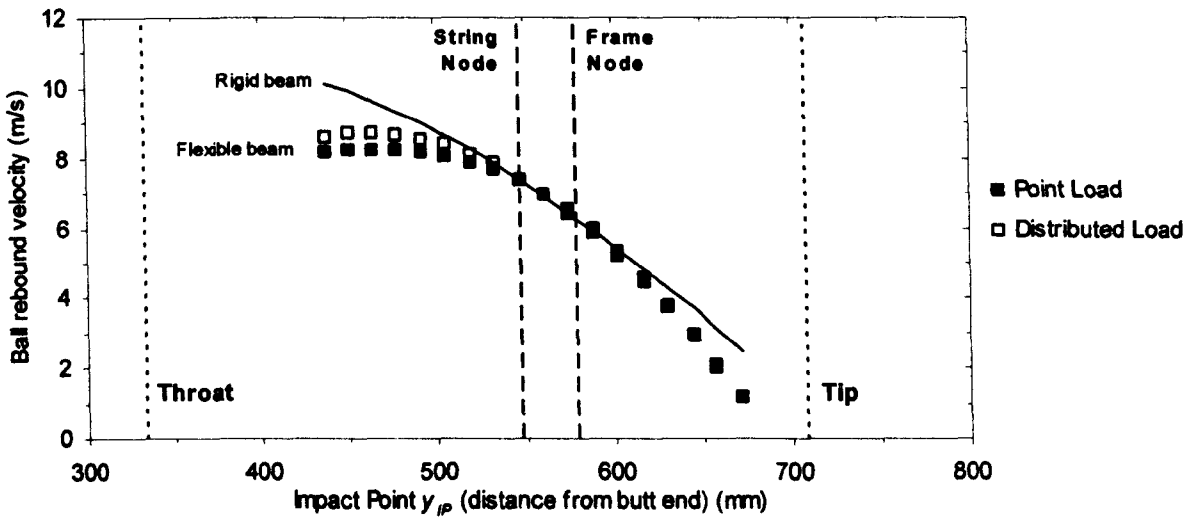

Figure D.5 Calculated ball rebound velocity for a range of ball impact positions on the beam. Data is presented for both a point loading and distributed loading on a flexible beam, and also for a point loading on a rigid beam. The beam model represents an *Yonex (1)* tennis racket. The positions of the throat and tip on the head of the racket, and the string and frame nodes are also given.

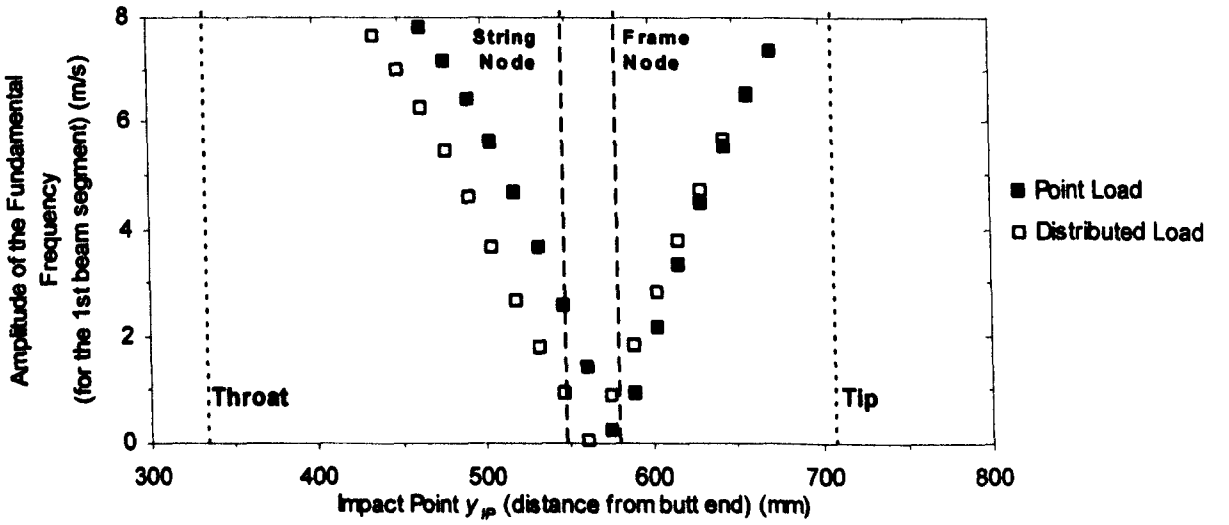

Figure D.6 Calculated amplitude of vibration of the fundamental frequency for a range of ball impact positions on the beam, for the vibration of the 1st beam segment (closest to the butt end). Data is presented for both a point loading and distributed loading on a flexible beam, and also for a point loading on a rigid beam. The data is presented for the *Yonex (1)* tennis racket. The positions of the throat and tip on the head of the racket, and the string and frame nodes are also given.

The comparisons, such as those above, were performed for all the tennis rackets which have been investigated in this study. In Figure D.6, a comparison is made between the impact position and the magnitude of vibration which is excited. An important feature of this comparison is the identification of the impact location which corresponds to minimal vibrations. This position is a function of the loading method, and the collated data for all seven rackets is shown in Table D.8. The positions of the string and frame nodes are also given in this table.

Table D.8 Comparison of the frame and stringbed nodes on the racket, and the impact locations corresponding to minimum vibrations of the beam.

Racket Type	Frame Node $(y_{NODE})_{Frame}$ (mm)	Stringbed Node $(y_{NODE})_{Stringbed}$ (mm)	Impact location corresponding to minimal vibrations of the beam (mm)	
			Point load (mm)	Distributed load
Yonex (1)	579	547	575	555
ITF Aluminium (2)	551	524	549	532
Head (3)	557	523	551	532
Spalding (4)	554	534	556	532
Miller (5)	561	538	559	540
ITF Carbon Fibre (6)	549	528	551	530
Wilson (7)	558	523	549	533

D.5 Method of storing the ball, stringbed and racket parameters in a database.

In section 9.5, a program called *Racket Impact* was discussed. This program performed the calculations that were required to solve for the displacements of the segments of the one dimensional beam segments and the components of the visco-elastic model. The ball, stringbed and racket parameters which were required by *Racket Impact* to model the impact are stored in an *MS Access 2000* database which contains three tables. These tables are defined as (1) Ball, (2) Stringbed and (3) Racket. The fields which compose each table are given in the following figures.

Table D.9 The field names contained with in the Ball table. All these parameters are determined using the methods described in sections 5.5 and 8.4.

Field name	Description
ID	
Ball type	
Mass	Mass of the ball in SI units
kBo	Value of the parameter $k_{B(0)}$
Ak	" " " A_K
Alpha	" " " α
Ac	" " " A_C
ro	" " " ρ
Picture	Filename of picture of ball (excludes the file extension)

Table D.10 The field names contained with in the Stringbed table. All these parameters are determined using the methods described in section 6.2.

Field name	Description
ID	
Stringbed type	
aks	Value of the parameter a_S
bks	" " " b_S
cks	" " " c_S

Table D.11 The field names contained with in the Racket table. All these parameters are determined using the methods described in sections 9.3.3 and D.2.1.

Field name	Description
ID	
Racket name	
Length	Total length of the beam
Mass	Total mass of the beam
Mass MI	Mass moment of inertia of the beam, around the butt end
Balance	Balance point measured from the butt end
Nseg	Number of segments N (equal to 51 in this study)
L1	The individual lengths of each of the five sections which compose the *five section* model beam.
L2	
L3	
L4	
L5	
N1	The number of segments in each of the five sections which compose the *five section* model beam.
N2	
N3	
N4	
N5	
M1	The individual masses of each of the five sections which compose the *five section* model beam.
M2	
M3	
M4	
M5	
EI1	The individual values of the flexural rigidity of each of the five sections which compose the *five section* model beam. (this value is constant for each section in this study, but is assigned individually)
EI2	
EI3	
EI4	
EI5	
1st Frequency	The fundamental frequency of the beam
Picture	Filename of picture of ball (excludes the file extension)

E. Impact between a Ball and Freely Suspended Racket

E.1 Comparison of ball rebound velocity

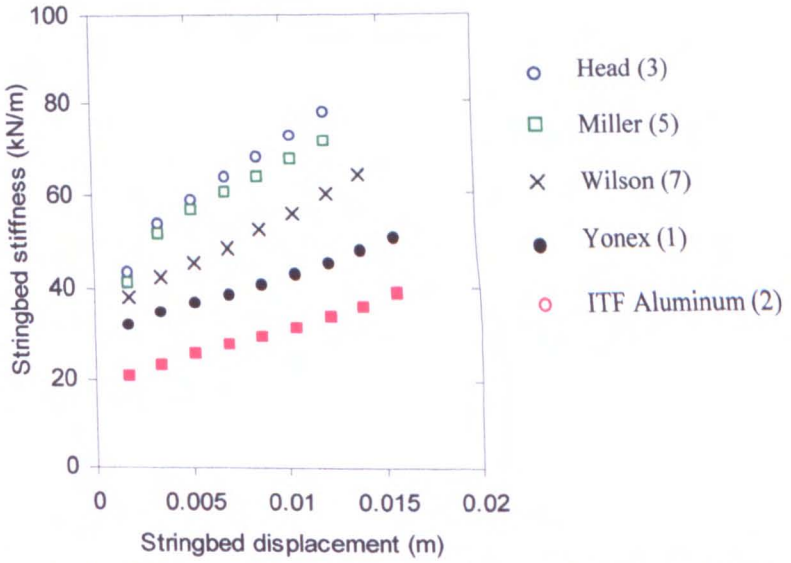

Figure E.1 The stringbed stiffness which was measured at the throat location (labelled *3* in Figure 10.1).

In section 10.2, experiments are conducted to measure the ball rebound velocity, for an impact between a ball and freely suspended racket. In this section, the *Racket Solver* software is also used to determine the ball rebound velocity for these impacts. This software requires the stringbed stiffness of the racket to be entered. This stiffness is given in Figure E.1 and Table E.1.

Table E.1 Second order polynomial trendline coefficients a_S, b_S and c_S for the five different rackets.

Racket Type	Tip			Geometric String Centre			Butt		
	a_S (kN/m^3)	b_S (kN/m^2)	c_S (kN/m)	a_S	b_S	c_S	a_S	b_S	c_S
Yonex (1)	33573	528	35.8	0	1053	27.43	4150	1151	30.6
ITF Aluminium (2)	30875	1211	24.6	-935.6	1160	18.59	8993	3067	19.0
Head (3)	0	3958	42.7	0	2690	41.71	0	2640	41.0
Miller (5)	0	2279	47.7	0	1550	43.605	0	1993	40.3
Wilson (7)	-22847	2599	28.9	27493	1040	38.35	-10291	2956	35.7

E.2 Ball, stringbed and racket deformation

In section 10.3, experiments were conducted to measure the ball, stringbed and racket displacement, during the impact between a ball and freely suspended tennis racket. Supplementary data for this study is presented in this appendix.

Table E.2 Second order polynomial trendline coefficients a_S, b_S and c_S for two *ITF Carbon Fibre* tennis rackets strung at different tensions.

String Tension	a_S (kN/m^3)	b_S (kN/m^2)	c_S (kN/m)
40lbs	10534	820.1	29.39
70lbs	40466	407	49.61

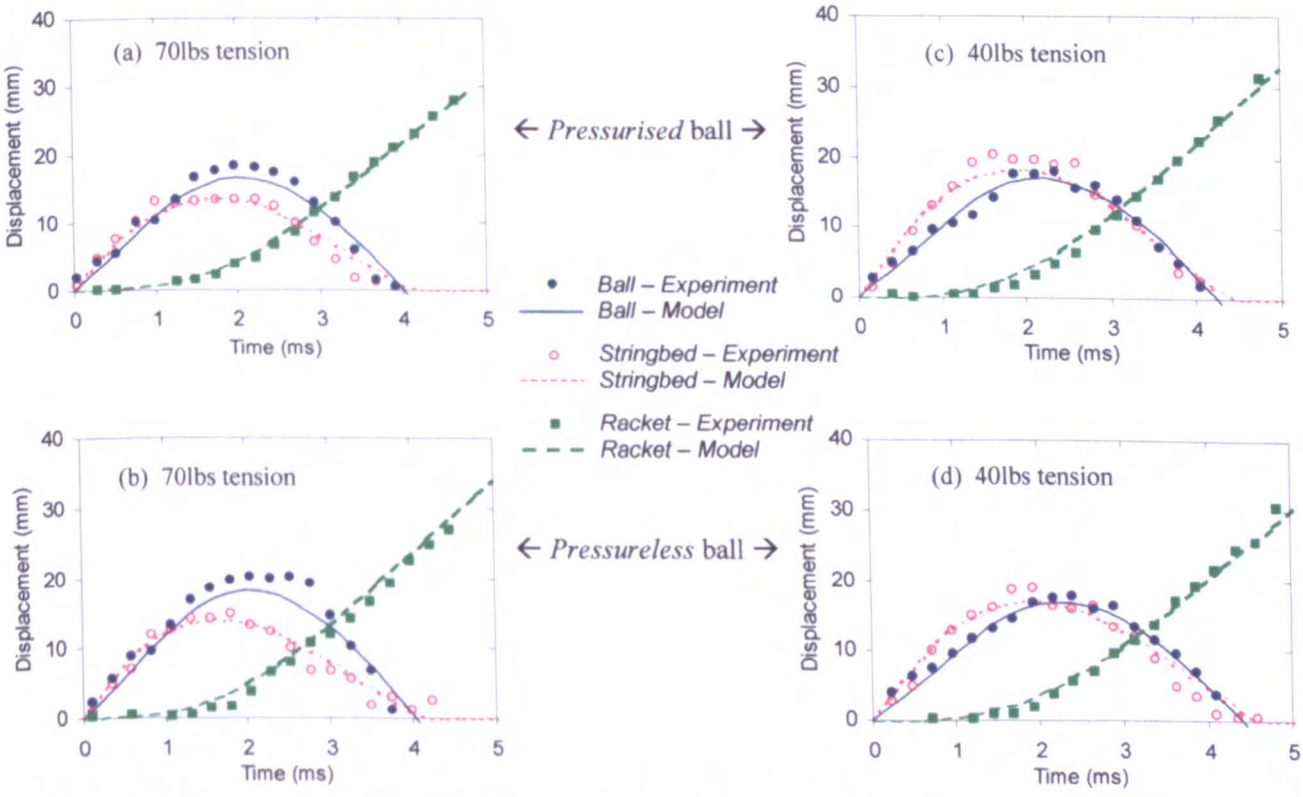

Figure E.2 Ball centre-of-mass displacement, stringbed displacement and racket impact point displacement for an impact between a ball and freely suspended racket, for four different combinations of string tension and ball type. The nominal ball impact velocity is 25m/s, and both the model and experimental data are presented.

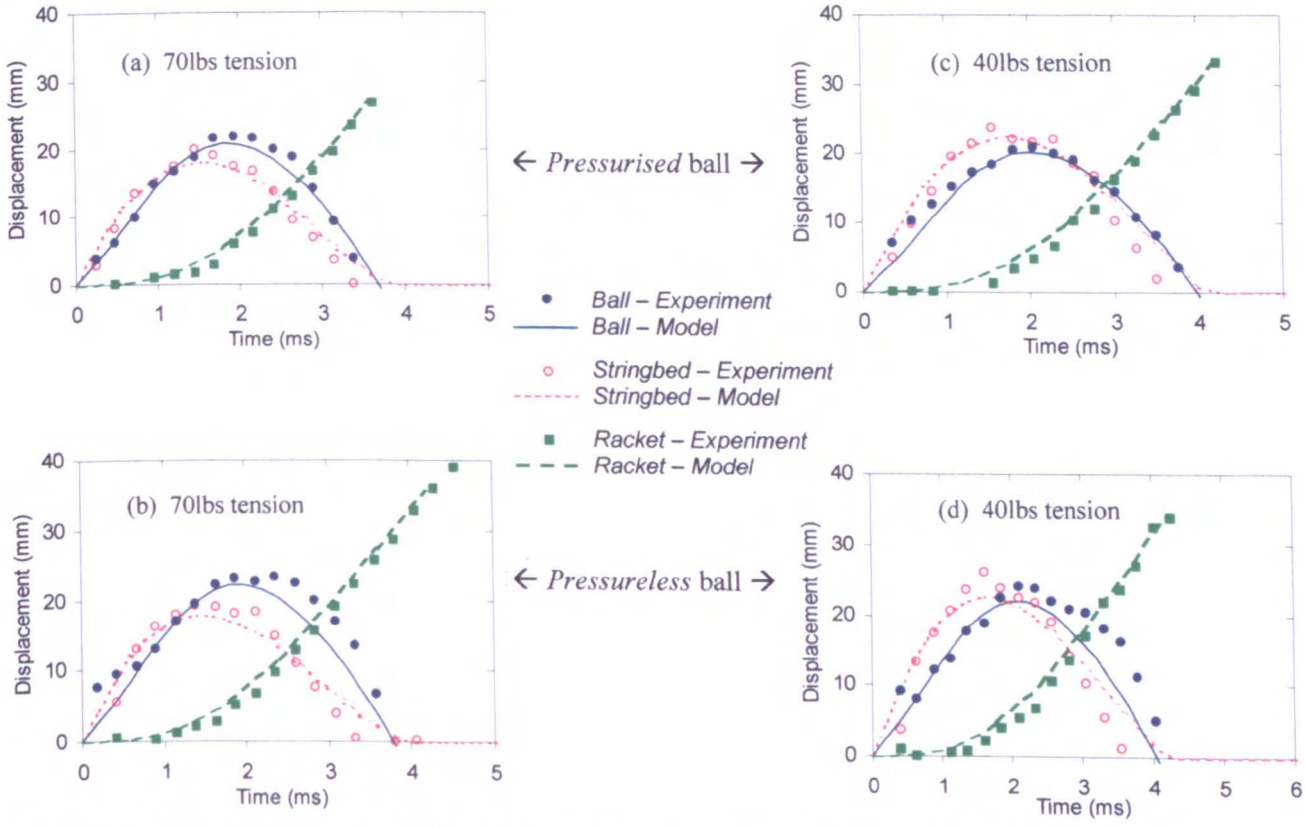

Figure E.3 Ball centre-of-mass displacement, stringbed displacement and racket impact point displacement for an impact between a ball and freely suspended racket, for four different combinations of string tension and ball type. The nominal ball impact velocity is 35m/s, and both the model and experiment data are presented.

E.3 Measuring Ball and Racket rebound velocity

E.3.1 Introduction

In section 10.4, the ball and racket rebound velocity were experimentally measured, for an impact between a ball and freely suspended tennis racket. The main details of this experiment are given in that section, and supplementary data is presented in this section.

Table E.3 Location of the four impact points which were tested on the racket.

	Distance between impact point and geometrical string centre (mm)	
	Head	*Spalding*
1	72	70
2	42	31
3	7	-9
4	-43	-53

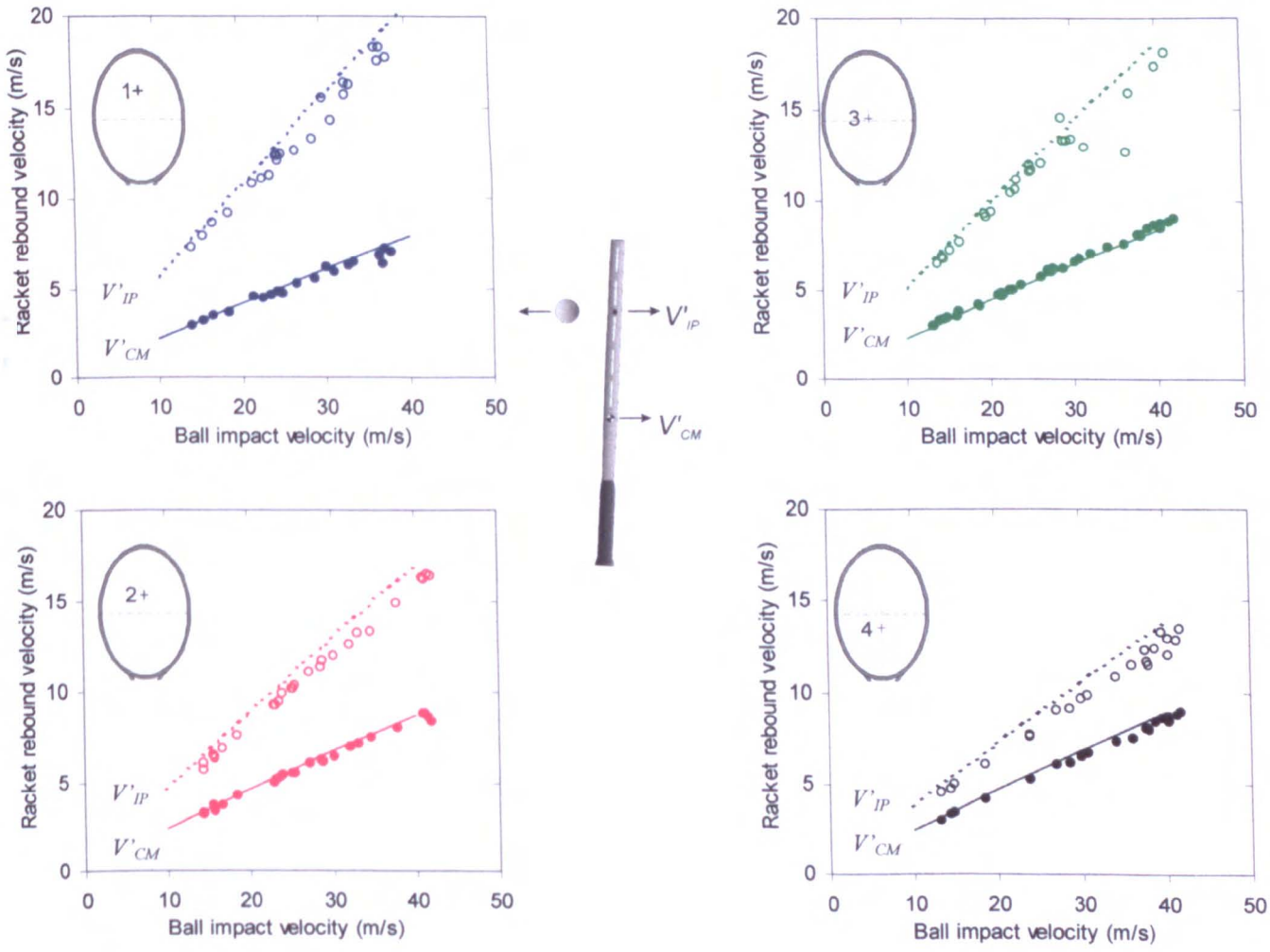

Figure E.4 The racket rebound velocity for the *Head* racket. The data points represent experimental data and the curves represent the data calculated by the model.

E.4 Comparison of beam/racket motion in the model and experiment

E.4.1 Introduction

In section 10.5, the displacement of the tip of the beam was experimentally measured using high speed video equipment. This experimental data was compared with the beam displacement data calculated by the *Racket Solver v1.1* software. This software uses the model of a ball impacting on a one-dimensional beam which has been developed in Chapter 9, and is used in the previous sections.

The experiments (and model) were conducted for a range of ball impact positions along the longitudinal axis of the tennis racket. In this current section, supplementary data is given for these different impact positions, as shown in Figure E.5.

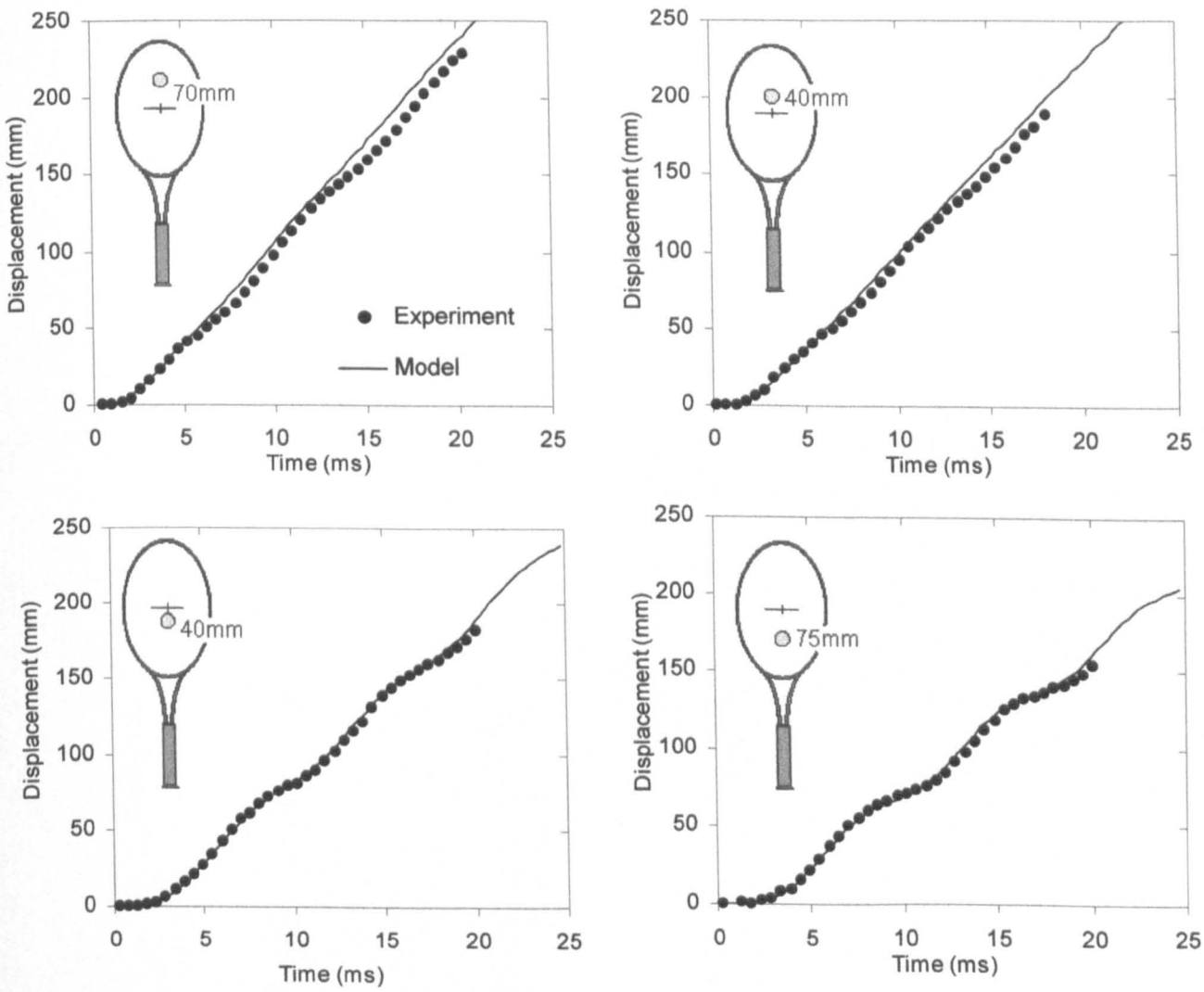

Figure E.5 The displacement of the tip of the racket/beam for a range of impact locations; the locations are referenced to the geometric string centre. Data is presented for both the experiment and model.